# Multi-scale Averaging and Analysis of Transport and Reaction Phenomena in Porous Media

A Dissertation

Presented to

the Faculty of the Department of Chemical and Biomolecular Engineering

University of Houston

In Partial Fulfillment

of the Requirements for the Degree

Doctor of Philosophy

in Chemical Engineering

by

Ram Ratan Ratnakar

May 2012

Dedicated to my family, friends and teachers

**Acknowledgements**

It is a great pleasure to express my immense gratitude and respect to my advisor, Prof. Vemuri Balakotaiah, whose encouragement, supervision and support from the preliminary to the concluding level enabled me to develop an understanding of the subject, which I am sure, is an asset in pursuing further research. The thesis would not have been possible without his help, not to mention his advice and unsurpassed knowledge of transport and reaction engineering. The long discussions with Prof. Bala on various problems have always been a source of inspiration and motivation. He has been extremely generous with his time, knowledge, ideas and allowed me great freedom in the research. His good advice, support and friendly nature have been invaluable on both an academic and a personal level, for which I am extremely grateful, and take this opportunity to thank him.

I sincerely appreciate the finantial support from the Robert A. Welch Foundation and Halliburton energy services. I would like to thank Dr. N. Kalia for her help, cooperation and discussions on the carbonate project. I greatly appriciate her for creating friendly and easy atmosphere during my internship at Halliburton.

I would like to thank these teachers, Prof. Economou, Prof. Luss, Prof. Mohanti and Dr. Birol for their valuable graduate training. I would like to thank Prof. Krishnamoorti, Dr. Conrad and Prof. Nikolaou for their valuable time and discussions in group meetings on porous media. I would also like to thank the supporting staff of the Chemical Engineering department and ISSSO for providing excellent support.

I am highly thankful to my labmates, Pankaj (Pankaaazzzz) and Santhosh (dealguru) for making my times in the lab joyful. They helped me in several ways from how to fill out taxes and other official forms to how to buy things from the internet more efficiently. I always enjoyed dicsussions on various topics (academic and non-academic) with them. Even in the end, when they were very busy in completing their degree, they made time to help me in preparing for a job interview. I wish

to thank my seniors, Saurabh, Robin, Ila, Jyoti, Ashok and Divesh for their valuble suggestions and times we spent during get togethers. I also wish to thank all my fellow lab mates Arun, Bijesh, Praneet, Priyank, and Richa for their support and for sharing their time with me.

I would like to thank my friends Anshul, Udit, Samaksh, Dhaval, Martin, Anthony and the alpha-psi-lambda community for various fun and adventurous activities which made my stay in Houston wonderful. I am thankful to Jay, Jeff, Kaushik, Radheshyam, Paras and AK for playing badminton with me. I would like to thank Manish, Gaurav, Chinmay, Kshitij, Swaroop, Surabhi, Ananya, Jyoti, Anita, Renu, Prasanna and Swati for good food and for playing volleyball and badminton with me. I am thankful to Amanda Wei (for being my partner in various fun actvities including dancing), our Salsa instructor Claudia and social dance clubs at UH (where I learned various latin and ballroom dancing), which helped me to improve my interpersonal skills. I am also thankful to my friends Aditya, Dhananjay, Ritesh, Rashmish, Abhishek, Prasat, Pathak Saab, Chandan, DJ, Alok, Manoj, Rajnish and Sudhanshu for moral support and other various activities we did together before grad school.

Finally, I would like to express my love and apreciation to my family for continuous support and encouragement in all my endevours. They have made me disciplined, confident and self-dependent. They struggled hard to give me the best possible education, for which I will always be thankful.

# Multi-scale Averaging and Analysis of Transport and Reaction Phenomena in Porous Media

An Abstract

of a

Dissertation

Presented to

the Faculty of the Department of Chemical and Biomolecular Engineering

University of Houston

In Partial Fulfillment

of the Requirements for the Degree

Doctor of Philosophy

in Chemical Engineering

by

Ram Ratan Ratnakar

May 2012

**Abstract**

In the first part, a systematic procedure of multi-scale averaging, based on Lyapunov-Schmidt (L-S) technique of bifurcation theory, is presented where low-dimensional models are derived for two problems: dispersion of a non-reacting tracer in laminar flow in a tube (Taylor dispersion); and, diffusion, convection and reaction in a catalytic monolith with porous washcoat. The averaged model for Taylor dispersion developed by the L-S procedure is exact for general inlet/initial conditions including point sources. It predicts no centroid displacement or variance deficit as other models in the literature. Truncated hyperbolic models are also presented along with inlet/initial conditions to the same accuracy. The reduced order model developed for catalytic monoliths is presented in terms of three concentration modes and it is shown for time-varying inlet conditions, the interfacial flux depends on all three modes. In such cases, in contrast to the traditional two-phase model, the three-mode reduced order model retains the feature of the detailed model.

In the second part, modeling and simulation of reactive dissolution of carbonates with in-situ gelling acids is presented. Stimulation of oil-wells in carbonate-reservoirs using an acidic-solution is a common practice to enhance oil production. However, due to heterogeneity, acid flows preferentially in high-permeability zones, which results into under stimulation of low-perm regions. Therefore, in-situ gelling acids are used that block the high-permeability region by forming a gel and diverts more acid to the low-permeability zones. Here, a rheological model for in-situ gelling acids is developed and combined with an extended two-scale-continuum model to describe the transport and reaction of in-situ gelling acids in carbonates. Three-dimensional simulations predict dissolution patterns in various flow regimes that are in accordance with experimental results. The effect of rheological parameters on flow diversion, optimum injection rates, wormhole diameter

and gel front-width and speed is studied using scaling analysis. Finally, guidelines for optimal stimulation of carbonates with in-situ gelling acids are presented.

# Table of Contents

**Acknowledgements** . . . . . **vi**

**Abstract** . . . . . **ix**

**Table of Contents** . . . . . **xi**

**List of Figures** . . . . . **xvi**

**List of Tables** . . . . . **xxiv**

**Nomenclature** . . . . . **xxv**

**Part I Multi-scale Averaging of Diffusion-convection-reaction Models** . . . . . **1**

**Chapter 1 Introduction** . . . . . **2**

1.1 Preamble . . . . . 2

1.2 Literature Review . . . . . 7

1.2.1 Top-down Approach . . . . . 7

1.2.2 Bottom-up Approach . . . . . 10

1.3 Objectives . . . . . 20

**Chapter 2 Liapunov-Schmidt Reduction** . . . . . **22**

2.1 Preamble . . . . . 22

2.2 Mathematical Aspects of L-S . . . . . 24

2.3 Illustration of the L-S Reduction . . . . . 28

2.3.1 Averaged Model in Terms of Exit Concentration $c_1$ . . . . . 38

2.4 Some Advantages of Averaging using the L-S procedure . . . . . 39

**Chapter 3 Exact Averaging of Laminar Dispersion** . . . . . **41**

3.1 Preamble . . . . . 41

3.2 Transverse Averaging of Laminar Dispersion using the L-S Method . 44

3.2.1 Model Formulation . . . . . 44

3.2.2 Transverse Averaging . . . . . 47
3.2.3 Solution of the Local Equation . . . . . 51
3.2.4 Convergence of the Perturbation Solution to the Local Equation 57
3.3 Analysis of Classical Taylor-Aris Dispersion . . . . . 61
3.3.1 Temporal Evolution of Spatial Moments . . . . . 64
3.3.2 Comparison of Lyapunov-Schmidt and Center Manifold Approaches for Averaging of Laminar Dispersion . . . . . 81
3.4 Truncated Regularized Two-Mode Models . . . . . 86
3.4.1 Case A: Convection Dominated Hyperbolic (Taylor) Limit: . . 88
3.4.2 Case B: The Taylor-Aris Limit: . . . . . 98
3.5 Conclusions and Discussion . . . . . 101
**Chapter 4 Reduced Order Model for recative dispersion in Catalytic monoliths . . . . . 105**
4.1 Preamble . . . . . 105
4.2 Model Formulation . . . . . 109
4.3 Transverse Averaging . . . . . 114
4.4 Interfacial flux and internal and external transfer coefficients . . . . . 127
4.5 Limiting cases of the reduced order model . . . . . 133
4.5.1 Thin washcoat and wall reaction limits $(\varepsilon_w \ll 1)$ . . . . . 133
4.5.2 steady-state model: . . . . . 135
4.5.3 Taylor dispersion with diffusion into the washcoat . . . . . 139
4.5.4 Flat Velocity Profile . . . . . 144
4.5.5 Comparison of Two-phase and Reduced Order Models . . . . 147
4.6 Conclusions and Discussion . . . . . 150
**Chapter 5 Summary and Future Scope of the Work . . . . . 153**
5.1 Summary . . . . . 153
5.2 Future Scope . . . . . 157

**Part II Reactive Transport of Gelling Acids and Wormhole Formation in Carbonates . . . . . 158**

**Chapter 6 Introduction . . . . . 159**

6.1 Preamble . . . . . 159

6.2 Literature Review . . . . . 167

6.2.1 Experimental Studies with Newtonian Acids . . . . . 167

6.2.2 Experimental Studies with Diverting Acids . . . . . 169

6.2.3 Mathematical Studies . . . . . 173

6.3 Objectives . . . . . 176

**Chapter 7 Mathematical Model for In-situ Gelling Acids . . . . . 178**

7.1 Preamble . . . . . 178

7.2 Rheological Modeling for Diverting Acids . . . . . 179

7.2.1 Effect of Temperature on Viscosity . . . . . 180

7.2.2 Effect of Pressure/Shear Rate on Viscosity . . . . . 182

7.2.3 Effect of pH on Viscosity . . . . . 188

7.2.4 A Complete Rheological Model . . . . . 194

7.3 Two-scale Continuum Model (TSC) for in-situ gelling Acids . . . . . 195

7.3.1 Darcy Law for in-situ gelling Acids . . . . . 197

7.3.2 Two-Scale Continuum Model . . . . . 199

7.3.3 Dimensionless Form of the Model . . . . . 209

**Chapter 8 Numerical Techniques for Wormhole Formation . . . . . 219**

8.1 Preamble . . . . . 219

8.2 Pressure Profile . . . . . 225

8.3 Concentration and Porosity Evolution . . . . . 231

8.3.1 Operator Splitting . . . . . 231

8.3.2 Finite Volume Discretization for Diffusion-Convection Operator 232

8.3.3 Solution of Reaction Operator . . . . . 236

8.3.4 Extrapolation . . . 238
**Chapter 9 One Dimensional Analysis: Gel Dynamics and Flow Diversion 241**
9.1 Preamble . . . 241
9.2 Single Core set-up . . . 243
9.2.1 Dimensionless TSC Model . . . 243
9.2.2 Gel Dynamics . . . 246
9.2.3 Breakthrough Curves and Optimum Injection Rate . . . 251
9.3 Dual Core Analysis . . . 256
9.3.1 Dimensionless TSC Model . . . 256
9.3.2 Flow Diversion in non-Reacting Case . . . 257
9.3.3 Flow Diversion by in-situ gelling Acids . . . 258
9.4 Conclusion and Discussion . . . 261
**Chapter 10 Two-Dimensional and Three-Dimensional Simulations: Dissolution Patterns . . . 264**
10.1 Preamble . . . 264
10.2 2-D Simulations . . . 265
10.2.1 Single Core Analysis . . . 265
10.2.2 Dual Core Analysis . . . 274
10.3 Three-dimensional Simulations of Wormholing with In-situ Gelling Acids . . . 280
10.3.1 Overall pressure drop . . . 283
10.3.2 Breakthrough Curves and Dissolution Patterns . . . 285
10.4 Conclusion and Discussion . . . 288
**Chapter 11 Summary and Future Scope of the Work . . . 292**
11.1 Summary . . . 292
11.2 Future Work . . . 295
**References . . . 298**

**Appendices** . . . . . **311**

**Appendix A: Solution of Local equation in Laminar Dispersion** . . . . . **312**

A.1 Eigenvalue problem in Cylindrical Coordinate . . . . . 312

A.2 Solution of Local Equation . . . . . 315

A.3 Moment Analysis . . . . . 318

A.3.1 Zeroth Moment . . . . . 321

A.3.2 First Moment . . . . . 321

A.3.3 Second Moment . . . . . 323

A.3.4 Third Moment for uniform release . . . . . 328

**Appendix B: Scaling Laws** . . . . . **332**

B.1 Gel Dynamics . . . . . 332

B.1.1 Speed of Reaction and Gel Fronts . . . . . 332

B.1.2 Width of Reaction and Gel Fronts . . . . . 334

B.2 Flow Diversion in Dual-core Set-up . . . . . 336

B.3 Optimum Injection rate . . . . . 338

# List of Figures


Figure 1.1 Heirarchy of length scales in various chemical engineering systems (a) Carbonate cores and (b) catalytic monoliths. . . . 3

Figure 1.2 Different approaches to averaging/dimension reduction. . . . 5

Figure 2.1 Schematic diagram illustrating the choice of the complementary spaces in the domain and codomain of the linear operator in the Liapunov-Schmidt Reduction. . . . . 25

Figure 2.2 Schematic diagram of a two-compartment discrete disffusion-convection model. . . . . 29

Figure 3.1 Time evolution of first moment for point release of solute at the tube center. . . . . 67

Figure 3.2 Centroid displacement versus time for point release of solute at different radial locations. . . . . 69

Figure 3.3 Centroid displacement versus time for point release at the center with varying $Pe_r$. . . . . 70

Figure 3.4 Temporal evolution of variance for uniform release and point release at the center. . . . . 72

Figure 3.5 Evolution of variance corresponding to point release at the center with varying $Pe_r$. . . . . 75

Figure 3.6 Evolution of the third central moment for uniform release of solute. . . . . 77

Figure 3.7 Log-Log plot of skewness versus time for uniform release and $\langle \zeta_2 \rangle = \langle \zeta_3 \rangle = 0$. . . . . 79

Figure 3.8 Dispersion curves predicted by the low-dimensional first order hyperbolic model [The dispersion curves include a Dirac-delta function of magnitude $Exp(-\frac{48}{p})$ at $\tau = 0$, which is not shown in the figure]. . . . . 95
Figure 4.1 Schematic diagram of a single straight monolithic channel of circular cross-section and with a uniformly thick washcoat. 109
Figure 4.2 Variation of the internal Sherwood number with washcoat volume fraction. . . . . 131
Figure 4.3 Steady state exit conversion $\varkappa_e$ corresponding to uniform feed conditions versus transverse peclet number p at various Thiele modulus for wall reaction case (comparison to exact solution). . . . . 138
Figure 4.4 Predicted dispersion/RTD curves for non-reacting case corresponding to various diffusivity ratios $\mu$ at $\varepsilon_f = 0.8$, $\varepsilon_{wc} = 0.5$ (or, $\gamma_w = 0.25$, $\gamma = 0.125$) and $p = 1$. . . . . 142
Figure 4.5 Predicted cumulative RTD function or F-curve for non-reacting case corresponding to various diffusivity ratio $\mu$ at $\varepsilon_f = 0.8$, $\varepsilon_{wc} = 0.5$ (or, $\gamma_w = 0.25$, $\gamma = 0.125$) and $p = 1$. . . . . 143
Figure 4.6 Dimensionless dispersion coefficient for various difusivity ratios for Taylor dispersion with diffusion into washcoat with parabolic velocity profile for $\varepsilon_{wc}\left(=\frac{\gamma}{\gamma_w}\right) = 0.5$. . . . . 144
Figure 4.7 Dimensionless dispersion coefficient for various difusivity ratios for Taylor dispersion with diffusion into washcoat with flat velocity profile for $\varepsilon_{wc}\left(=\frac{\gamma}{\gamma_w}\right) = 0.5$. . . . . 148
Figure 6.1 Schematic view of a wellbore, damaged zone and reservoir. 160
Figure 6.2 Dissolution patterns formed at different injection rates of acidic solution (Fredd and Fogler, 1998). . . . . 162

Figure 6.3 Increase in permeability due to dissolution with 0.25 M EDTA at various injection rates in a core (0.8-2 mD) of length 10.2 cm and diameter 3.8 cm (Fredd and Fogler, 1998). . . . . 163

Figure 6.4 Breakthrough curve (here, pore volume to breakthrough is defined as the number of pore volume of acidic solution injected to increase the permeability of the core by a factor $100$). . . . . 164

Figure 6.5 Breakthrough curve and wormhole patterns for various acids with different reactivity. . . . . 165

Figure 6.6 Wormholes created by injecting water through a radial core (of diameter 2 mm and length 50 mm) made of plaster (Daccord, 1987). . . . . 168

Figure 6.7 Dissolution patterns and flow diversion in dual-core experiments with diverting acids at various injection rates (a) experiments 3 (Gomaa et al., 2011) with injection rate, $Q = 1cm^3min^{-1}$ and permeability ratio, $\frac{K_{high}}{K_{low}} \sim 25$, (b) experiments 8 (Gomaa et al., 2011) with injection rate, $Q = 15cm^3min^{-1}$ and permeability ratio, $\frac{K_{high}}{K_{low}} \sim 20$, (c) experiments 10 (Gomaa et al., 2011) with injection rate, $Q = 2.5cm^3min^{-1}$ and permeability ratio, $\frac{K_{high}}{K_{low}} \sim 21$. . . . . 172

Figure 7.1 Schematic of different length scales associated in a lcarbonate core used in laboratory experiments. . . . . 178

Figure 7.2 Effect of temerature coefficient of viscosity, $\alpha$, on viscosity vs temperature profile. . . . . 181

Figure 7.3 Schematic diagram illustrating the time independent non-Newtonian fluid behavior. . . . . 183

Figure 7.4 Schematic diagram illustrating the general viscosity behavior of a shear thinning fluid. . . . . 186
Figure 7.5 Experimental data for viscosity of ZCA (1.5 % SGA-III) vs pH. 189
Figure 7.6 Effect of $\mu_m$ on viscosity vs pH profile for $a = 10$ and $pH_m = 5$.191
Figure 7.7 Effect of $pH_m$ on viscosity vs. pH profile for $\mu_m = 20$ and $a = 10$. . . . . 192
Figure 7.8 The effect of the parameter $a$ on viscosity vs. pH profile. . . 193
Figure 7.9 Comparison of experimental and theoretical plot for viscosity vs. pH for various shear rates. . . . . 196
Figure 7.10 Variation in permeability with porosity due to dissolution for typical values of $\beta = 0.5$, $1.0$ and $1.5$. . . . . 205
Figure 7.11 Change in pore radius with porosity due to dissolution for typical values of $\beta = 0.5$, $1.0$ and $1.5$. . . . . 206
Figure 7.12 Change in area per unit volume available for reaction as porosity changes due to dissolution for typical values of $\beta = 0.5$, $1.0$ and $1.5$. . . . . 207
Figure 7.13 Schematic diagram of a single core set-up. . . . . 209
Figure 7.14 Schematic diagram of a multicore set-up. . . . . 213
Figure 8.1 Finite volume descretization in 1D (solid circles denote the node points where concentrations, porosity and pressure are defined; w and e define the west and east face of the element where velocity vector are defined). . . . . 221

Figure 8.2 Finite volume descretization in 2D (solid circles denote the node points where concentrations, porosity and pressure are defined; w and e denote the west and east faces of the element where x-component of velocity vector are defined; s and n denote the south and east faces of the element where y-component of velocity vector are defined). . . . . 221
Figure 8.3 Finite volume descretization in 3D (solid circles denote the node points where concentrations, porosity and pressure are defined; w and e denote the west and east faces of the element where x-component of velocity vector are defined; s and n denote the south and east faces of the element where y-component of velocity vector are defined; b and t denote the bottom and top faces of the element where z-component of velocity vector are defined), (a) meshing (b) control volume.222
Figure 8.4 The main steps used in obtaining numerical solution of the two-scale continuum models in single or dual core set ups. . 224
Figure 8.5 Surface of control volume at the boundaries, (a) west boundary, $i = 1$, (b) east boundary, $i = N_x$, (c) south boundary, $j = 1$, (d) north boundary, $j = N_y$, (e) bottom boundary, $k = 1$, (a) top boundary, $k = N_z$. . . . . 226
Figure 9.1 Schematic diagram of (a) single core set-ups (b) dual core set-ups in laboratory core experiments. . . . . 242
Figure 9.2 PH/concentration profile from 1-D simulation for $Da = 100.$ . 246
Figure 9.3 Viscosity profile (presence of gel) in the core the from 1-D simulation for $Da = 100.$ . . . . . 247
Figure 9.4 Gel propagation (viscosity profile) at $Da = 100$ in the core for various pore volume of acid injected. . . . . 248

Figure 9.5 Width of gel and reaction fronts in cores of different initial permeabilities at constant injection rate, $u_0 = 9.8 \times 10^{-4}$cm $s^{-1}$.250
Figure 9.6 Overall pressure drop for gelling and Newtonian acids from 1-D simulation at $Da = 100.$ . . . . . 252
Figure 9.7 Comparison of breakthrough curves for gelling acids and Newtonian acids at $\phi^2 = 0.047.$ . . . . . 253
Figure 9.8 Effect of initial core permeability on breakthrough curves for gelling acids at $\phi^2 = 0.047.$ . . . . . 255
Figure 9.9 Gel dynamics in dual core set-up at $\phi^2 = 0.07$ and $Da = 100$ from 1-D simulation. . . . . 259
Figure 9.10 Flow splitting in dual core set-up at $\phi^2 = 0.047$ and $Da = 100.$ 260
Figure 9.11 Ratio of inlet flow rates in low-perm to high-perm cores from 1-D simulation at $\phi^2 = 0.047$ and $Da$=100. . . . . 261
Figure 10.1 Evolution of effective mobility in time for Newtonian acids at various injection rates from 2-D simulation. . . . . 267
Figure 10.2 Evolution of effective mobility in time foi gelling acids at various injection rates from 2-D simulation. . . . . 268
Figure 10.3 Breakthrough-curves for Newtonian and gelling acids at $\phi^2 = 0.047.$ . . . . . 269
Figure 10.4 Dissolution patterns at optimum for gelling acids and Newtonian acids from 2-D simulation in a core of 5 cm length at (a) color-scale for porosity, (b) initial heterogeneious porosity field, (c) porosity field (wormhole structure) at breakthrough for Newtonian acids, and (d) porosity field (wormhole structure) at breakthrough for in-situ gelling acids. . . . . 270

Figure 10.5 pH profile and demonstration of reaction and gelled zones (a) color-scale for pH, (b) Newtonian acids, and (c) in-situ gelling acids. . . . . 271
Figure 10.6 Dissolution patterns in a core of length 10 cm and height 4 cm at $\phi^2 = 0.047$ for (a) Newtonian acids and (b) in-situ gelling acids. . . . . 273
Figure 10.7 Flow diversion in a dual core set-up from 2-D simulation, inset show the plot at shorter times. . . . . 277
Figure 10.8 Fractional flow (ratio of flow rates in low-perm to high-perm cores), inset show the plot at shorter times. . . . . 278
Figure 10.9 Disoolution pattern in dual core study when optimum exist in high-perm core (a) simulation results (b) experimental results (Gomaa, et al., 2011). . . . . 279
Figure 10.10 Disoolution pattern in dual core study when optimum exist in low-perm core (a) simulation results (b) experimental results (Gomaa, et al., 2011). . . . . 281
Figure 10.11 Comparison of pressure profile from 3-D simulations and experiments; (a) Pressure profile for gelling acids, (b) pressure profile for Newtonian acids, and (c) experimental profile (Gomaa, et al., 2011). . . . . 284
Figure 10.12 Breakthrough curves for gelling acids and newtonian acids from 3-D simulation at $\phi^2 = 0.047$. . . . . 285
Figure 10.13 Experimental breakthrough curve for DTPA (Fredd and Fogler, 1998). . . . . 286
Figure 10.14 3-D dissolution patterns at optimum for (a) Gelling acids ($0.01 cm^3 s^{-1}$) and (b) Newtonian acids ($0.04 cm^3 s^{-1}$). . . . . 287

Figure 10.15 (a) Breakthrough curves for in-situ gelling acids and Newtonian acids; Dissolution patterns in wormhole, conical and ramified dissolution regimes (b) for in-situ gelling acids, (c) for Newtonian acids, and (d) from experiments (Fredd and Fogler, 1998). . . . . 289

# List of Tables

Table 4.1 Various transverse functions and coefficients for fully developed laminar flow in a circular channel with a washcoat of uniform thickness . . . . . 121

Table 4.2 Transverse functions and coefficients for flat velocity profile/developing flow . . . . . 145

Table 6.1 Set of dual-core experiments with diverting acids at various injection rates (Gomaa et al., 2011). . . . . 171

Table 7.1 List of dimensionless quantities used for single core analysis. . 210

Table 7.2 List of dimensionless quantities used for dual core analysis. . . 214

Table 9.1 List of parameters and dimensionless numbers used in the simulation . . . . . 245

# Nomenclature

## Part I

*Roman letters*

$a =$ radius of the tube

$a_v =$ area per unit volume

$c =$ dimensionless solute concentration

$C_f =$ dimensional solute concentration in fluid phase

$c_f =$ dimensionless solute concentration in fluid phase

$C_{f,in} =$ dimensional inlet solute concentration in fluid phase

$c_{f,in} =$ dimensionless inlet solute concentration in fluid phase

$C_{f0} =$ dimensional initial solute concentration in fluid phase

$c_{f0} =$ dimensionless initial solute concentration in fluid phase

$c_{in} =$ dimensionless inlet solute concentration

$c_j, c'_j, c'_{i,j} =$ fluctuation in dimensionless solute concentration of the $O(p^j)$

$c_m =$ dimensionless cup-mixing or velocity weighted concentration

$c_{m,in} =$ dimensionless inlet cup-mixing or velocity weighted concentration

$c_{pf} =$ specific heat capacity in fluid phase

$C_R =$ reference concentration

$C_w =$ dimensional wall concentration

$c_w =$ dimensionless wall concentration

$C_{w0} =$ dimensional initial solute concentration in washcoat

$c_{w0} =$ dimensionless initial solute concentration in washcoat

$c' =$ local fluctuation in dimensionless concentration

$c_0 =$ dimensionless initial solute concentration

$\langle c \rangle =$ dimensionless overall cross-sectional averaged solute concentration

$\langle c_0 \rangle =$ dimensionless average initial solute concentration

$\langle c \rangle_f =$ dimensionless cross-sectionally averaged concentration in fluid phase

$\langle c_s \rangle =$ dimensionless peripheral averaged concentration at fluid-washcoat interface

$\langle c \rangle_w =$ dimensionless cross-sectionally averaged concentration in washcoat

$D =$ Dimensionless molecular diffusivity of solute

$Da =$ Damköhler number (corresponding to homogeneous reaction in washcoat)

$Da_s =$ Damköhler number (corresponding to equivalent surface reaction in washcoat)

$D_f =$ Dimensional molecular diffusivity of solute in fluid phase

$D_w =$ Dimensional molecular diffusivity of solute in washcoat

$E =$ Residence time distribution (RTD)

$\overline{E} =$ RTD in Laplace domain

$F =$ non-linear diffusion-convection-reaction operator

$h =$ heat transfer coefficient

$I_1 =$ first order modified Bessel function of first kind

$J =$ interfacial molecular flux at fluid-washcoat interface (dimensionless)

$J_{fw} =$ interfacial molecular flux at fluid-washcoat interface (dimensional)

$k_{ext} =$ external mass transfer coefficient (dimensional)

$k_f =$ heat conductivity in fluid phase

$k_{int} =$ internal mass transfer coefficient (dimensional)

$k_o =$ overall mass transfer coefficient (dimensional)

$L =$ Length of the monolith

$m_k =$ k$^{th}$ spatial moment

$M_k =$ k$^{th}$ spatial moment in Laplace domain

$Nu =$Nusselt number

$\mathbf{n}, \mathbf{n}_\Omega =$ normal unit vector to $\partial\Omega$

$\mathbf{n}_{\Omega_f} =$ normal unit vector to $\partial\Omega_f$

$\mathbf{n}_{\Omega_w} =$ normal unit vector to $\partial\Omega_w$

$p =$ transverse Peclet number

$Pe_r =$ radial Peclet number

$Pe_L =$ axial Peclet number

$r =$ radial coordinate (dimensional)

$R =$ homogeneous reaction in washcoat (dimensionless)

$R_w =$ homogeneous reaction in washcoat (dimensional)

$R_{\Omega_f} =$ hydraulic radius for flow channel

$R_{\Omega_w} =$ effective (diffusion) length scale in washcoat

$s =$ dimensionless source term containing initial and inlet conditions

$s' =$ deviation of source term from its average

$\langle s \rangle =$ average of source term

$s_f =$ dimensionless source term containing initial and inlet conditions in fluid phase

$s_f =$ dimensionless source term containing initial in washcoat

$Sh_e =$ external Sherwood number

$Sh_{e,flat} =$ external Sherwood number corresponding to flat velocity profile

$Sh_{e,non-react} =$ external Sherwood number corresponding no reaction in washcoat

$Sh_{e,ss} =$ external Sherwood number coefficient corresponding to steady state

$Sh_o =$ overall Sherwood number

$Sh_{\Omega i} =$ internal Sherwood number

$T =$ temperature

$T_{in} =$ inlet temperature

$T_m =$ mixing-cup temperature

$T_w =$ wall temperature

$t =$ dimensionless time

$t' =$ dimensional time

$u =$ velocity in the axial direction (dimensionless)

$u' =$ fluctuation in velocity in the axial direction (dimensionless)

$U_f =$ fluid velocity in the axial direction (dimensional)

$u_f =$ fluid velocity in the axial direction (dimensionless)

$\overline{u} =$ averaged fluid velocity in the axial direction (dimensionless)

$\langle u \rangle =$ averaged velocity in the axial direction (dimensionless)

$x' =$ coordinate along the length of the reactor (dimensional)

$x =$ dimensionless coordinate along the length of the reactor

*Greek letters*

$\alpha =$ Laplace domain variable

$\beta =$ dimensionless catalyst activity profile

$\beta' =$ deviation in activity profile from its average

$\langle \beta \rangle =$ average catalyst activity profile

$\psi, \psi_n, \psi_{mn} =$ eigenfunctions of a linear operator $\mathbb{L}$

$\varepsilon_f =$ macroscopic volume fraction of flow channel

$\varepsilon_w =$ macroscopic volume fraction of washcoat

$\varepsilon_{wc} =$ porosity of the washcoat

$\gamma =$ capacitance ratio in washcoat to the fluid phase

$\gamma_w =$ volume ratio of washcoat to the flow channel

$\Gamma =$ transverse function that depends on flow profile

$\chi =$ transverse function that depends on activity profile

$\varkappa =$ exit conversion

$\lambda =$ ratio of washcoat thickness to radius of flow channel

$\Lambda =$ dimensionless dispersion coefficient

$\mu =$ ratio of solute diffusivities in fluid to washcoat

$\mu_k =$ k$^{th}$ eigenvalues of transverse Laplacian operator

$\nu_k =$ k$^{th}$ central moment

$\phi_s^2 =$ Thiele modulus corresponding to equivalent surface reaction in washcoat

$\rho_f =$ density of fluid phase

$\sigma =$ transverse function that depends on Dirac-delta at interface

$\sigma^2 =$ variance

$\sigma_D^2 =$ dimensionless normalized second central moment

$\theta =$ azimuthal (angular) coordinate

$\tau_D =$ transverse diffusion time

$\tau_{cD} =$ diffusion-convection time

$\tau_C =$ convection time

$\tau_R =$ reaction time

$\Omega =$ overall cross-section (flow channel + washcoat)

$\Omega_f =$ cross-section of flow channel

$\Omega_w =$ cross-section of washcoat

$\xi =$ dimensionless radial coordinate

$\zeta =$ transverse function that depends on flow profile

*Subscripts*

$f =$fluid phase

$s =$solid phase

$w$ = washcoat

$m =$cup-mixing

$\infty =$asymptotic value

$X, L =$flow direction

$T =$Transverse direction

*Operators*

$\nabla^2_{\perp'}$ = transverse Laplacian operator (dimensional)

$\nabla^2_{\perp}$ = transverse Laplacian operator (dimensionless)

$\langle\rangle$ = Inner product over whole cross-section (flow channel + washcoat)

$\langle\rangle_c$ = Inner product with velocity profile as weighting function

$\langle\rangle_f$ = Inner product over flow channel

$\langle\rangle_w$ = Inner product over washcoat

$\mathbb{L}$ = linear operator

## Part II

*Roman letters*

$a$ =rheological parameter signifying the pH range of gel formation

$a_v$ =area perunit volume available for reaction

$a_{v0}$ =initial value of $a_v$

$A_v$ = dimensionless area perunit volume available for reaction

$C_f$ = acid concentration in the fluid

$C_{fin}$ =inlet acid concentration

$C_s$ =acid concentration in the solid-fluid interface

$c_f$ = dimensionless acid concentration in the fluid

$c_s$ = dimensionless acid concentration in the solid-fluid interface

$d_p$ =particle diameter

$D_e$ =effective dispersion coefficient of acid/protons

$D_{ep}$ = effective dispersion coefficient of polymers

$D_{eX}$ = effective dispersion coefficient of acid/protons in axial direction

$D_{eT}$ =effective dispersion coefficient of acid/protons in transverse direction

$Da$ = Damköhler number based on reaction time

$Da_{opt}$ = optimum Damköhler number based on reaction time

$fr$ =fraction of total flow going through low-perm core

$K$ =permeability

$K_0$ =initial permeability

$k_c$ =mass-transfer coefficient

$k_s$ =reaction rate constant

$k_{eff}$ =effective rate constant

$L$ = length of catalytic wire

$m$ =pore length to diameter ratio

$M$ = Mobility

$n$ =power index

$N_{ac}$ =acid capacity number

$P$ =pressure

$p$ =dimensionless pressure

$p_{exit}$ =exit pressure

$pH_m = pH$ value at which viscosity is maximum due to gel formation

$PV$ =pore volume

$PV_{BT}$ =pore volume to breakthrough

$Q$ = fluid volumetric flow rate

$Q_{opt}$ = optimum fluid volumetric flow rate

$r$ =dimensionless pore radius

$r_p$ =pore radius

$r_{p0}$ =initial pore radius

$R$ = reaction rate

$R_{ep}$ =Reynold's number

$Sc$ =Schmidt number

$Sh$ =Sherwood number

$Sh_\infty$ =asymptotic value of Sherwood number

$t$ = time (dimensionless)

$t'$ =dimensional time

$t^*$ =time in wave coordinate

$T$ = temperature

$T_0$ =reference temperature

$T_s$ = solid phase temperature

$U$ =dimensional velocity

$u$ =dimensionless velocity

$u_0$ =inlet velocity

$u_{opt}$ =optimum injection rate

$v$ =velocity

$x$ =dimensionless axial/flow direction

$x'$ = axial direction

$x^*$ =axial direction in wave coordinates

$y', z'$ =transverse direction

$y, z$ = dimensionless transverse direction

*Greek letters*

$\alpha$ = temperature coefficient of viscosity

$\alpha_c$ = acid capacity

$\beta$ = parameter used in structure-property relation

$\dot{\gamma}$ = shear rate

$\varepsilon$ = porosity of the rock

$\varepsilon_0$ =initial porosity

$\langle \varepsilon_0 \rangle$ =average initial porosity

$\Delta\varepsilon$ =magnitude of heterogeneity

$\phi^2$ = pore-scale Thiele modulus

$\Phi^2$ = macro-scale Thiele modulus

$\eta_0$ =polymer viscosity

$\kappa$ =dimensionless permeability

$\mu =$ viscosity

$\mu_0 =$base viscosity

$\mu_a =$aparent viscosity

$\mu_{eff} =$effective viscosity term

$\mu_m =$maximum increase in viscosity from the base value due to gel formation

$\langle \mu \rangle_c =$average viscosity in reaction zone

$\langle \mu \rangle_{gel} =$average viscosity of gel

$\rho_s =$solid density

$\tau =$shear stress

# Part I

# Multi-scale Averaging of Diffusion-convection-reaction Models

# Chapter 1 Introduction

## 1.1 Preamble

Modeling and analysis of the transport and reaction phenomena is one of the core activities of the chemical engineering discipline. Models of chemical reactors and other process equipment are obtained by applying the fundamental conservation laws and combining them with the constitutive equations for the various rate processes. These systems have hierarchy of length scales as can be seen from Figure 1.1. For example, it can be seen from Figure 1.1(a) that length-scales in a carbonate core (which are used to analyze the oil production from reservoirs that are spread in kilometers) varies from core scale ($cm$) to intermediate Darcy-scale ($mm$) to pore scale ($\mu m$). The Darcy-scale is where Darcy law are applied for describing flow equations and pore-scale is where conservation laws are applicable. Similarly, in a catalytic monoliths, the length scale varies from few centimeters to few $\mathring{A}$ as can be seen from Figure 1.1(b). These length scales are typically characterized by three representative ones, namely, microscale, mesoscale and macroscale. Microscale is the molecular scale where conservation laws applied and molecular properties are expressed. Macroscale is the reactor or process scale where laboratory experiments are performed to measure the quantities that interest to scientists and engineers. Mesoscale or intermediate scale which is smaller than macroscale and bigger than microscale, represents the smaller length scale of the reactor. For example, in case of a tubular reactors, the mesoscale is the tube or catalyst particle diameter while in case of porous media, the mesoscale is the heterogeneity length-scale. These length scales can also be interpreted in terms of time scales. For example, the residence time in the reactor varies usually between $1$ to $1000$ seconds while the intraparticle diffusion time is of the order of $0.1s$. Similarly, inside a pore, the diffusion time is of order of microseconds and

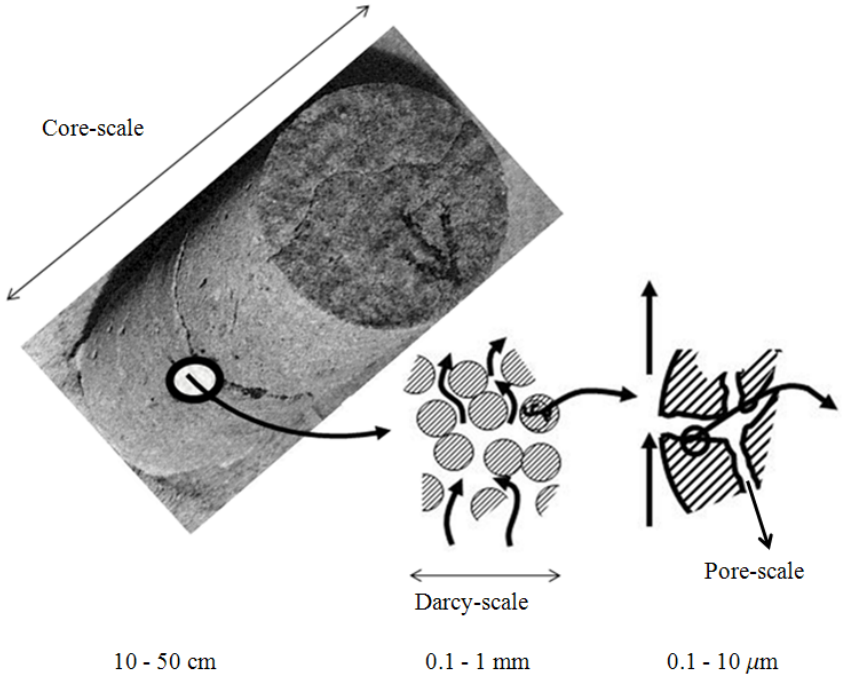


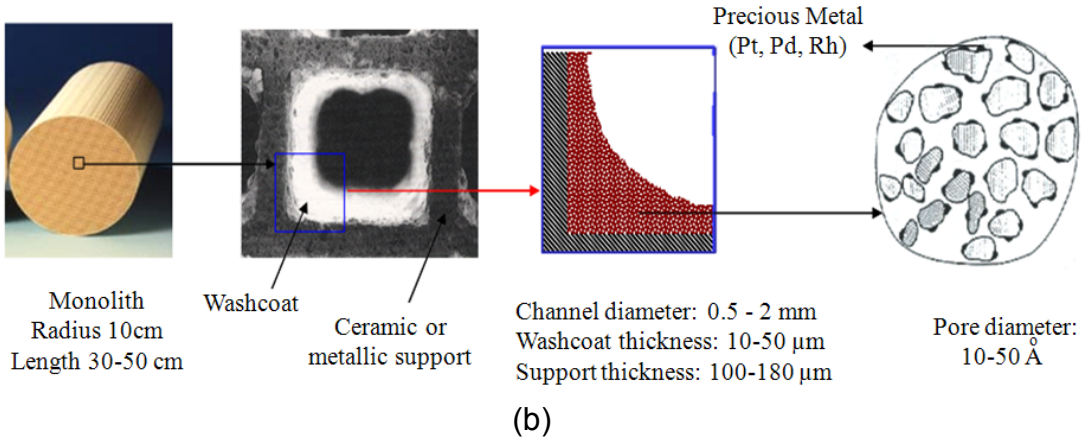


Figure 1.1: Heirarchy of length scales in various chemical engineering systems (a) Carbonate cores and (b) catalytic monoliths.

the time scale associated with adsorption is typically less than a microsecond and could be as small as a nanosecond. Depending on the level of detail included at various length and time scales, mathematical models can vary in complexity, from a few algebraic or ordinary differential equations to several coupled partial differential equations in three spatial coordinates and time. In addition, due to the strong coupling between the transport and reaction processes and the dependence of the kinetic and transport parameters on the state variables, the model equations are usually nonlinear and may exhibit a variety of complex spatio-temporal patterns. For most cases of practical interest, even with the present day computational power, it is impractical to solve such detailed models and explore all the different types of solutions that may exist in the multi-dimensional parameter spaces. Even in cases where detailed solutions can be obtained, the numerical results may have to be coarse-grained to determine quantities, such as the average exit conversion of a reactant or speed of an adsorption or thermal front, that are of interest to the design engineer. For these reasons, it is of practical interest to have accurate low-dimensional models in terms of experimentally measurable variables, such as cup-mixing concentrations or temperatures, for the purpose of design, control and optimization of chemical processes. Since reaction and transport processes can create a scale separation, an averaged low-dimensional model can be developed at macroscale in terms of experimentally measurable quantities that retains all the essential physics at microscale in terms of transfer/dispersion coefficients.

Figure 1.2 shows the schematic diagram of various approaches used in literatures to reduce the dimension and develop a low dimensional model for a given system. The top-down approach is the most common procedure to develop low-dimensional models of reactors where certain *a prior* assumptions are made on the length and time scales of diffusion, convection and reaction, and, conservation laws are applied at the meso or macro scales only. For example, the most fa-

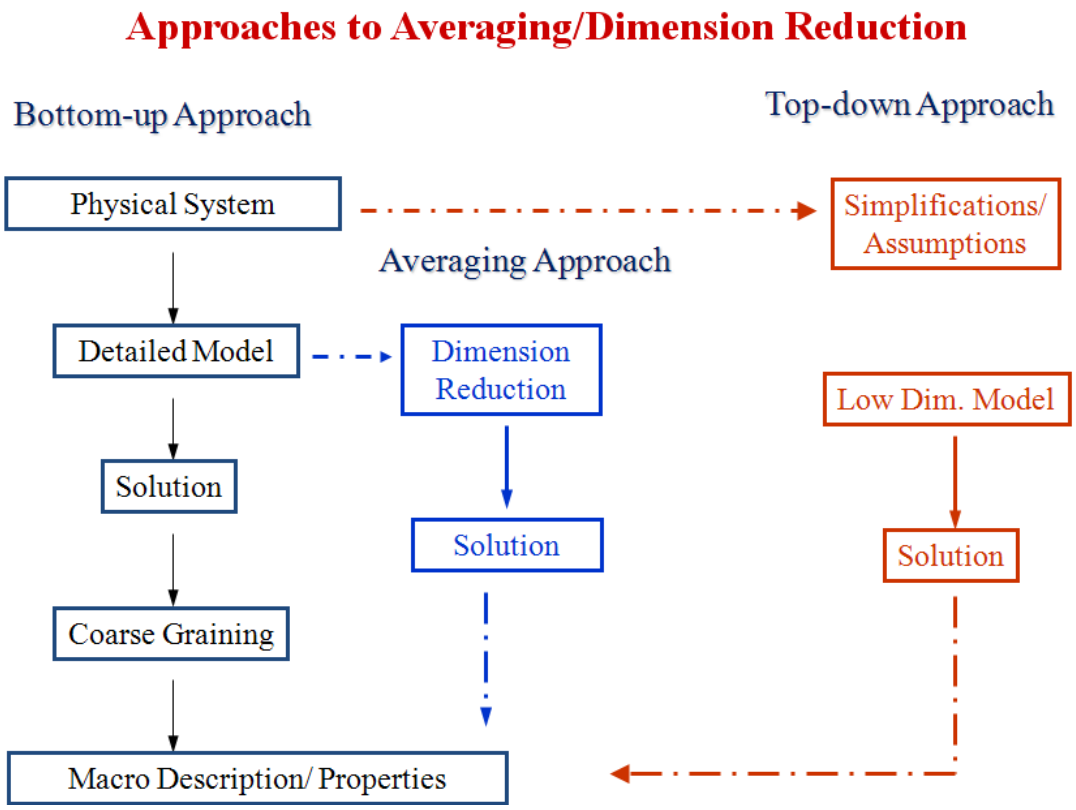


Figure 1.2: Different approaches to averaging/dimension reduction.

mous and widely used chemical reactor model, namely the continuous-flow stirred tank reactor (CSTR), is obtained by assuming the negligible diffusion time (or complete mixing) in every directions (flow and transverse direction) that expresses the species and energy balances at macroscale in terms of few ordinary differential equations. Similarly, the plug-flow reactor model (PFR) assumes the complete mixing in transverse direction and expresses the conservation laws at mesoscale as partial differential equation in time and one spatial coordinate in flow direction. These models are computationally very simple. However, assumptions made in the top-down approach are not justified for most cases of practical interests and thus, the models developed using this approach such as the CSTR, the PFR, the axial dispersion model with/without Danckwerts boundary conditions, the two-phase catalytic reactor model, pseudo-homogeneous models of multiphase reac-

tors etc., ignore the physics at small length scales. In fact, the shortcomings of these models (such as the inability to predict micromixing effects on conversion and yield/selectivity of an intermediate product for the case of fast reactions) are well known. For example, the conversion predicted from ideal CSTR model is independent of how input and output streams enter the reactor and so on.

The other extreme is the numerical approach where detail diffusion-convection-reaction models for given system are applied at micro-scale and are solved numerically such as by using computational fluid dynamics (CFD). While this approach is certainly feasible (at least for single phase systems) due to the recent availability of computational power and more accurate than the top-down approach, it may be computationally prohibitive, especially for multi-phase systems with complex geometries and fast kinetics. It is also not practical when design, control and optimization of the reactor or the process is of main interest. The main drawbacks/criticism of this approach are that:

(i) It uses discrete models of very high dimension that are not only difficult to incorporate into design and control schemes but also may not represent the original problem due to discretization.

(ii) Due to the strong coupling between the transport and reaction processes, the model equations are usually nonlinear and may exhibit a variety of complex spatio-temporal patterns. Without having prior parametric studies, these patterns may not be explored numerically. Even when appropriate set of parameters are considered, right initial conditions or initial guess are essential in numerical approach. In addition, design engineers are interested usually in averaged quantities such as the average exit conversion of a reactant or speed of an adsorption or thermal front, so when detailed solutions are obtained, the numerical results may have to be coarse-grained to determine those quantities.

(iii) For highly nonlinear cases where length scale of separation is very high, the mesh size needed to avoid spurious solutions may be so small that this approach is not feasible. For example, in case of a carbonate core where length scale separation is of order of $10^5$ (core scale of around $10$ cm to pore scale of around $1\mu m$), the number of mesh needed in every direction is $10^5$, i.e., for a typical core ($10 \times 4 \times 4$ cm$^3$), the number of mesh points needed for 3-D simulation is of order of $10^{14}$ which is not practical.

(iv) Numerical approach such as the CFD also uses averaged models (e.g $k - \epsilon$ model for turbulent flows, Prandtl mixing length theory etc.) with closure schemes that are not always justified and contains adjustable constants.

Thus, the intermediate approach where the full convection-diffusion-reaction equations are averaged spatially using systematic procedure, are preferred to develop low-dimensional models as it retain the essential features of the system and computationally less expansive than the numerical approach. In this approach, the full model is averaged over small length scales to describe the process at macro or meso scale in terms of effective coefficients such as transfer coefficients, dispersion coefficients, effectiveness factors etc. Another advantage of this approach is the ability to predict and verify the range of convergence and validity of the averaged model. Before going into detail, we give a brief history of some important reactor models and discuss the averaging procedures used in the literature in following section.

## 1.2 Literature Review

### 1.2.1 Top-down Approach

The most widely used simplified reactor models are the three classical ideal reactor models: (i) the ideal batch reactor (BR) model, (ii) the ideal plug-flow reactor (PFR) model and (iii) the ideal continuous-flow stirred tank reactor (CSTR) model.

The BR model describe the evolution of concentration/temperature profile as reaction occurs in terms of one dimensional ordinary differential equation in time as follows:

$$\frac{d\mathbf{C}}{dt} = \boldsymbol{\nu}\ \mathbf{R}(\mathbf{C}) \quad \text{with } \mathbf{C} = \mathbf{C}_0 \text{ @ } t = 0, \tag{1.1}$$

where $\mathbf{C}$ is concentration vectors for various species, $\mathbf{R}\left(\mathbf{C}\right)$ is reaction vector, $\boldsymbol{\nu}$ is the stoichiometric coefficient matrix and $\mathbf{C}_0$ is the initial concentration vector. For energy balance, concentration vector in transient term is replaced by temperature, $T$ and reaction term is multiplied by corresponding enthalpy of reaction. Similarly, the PFR model assumes no gradient in transverse (to flow) direction and expresses the species and energy balance as a first order partial differential equation in time, $t$ and one spatial coordinate, $x$ (corresponding to flow direction) by neglecting axial mixing as follows:

$$\begin{gathered} \frac{\partial \mathbf{C}}{\partial t} + \langle u \rangle \frac{\partial \mathbf{C}}{\partial x} = \boldsymbol{\nu}\ \mathbf{R}(\mathbf{C}), \\ \mathbf{C} = \mathbf{C}_{in} \text{ @ } x = 0 \text{ and } \mathbf{C} = \mathbf{C}_0 \text{ @ } t = 0, \end{gathered} \tag{1.2}$$

where $\mathbf{C}_{in}$ is the inlet concentration vector and $\langle u \rangle$ is the average velocity. It should be noted that it is an hyperbolic model and describes how the concentration/temperature profile varies in flow direction. While the BR model and the PFR model have existed since the late eighteenth century, a conceptual leap came in the form of the CSTR model (Bodenstein and Wolgast, 1908) which assumes complete mixing at all scales and expresses the balance equations as follows:

$$\frac{d\mathbf{C}}{dt} = \frac{\mathbf{C}_{in} - \mathbf{C}}{\tau_C} + \boldsymbol{\nu}\ \mathbf{R}(\mathbf{C}),\ \ (j = 1, 2, ..., M) \tag{1.3}$$

where $\tau_C$ is the total residence time of the reactor. It should be noted that these reactor models are expressed in terms of a single mode $\mathbf{C}$ and do not distinguish

between spatially averaged concentration, $\langle \mathbf{C} \rangle$, and cup-mixing or flow averaged concentration, $\mathbf{C}_m$.

The assumption of no axial mixing in PFR model was later relaxed by using finite axial mixing by Irving Langmuir (1908), who dealt with both the limiting cases of "mixing nearly complete" and "only slight mixing" and replaced the Dirichlet boundary condition ($\mathbf{C} = \mathbf{C}_{in}$ @ $x = 0$) by a flux type boundary condition:

$$\mathbf{D}\frac{d\mathbf{C}}{dx} = \langle u \rangle \left[\mathbf{C} - \mathbf{C}_{in}\right] \text{ @ } x = 0, \tag{1.4}$$

where $\mathbf{D}$ is the diagonal matrix of molecular diffusivity of the species. The above boundary condition was rediscovered first by Förster and Geib (1934), which was quoted and applied by Damköhler (1937) and then finally by Danckwerts (1953), and since then, it has been known as 'Danckwerts' boundary condition'. Förster and Geib (1934) in their paper, introduced the concept of residence time distribution (RTD) and obtained the RTD curves for the axial dispersion model using Danckwerts boundary condition. Damköhler (1937) in his historic paper, summarized various reactor models and formulated the two-dimensional DCR model for tubular reactors (by using the Danckwerts boundary condition with parabolic velocity profile corresponding to laminar flow in tubes) to describe finite mixing both in the flow and transverse directions. Later, Danckwerts (1953) introduced the concepts of "hold-back" and "segregation" and devised a generalized treatment of RTD. Following this, Zwietering (1959) introduced the concept of *micromixing* (mixing caused by local diffusion, local velocity gradients and reaction at the small scales) and quantified the degrees of mixing with the ideas of "complete segregation" and "maximum mixedness". Since then, the topic of micromixing has become a part of classical Chemical Reaction Engineering and has been discussed in various textbooks [Levenspiel (1999), Froment & Bischoff (1990), Westerterp, van

Swaaij & Beenackers (1984)] and review articles (Villermaux, 1991).

Though the top-down approach is the one that chemical engineers have followed historically to develop low-dimensional models of various reactors at macroscale by making certain *a prior* assumptions on the length and time scales, these assumptions are usually not justified since it involves comparison of the solutions obtained with more detailed (fundamental) models, which are not available. Because of the *a prior* assumptions, these models cannot explain many experimentally observed features that arise due to strong coupling between transport and reaction processes at small scales. When the predictions of such ad-hoc models do not match with experimental results, the low-dimensional models are modified by expanding the degrees of freedom using concepts such as residence time distribution, non-ideal flow and mixing, which express the models in terms of effective quantities such as effectiveness factors or effective dispersion coefficients (Danckwerts, 1958; Zwietering, 1959; Levenspiel, 1999). The short-comings of this approach (such as the dependence of these effective coefficients on the kinetic parameters and inconsistencies such as infinite propagation speed of signals even in convection dominated systems) are well known (Balakotaiah and Chang, 2003; Balakotaiah and Ratnakar, 2010).

### 1.2.2 Bottom-up Approach

#### Numerical Approach

The numerical approach is the discretization of the convection and the diffusion operators of the PDEs that gives rise to a system of effective low-dimensional models of very high order depending on the mesh size (/discretization interval) required to avoid spurious solutions. For example, the minimum number of mesh points ($N_{xyz}$) necessary for direct numerical simulation (DNS) of non-reacting tur-

bulent flow is given by (Baldyga and Bourne, 1999)

$$N_{xyz} \approx Re^{9/4} Sc^{3/2}, \tag{1.5}$$

where $Re$ and $Sc$ are the Reynolds and turbulent Schmidt numbers, respectively. [ For $Re = 10^4$ and $Sc = 10^3$, $N_{xyz} \sim 10^{13}$, which is quite large.] For the case of steady-state one-dimensional laminar reacting flows in a tube of radius $a$ and length $L$, the minimum number of mesh points required is given by (Dommeti & Balakotaiah, 2000)

$$N_x = \sqrt{\frac{Pe^3}{24q}\left(q - 1 - \frac{2Da}{Pe} + \frac{2Da^2}{Pe^2}\right)}, \tag{1.6}$$

where

$$q = \sqrt{1 + \frac{4Da}{Pe}}, \tag{1.7}$$

$Da$ is the Damköhler number, $Pe$ is the Peclet number based on the reactor length, given by

$$Pe = \frac{L}{2a} Re\ Sc. \tag{1.8}$$

For very fast reactions, i.e. $Da \gg 1$, criterion to avoid spurious solutions for a 3-dimensional scalar CDR is simplified as

$$N_{xyz} = \left(\frac{\phi^2}{24}\right)^{3/2}, \tag{1.9}$$

where $\phi^2$ ($= Pe\ Da$) is Theile-modulus. For the case of non-isothermal kinetics, $\phi^2 = \phi_0^2\ exp[B]$, where $\phi_0^2$ is the value based on the reference temperature and $B$ is the Zeldovich number (dimensionless adiabatic temperature rise). Thus, for a typical value of $B$ of $20$ (that is very common for partial oxidation and combustion reactions) and $\phi_0^2 = 1$, $N_{xyz} = 3 \times 10^{17}$, which is very large and the problem is

rendered numerically unsolvable. Similar examples can be given for other systems where the number of mesh size required to avoid spurious solution and to capture the essential physics of the system, is very large. These systems of such high order cannot be easily incorporated for control and optimization purposes. Thus, the numerical solution of the three-dimensional transport equations for reacting flows using CFD codes or other methods are prohibitive in terms of the numerical effort required, especially for the case of fast/ non-isothermal kinetics. In such cases, low dimensional models are a natural alternative.

**Averaging or Dimension Reduction Approach**

In this intermediate approach, the full model is averaged over small length scales to describe the process at macro or meso scale. Several different empirical as well as rigorous averaging techniques (with different terminology such as homogenization, dimension reduction, adiabatic elimination, multi-scale method, slaving principle, etc.) are used in different fields for obtaining low-dimensional models. In chemical engineering literature, the two most important concepts that have appeared in the past century to provide a simplified description of the transport processes are that of the transfer coefficient and the dispersion coefficient. Both these concepts reduce the local degrees of freedom and provide a coarse-grained low-dimensional description of the transport process in terms of macroscale averaged variables such as cup-mixing and/or wall temperatures, and some weighted average concentrations. While both concepts have been applied successfully for many decades for non-reacting systems, their application to reacting systems or transient problems with sources or sinks, leads to identification of sharp differences between them.

**The Transfer Coefficient Concept:** The transfer coefficient concept is almost a century old and was introduced by Lewis (1916) and Lewis and Whitmann (1924),

in the context of film models for heat and mass transfer. It is closely related to the boundary layer theory introduced by Prandtl (1904) and Von Karman (1921) in the context of momentum transfer. In text books, the heat transfer coefficient concept is often illustrated by the classical Graetz-Nusselt problem describing steady-state heat transfer in laminar flow in a circular tube (with length to diameter ratio $>>$1). In this case, the detailed model describing the fluid temperature variation in the tube as a function of axial and radial position (assuming azimuthal symmetry) is described by the partial differential equation

$$2\left\langle u\right\rangle \rho_f c_{pf}\left(1-\frac{r^2}{a^2}\right)\frac{\partial T}{\partial x}=k_f\frac{1}{r}\frac{\partial}{\partial r}\left(r\frac{\partial T}{\partial r}\right);\ 0<r<a, x>0 \tag{1.10}$$

with initial (inlet) and boundary conditions

$$T(x=0,r)=T_{in}\ ,\quad T(x,r=a)=T_w, \frac{\partial T}{\partial r}(x,r=0)=0, \tag{1.11}$$

while the coarse-grained low-dimensional model is given by

$$\left\langle u\right\rangle \rho_f c_{pf}\frac{dT_m}{dx}=a_v q\ \ ;\ \ T_m(x=0)=T_{in};\ \ a_v=\frac{2}{a}, \qquad \text{(Global equation)} \tag{1.12}$$

$$q=h(x)\left(T_w-T_m\right); \qquad \text{(Local equation)} \tag{1.13}$$

where $T_m$ is the cup-mixing (or velocity weighted or bulk) temperature defined by

$$T_m=\frac{\int_0^a 4\pi r\left\langle u\right\rangle\left(1-\frac{r^2}{a^2}\right)T(x,r)dr}{\pi a^2\left\langle u\right\rangle}. \tag{1.14}$$

Here, $a_v$ is the heat transfer area per unit tube volume, and the local heat transfer coefficient and the dimensionless heat transfer coefficient (Nusselt number) are defined by

$$h(x)=\frac{-k_f\frac{\partial T}{\partial r}(x,r=a)}{T_m-T_w}\quad ;\quad Nu_T(x)=\frac{2a\ h(x)}{k_f} \tag{1.15}$$

The coarse-grained model is expressed in terms of the experimentally measurable cup-mixing temperature and eliminates the dependence of the temperature on the smaller scale (radial coordinate) and hence the associated transverse degrees of freedom. To complete the low-dimensional description, we have to specify the dependence of $h(x)$ (or $Nu_T(x)$) on the parameters appearing in the detailed model. For this specific case, this can be done either by exact solution of the full model or by analyzing the two limiting cases of short and long axial distances from inlet (corresponding to the Leveque solution and the asymptotic downstream solution with fully developed velocity and temperature profiles). Since these expressions can be found in standard heat transfer books (Kays et al. (2004)), we will not repeat them here but note the following key observations about the low-dimensional model given by equations (1.12,1.13 ): (i) The global equation gives the variation of the measurable global variable, namely the cup-mixing temperature, along the tube length (which is the global or large scale). (ii) The local equation (1.13) uses two temperature modes to express the local gradients in terms of the eliminated smaller scale. (iii) For the practical case of tube length being much larger than the radius ($L/a >> 1$) or when there is a clear separation of length scales, the heat transfer coefficient over most of the tube length is given by an asymptotic value that depends only on the local length scales and molecular properties, i.e.,

$$Nu_{T\infty} = 3.656 \text{ or } h_\infty = \frac{3.656 k_f}{2a}. \tag{1.16}$$

The asymptotic Nusselt number is just the first eigenvalue of the convection-diffusion (C-D) operator appearing in the Graetz-Nusselt problem. When there is a clear separation of length scales, only the first transverse mode of the C-D operator is important and all other transverse modes (degrees of freedom) are eliminated. For short distances, where a thermal boundary layer may exist, the spectrum of the

C-D operator is continuous and in the general case of arbitrary inlet conditions, it is not possible to reduce the transverse degrees of freedom. However, for special inlet conditions such as that of a uniform inlet temperature, the inlet boundary layer can be characterized and the low-dimensional model can be extended by using a position dependent heat transfer coefficient. The key point to note here is that once a two-mode low-dimensional model is available, its range of validity can be extended by using position dependent transfer coefficient. In fact, in this classical Graetz-Nusselt problem, use of exact expression for $h(x)$ makes the solution of the low-dimensional model to be identical to that of the detailed model (but the low-dimensional model cannot treat or is not accurate for other types of inlet conditions).

The low-dimensional model can easily be generalized to other situations such as constant flux boundary condition at the wall (for which $Nu_{H\infty} = \frac{48}{11}$), ducts of other shapes, complex geometries (porous media or packed-beds), developing flows, turbulent flows and flows with phase change. In all these cases, the expressions or correlations for $h(x)$ change but the main concept of eliminating the local degrees of freedom using a global and a local equation with two temperature modes and the transfer coefficient concept remains valid.

**The Dispersion Coefficient Concept:** The dispersion coefficient concept is older than that of the transfer coefficient and was first introduced by Boussinesq (1877) as *eddy viscosity* for describing momentum transport in turbulent flows. In the chemical engineering literature, the popularity of the dispersion coefficient in mass transfer traces its origin to the papers of Taylor (1953) and Aris (1956). The classical Taylor-Aris problem considers the dispersion of a non-reactive solute in a circular tube of constant cross-section in which the flow is laminar. In this case, the detailed model describing the solute concentration $C(r, \theta, x, t)$ is described by the

convective-diffusion equation

$$\begin{aligned} \frac{\partial C}{\partial t} + 2\left\langle u \right\rangle \left(1 - \frac{r^2}{a^2}\right) \frac{\partial C}{\partial x} &= D_m \left[\frac{1}{r}\frac{\partial}{\partial r}\left(r\frac{\partial C}{\partial r}\right) + \frac{1}{r^2}\frac{\partial^2 C}{\partial \theta^2}\right] + D_m \frac{\partial^2 C}{\partial x^2}; \quad (1.17) \\ 0 &< r < a,\ x > 0,\ t > 0 \end{aligned}$$

with boundary conditions

$$\frac{\partial C}{\partial r} = 0 \ @ \ r = a; C \text{ finite } @ \ \ r = 0. \quad (1.18)$$

and appropriate inlet and initial conditions. Taylor (1953) and Aris (1956) showed that the cross-sectional averaged concentration

$$\left\langle C \right\rangle (x,t) = \frac{1}{\pi a^2} \int_0^{2\pi} \int_0^a r\ C(r,\theta,x,t) dr d\theta, \quad (1.19)$$

is given by the coarse-grained low-dimensional model

$$\frac{\partial \left\langle C \right\rangle}{\partial t} + \left\langle u \right\rangle \frac{\partial \left\langle C \right\rangle}{\partial x} = D_{eff} \frac{\partial^2 \left\langle C \right\rangle}{\partial x^2} \quad ; \quad D_{eff} = D_T + D_m \ ; \ D_T = \frac{a^2 \left\langle u \right\rangle^2}{48 D_m}, \quad (1.20)$$

where $D_{eff}$ is the effective dispersion coefficient. The first term in $D_{eff}$ is known as the Taylor dispersion coefficient and arises due to the combined effect of velocity profile and transverse molecular diffusion. Defining a transverse diffusion time (for circular tube) as

$$t_D = \frac{a^2}{48 D_m}, \quad (1.21)$$

the Taylor dispersion coefficient may be expressed as

$$D_T = \left\langle u \right\rangle^2 t_D. \quad (1.22)$$

The second contribution to $D_{eff}$ in equations (1.20) (known as the Aris contribution) is the axial diffusion term that is already present in the detailed model and is often neglected when the tube length is much larger than the diameter (or more precisely, when $L \gg \langle u \rangle t_D$ and the radial Peclet number $Pe_r = \frac{a\langle u \rangle}{D_m} \gg \sqrt{48}$). As the heat transfer model, this coarse-grained model eliminates the dependence of the concentration on the smaller scales (transverse radial coordinate $r$ and azimuthal coordinate $\theta$) using the effective dispersion coefficient concept, which depends only on the eliminated length scale and molecular properties. The model given by equations (1.20)) is widely used in the chemical engineering literature, often with added inlet and exit boundary conditions. In the literature, there is no general agreement or justification for these inlet and exit conditions.

The following observations may be made on the Taylor-Aris low-dimensional description of the non-reactive solute dispersion model: (i) The average concentration $\langle C \rangle (x,t)$ is not an easily measurable quantity. In fact, Taylor (1953) himself measured experimentally the cup-mixing or velocity weighted concentration $C_m(x,t)$ (also known as the bulk concentration), which can be done by collecting small samples of fluid exiting the tube. As we show below, the distinction between $C_m(x,t)$ and $\langle C \rangle (x,t)$ is important but is often ignored in most publications on this topic (and also in most textbooks). (ii) The Taylor-Aris model uses a single concentration mode and represents what is a local phenomenon (exchange of solute by molecular diffusion between fast moving fluid near the center of the tube and slow moving fluid near the wall) as a diffusion term in the macroscale equation. It represents the local (transverse) gradient in concentration as a gradient in the global (longitudinal) variable with respect to the global scale in the low-dimensional description. As can be seen intuitively, this is not an accurate description of the true physical situation and hence is the main reason for the many conceptual difficulties (such as upstream diffusion of the solute, infinite speed of propagation of signals

even in the convection dominated limit, etc.) associated with this model. (iii) Since the model is parabolic and is similar to the diffusion equation (in a coordinate system moving with the average velocity), it requires additional boundary conditions or physical constraints. Further, it can not describe the bypass behavior or the segregated flow limit that may be reached in the case of laminar flow in a tube with negligible molecular diffusion effects ($D_m \to 0$).

**Rigorous Procedures:** There are several other averaging techniques used in literature. For example, in fluid dynamics, Reynolds averaging is widely used to obtain time-smoothed transport equation that describes micromixing effectively. However, this technique leads to the closure problem (more number of unknowns than the number of equations). Several schemes have been proposed to close the two terms in the time-smoothed equations, namely, scalar turbulent flux in reactive mixing, and the mean reaction rate (Bourne and Toor, 1977; Brodkey and Lewalle, 1985; Li and Toor, 1986; Dutta and Tarbell, 1989; Fox, 1992). However, these are not justified for fast/non isothermal kinetics as well as for the case where strong boundary layers are present.

For dynamical systems with scale separation, the Center Manifold theorem (Carr, 1981) has been used extensively in recent years to eliminate the slave (or fast decaying) modes and obtain low dimensional models described by a few ordinary differential equations (Mercer and Roberts, 1990; Balakotaiah and Chang, 1995; Balakotaiah and Dommeti, 1999). While this is a powerful technique and can describe the asymptotic behavior of a physical system near a fixed/steady point (such as a trivial solution), a major limitation of this technique is its inability to describe the transient evolution of initial conditions or dispersion process at short times (Ratnakar and Balakotaiah, 2011a). In addition, it can not be used for algebraic equations or elliptic problems (steady-state boundary value problems).

Similarly, the method of moments (Aris, 1956; Chatwin, 1970; Barton 1983) are one of the well known techniques to analyze the spreading process and to determine the spatial moments. Aris (1956) analyzed the dispersion of non-reacting solute in a tube using this method and derived the asymptotic solution for first few moments where he presented the contribution of axial mixing on overall spreading process. Chatwin(1970) revised the work of Aris (1970) further and derived the solution of diffusion-convection model asymptotically. However, the double zero in Laplace transform inversion was neglected in his derivation that lead to physically incorrect results, which was corrected later by Barton (1983). Though this method can predict the moments accurately, it can not be applied for non-linear problems. In addition, the first few moments are not enough to determine the solution. For example, in a tubular reactor, the spatial moments can not predict the exit conversion. the third central moments.

The most superior averaging technique of all is the Lyapunov-Schmidt (L-S) technique of classical bifurcation theory which eliminates the degrees of freedom near a zero eigenvalue and analyze the bifurcation behavior of a nonlinear operator (Golubitsky and Schaeffer, 1984; Balakotaiah et al.,1985). Recently, this technique has been used for spatial averaging of convection-diffusion-reaction models provided a scale separation exists (Balakotaiah and Chang, 2003; Balakotaiah, 2004; Bhattacharya at al., 2004; Chakraborty and Balakotaiah, 2005, Ratnakar and Balakotaiah, 2011 a,b; Balakotaiah and Ratnakar, 2010). Intuitively speaking, the L-S method of averaging is equivalent to Taylor expansion of a more detailed model in terms of one or more small parameters representing the ratio of length or time scales present in the detailed model. In such an expansion, the lowest (zeroth) order term (which ignores the physics at the small scales) is the simplified model (such as the ideal PFR or CSTR model) while the higher order corrections modify it by including the small but significant physical phenomena (such as local velocity

gradients, molecular diffusion, finite rates of adsorption, reaction, etc.) present at various length and time scales.

## 1.3 Objectives

As discussed in introduction, there are three approaches to obtain low-dimensional models in the chemical engineering literature: (i) top-down approach, where a certain a prior assumptions are made to simplify the detail models; (ii) numerical approach, where the detailed model is discretized and solved numerically; and (iii) averaging approach, where a low-dimensional model is developed by averaging the detailed model over small length scales. We also discussed that the first two approach have various shortcomings. Therefore, one of the main objective of this part of thesis is to present a rigorous and systematic procedure for averaging of full diffusion-convection-reaction model for various reactors that can be used for general sources including non-linear and point sources. Since most of the averaging techniques such as Center Manifold, method of moments and volume averaging techniques have various shortcomings and L-S procedure overcomes these shortcomings, we develop low-dimensional models for transport and reaction processes based on L-S procedure. Another objective is to analyze the range of convergence and validity of the averaged model in parameter spaces. After we have the averaged model, one of the important objective is to determine experimentally measurable quantities to gain physical insight that can be helpful to design better experiments or develop better low-dimensional models.

In the next chapter, we present the mathematical aspect of L-S procedure and illustrate its application with an example of two-compartment discrete diffusion-convection model transport. We also analyze the range of convergence and validity of the model. In the third chapter, we present the exact averaging of laminar dispersion in a tube with general sources including point release and analyze the range of convergence and validity of the model. In this chapter, we present the evo-

lution of spatial moments and demonstrate the superiority of L-S procedure over other techniques. We also analyze the truncated models and show that the regularization of truncated model increases its range of validity. In the forth chapter, we derive reduced order model for describing dispersion in catalytic monoliths where we analyze the transfer coefficient concept in detail. In the last chapter, summarize the main conclusion of the first part of the thesis and recommends for future work.

# Chapter 2 Liapunov-Schmidt Reduction

## 2.1 Preamble

In this chapter, we present multi-scale averaging of a general non-linear operator corresponding to transport and reaction processes in a chemical reactor based on the Lyapunov-Schmidt technique of classical bifurcation theory. This method is best suited for spatial averaging near a zero eigenvalue (corresponding to the vanishing of a small parameter representing the ratio of length or time scales in the system). For the case of diffusion-convection-reaction problems, local equilibrium exists in the limit when local diffusion is very fast as compared to convection and reaction [Remark: The convection time scale varies as $L/\langle u\rangle$, where $L$ is the macro length scale and $\langle u\rangle$ is the average velocity. The reaction time scale varies as $C_R/R(C_R)$,where $C_R$ is a reference concentration and $R(C_R)$ is the reaction rate. The local diffusion time scale varies as $\ell_T^2/D_m$, where $\ell_T$ is the meso or micro length scale (tube radius in case of tubular reactor) and $D_m$ is the molecular (or effective) diffusivity. When $\ell_T \to 0$, local diffusion becomes dominant as the other scales are independent of $\ell_T$. Conversely, by choosing the appropriate length scale $\ell_T$, the local diffusion can be made to be the dominant process and hence, the spatial degrees of freedom associated with this length scale can be eliminated]. Dimension reduction based on Lyapunov-Schmidt technique uses two orthogonal set of vector spaces and orthogonal projection of the convection-diffusion-reaction operator and state variables (concentration/temperature) on those spaces. The resultant low-dimensional models are described by multiple concentration and temperature variables, unlike the traditional low-dimensional models which are described by a single concentration and a single temperature variable. Each of these variables is representative of a physical scale of a system and is called a “mode,” and the averaged models are called “multi-mode models.” Moreover, spatial aver-

aging by the Lyapunov-Schmidt method retains all the parameters present in the full CDR equation. Therefore, within their region of validity these low-dimensional models retain the complex spatio-temporal behaviors (multiple solutions, oscillations, micromixing effects, etc.) that are exhibited by the detailed model that are often missed by the traditional low-dimensional models. Intuitively speaking, the L-S method of averaging is equivalent to Taylor expansion of a more detailed model in terms of one or more small parameters representing the ratio of length or time scales present in the detailed model. In such an expansion, the lowest (zeroth) order term (which ignores the physics at the small scales) is the simplified model (such as the ideal PFR or CSTR model) while the higher order corrections modify it by including the small but significant physical phenomena (such as local velocity gradients, molecular diffusion, finite rates of adsorption, reaction, etc.) present at various length and time scales

The Lyapunov-Schmidt method is a well known techniques for eliminating the degrees of freedom near a zero eigenvalue. It has been used for analyzing the bifurcation behavior of a nonlinear operator near a zero eigenvalue (Golubitsky and Schaeffer, 1984; Balakotaiah et al.,1985). Recently, this technique has been used for spatial averaging of convection-diffusion-reaction models provided a scale separation exists (Balakotaiah and Chang, 2003; Balakotaiah, 2004; Bhattacharya at al., 2004; Chakraborty and Balakotaiah, 2005, Ratnakar and Balakotaiah, 2011 a,b; Balakotaiah and Ratnakar, 2010). Here, we illustrate the main steps of this averaging procedure by considering a single partial differential equation of the convection-diffusion-reaction type and show how the local spatial degrees of freedom (present in the diffusion operator) may be eliminated by averaging. Application of the procedure for more general cases may be found in the cited references.

## 2.2 Mathematical Aspects of L-S

We explain here briefly the mechanism of the Lyapunov-Schmidt reduction when the linear operator is Fredholm of index zero. Finite dimensional (matrix) operators and elliptic differential operators such as the transverse diffusion operator considered in the next section fall into this category.

We consider a linear or nonlinear equation of the form

$$F(c,p) \equiv \mathbb{L}c - pN(c,p) = 0\ , \tag{2.1}$$

where $c$ is a state variable, $p$ is a parameter (not necessarily small), $\mathbb{L}$ is a linear operator, independent of $p$, and $N\,(c,p)$ is a smooth function. We assume that $\mathbb{L}$ has a simple zero eigenvalue with eigenvector $y_0$, i.e.,

$$\mathbb{L}\ y_0 = 0; \quad y_0 \neq 0. \tag{2.2}$$

Let $\mathbb{L}^* =$ adjoint operator to $\mathbb{L}$ and $v_0$ be the eigenvector of $\mathbb{L}^*$ corresponding to zero eigenvalue, i.e.,

$$\mathbb{L}^*\ v_0 = 0; \quad v_0 \neq 0. \tag{2.3}$$

We use orthogonal complementary spaces to decompose the domain and codomain as shown in Figure 2.1. Let $E$ be the projection operator onto $range\,\mathbb{L}$. Then, equation (2.1) is equivalent to

$$E\ F(c,p) = 0, \tag{2.4}$$

$$(I-E)\ F(c,p) = 0. \tag{2.5}$$

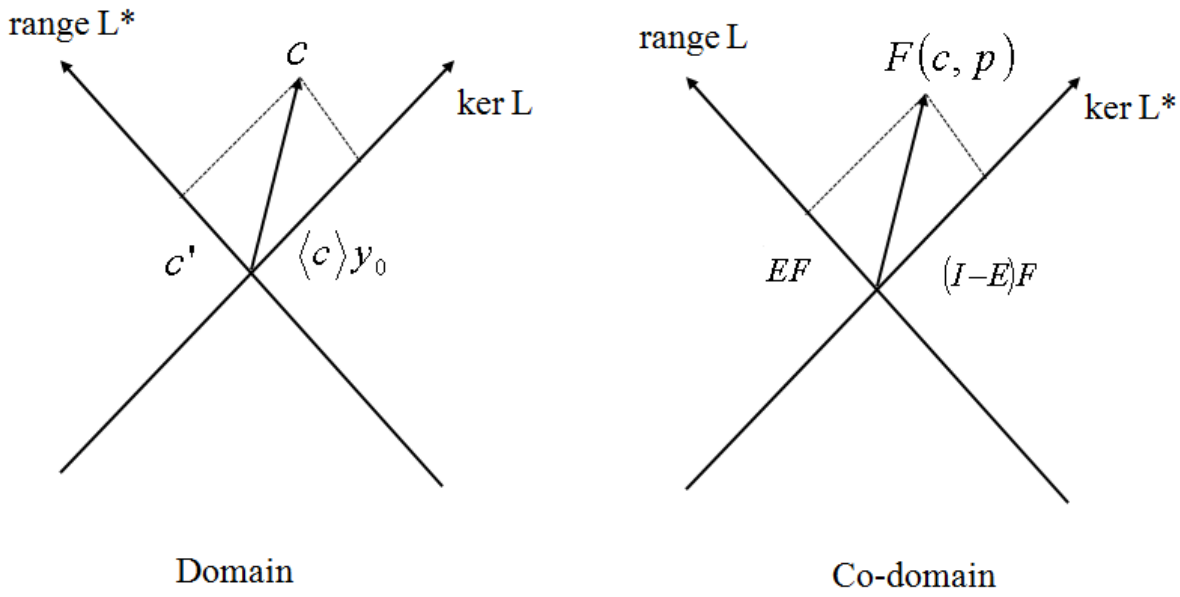


Figure 2.1: Schematic diagram illustrating the choice of the complementary spaces in the domain and codomain of the linear operator in the Liapunov-Schmidt Reduction.

In the domain, $c$ may be expressed as

$$c = \langle c \rangle \ y_0 + c' \tag{2.6}$$

where $\langle c \rangle \, y_0$ is the component of the solution $c$ projected onto $ker\ \mathbb{L}$. [If the eigenvector is normalized so that $\langle y_0, v_0 \rangle = 1$, then $\langle c \rangle$ may be interpreted as the amplitude of the projection of $c$ onto $ker\ \mathbb{L}$]. Thus, equation (2.4,2.5) become

$$E\ F(\langle c \rangle \ y_0 + c', p) \ = \ 0, \tag{2.7}$$

$$(I - E)\ F(\langle c \rangle \ y_0 + c', p) \ = \ 0. \tag{2.8}$$

We call equation (2.7) and equation (2.8) as the *local* and the *global* equations, respectively. Since the operator $EF : range\ \mathbb{L}^* \rightarrow range\ \mathbb{L}$ is invertible, it follows from the implicit function theorem that equation (2.7) can be solved *uniquely* for $c'$

as

$$c' = c'(\langle c \rangle \ y_0, p). \tag{2.9}$$

This is the key step of the elimination process for $c'$ that contains all the slave modes. Substitution of equations (2.9) in (2.8) gives

$$(I - E)\ F(\langle c \rangle \ y_0 + c'(\langle c \rangle \ y_0, p), p) = 0. \tag{2.10}$$

Defining

$$f(\langle c \rangle, p) = (I - E)F(\langle c \rangle y_0 + c' \langle c \rangle y_0, p), p), \tag{2.11}$$

we note that $f : \ker \mathbb{L} \to \ker \mathbb{L}^*$ is a mapping between the one dimensional spaces $\ker \mathbb{L}$ and $\ker \mathbb{L}^*$. We define the *averaged equation* or the *reduced order model* for the amplitude $\langle c \rangle$ by

$$\langle (I - E)\ F(\langle c \rangle y_0 + c'(\langle c \rangle y_0, p), p), v_0 \rangle = 0, \tag{2.12}$$

where $\langle \cdot, \cdot \rangle$ denotes inner product and $c'(\langle c \rangle y_0, p)$ is defined implicitly by the equation

$$E\ F(\langle c \rangle y_0 + c'(\langle c \rangle y_0, p), p) = 0. \tag{2.13}$$

Now, since $E\ F \in range\ \mathbb{L}$ and $v_0 \perp$ range $\mathbb{L}$, the averaged model equation (2.12) may be simplified to

$$\langle\ F(\langle c \rangle y_0 + c'(\langle c \rangle y_0, p), p), v_0 \rangle = 0. \tag{2.14}$$

For the special form of $F$ given by equation (2.1), the local equation (after noting that $E\mathbb{L} = \mathbb{L}$) simplifies to the equation

$$\mathbb{L}c' = pEN(\langle c \rangle y_0 + c'(\langle c \rangle y_0, p), p) \tag{2.15}$$

while the averaged model is given by

$$\langle N(\langle c\rangle\, y_0 + c'(\langle c\rangle\, y_0, p), p), v_0\rangle = 0. \tag{2.16}$$

In applications, the elimination of the slave vector $c'$ from equation (2.15) can be done in many ways. For example, when $N$ is a linear operator in $c$ then the local equation (2.15) can be solved exactly for $c'$ in terms of $\langle c\rangle$ as

$$c' = (\mathbb{L} - p\; EN)^{-1}\, p\; EN(\langle c\rangle\, y_0, p), \tag{2.17}$$

provided the linear operator $(\mathbb{L} - p\; EN)$ is invertible. Substitution of equation (2.17) in equation (2.16) gives an exact averaged equation for $\langle c\rangle$. A second approach to solve the local equation is to take advantage of scale separation that may be present in the physical problem. For example, when $p$ is small, we can use a perturbation expansion

$$c' = \sum_{n=1}^{\infty} p^n c'_n \tag{2.18}$$

and solve a sequence of linear inhomogeneous equations of the form

$$\mathbb{L}\; c'_n = b(\langle c\rangle\, y_0, c'_1, ..c'_{n-1}). \tag{2.19}$$

In this case, the averaged model can be expressed in powers of $p$ to any desired order. Similarly, when the scale separation is such that $p$ is large, we can use a perturbation expansion of the form

$$c' = \sum_{n=0}^{\infty} \frac{c'_n}{p^n} \tag{2.20}$$

to solve the local equation.

We note that the solvability condition for equation (2.15, 2.19) is always satis-

fied due to the decomposition of $c$ and our choice of complementary spaces, and, having a small parameter or the introduction of a small parameter (and hence scale separation) is convenient but not necessary in the L-S procedure. If the local equation (2.15) for $c'$ can be solved exactly, then the reduced order model is exact for any finite $p$. The L-S procedure can be applied for general (asymmetric) problem as well as symmetric problem where operator $\mathbb{L}$ is self-adjoint, i.e., $\mathbb{L}^* = \mathbb{L}$. We provide here a simple example that illustrates the L-S procedure and has many features that are similar to the laminar dispersion problem discussed in the subsequent sections.

## 2.3 Illustration of the L-S Reduction

We consider the two compartment discrete diffusion-convection model shown in Figure 2.2. Each compartment (cell) is assumed to be perfectly mixed and the exchange flow rate $Q$ between the compartments is assumed to be constant. The convective (in and out) flow rate is $q$, while the inlet solute concentration is $c_{in}(t)$. In applications such as those in chemical engineering (residence time distribution theory) and biomedical engineering (pharmacokinetics), the second compartment represents stagnant (no flow) regions (Wen and Fan, 1975; Himmelblau and Bischoff, 1968). The mathematical model for this system is given by

$$\frac{V}{2}\frac{dc_1}{dt} = -Q\ c_1 + Q\ c_2 + q\ c_{in}(t) - q\ c_1 + \frac{V}{2}c_{10}\delta(t) \tag{2.21}$$

$$\frac{V}{2}\frac{dc_2}{dt} = Q\ c_1 - Q\ c_2 + \frac{V}{2}c_{20}\delta(t), \qquad t \geq 0 \tag{2.22}$$

where the last terms in equation (2.21,2.22) containing the Dirac delta function $\delta\,(t)$, represent the initial conditions. Defining characteristic times

$$\tau_E = \frac{V}{Q},\ \tau_c = \frac{V}{q}, \tag{2.23}$$

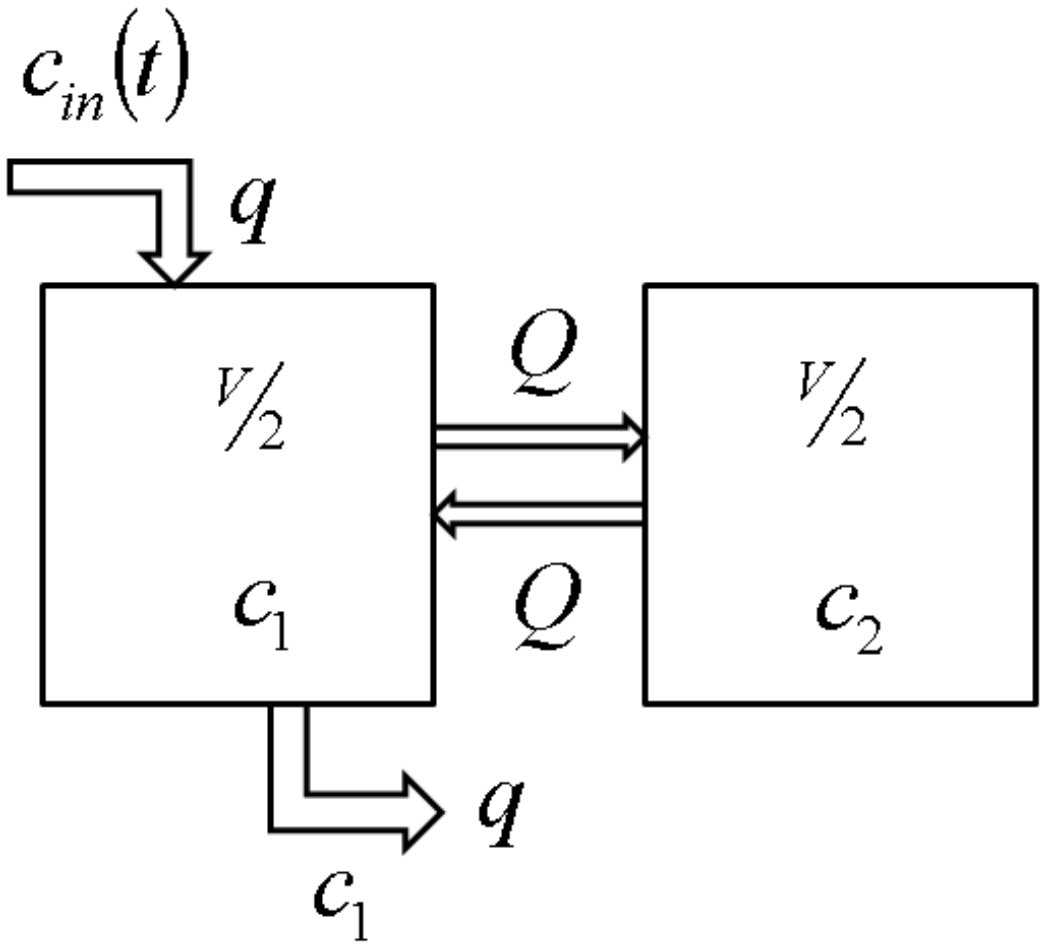


Figure 2.2: Schematic diagram of a two-compartment discrete disffusion-convection model.

and dimensionless variables

$$\tau = \frac{t\,q}{V}, \quad p = \frac{q}{Q} = \frac{\tau_E}{\tau_c}, \tag{2.24}$$

the model may be expressed as

$$\mathbf{A}\,\mathbf{c} = p\,\mathbf{f}\ , \tag{2.25}$$

where

$$\mathbf{A} = \begin{pmatrix} -2 & 2 \\ 2 & -2 \end{pmatrix}, \ \mathbf{c} = \begin{pmatrix} c_1 \\ c_2 \end{pmatrix} \tag{2.26}$$

and

$$\mathbf{f} = \begin{pmatrix} f_1 \\ f_2 \end{pmatrix} = \begin{pmatrix} \frac{dc_1}{d\tau} + 2\ c_1 - 2\ c_{in}(\tau) - c_{10}\delta(\tau) \\ \frac{dc_2}{d\tau} - c_{20}\delta(\tau) \end{pmatrix}. \tag{2.27}$$

Here, $\tau_E$ is the local exchange time while $\tau_c$ is the convection or residence time. The matrix $\mathbf{A}$, which is symmetric has eigenvalues $\lambda_0 = 0$, $\lambda_1 = -4$ and corresponding eigenvectors $\mathbf{y}_0 = \begin{pmatrix} 1 \\ 1 \end{pmatrix}$, $\mathbf{y}_1 = \begin{pmatrix} 1 \\ -1 \end{pmatrix}$. Thus, defining the canonical variables

$$\langle c \rangle = \frac{c_1 + c_2}{2}, \ c' = \frac{c_1 - c_2}{2}, \tag{2.28}$$

or equivalently,

$$c_1 = \langle c \rangle + c', c_2 = \langle c \rangle - c', \tag{2.29}$$

and the projection matrix $\mathbf{E} = \begin{pmatrix} \frac{1}{2} & -\frac{1}{2} \\ -\frac{1}{2} & \frac{1}{2} \end{pmatrix}$, the averaged equation and local equation are given by

$$\frac{d\langle c \rangle}{d\tau} + \langle c \rangle - \ c_{in}(\tau) - \frac{(c_{10} + c_{20})}{2}\delta(\tau) + c' = 0 \tag{2.30}$$

$$-4c' = p\left[\frac{dc'}{d\tau} + c' + \langle c \rangle - \ c_{in}(\tau) - \frac{(c_{10} - c_{20})}{2}\delta(\tau)\right]. \tag{2.31}$$

Using the averaged equation (2.30), the local equation (2.31) may be written as

$$-4c' = p\left[\frac{dc'}{d\tau} - \frac{d\langle c \rangle}{d\tau} + c_{20}\delta(\tau)\right]. \tag{2.32}$$

We note that if the local equation (2.32) can be solved exactly for $c'$ in terms of $\langle c \rangle$, the reduced order model will be exact. To show that the L-S procedure is a pure elimination process, we write the averaged and local equations in the Laplace domain by defining

$$\widehat{\langle c \rangle} = \mathcal{L}\left\{\langle c \rangle(\tau)\right\} = \int_0^\infty \exp\left(-\omega\ \tau\right)\ \ \langle c \rangle(\tau)\ \ d\tau. \tag{2.33}$$

Taking Laplace Transform of equation (2.30) & (2.32), we get

$$\omega\ \widehat{\langle c \rangle} + \widehat{\langle c \rangle} - \widehat{\langle c_{in} \rangle}(\omega) - \frac{(c_{10} + c_{20})}{2} + \widehat{c'} = 0 \tag{2.34}$$

$$-4\ \widehat{c'} = p\left[\omega\ \widehat{c'} - \omega\ \widehat{\langle c \rangle} + c_{20}\right]. \tag{2.35}$$

Solving equation (2.35) for $c'$, we get

$$\widehat{c'} = \frac{p}{4 + \omega\ p}\left[\omega\ \widehat{\langle c \rangle} - c_{20}\right], \tag{2.36}$$

which after taking the inverse Laplace transform leads to the result

$$c' = \int_0^\tau \exp\left(\frac{-4(\tau - t')}{p}\right)\frac{d\langle c \rangle}{d\tau}(t')\ \ dt' - c_{20}\int_0^\tau \exp\left(\frac{-4(\tau - t')}{p}\right)\delta(t')\ \ dt'. \tag{2.37}$$

Thus, the *exact averaged equation* in the Laplace domain is given by

$$\omega\ \widehat{\langle c \rangle} + \widehat{\langle c \rangle} - \widehat{\langle c_{in} \rangle}(\omega) - \frac{(c_{10} + c_{20})}{2} + \frac{\frac{p}{4}}{1 + \omega\frac{p}{4}}\left[\omega\widehat{\langle c \rangle} - c_{20}\right] = 0. \tag{2.38}$$

In the time domain, we can write the above equation (2.38) in the following form:

$$\frac{d\langle c \rangle}{d\tau} + \langle c \rangle + \int_0^\tau \exp\left(\frac{-4(\tau - t')}{p}\right)\frac{d\langle c \rangle}{d\tau}(t')\ \ dt' -\ \ c_{in}(\tau)$$

$$-\frac{(c_{10}+c_{20})}{2}\delta(\tau)-c_{20}\int_0^{\tau}\exp\left(\frac{-4(\tau-t')}{p}\right)\delta\left(t'\right)\,dt'=0. \quad (2.39)$$

For $p=0$, the leading order equation is given by

$$\frac{d\left\langle c\right\rangle_0}{d\tau}+\left\langle c\right\rangle_0-\ c_{in}(\tau)-\frac{(c_{10}+c_{20})}{2}\delta(\tau)=0. \quad (2.40)$$

It is clear from above equation that the base state $\left\langle c\right\rangle_0(\tau)$, in general, is time dependent. Even when there is no solute present in the cells initially $(c_{10}=c_{20}=0)$, the base state can be time dependent whenever the inlet condition $c_{in}(\tau)$ is time dependent.

We note that in this specific case, the exact averaged model could also be obtained by solving equation (2.30) for $c'$ and substituting the result in equation (2.32). This leads to the averaged model in the form:

$$\frac{d\left\langle c\right\rangle}{d\tau}+\left\langle c\right\rangle-\ c_{in}(\tau)-\frac{(c_{10}+c_{20})}{2}\delta(\tau)+ \\ \frac{p}{4}\left[\frac{d^2\left\langle c\right\rangle}{d\tau^2}+2\frac{d\left\langle c\right\rangle}{d\tau}-\ \frac{dc_{in}}{d\tau}-\frac{(c_{10}+c_{20})}{2}\delta'(\tau)-c_{20}\delta\left(\tau\right)\right]=0. \quad (2.41)$$

The L-S method also leads to the same form if equation (2.38) is multiplied by $\left(1+\frac{\omega p}{4}\right)$ before taking the inverse Laplace transform. It can be seen easily that the two forms of the averaged model, equation (2.39) and (2.41) are equivalent.

It should be noted that equation (2.41) is a second order equation with two initial conditions. For $\tau>0$, equation (2.41) gives

$$\frac{d\left\langle c\right\rangle}{d\tau}+\left\langle c\right\rangle-\ c_{in}(\tau)+\frac{p}{4}\left[\frac{d^2\left\langle c\right\rangle}{d\tau^2}+2\frac{d\left\langle c\right\rangle}{d\tau}-\ \frac{dc_{in}}{d\tau}\right]=0. \quad (2.42)$$

Multiplying equation (2.41) by $\tau$ and followed by integration from $\tau=0$ to $0^+$, we

get one initial condition for $\langle c \rangle$ as

$$\langle c \rangle|_{\tau=0^+} = \frac{c_{10} + c_{20}}{2}. \tag{2.43}$$

Integration of equation (2.41) from $\tau = 0$ to $0^+$ gives

$$\langle c \rangle - \frac{(c_{10} + c_{20})}{2} + \frac{p}{4}\left[\frac{d\langle c \rangle}{d\tau} + 2\langle c \rangle - c_{in} - c_{20}\right] = 0 \ @\tau = 0^+ \tag{2.44}$$

that can be further simplified by using equation (2.43) as

$$\left.\frac{d\langle c \rangle}{d\tau}\right|_{\tau=0^+} = c_{in}|_{\tau=0^+} - c_{20}. \tag{2.45}$$

The averaged models given by equations(2.39) and (2.41) are exact and valid for any $p \geq 0$. An alternate method to solve the local equation (2.32) for $c'$ in terms of $\langle c \rangle$ is to use perturbation expansion. If $p$ is small, we express the local variable $c'$ as

$$c' = \sum_{i=1}^{\infty} p^i \ c'_i, \tag{2.46}$$

and obtain the result

$$c' = \sum_{i=1}^{\infty} \left(\frac{p}{4}\right)^i (-1)^{i-1} \ \frac{d^i \langle c \rangle}{d\tau^i} - c_{20} \sum_{i=1}^{\infty} \left(\frac{p}{4}\right)^i (-1)^{i-1} \ \delta^{i-1}(\tau), \tag{2.47}$$

where $\delta^{i-1}(\tau)$ is the $(i-1)^{th}$ derivative of the Dirac delta distribution. We show that the solution for $c'$ given by equation (2.47) is same as the exact solution of $c'$ given by equation (2.37). For this, we note that

$$\mathcal{L}^{-1}\left\{\frac{p}{1+\omega p}\right\} = \int_0^{\tau} \exp\left(\frac{-4(\tau - t')}{p}\right) \delta(t') \ dt', \ \ \tau \geq 0 \tag{2.48}$$

while for $|\omega\ p| < 1$, we can write

$$\begin{aligned}\mathcal{L}^{-1}\left\{\frac{p}{1+\omega p}\right\} &= \mathcal{L}^{-1}\left\{p-\omega\ p^2+\omega^2\ p^3-.....\right\} \\ &= \delta\left(\frac{\tau}{p}\right)-\delta'\left(\frac{\tau}{p}\right)+\delta''\left(\frac{\tau}{p}\right)-..... \end{aligned} \tag{2.49}$$

Thus, for $|\omega p| < 1$, we have the identity

$$\int_0^\tau \exp\left(\frac{-4(\tau-t')}{p}\right)\delta\left(t'\right)\ dt' = \delta\left(\frac{\tau}{p}\right)-\delta'\left(\frac{\tau}{p}\right)+\delta''\left(\frac{\tau}{p}\right)-....., \tag{2.50}$$

while for $|\omega p| > 1$, we can write

$$\begin{aligned}\mathcal{L}^{-1}\left\{\frac{p}{1+\omega p}\right\} &= \mathcal{L}^{-1}\left\{\frac{1}{\omega}-\frac{1}{\omega^2 p}+\frac{1}{\omega^3 p^2}-.....\right\} \\ &= 1-\left(\frac{\tau}{p}\right)+\left(\frac{\tau}{p}\right)^2\frac{1}{2!}-\left(\frac{\tau}{p}\right)^3\frac{1}{3!}....=\exp\left(-\frac{\tau}{p}\right). \end{aligned} \tag{2.51}$$

Thus, using equation (2.50) and the property of the distributional derivatives

$$\int_0^\tau \delta^j\left(\tau-t'\right)\frac{d\left\langle c\right\rangle}{d\tau}\left(t'\right)\ dt' = (-1)^j\frac{d^{j+1}\left\langle c\right\rangle}{d\tau^{j+1}}, \tag{2.52}$$

we can express the perturbation solution given by equation (2.47) as

$$c' = \int_0^\tau \exp\left(\frac{-4(\tau-t')}{p}\right)\frac{d\left\langle c\right\rangle}{d\tau}\left(t'\right)\ dt' - c_{20}\int_0^\tau \exp\left(\frac{-4(\tau-t')}{p}\right)\delta\left(t'\right)\ dt', \tag{2.53}$$

which is same as the exact solution given by equation (2.37).

We can also solve the local equation (2.32) using a perturbation expansion in terms of reciprocal powers of $p$ as

$$c' = \sum_{n=0}^{\infty}\frac{c'_n}{p^n} \tag{2.54}$$

and obtain the solution in the Laplace domain in the form

$$\widehat{c'} = \sum_{i=0}^{\infty} \left( -\frac{4}{p\omega} \right)^{i} \left[ \widehat{\langle c \rangle} - \frac{c_{20}}{\omega} \right], \tag{2.55}$$

that is same as the exact solution given by equation (2.36) or given by equation (2.37) in time domain.

The perturbation expansion, equation (2.47), in powers of $p$ converges absolutely provided $\frac{1}{|\omega|} > \frac{p}{4}$ (or equivalently, $p\,|\omega| < 4$) while the same in powers of $\frac{1}{p}$, equation (2.55), converges absolutely if $\frac{1}{|\omega|} < \frac{p}{4}$ (or equivalently, $p\,|\omega| > 4$). The key point is that the local equation can be solved by various methods exactly using different scaling. For example, expansion in powers of $p$ corresponds to the long time scaling while expansion in reciprocal powers of $p$ may correspond to short time scaling. Once the local equation is solved, the reduced order model is exact and is valid for all times within the range of convergence of the local equation.

It should be emphasized that in the long time scaling, the L-S procedure captures the exponentially small terms in time through the distributional derivatives or in the form of higher order derivatives of $\langle c \rangle (\tau)$. Similarly, it may be seen that the short time scaling leads to a solution in powers of $\left(\frac{\tau}{p}\right)$. It is also clear that the identity given by equation (2.51) is derived for $p\,|\omega| > 1$ but the expansion converges for all $\tau$ and $p$ as long as we include all terms. The same is true for equation (2.50). Thus, whether we use a perturbation expansion method for small $p$ or large $p$ to solve the local equation for $c'$, the averaged model is exact (within the range of convergence of the local equation) as long as all order terms are included in the expansion. However, truncation of the local equation at any finite order will reduce the accuracy of the averaged model. In such cases, it may be shown that the solution of the complete model agrees with that of averaged model up to all orders to which the local equation is valid.

As stated earlier, the reduced order model when expressed as a perturbation series in $p$ contains higher order time derivatives of $\langle c \rangle$ as well as distributional derivatives of $\delta(\tau)$, i.e.,

$$\frac{d\langle c\rangle}{d\tau} + \langle c\rangle - \ c_{in}(\tau) - \frac{(c_{10}+c_{20})}{2}\delta(\tau) + \sum_{i=1}^{\infty}\left(\frac{p}{4}\right)^i (-1)^{i-1} \ \frac{d^i\langle c\rangle}{d\tau^i} \\ -c_{20}\sum_{i=1}^{\infty}\left(\frac{p}{4}\right)^i (-1)^{i-1} \ \delta^{i-1}(\tau) = 0. \qquad (2.56)$$

However, the solution of the above model does not require any additional initial conditions. This can be seen if we express the solution $\langle c\rangle(\tau)$ also in a perturbation series:

$$\langle c\rangle = \langle c\rangle_0 + \sum_{i=1}^{\infty} p^i \ \langle c\rangle_i \qquad (2.57)$$

Now, the evolution equation for each $\langle c\rangle_i$, $i = 0, 1, 2...$ is a first order ODE, e.g.

$$\frac{d\langle c\rangle_0}{d\tau} + \langle c\rangle_0 = c_{in}(\tau) + \frac{(c_{10}+c_{20})}{2}\delta(\tau)$$
$$\frac{d\langle c\rangle_n}{d\tau} + \langle c\rangle_n = \sum_{i=1}^{n}\left(\frac{-1}{4}\right)^i \ \frac{d^i\langle c\rangle_{n-i}}{d\tau^i} - c_{20}\left(\frac{-1}{4}\right)^n \ \delta^{n-1}(\tau) \qquad , \quad n > 0 \ (2.58)$$

As can be seen from equation (2.58), the R.H.S. of the evolution equation for $\langle c\rangle_n$ is independent of $\langle c\rangle_n$ and depends only on $\langle c\rangle_{n-1}$, $\langle c\rangle_{n-2}$, ..... ,$\langle c\rangle_0$. Thus, the equation (2.58) can be solved sequentially up to desired accuracy without providing any additional initial conditions.

While the two forms of the exact averaged model, equations(2.41) and (2.41), are valid for any finite $p$, the perturbation expansion, equation (2.56), is valid only for small $p$ (given by the convergence criterion, $p|\omega| < |\lambda_1|$). Thus, if equation (2.56) is truncated at some finite order and applied to $p$ values of order unity or larger, it can give inconsistent (non-physical) results. [The initial conditions for the truncated form of equation (2.56) may be obtained by multiplying it by $\tau^k$ ($k = 0, 1, ..$) and

integrating from $\tau = 0$ to $0^+$.] This is due to the fact that for finite values of $p$, the higher order derivatives dominate the behavior, which is inconsistent with the (long time) perturbation scaling. However, if the solution is also expressed as a perturbation series in $p$ (as in equation (2.57), the higher order derivatives describe the behavior for shorter times, consistent with the scaling.

We now discuss another procedure for solving the truncated form of the averaged model (2.56). Suppose that we truncate equation (2.56) at some finite order. This truncated equation can be rewritten using lower order truncated equation to eliminate the higher order derivatives but without changing the accuracy. For example, if we truncate the reduced order model (2.56) at $O\left(p^2\right)$ and write it for the special case of $c_{10} = c_{20} = 0$ as follows:

$$\frac{d\left\langle c\right\rangle}{d\tau} + \left\langle c\right\rangle - c_{in}(\tau) + \frac{p}{4}\frac{d\left\langle c\right\rangle}{d\tau} - \left(\frac{p}{4}\right)^2 \frac{d^2\left\langle c\right\rangle}{d\tau^2} = 0 + O\left(p^3\right). \tag{2.59}$$

We can rewrite this equation by using the following approximations from lower order truncated models

$$\frac{d\left\langle c\right\rangle}{d\tau} = c_{in}(\tau) - \left\langle c\right\rangle - \frac{p}{4}\frac{d\left\langle c\right\rangle}{d\tau} + O\left(p^2\right) \tag{2.60}$$

and

$$\frac{d^2\left\langle c\right\rangle}{d\tau^2} = \frac{dc_{in}(\tau)}{d\tau} - \frac{d\left\langle c\right\rangle}{d\tau} + O\left(p\right) \tag{2.61}$$

and rewrite the truncated model, equation (2.59) as

$$\begin{aligned}\frac{d\left\langle c\right\rangle}{d\tau} + \left\langle c\right\rangle + \frac{p}{4}\left(c_{in}(\tau) - \left\langle c\right\rangle - \frac{p}{4}\frac{d\left\langle c\right\rangle}{d\tau} + O\left(p^2\right)\right) - \\ \left(\frac{p}{4}\right)^2\left(\frac{dc_{in}(\tau)}{d\tau} - \frac{d\left\langle c\right\rangle}{d\tau} + O\left(p\right)\right) - c_{in}(\tau) \;\; = \;\; 0 + O\left(p^3\right)\end{aligned} \tag{2.62}$$

or,

$$\frac{d\left\langle c\right\rangle}{d\tau} = \left(1 - \frac{p}{4}\right)\left(c_{in}(\tau) - \left\langle c\right\rangle\right) + \frac{p^2}{16}\frac{dc_{in}(\tau)}{d\tau} + O\left(p^3\right). \tag{2.63}$$

It is straightforward to verify that the solutions of equations(2.59) and (2.63) agree with the exact solution to $O\left(p^2\right)$. Thus, the rewriting by using lower order truncated models appropriately, does not change the accuracy but can remove the higher order derivatives and this procedure is consistent with long time scaling. As discussed later, this rewriting may also be used to increase the range of validity of the model (without changing the accuracy) by a procedure called *regularization*.

### 2.3.1 Averaged Model in Terms of Exit Concentration $c_1$

As explained above, the L-S method gives the averaged model in terms of $\langle c \rangle$, which is the amplitude of the projection of the state vector onto ker **A**. However, in applications, it is preferable to express the averaged model in terms of an experimentally measured variable. For example, in the compartment model discussed above, the volume averaged concentration $\langle c \rangle$ is not easily measurable but the flow averaged concentration $c_1$ can be measured. Therefore, we derive the averaged model in terms of exit concentration $c_1$ by rewriting the equation (2.29) as

$$\langle c \rangle = c_1 - c'$$

Thus, the global equation (2.34) in the Laplace domain can be rewritten as

$$\omega\ \widehat{c_1} + \widehat{c_1} - \widehat{\langle c_{in} \rangle}\left(\omega\right) - \frac{\left(c_{10} + c_{20}\right)}{2} - \omega\ \widehat{c'} = 0 \tag{2.64}$$

while the local equation given by equation (2.36) in the Laplace domain can be rewritten as

$$\widehat{c'} = \frac{p}{4 + 2\ \omega\ p}\left[\omega\ \widehat{c_1} - c_{20}\right]. \tag{2.65}$$

and in time domain as

$$c' = \frac{1}{2}\int_0^\tau \exp\left(\frac{-2(\tau - t')}{p}\right)\frac{dc_1}{d\tau}\left(t'\right)\ dt' - \frac{c_{20}}{2}\int_0^\tau \exp\left(\frac{-2(\tau - t')}{p}\right)\delta\left(t'\right)\ dt'. \tag{2.66}$$

By combining equations(2.64 and 2.65), the exact averaged equation in the Laplace domain is given by

$$\omega\ \widehat{c_1} + \widehat{c_1} - \widehat{\langle c_{in} \rangle}\,(\omega) - \frac{(c_{10} + c_{20})}{2} - \frac{p}{4 + 2\ \omega\ p}\left[\omega^2\ \widehat{c_1} - \omega c_{20}\right] = 0 \tag{2.67}$$

while in time domain, it is given by

$$\frac{dc_1}{d\tau} + c_1 - \ c_{in}(\tau) - \frac{1}{2}\int_0^\tau \exp\left(\frac{-2(\tau - t')}{p}\right)\frac{d^2c_1}{d\tau^2}\,(t')\ dt' - \frac{(c_{10} + c_{20})}{2}\delta(\tau) + \frac{c_{20}}{2}\int_0^\tau \exp\left(\frac{-2(\tau - t')}{p}\right)\delta'\,(t')\ dt' = 0. \tag{2.68}$$

Using the identity (for $c_1\,(\tau = 0) = 0$)

$$\int_0^\tau \exp\left(\frac{-2(\tau - t')}{p}\right)\frac{dc_1}{d\tau}\,(t')\ dt' = c_1 - \frac{2}{p}\int_0^\tau \exp\left(\frac{-2(\tau - t')}{p}\right)c_1\,(t')\ dt', \tag{2.69}$$

the exact averaged model in terms of exit concentration $c_1$ may be expressed as

$$\frac{1}{2}\frac{dc_1}{d\tau} + c_1 - \ c_{in}(\tau) + \frac{1}{p}\int_0^\tau \exp\left(\frac{-2(\tau - t')}{p}\right)\frac{dc_1}{d\tau}\,(t')\ dt' - \frac{c_{10}}{2}\delta(\tau) - \frac{c_{20}}{p}\int_0^\tau \exp\left(\frac{-2(\tau - t')}{p}\right)\delta\,(t')\ dt' = 0. \tag{2.70}$$

Alternatively, we can express $c_1$ in terms of $\langle c \rangle$ using equations(17b) and (31).

## 2.4 Some Advantages of Averaging using the L-S procedure

It is of interest to compare the L-S method with other averaging techniques such as the Center Manifold (CM) method. While a detailed comparison is beyond the scope of this work, we summarize here some important differences for future investigation: (i) The L-S method of averaging can be applied to steady-state or

equilibrium models where the governing equation is not an evolution equation either in space or time. In contrast, the CM method and other methods based on dynamical systems theory have limited applicability to such models. (ii) In the L-S method, the base state can be time dependent, and, time dependent inlet conditions/sources can be treated. In the CM method, base state (fixed point) is generally assumed to be time independent. While time dependent center manifolds can be treated (Cox and Roberts, 1991), the forcing terms have to be small (quadratic or higher order). Also, in the CM approach, the initial/inlet conditions are assumed to be close to the fixed point. In contrast, there is no restriction on initial/inlet conditions in the L-S technique. (iii) When applied to the averaging of transient models, the L-S method can capture exponentially small terms in time while these terms are ignored in the CM method (Carr, 1981). For example, in the compartment model discussed above, the L-S method leads to reduced order model containing higher order derivatives in time when a perturbation expansion is used for small $p$. As illustrated above, these higher order time derivatives extend the validity of the model to short times (or, capture the exponentially small transients). (iv) When a perturbation expansion is used to solve for the CM, the range of validity of the CM expansion can not be greater than that given by $\left|\frac{\omega\ p}{\gamma}\right| < 1$, where $\gamma$ is the real part of eigenvalue close to zero and $\omega$ is frequency or wave number (Mercer and Roberts, 1994; Cox and Roberts, 1995). In contrast, as shown in the example above, when a perturbation expansion is used to solve the local equation in the L-S method, the region of convergence of the expansion appears to be at least as large as that given by $\left|\frac{\omega\ p}{\gamma}\right| < 1$. In addition, as illustrated above, time scale separation is convenient but not necessary in the L-S formalism. In contrast, the application of CM method requires time scale separation.

# Chapter 3 Exact Averaging of Laminar Dispersion

## 3.1 Preamble

In the most frequently cited of his articles, Sir Geoffrey Ingram Taylor examined the dispersion of a non-reactive solute in laminar flow through a tube and showed that the cross-section averaged concentration satisfies, in a coordinate moving with the mean flow velocity, a diffusion equation (Taylor, 1953, 1954). Taylor found that the apparent diffusion coefficient to be equal to $a^2 \langle u \rangle^2 / 48 D_m$, where $a$ is the tube radius, $\langle u \rangle$ is the mean velocity and $D_m$ is the molecular diffusion coefficient. As the methodology and the physical arguments used by Taylor to obtain a coarse-grained low-dimensional model with an effective dispersion coefficient are of enormous importance in the simplification of many problems in the applied sciences and engineering, the literature on Taylor dispersion theory is extensive. We refer to the review article by Young and Jones (1991), the monograph by Brenner and Edwards (1993) and recent articles by Gill and Subramanian (1980), Mercer and Roberts (1990, 1994), Vandenbroeck (1990), Watt and Roberts (1995), Dorfman and Brenner (2003), Balakotaiah (2004), Mikelic et al. (2006), Biswas and Sen (2007), Balakotaiah (2008), Lee et al. (2008) and Balakotaiah and Chang (1995, 2003) for a discussion of the various contributions to Taylor dispersion theory.

In his seminal paper, Taylor used simple scaling and intuitive arguments to derive a low-dimensional model for laminar dispersion (Taylor, 1953, 1954). His approach dealt only with the derivation of the reduced order model but not the inlet or initial conditions that are needed to solve the model. Taylor's approach has been extended by many authors using other techniques that take advantage of either the separation of scales (e.g. method of multiple scales, the center manifold theorem of dynamical systems theory, etc.) or the linearity of the classical Taylor dispersion problem (e.g. method of moments). In our opinion, the most successful of these

techniques for describing the long time behavior is the center manifold approach (Carr, 1981) used by Mercer and Roberts (1990, 1994). However, as discussed by Young and Jones (1991), a major limitation of all these techniques is their inability to describe the dispersion process accurately at short times, leading to the so called *centroid displacement* and *variance deficits*. For example, the center manifold approach is applicable only for times exceeding a critical value that is determined by the non-zero eigenvalues of the transverse diffusion operator. For comparison with experimental data, the existing reduced order models have also other limitations. For example, most literature studies do not make a clear distinction between the cross-sectional averaged and the experimentally measured velocity weighted or cup-mixing (or bulk) concentration. This distinction is very important especially for the case of non-uniform inlet or initial conditions where the difference between these two concentrations is present initially. This difference is maximum for the point release at the center where the cup-mixing concentration is twice the cross-section averaged concentration. Most earlier studies use a single diffusive mode (the cross-section averaged concentration) to represent the dispersion flux in terms of the macroscale gradient of this mode, which is inconsistent with the physical picture, i.e., laminar dispersion arises due to the local phenomenon of exchange of solute between fast moving fluid near the center and the slow moving fluid near the wall by transverse molecular diffusion. Hence, the dispersion flux should be proportional to the local gradient, namely, the difference between the cup-mixing and cross-section averaged concentrations (transverse gradient) and not the large scale gradient of the cross-section averaged concentration. Finally, most literature studies use a parabolic reduced order model even in the convection dominated (hyperbolic) limit that leads to many conceptual difficulties such as upstream diffusion of the solute, infinite speed of propagation and negative effective dispersion coefficients for fast reactions or short times.

The main focus of this chapter is to present an alternate method for obtaining coarse-grained low-dimensional models from the three dimensional convection-diffusion-reaction models. Specifically, we show that the Lyapunov-Schmidt (L-S) technique of classical bifurcation theory may be used to obtain coarse-grained low-dimensional models in a systematic way. Though we use the laminar dispersion problem to illustrate the method and compare the results obtained with other methods, the L-S method is applicable to a wide range of problems. It is best suited for spatial averaging near one or more zero eigenvalues of the first Fréchet derivative (linearization) of a governing nonlinear operator corresponding to the vanishing of a small parameter representing the ratio of time or length scales in the system. It can be used to eliminate the local spatial degrees of freedom (such as those associated with the local diffusion operator) and derive accurate low-dimensional models to any order in that small parameter. Intuitively, this method is similar to the Maclaurin's series expansion of the nonlinear model in that small parameter. The mathematical details of the Lyapunov-Schmidt technique and its application to the engineering problems are already discussed in the literature (Balakotaiah and Chang, 2003; Balakotaiah et al., 1985; Golubitsky and Schaeffer, 1984; Ambrosetti and Prodi, 1993) and in the second chapter we reviewed it briefly as an averaging technique. In the next section, we apply the L-S procedure to the laminar dispersion problem where the transverse Laplacian is self-adjoint with respect to the standard cylindrical inner product.

## 3.2 Transverse Averaging of Laminar Dispersion using the L-S Method

### 3.2.1 Model Formulation

The detailed model describing the dispersion of a non-reactive solute in laminar flow in a tube is given by the transient convection-diffusion equation

$$\frac{\partial C}{\partial t} + U(r)\frac{\partial C}{\partial x} = D_m \left[\frac{1}{r}\frac{\partial}{\partial r}\left(r\frac{\partial C}{\partial r}\right) + \frac{1}{r^2}\frac{\partial^2 C}{\partial \theta^2}\right] + D_m \frac{\partial^2 C}{\partial x^2} + S_f\left(r,\theta,x,t\right), \quad 0 < r < a,\ 0 < \theta < 2\pi, \quad x > 0, t > 0 \tag{3.1}$$

with inlet, initial and boundary conditions:

$$\left[-D_m \frac{\partial C}{\partial x} + U(r)\ C\right]\Big|_{@x=0} = U(r)\ C_{in}(r,\theta,t) \tag{3.2}$$

$$C = C_0(r,\theta,x) \quad @\ \ t = 0, \tag{3.3}$$

$$C \text{ finite } @\ r = 0\ ;\ \frac{\partial C}{\partial r} = 0\ @\ r = \ a, \tag{3.4}$$

$$C(r,\theta,x,t) = C(r,\theta+2\pi,x,t), \tag{3.5}$$

where

$$U(r) = 2\ \langle u\rangle\ \ \left(1 - \frac{r^2}{a^2}\right) \tag{3.6}$$

is the velocity profile, $\langle u\rangle$ is the average velocity, $D_m$ is the molecular diffusion coefficient and other terms have their usual meanings. Here, we have made the usual assumptions for the continuity and momentum equation. We consider no-flux boundary condition at the wall and use the Danckwerts boundary condition (Danckwerts, 1953) at inlet which is physically consistent whenever the axial molecular diffusion term is included in the evolution equation (3.1). The term $S_f\left(r,\theta,x,t\right)$ represents sources/sinks for solute at $x > 0$ and $t > 0$.

We include the inlet and initial conditions as source/sink terms in the evolution

equation as explained by Balakotaiah and Ratnakar (2010) and express it as

$$\frac{\partial C}{\partial t} + U(r)\frac{\partial C}{\partial x} = D_m \left[\frac{1}{r}\frac{\partial}{\partial r}\left(r\frac{\partial C}{\partial r}\right) + \frac{1}{r^2}\frac{\partial^2 C}{\partial \theta^2}\right] + D_m \frac{\partial^2 C}{\partial x^2} + S_f\left(r,\theta,x,t\right) + U(r)\, C_{in}(r,\theta,t)\, \delta(x) + C_0(r,\theta,x)\, \delta(t) \quad (3.7)$$

with the same boundary conditions (3.4, 3.5). It can be easily seen that equation (3.7) is identical to equation (3.1) for $x > 0$ and $t > 0$ and leads to the inlet and initial conditions (3.2,3.3) after integration w.r.t. $x$ from $x = 0$ to $0^+$ and w.r.t. $t$ from $t = 0$ to $0^+$, respectively. Here $t = 0^+$ should be interpreted as $t = \varepsilon \ll \tau_D$ with $\varepsilon \to 0$, where $\tau_D = \frac{a^2}{D_m}$ is the transverse diffusion time.

Non-dimensionalizing the above equation (3.7) by defining

$$z = \frac{x}{L}, \tau = \frac{\langle u\rangle\ t}{L}, \xi = \frac{r}{a}, u(\xi) = \frac{U(r)}{\langle u\rangle} = 2\left(1-\xi^2\right) \quad (3.8)$$

$$p = \frac{\langle u\rangle\ a^2}{D_m L}, Pe_r = \frac{\langle u\rangle\ a}{D_m}, c(\xi,\theta,z,\tau) = \frac{C(r,\theta,x,t)}{C_R}, \quad s_f\left(\xi,\theta,z,\tau\right) = \frac{S_f\left(r,\theta,x,t\right) L}{\langle u\rangle\, C_R} \quad (3.9)$$

$$s(\xi,\theta,z,\tau)\ = s_f\left(\xi,\theta,z,\tau\right) + u(\xi)\, c_{in}(\xi,\theta,\tau)\, \delta(z) + c_0(\xi,\theta,z)\, \delta(\tau), \quad (3.10)$$

we express it as,

$$F\left(c,p\right) \equiv \nabla_\perp^2\, c\ - p\ \left[\frac{\partial c}{\partial \tau} + u(\xi)\frac{\partial c}{\partial z} - \frac{p}{Pe_r^2}\frac{\partial^2 c}{\partial z^2} -\ s(\xi,\theta,z,\tau)\right] = 0\ \text{ in } \Omega, \quad (3.11)$$

with boundary conditions given by

$$\boldsymbol{\nabla}_\perp c \cdot \mathbf{n}\ = 0 \text{ on } \partial\Omega, \quad (3.12)$$

$$c(\xi,\theta,z,\tau) = c(\xi,\theta+2\pi,z,\tau), \tag{3.13}$$

where $\mathbf{n}$ is outward normal to the boundary $\partial\Omega$ (tube wall) and

$$\nabla_{\perp}^{2}\, c = \frac{1}{\xi}\frac{\partial}{\partial\xi}\left(\xi\frac{\partial c}{\partial\xi}\right) + \frac{1}{\xi^{2}}\frac{\partial^{2}c}{\partial\theta^{2}} \tag{3.14}$$

is transverse Laplacian operator in the domain $\Omega$ (tube cross-section) subjected to the zero flux boundary conditions on $\partial\Omega$. Here, $c\left(\xi,\theta,z,\tau\right)$ is the concentration non-dimensionalized by some reference concentration ($C_R$); $u\left(\xi\right)$ is the dimensionless velocity profile with dimensionless average velocity $\langle u\left(\xi\right)\rangle = 1$; $\xi$ and $z$ are dimensionless radial and axial coordinates, respectively; $\tau$ is time non-dimensionalized by the convection time $\tau_c = \frac{L}{\langle u\rangle}$, and $p$ is the local (transverse) Peclet number which represents the ratio of two time scales, the transverse diffusion time $\tau_D\left(=\frac{a^2}{D_m}\right)$ to the convection time $\tau_c$. The parameter $p$ is the non-dimensionalized local or transverse diffusion time and could also be interpreted as the dimensionless wave number (or frequency). In this specific problem, due to the zero flux boundary condition, the transverse operator has a zero eigenvalue for any value of $p$, so the L-S procedure will lead to the exact averaging even for finite values of $p$ if the local equation can be solved exactly. However, as discussed in more detail below, in most practical cases, only small values of $p$ are of interest and the smallness (magnitude) of $p$ is an indication of scale separation in the physical system. The parameter $Pe_r$ is radial Peclet number (ratio of transverse diffusion time and convection time based on tube radius) while $s(\xi,\theta,z,\tau)$ is source/sink term including inlet and initial conditions. The L-S procedure presented in the previous section can be extended to the general case in which the source/sink terms include nonlinear volumetric and/or surface reactions. We restrict it here to the non-reacting cases, i.e., $s\left(\xi,\theta,z,\tau\right)$ representing inlet/initial conditions and/or sources/sinks of solute for $z>0$ and $\tau>0$.

In the present approach, the inlet and initial conditions are included in the transverse averaging procedure. As shown later, this leads to the identification of the inlet/initial conditions of the reduced order model.

### 3.2.2 Transverse Averaging

We represent the detailed model given by equation (3.11) in the following form:

$$\begin{aligned} F(c,p,Pe_r) &\equiv \nabla_\perp^2 c - p\left[\frac{\partial c}{\partial \tau} + u(\xi)\frac{\partial c}{\partial z} - \frac{p}{Pe_r^2}\frac{\partial^2 c}{\partial z^2} - s(\xi,\theta,z,\tau)\right] = 0 \quad (3.15) \\ &\equiv \mathbb{L}c - pN\left(c,p,Pe_r\right) = 0, \end{aligned}$$

where the concentration $c\left(\xi,\theta,z,\tau\right)$ depends on the local (transverse) variables $(\xi,\theta)$ as well as the macroscopic variables $z$ and $\tau$. The parameter $\frac{Pe_r^2}{p}\left(=\frac{\langle u\rangle\ L}{D_m}=Pe_L\right)$ is also known as axial Peclet number and represents the ratio of convection time $\tau_c$ and the axial diffusion time $\tau_{DL}=\frac{L^2}{D_m}$. We note that $\mathbb{L}\equiv\nabla_\perp^2$ is the transverse diffusion (Laplacian) operator in the region $\Omega=\{0<\xi<1\ \&\ 0<\theta<2\pi\}$ with Neumann (or periodic) boundary conditions on the boundary $\partial\Omega=\{\xi=1 \quad \& \quad 0<\theta<2\pi\}$. This is symmetric and has a simple zero eigenvalue with a constant eigenfunction independent of transverse coordinates. Equivalently, the eigenvalue problem

$$\begin{aligned} \mathbb{L}\psi \equiv \nabla_\perp^2\psi = -\mu\ \psi \text{ in } \Omega \quad , \\ \boldsymbol{\nabla}_\perp\psi\cdot\mathbf{n} = 0 \text{ on } \partial\Omega \end{aligned} \quad (3.16)$$

is self-adjoint ($\mathbb{L}^*=$ adjoint operator $=\mathbb{L}$) with respect to the inner product,

$$\langle v(\xi,\theta),\ w(\xi,\theta)\rangle = \frac{1}{A_\Omega}\iint_\Omega \xi\ \ v(\xi,\theta)\ \ w(\xi,\theta)\ d\xi\ d\theta \quad (3.17)$$

with $A_\Omega=\pi$. This eigenvalue problem has a simple zero eigenvalue $\mu_0=0$ with a constant eigenfunction $\psi_0\left(\xi,\theta\right)=1$. Moreover, for all $j\geqslant 0$, the eigenfunctions

$\psi_j(\xi,\theta)$ are chosen to satisfy the orthonormality condition

$$\left\langle \psi_i(\xi,\theta),\ \psi_j(\xi,\theta)\right\rangle = \delta_{ij} = \begin{cases} 0,\ i \neq j \\ 1,\ i = j \end{cases} \tag{3.18}$$

The range of $\mathbb{L}$ (containing transverse decaying modes) and the ker of $\mathbb{L}$ (containing master or transverse average mode) form an orthogonal complementary spaces which are used to split $c$ and $F(c,p)$ in the L-S procedure as explained earlier. Thus, we express concentration $c$ as,

$$c(\xi,\theta,z,\tau) = \langle c\rangle(z,\tau)\,\psi_0 + c'(\xi,\theta,z,\tau) \tag{3.19}$$

where, $\langle c\rangle$ is cross-sectional average concentration defined by

$$\langle c\rangle = \frac{1}{A_\Omega}\iint_\Omega \xi\ c(\xi,\theta,z,\tau)\ d\xi\ d\theta = \langle c,\psi_0\rangle, \tag{3.20}$$

and $c'(\xi,\theta,z,\tau)$ is the local (transverse) fluctuation. It follows from the orthogonality conditions that

$$\langle c',\psi_0\rangle = 0. \tag{3.21}$$

Similarly, the projection of the operator $F$ onto ker($\mathbb{L}$) leads to the coarse-grained model as given by equation (2.16) in the following form:

$$\langle N(c,p,Pe_r),\psi_0\rangle \equiv \frac{\partial\langle c\rangle}{\partial\tau} + \frac{\partial c_m}{\partial z} - \frac{p}{Pe_r^2}\frac{\partial^2\langle c\rangle}{\partial z^2} - \langle s\rangle(z,\tau) = 0 \tag{3.22}$$

where $c_m$ is the cup-mixing or velocity weighted concentration defined by

$$c_m = \langle u(\xi),c\rangle = \frac{1}{A_\Omega}\iint_\Omega \xi\ u(\xi)\ c(\xi,\theta,z,\tau)\ d\xi\ d\theta = \langle c\rangle + \langle u(\xi),c'\rangle, \tag{3.23}$$

and $\langle s\rangle(z,\tau)$ is transverse average of source/sink. We note that the global equa-

tion (3.22) is not in closed form since it contains two modes (cross-section averaged and cup-mixing concentrations). If we do not make distinction between the cup-mixing concentration and cross-sectional averaged concentration, the global equation (3.22) is in closed form. However, in that case, we neglect the effect of transverse dependency of concentration (caused by transverse molecular diffusion, velocity profile, and initial or inlet conditions). Therefore, the distinction between cup-mixing concentration and cross-sectional average concentration is necessary to include the transverse variations and to develop an accurate low-dimensional model.

It should be noted that there is also a compelling physical (and mathematical) reason for using the two modes $\langle c \rangle$ and $c_m$. The *diffusive modes* defined by the eigenvalue problem, equation (3.16), are useful to describe the evolution in time. When the velocity profile is not flat, the evolution in $z$ is described in terms of the *convective modes* defined by the following Graetz-Nusselt eigenvalue problem:

$$\begin{aligned} \nabla_{\perp}^2 \phi &= -\lambda \, u(\xi) \; \phi \quad \text{in } \Omega \\ \boldsymbol{\nabla}_{\perp} \phi \cdot \mathbf{n} &= 0 \quad \text{on } \partial\Omega. \end{aligned} \tag{3.24}$$

This is also a self-adjoint eigenvalue problem w.r.t. the convective (velocity-weighted) inner product

$$\langle v(\xi,\theta),\; w(\xi,\theta) \rangle_c = \frac{1}{A_\Omega} \iint_\Omega \xi \; u(\xi) \; v(\xi,\theta) \; w(\xi,\theta) \, d\xi \, d\theta \tag{3.25}$$

and has a simple zero eigenvalue $\lambda_0 = 0$ with a constant eigenfunction $\phi_0(\xi,\theta) = 1$. The cup-mixing concentration $c_m$ can be given by the convective inner product, $\langle \cdot, \cdot \rangle_c$, of the dominant convective mode $\phi_0$ with the concentration $c(\xi,\theta,z,\tau)$, i.e.,

$$c_m(z,\tau) = \langle c(\xi,\theta,z,\tau), \phi_0 \rangle_c . \tag{3.26}$$

We note that both eigenvalue problems are relevant in the transverse averaging method. In the following discussion, we present the averaging procedure using the diffusive eigenfunctions $\psi_i$ but consider some special cases where only either the diffusive or convective modes appear.

The last term of equation (3.23) implies that the local or transverse (diffusion and velocity gradient) effect on the macroscopic scale is included through the cup-mixing concentration. To quantify the local effect, we need to solve the local equation for $c^{'}$, which is obtained by the projection of the operator $F(c, p, Pe_r)$ onto range($\mathbb{L}$) and can be rewritten as

$$\mathbb{L}c' = p\ \left[\frac{\partial c'}{\partial \tau} + u(\xi)\frac{\partial c'}{\partial z} - \left\langle u(\xi), \frac{\partial c'}{\partial z}\right\rangle - \frac{p}{Pe_r^2}\frac{\partial^2 c'}{\partial z^2} + u'(\xi)\frac{\partial \langle c\rangle}{\partial z} - s'(\xi, \theta, z, \tau)\right] \tag{3.27}$$

where $u'(\xi)\ \left(= u(\xi) - 1 = 1 - 2\xi^2\right)$ is dimensionless velocity fluctuation and $s'(= s - \langle s\rangle)$ is the source fluctuation. Since $\mathbb{L}$ : Range($\mathbb{L}$)$\longrightarrow$ Range($\mathbb{L}$) is invertible with the orthogonality constraint given by equation (3.21), the implicit function theorem makes sure that the local equation (3.27) can be solved uniquely for $c'$ in terms of $\langle c\rangle$.

As discussed in the previous section, the local equation can be solved in various ways. One way is to use perturbation expansion in terms of powers of $p$ or reciprocal powers of $p$. The expansion in terms of powers of $p$ corresponds to the long time scaling that extends the validity of the averaged model at shorter times through the higher order derivatives in time and distributional derivatives, while the expansion in terms of reciprocal powers of $p$ corresponds to the short time scaling and leads to a polynomial in $\frac{\tau}{p}$. Since in most practical cases, only small $p$ are of interest and both perturbation expansions will lead to the exact solution of local equation when all order terms are included in the expansion, we use the long time scaling (expansion in $p$) to solve the local equation (3.27) for $c'$ in this section.

### 3.2.3 Solution of the Local Equation

To use a perturbation expansion in $p$ properly, we must assume the order of other parameters present in the model such that each term has proper order in $p$. Here, we assume that the radial Peclet number $Pe_r$ is of order $p^\gamma$ i.e., $Pe_r \sim O(p^\gamma)$ or $Pe_L \sim O(p^{2\gamma-1})$, $\gamma \leq \frac{1}{2}$. Three specific values of $\gamma$ are of interest: $\gamma = -\frac{1}{2}$ corresponding to the classical Taylor case (where the contribution of axial molecular diffusion to the overall dispersion is small as it appears only at orders $p^2$ and higher); $\gamma = 0$ corresponding to the Taylor-Aris case (where both the Taylor contribution and the axial molecular contribution or the Aris term are equally important and appear at order $p$); and, $\gamma = \frac{1}{2}$ corresponding to the Danckwerts limit (where the Taylor contribution is negligible). We note that for the first two cases, the leading order model is hyperbolic (or the solute dispersion is described by a Cauchy problem for $p = 0$) while for the third case, the leading order model is parabolic and is described by a boundary value problem, requiring an additional boundary condition at the exit of the tube. Though our procedure is applicable to all cases, our focus will be on the first two cases and in what follows, we present the averaging procedure for the case of $\gamma = 0$.

For the base state ($p = 0$), the local equation (3.27) with orthogonality constraint, equation (3.21), results in the local variable $c' = 0$ i.e., no transverse gradient of concentration. In this limit, the cup-mixing and the cross-sectional average concentrations are same. Hence, the local variable $c'$ can be expanded perturbatively in powers of the transverse Peclet number $p$ starting from the first power, as follows:

$$c'(\xi, \theta, z, \tau) = \sum_{n=1}^{\infty} p^n c'_n(\xi, \theta, z, \tau), \tag{3.28}$$

where $c_n$ are referred as the $n^{th}$ order correction. This expansion is similar to Maclaurin's series expansion where higher order corrections may be neglected

in the limit $p \to 0$. Using the expansion (3.28) in the local equation followed by comparison of the coefficients of each powers of $p$, we can write the equation for perturbed variable of each order as follows:

$$\nabla_{\perp}^2 c_1' = u'(\xi)\frac{\partial \langle c \rangle}{\partial z} - s'(\xi,\theta,z,\tau), \tag{3.29}$$

$$\nabla_{\perp}^2 c_2' = \frac{\partial c_1'}{\partial \tau} + u(\xi)\frac{\partial c_1'}{\partial z} - \left\langle u(\xi), \frac{\partial c_1'}{\partial z} \right\rangle, \tag{3.30}$$

$$\nabla_{\perp}^2 c_{n+1}' = \frac{\partial c_n'}{\partial \tau} + u(\xi)\frac{\partial c_n'}{\partial z} - \left\langle u(\xi), \frac{\partial c_n'}{\partial z} \right\rangle - \frac{1}{Pe_r^2}\frac{\partial^2 c_{n-1}'}{\partial z^2}, \qquad n \geq 2 \tag{3.31}$$

with boundary condition and orthogonality constraint given by

$$\boldsymbol{\nabla}_{\perp} c_n' \cdot \mathbf{n} = 0 \quad \text{on } \partial\Omega \text{ and } \langle c_n', \psi_0 \rangle = 0 \quad \forall\, n. \tag{3.32}$$

[As pointed out earlier, the above equations assume $\gamma = 0$ or $Pe_r$ is of order unity. For other values of $\gamma$, the equation for $c_n'$, $n \geq 2$ may be different]. The first order correction (perturbed variable $c_1'$) can be solved uniquely in terms of cross-sectional concentration ($\langle c \rangle$) using equations(3.29,3.32). The second order correction ($c_2'$) can be evaluated uniquely in terms of $c_1'$ and hence in terms of $\langle c \rangle$. Similarly the $n^{th}$ order correction ($c_n'$) can be solved uniquely in terms of $c_{n-1}'$ and hence in terms of $\langle c \rangle$ . Thus, we can solve each order correction $c_i'$ one by one, uniquely in terms of the cross-sectional average concentration $\langle c \rangle$ . Using the double Laplace transform in $z$ and $\tau$, the solution of local equation is given as follows (details in appendix):

$$c' = \sum_{n=1}^{\infty} p^n \sum_{j=1}^{n} \frac{\partial^{n-1} c_{n,j}'}{\partial z^{j-1}\, \partial \tau^{n-j}}, \ , \tag{3.33}$$

where, $c_{n,j}'$ are given by

$$\nabla_{\perp}^2\, c_{1,1}' = u'(\xi)\frac{\partial \langle c \rangle}{\partial z} - s'(\xi,\theta,z,\tau) \tag{3.34}$$

$$\nabla_{\perp}^{2}\, c'_{n+1,j} = c'_{n,j} + \left(u c'_{n,j-1} - \left\langle u, c'_{n,j-1}\right\rangle\right) - \frac{1}{Pe_r^2} c'_{n-1,j-2,} \tag{3.35}$$

with the zero flux boundary condition at $\xi = 1$ and satisfy the constraints $c'_{n,\,j}(\xi) = 0$ for $j \leqslant 0$ or $j > n$ and $\left\langle \psi_0,\ c'_{n,\,j}\right\rangle = 0$. For the special case of uniform release and no source/sink for $z$ and $\tau > 0$ where the source fluctuation $s' = 0$, the solution for $c'$ can be expressed in the form:

$$c' = \sum_{n=1}^{\infty} p^n \sum_{j=1}^{n} \Lambda_{n,\,j} \frac{\partial^n \langle c\rangle}{\partial z^j\ \partial \tau^{n-j}}, \tag{3.36}$$

where $\Lambda_{n,\,j}(\xi)$ are given by

$$\nabla_{\perp}^{2} \Lambda_{1,1} = u'(\xi), \tag{3.37}$$

$$\nabla_{\perp}^{2} \Lambda_{n+1,\,j} = \Lambda_{n,\,j} + u(\xi)\ \Lambda_{n,\,j-1} - \langle u(\xi),\ \Lambda_{n,\,j-1}\rangle - \frac{1}{Pe_r^2} \Lambda_{n-1,\,j-2},\ n \geq 1 \tag{3.38}$$

with the zero flux boundary condition at $\xi = 1$ and satisfy the constraints $\Lambda_{n,\,j}(\xi) = 0$ for$j \leqslant 0$ or $j > n$ and $\langle \psi_0,\ \Lambda_{n,\,j}\rangle = 0$.

For the general case of source/sink (initial, inlet or feed conditions), the solution for $c'$ given by equations(3.33-3.35) contains extra terms that arise due to the source fluctuation $s'(\xi, \theta, z, \tau)$. In this more general case, the cup-mixing concentration can be expressed in terms of cross-sectional average concentration $\langle c\rangle$ (details in appendix) as follows:

$$c_m - \langle c\rangle = \sum_{n=1}^{\infty} p^n \sum_{j=1}^{n} \langle u(\xi),\ \Lambda_{n,\,j}\rangle \frac{\partial^n \langle c\rangle}{\partial z^j\ \partial \tau^{n-j}} - \sum_{n=1}^{\infty} p^n \sum_{j=1}^{n} \left\langle \frac{\partial^{n-1} s'}{\partial z^{j-1}\ \partial \tau^{n-j}},\ \Lambda_{n,\,j}\right\rangle, \tag{3.39}$$

where $\Lambda_{n,j}(\xi)$, given by equation (3.37,3.38), are independent of $\theta$. We refer to the

above equation (3.39) as local equation.

It is interesting to note that the local equation (3.39) contains mixed derivative terms in time and space. These terms are very important in the accurate description of the evolution at short times (or distances). Once again, this accurate description of the evolution at short times through the proper solution of the local equation is the main difference between our approach and those in the literature. For example, the averaged model derived by the Central Manifold (CM) approach (Young and Jones, 1991; Mercer and Roberts, 1990; Balakotaiah and Chang, 1995) contains only spatial derivatives of $\langle c \rangle$ that results in loss of accuracy while describing short time behavior. The main reason for this is that the master mode in the CM approach is a (time independent) fixed or trivial state (such as $c = 0$) and hence can not describe the system behavior all the way back to initial times. For example, the CM expansion of Mercer and Roberts (1990, 1994) and Young and Jones (1991) for the laminar dispersion problem uses the wave number $\alpha$ as a perturbation parameter with base state $(\alpha, c) = (0, 0)$ that corresponds to $t \to \infty$, which is inconsistent with the initial condition at $t = 0$. In contrast, the master mode ($\langle c \rangle (z, \tau)$) considered in the L-S procedure can be time dependent. For example, for $p = 0$ and $Pe_r$ is of order unity, it satisfies the hyperbolic equation

$$\frac{\partial \langle c \rangle_0}{\partial \tau} + \frac{\partial \langle c \rangle_0}{\partial z} - \langle s \rangle (z, \tau) = 0. \tag{3.40}$$

Once again, we emphasize the limit $p = 0$ or the case of transverse diffusion time being zero. From the physics of the problem, this limit corresponds to the case of no radial gradients in the solute concentration, which is determined by a first-order hyperbolic equation or a Cauchy problem [In the Chemical Engineering literature, this convection dominated limit with zero radial diffusion time and infinite axial diffusion time is called plug flow limit]. Thus, the L-S technique uses an

expansion around the non-trivial plug flow base state that can vary with $z$ and $\tau$. A detailed comparison of the CM and L-S methods is considered in the next section.

Substitution of the local equation (3.39) in the global equation (3.22) gives the following exact averaged model in terms of the cross-section averaged concentration $\langle c\rangle(z,\tau)$:

$$\frac{\partial\langle c\rangle}{\partial\tau}+\frac{\partial\langle c\rangle}{\partial z}-\frac{p}{Pe_r^2}\frac{\partial^2\langle c\rangle}{\partial z^2}+\sum_{n=1}^{\infty}p^n\sum_{j=1}^{n}\langle u(\xi),\Lambda_{n,\,j}\rangle\frac{\partial^{n+1}\langle c\rangle}{\partial z^{j+1}\partial\tau^{n-j}} = \langle s\rangle(z,\tau)+\sum_{n=1}^{\infty}p^n\sum_{j=1}^{n}\frac{\partial^n\langle s',\Lambda_{n,\,j}\rangle}{\partial z^j\partial\tau^{n-j}}. \quad (3.41)$$

We note that the above reduced order model is valid for $z\geq 0$ and $\tau\geq 0$. We can separate the governing equation from the initial and inlet conditions by integration w.r.t. $z$ from $z=0$ to $0^+$ and w.r.t. $\tau$ from $\tau=0$ to $0^+$, which leads to the governing equation as

$$\frac{\partial\langle c\rangle}{\partial\tau}+\frac{\partial\langle c\rangle}{\partial z}-\frac{p}{Pe_r^2}\frac{\partial^2\langle c\rangle}{\partial z^2}+\sum_{n=1}^{\infty}p^n\sum_{j=1}^{n}\langle u(\xi),\ \Lambda_{n,\,j}\rangle\frac{\partial^{n+1}\langle c\rangle}{\partial z^{j+1}\partial\tau^{n-j}} = \langle s_f\rangle(z,\tau)+\sum_{n=1}^{\infty}p^n\sum_{j=1}^{n}\frac{\partial^n\left\langle s_f',\Lambda_{n,\,j}\right\rangle}{\partial z^j\partial\tau^{n-j}} \quad , \quad (3.42)$$

or, in two-mode form:

$$\frac{\partial\langle c\rangle}{\partial\tau}+\frac{\partial c_m}{\partial z}-\frac{p}{Pe_r^2}\frac{\partial^2\langle c\rangle}{\partial z^2}-\langle s_f\rangle(z,\tau)=0;\quad \tau>0,\quad z>0 \quad (3.43)$$

$$c_m-\langle c\rangle=\sum_{n=1}^{\infty}p^n\sum_{j=1}^{n}\langle u(\xi),\Lambda_{n,\,j}\rangle\frac{\partial^n\langle c\rangle}{\partial z^j\ \partial\tau^{n-j}} -\sum_{n=1}^{\infty}p^n\sum_{j=1}^{n}\frac{\partial^{n-1}\left\langle s_f',\ \Lambda_{n,\,j}\right\rangle}{\partial z^{j-1}\ \partial\tau^{n-j}};\ \tau>0,\ z>0 \quad (3.44)$$

while the inlet and initial conditions are given by

$$\langle c\rangle + \sum_{n=1}^{\infty} p^n \sum_{j=1}^{n} \langle u, \Lambda_{n,\,j}\rangle \frac{\partial^n \langle c\rangle}{\partial z^j \partial \tau^{n-j}} - \frac{p}{Pe_r^2}\frac{\partial \langle c\rangle}{\partial z}$$
$$= c_m - \frac{p}{Pe_r^2}\frac{\partial \langle c\rangle}{\partial z} = \langle u, c_{in}\rangle = c_{m,in}(\tau) \;\; @\; z = 0 \tag{3.45}$$

$$\langle c\rangle + \sum_{n=1}^{\infty} p^n \sum_{j=1}^{n-1} \langle u, \Lambda_{n,\,j}\rangle \frac{\partial^n \langle c\rangle}{\partial z^{j+1} \partial \tau^{n-1-j}}$$
$$= \langle c_0\rangle (z) + \sum_{n=1}^{\infty} p^n \frac{\partial^n}{\partial z^n} \langle c_0(\xi, \theta, z), \Lambda_{n,n}\rangle \quad @\; \tau = 0. \tag{3.46}$$

Here,

$$s_f'(\xi, \theta, z, \tau) = s_f(\xi, \theta, z, \tau) - \langle s\rangle_f (z, \tau). \tag{3.47}$$

Also note that, the existence of source/sinks of solute for $z$ or $\tau > 0$ does not change the initial or inlet conditions (as can be expected) but leads to additional terms in the governing equation. In case where the source/sink terms are only due to initial or inlet conditions, the coarse-grained model simplifies to,

$$\frac{\partial \langle c\rangle}{\partial \tau} + \frac{\partial \langle c\rangle}{\partial z} - \frac{p}{Pe_r^2}\frac{\partial^2 \langle c\rangle}{\partial z^2},$$
$$+ \sum_{n=1}^{\infty} p^n \sum_{j=1}^{n} \langle u(\xi),\ \Lambda_{n,\,j}\rangle \frac{\partial^{n+1} \langle c\rangle}{\partial z^{j+1}\, \partial \tau^{n-j}} = 0, \qquad \tau > 0,\ z > 0; \tag{3.48}$$

with the same inlet and initial conditions as given by equations (3.45,3.46).

We note that the reduced order model for $\langle c\rangle (z, \tau)$ contains higher order derivatives of $\langle c\rangle (z, \tau)$ w.r.t $z$ and $\tau$ while the original/detailed model contained only first derivative w.r.t $\tau$ and first and second derivatives w.r.t $z$. However, we do not require any additional initial/inlet conditions. This can be seen easily if we expand the solution $\langle c\rangle (z, \tau)$ also in a perturbation series in $p$ as follows:

$$\langle c\rangle = \langle c\rangle_0 + \sum_{i=1}^{\infty} p^i \langle c\rangle_i . \tag{3.49}$$

This leads to the following model equations at each order:

$$\begin{aligned}
\frac{\partial \langle c\rangle_0}{\partial \tau}+\frac{\partial \langle c\rangle_0}{\partial z} &= \langle s_f\rangle(z,\tau), \quad \tau>0,\ z>0\\
\langle c\rangle_0 &= \langle c_0\rangle(z) \ @\ \tau=0\\
\langle c\rangle_0 &= \langle u, c_{in}\rangle \ @\ z=0;
\end{aligned} \tag{3.50}$$

$$\begin{aligned}
\frac{\partial \langle c\rangle_1}{\partial \tau}+\frac{\partial \langle c\rangle_1}{\partial z}-\frac{1}{Pe_r^2}\frac{\partial^2 \langle c\rangle_0}{\partial z^2}+\langle u(\xi),\ \Lambda_{1,1}\rangle\frac{\partial^2 \langle c\rangle_0}{\partial z^2} &= \frac{\partial \langle s_f', \Lambda_{1,1}\rangle}{\partial z}, \ \ \tau>0,\ z>0\\
\langle c\rangle_1 &= \frac{\partial}{\partial z}\langle c_0(\xi,\theta,z),\Lambda_{1,1}\rangle \ @\ \tau=0\\
\langle c\rangle_1+\langle u,\Lambda_{1,1}\rangle\frac{\partial \langle c\rangle_0}{\partial z}-\frac{1}{Pe_r^2}\frac{\partial \langle c\rangle_0}{\partial z} &= 0 \ @\ z=0;
\end{aligned} \tag{3.51}$$

and for $i \geqslant 2$,

$$\begin{aligned}
\frac{\partial \langle c\rangle_i}{\partial \tau}+\frac{\partial \langle c\rangle_i}{\partial z}-\frac{1}{Pe_r^2}\frac{\partial^2 \langle c\rangle_{i-1}}{\partial z^2}+\sum_{n=1}^{i}\sum_{j=1}^{n}\langle u(\xi),\Lambda_{n,j}\rangle\frac{\partial^{n+1}\langle c\rangle_{i-n}}{\partial z^{j+1}\partial \tau^{n-j}} &\\
= \sum_{j=1}^{i}\frac{\partial^i \langle s_f', \Lambda_{i,\,j}\rangle}{\partial z^j \partial \tau^{i-j}}, \qquad \tau>0,\ z>0 &\\
\langle c\rangle_i+\sum_{n=1}^{i}\sum_{j=1}^{n-1}\langle u(\xi),\Lambda_{n,j}\rangle\frac{\partial^n \langle c\rangle_{i-n}}{\partial z^{j+1}\partial \tau^{n-1-j}} &= \frac{\partial^i}{\partial z^i}\langle c_0(\xi,\theta,z),\Lambda_{i,i}\rangle \ @\ \tau=0\\
\langle c\rangle_i-\frac{1}{Pe_r^2}\frac{\partial \langle c\rangle_{i-1}}{\partial z}+\sum_{n=1}^{i}\sum_{j=1}^{n}\langle u(\xi),\Lambda_{n,j}\rangle\frac{\partial^n \langle c\rangle_{i-n}}{\partial z^j \partial \tau^{n-j}} &= 0 @\ z=0.
\end{aligned} \tag{3.52}$$

Thus, the equation for each perturbed variable $\langle c\rangle_i$ is a first order PDE in $z$ and $\tau$ and does not need any additional inlet/initial condition.

### 3.2.4 Convergence of the Perturbation Solution to the Local Equation

Due to the coupling of the diffusive and convective modes, the coefficients appearing in the local equation or the averaged model can only be determined numerically (except for the first few). A further complication arises due to the double summation/mixed derivatives of $\langle c\rangle$ w.r.t. $z$ and $\tau$. Thus, we are not able to ob-

tain any analytical results related to the convergence of the local equation or the averaged model for arbitrary inlet or initial conditions. Here, we examine the convergence of the local equation for two special cases with negligible axial diffusion:

**Case 1: Flat Velocity Profile**

In this case, $u(\xi) = 1$, i.e., $u'(\xi) = 0$ or equivalently, there is no difference between the cup-mixing concentration and the transverse average concentration. Also, in this case , $\phi_i = \psi_i \ \forall \ i$ and $\langle \cdot, \cdot \rangle = \langle \cdot, \cdot \rangle_c$, i.e., the diffusive and convective modes are identical. The local equation in this case is given by

$$\nabla_{\perp}^2 c' = p \ \left[ \frac{\partial c'}{\partial \tau} + \frac{\partial c'}{\partial z} - s'(\xi, \theta, z, \tau) \right] \tag{3.53}$$

with zero flux boundary condition at $\xi = 1$. After taking double Laplace transform $\tau \rightarrow \omega$, $z \rightarrow \alpha$ and $c' \rightarrow \widehat{c'}$, equation (3.53) can be rewritten in Laplace domain as

$$\nabla_{\perp}^2 \widehat{c'} = p \ \left[ (\omega + \alpha) \, \widehat{c'} - \widehat{s'}\,(\xi, \theta, \alpha, \omega) \right], \tag{3.54}$$

with zero flux boundary condition at $\xi = 1$ and leads to the solution in the Laplace domain as

$$\widehat{c'} = \sum_{i=1}^{\infty} \frac{p \left\langle \widehat{s'}\,(\xi, \theta, \alpha, \omega), \psi_i \right\rangle}{\mu_i \left( 1 + p \frac{\omega + \alpha}{\mu_i} \right)} \psi_i, \tag{3.55}$$

or,

$$\widehat{c'} = \sum_{i=1}^{\infty} \sum_{j=0}^{\infty} (-1)^j \left( \frac{p}{\mu_i} \right)^{j+1} \left\langle (\omega + \alpha)^j \ \widehat{s'}\,(\xi, \theta, \alpha, \omega), \psi_i \right\rangle \psi_i. \tag{3.56}$$

The solution in the time domain may be expressed as

$$\widehat{c'} = \sum_{i=1}^{\infty} \sum_{j=0}^{\infty} (-1)^j \left( \frac{p}{\mu_i} \right)^{j+1} \left\langle \sum_{k=0}^{j} \begin{pmatrix} j \\ k \end{pmatrix} \frac{\partial^j s'\,(\xi, \theta, z, \tau)}{\partial z^k \partial \tau^{j-k}}, \psi_i \right\rangle \psi_i. \tag{3.57}$$

It follows from equation (3.56) that the solution given by equation (3.57) in powers of $p$ contains mixed derivatives in $z$ and $\tau$ and converges absolutely if $\frac{p(|\omega|+|\alpha|)}{\mu_1} < 1$, where $\mu_1$ is the non-zero eigenvalue of the transverse diffusion operator closest to the origin [$\mu_1 = 14.68\ (3.39)$ for axisymmetric (non-axisymmetric) inlet/initial conditions]. We also note that the Laplace domain solution for $\widehat{c'}$ given by equation (3.55) converges for all values of $p$. In other words, if the solution is expressed in terms of perturbation expansion as given in equation (3.57) or (3.56), the range of absolute convergence may be finite while if the series can be summed in a closed functional form as given in equation (3.55), the solution converges for all frequencies and for all values of $p$. For this special case, the averaged model is decoupled from the local equation. However, there is dispersion whenever the inlet or initial conditions are not uniform in the transverse coordinates. All the information about dispersion is contained in the local equation and the L-S method captures these exponentially small terms (in $z$ and $\tau$) in the form of mixed higher order derivatives w.r.t. $z$ and $\tau$.

**Case 2: Steady Laminar Flow**

The second limiting case we consider is that of steady-state dispersion, i.e., no dependence of $c$ and $s$ on time. In this case, the detailed model is given by

$$\frac{1}{u\left(\xi\right)}\nabla_{\perp}^{2}c = p\left[\frac{\partial c}{\partial z} - \frac{s(\xi,\theta,z)}{u\left(\xi\right)}\right] \tag{3.58}$$

with zero flux boundary condition at $\xi = 1$. If the source term contains only the inlet condition, i.e.,

$$s(\xi,\theta,z) = u\left(\xi\right)c_{in}\left(\xi,\theta\right)\delta\left(z\right),$$

the averaged model is given in terms of cup-mixing concentrations, $c_m = \langle c, \phi_0 \rangle_c$, as follows:

$$\frac{dc_m}{dz} - c_{m,in}\delta\left(z\right) = 0, \tag{3.59}$$

where $c_{m,in} = \langle c_{in}, \phi_0 \rangle_c$, while the local equation is given by

$$\frac{1}{u\left(\xi\right)} \nabla_{\perp}^2 c_m' = p \left[ \frac{\partial c_m'}{\partial z} - c_{m,in}'(\xi,\theta) \delta\left(z\right) \right], \tag{3.60}$$

with zero flux boundary condition at $\xi = 1$, where the local variable

$$c_m' = c - \langle c, \phi_0 \rangle_c \, \phi_0 = c - c_m \phi_0$$

and

$$c_{m,in}' = c_{in} - c_{m,in} \; \phi_0,$$

are orthogonal to the dominant convective mode $\phi_0$. Here, the local equation (3.60) can be solved exactly in terms of Graetz-Nusselt eigenfunctions $\phi_i\left(\xi,\theta\right)$:

$$c_m' = \mathcal{L}^{-1} \left[ \sum_{i=1}^{\infty} \frac{\langle c_{in}, \phi_i \rangle_c}{\alpha + \frac{\lambda_i}{p}} \phi_i \right] = \sum_{i=1}^{\infty} \exp\left( -\frac{\lambda_i \; z}{p} \right) \langle c_{in}, \phi_i \rangle_c \, \phi_i \tag{3.61}$$

$$\text{or,} \qquad c_m' = \sum_{i=1}^{\infty} \sum_{j=0}^{\infty} (-1)^j \left( \frac{p}{\lambda_i} \right)^{j+1} \delta^j\left(z\right) \langle c_{in}\left(\xi,\theta\right), \phi_i \rangle_c \, \phi_i. \tag{3.62}$$

For the general source $s\left(\xi,\theta,z\right)$, the solution of the local equation is given by

$$\begin{aligned} c_m' &= \mathcal{L}^{-1} \left[ \sum_{i=1}^{\infty} \frac{\left\langle \frac{\widehat{s}}{u}, \phi_i \right\rangle_c}{\alpha + \frac{\lambda_i}{p}} \phi_i \right] \\ &= \sum_{i=1}^{\infty} \int_0^z \exp\left[ -\frac{\lambda_i \; (z - z')}{p} \right] \left\langle \frac{s\left(\xi,\theta,z'\right)}{u\left(\xi\right)}, \phi_i \right\rangle_c \phi_i \; dz' \end{aligned} \tag{3.63}$$

$$\text{or,} \qquad c_m' = \sum_{i=1}^{\infty} \sum_{j=0}^{\infty} (-1)^j \left( \frac{p}{\lambda_i} \right)^{j+1} \left\langle \frac{\partial^j}{\partial z^j} \left[ \frac{s\left(\xi,\theta,z\right)}{u\left(\xi\right)} \right], \phi_i \right\rangle_c \phi_i. \tag{3.64}$$

We note that in this case, the natural modes appearing are the convective modes and the cup-mixing concentration $c_m$. Also, the solution given by equation (3.62) in powers of $p$ contains spatial derivatives in $z$ and converges absolutely if $\frac{p|\alpha|}{\lambda_1} < 1$,

where $\lambda_1$ is the first non-zero eigenvalue of the Graetz-Nusselt eigenvalue problem [$\lambda_1 = 12.84\ (4.16)$ for axisymmetric (non-axisymmetric) inlet conditions]. However, if the solution is summed in the closed functional form as in equation (3.61 or 3.63), it converges for all frequencies and for all values of $p$. Once again, the local and global equation are decoupled and all information about dispersion (or in this case the so called mixing length) is contained in the local equation and the L-S method captures these exponentially small terms (in $z$) in the form of higher order spatial derivatives w.r.t. $z$.

The two special cases examined above lead to the following observations: (i) When all the terms are retained, the perturbation solution to the local equation is identical to the exact solution within its range of convergence. (ii) The smallest range of absolute convergence of the perturbation expansion is obtained for the case of non-axisymmetric inlet/initial conditions and flat velocity profile. Thus, while a rigorous proof for the general case is difficult due to double expansion in $\tau$ and $z$, it appears that the averaged model given by equation (3.41) for the general case, converges absolutely (for $Pe_r \rightarrow \infty$ or negligible axial diffusion) provided $p(|\omega| + |\alpha|) < 3.39$. The range of absolute convergence for the case of finite $Pe_r$ has to be determined numerically and we do not pursue it here. (iii) If the perturbation series can be summed to a closed functional form, the solution converges for all frequencies and for all values of $p$ implying the exactness of the solution derived by L-S procedure. For further discussion on the convergence of the reduced order/truncated model, we refer to the recent article by Choquet and Mikelic (2009).

## 3.3 Analysis of Classical Taylor-Aris Dispersion

In the classical Taylor-Aris dispersion problem (dispersion in an infinitely long tube), only the radial scale is present i.e., $Pe_r$ is the only physical parameter present and there is no inlet condition. Hence, we can get rid off the transverse

Peclet number $p$ and represent the local and global equations(3.22,3.39) in terms of the radial Peclet number $Pe_r$ by non-dimensionalizing time and axial coordinate by transverse diffusion time and tube radius, respectively. Defining $t^* = \frac{t}{\tau_D} = \frac{\tau}{p}$ and $x^* = \frac{x}{a}$, leads to the low-dimensional model for classical Taylor-Aris dispersion in the following form:

$$\frac{\partial \langle c \rangle}{\partial t^*} + Pe_r \frac{\partial c_m}{\partial x^*} - \frac{\partial^2 \langle c \rangle}{\partial x^{*2}} - \langle s^* \rangle = 0; \tag{3.65}$$

$$c_m - \langle c \rangle = Pe_r \sum_{n=1}^{\infty} \sum_{j=1}^{n} \langle u',\ \Gamma_{n,j} \rangle \frac{\partial^n \langle c \rangle}{\partial x^{*j}\ \partial t^{*n-j}} - \sum_{n=1}^{\infty} \sum_{j=1}^{n} \left\langle \frac{\partial^{n-1} s^{*\prime}}{\partial x^{*j-1}\ \partial t^{*n-j}},\ \Gamma_{n,j} \right\rangle, \tag{3.66}$$

where

$$\Gamma_{n,j} = Pe_r^{j-1}\ \Lambda_{n,j}(\xi)\ = 0 \ \text{ for } \ j \leq 0 \ \text{ or } \ j > n,$$

and $\langle \psi_0,\ \Gamma_{n,\,j} \rangle = 0$, are given by

$$\nabla_\perp^2 \Gamma_{1,1} \ = \ u'(\xi), \tag{3.67}$$

$$\nabla_\perp^2 \Gamma_{n+1,\,j} \ = \ \Gamma_{n,\,j} + Pe_r \left( u(\xi)\ \Gamma_{n,\,j-1} - \langle u(\xi),\ \Gamma_{n,\,j-1} \rangle \right) - \Gamma_{n-1,\,j-2}, \tag{3.68}$$

with the zero flux boundary condition at $\xi = 1$, and, the source

$$s^*(\xi, \theta, x^*, t^*) = \zeta(\xi, \theta, x^*)\ \delta(t^*)$$

accounts only for the initial condition

$$c(t^* = 0) = \zeta(\xi, \theta, x^*).$$

The global and local equations(3.65,3.66) can be combined to give a coarse-grained model in terms of $\langle c \rangle$ as follows:

$$\frac{\partial \langle c \rangle}{\partial t^*} + Pe_r \frac{\partial \langle c \rangle}{\partial x^*} + Pe_r^2 \sum_{n=1}^{\infty} \sum_{j=1}^{n} \langle u', \Gamma_{n,j} \rangle \frac{\partial^{n+1} \langle c \rangle}{\partial x^{*j+1} \partial t^{*n-j}} - \frac{\partial^2 \langle c \rangle}{\partial x^{*2}} = \langle \zeta \rangle \delta(t^*) + Pe_r \sum_{n=1}^{\infty} \sum_{j=1}^{n} \frac{\partial^j \langle \zeta, \Gamma_{n,j} \rangle}{\partial x^{*j}} \delta^{n-j}(t^*). \quad (3.69)$$

Alternatively, if we do not scale $x$ and $t$, we get the averaged model in terms of powers of $\tau_D$ as

$$\frac{\partial \langle C \rangle}{\partial t} + \langle u \rangle \frac{\partial \langle C \rangle}{\partial x} - \frac{\langle u \rangle^2 \tau_D}{Pe_r^2} \frac{\partial^2 \langle C \rangle}{\partial x^2} + \sum_{n=1}^{\infty} \tau_D^n \sum_{j=1}^{n} \langle u(\xi), \Lambda_{n,\, j} \rangle \langle u \rangle^{j+1} \frac{\partial^{n+1} \langle C \rangle}{\partial x^{j+1} \partial t^{n-j}} = \langle C_0 \rangle (x)\ \delta(t) + \sum_{n=1}^{\infty} \tau_D^n \sum_{j=1}^{n} \langle u \rangle^j \frac{\partial^j \langle C_0, \Lambda_{n,j} \rangle}{\partial x^j} \delta^{n-j}(t). \quad (3.70)$$

Thus, the zeroth order model (that corresponds to $\tau_D = 0$) is hyperbolic in nature and is given by

$$\frac{\partial \langle C \rangle}{\partial t} + \langle u \rangle \frac{\partial \langle C \rangle}{\partial x} = \langle C_0 \rangle (x)\ \delta(t). \quad (3.71)$$

Similarly the first order model is given by

$$\frac{\partial \langle C \rangle}{\partial t} + \langle u \rangle \frac{\partial \langle C \rangle}{\partial x} - \langle u \rangle^2 \tau_D \left( \frac{1}{Pe_r^2} - \langle u(\xi), \Lambda_{1,1} \rangle \right) \frac{\partial^2 \langle C \rangle}{\partial x^2} = \langle C_0 \rangle (x)\ \delta(t) + \langle u \rangle \tau_D \frac{\partial \langle C_0, \Lambda_{1,1} \rangle}{\partial x} \delta(t), \quad (3.72)$$

and so forth. The form given by equation (3.70) is convenient for physical interpretation while equation (3.69) is convenient to evaluate the spatial moments and compare them with the exact results where the same scaling is used (Barton, 1983).

The coarse-grained model equation (3.69) may be used to evaluate the spatial moments or the actual concentration distribution to any desired degree of accu-

racy. This section is mainly focused on the analysis of temporal evolution of spatial moments using the averaged model (equation3.69) and comparison of the results with those obtained by direct methods (which do not use averaging) as well as other averaging methods such as the CM approach.

### 3.3.1 Temporal Evolution of Spatial Moments

The spatial moments are helpful in the understanding of the spreading process of the solute. Once we have low-dimensional model, spatial moments of any order can be determined. For example, integrating the coarse-grained model equation (3.69) over the entire axial domain ($x^*$ from $-\infty$ to $\infty$), we can find the zeroth moment which can be normalized to unity. Multiplying equation (3.69) by $x^*$ and integrating over the axial domain, we get the evolution equation for the first moment. Similarly, the evolution equation for $k$-th spatial moment ($k \geq 1$) can be derived by multiplying equation (3.69) by $x^{*k}$ and integrating it w.r.t. $x^*$ over the entire domain (from $-\infty$ to $\infty$), which results in the moment equation as follows:

$$\begin{aligned}
&\frac{dm_k}{dt^*} - k\ Pe_r\ m_{k-1} - k(k-1)\ m_{k-2} \\
&+Pe_r^2 \sum_{n=1}^{\infty}\sum_{j=1}^{n} \langle u', \Gamma_{n,j}\rangle \frac{\partial^{n-j} m_{k-j-1}}{\partial t^{*n-j}} (-1)^{j+1} \prod_{i=1}^{j+1}(k-i+1) - \langle \zeta_k \rangle\ \delta(t^*) \\
&\quad - Pe_r \sum_{n=1}^{\infty}\sum_{j=1}^{n} \left\langle \zeta_{k-j},\ \Gamma_{n,j} \right\rangle\ \delta^{n-j}(t^*)\ (-1)^j \prod_{i=1}^{j}(k-i+1) = 0. \qquad (3.73)
\end{aligned}$$

Here, $m_k$ are $k^{th}$ moment corresponding to cross-sectional average concentration $\langle c\rangle\,(x^*, t^*)$ and defined as follows:

$$m_k(t^*) = \frac{1}{A_\Omega} \int_{-\infty}^{\infty}\int_{0}^{2\pi}\int_{0}^{1} x^{*k}\xi\ c(\xi, \theta, x^*, t^*)\ d\xi\ d\theta\ dx^* = \int_{-\infty}^{\infty} x^{*j}\ \langle c\rangle\,(x^*, t^*)\ dx^*. \quad (3.74)$$

Similarly, $\zeta_k$ and $\langle \zeta_k \rangle$ are $k^{th}$ moment corresponding to initial concentration $c_0(\xi, \theta, x^*)$ and initial cross-sectional average concentration $\langle c_0\rangle\,(x^*)$, respectively; $\delta^n(t^*)$ is $n^{th}$

order distributional derivatives of the Dirac delta function in time $t^*$ and the transverse functions $\Gamma_{n,j}$ defined by equation (3.67, 3.68), depend only on the velocity profile (or geometry of the tube) and transverse boundary condition.

While any order moment can be evaluated sequentially using the equation (55), due to presence of distributional derivatives of Dirac delta function, it is convenient to analyze the moments in the Laplace domain ($t^* \rightarrow \omega$). The moment equation (3.73) in the Laplace domain can be written as

$$\omega M_k = k\ Pe_r\ M_{k-1} + k(k-1)\ M_{k-2} + Pe_r^2 \sum_{j=1}^{k-1} (-1)^j\ \frac{k!}{(k-j-1)!}\ \langle u', Y_j \rangle\ \ M_{k-j-1} + \langle \zeta_k \rangle\ +\ Pe_r \sum_{j=1}^{k} (-1)^j \frac{k!}{(k-j)!} \left\langle \zeta_{k-j},\ Y_j \right\rangle, \tag{3.75}$$

where, $\omega$ is the Laplace domain variable, $M_k(\omega)$ is the Laplace transform of the $k^{th}$ moment $m_k(t^*)$, and $Y_j$ are given in appendix by

$$Y_j = \sum_{n=1}^{\infty} \Gamma_{n,j} \omega^{n-j} = -\ \sum_m \frac{\langle Pe_r\ u\ Y_{j-1} - Y_{j-2}, \psi_m \rangle}{\mu_m + \omega} \psi_m, \tag{3.76}$$

$$\text{where } Y_1 = -\sum_m \frac{\langle u', \psi_m \rangle}{\mu_m + \omega} \psi_m.$$

They depend on the flow profile or geometry of the tube and can be expressed in terms of eigenvalues and eigenfunctions of the transverse diffusion operator given as follows:

$$\psi_{nm}(\xi, \theta) = \begin{cases} \psi^s_{nm} = \sqrt{2}\ \sin(n\theta)\ \frac{J_n\left(\sqrt{\mu_{nm}}\xi\right)}{\sqrt{\left(1 - \frac{n^2}{\mu_{nm}}\right)} J_n\left(\sqrt{\mu_{nm}}\right)}, & n \neq 0 \\ \psi^c_{nm} = \sqrt{2}\ \cos(n\theta)\ \frac{J_n\left(\sqrt{\mu_{nm}}\xi\right)}{\sqrt{\left(1 - \frac{n^2}{\mu_{nm}}\right)} J_n\left(\sqrt{\mu_{nm}}\right)}, & n \neq 0\ , \\ \psi_m = \frac{J_0\left(\sqrt{\mu_{0m}}\xi\right)}{J_0\left(\sqrt{\mu_{0m}}\right)}, & n = 0 \end{cases} \tag{3.77}$$

where $\mu_{nm}$ are roots of the equation:

$$J_n'\left(\sqrt{\mu}\right) = -\sqrt{\mu} J_{n+1}\left(\sqrt{\mu}\right) + n J_n\left(\sqrt{\mu}\xi\right) = 0. \tag{3.78}$$

Though a general initial release can be analyzed (in appendix), we consider here the initial release of a unit amount of solute distributed evenly, i.e., $\langle \zeta_0 \rangle = 1$ and $\zeta_1 = 0$, as considered by Chatwin (1970) and Barton (1983). In this case, zeroth moment turns out as,

$$m_0(t^*) = 1. \tag{3.79}$$

This is the total amount of solute present in the system at any time, which should be a constant as expected according to the material balance of the solute.

**Centroid**

The first moment is simplified (in appendix) as

$$m_1(t^*) = Pe_r \;\; t^* + \;\; Pe_r \sum_m a_m \; b_m \; \beta_m(t^*), \tag{3.80}$$

where,

$$\beta_m(t^*) = \frac{1}{\mu_m}\left(1 - e^{-\mu_m t^*}\right); \; a_m = \langle u', \psi_m \rangle = -\frac{8}{\mu_m}; \;\; b_m = \langle \zeta_0', \psi_m \rangle . \tag{3.81}$$

Here, $\psi_m$ are the azimuthally symmetric eigenfunctions of the transverse Laplacian operator corresponding to non-zero eigenvalues $\mu_m$, i.e.,

$$\psi_m(\xi) = \frac{J_0(\sqrt{\mu_m}\xi)}{J_0(\sqrt{\mu_m})}, \tag{3.82}$$

where $\mu_m$ ($> 0$) are the roots of equation $J_1(\sqrt{\mu}) = 0$. equation (3.80) derived from the averaged model agrees with the exact result derived by Barton (1983) using the full model. For the case of uniform release, $b_m = 0$ and hence the second term

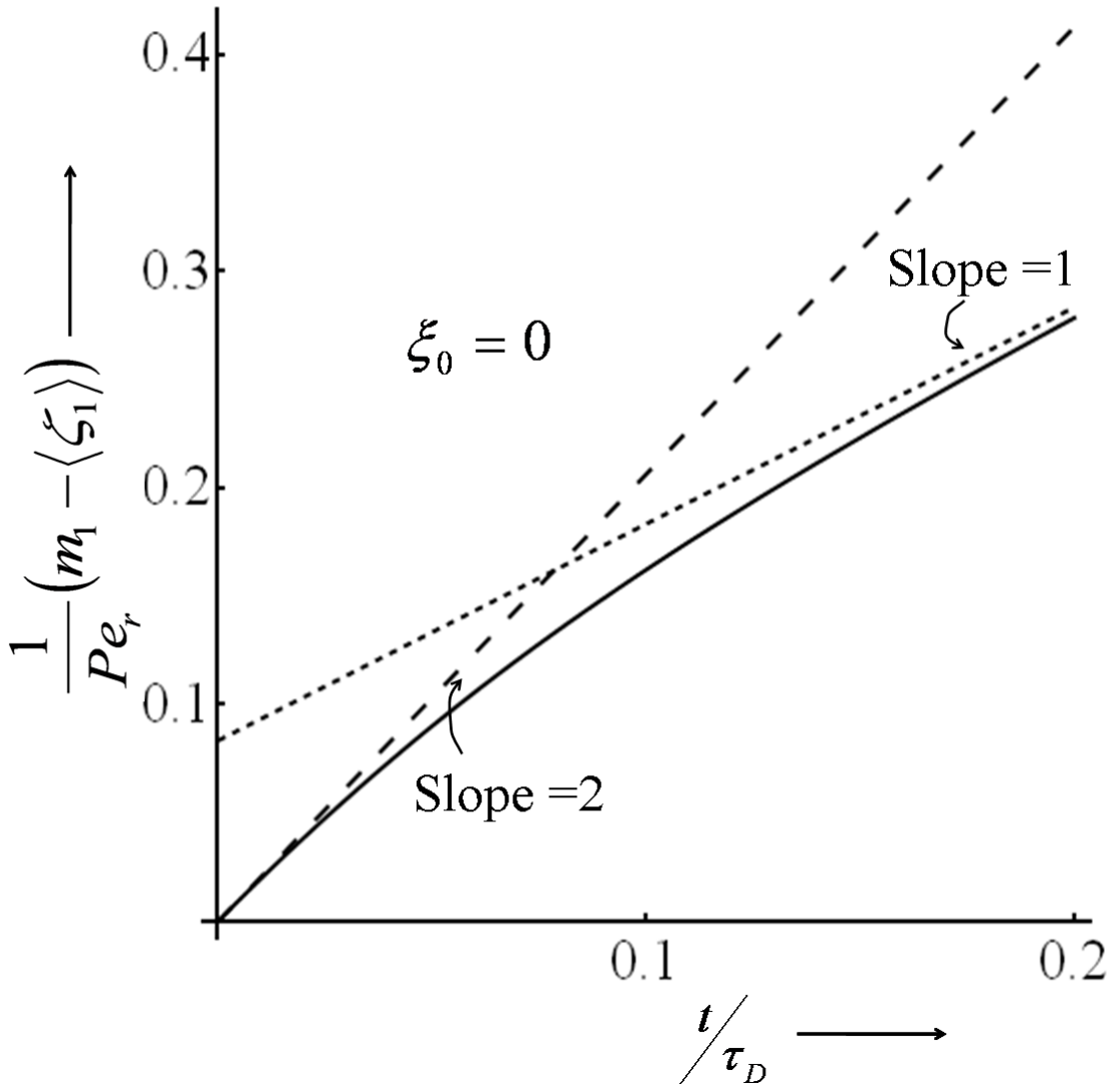


Figure 3.1: Time evolution of first moment for point release of solute at the tube center.

in equation (3.80) is zero that implies the centroid moves linearly with time with the transverse average velocity.

We note from equations(3.80, 3.81) that

$$\text{as } t^* \to 0,\ \beta_m(t^*) = \frac{1}{\mu_m}\left(1 - e^{-\mu_m t^*}\right) \to 0,$$

so the centroid $m_1(t^*) \to 0$, i.e., there is no centroid displacement. This can be seen from the Figures (3.1-3.3). The long time approximation of the centroid loca-

tion is given by

$$m_{1,long}(t^*) = \ Pe_r \ (t^* - \ \langle \zeta_0, \Gamma_{11} \rangle) \,, \tag{3.83}$$

where

$$\Gamma_{11} = \Lambda_{11} = -\frac{1}{24} \left(2 - 6\xi^2 + 3\xi^4\right) ,$$

i.e., after very long time, the centroid moves with average velocity and has a centroid displacement, $-Pe_r \ \langle \zeta_0, \Gamma_{11} \rangle$ as shown by dotted line in the Figure 3.1. Again, this long time asymptote agrees with the result derived by method of moments (Aris, 1956) and also by Center Manifold theory (Young and Jones, 1991; Mercer and Roberts, 1994). Similarly, the short time behavior can be observed by expanding exponential dependence $e^{-\mu_m t^*}$ in its Maclaurin's series and neglecting the higher order terms, which results in the centroid location as

$$m_{1,short}(t^*) = \ Pe_r \ \langle \zeta_0, u \rangle \ t^*. \tag{3.84}$$

This indicates that the overall movement of solute evolves linearly in time $t^*$ with its overall macroscopic or convective velocity $\langle \zeta_0, u \rangle$. In particular, for the special case of point release at any radial position $r = r_0$ or $\xi = \xi_0$, the short time approximation of the centroid location is given by $m_{1,short}(t^*) = Pe_r \ u(\xi_0) t^*$ in dimensionless form, or, $U(r_0) \, t$ in dimensional form. In other words, at smaller times, the centroid moves with the fluid velocity at the point of release (as expected).

While the general release can be analyzed, here we discuss the case of point release and compare our results with those in the literature. The temporal evolution of centroid for various points of solute release is shown in Figure 3.2. We see here that the initial slope of centroid increases monotonically from $0$ (corresponding to release at the wall, $\xi_0 = 1$) to 2 (corresponding to release at the center, $\xi_0 = 0$) corresponding to the velocities $u(\xi_0 = 1) = 0$ and $u(\xi_0 = 1) = 2$. Since, after long time, the centroid moves with average velocity as discussed above, the slope

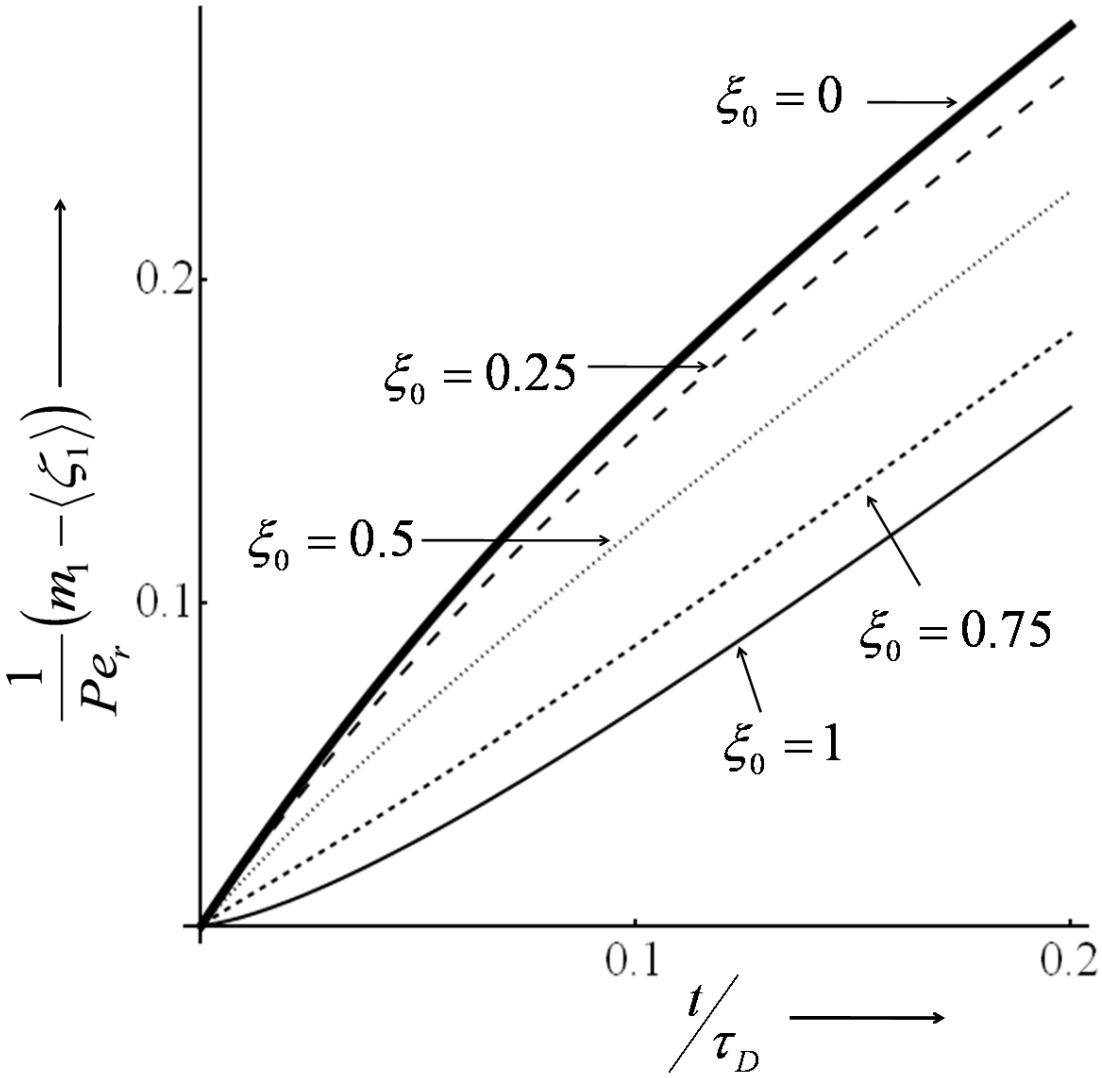


Figure 3.2: Centroid displacement versus time for point release of solute at different radial locations.

of centroid displacement versus time curve becomes unity (and independent of the point where the solute is released). In addition, all the curves are bounded between the curves for point release at the wall and at the center.

It is interesting to note that the intersection time for short and long time asymptotes of centroid is independent of radial Peclet number $Pe_r$ and depends only on the type of release. This time is given by

$$t_{inter\,sec\,tion} = \kappa_1 \tau_D, \quad \text{where} \quad \kappa_1 = -\frac{\langle\, \zeta_0, \Gamma_{11} \rangle}{\langle\, \zeta_0, u' \rangle}. \tag{3.85}$$

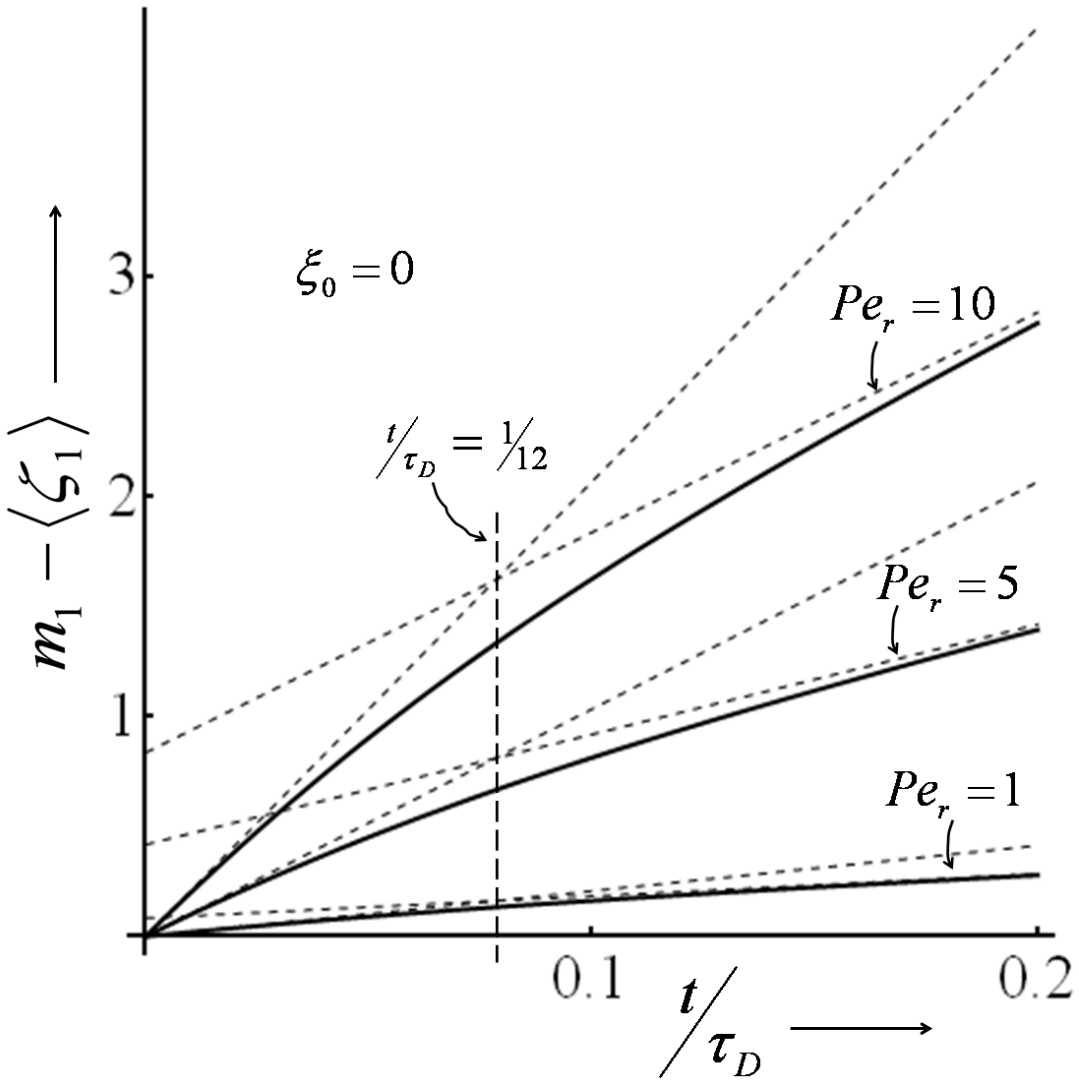


Figure 3.3: Centroid displacement versus time for point release at the center with varying $Pe_r$.

Thus, for point release at $\xi = \xi_0$,

$$\kappa_1 = \frac{\left(2 - 6\xi_0^2 + 3\xi_0^4\right)}{24\left(1 - 2\xi_0^2\right)}. \tag{3.86}$$

This can be seen from Figure 3.3 (for release at the center, $\kappa_1 = \frac{1}{12}$). For the point release at $\xi = \frac{1}{\sqrt{2}}$, the value of $\kappa_1 \to \infty$, i.e., the centroid curves at short and long times become parallel to each other. In addition, these figures also indicate that the difference between the centroid position and its long time approximation increases

with increase in the radial Peclet number $Pe_r$ at any fixed time. In other words, the time after which long time approximation is valid, increases with increase in $Pe_r$.

**Variance**

The second central moment or variance can be simplified (in appendix) for unit amount of release ($\langle\zeta_0\rangle = 1$) distributed evenly ($\zeta_1 = 0$) as follows:

$$\begin{aligned}\sigma^2(t^*) &= \langle\zeta_2\rangle + 2\left(1 + Pe_r^2 \sum_m \frac{a_m^2}{\mu_m}\right) t^* - 2Pe_r^2 \sum_m \frac{a_m^2\ \beta_m(t^*)}{\mu_m} \\ &\quad +2Pe_r^2 \sum_m a_m\ b_m \langle u'\ \psi_m, \psi_m\rangle \left(\frac{\beta_m(t^*) - t^* e^{-\mu_m t^*}}{\mu_m}\right) \\ &\quad +2Pe_r^2 \sum_m \sum_{n\neq m} a_n\ b_m \langle u'\ \psi_n, \psi_m\rangle \left(\frac{\beta_m(t^*) - \beta_n(t^*)}{\mu_n - \mu_m}\right) \\ &\quad -Pe_r^2 \left(\sum_m a_m\ b_m\ \beta_m(t^*)\right)^2,\end{aligned} \tag{3.87}$$

where the term

$$\left(1 + Pe_r^2 \sum_m \frac{a_m^2}{\mu_m}\right) = \left(1 + \frac{Pe_r^2}{48}\right) = D_{eff}$$

is the dimensionless effective (or Taylor-Aris) dispersion coefficient. Once again, we note that the above expression derived from the averaged model equation (3.69) is identical to that derived by Barton (1983) from the full model using the Fourier-Bessel expansions. We note from equations(3.81, 3.87) that

$$\text{as } t^* \to 0,\ \beta_m(t^*) = \frac{1}{\mu_m}\left(1 - e^{-\mu_m t^*}\right) \to 0,$$

and so the variance $\sigma^2(t^*) - \langle\zeta_2\rangle \to 0$, i.e., there is no variance deficit. This can be seen from the Figure 3.4 also, where, the temporal evolution of variance for uniform release and point release at the center is plotted. For the case of uniform release

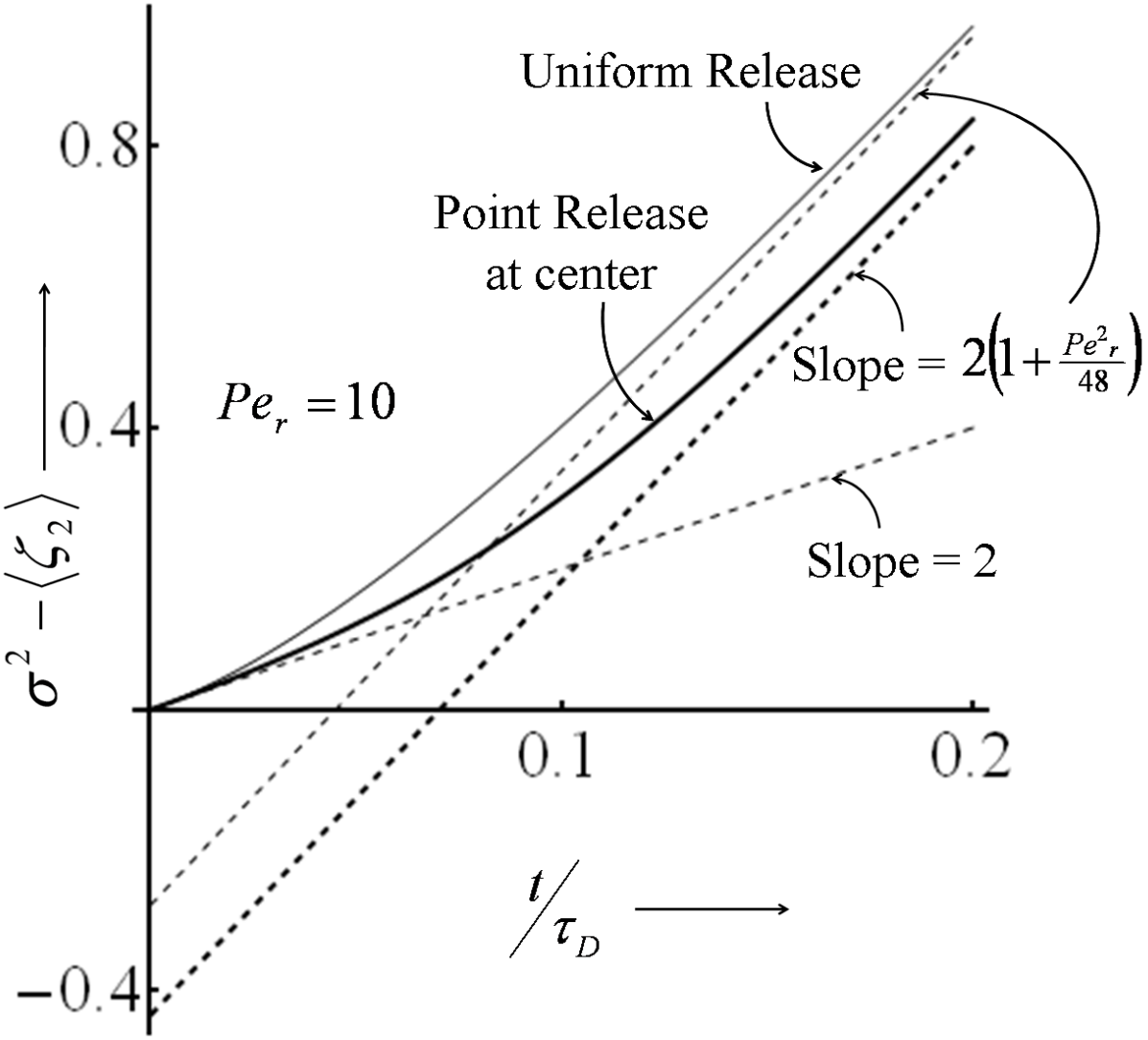


Figure 3.4: Temporal evolution of variance for uniform release and point release at the center.

($b_m = 0$), the variance is simplified as follows:

$$\sigma^2_{uniform\ release}(t^*) - \langle\zeta_2\rangle = 2D_{eff}\ t^* - \frac{Pe_r^2}{360} + 128Pe_r^2 \sum_m \frac{e^{-\mu_m t^*}}{\mu_m^4}\ , \qquad (3.88)$$

which shows the variance deficit $-\frac{Pe_r^2}{360}$ at large times. For any finite $Pe_r$, the variance deficit arising at very long time, is much smaller than the effective dispersion contribution $2D_{eff}\ t^*$. We note that for $t^* \to 0$, the term $-\frac{Pe_r^2}{360}$ cancels out with the series summation, $128Pe_r^2 \sum_m \frac{1}{\mu_m^4}$, which results in no variance deficit as shown in

Figure 3.4.

The long time approximation ($t^* \to \infty$, $e^{-\mu_m t^*} \to 0$) of variance for the general release is given by,

$$\sigma^2_{long\ time}(t^*) - \langle \zeta_2 \rangle = 2D_{eff}\, t^* + 2Pe_r \langle \zeta_0, \Gamma_{22} \rangle - Pe_r^2 \left( \frac{1}{360} + 2 \langle \zeta_0, \Gamma_{21} \rangle + \langle \zeta_0, \Gamma_{11} \rangle^2 \right), \tag{3.89}$$

where $\Gamma_{n,\,j}$ are given by equation (3.67, 3.68). The same result is obtained by the complete model using CM approach (Young and Jones, 1991; Mercer and Roberts, 1990, 1994). The long time asymptote shown in Figure 3.4 by dotted line, has a slope $2D_{eff}$ and a variance deficit equals to

$$\sigma^2_{deficit} = Pe_r^2 \left( \frac{1}{360} + 2 \langle \zeta_0, \Lambda_{22} - \Lambda_{21} \rangle + \langle \zeta_0, \Lambda_{11} \rangle^2 \right).$$

The amount of deficit depends upon the nature of the release and increases quadratically with $Pe_r$. For example, the point release at radial coordinates $(\xi_0, \theta_0)$ gives the deficit

$$\sigma^2_{deficit} = -\frac{Pe_r^2}{1152}(5 - 12\xi_0^2 + 36\xi_0^4 - 32\xi_0^6 + 9\xi_0^8)$$

while the uniform release gives the deficit equals to $-\frac{Pe_r^2}{360}$. Also, the variance deficit for the point release is non-monotonic in $\xi_0$, i.e., the variance curves for point release are not bounded by those for $\xi_0 = 0$ and $\xi_0 = 1$.

The short time approximation ($t^* \to 0$) for the general release leads to the variance as follows:

$$\sigma^2_{short\ time}(t^*) - \langle \zeta_2 \rangle = 2t^* + Pe_r^2 t^{*2} \left[ \langle \zeta_0, u^2 \rangle - \langle \zeta_0, u \rangle^2 \right] + O(t^{*3}) \tag{3.90}$$

This clearly shows that there is no variance deficit at $t^* \to 0$. For point release at

$(\xi_0, \theta_0)$, it reduces to

$$\sigma^2_{short\ time}(t^*) - \langle \zeta_2 \rangle = 2t^* = 2D_m t$$

in dimensional form, while for uniform release, it reduces to

$$\sigma^2_{short\ time}(t^*) - \langle \zeta_2 \rangle = 2t^* + \frac{Pe_r^2 t^{*2}}{3} = 2D_m t + \frac{\langle u \rangle^2 t^2}{3}$$

in dimensional form. It is interesting to note from equations(3.89, 3.90) or Figure 3.4 that the short time evolution of variance is governed by pure axial molecular diffusion

$$\left( \frac{1}{2} \frac{\partial\, \sigma^2}{\partial\, t^*} \bigg|_{t^* \to 0} = 1 \right)$$

while long time evolution is governed by effective dispersion

$$\left( \frac{1}{2} \frac{\partial\, \sigma^2}{\partial\, t^*} \bigg|_{t^* \to \infty} = D_{eff} \right).$$

This implies that the solute spreading process is dominated by axial molecular diffusion at short times and convection effects become important at larger time. Thus, there exists a critical time scale $\tau_{CD}$ beyond which the convection effects become important in the evolution process. This critical time scale can be quantified by analyzing the short time behavior. For the case of uniform release,

$$\sigma^2_{short\ time}(t^*) - \langle \zeta_2 \rangle = 2t^* + \frac{Pe_r^2 t^{*2}}{3} + O(t^{*3}) or 2D_m t + \frac{\langle u \rangle^2 t^2}{3} + O(t^3)$$

in dimensional form. The first term represents the effect of axial molecular diffusion and the second and higher order terms represent the effect of convection. If we have $\frac{\langle u \rangle^2 t^2}{3} << 2D_m t$ or equivalently, $t << \frac{6D_m}{\langle u \rangle^2}$, convection effects are much less important than the molecular diffusion effects. Thus, the critical time scale

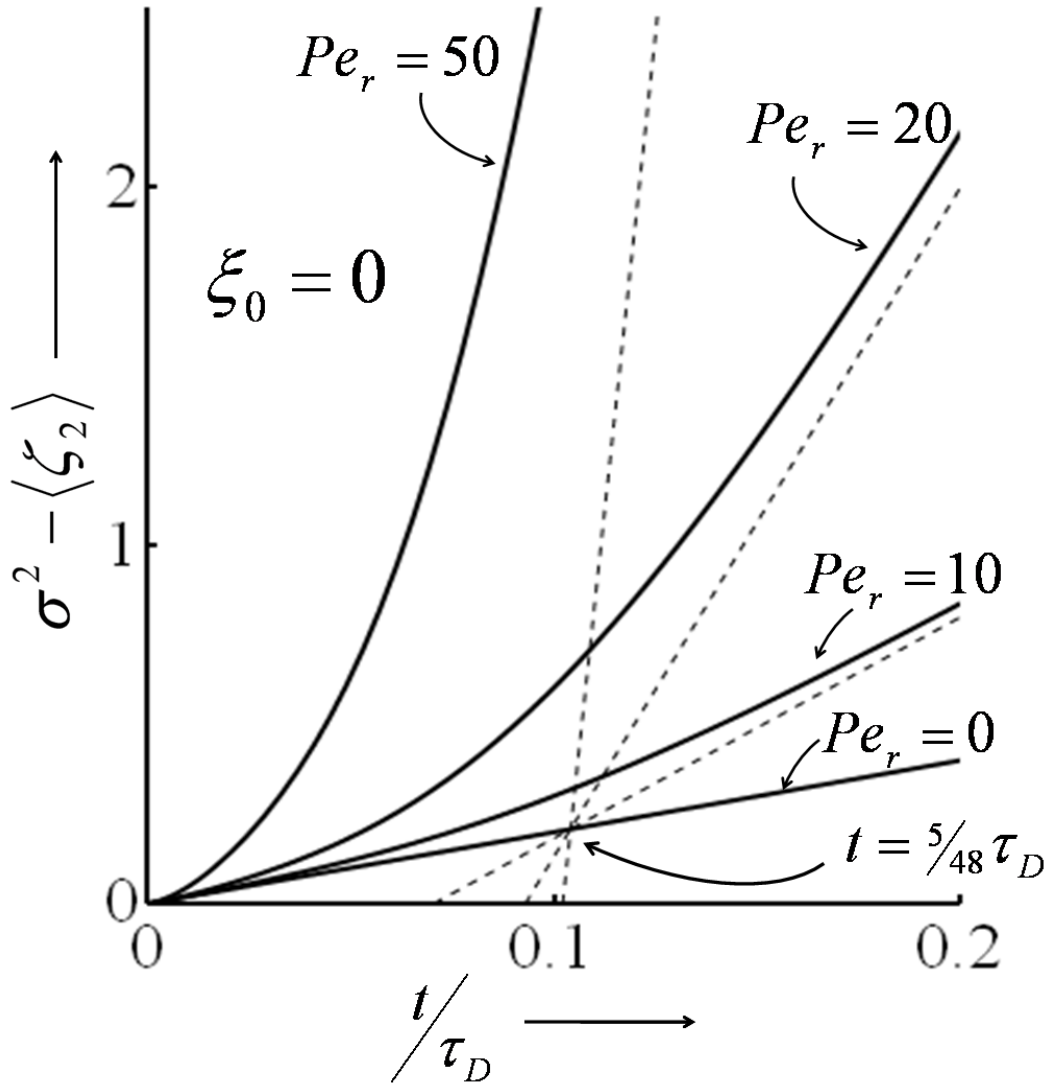


Figure 3.5: Evolution of variance corresponding to point release at the center with varying $Pe_r$.

$\tau_{CD} = \frac{D_m}{\langle u \rangle^2}$ (which we may term as "convection-diffusion time") characterizes the dominance of pure diffusion over convection effects. We note that the ratio of $\tau_D$ to $\tau_{CD}$ is the square of the radial Peclet number, $Pe_r$.

It is interesting to note from Figure 3.5 that the intersection time of the short and long time asymptote of variance is independent of the radial Peclet number $Pe_r$ and depends only on the nature of release. This time is given by

$$t_{inter\,sec\,tion} = \kappa_2 \tau_D,$$

where

$$\kappa_2 = 24\left(\frac{1}{360} + 2\left\langle\zeta_0, \Lambda_{22} - \Lambda_{21}\right\rangle + \left\langle\zeta_0, \Lambda_{11}\right\rangle^2\right).$$

For example, $\kappa_2 = \frac{1}{15}$ for uniform release and

$$\kappa_2 = \frac{Pe_r^2}{48}(5 - 12\xi_0^2 + 36\xi_0^4 - 32\xi_0^6 + 9\xi_0^8)$$

for point release at $(\xi_0, \theta_0)$. At the intersection point, the variance is given by

$$\sigma^2_{inter\,sec\,tion}(t^*) - \langle\zeta_2\rangle = 2\ \kappa_2.$$

In addition, the convection process is dominant after times $t >> t_{inter\,sec\,tion}$. However, the difference between variance and its asymptote increases with $Pe_r^2$, i.e., for large $Pe_r$, it takes very long time where convection dominates over transverse diffusion.

**Skewness**

The third central moment for the case of unit amount of solute distributed uniformly is simplified (in appendix) as,

$$\begin{aligned}\nu_3(t^*) - \langle\zeta_3\rangle = \\ 6Pe_r^3\ t^* \sum_m \sum_n \frac{a_n a_m}{\mu_m\ \mu_n}\left\langle u'\psi_n, \psi_m\right\rangle + 6Pe_r^3\ \sum_m \frac{a_m^2}{\mu_m^2}\left\langle u'\psi_m, \psi_m\right\rangle \left(t^*\ e^{-\mu_m t^*}\right) \\ -12Pe_r^3\ \sum_m \frac{a_m}{\mu_m}\left\{\frac{a_m}{\mu_m}\left\langle u'\psi_m, \psi_m\right\rangle + \sum_{n\,\neq\,m} \frac{a_n}{(\mu_n - \mu_m)}\left\langle u'\ \psi_n, \psi_m\right\rangle\right\}\beta_m(t^*).\end{aligned} \tag{3.91}$$

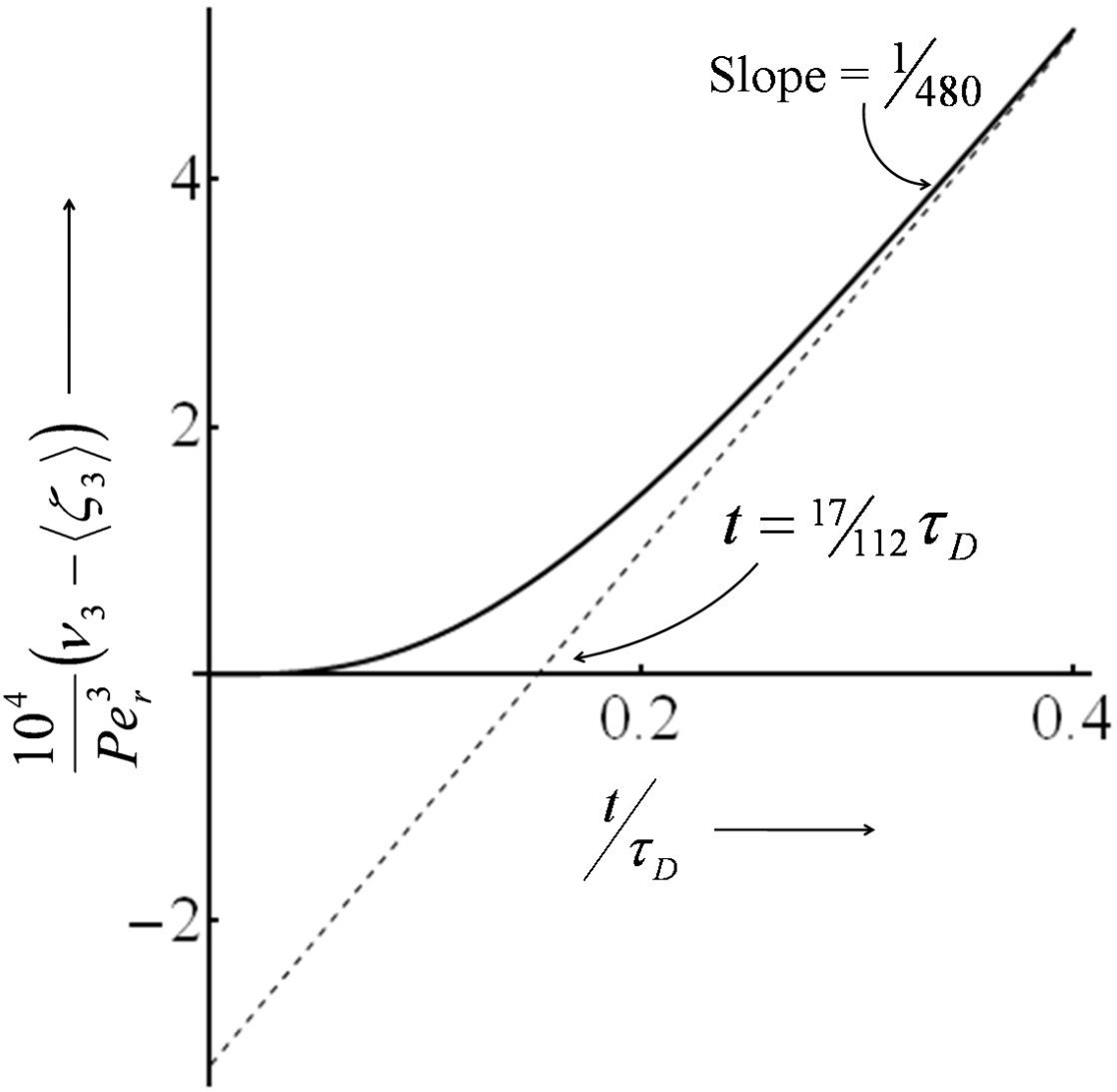


Figure 3.6: Evolution of the third central moment for uniform release of solute.

The above expression is identical to that given by Barton (1983) and can be further simplified to

$$\nu_3(t^*) - \langle\zeta_3\rangle = \frac{Pe_r^3}{480}\left(t^* - \frac{17}{112}\right) + 128Pe_r^3 \sum_m \frac{(t^*\mu_m^2 + 18\mu_m - 240)}{\mu_m^6} e^{-\mu_m t^*}. \quad (3.92)$$

equation (3.91, 3.92) leads to the third central moment consistent with the initial condition, i.e., for $t^* \to 0$, $\nu_3(t^*) - \langle\zeta_3\rangle \to 0$, as shown in Figure 3.6. The long time

approximation of the third central moment is given by

$$\nu_{3,long}(t^*) - \langle\zeta_3\rangle = \frac{Pe_r^3}{480}\left(t^* - \frac{17}{112}\right). \tag{3.93}$$

This expression is same as that derived by Central Manifold theory by Young and Jones (1991). The short time analysis shows that the third central moment satisfies the following condition

$$\left.\frac{d}{dt^*}\nu_3(t^*)\right|_{t^*=0} = \left.\frac{d^2}{dt^{*2}}\nu_3(t^*)\right|_{t^*=0} = \left.\frac{d^3}{dt^{*3}}\nu_3(t^*)\right|_{t^*=0} = 0,$$

and is given by

$$\nu_{3,short}(t^*) - \langle\zeta_3\rangle = \frac{8}{3}Pe_r^3\ t^{*4}, \tag{3.94}$$

which can be observed from the flatness of the curve near the origin in Figure 3.6. For the case of $\langle\zeta_2\rangle = \langle\zeta_3\rangle = 0$, the non-dimensional third central moment or skewness ($skew = \frac{\nu_3}{\sigma^3}$) is plotted on log-log graph in Figure 3.7, which shows that the skewness first increases and then decreases with time. As discussed above, if $\langle\zeta_2\rangle = \langle\zeta_3\rangle = 0$,

$$\nu_3 \sim \frac{8}{3}Pe_r^3\ t^{*4}$$

while

$$\sigma^2 \sim 2t^* + \frac{Pe_r^2}{3}t^{*2}$$

at short times ($t^* \to 0$). This implies that skewness evolves at short times as

$$skew_{short}(t^*) = \frac{Pe_r^3\ t^{*2}\sqrt{t^*}}{3\left(1 + \frac{Pe_r^2}{6}t^*\right)^{\frac{3}{2}}}, \tag{3.95}$$

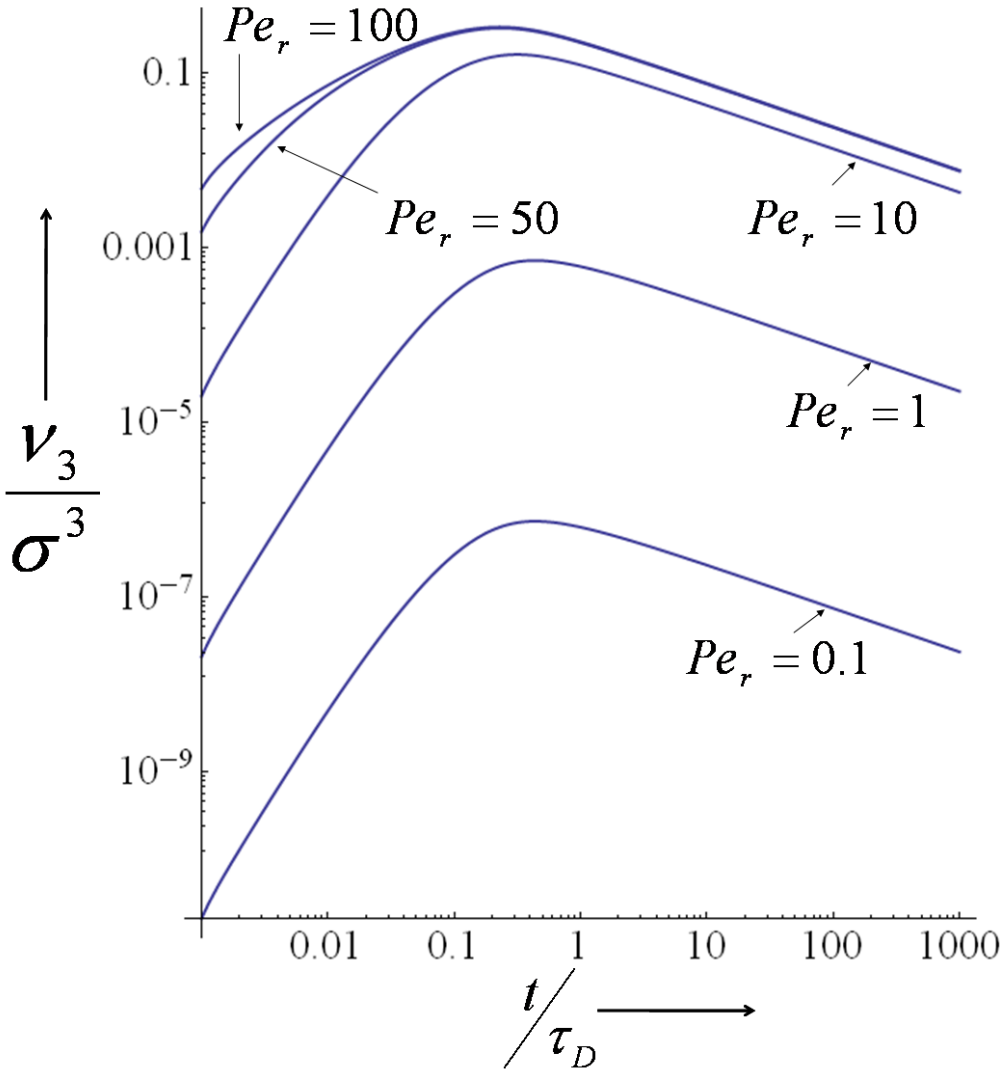


Figure 3.7: Log-Log plot of skewness versus time for uniform release and $\langle\zeta_2\rangle = \langle\zeta_3\rangle = 0$.

which is an increasing function of time. On the other hand, both the third central moment and the variance goes linearly with time, i.e.,

$$\nu_3 \sim \frac{Pe_r^3\, t^*}{480}$$

and

$$\sigma^2 \sim 2(1 + \frac{Pe_r^2}{48})t^*$$

at large times ($t^* \rightarrow \infty$). This implies that the skewness varies at large times as

$$skew_{long}(t^*) = \frac{Pe_r^3}{960(1+\frac{Pe_r^2}{48})^{\frac{3}{2}}} \frac{1}{\sqrt{2t^*}}. \tag{3.96}$$

Thus, for smaller values of $Pe_r$ ($Pe_r^2 << 48$), skewness varies as $skew \sim Pe_r^3\, t^{*2}\sqrt{t^*}$ at short times and $skew \sim Pe_r^3\, \frac{1}{\sqrt{t^*}}$ at large times, while at larger values of $Pe_r$ ($Pe_r^2 >> 48$), the skewness varies as $skew \sim \ t^*$ at short times and $skew \sim \frac{1}{\sqrt{t^*}}$ at large times (i.e., independent of $Pe_r$). These short and long time asymptotes can be seen clearly in Figure 3.7. The initial slope of the log-log curve is $\frac{5}{2}$ for smaller values of $Pe_r$ and becomes unity for large $Pe_r$ while the slope for $t \rightarrow \infty$ is $\left(-\frac{1}{2}\right)$, indicating that the skewness decreases slowly with time. Thus, the solute distribution approaches the Gaussian profile only at very large times. In addition, in the convection dominated limit ($Pe_r^2 >> 48$ and $t >> \tau_{CD}$), the variance varies as square of radial Peclet number $Pe_r$ leading to the skewness as follows:

$$skew_{convection}(t^*) = \frac{\left[\frac{1}{480}\left(t^* - \frac{17}{112}\right) + 128 \sum_m \frac{\left(t^*\mu_m^2 + 18\mu_m - 240\right)}{\mu_m^6} e^{-\mu_m t^*}\right]}{\left[\frac{1}{24}\ \left(t^* - \frac{1}{15}\right) + 128 \sum_m \frac{e^{-\mu_m t^*}}{\mu_m^4}\right]^{\frac{3}{2}}}, \tag{3.97}$$

$$= \begin{cases} \sqrt{24}\ t^* \text{ for } t^* \rightarrow 0 \\ \frac{\sqrt{6}}{10}\ \frac{1}{t^*} \text{ for } t^* \rightarrow \infty \end{cases} \tag{3.98}$$

i.e., in this limit, the skewness is independent of the radial Peclet number (Figure 3.7).

We note that the first three spatial moments predicted by the low-dimensional model are identical to the exact moments derived directly from the full model. We believe that this result extends also to the higher order spatial moments. This is due to the fact that the reduced order model derived by L-S technique is the exact Maclaurin's series expansion of the full model in terms of the transverse diffusion

time. Hence, it is valid for all times and converges for any general source/sink including point sources. In addition, while method of moments (Chatwin, 1970; Barton, 1983) can be used to determine spatial moments, the method is limited to linear problems only and can not provide exact concentration or any averaged concentration. Thus, the traditional method of determining spatial moments is not useful in determining the conversion of a reacting solute. On the contrary, as shown in previous sections, the L-S technique leads to the accurate low-dimensional model that can be used to calculate spatial or temporal moments as well as exact concentration $c(\xi, \theta, z, \tau)$ or any averaged concentration including experimentally measurable cup-mixing concentration.

### 3.3.2 Comparison of Lyapunov-Schmidt and Center Manifold Approaches for Averaging of Laminar Dispersion

In this section, we illustrate some of the advantages of L-S approach over CM approach. In an article titled "A Complete Model of Shear Dispersion in Pipes," Mercer and Roberts (1994) used the CM approach to obtain a reduced order model (Mercer and Roberts, 1994) in terms of cross-sectional average concentration to all orders in terms of the wave number. Their model consists of the governing equation

$$\frac{\partial \langle c \rangle}{\partial t^*} + Pe_r \frac{\partial \langle c \rangle}{\partial x^*} - D_{eff} \frac{\partial^2 \langle c \rangle}{\partial x^{*2}} - \sum_{n=3}^{\infty} A_n \, Pe_r^n \frac{\partial^n \langle c \rangle}{\partial x^{*n}} = 0; \qquad t^* > 0, \ -\infty < x^* < \infty, \tag{3.99}$$

and the projected initial conditions:

$$\langle c \rangle = \langle \zeta \rangle + Pe_r \frac{\partial \langle \zeta, f_1 \rangle}{\partial x^*} + Pe_r^2 \frac{\partial^2}{\partial x^{*2}} \left( \langle \zeta, f_2 \rangle - \frac{1}{720} \langle \zeta \rangle \right) + \sum_{n=3}^{\infty} Pe_r^n \frac{\partial^n \langle \zeta, V_n \rangle}{\partial x^{*n}}, \ @ \ t^* = 0, \tag{3.100}$$

where $A_n$ are constants, $V_n$ are some transverse functions, and

$$\begin{aligned} f_1 &= -\frac{1}{24}\left(2 - 6\xi^2 + 3\xi^4\right), \\ f_2 &= \frac{1}{11520}\left(31 - 180\xi^2 + 300\xi^4 + 200\xi^6 + 45\xi^8\right) \end{aligned} \tag{3.101}$$

and so on (Mercer and Roberts, 1994). Thus, using the definition of moments, we can determine them sequentially by multiplying the above model (3.99, 3.100) by $x^{*k}$ and integrating from $-\infty$ to $\infty$ with $k = 1, 2, 3....$For the case of unit amount of solute released at $x^* = 0$ (i.e., $\zeta_i = 0 \; \forall \; i \neq 0$ and $\langle \zeta_0 \rangle = 1$), the zeroth moment is given by

$$\begin{aligned} \frac{dm_0}{dt^*} &= 0; \quad t^* > 0, \\ m_0 = \; \langle \zeta_0 \rangle &= 1, \quad @ \;\; t^* = 0, \end{aligned} \tag{3.102}$$

which leads to

$$m_0 = \langle \zeta_0 \rangle = 1. \tag{3.103}$$

Similarly, the first moment is given by

$$\begin{aligned} \frac{dm_1}{dt^*} - Pe_r \; m_0 &= 0; \;\; t^* > 0, \\ m_1 = \langle \zeta_1 \rangle - Pe_r \;\; \langle \zeta_0, f_1 \rangle \quad &, \quad @ \;\; t^* = \;\; 0, \end{aligned} \tag{3.104}$$

which leads to

$$m_1 = Pe_r \;\; (t^* - \langle \zeta_0, f_1 \rangle) \;\; = 0, \tag{3.105}$$

and the second moment is given by

$$\begin{aligned} \frac{dm_2}{dt^*} - 2Pe_r \; m_1 - 2D_{eff} \; m_0 &= 0; \;\; t^* > 0, \\ m_2 = \langle \zeta_2 \rangle - 2Pe_r \;\; \langle \zeta_1, f_1 \rangle + 2 \; Pe_r^2 \left( \langle \zeta_0, f_2 \rangle - \frac{1}{720} \langle \zeta_0 \rangle \right), \;\; @ \;\; t^* &= 0, \end{aligned} \tag{3.106}$$

which leads to

$$m_2 = 2\ Pe_r^2 \left( \langle \zeta_0, f_2 \rangle - \frac{1}{720} \right) + 2D_{eff}\ t^* + Pe_r^2\ \left( t^{*2} - 2\ \langle \zeta_0, f_1 \rangle\ t^* \right) \tag{3.107}$$

This results in the following formula for the variance:

$$\sigma^2 = m_2 - m_1^2 = 2D_{eff}\ t^* + \ Pe_r^2 \left( 2\ \langle \zeta_0, f_2 \rangle - \langle \zeta_0, f_1 \rangle^2 - \frac{1}{360} \right). \tag{3.108}$$

We note that the centroid location and variance predicted by the complete model (Mercer and Roberts, 1994) derived from CM approach, is same as the long time approximation of that derived by the L-S procedure and have centroid displacement as well as variance deficit. We note that these results for the first two moments do not change even if we include third or all other higher order terms in the wave number (Mercer and Roberts, 1994). In fact, it is easily seen that the above model predicts correctly the asymptotic behavior of all the moments in the limit of $t \to \infty$ but can lead to negative moments for short times, i.e., the higher order terms (in the wave number expansion) lead to correct asymptotic behavior of higher moments but do not lead to any systematic improvement of the lower moments. On the contrary, higher order terms in the reduced order model derived by L-S procedure improve the moments in terms of distributional derivatives of Dirac-delta functions that capture the exponentially small terms. It can be illustrated by the truncated third order ($O(p^3)$) model (with uniform release):

$$\begin{aligned} &\frac{\partial \langle c \rangle}{\partial t^*} + Pe_r\ \frac{\partial \langle c \rangle}{\partial x^*} - (1 - \langle u', \Gamma_{1,1} \rangle)\ \frac{\partial^2 \langle c \rangle}{\partial x^{*2}} \\ &\quad + Pe_r^2\ \left[ \langle u', \Gamma_{2,1} \rangle\ \frac{\partial^3 \langle c \rangle}{\partial x^{*2}\ \partial t^*} + \langle u', \Gamma_{2,2} \rangle\ \frac{Pe_r}{576} \frac{\partial^3 \langle c \rangle}{\partial x^{*3}} \right] \\ &\quad + Pe_r^2\ \left[ \langle u', \Gamma_{3,1} \rangle\ \frac{\partial^4 \langle c \rangle}{\partial x^{*2}\ \partial t^{*2}} + \langle u', \Gamma_{3,2} \rangle\ \frac{\partial^4 \langle c \rangle}{\partial x^{*3}\ \partial t^*} + \langle u', \Gamma_{3,3} \rangle\ \frac{\partial^4 \langle c \rangle}{\partial x^{*4}} \right] \\ &\qquad = \delta(x^*)\delta(t^*) \end{aligned} \tag{3.109}$$

that leads to the variance

$$\sigma^2_{truncated}(t^*) = 2\left[1 - Pe_r^2\left\langle u', \Gamma_{1,1}\right\rangle\right] t^* - 2Pe_r^2\left[\left\langle u', \Gamma_{2,1}\right\rangle + \left\langle u', \Gamma_{3,1}\right\rangle \delta\left(t^*\right)\right]$$
$$= 2\left(1 + \frac{Pe_r^2}{48}\right) t^* - \frac{Pe_r^2}{360} - \frac{13Pe_r^2}{69120}\delta\left(t^*\right), \tag{3.110}$$

which contains the long time variance deficit $\frac{Pe_r^2}{360}$ as derived by the method of moments (Aris, 1956) and the CM approach (Young and Jones, 1991; Mercer and Roberts, 1994), as well as the term containing the Delta function. If we include all higher order derivative terms in time but only up to second order derivative in $x^*$, the terms containing distributional derivatives may be summed in closed functional form to give the exponential term $\left(128Pe_r^2\sum_m \frac{\exp(-\mu_m t^*)}{\mu_m^4}\right)$ in equation (3.88). As explained earlier, the higher order time derivative terms extend the validity of the reduced order model derived by the L-S procedure to shorter times. In fact, to obtain the $n^{th}$ spatial moment accurately for all time including $t \to 0$, the spatial derivatives of order higher than $n$ can be dropped out in the reduced order model, but we must retain temporal derivative terms of all orders. In contrast, to obtain the $n^{th}$ order spatial moment for long times ($t \to \infty$), we need to retain only spatial or mixed derivative terms of order $\tau_D^n$ in the reduced order model, equation (3.70).

The CM approach as applied to the shear dispersion problem (Mercer and Roberts, 1994) uses a perturbation expansion in terms of the wave number $\alpha\left(=\frac{\partial}{\partial x}\right)$ around the base state $(\alpha, c) = (0, 0)$. However, for $\alpha = 0$, the projected initial condition in the complete model (Mercer and Roberts, 1994) reduces to $\langle c\rangle = \langle\zeta\rangle$ @ $\tau = 0$ that is inconsistent with the base state. While the complete model (Mercer and Roberts, 1994) derived by CM approach leads to correct asymptotic moments ($t \to \infty$), no improvement is possible at short times because of the following reasons: (i) CM theorem (Carr, 1981) states that the reduced order model derived by the CM approach has an error of order $\exp\left(-\frac{\mu_1 t}{\tau_D}\right)$, i.e., it can not capture the

exponentially small transients and (ii) The projected initial condition (Mercer and Roberts, 1994) is selected such that the solution given by the reduced order model agrees with that of the exact solution in the limit of $t \to \infty$. Thus, in the CM approach, the true dynamics is missed by the reduced order model from $t = 0$ to the time of approach to the CM (which is of the order of $\frac{\tau_D}{\mu_1}$). Hence, only the zeroth moment is predicted exactly by the CM approach as it is independent of time.

The range of convergence of the complete model (Mercer and Roberts, 1994) derived by CM approach can not be larger than that given by $|\alpha| < \frac{\mu_1}{p}$. In fact, as shown by Mercer and Roberts (1994), the actual range of convergence is even smaller $(p\,|\alpha| < 2.2)$. In contrast, the range of convergence of the reduced order model derived by L-S procedure is at least as large as given by $|\alpha| < \frac{\mu_1}{p}$. We also note that for the case of time dependent sources, the *ansatz* used for $c'$ in the CM approach (Young and Jones, 1991) does not have the correct form as it is expressed in terms of only spatial derivatives of transverse averaged concentration while the exact expression must contain the mixed time and spatial derivatives as illustrated. While a detailed comparison is beyond the scope of this work, we summarize here some important differences for future investigation: (i) The L-S method of averaging can be applied to steady-state or equilibrium models where the governing equation is not an evolution equation either in space or time. In contrast, the CM method has limited applicability to such models. (ii) In the L-S method, the base state can be time dependent, and, time dependent inlet conditions/sources can be treated. In the CM method, base state (fixed point) is generally assumed to be time independent. While time dependent center manifolds can be treated (Cox and Roberts, 1991), the forcing terms have to be small (quadratic or higher order). Also, in the CM approach, the initial/inlet conditions are assumed to be close to the fixed point. In contrast, there is no restriction on initial/inlet conditions in the L-S technique. (iii) When applied to the averaging of transient models, the L-S method

can capture exponentially small terms in time while these terms are ignored in the CM method (Carr, 1981). As illustrated earlier, the L-S method leads to reduced order model containing higher order derivatives in time when a perturbation expansion is used for small $p$. These higher order time derivatives extend the validity of the model to short times (or, capture the exponentially small transients). (iv) When a perturbation expansion is used to solve for the CM, the range of validity of the CM expansion can not be greater than that given by $\left|\frac{\omega\ p}{\gamma}\right| < 1$, where $\gamma$ is the real part of eigenvalue close to zero and $\omega$ is frequency or wave number (Mercer and Roberts, 1994; Cox and Roberts, 1995). In contrast, when a perturbation expansion is used to solve the local equation in the L-S method, the region of convergence of the expansion appears to be at least as large as that given by $\left|\frac{\omega\ p}{\gamma}\right| < 1$. In addition, time scale separation is convenient but not necessary in the L-S formalism. In contrast, the application of CM method requires time scale separation.

## 3.4 Truncated Regularized Two-Mode Models

The classical Taylor-Aris dispersion problem discussed in the previous section, while theoretically simpler and interesting, is unrealistic from a practical point of view for the following reasons: (a) In real situations, the tube is of finite length and hence entrance and exit conditions must be considered. (b) It is difficult to measure the spatial moments at any fixed time as it requires the simultaneous evaluation of the solute axial concentrations at all different locations. (c) The cross-section averaged concentration $\langle c \rangle (z, \tau)$ is not the measured concentration in the experiments but it is the velocity weighted or cup-mixing concentration $c_m(z, \tau)$. (d) The measurement of $c_m(z, \tau)$ either at the tube exit or some other fixed location as a function of time leads to the experimental determination of the temporal moments instead of the spatial moments considered in the classical Taylor dispersion theory. In addition to these practical considerations, we note that while it is possible to derive the low-dimensional model using the L-S technique to any order in the perturba-

tion parameter, the main reason for seeking reduced order models is to include the small scale (local) effects without complicating the model. Thus, in most practical applications, the first few terms may be sufficient to retain the essential physics of the system with sufficient quantitative accuracy. For these reasons, we would like to truncate the reduced order model at some finite order (preferably at the lowest order at which all scales are represented) and express it in terms of experimentally measurable quantities. In this section, we consider these practical aspects, compare the different forms of the truncated models and discuss how to extend their range of validity by a procedure called regularization (Takeshi, 1999).

We note that the two-mode form of the averaged model consisting of $\langle c \rangle$ and $c_m$ , equations(3.43-3.46), is applicable for a semi-infinite tube or a finite tube provided the axial length scale $L$ is interpreted as the downstream distance at which the solute concentration is measured. As we have noted earlier, the two-mode form is more convenient than the single mode form for physical interpretation of the local and global equations. Further, we note that in the two-mode form, the global equation (3.43) is exact to all orders in $p$. Thus, any error in the averaged model is due to the finite truncation of the local equation (3.44) and the initial/inlet condition.

As noted earlier, the two-mode model given by equation (3.43-3.46)) is valid only when $Pe_r = O(p^\gamma)$ with $\gamma \leq 0$. Due to space limitation, here we discuss only two limiting cases within this region of parameters: Case (A) with $\gamma = -\frac{1}{2}$ or the convection dominated (Taylor) case in which the axial diffusion term is negligible, and Case (B) with $\gamma = 0$ or the diffusion-convection (Taylor-Aris) case in which both axial and transverse diffusional effects are comparable. A third limiting case of $\gamma = \frac{1}{2}$ or the (Danckwerts limit) in which the effect of transverse velocity gradients and molecular diffusion are small compared to the axial diffusion and convection, will be considered in future publications.

### 3.4.1 Case A: Convection Dominated Hyperbolic (Taylor) Limit:

The case of $Pe_r = O(p^{-1/2})$ corresponds to negligible axial (or macroscale) diffusion (mixing). In this limit, truncation of the two-mode model, equation (3.43-3.46)) at order $p$ leads to the model

$$\frac{\partial \langle c \rangle}{\partial \tau} + \frac{\partial c_m}{\partial z} - \langle s_f \rangle (z, \tau) = 0, \tag{3.111}$$

$$c_m - \langle c \rangle = -\frac{p}{48} \frac{\partial \langle c \rangle}{\partial z} - p \left\langle s'_f, \Lambda_{1,1} \right\rangle + O(p^2), \quad \tau > 0, z > 0 \tag{3.112}$$

with inlet and initial conditions:

$$c_m = c_{m,in}(\tau) + O(p^2) \ @ \ z = 0, \tag{3.113}$$

$$\langle c \rangle = \langle c_0 \rangle (z) + p \frac{\partial}{\partial z} \langle c_0(\xi, \theta, z), \ \Lambda_{1,1} \rangle + O(p^2) \quad @ \quad \tau = 0, \tag{3.114}$$

where $\Lambda_{1,1}(\xi) = -\frac{1}{24}\left(2 - 6\xi^2 + 3\xi^4\right)$. Based on our earlier discussion, we note that the above truncation of the perturbation expansion is valid only for wave numbers or frequencies satisfying $p|\omega| < \mu_1$. Here, $\mu_1 = 14.68$ $(3.39)$ is the first non-zero eigenvalue of the transverse diffusion operator for axisymmetric (non-axisymmetric) inlet/initial conditions. Thus, the truncated first order model, equation (3.111-3.114), has error of $O(p^2)$ provided the spatial frequencies contained in the initial conditions $c_0(\xi, \theta, z)$ or the temporal frequencies contained in the inlet conditions $c_{in}(\xi, \theta, \tau)$ satisfy $p|\omega| < \mu_1$. For step or pulse (Delta function) inputs where the condition is not satisfied, the error is $O(p^2)$ provided $z, \tau > \frac{p}{\mu_1}$. In all other cases, the error may not be small.

The local equation (3.112) describes the micromixing (or the exchange of solute in the transverse direction due to the combined effect of velocity gradient and molecular diffusion) using the transfer coefficient concept in terms of the difference between the two modes $c_m$ and $\langle c \rangle$. As expected, when $p = 0$, $c_m = \langle c \rangle$ and the model

equation (3.111-3.114) reduces the plug flow hyperbolic model which is symmetric in $z$ and $\tau$. Eliminating the convective mode ($c_m$) from the local equation (3.112), we can write the coarse-grained first order model in terms of $\langle c \rangle$ as

$$\frac{\partial \langle c \rangle}{\partial \tau} + \frac{\partial \langle c \rangle}{\partial z} - \frac{p}{48}\frac{\partial^2 \langle c \rangle}{\partial z^2} = \langle s_f \rangle (z,\tau) + p\frac{\partial}{\partial z}\left\langle s_f', \Lambda_{1,1} \right\rangle + O(p^2); \quad z > 0, \tau > 0 \tag{3.115}$$

with initial and inlet conditions:

$$\langle c \rangle - \frac{p}{48}\frac{\partial \langle c \rangle}{\partial z} = \langle u(\xi),\ \ c_{in}(\xi,\theta,\tau) \rangle + O(p^2) \quad @ \ \ z = 0 \tag{3.116}$$

$$\langle c \rangle = \langle c_0 \rangle (z) \ + \ p\frac{\partial}{\partial z}\langle \Lambda_{1,1}, c_0(\xi,\theta,z) \rangle + O(p^2) \ @ \quad \tau = 0. \tag{3.117}$$

This is the classical Taylor dispersion model derived by many authors in the literature except that we have also added the inlet/initial/feed conditions to the same accuracy as the evolution equation (3.115). Since the reduced order model (3.115) contains a second order spatial derivative in $z$ and there is only one inlet condition (3.117), the model appears to be not complete. However, as explained earlier, a second boundary condition is not required if we express the solution in a perturbation series in $p$ or we rewrite the truncated model by eliminating the higher order derivatives using truncated lower order models. We consider both of these below.

If we express the solution of equations (3.115-3.117) as

$$\langle c \rangle = \langle c \rangle_0 + p \langle c \rangle_1 + O(p^2) \tag{3.118}$$

we obtain the following hyperbolic/Cauchy problems at each order

$$\begin{aligned} \frac{\partial \langle c \rangle_0}{\partial \tau} + \frac{\partial \langle c \rangle_0}{\partial z} &= \langle s_f \rangle (z,\tau); z > 0, \tau > 0 \\ \langle c \rangle_0 &= \langle u(\xi),\ \ c_{in}(\xi,\theta,\tau) \rangle \ \ @ \ \ z = 0 \end{aligned} \tag{3.119}$$

$$\langle c\rangle_0 \;=\; \langle c_0\rangle(z) \;\;@\;\; \tau = 0.$$

$$\begin{aligned}
\frac{\partial \langle c\rangle_1}{\partial \tau} + \frac{\partial \langle c\rangle_1}{\partial z} &= \frac{1}{48}\frac{\partial^2 \langle c\rangle_0}{\partial z^2} + \frac{\partial}{\partial z}\left\langle s'_f, \Lambda_{1,1}\right\rangle; z>0, \tau>0 \\
\langle c\rangle_1 &= \frac{1}{48}\frac{\partial \langle c\rangle_0}{\partial z} \;\;@\;\; z=0 \\
\langle c\rangle_1 &= \frac{\partial}{\partial z}\langle \Lambda_{1,1}, c_0(\xi,\theta,z)\rangle \;\;@\;\; \tau = 0.
\end{aligned} \tag{3.120}$$

These equations can be solved sequentially. For example, for the case of a unit impulse input at the inlet and no other sources or sinks, i.e.,

$$s_f = 0;\; c_0(\xi,\theta,z) = 0;\; c_{in}(\xi,\theta,\tau) = \delta(\tau),$$

the solution may be expressed as

$$\langle c\rangle(z,\tau) = \delta(\tau - z) + \frac{p}{48}\left[z\,\delta''(\tau - z) - \delta'(\tau - z)\right] + O(p^2) \tag{3.121}$$

Alternatively, we can use the leading order approximation:

$$\frac{\partial \langle c\rangle}{\partial \tau} = \frac{\partial \langle c\rangle}{\partial z} - \langle s\rangle(z,\tau) + O(p) \tag{3.122}$$

in the model equation (3.115) for $z > 0, \tau > 0$, and rewrite the coarse-grained model as follows (without changing the accuracy):

$$\frac{\partial \langle c\rangle}{\partial \tau} + \frac{\partial \langle c\rangle}{\partial z} + \frac{p}{48}\frac{\partial^2 \langle c\rangle}{\partial z \partial \tau} = \langle s_f\rangle(z,\tau) + \frac{p}{48}\frac{\partial \langle s_f\rangle}{\partial z} + p\frac{\partial}{\partial z}\left\langle s'_f, \Lambda_{1,1}\right\rangle + O(p^2); \quad z>0, \tau>0 \tag{3.123}$$

with initial and inlet conditions:

$$\left(1 - \frac{p}{48}\frac{\partial}{\partial z}\right)\langle c\rangle = \langle u(\xi),\;\; c_{in}(\xi,\theta,\tau)\rangle + O(p^2) \;\;@\;\; z = 0 \tag{3.124}$$

$$\langle c\rangle(z,\tau) = \langle c_0\rangle(z) \; + \; p\frac{\partial}{\partial z}\langle \Lambda_{1,1}, c_0(\xi,\theta,z)\rangle + O(p^2) \; @ \quad \tau = 0. \tag{3.125}$$

Now, the reduced model (3.123-3.125) is a Cauchy problem which does not need any additional boundary condition and has the same accuracy as the parabolic model (3.115-3.117). Since the leading order model (for $p = 0$) is itself a hyperbolic/initial value problem, the $O(p)$ corrections in the reduced order hyperbolic model (3.123-3.125) represent the transverse dispersion effects.

As explained earlier, if the truncated model, equation (3.115-3.117) is used for finite values of $p$, it can lead to physical inconsistencies. While both forms, equation (3.115-3.117) and (3.123-3.125) have the same accuracy for $p \to 0$, in our view, the hyperbolic model, equation (3.123-3.125), is preferred over the parabolic model to represent the Taylor dispersion phenomena. As discussed below, the error in the parabolic model increases rapidly for finite values of $p$. Further, in some literature studies (Mercer and Roberts, 1994; Roberts, 1992; Smith, 1988), the parabolic model is used by adding an additional boundary condition at $z = 1$ (or $x = L$). It is known in the chemical engineering literature (Wen and Fen, 1975; Himmelblau and Bischoff, 1968; Wehner and Wilhelm, 1956; Froment and Bischoff, 1990) and shown below that the addition of an exit boundary condition does not change the variance in the limit of $p \to 0$, but may lead to physical inconsistencies for $p$ values of order unity or larger. An exit boundary condition is justified for $Pe_L = \frac{\langle u\rangle L}{D_m} = \frac{Pe_r^2}{p}$ values of order unity in which case, the leading order model is not hyperbolic or axial diffusion effect is not small and the original full PDE model must include an exit boundary condition.

It should be emphasized again that once the reduced order model is known to order $p$, it can be rewritten in other equivalent forms without losing accuracy. This rewriting is important for several reasons such as interpretation of experimental data, ease of numerical computations, and extension of the range of validity of the

model (for finite values of $p$). Since the cup-mixing concentration $c_m(z,\tau)$ is the one that is measured experimentally, we use an equivalent form of the local equation (3.112) as

$$\begin{aligned}\langle c\rangle &= c_m(z,\tau) + p\left\langle s'_f, \Lambda_{1,1}\right\rangle + \frac{p}{48}\,\frac{\partial\langle c\rangle}{\partial z} + O(p^2)\\ &= c_m(z,\tau) + \frac{p}{48}\,\frac{\partial c_m}{\partial z} + p\left\langle s'_f, \Lambda_{1,1}\right\rangle + O(p^2), \quad z>0, \tau>0 \end{aligned} \tag{3.126}$$

to express the reduced order model in terms of the experimentally measurable $c_m$ as

$$\frac{\partial c_m}{\partial \tau} + \frac{\partial c_m}{\partial z} + \frac{p}{48}\frac{\partial^2 c_m}{\partial z\,\partial \tau} = \langle s_f\rangle(z,\tau) - p\frac{\partial}{\partial \tau}\left\langle s'_f, \Lambda_{1,1}\right\rangle + O(p^2); \quad \tau>0, \quad z>0 \tag{3.127}$$

$$\left(1+\frac{p}{48}\frac{\partial}{\partial z}\right)c_m = \langle c_0\rangle(z) + p\frac{\partial}{\partial z}\langle \Lambda_{1,1}, c'_0(\xi,\theta,z)\rangle + O(p^2) \;\; @ \;\; \tau=0 \tag{3.128}$$

$$c_m = \langle u(\xi)\, c_{in}(\xi,\theta,\tau)\rangle + O(p^2) \quad @ \quad z=0. \tag{3.129}$$

[Balakotaiah and Chang (2003) were the first to derive equation (3.127) for $s_f = 0$, but they did not consider the order $p$ corrections in the initial and inlet conditions, equations(3.128, 3.129)]. Comparing the reduced order models for $\langle c\rangle$ and $c_m$, equations (3.123-3.125 and 3.127-3.129), we note that they are identical only for $p=0$. For $p>0$, though the evolution equations equation (3.123 and 3.127) are symmetric in $z$ and $\tau$ (for $s'_f = 0$), the coarse-grained model is asymmetric because of the asymmetry in the inlet and initial conditions. Since the initial condition given by equation (3.128) is not convenient to implement, we can simplify it further without changing the accuracy to order $p$ as follows:

$$\begin{aligned} c_m(z,\tau)|_{\tau=0} &= \left(1+\frac{p}{48}\frac{\partial}{\partial z}\right)^{-1}\left(\langle c_0(\xi,\theta,z)\rangle + p\frac{\partial}{\partial z}\langle \Lambda_{1,1}, c_0(\xi,\theta,z)\rangle\right) + O(p^2)\\ &= \langle c_0(\xi,\theta,z)\rangle + p\frac{\partial}{\partial z}\langle \Lambda_{1,1}, c_0(\xi,\theta,z)\rangle - \frac{p}{48}\frac{\partial}{\partial z}\langle c_0(\xi,\theta,z)\rangle + O(p^2)\end{aligned}$$

(3.130)

Once again, the hyperbolic models defined by equations (3.127, 3.130, 3.129) or equations (3.123-3.125) are preferred over parabolic model defined by equations (3.115-3.117) for the following reasons: (i) $c_m(z,\tau)$ is the concentration measured in experiments (ii) Like the detailed model, for negligible axial mixing, the hyperbolic model, equations (3.127, 3.130, 3.129), is a Cauchy problem i.e., an initial value problem in both $z$ and $\tau$, and does not need any additional physical constraints.

The differences between the parabolic and hyperbolic forms of the reduced order model can be seen better by examining their solutions for the special case of transversely uniform initial and inlet conditions, particularly an impulse input ($c_{in}(\xi,\theta,\tau) = \delta(\tau)$ and $c_0(\xi,\theta,z) = 0$) with no feed ($s_f = 0$) and determining the dispersion (or the residence time distribution, RTD) curve $E(\tau) = c(z=1,\tau)$, or comparing their temporal moments. For the parabolic model, we have (with $\widehat{p} = \frac{p}{48}$)

$$\frac{\partial \langle c\rangle}{\partial \tau} + \frac{\partial \langle c\rangle}{\partial z} - \widehat{p}\frac{\partial^2 \langle c\rangle}{\partial z^2} = 0; \quad z>0, \tau>0 \tag{3.131}$$

$$\langle c\rangle (z,0) = 0; \qquad \langle c\rangle (0,\tau) - \widehat{p}\frac{\partial \langle c\rangle}{\partial z}(0,\tau) = \delta(\tau); \tag{3.132}$$

and the solution in the Laplace transform domain ($t \rightarrow \omega$) may be written as

$$\widehat{E}(\omega) = \widehat{\langle c\rangle}(1,\omega) = \exp(-\omega)\left[1 - \widehat{p}\omega + \widehat{p}\omega^2\right] + O\left(\widehat{p}^2\right) \tag{3.133}$$

$$= 1 - \omega\left[1 + \widehat{p} + O\left(\widehat{p}^2\right)\right] + \frac{\omega^2}{2!}\left[1 + 4\widehat{p} + O\left(\widehat{p}^2\right)\right] + O(\omega^3) \tag{3.134}$$

$$= M_0 - M_1\omega + \frac{\omega^2}{2!}M_2 + O(\omega^3), \tag{3.135}$$

where $M_i$ is the i-th temporal moment (of the exit concentration). It is interesting to note that the parabolic model predicts correctly that the centroid of the transverse average concentration moves slower than the mean flow (and hence takes longer

time to reach the measuring point). The normalized second central moment of the RTD curve is given by,

$$\sigma^2 = \frac{M_2}{M_1^2} - 1 = 2\widehat{p} \ + O\left(\widehat{p}^2\right). \tag{3.136}$$

It should be emphasized again that the model is accurate only for small values of $\widehat{p}$, and if applied for $\widehat{p}$ values of order unity, the results predicted by it may lose physical meaning or need to be interpreted very carefully. For example, for $\widehat{p}$ values of order unity, the solution of the parabolic model when the exit boundary condition is taken as $\langle c \rangle \, (\infty, \tau) \rightarrow 0$ is given by

$$\widehat{E}(\omega) = \widehat{\langle c \rangle}(1,\omega) = \frac{2}{\left(1+\sqrt{1+4\omega\widehat{p}}\right)} \exp\left(\frac{1-\sqrt{1+4\omega\widehat{p}}}{2p}\right) \tag{3.137}$$

$$= 1 - (1+\widehat{p})\omega + \frac{\omega^2}{2!}(1+2\widehat{p})^2 + O(\omega^3) \tag{3.138}$$

$$= M_0 - M_1\omega + \frac{\omega^2}{2!}M_2 + O(\omega^3), \tag{3.139}$$

leading to

$$\sigma^2 = \left(\frac{1+2\widehat{p}}{1+\widehat{p}}\right)^2 - 1 = \frac{2\widehat{p}+3\widehat{p}^2}{1+2\widehat{p}+\widehat{p}^2} \approx 2\widehat{p} \text{ for } \widehat{p} \rightarrow 0. \tag{3.140}$$

Similarly, when the Danckwerts exit boundary condition ($\frac{\partial \langle c \rangle}{\partial z}(1,\tau) = 0$ ) is used, one obtains (Wen and Fen, 1975; Himmelblau and Bischoff, 1968; Wehner and Wilhelm, 1956; Froment and Bischoff, 1990).

$$M_1 = 1$$

$$\sigma^2 = 2\widehat{p} \ - 2\widehat{p}^2(1-e^{-1/\widehat{p}}) \approx 2\widehat{p} \text{ for } \widehat{p} \rightarrow 0. \tag{3.141}$$

Thus, the variance predicted by the parabolic model is the same for all exit boundary conditions examined in the limit of $\widehat{p} \rightarrow 0$. [In the Chemical Engineering literature (Himmelblau and Bischoff, 1968; Froment and Bischoff, 1990), the limit $\widehat{p} = 0$

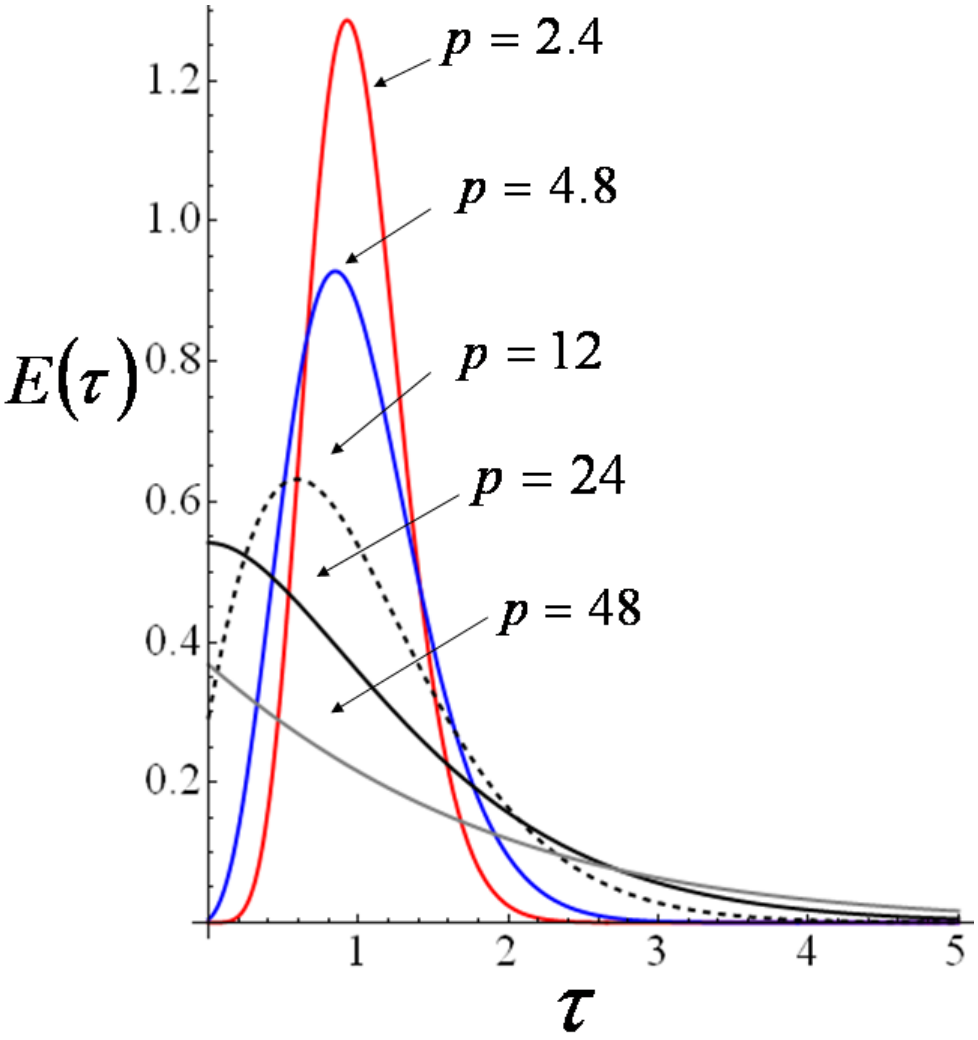


Figure 3.8: Dispersion curves predicted by the low-dimensional first order hyperbolic model [The dispersion curves include a Dirac-delta function of magnitude $Exp(-\frac{48}{p})$ at $\tau = 0$, which is not shown in the figure].

is called the *plug flow* while the opposite limit of $\widehat{p} \to \infty$ is called the *segregated flow*. In the latter case, there is no molecular diffusion either in the axial or radial directions and the dispersion of the solute is purely due to transverse velocity gradients.]

For the hyperbolic model, the dispersion (RTD) curve is obtained by solving

$$\frac{\partial c_m}{\partial \tau} + \frac{\partial c_m}{\partial z} + \widehat{p}\frac{\partial^2 c_m}{\partial z\, \partial \tau} = 0; \qquad \tau > 0, \qquad z > 0 \tag{3.142}$$

$$c_m(z,0) = 0; \quad c_m(0,\tau) = \delta(\tau). \tag{3.143}$$

The solution in the Laplace transform domain may be written as

$$\widehat{E}(\omega) = \widehat{c_m}(1,\omega) = \exp\left(-\frac{\omega}{1+\omega\widehat{p}}\right) \tag{3.144}$$

$$= 1 - \omega + \frac{\omega^2}{2!}(1+2\widehat{p}) + O(\omega^3) \tag{3.145}$$

Thus, the hyperbolic model predicts that the centroid of the cup-mixing concentration moves with the mean flow. The normalized second central moment of the RTD curve is given by

$$\sigma^2 = \frac{M_2}{M_1^2} - 1 = 2\widehat{p}. \tag{3.146}$$

In fact, the dispersion curve may be expressed explicitly as

$$E(\tau) = \exp\left(-\frac{\tau+1}{\widehat{p}}\right)\left[\delta(\tau) + \frac{1}{\widehat{p}\sqrt{\tau}} I_1\left(\frac{2\sqrt{\tau}}{\widehat{p}}\right)\right], \tag{3.147}$$

and is shown in Figure 3.8 (without the Dirac delta function of magnitude $\exp\left(-\frac{1}{\widehat{p}}\right)$ at $\tau = 0$) for various values of $\widehat{p}(= \frac{p}{48})$. We note that for small values of $\widehat{p}$, the predictions of the parabolic model (with any exit boundary condition) and hyperbolic model agree and the behavior is close to that of plug flow (with small variance $\sigma^2 \approx 2\widehat{p}$). As $\widehat{p}$ increases (or transverse or local gradients increase), the hyperbolic model predicts that the peak of the RTD curve shifts to $\tau$ values below unity (as can be expected based on the physics). For $\widehat{p} = \frac{1}{2}$ (or, $p = 24$), the predicted RTD curve is very similar to that of an ideal CSTR ($E(\tau) = e^{-\tau}$ with peak at $\tau = 0$) and for $\widehat{p} > \frac{1}{2}$, the predicted curve has long tails, typical of laminar flow. For the extreme case of $\widehat{p} \to \infty$ (segregated flow limit or the limit where radial diffusivity goes to

zero), the true RTD curve is given by

$$E(\tau) = \begin{cases} 0; \tau < \frac{1}{2} \\ \frac{1}{2\tau^3}; \tau > \frac{1}{2} \end{cases} \tag{3.148}$$

and the second central moment goes to infinity. *The hyperbolic model predicts qualitatively correct behavior even for large values of $\widehat{p}$, including the extreme (segregated flow) limit of $\widehat{p} \to \infty$.* Thus, the hyperbolic model (which is a Cauchy problem) can predict RTD curves ranging from the plug flow (PFR) limit to the perfectly mixed (CSTR) limit, and also the bypass and segregated flow limits associated with laminar flow (but only qualitatively). We conclude that the hyperbolic model given by equations(3.127, 3.130, 3.129) and expressed in terms of experimentally measurable cup-mixing concentration, retains the proper physics, requires no extra inlet or exit conditions, can describe dispersion effects better than the parabolic model equations(3.115, 3.116, 3.117) and is valid in a much larger domain of the physical parameter space, i.e., for all $\widehat{p}$. This last property is due to use of physically meaningful cup-mixing concentration (or use of two modes with a transfer coefficient) and rewriting the local equation (equation3.112) as equation (3.126). This *regularization* is a crucial step in expanding the range of validity of the coarse-grained model (qualitatively). A good analogy between the parabolic and hyperbolic models (and the regularization procedure) is the approximation of the function $e^{-\widehat{p}}$ for small $\widehat{p}$ by $f_P(\widehat{p}) = 1 - \widehat{p}$ and $f_H(p) = \frac{1}{1+\widehat{p}}$. Both approximations have the same accuracy for $\widehat{p} \to 0$ but the first approximation breaks down qualitatively for $\widehat{p} > 1$ while the second approximation is valid qualitatively for all $\widehat{p}$. The second (Pade) approximation is a regularized version of the first function and is closely connected with how we write the local equation. In this specific case for no feed source, we

replace the local equation (87b)

$$c_m = \left(1 - \widehat{p}\frac{\partial}{\partial z}\right)\langle c\rangle \tag{3.149}$$

by the regularized version

$$\langle c\rangle = \left(1 + \widehat{p}\frac{\partial}{\partial z}\right)c_m. \tag{3.150}$$

From a physical point of view, this regularization of the local equation forces the use of the two-mode model, or equivalently, the elimination of $\langle c\rangle$ from the local equation, instead of the physically relevant concentration $c_m$.

### 3.4.2 Case B: The Taylor-Aris Limit:

When $Pe_r$ is of order unity, both axial and transverse diffusional effects are comparable and the truncation of the averaged model at ($O(p)$) gives

$$\frac{\partial\langle c\rangle}{\partial\tau} + \frac{\partial c_m}{\partial z} - \frac{p}{Pe_r^2}\frac{\partial^2\langle c\rangle}{\partial z^2} - \langle s_f\rangle(z,\tau) = 0, \quad \tau > 0, \quad z > 0 \tag{3.151}$$

$$c_m - \langle c\rangle = -\frac{p}{48}\frac{\partial\langle c\rangle}{\partial z} - p\left\langle s_f', \Lambda_{1,1}\right\rangle + O(p^2), \quad \tau > 0, \quad z > 0 \tag{3.152}$$

with inlet and initial conditions:

$$c_m - \frac{p}{Pe_r^2}\frac{\partial\langle c\rangle}{\partial z} = c_{m,in}(\tau) + O(p^2) \;\; @ \;\; z = 0, \tag{3.153}$$

$$\langle c\rangle = \langle c_0\rangle(z) + p\frac{\partial}{\partial z}\langle c_0(\xi,\theta,z),\ \Lambda_{1,1}\rangle + O(p^2) \quad @ \quad \tau = 0, \tag{3.154}$$

where $\Lambda_{1,1}(\xi) = -\frac{1}{24}\left(2 - 6\xi^2 + 3\xi^4\right)$. The conditions for validity of this model are same as those for the Taylor model. The global equation (3.151) represents the macroscopic (overall) evolution of the solute with axial mixing. The local equation (3.152) represents the local or microscopic phenomena (exchange of solute between fast flowing fluid near the tube center and slow moving fluid near the tube wall) as the transfer between the two modes $c_m$ and $\langle c\rangle$. equations (3.153, 3.154)

represents the modified inlet and initial conditions caused by velocity gradient and transverse diffusion.

Eliminating the convective mode ($c_m$) from the local equation, we can write the coarse-grained first order model in terms of $\langle c \rangle$ as

$$\frac{\partial \langle c \rangle}{\partial \tau} + \frac{\partial \langle c \rangle}{\partial z} - p\left(\frac{1}{48} + \frac{1}{Pe_r^2}\right)\frac{\partial^2 \langle c \rangle}{\partial z^2} = \langle s_f \rangle (z,\tau) + p\frac{\partial}{\partial z}\left\langle s_f', \Lambda_{1,1}\right\rangle + O(p^2)\,, \quad \tau > 0, \quad z > 0 \tag{3.155}$$

with initial and inlet condition as

$$\langle c \rangle - p\left(\frac{1}{48} + \frac{1}{Pe_r^2}\right)\frac{\partial \langle c \rangle}{\partial z} = c_{m,in}(\tau) + O(p^2) \;\; @ \;\; z = 0, \tag{3.156}$$

$$\langle c \rangle = \langle c_0 \rangle (z) + p\frac{\partial}{\partial z}\left\langle c_0(\xi,\theta,z),\ \Lambda_{1,1}\right\rangle + O(p^2) \quad @ \quad \tau = 0, \tag{3.157}$$

This is same as classical Taylor model except with modified inlet and initial condition. Once, $\langle c \rangle$ is known, $c_m$ can be calculated. Once again, we see that the reduced order model equation (3.155) contains a second spatial derivative term, but there is only one inlet condition equation (3.156). Hence model is not complete without a second boundary or inlet condition. This can be avoided by using leading order approximation equation (3.122) in the coarse-grained model equation (3.155) for $t > 0, z > 0$ which leads to the following hyperbolic model,

$$\frac{\partial \langle c \rangle}{\partial \tau} + \frac{\partial \langle c \rangle}{\partial z} + p\left(\frac{1}{48} + \frac{1}{Pe_r^2}\right)\frac{\partial^2 \langle c \rangle}{\partial z \partial \tau} = \langle s_f \rangle (z,\tau) + p\frac{\partial}{\partial z}\left\langle s_f', \Lambda_{1,1}\right\rangle + p\left(\frac{1}{48} + \frac{1}{Pe_r^2}\right)\frac{\partial \langle s_f \rangle}{\partial z}O(p^2)\,, \quad \tau > 0, \quad z > 0 \tag{3.158}$$

with the same inlet and initial condition as given by equations (3.156, 3.157). It is interesting to note that after using leading order approximation, the parabolic model is transformed into a Cauchy (initial value) problem which is easier to solve. Sim-

ilarly, using the regularized version (equation3.126) of the local equation (3.152), the reduced first order model can be written in terms of $c_m$ as follows:

$$\frac{\partial c_m}{\partial \tau} + \frac{\partial c_m}{\partial z} + \frac{p}{48}\frac{\partial^2 c_m}{\partial z \partial \tau} - \frac{p}{Pe_r^2}\frac{\partial^2 c_m}{\partial z^2} = \langle s_f \rangle (z,\tau) - p\frac{\partial}{\partial \tau}\left\langle s_f', \Lambda_{1,1}\right\rangle + O(p^2), \quad \tau > 0, \quad z > 0 \tag{3.159}$$

with inlet and initial conditions:

$$c_m - \frac{p}{Pe_r^2}\frac{\partial c_m}{\partial z} = c_{m,in}(\tau) + O(p^2) \;\; @ \;\; z = 0, \tag{3.160}$$

$$c_m + \frac{p}{48}\frac{\partial c_m}{\partial z} = \langle c_0 \rangle (z) + p\frac{\partial}{\partial z}\left\langle c_0(\xi,\theta,z),\ \Lambda_{1,1}\right\rangle + O(p^2) \quad @ \quad \tau = 0, \tag{3.161}$$

We note that the reduced order model (3.159) also contains a second order spatial derivative in $z$, which again can be avoided by using the leading order approximation for $\tau > 0,\ z > 0$ and rewriting the model without changing accuracy as follows:

$$\frac{\partial c_m}{\partial \tau} + \frac{\partial c_m}{\partial z} + \left(\frac{p}{48} + \frac{p}{Pe_r^2}\right)\frac{\partial^2 c_m}{\partial z \partial \tau} = \langle s_f \rangle (z,\tau) + \frac{p}{Pe_r^2}\frac{\partial \langle s_f \rangle}{\partial z} - p\frac{\partial}{\partial \tau}\left\langle s_f', \Lambda_{1,1}\right\rangle + O(p^2), \quad \tau > 0, \quad z > 0 \tag{3.162}$$

with inlet and initial conditions same as given by equations (3.160, 3.161). We note that the above reduced order model is more appropriate to describe the solute dispersion as it is hyperbolic and is written in terms of experimentally measurable concentration $c_m$. The initial conditions (3.161) can be further simplified by inverting

as

$$c_m = \langle c_0(\xi,\theta,z)\rangle + p\frac{\partial}{\partial z}\langle c_0(\xi,\theta,z),\ \Lambda_{1,1}\rangle - \frac{p}{48}\frac{\partial}{\partial z}\langle c_0(\xi,\theta,z)\rangle + O(p^2) \quad @ \quad \tau = 0, \tag{3.163}$$

For the case of uniform impulse input ($c_{in}(\xi,\theta,\tau) = \delta(\tau)$ and $c_0(\xi,\theta,z) = 0$) and no feed ($s_f = 0$), the solution of parabolic form given by equation (3.155-3.157) is same as that of parabolic model (3.131, 3.132) with $\widehat{p} = \frac{p}{48} + \frac{p}{Pe_r^2}$. Similarly for this case, the solution of hyperbolic model given by equations (3.158, 3.155, 3.156) or equations (3.162, 3.163, 3.160) is same as that of hyperbolic model equations (3.142, 3.143) with $\widehat{p} = \frac{p}{48} + \frac{p}{Pe_r^2}$. Here, $\widehat{p}\left(= \frac{p}{48} + \frac{p}{Pe_r^2}\right)$ is the well known effective dispersion coefficient in dimensionless form. However, in the hyperbolic model, $\widehat{p}$ is an effective local exchange/transfer time.

## 3.5 Conclusions and Discussion

The main contribution of this work is the presentation of a systematic averaging procedure based on the Lyapunov-Schmidt (L-S) method for deriving coarse-grained low-dimensional models from the detailed diffusion-convection-reaction equations. As outlined in earlier section, this method has some advantages compared to other methods presented in the literature. When there is scale separation in the detailed model, the L-S method is equivalent to the exact Maclaurin's series expansion of the detailed model in terms of the small parameter representing the scale separation. While we have illustrated it here only for the non-reacting solute dispersion case, it can be applied to a wide range of reacting as well as non-reacting cases described by diffusion-convection-reaction models. For the case of classical Taylor dispersion problem, we have derived the reduced order model to all orders in the transverse diffusion time. By summing the resulting infinite series in closed functional form, we were able to show that the reduced order model derived by the L-S technique is exact in the sense that it can predict the moments of

the solute distribution exactly for all times.

A second contribution of this work is the analysis of the solute dispersion at short times using the coarse-grained model derived by the L-S method. Specifically, we have shown that, as expected, the centroid displacement arises due to the fact that for point release at $(r_0, \theta_0)$, the centroid moves with the local fluid velocity $u(r_0)$ at short times while it moves with the mean velocity at large times. Thus, it is not possible to predict the location of centroid (and hence the second central moment or the variance) correctly by any coarse-grained model that is not valid for $t \to 0$. Similarly, the short time approximation of variance shows that solute spreading process evolves with pure diffusion for $t \to 0$, and after some critical time $\tau_{CD} = \frac{D_m}{\langle u \rangle^2}$, convection effects start to contribute and introduce asymmetry in the concentration distribution. For long times ($t \gg \tau_D = \frac{a^2}{D_m}$), the spreading process is governed by the Taylor (when $Pe_r \approx O(\frac{1}{\sqrt{p}})$) or Taylor-Aris mechanism (when $Pe_r \approx O(1)$). Thus, the solute spreading process may be divided into three time intervals; $0 < t < \tau_{CD}$ where axial molecular diffusion dominates, $t \in (\tau_{CD}, \tau_D)$ where the dispersion is due to the combined effects, and $t >> \tau_D$ where convection and transverse diffusion dominates. Our analysis in section 4.1 also shows that for the practical case of $Pe_r >> 1$, the skewness of the solute concentration profile increases as $\left(\frac{t}{\tau_D}\right)$ for short times while it decreases as $\sqrt{\frac{\tau_D}{t}}$ for long times. Thus, while the Gaussian profile is approached for $t \to \infty$ (Chatwin, 1970), the skewness is never zero for any finite time and goes through a maxima for $t$ values of order $\tau_D$. In our view, this important observation has not been recognized in the literature.

A third contribution of our work is the clear distinction between the dominant convective mode represented by the cup-mixing concentration ($c_m$) and the dominant diffusive mode represented by the cross-sectional averaged concentrations ($\langle c \rangle$). We have shown how these two modes arise naturally in the averaging of the

convective diffusion equation. With the use of these two modes, the local gradients can be quantified more accurately than the traditional use of a single concentration mode and its large scale gradient. In our opinion, there is a fundamental physical inconsistency in representing the Taylor dispersion phenomenon using a single diffusive mode (the cross-section averaged concentration) and its large scale gradient. This parabolic description of the dispersion flux, first used by Taylor (1953) and later by many others, makes the local phenomenon of exchange of solute between the (fast moving or large scale) convective mode ($c_m$) and nearly stationary and small scale diffusive mode($\langle c \rangle$) into a large scale phenomenon (effective diffusion on the larger scale). It is mainly for this reason, the traditional coarse-grained parabolic models fail to describe the solute dispersion process accurately for short times or for the case of a reactive solute, for fast reactions and for finite values of the transverse diffusion time. In fact, as shown elsewhere (Balakotaiah and Ratnakar, 2010), the single mode description of the Taylor dispersion phenomenon for reacting flows in terms of $\langle c \rangle$ can lead to negative effective dispersion coefficients! Based on these and other comparisons, we conclude that Taylor dispersion phenomena are better described in terms of hyperbolic models using either a single convective mode (for the non-reactive case) or multiple concentration modes coupled through the concept of a transfer coefficient (Balakotaiah and Ratnakar, 2010).

Finally, it should be noted that exact averaging is possible in the classical Taylor-Aris problem due to two special properties, namely, linearity of the model and the existence of zero eigenvalue for the transverse diffusion operator for all values of $p$. Due to these properties, it was possible to derive the coarse-grained model to all orders in $p$ and sum the resulting infinite series for the moments in closed functional form so that the dispersion due to point sources (in space or time) can be treated accurately. However, in many practical applications involving homogeneous and

multiphase reacting systems with point sources or sinks (e.g. spark-ignited internal combustion engine models, wall catalyzed reactions with small metallic crystallites acting as reaction sources or sinks and homogeneous reactions with concentrated feeding of one or more of the reactants), we have found that the traditional Taylor dispersion approach is not adequate as the coarse-grained models may not converge when the local Damköhler number exceeds a critical value. In such cases, the higher order terms in the coarse-grained model derived using the L-S method are necessary to determine the region of convergence of the reduced order model and to improve its accuracy.

# Chapter 4 Reduced Order Model for recative dispersion in Catalytic monoliths

## 4.1 Preamble

The monolith reactor is widely used in the treatment of exhaust gases from automobiles, oxidation of volatile organic compounds, catalytic partial oxidation or combustion of hydrocarbons, removal of nitrogen oxides from power plant and furnace exhaust gases and many other applications. The monolith reactor consists of a large number of parallel channels of diameter in the range 0.2 to 10 mm and length 1 to 100 cm through which the reactant, product and carrier gases flow. The catalyst containing various precious metals is deposited on the wall of the monolith channels as a porous washcoat layer with a mean thickness of about 10 to 50 $\mu m$. In most applications, the Reynolds number is well below 2000 and hence the flow in the channel is laminar (though in some cases it may not be fully developed). The reactants are transported mainly by convection in the axial direction, by molecular diffusion in the radial direction, while the transport in the washcoat may be due to a combined mechanism of molecular and Knudsen diffusion. In addition to the above applications, the problem of laminar flow in a channel with a porous layer on the wall is also important in coated tube chromatography, catalytic micro-reaction engineering, reactive dissolution of porous media and contaminant transport in soil and other applications.

In the automobile exhaust treatment applications, the monolith operates under highly transient conditions where the inlet composition and temperature vary with time. Various control and optimization algorithms related to fuel efficiency and emissions constraints may be implemented in real time if reduced order models for various sub-systems are available. In addition to this important application, the development of low-dimensional models for catalytic reactors has other advan-

tages such as speed-up of transient reactor calculations by three to five orders of magnitude (Joshi et al., 2009a), parametric studies and bifurcation analysis of catalytic reactors, estimation of kinetic and transport parameters from limited number of macroscopic experimental observations (or the solution of the so called *inverse problem*), and incorporation of the model in larger scale process and optimization schemes. These reasons are the primary motivation for the present study.

The literature relevant to this work falls into two groups: one dealing with monoliths and catalytic after-treatment aspects and the second dealing with coarse graining of diffusion-convection-reaction models. As the literature is extensive in both groups we review here only the recent literature that is directly relevant to this work and refer to monographs or review articles for older literature.

The most widely used monolith models in the chemical engineering literature are the one-dimensional two-phase models that use various average concentrations with effective external heat and mass transfer coefficients (Froment and Bischoff, 1990; Heck and Farrauto, 2009; Cybulski and Moulijn, 2006). For example, for the case of an isothermal monolith, the two-phase model consists of a species balance equation for some average concentration in each phase and an interphase transfer term. (In the fluid phase, the average concentration used is the experimentally measurable mixing-cup or velocity weighted concentration, while in the solid phase the concentration used is the average solid-fluid interfacial concentration). The gradients in the washcoat are accounted for by using the effectiveness factor concept, which is only applicable for the case of a single reaction (Joshi et al., 2009). As reviewed by Chakraborty and Balakotaiah (2005), though these two-phase models are derived for describing the interphase transport at steady-state and in the absence of reactions, the common practice is to use them for unsteady state conditions and with chemical reactions. The validity of this assumption for steady-state conditions has been established in the literature by making the transfer coefficients

as a function of the local Damköhler number and position and calculation of these transfer coefficients for the case of wall reaction or reaction in the washcoat (Tronconi and Forzatti, 1992; Gupta and Balakotaiah, 2001; Bhattacharya et al. 2004). More recently, various averaging methods have been used to obtain the two-phase models as well as other such reduced order models for monoliths and other reacting systems (Chakaraborty and Balakotaiah, 2005; Mikelic et al., 2006). In our view, the main unresolved issue at present is the validity of the transfer coefficient concept for reacting systems under transient conditions.

A second important concept in obtaining the reduced order models is that of the dispersion coefficient, popularized by the work of Taylor (1953) and Aris (1956). While this concept was initially introduced to describe the spreading of a non-reactive solute in laminar flow in a channel due to velocity gradients and molecular diffusion, it has also been used extensively for reacting systems (Brenner and Edwards, 1993). This approach uses a single concentration mode and obtains the reduced order model in parabolic form with an effective velocity, dispersion coefficient and rate constant (for reacting systems). However, in recent years, some shortcomings of the Taylor-Aris parabolic model have been identified (Balakotaiah and Chang, 2003; Balakotaiah, 2004; Balakotaiah and Ratnakar, 2010). To overcome these, several authors have introduced, derived and justified the use of hyperbolic models (Camacho,1993; Mauri, 1991; Maas, 1999; Balakotaiah and Chang, 2003; Mikelic et al., 2006; Ratnakar and Balakotaiah, 2011) to describe dispersion effects under non-reactive as well as reactive conditions. The main goal of most of these earlier works was to obtain an effective transport equation (parabolic or hyperbolic partial differential equation) in terms of a single concentration mode. However, earlier work on coarse-graining of reacting flows has shown that it is not possible to obtain a reduced order hyperbolic model in terms of a single mode (Chakraborty and Balakotaiah, 2005). The current work is a further

extension of this earlier work where we obtain reduced order models in the form of multiple interacting modes. The main focus of the present work is on the minimum number of modes needed to express the reduced order model, the expressions for the solid-fluid interfacial flux in terms of various concentration modes and the proper initial and inlet conditions to be used on the reduced order model.

In this chapter, we consider a detailed partial differential equation model that describes the transient diffusion, convection and reaction in a monolith channel with a porous washcoat layer and average it over the transverse dimensions to obtain a reduced order model in terms of the axial length scale and time. The reduced order model is expressed in terms of physically meaningful or measurable concentration modes. We provide a physical interpretation of the various terms and the *effective transport coefficients* that appear due to transverse averaging. We also obtain the appropriate inlet and initial conditions to be used on the reduced order model. We examine various limiting cases of the general model and compare our results with those in the literature. Our main conclusion is that the traditional transfer or dispersion coefficient concepts that are extensively applied either for non-reacting cases or for steady-reacting cases are not applicable in the general case in which various transport, reaction and transient processes in different phases interact. For example, we show that the traditional external mass transfer coefficient concept where the flux at the fluid-solid interface is expressed in terms of the difference between two concentration modes is not applicable under transient reacting conditions. In our approach, the reduced order model is expressed in terms of interacting multiple modes.

This chapter is organized as follows. In the next section, we present a detailed model for a monolith channel with a porous washcoat layer on the wall in which a reaction occurs. In section 3, we average the detailed model over the small transverse scales to obtain a coarse-grained model. We also present the reduced order

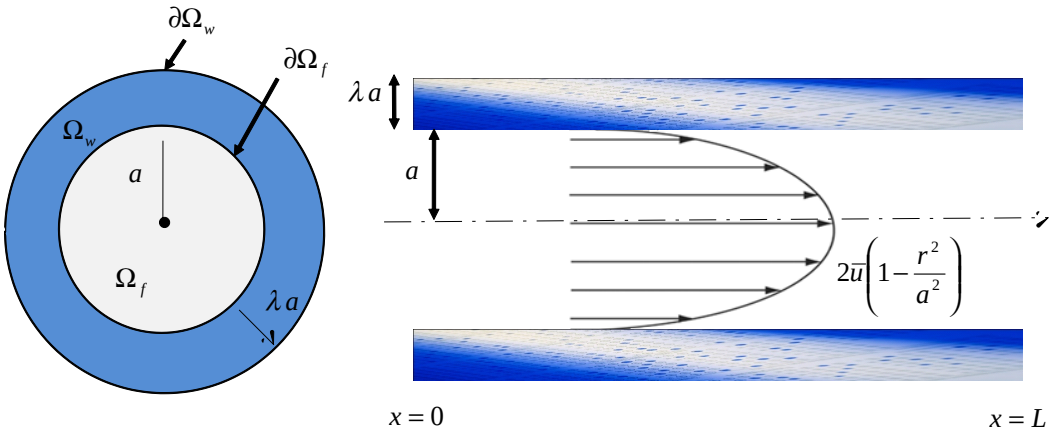


Figure 4.1: Schematic diagram of a single straight monolithic channel of circular cross-section and with a uniformly thick washcoat.

model in single and various multi-mode forms. In section 4, we examine the solid-fluid interfacial flux and obtain expressions for it in terms of various concentration modes. We also identify the effective mass transfer coefficients that appear in these flux expressions. In section 5, we examine some limiting cases of the model and compare our results with those in the literature or with the exact numerical solutions. In the last section, we summarize the main contributions of this work and discuss some possible extensions.

## 4.2 Model Formulation

We consider a straight monolith channel of circular cross-section in which the flow is laminar and fully developed and having a washcoat of uniform thickness in the circumferential direction as shown in Figure 4.1. We consider here only the case in which the concentration of the reactant is small so that any non-isothermal (temperature) effect may be neglected. We also assume that the length to diameter ratio of the channel is large so that axial diffusion may be neglected in both the solid and fluid phases. With these assumptions, the detailed model describing the

transient diffusion, convection and reaction in the channel may be expressed as

$$\frac{\partial C_f}{\partial t'} + U_f(r)\,\frac{\partial C_f}{\partial x'} = D_f \nabla^2_{\perp'} C_f \;\text{ in } \Omega_f, 0 < x' < L,\; t' > 0 \tag{4.1}$$

$$\varepsilon_{wc}\frac{\partial C_w}{\partial t'} = D_w \nabla^2_{\perp'} C_w \; - R_w(C_w) \text{ in } \Omega_w, 0 < x' < L,\; t' > 0 \tag{4.2}$$

with zero flux boundary condition at the outer surface $\partial\Omega_w$ given by

$$\mathbf{n}_{\Omega_w} \cdot D_w \boldsymbol{\nabla}_{\perp'} C_w = 0 \text{ on } \partial\Omega_w, \tag{4.3}$$

and the continuity of concentration and reactant flux at the fluid-washcoat interface as given by

$$C_f \;=\; C_w \quad \text{on } \partial\Omega_f, \tag{4.4}$$

$$J_{fw} \;=\; -\mathbf{n}_{\Omega f} \cdot D_f \boldsymbol{\nabla}_{\perp'} C_f = -\mathbf{n}_{\Omega f} \cdot D_w \boldsymbol{\nabla}_{\perp'} C_w \text{ on } \partial\Omega_f. \tag{4.5}$$

The initial and inlet conditions are given by

$$C_f \;=\; C_{f0}\,(r, \theta, x') \;@\; t' = 0, \tag{4.6}$$

$$C_w \;=\; C_{w0}\,(r, \theta, x') \,@\, t' = 0, \tag{4.7}$$

$$C_f = \;\; C_{f,in}\;\; (r, \theta, t') \,@\;\; x' = 0, \tag{4.8}$$

where $\Omega_f$ and $\Omega_w$ represent the cross-sectional area of the flow channel (fluid) and the washcoat, respectively as shown in Figure 4.1. $C_f$ and $C_w$ are the solute concentrations in fluid phase and washcoat, respectively. [Remark: $C_w$ is the concentration in the interstitial space of the washcoat]. Here, $D_f$ and $D_w$ are molecular diffusivity of the reacting species in the fluid phase and effective diffusivity in the washcoat, respectively. $\varepsilon_{wc}$ is the porosity of the washcoat, which is assumed to

be a constant (independent of position and time). The function

$$U_f(r) = 2\overline{u}\left(1 - \frac{r^2}{a^2}\right)$$

is the velocity profile in the channel with average fluid velocity $\overline{u}$. $R_w\left(C_w\right)$ is the global rate expression for the consumption of the reactant in moles per unit time per unit washcoat volume. In equations(1e), $J_{fw}$ is the flux of the reactant at the fluid-washcoat interface from fluid phase into the washcoat. The operator

$$\nabla^2_{\perp'} = \frac{1}{r}\frac{\partial}{\partial r}\left(r\frac{\partial}{\partial r}\right) + \frac{1}{r^2}\frac{\partial^2}{\partial \theta^2}$$

is the transverse Laplacian, $\mathbf{n}_{\Omega_f}$ and $\mathbf{n}_{\Omega_w}$ are unit normal vectors radially outward to the fluid-washcoat interface $\partial\Omega_f$ $(r = a)$ and the outer washcoat boundary $\partial\Omega_w$ (at $r = a + \lambda a$) , respectively.

The above model may be written in dimensionless form by defining

$$\xi = \frac{r}{a};\ x = \frac{x'}{L};\ t = \frac{\overline{u}\ t'}{L};\ u_f\left(\xi\right) = \frac{U_f\left(r\right)}{\overline{u}};\ \mu = \frac{D_f}{D_w};\ p = \frac{\overline{u}\ \ a^2}{D_f\ L};$$
$$\left(c_w, c_f\right) = \left(C_w, C_f\right)/C_R;\ R\left(c_w\right) = \frac{R_w\left(C_R c_w\right)}{R_w\left(C_R\right)};\ Da = \frac{R_w\left(C_R\right)}{C_R}\frac{L}{\overline{u}},$$

and including the inlet/initial conditions as source/sink terms in the evolution equation as explained by Balakotaiah and Ratnakar (2010) and Ratnakar and Balakotaiah (2011). Thus, we can express the detailed model in the domain of interest as

$$F\left(c, p, \mu\right) \equiv \mathbb{L}c - p\left[\frac{\partial c}{\partial t} + u\left(\xi, \theta\right)\frac{\partial c}{\partial x} + Da\ \beta\left(\xi, \theta\right)\ R\left(c\right) - s\left(\xi, \theta, x, t\right)\right] = 0 \text{ in } \Omega \tag{4.9}$$

with the zero flux boundary condition at the outer surface of the washcoat

$$\mathbf{n}_{\Omega}\cdot\boldsymbol{\nabla}_{\perp}\, c = \frac{\partial c}{\partial \xi} = 0 \text{ on } \partial\Omega \;\; (\equiv \xi = \lambda + 1), \tag{4.10}$$

where

$$\mathbb{L}c = \frac{1}{\rho}\boldsymbol{\nabla}_{\perp}\cdot\left(D\;\boldsymbol{\nabla}_{\perp}\, c\right) = \frac{1}{\rho}\left[\frac{1}{\xi}\frac{\partial}{\partial \xi}\left(\xi D\left(\xi\right)\frac{\partial c}{\partial \xi}\right) + \frac{D\left(\xi\right)}{\xi^2}\frac{\partial^2 c}{\partial \theta^2}\right]$$

is the transverse diffusion operator in the region $\Omega \;\left(= 0 < \xi < \lambda + 1, 0 < \theta \leq 2\pi\right)$ in the dimensionless transverse variables $(\xi, \theta)$ in cylindrical coordinates. Here, $\rho$ is the capacitance function. Though our procedure is valid for general case in which $\rho$ varies with position, the focus here will be on the special case in which $\rho$ is constant in each phase. $x$ is the dimensionless axial coordinate and $t$ is the dimensionless time, non-dimensionalized by convection time $\tau_C \left(= \frac{L}{\overline{u}}\right)$, $u_f\left(\xi\right)$ is the dimensionless velocity profile through the open part of the channel. The parameter $\mu$ is the ratio of diffusion coefficient of the reactant in fluid phase to that in the washcoat. The perturbation parameter $p$ is the local (transverse) Peclet number which can be interpreted as the ratio of two time scales, namely, the transverse diffusion time $\tau_D = \left(\frac{a^2}{D_f}\right)$ and the convection time $\tau_C$ or transverse to axial length scales. The parameter $p$ represents the scale separation in the physical system. It could also be interpreted as the dimensionless frequency/wave number in the macro variables $x$ or $t$. The Damköhler number, $Da$, represents the ratio of convection time ($\tau_C$) to the characteristic reaction time $\tau_R \left(= \frac{C_R}{R_w(C_R)}\right)$ in the washcoat.

The concentration is non-dimensionalized by some reference concentration $(C_R)$ and is expressed as

$$c\left(\xi, \theta, x, t\right) = \begin{cases} c_f\left(\xi, \theta, x, t\right), & 0 < \xi < 1 \;\; (\equiv \Omega_f) \\ c_w\left(\xi, \theta, x, t\right), & 1 < \xi < \lambda + 1 \;\; (\equiv \Omega_w) \end{cases} \tag{4.11}$$

Similarly, the dimensionless velocity profile may be expressed as

$$u(\xi,\theta)=\begin{cases} u_f(\xi)=2\left(1-\xi^2\right), & 0<\xi<1 \\ 0, & 1<\xi<\lambda+1 \end{cases}, \tag{4.12}$$

the molecular diffusivity expressed as

$$D(\xi,\theta)=\begin{cases} 1, & 0<\xi<1 \\ \frac{1}{\mu}, & 1<\xi<\lambda+1 \end{cases}, \tag{4.13}$$

the reaction/catalyst activity profile as

$$\beta(\xi,\theta)=\begin{cases} 0, & 0<\xi<1 \\ \frac{1}{\varepsilon_{wc}}, & 1<\xi<\lambda+1 \end{cases}, \tag{4.14}$$

the capacitance function $\rho$ as

$$\rho(\xi,\theta)=\begin{cases} 1, & 0<\xi<1 \\ \varepsilon_{wc}, & 1<\xi<\lambda+1 \end{cases}, \tag{4.15}$$

and the source term $s(\xi,\theta,x,t)$ as

$$\begin{aligned} &s(\xi,\theta,x,t)=c_0(\xi,\theta,x)\,\delta(t)+u(\xi)\,c_{in}(\xi,\theta,t)\,\delta(x) \\ &=\begin{cases} s_f(\xi,\theta,x,t)=c_{f0}(\xi,\theta,x)\,\delta(t)+u(\xi)\,c_{fin}(\xi,\theta,t)\,\delta(x), & \text{in } \Omega_f \\ s_w(\xi,\theta,x,t)=c_{w0}(\xi,\theta,x)\,\delta(t). & \text{in } \Omega_w \end{cases} \end{aligned} \tag{4.16}$$

It should be noted that equations (4.9, 4.10) is equivalent to the equations (4.1-4.8) for $x>0$ and $t>0$ and leads to the same inlet/initial condition (equations 4.6 - 4.8) after integrating w.r.t. $x$ from $x=0$ to $0^+$ and w.r.t.. $t$ from $t=0$ to $0^+$. Here $t=0^+$ should be interpreted as $t=\varepsilon\ll\tau_D$. Also, the activity profile $\beta$ vanishes in $\Omega_f$

because there is no (homogeneous) reaction occurring in the channel. In the more general case, the source function $s(\xi, \theta, x, t)$ can also represent the source/sink terms at $x > 0$ and $t > 0$. We show later that the inclusion of inlet/initial conditions as source terms in the evolution equation leads to the identification of inlet/initial conditions for the averaged model. It should also be noted that the model given by equations(4.9, 4.10) can be extended to the more general case of a monolith of arbitrary cross-section where catalyst activity, diffusivity and velocity may be functions of transverse coordinates. However, for simplicity, we consider the present case of a straight circular channel with a washcoat of uniform thickness. [For an extension of the averaging procedure to other channel and washcoat geometries, see Bhattacharya, 2004].

## 4.3 Transverse Averaging

Since the details of transverse averaging using the Lyapunov-Schmidt method have been discussed in prior work (Balakotaiah and Chakraborty, 2002; Balakotaiah and Chang, 2003; Ratnakar and Balakotaiah, 2011), we report here only some steps in the application of the procedure and focus on the results.

We note that the operator that appears in transverse averaging is $\mathbb{L} = \frac{1}{\rho}\boldsymbol{\nabla}_\perp \cdot (D\ \boldsymbol{\nabla}_\perp\ )$, which is symmetric and has a simple zero eigenvalue with an eigenfunction that is independent of transverse coordinates. Equivalently, the eigenvalue problem

$$\begin{aligned} \mathbb{L}\psi_i \equiv \frac{1}{\rho}\boldsymbol{\nabla}_\perp \cdot (D\ \boldsymbol{\nabla}_\perp\ \psi_i) &= -\lambda_i \psi_i \text{ in } \Omega \\ \mathbf{n}_\Omega \cdot\ \boldsymbol{\nabla}_\perp\ \psi_i &= 0 \qquad \text{on } \partial\Omega \end{aligned} \tag{4.17}$$

is self-adjoint ($\mathbb{L}^*$ = adjoint operator $= \mathbb{L}$) with respect to the (capacitance weighted)

inner product defined by

$$\langle u, v \rangle = \frac{1}{A_\Omega} \int_0^{2\pi} \int_0^{1+\lambda} \xi \ \rho\left(\xi, \theta\right) \ u\left(\xi, \theta\right) \ v\left(\xi, \theta\right) \ d\xi d\theta \tag{4.18}$$

with

$$A_\Omega = \int_0^{2\pi} \int_0^{1+\lambda} \xi \ \rho\left(\xi, \theta\right) \ d\xi d\theta = \pi[1 + \varepsilon_{wc} \lambda \left(\lambda + 2\right)],$$

and has a simple zero eigenvalue $\lambda_0 = 0$ with a constant eigenfunction $\psi_0\left(\xi, \theta\right) = 1$. Moreover, all eigenfunctions $\psi_j$ may be chosen such that they are normalized w.r.t.. inner product defined by equations (4.18), i.e.,

$$\left\langle \psi_i, \psi_j \right\rangle = \delta_{ij} = \begin{cases} 0, \ i \neq j \\ 1, \ i = j \end{cases} \tag{4.19}$$

The concentration $c$ is expressed as

$$c\left(\xi, \theta, x, t\right) = \langle c \rangle \left(x, t\right) \ \psi_0 + c'\left(\xi, \theta, x, t\right) \tag{4.20}$$

where, the projection of $c$ on to ker$(\mathbb{L})$ is the (capacitance weighted) cross-sectional averaged concentration,

$$\langle c \rangle \left(x, t\right) = \langle c, \psi_0 \rangle = \frac{1}{A_\Omega} \iint_\Omega \xi \ \rho\left(\xi, \theta\right) c\left(\xi, \theta, x, t\right) \ d\xi d\theta, \tag{4.21}$$

and the projection of $c$ on to Range$(\mathbb{L}^*)$ is the concentration fluctuation about its average value, satisfying the following orthogonality constraint

$$\langle c', \psi_0 \rangle = 0. \tag{4.22}$$

Similarly, in codomain, projecting the operator $F$ onto ker$(\mathbb{L}^* = \mathbb{L})$, we get the

global equation $(I-E)F \equiv \langle F, \psi_0 \rangle \psi_0 = 0$ as follows

$$\frac{\partial \langle c \rangle}{\partial t} + \langle u \rangle \frac{\partial c_m}{\partial x} + Da \ \langle \beta(\xi, \theta) \ R(c) \rangle - \langle s \rangle = 0 \tag{4.23}$$

where, $c_m$ is the cup-mixing or velocity weighted averaged concentration defined by

$$c_m = \frac{\langle c, u \rangle}{\langle u \rangle} = \langle c \rangle + \frac{\langle c', u' \rangle}{\langle u \rangle}, \tag{4.24}$$

and $\langle s \rangle$ is the transverse average of the source/sinks. The reaction term can be simplified as

$$\begin{aligned} \beta \ R(c) &= \beta R(\langle c \rangle) + \sum_{i=1}^{\infty} \beta \frac{R^{[i]}}{i!} (\langle c \rangle) (c - \langle c \rangle)^i \\ &= \beta R(\langle c \rangle) + \beta R'(\langle c \rangle) (c - \langle c \rangle) + O\left((c - \langle c \rangle)^2\right), \end{aligned} \tag{4.25}$$

and hence

$$\langle \beta \ R(c) \rangle = \langle \beta \rangle R(\langle c \rangle) + \langle \beta \rangle R'(\langle c \rangle) (\langle c \rangle_w - \langle c \rangle) = \langle \beta \rangle R(\langle c \rangle_w) + O\left((c - \langle c \rangle)^2\right), \tag{4.26}$$

where $\langle c \rangle_w$ is the activity weighted averaged concentration (which is same as washcoat average concentration because the activity profile within the washcoat is uniform in the transverse directions) and is given by

$$\langle c \rangle_w = \frac{\langle c, \beta \rangle}{\langle \beta \rangle} = \langle c \rangle + \frac{\langle c', \beta' \rangle}{\langle \beta \rangle}. \tag{4.27}$$

Thus, using equations (4.26), we simplify the global equation (4.23) as follows:

$$\frac{\partial \langle c \rangle}{\partial t} + \langle u \rangle \frac{\partial c_m}{\partial x} + Da \ \langle \beta \rangle R(\langle c \rangle_w) - \langle s \rangle = 0 \tag{4.28}$$

We note that the global model equations (4.28) is exact for linear kinetics and is

valid for non-linear kinetics to first order when the transverse variation in concentration is small. Also, it is not closed since it contains three concentration modes $\langle c \rangle$ , $c_m$ and $\langle c \rangle_w$ appearing naturally. The mode $\langle c \rangle$ appears due to transient nature of the problem while the modes $c_m$ and $\langle c \rangle_w$ appear due to transverse dependency of velocity profile and catalytic activity, respectively. These modes contains the effect of concentration variation at smaller scales. To quantify these smaller scale effects, we solve the local equation for $c'$ which is obtained by projecting $F$ onto range ($\mathbb{L}$), leading to the following equation:

$$EF \equiv \mathbb{L}c' - p \left[ \begin{array}{c} \frac{\partial c'}{\partial t} + \frac{\partial}{\partial x}\left(uc' - \langle u'c' \rangle\right) + DaR'\left(\langle c \rangle\right)\left(\beta c' - \langle \beta' c' \rangle\right) \\ + u' \frac{\partial \langle c \rangle}{\partial x} + Da\ \beta'\ R\left(\langle c \rangle\right) - s'\left(\xi, \theta, x, t\right) \end{array} \right] = 0 \text{ in } \Omega \quad (4.29)$$

with the zero flux boundary condition at outer surface of the washcoat

$$\mathbf{n}_\Omega \cdot \boldsymbol{\nabla}_\perp\ c' = 0 \text{ on } \partial\Omega, \quad (4.30)$$

where $c'$ represents the fluctuation/deviation from the cross-sectional average and $s' = s - \langle s \rangle$. Since $\mathbb{L} : range\left(\mathbb{L}\right) \rightarrow range\left(\mathbb{L}\right)$ is invertible with the orthogonality constraint (4.22), it follows from implicit function theorem that the local equation (4.29) with boundary condition (4.30) can be solved for $c'$ uniquely in terms of all the modes appearing in the local equation.

Here, we use the perturbation expansion in local (transverse) Peclet number $p$ to solve the local equation. To use the perturbation expansion in $p$ properly, we must assign the order of other parameters present in the model such that each term can be compared in terms of order of $p$ properly. Here, we assume $Da \sim O(p^{\gamma_1})$. Time or length scale separation (perturbation in power series of small $p$) exists only when we have $\gamma_1 \geq 0$ (slow kinetics compared to transverse diffusion time). We consider here the case of Damkohler number of order unity, i.e., $\gamma_1 = 0$. It should

be noted that in this case, the leading order model (corresponding to $p = 0$) is hyperbolic (first order partial differential equation) in $x$ and $t$ :

$$\frac{\partial \langle c \rangle}{\partial t} + \langle u \rangle \frac{\partial \langle c \rangle}{\partial x} + Da \ \langle \beta \rangle R(\langle c \rangle) - \langle s \rangle = 0, \tag{4.31}$$

For $p = 0$, the local equation (4.29) with boundary condition (4.30) and orthogonality constraint (4.22) leads to $c' = 0$, i.e., there is no transverse variation in concentration. In this limit, all the modes are same and the global equation becomes exact. Since $c' = 0$ for $p = 0$, the perturbation expansion of $c'$ in terms of $p$ may be expressed as follows:

$$c'(\xi, \theta, x, t) = \sum_{i=1}^{\infty} p^i c_i(\xi, \theta, x, t) \tag{4.32}$$

where $c_i$ is the $i^{th}$ order correction. Using the expansion (4.32) in the local equation (4.29), we can write the equation for each order correction as follows:

$$\mathbb{L}c_1 = u' \frac{\partial \langle c \rangle}{\partial x} + Da \ \beta' \ R(\langle c \rangle) - s'(\xi, \theta, x, t), \text{ in } \Omega \tag{4.33}$$

$$\mathbb{L}c_2 = \frac{\partial c_1}{\partial t} + \frac{\partial}{\partial x}(uc_1 - \langle u'c_1 \rangle) + DaR'(\langle c \rangle)(\beta c_1 - \langle \beta' c_1 \rangle), \text{ in } \Omega \tag{4.34}$$

$$\mathbb{L}c_i = \frac{\partial c_{i-1}}{\partial t} + \frac{\partial}{\partial x}(uc_{i-1} - \langle u'c_{i-1} \rangle) + DaR'(\langle c \rangle)(\beta c_{i-1} - \langle \beta' c_{i-1} \rangle), \text{ in } \Omega \ \forall \ i \geq 3 \tag{4.35}$$

subject to the same zero flux boundary condition (4.30) and the same orthogonality constraint (4.22). It should be noted that other values of $\gamma_1$ will lead to different form of equations for each order correction $c_i$. It can be easily seen from equations (4.33, 4.34 and 4.35) that $i^{th}$ order correction $c_i$ can be solved in terms of first$(i-1)^{st}$ order corrections while the first order corrections can be solved in terms of $\langle c \rangle$.

While it is possible to derive the low-dimensional model to any order in the perturbation parameter using this approach, the main purpose of obtaining the reduced order model is to retain all the essential physics occurring at small scales without increasing the complexity of the model. For most practical applications, the first few corrections may be sufficient to capture the small scale (local) effects with sufficient quantitative accuracy. Therefore, we consider the solution of the local equation up to the first order in $p$ and express it in terms of measurable or physically meaningful quantities.

Solving the equations (4.33), we get

$$c_1 = \Gamma(\xi,\theta)\frac{\partial \langle c\rangle}{\partial x} + Da\ \chi(\xi,\theta)\ R(\langle c\rangle) - \zeta(\xi,\theta,x,t) \tag{4.36}$$

where the transverse functions $\Gamma$ and $\chi$, and $\zeta$ are given by

$$\mathbb{L}\Gamma = u';\ \mathbb{L}\chi = \beta';\ \ \mathbb{L}\zeta = s'(\xi,\theta,x,t),\ \text{in } \Omega \tag{4.37}$$

with the same boundary condition (4.30) and the same orthogonality constraint (4.22). It is easy to show that if $\mathbb{L}H_1 = h_1$ and $\mathbb{L}H_2 = h_2$, then $\langle H_1, h_2\rangle = \langle H_2, h_1\rangle$ as long as $H_1$, $H_2$, $h_1$ and $h_2$ satisfy the orthogonality constraint (4.22) and, $H_1$ and $H_2$ satisfy the zero flux boundary condition (4.30). Thus, using this property with equations(4.24-4.27), other modes can be written as

$$\begin{aligned}\langle u\rangle(c_m - \langle c\rangle) &= \langle c', u'\rangle \\ &= p\left[\langle \Gamma, u'\rangle\frac{\partial\langle c\rangle}{\partial x} + Da\ \langle\Gamma,\beta'\rangle\ R(\langle c\rangle) - \langle\Gamma, s'\rangle\right] + O(p^2) \qquad (4.38)\\ \langle\beta\rangle(\langle c\rangle_w - \langle c\rangle) &= \langle c', \beta'\rangle \\ &= p\left[\langle \chi, u'\rangle\frac{\partial\langle c\rangle}{\partial x} + Da\ \langle\chi,\beta'\rangle\ R(\langle c\rangle) - \langle\chi, s'\rangle\right] + O(p^2) \qquad (4.39)\end{aligned}$$

These transverse functions and the coefficients appearing in the above equations

(4.38, 4.39) are listed in Table 4.1.

Thus, the global equation (4.28) and local equations (4.38 and 4.39) form the averaged model. We can combine these equations to write a first order coarse-grained model in terms of $\langle c \rangle$ as follows:

$$\frac{\partial \langle c \rangle}{\partial t} + \langle u \rangle \frac{\partial \langle c \rangle}{\partial x} + p\frac{\partial}{\partial x}\left[\langle \Gamma, u' \rangle \frac{\partial \langle c \rangle}{\partial x} + Da\ \langle \Gamma, \beta' \rangle\ R(\langle c \rangle) - \langle \Gamma, s' \rangle\right] + Da\ \langle \beta \rangle R(\langle c \rangle) + pDa\ R'(\langle c \rangle)\left[\langle \chi, u' \rangle \frac{\partial \langle c \rangle}{\partial x} + Da\ \langle \chi, \beta' \rangle\ R(\langle c \rangle) - \langle \chi, s' \rangle\right] - \langle s \rangle = 0 + O\left(p^2\right) \quad . \tag{4.40}$$

It should be noted that the above coarse-grained model is valid for $x, t \geq 0$. We can separate the governing equation from inlet(/initial) conditions by integrating w.r.t.. $x\,(/t)$ from $x\,(/t) = 0$ to $0^+$. The governing equation for $x, t > 0$ is given by

$$\frac{\partial \langle c \rangle}{\partial t} + \left[\langle u \rangle + pDa\ \left(\langle \Gamma, \beta' \rangle + \langle \chi, u' \rangle\right)\ R'(\langle c \rangle)\right] \frac{\partial \langle c \rangle}{\partial x} + p \langle \Gamma, u' \rangle \frac{\partial^2 \langle c \rangle}{\partial x^2} + \left[\langle \beta \rangle + pDa\ \langle \chi, \beta' \rangle\ R'(\langle c \rangle)\right] Da\ R(\langle c \rangle) = 0 + O\left(p^2\right) \tag{4.41}$$

with inlet and initial conditions as follows:

$$\langle u \rangle \langle c \rangle + p \langle \Gamma, u' \rangle \frac{\partial \langle c \rangle}{\partial x} + pDa\ \langle \Gamma, \beta' \rangle\ R(\langle c \rangle) + pDa\ R(\langle c \rangle)\ \langle \chi, u' \rangle = \langle u\ c_{in} \rangle + pDa\ R'(\langle c \rangle) \langle \chi, u c_{in} \rangle + O\left(p^2\right) \quad @ \quad x = 0 \tag{4.42}$$

$$\langle c \rangle - pDa\ R'(\langle c \rangle) \langle \chi, c_0 \rangle - p\left\langle \Gamma, \frac{\partial c_0}{\partial x} \right\rangle - \langle c_0 \rangle = 0 + O\left(p^2\right)\ @\ t = 0. \tag{4.43}$$

The reduced order model given by equations (4.41-4.43), which is accurate to first order in $p$, is one of the main results of this work. We note that for $p = 0$, it reduces to the zeroth order hyperbolic model. For $0 < p \ll 1$, the governing equations (4.41) contains four first order correction terms. The term containing $\langle \Gamma, u' \rangle$ is the

Table 4.1: Various transverse functions and coefficients for fully developed laminar flow in a circular channel with a washcoat of uniform thickness

| | |
|---|---|
| $\Gamma$ | Fluid $\Gamma_f = \frac{(1+2\gamma)}{4(1+\gamma)}\xi^2 - \frac{1}{8}\xi^4 - \frac{\left(2+8\gamma+9\gamma^2\right)}{24(1+\gamma)^2} + \frac{\mu\gamma^2}{8(1+\gamma)^2\gamma_w^2}\left[2\gamma_w + 3\gamma_w^2 - 2\left(1+\gamma_w\right)^2 \mathsf{Ln}\left(1+\gamma_w\right)\right]$<br>Washcoat $\Gamma_w = -\frac{\mu\gamma}{4\gamma_w(1+\gamma)}\left[\xi^2 - 2\left(1+\gamma_w\right)\mathsf{Ln}\left(\xi\right)\right] + \frac{(1+4\gamma)}{24(1+\gamma)^2} + \frac{\mu\gamma}{8(1+\gamma)^2\gamma_w^2}\left[2\gamma_w + 4\gamma\gamma_w + 3\gamma\gamma_w^2 - 2\gamma\left(1+\gamma_w\right)^2 \mathsf{Ln}\left(1+\gamma_w\right)\right]$ |
| $\chi$ | Fluid $\chi_f = -\frac{\gamma_w}{4(1+\gamma)}\xi^2 + \frac{\gamma_w(1+2\gamma)}{8(1+\gamma)^2} - \frac{\mu\gamma}{8(1+\gamma)^2\gamma_w}\left[2\gamma_w + 3\gamma_w^2 - 2\left(1+\gamma_w\right)^2 \mathsf{Ln}\left(1+\gamma_w\right)\right]$<br>Washcoat $\chi_w = \frac{\mu}{4(1+\gamma)}\left[\xi^2 - 2\left(1+\gamma_w\right)\mathsf{Ln}\left(\xi\right)\right] - \frac{\mu\gamma_w}{8(1+\gamma)^2} - \frac{\mu}{8(1+\gamma)^2\gamma_w}\left[2\gamma_w + 4\gamma\gamma_w + 3\gamma\gamma_w^2 - 2\gamma\left(1+\gamma_w\right)^2 \mathsf{Ln}\left(1+\gamma_w\right)\right]$ |
| $\sigma$ | Fluid $\sigma_f = -\frac{\xi^2}{4} + \frac{(1+2\gamma)}{8(1+\gamma)} + \frac{\mu\gamma^2}{8(1+\gamma)\gamma_w^2}\left[2\gamma_w + 3\gamma_w^2 - 2\left(1+\gamma_w\right)^2 \mathsf{Ln}\left(1+\gamma_w\right)\right]$<br>Washcoat $\sigma_w = \frac{\mu\gamma}{4\gamma_w}\left[-\xi^2 + 2\mathsf{Ln}\left(\xi\right)\right] - \frac{1}{8(1+\gamma)} + \frac{\mu\gamma}{8(1+\gamma)^2\gamma_w^2}\left[2\gamma_w + 4\gamma\gamma_w + 3\gamma\gamma_w^2 - 2\gamma\left(1+\gamma_w\right)^2 \mathsf{Ln}\left(1+\gamma_w\right)\right]$ |
| $\langle\Gamma, u'\rangle$ | $-\frac{\left(1+6\gamma+11\gamma^2\right)}{48(1+\gamma)^3} + \frac{\mu\gamma^2}{8(1+\gamma)^3\gamma_w^2}\left[2\gamma_w + 3\gamma_w^2 - 2\left(1+\gamma_w\right)^2 \mathsf{Ln}\left(1+\gamma_w\right)\right]$ |
| $\langle\chi, u'\rangle$ = $\langle\Gamma, \beta'\rangle$ | $\frac{(1+4\gamma)\gamma_w}{24(1+\gamma)^3} - \frac{\mu\gamma}{8(1+\gamma)^3\gamma_w}\left[2\gamma_w + 3\gamma_w^2 - 2\left(1+\gamma_w\right)^2 \mathsf{Ln}\left(1+\gamma_w\right)\right]$ |
| $\langle\sigma, u'\rangle$ | $\frac{(1+4\gamma)}{24(1+\gamma)^2} + \frac{\mu\gamma^2}{8(1+\gamma)^2\gamma_w^2}\left[2\gamma_w + 3\gamma_w^2 - 2\left(1+\gamma_w\right)^2 \mathsf{Ln}\left(1+\gamma_w\right)\right]$ |
| $\langle\chi, \beta'\rangle$ | $-\frac{\gamma_w^2}{8(1+\gamma)^3} + \frac{\mu}{8(1+\gamma)^3}\left[2\gamma_w + 3\gamma_w^2 - 2\left(1+\gamma_w\right)^2 \mathsf{Ln}\left(1+\gamma_w\right)\right]$ |
| $\langle\sigma, \beta'\rangle$ | $-\frac{\gamma_w}{8(1+\gamma)^2} - \frac{\mu\gamma}{8(1+\gamma)^2\gamma_w}\left[2\gamma_w + 3\gamma_w^2 - 2\left(1+\gamma_w\right)^2 \mathsf{Ln}\left(1+\gamma_w\right)\right]$ |
| $2\left.\frac{\partial\Gamma}{\partial\xi}\right\|_{\xi=1^-}$ | $\frac{\gamma}{(1+\gamma)}$ |
| $2\left.\frac{\partial\chi}{\partial\xi}\right\|_{\xi=1^-}$ | $-\frac{\gamma_w}{(1+\gamma)}$ |

Taylor dispersion that arises due to velocity gradients. The term $\langle \chi, \beta' \rangle$ arises due to activity variation in the transverse direction. The terms containing $\langle \Gamma, \beta' \rangle$ and $\langle \chi, u' \rangle$ arise due to the coupling between chemical reaction and transverse velocity gradients.

It can be seen from equations (4.41) that if the coarse-grained model is represented in terms of a single mode, the apparent mean velocity and effective Damköhler number depend on kinetics and may lead to unphysical results for fast non-linear reactions. For example, the reaction term can change sign where $pDa\ R'\left(\langle c \rangle\right) > -\frac{\langle \beta \rangle}{\langle \chi, \beta \rangle}$ and so on. The single mode model has other disadvantages discussed elsewhere (Balakotaiah and Ratnakar, 2010). Therefore, we regularize the local equations and express the low-dimensional model in multi-mode form as follows:

$$\frac{\partial \langle c \rangle}{\partial t} + \langle u \rangle \frac{\partial c_m}{\partial x} + Da\ \langle \beta \rangle R\left(\langle c \rangle_w\right) = 0 \tag{4.44}$$

$$\langle u \rangle \left(c_m - \langle c \rangle\right) = p \left[ \langle \Gamma, u' \rangle \frac{\partial c_m}{\partial x} + Da\ \langle \Gamma, \beta' \rangle\ R\left(\langle c \rangle_w\right) \right] + O(p^2) \tag{4.45}$$

$$\beta \left(\langle c \rangle_w - \langle c \rangle\right) = p \left[ \langle \chi, u' \rangle \frac{\partial c_m}{\partial x} + Da\ \langle \chi, \beta' \rangle\ R\left(\langle c \rangle_w\right) \right] + O(p^2),\ \ x, t > 0 \tag{4.46}$$

where, the inlet and initial conditions can be simplified by using leading order approximations as follows:

$$c_m + pDa\ R\left(c_m\right) \left\langle \frac{u}{\langle u \rangle}, \chi \right\rangle = c_{m,in} + pDa\ R'\left(c_{m,in}\right) \left\langle \chi, \frac{u c_{in}}{\langle u \rangle} \right\rangle + O\left(p^2\right) \quad @ \quad x = 0, \tag{4.47}$$

$$\langle c \rangle = \langle c_0 \rangle + p \left\langle \Gamma, \frac{\partial c_0}{\partial x} \right\rangle + pDa\ R'\left(\langle c_0 \rangle\right) \langle \chi, c_0 \rangle + O\left(p^2\right)\ @\ t = 0 \tag{4.48}$$

where $c_{m,in} = \frac{\langle u c_{in} \rangle}{\langle u \rangle}$ is the inlet cup-mixing concentration. The local equations (4.45, 4.46) are regularized version of local equations (4.38, 4.39). It should be noted

that the initial/inlet conditions for the reduced order model depend not only on the transverse dependency of the inlet/initial conditions of the detailed model but also contain order $p$ terms that depend on the kinetics for the case of non-uniform catalyst activity profile. [For an explanation of regularization and how it expands the the range of validity of the reduced order model, we refer to the article by Chakraborty and Balakotaiah, 2005].

The concentrations $\langle c \rangle$ and $\langle c \rangle_w$ are not easily measurable and not used in practice. To express the reduced order model in a convenient form for applications, we define two different inner products in fluid phase and washcoat as follows:

$$\langle u, v \rangle_f = \frac{1}{A_{\Omega_f}} \int_0^{2\pi} \int_0^1 \xi \, u(\xi, \theta) \; v(\xi, \theta) \; d\xi d\theta \, ; \quad \langle u, v \rangle_w = \frac{1}{A_{\Omega_w}} \int_0^{2\pi} \int_1^{1+\lambda} \xi \, u(\xi, \theta) \; v(\xi, \theta) \; d\xi d\theta \tag{4.49}$$

where $A_{\Omega_f} = \pi$ and $A_{\Omega w} = \pi\lambda(\lambda + 2)$. If $\varepsilon_f$ is the fraction of the cross-section area of the channel open to flow and $\varepsilon_w$ is the fraction of cross-section area of the washcoat, i.e.,

$$\varepsilon_f = \frac{A_{\Omega_f}}{A_{\Omega_f} + A_{\Omega_w}} = \frac{1}{(1+\lambda)^2}; \text{ and } \varepsilon_w = 1 - \varepsilon_f = \frac{A_{\Omega_w}}{A_{\Omega_f} + A_{\Omega_w}} = \frac{\lambda(\lambda+2)}{(1+\lambda)^2}, \tag{4.50}$$

then we can define the volume ratio of washcoat to flow channel ($\gamma_w$) and capacitance ratio ($\gamma$) as

$$\gamma_w = \frac{\varepsilon_w}{\varepsilon_f}; \quad \text{and} \quad \gamma = \frac{\varepsilon_{wc}\varepsilon_w}{\varepsilon_f}. \tag{4.51}$$

Thus the inner products can be written as follows:

$$\langle u, v \rangle = \frac{\langle u, v \rangle_f + \gamma \langle u, v \rangle_w}{1 + \gamma} \tag{4.52}$$

and hence,

$$\langle u\rangle = \frac{1}{1+\gamma};\ \ \langle \beta\rangle = \frac{\gamma_w}{1+\gamma}; \langle c\rangle = \frac{\langle c\rangle_f + \gamma \langle c\rangle_w}{1+\gamma}; \frac{\langle \beta c\rangle}{\langle \beta\rangle} = \langle c\rangle_w \tag{4.53}$$

$$c_m = \frac{\langle uc\rangle}{\langle u\rangle} = \langle uc\rangle_f = c_{mf}\ ;\ \ \langle s\rangle = \frac{\left(\langle c_{f0}\rangle_f + \gamma \langle c_{w0}\rangle_w\right)\delta(t) + \langle uc_{in}\rangle_f \delta(x)}{1+\gamma} \tag{4.54}$$

where $\langle c\rangle_f$ and $\langle c\rangle_w$ are the cross-sectional average concentrations in fluid phase and washcoat, respectively. $c_{mf}$ is the cup-mixing concentration in the fluid-phase. Now, integrating the dimensionless form of the full model equation (4.9) over the fluid phase ($\Omega_f$), we get the averaged equation for fluid phase as follows:

$$\frac{\partial \langle c\rangle_f}{\partial t} + \frac{\partial c_m}{\partial x} - \langle s\rangle_f = \frac{1}{2\pi}\int_0^{2\pi} \frac{2}{p}\left.\frac{\partial c}{\partial \xi}\right|_{\xi=1^-} d\theta = -J \tag{4.55}$$

which is exact and valid to all orders in $p$ (provided the exact flux $J$ is also determined to all order in $p$). Similarly, integrating the same equation (4.9) over washcoat ($1 < \xi < 1+\lambda$) with zero flux boundary condition (4.10) leads to the averaged equation in washcoat as follows:

$$\frac{\partial \langle c\rangle_w}{\partial t} + \frac{\gamma_w}{\gamma} Da\ R\left(\langle c\rangle_w\right) - \langle s\rangle_w = -\frac{1}{\mu\gamma}\frac{1}{2\pi}\int_0^{2\pi} \frac{2}{p}\left.\frac{\partial c}{\partial \xi}\right|_{\xi=1^+} d\theta = \frac{1}{\gamma}J \tag{4.56}$$

which is also exact in $p$ for the case of linear reactions and accurate to $O\left(p^2\right)$ for non-linear reactions. Here, $J$ is the dimensionless diffusive flux from fluid phase to the washcoat, averaged over the periphery of the fluid-washcoat interface. An expression for the flux $J$ can be obtained by subtracting equations (4.55) from

equations (4.56):

$$J = -\frac{\gamma}{1+\gamma}\left[\frac{\partial c_m}{\partial x} - \frac{\gamma_w}{\gamma} Da\ R\left(\langle c\rangle_w\right) - \langle s\rangle_f + \langle s\rangle_w + \frac{\partial}{\partial t}\left(\langle c\rangle_f - \langle c\rangle_w\right)\right] \quad (4.57)$$

It should be noted that only two of the above equations (4.55, 4.56 and 4.57) are independent. They contain four unknowns, namely, the averaged concentration in washcoat and fluid phase ($\langle c\rangle_w$ and $\langle c\rangle_f$), cup-mixing concentration $(c_{mf})$ and peripheral averaged interfacial flux $(J)$. Hence, we need two local equations to close the model. Using equations (4.44-4.48) and equations (4.53, 4.54) we can write the difference between cross-sectional average concentrations in fluid phase, washcoat and overall cross-section as follows:

$$\begin{aligned}\langle c\rangle_w - \langle c\rangle &= \frac{1}{\gamma}\left(\langle c\rangle - \langle c\rangle_f\right) = \frac{1}{1+\gamma}\left(\langle c\rangle_w - \langle c\rangle_f\right) \\ &= \frac{p}{\langle\beta\rangle}\left[\langle\chi, u'\rangle\frac{\partial c_m}{\partial x} + \langle\chi, \beta'\rangle\, Da\ R\left(\langle c\rangle_w\right) - \langle\chi, s'\rangle\right]. \quad (4.58)\end{aligned}$$

while the difference between cup-mixing and cross-sectional averaged concentration in fluid phase can be written as follows:

$$c_m - \langle c\rangle_f = \frac{p}{\langle u\rangle}\left[\left\langle\Gamma + \frac{\gamma}{\gamma_w}\chi, u'\right\rangle\frac{\partial c_m}{\partial x} + \left\langle\Gamma + \frac{\gamma}{\gamma_w}\chi, \beta'\right\rangle Da\ R\left(\langle c\rangle_w\right) - \left\langle\Gamma + \frac{\gamma}{\gamma_w}\chi, s'\right\rangle\right] \quad (4.59)$$

Now, we can write the averaged model in several forms in terms of various concentration modes ($\langle c\rangle_f, \langle c\rangle_w, c_{mf}, \langle c\rangle$) and interfacial flux $(J)$. However, as discussed by Balakotaiah and Ratnakar (2010), we need at least three modes (two modes in flow channel to express the effect of transients and convection, and one mode in washcoat to describe the transients and reaction) to describe the various phenomena accurately. The three mode form of the averaged model in terms of $\langle c\rangle_w, c_{mf}$

and $\langle c \rangle$ is given by

$$\frac{\partial \langle c \rangle}{\partial t} + \langle u \rangle \frac{\partial c_m}{\partial x} + \langle \beta \rangle \, Da \; R\left(\langle c \rangle_w\right) = 0 \tag{4.60}$$

$$c_m - \langle c \rangle = \frac{p}{\langle u \rangle} \left[ \langle \Gamma, u' \rangle \frac{\partial c_m}{\partial x} + Da \;\; \langle \Gamma, \beta' \rangle \;\; R\left(\langle c \rangle_w\right) \right] + O(p^2) \tag{4.61}$$

$$\langle c \rangle_w - \langle c \rangle = \frac{1}{\gamma} \left( \langle c \rangle - \langle c \rangle_f \right) = \frac{p}{\langle \beta \rangle} \left[ \langle \chi, u' \rangle \frac{\partial c_m}{\partial x} + Da \;\; \langle \chi, \beta' \rangle \;\; R\left(\langle c \rangle_w\right) \right] + O(p^2) \tag{4.62}$$

$$\langle c \rangle = \frac{\langle c \rangle_f + \gamma \langle c \rangle_w}{1 + \gamma} \tag{4.63}$$

with inlet/initial conditions as follows:

$$c_m + pDa \; R\left(c_m\right) \;\; \langle u, \chi \rangle_f = c_{m,in} + pDa \; R'\left(c_{m,in}\right) \langle \chi, u c_{in} \rangle_f + O\left(p^2\right) \quad @ \quad x = 0, \tag{4.64}$$

$$\langle c \rangle = \langle c_0 \rangle + p \left\langle \Gamma, \frac{\partial c_0}{\partial x} \right\rangle + pDa \; R'\left(\langle c_0 \rangle\right) \langle \chi, c_0 \rangle + O\left(p^2\right) \;\; @ \, t = 0 \tag{4.65}$$

Here, the global equations (4.60) represents the reactant balance in the whole domain (flow channel + washcoat) while the local equations(4.61, 4.62) represent the concentration differences due to transverse diffusion and catalytic reaction in the flow channel and washcoat.

We can also write the averaged model in other forms such as in terms of averaged concentration in washcoat and fluid phase $\left(\langle c \rangle_w \text{ and } \langle c \rangle_f\right)$ and cup-mixing concentration $(c_{mf})$ as follows:

$$\frac{\partial \langle c \rangle_f}{\partial t} + \frac{\partial c_{mf}}{\partial x} = - \, J = - \left[ \gamma \frac{\partial \langle c \rangle_w}{\partial t} + \gamma_w Da \; R\left(\langle c \rangle_w\right) \right] \tag{4.66}$$

$$c_{mf} - \langle c \rangle_f = \frac{p}{\langle u \rangle} \left[ \left\langle \Gamma + \frac{\gamma}{\gamma_w} \chi, u' \right\rangle \frac{\partial c_{mf}}{\partial x} + \left\langle \Gamma + \frac{\gamma}{\gamma_w} \chi, \beta' \right\rangle Da \; R\left( \langle c \rangle_w \right) \right] \quad (4.67)$$

$$c_{mf} - \langle c \rangle_w = p \left[ \left\langle \frac{\Gamma}{\langle u \rangle} - \frac{\chi}{\langle \beta \rangle}, u' \right\rangle \frac{\partial c_{mf}}{\partial x} + \left\langle \frac{\Gamma}{\langle u \rangle} - \frac{\chi}{\langle \beta \rangle}, \beta' \right\rangle Da \; R\left( \langle c \rangle_w \right) \right] \quad (4.68)$$

Now, the local equation (4.67) is expressed in terms of the difference between convective mode $c_{mf}$ and diffusive mode $\langle c \rangle_f$ in the flow channel where the coefficient $\frac{p}{\langle u \rangle} \left\langle \Gamma + \frac{\gamma}{\gamma_w} \chi, u' \right\rangle$ is the dimensionless Taylor dispersion coefficient that depends on the volume fraction of the flow channel as well as the ratio of diffusivity in flow channel and washcoat. The second coefficient $\frac{p}{\langle u \rangle} \left\langle \Gamma + \frac{\gamma}{\gamma_w} \chi, \beta' \right\rangle$ represents the effect of washcoat catalytic reaction on dispersion in the flow channel. The local equations(4.68) represents the mass transfer between convective mode $c_{mf}$ in the flow channel and reactive mode $\langle c \rangle_w$ in the washcoat. The corresponding inlet and initial condition with $O(p)$ modification are given by

$$c_{mf} + pDa \; R\left( c_{mf} \right) \; \langle \chi, u \rangle_f = c_{m,in} + pDa \; R'\left( c_{m,in} \right) \langle \chi, u c_{in} \rangle_f \; @ \quad x = 0, \quad (4.69)$$

$$\langle c \rangle_f = \langle c_{f0} \rangle_f + p \frac{\partial}{\partial x} \langle \Gamma, c_{f0} \rangle_f + pDa \; R'\left( c_{f0} \right) \langle \chi, c_{f0} \rangle_f \; @ \, t = 0, \quad (4.70)$$

and

$$\langle c \rangle_w = \langle c_{w0} \rangle_w + p \frac{\partial}{\partial x} \langle \Gamma, c_{w0} \rangle_w + pDa \; R'\left( c_{w0} \right) \langle \chi, c_{w0} \rangle_w \; @ \, t = 0 \quad (4.71)$$

As stated in the introduction, in the literature, the transfer coefficient concept is used to express the interfacial flux in terms of the difference between various concentration modes that includes the interfacial concentration. This is examined in the next section.

## 4.4 Interfacial flux and internal and external transfer coefficients

The peripheral average concentration and flux at the fluid-washcoat interface play an important role in the understanding of the intra and interphase gradients.

In this section, we introduce the peripheral average concentration mode and represent the interfacial flux in terms of the difference between various concentration modes and determine the external or internal mass transfer coefficients, when they are meaningful.

The peripheral average fluid-washcoat interfacial concentration is defined by

$$\langle c_s \rangle = \frac{1}{2\pi} \int_0^{2\pi} c\left(\xi = 1, \theta\right) d\theta = \frac{1}{\pi} \int_0^{2\pi} \int_0^{1+\lambda} \xi \;\; c\left(\xi, \theta\right) \;\; \delta_2\left(\xi - 1\right) \;\; d\xi d\theta \; ; \tag{4.72}$$

where, $\delta_2\left(\xi - 1\right)$ is the standard cylindrical Dirac-delta function at the fluid-washcoat interface $(\xi = 1)$. Thus, the peripheral average surface concentration may be expressed as follows:

$$\langle c_s \rangle - \langle c \rangle = p \left\langle c_1, \frac{A_\Omega}{\pi} \delta_2\left(\xi - 1\right) \right\rangle = p \left[ \langle \sigma, u' \rangle \frac{\partial c_{mf}}{\partial x} + \langle \sigma, \beta' \rangle \, Da \; R\left(\langle c \rangle_w\right) \right] \tag{4.73}$$

where the transverse function $\sigma\left(\xi, \theta\right)$ is given by

$$\mathbb{L}\sigma = \frac{A_\Omega}{\pi} \delta_2\left(\xi - 1\right) - 1, \quad 0 < \xi < 1 + \lambda \tag{4.74}$$

subject to the zero flux boundary condition at the outer surface of washcoat as $\left.\frac{\partial \sigma}{\partial \xi}\right|_{\xi = 1+\lambda} = 0$ and the orthogonality constraint $\langle \sigma \rangle = 0$. This can be further simplified as follows:

$$\sigma = \begin{cases} \sigma_f : \nabla_\perp^2 \sigma_f = -1 \quad \text{in } \; \Omega_f \\ \sigma_w : \frac{1}{\mu} \nabla_\perp^2 \sigma_w = -1 \quad \text{in } \; \Omega_w \end{cases} \tag{4.75}$$

subject to zero flux boundary, $\left.\frac{\partial \sigma}{\partial \xi}\right|_{\xi = 1+\lambda} = 0$, orthogonality constraint $\langle \sigma, \psi_0 \rangle = 0$ and the continuity $\sigma_f = \sigma_w$ at $\xi = 1$. It must be noted that this transverse function $\sigma\left(\xi, \theta\right)$ does not satisfy the flux continuity at the interface due to presence of Dirac-

delta function $\delta_2(\xi-1)$. In fact, we can show from equations(4.75) that

$$\left(\frac{1}{\mu}\left.\frac{\partial\sigma_w}{\partial\xi}\right|_{\xi=1}-\left.\frac{\partial\sigma_f}{\partial\xi}\right|_{\xi=1}\right)=\frac{1}{2}\frac{A_\Omega}{\pi}. \tag{4.76}$$

However, this condition is automatically satisfied when solved for $\sigma(\xi,\theta)$. We have listed $\sigma(\xi,\theta)$ and coefficients ($\langle\sigma,u'\rangle\ \langle\sigma,\beta'\rangle$) in equations (4.73) in Table 4.1.

Now, the interfacial flux can be expressed as follows:

$$\begin{aligned}J=&-\frac{\gamma}{1+\gamma}\left[\frac{\partial c_{mf}}{\partial x}-\frac{\gamma_w}{\gamma}Da\ R\left(\langle c\rangle_w\right)\right]\\&+p\frac{\gamma}{\gamma_w}\left[\langle\chi,u\rangle_f\frac{\partial^2 c_{mf}}{\partial x\partial t}-Da\ \langle\chi,\beta'\rangle\ R'\left(\langle c\rangle_w\right)\left(\frac{\partial c_{mf}}{\partial x}+\gamma_w Da\ R\left(\langle c\rangle_w\right)\right)\right]\end{aligned} \tag{4.77}$$

while the difference between cup-mixing concentration $c_m$ and average interfacial concentration $c_s$ using Table 4.1 may be expressed as follows:

$$\begin{aligned}c_{mf}-\langle c_s\rangle &= p\left[\left\langle\frac{\Gamma}{\langle u\rangle}-\sigma,u'\right\rangle\frac{\partial c_{mf}}{\partial x}+\left\langle\frac{\Gamma}{\langle u\rangle}-\sigma,\beta'\right\rangle Da\ R\left(\langle c\rangle_w\right)\right] &(4.78)\\ &= p\left[\left(-\frac{3+11\gamma}{48\left(1+\gamma\right)}\right)\frac{\partial c_{mf}}{\partial x}+\frac{\gamma_w}{6\left(1+\gamma\right)}Da\ R\left(\langle c\rangle_w\right)\right] &(4.79)\end{aligned}$$

Similarly, the difference between average interfacial concentration $c_s$ and average concentration in washcoat $\langle c\rangle_w$) using Table 4.1 as follows:

$$\langle c_s\rangle-\langle c\rangle_w=p\left[\left\langle\sigma-\frac{\chi}{\langle\beta\rangle},u'\right\rangle\frac{\partial c_{mf}}{\partial x}+\left\langle\sigma-\frac{\chi}{\langle\beta\rangle},\beta'\right\rangle Da\ R\left(\langle c\rangle_w\right)\right] \tag{4.80}$$

$$=\frac{p\mu\gamma\left(2\gamma_w+3\gamma_w^2-2\left(1+\gamma_w\right)^2\mathsf{Ln}\left(1+\gamma_w\right)\right)}{8\left(1+\gamma\right)\gamma_w^2}\left[\frac{\partial c_{mf}}{\partial x}-\frac{\gamma_w}{\gamma}Da\ R\left(\langle c\rangle_w\right)\right] \tag{4.81}$$

It can be seen from equations (4.77) and equations (4.80-4.82) that the difference between the concentration modes $\langle c_s\rangle$ and $\langle c\rangle_w$ is proportional to the interfacial

flux $J$ to leading order, i.e.,

$$\langle c_s \rangle - \langle c \rangle_w = -\frac{\mu \left(2\gamma_w + 3\gamma_w^2 - 2\left(1+\gamma_w\right)^2 \mathsf{Ln}\left(1+\gamma_w\right)\right)}{\left(8\gamma_w^2\right)} pJ \tag{4.82}$$

Equivalently, the interfacial flux can be expressed in terms of the difference (or driving force), $(\langle c_s \rangle - \langle c \rangle_w)$ using the internal transfer coefficient concept (Balakotaiah, 2008). The internal mass transfer coefficient is defined as the ratio of average peripheral flux to the concentration difference, i.e.,

$$k_{int} = \frac{\frac{1}{2\pi}\int_0^{2\pi} (-D_w \left.\frac{\partial c}{\partial r}\right|_{r=a^+}) d\theta}{\langle c_s \rangle - \langle c \rangle_w}. \tag{4.83}$$

Therefore, the dimensionless internal mass transfer coefficient or Sherwood number $(Sh_{\Omega i})$ may be expressed as

$$\begin{aligned} Sh_{\Omega i} &= \frac{k_{int} R_{\Omega_w}}{D_w} = -\frac{\mu}{4}\frac{\gamma_w^2}{(1+\gamma)} \left\langle \sigma - \frac{\chi}{\langle\beta\rangle}, \beta' \right\rangle^{-1} \\ &= \frac{2\gamma_w^3}{\left(2\gamma_w + 3\gamma_w^2 - 2\left(1+\gamma_w\right)^2 \mathsf{Ln}\left(1+\gamma_w\right)\right)} \end{aligned} \tag{4.84}$$

[Here, $R_{\Omega_w}$ is the effective washcoat thickness, defined as the washcoat cross-sectional area over the fluid-washcoat interfacial perimeter]. The internal Sherwood number is plotted in Figure 4.2. We note that when the washcoat thickness is small $(\varepsilon_w \to 0$ or $\gamma_w \to 0)$, the curvature effect may be neglected and $Sh_{\Omega i}$ approaches the thin washcoat limit of $3$, verifying the previous results of Balakotaiah (2008) and Joshi et al. (2009).

In the chemical reaction engineering and heat and mass transfer literature, the interfacial flux is also expressed in terms of the concentration modes $c_{mf}$ and $\langle c_s \rangle$ using the external mass transfer coefficient. We note from equations (4.77) and 4.79) that $J$ is not proportional to the difference $(c_{mf} - \langle c_s \rangle)$. It is also not pro-

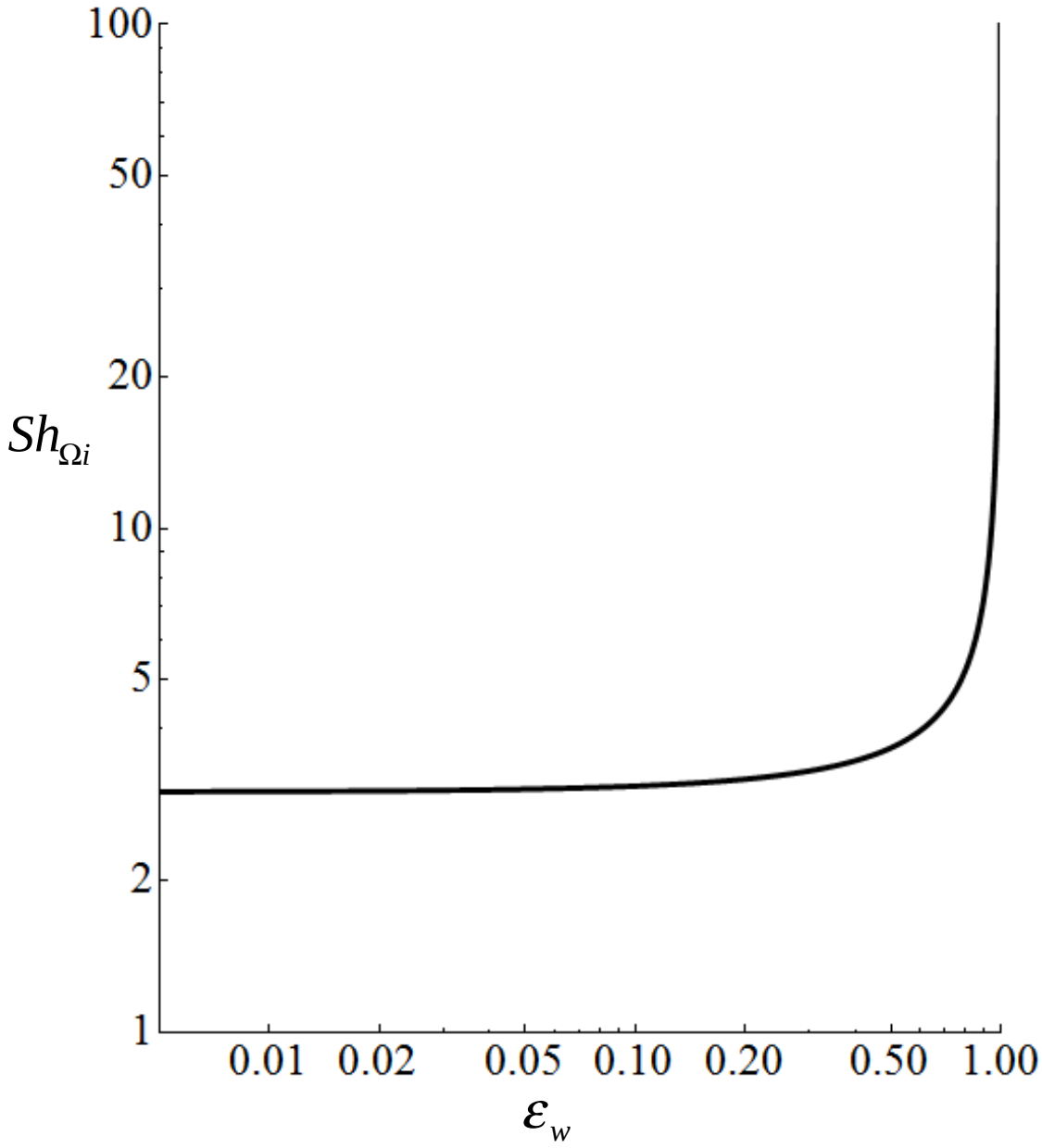


Figure 4.2: Variation of the internal Sherwood number with washcoat volume fraction.

portional to the difference $\left(\langle c\rangle_f - \langle c_s\rangle\right)$. However, combining equations(4.67, 4.77 and 4.79), we can express the flux in terms of the interfacial mode $\langle c_s\rangle$ and the two external fluid phase modes $c_{mf}$ and $\langle c\rangle_f$ as

$$J = \frac{24}{p}\left(3\langle c\rangle_f - \langle c_s\rangle - 2c_{mf}\right) + O(p) \tag{4.85}$$

It can be seen from above expression that in the general case in which the transverse or local gradients are due to the interaction of catalytic reaction, velocity gradients and molecular diffusion in the channel and varying inlet or initial conditions, the flux $J$ can not be written in terms of difference between an external mode and the interfacial mode but depends on both external modes and the interfacial mode and must be expressed as

$$J = \alpha_1\left(\langle c\rangle_f - c_{mf}\right) + \alpha_2\left(\langle c\rangle_f - \langle c_s\rangle\right); \tag{4.86}$$

where $\alpha_1 = \frac{48}{p}$ and $\alpha_2 = \frac{24}{p}$ for the fully developed laminar flow through cylindrical channel. However, for the three special cases of steady-state conditions, or no reaction case, or flat velocity profile, the the interfacial flux can be expressed in terms of the difference (or driving force), $(c_m - \langle c_s\rangle)$ using the external transfer coefficient concept. The external mass transfer coefficient is defined as the ratio of average peripheral flux to the concentration difference, i.e.,

$$k_{ext} = \frac{\frac{1}{2\pi}\int_0^{2\pi}(-D_f\ \frac{\partial c}{\partial r}\big|_{r=a^-})d\theta}{c_m - \langle c_s\rangle} \tag{4.87}$$

Therefore, the dimensionless external mass transfer coefficient or Sherwood num-

ber $(Sh_e)$ may be expressed as

$$Sh_e = \frac{k_{ext}(4R_{\Omega_f})}{D_m} \tag{4.88}$$

[Here, $d_h = 4R_{\Omega_f}$ is the hydraulic diameter of the flow channel defined as the four times flow area over the fluid-washcoat interfacial perimeter]. Thus, in special cases of steady-state conditions, or no reaction case, or flat velocity profile, the interfacial flux can be expressed in terms of the difference (or driving force), $(c_m - \langle c_s \rangle)$ as follows:

$$c_{mf} - \langle c_s \rangle = Sh_e^{-1} \;\; p \; J \tag{4.89}$$

where the external Sherwood number $Sh_e$ in these cases is given by

$$\begin{aligned} Sh_{e,ss} &= \left\langle \frac{\Gamma}{\langle u \rangle} - \sigma, \frac{1}{\gamma_w}\beta' - u' \right\rangle^{-1} = \frac{48}{11} \\ Sh_{e,non-react} &= -\frac{\gamma}{1+\gamma} \left\langle \frac{\Gamma}{\langle u \rangle} - \sigma, u' \right\rangle^{-1} = \frac{48\gamma}{3+11\gamma} \\ Sh_{e,flat} &= k_{er,flat} = \gamma_w \left\langle (1+\gamma_w)\,\Gamma - \sigma, \beta' \right\rangle^{-1} \Big|_{flat} = 8. \end{aligned} \tag{4.90}$$

In the next section, we simplify the general multi-mode model for these special cases and give a physical interpretation of transfer/dispersion coefficients in the final reduced order models. We also obtain the solution of the reduced order model for some special cases and compare it with exact solutions when available.

## 4.5 Limiting cases of the reduced order model

### 4.5.1 Thin washcoat and wall reaction limits $(\varepsilon_w \ll 1)$

When the washcoat thickness is small compared to the channel hydraulic diameter, the curvature effect can be neglected and diffusion in the washcoat can be treated by assuming that it is a flat layer. In this case, the main simplification is in

the local equation that gives the difference between average interfacial concentration $c_s$ and average concentration in the washcoat $\langle c \rangle_w$). For a thin washcoat, the reduced order model equations may be expressed as follows:

$$\frac{\partial \langle c \rangle_f}{\partial t} + \frac{\partial c_{mf}}{\partial x} = - J = - \left[ \gamma \frac{\partial \langle c \rangle_w}{\partial t} + \gamma_w Da \; R\left( \langle c \rangle_w \right) \right] \tag{4.91}$$

$$c_{mf} - \langle c \rangle_f = p \left[ -\frac{1}{48} \left( \frac{1+3\gamma}{1+\gamma} \right) \frac{\partial c_{mf}}{\partial x} + \frac{1}{24} \left( \frac{\gamma_w}{1+\gamma} \right) \; Da \; R\left( \langle c \rangle_w \right) \right] \tag{4.92}$$

$$c_{mf} - \langle c_s \rangle = p \left[ -\frac{1}{48} \left( \frac{3+11\gamma}{1+\gamma} \right) \frac{\partial c_{mf}}{\partial x} + \frac{1}{6} \left( \frac{\gamma_w}{1+\gamma} \right) \; Da \; R\left( \langle c \rangle_w \right) \right] \tag{4.93}$$

$$\langle c_s \rangle - \langle c \rangle_w = -p \frac{\mu \gamma \gamma_w}{12\left(1+\gamma\right)} \left[ \frac{\partial c_{mf}}{\partial x} - \; \frac{\gamma_w}{\gamma} Da R\left( \langle c \rangle_w \right) \right] \tag{4.94}$$

with the initial and inlet conditions given by equations (4.70, 4.71). A further simplification of the above model can be obtained if the gradients in the washcoat are neglected without diluting the catalytic sites. This wall reaction case corresponds to the limit of $\varepsilon_w \to 0$ (or $\gamma_w \to 0$) but $\underset{\gamma_w \to 0}{Lt} \left( \gamma_w Da \right) = Da_s$ is finite and of order unity. For this wall reaction case, the difference between average interfacial concentration $c_s$ and average concentration in the washcoat $\langle c \rangle_w$ vanishes and we obtain the three mode model:

$$\frac{\partial \langle c \rangle_f}{\partial t} + \frac{\partial c_{mf}}{\partial x} = - J = -Da_s \; R\left( \langle c \rangle_w \right) \tag{4.95}$$

$$c_{mf} - \langle c \rangle_f = p \left[ \frac{-1}{48} \frac{\partial c_{mf}}{\partial x} + \frac{1}{24} \; Da_s \; R\left( \langle c \rangle_w \right) \right] \tag{4.96}$$

$$c_{mf} - \langle c \rangle_w = p \left[ \frac{-1}{16} \frac{\partial c_{mf}}{\partial x} + \frac{1}{6} \; Da_s \; R\left( \langle c \rangle_w \right) \right] \tag{4.97}$$

which corresponds to the laminar flow through circular channel with catalytic reaction at the wall (and the assumption of no accumulation of reactant on catalytic sites on the wall). The above model equations were derived earlier by Balakotaiah (2004), the main addition being the $O(p)$ corrections to the inlet and initial con-

ditions and the expression for the flux. We note that even for this widely studied case, the flux at the wall is given by

$$J = \frac{24}{p}\left(3\left\langle c\right\rangle_f - \left\langle c_s\right\rangle - 2c_{mf}\right), \tag{4.98}$$

which is the same expression as that obtained for a washcoat of finite thickness. This limiting case is the simplest example that illustrates one of the main results of this work, i.e., under unsteady-state conditions and when velocity gradients exist in the fluid phase, the flux of the reactant to the wall cannot be written as a transfer coefficient times the difference between any two concentration modes. Here, the coefficient $\frac{1}{48}$ is the dimensionless Taylor-diffusivity under non-reactive conditions. The addition of wall reaction couples the three modes and adds the terms with coefficients $\frac{1}{24}$ and $\frac{1}{6}$, in equations (4.96, 4.97). Only for the case of steady-state conditions, the flux may be expressed in terms of two modes:

$$c_{mf} - \left\langle c\right\rangle_w = \frac{11}{48}\, pDa_s\, R\left(\left\langle c\right\rangle_w\right) = \frac{11}{48}\, pJ \tag{4.99}$$

where the coefficient $\frac{48}{11}$ is the dimensionless external mass transfer coefficient (Sherwood number, $Sh_e$).

### 4.5.2 steady-state model:

An important limiting case that is of interest in applications is the steady-state operation of the monolith. For this case, it is possible to solve the detailed model to obtain analytical expressions for the reactant conversion for the special case of linear kinetics and the limits of very small and large Schmidt numbers, or flat and parabolic velocity cases (Bhattacharya et al., 2004a,b; Gupta and Balakotaiah, 2001). These solutions can be used to compare the accuracy of the reduced order model.

For steady-state conditions, the multi-mode model describing the evolution of

the cup-mixing concentration along the length may be expressed as

$$\frac{dc_{mf}}{dx} = -J \tag{4.100}$$

$$J = \gamma_w Da\ R\left(\langle c\rangle_w\right) \tag{4.101}$$

$$= \frac{(8\gamma_w^2)}{\left(2\gamma_w + 3\gamma_w^2 - 2\left(1+\gamma_w\right)^2 \mathsf{Ln}\left(1+\gamma_w\right)\right)} \frac{\left(\langle c_s\rangle - \langle c\rangle_w\right)}{\mu\ p} \tag{4.102}$$

$$= \frac{\left(c_{mf} - \langle c_s\rangle\right)}{p}\frac{48}{11} \tag{4.103}$$

with modified inlet condition given by

$$c_{mf} + pDa\ R\left(c_{mf}\right)\ \langle \chi, u\rangle_f = c_{m,in} + R'\left(c_{m,in}\right)\langle \chi, uc_{in}\rangle_f \ @ \quad x = 0. \tag{4.104}$$

The above model can be further simplified by eliminating the flux and the interfacial mode $\langle c_s\rangle$ to obtain a single differential equation coupled to an algebraic equation:

$$\frac{dc_{mf}}{dx} + \gamma_w Da\ R\left(\langle c\rangle_w\right) = 0 \tag{4.105}$$

$$\frac{c_{mf} - \langle c\rangle_w}{p} = \gamma_w Da\ R\left(\langle c\rangle_w\right)\left[\frac{11}{48} + \frac{\left(2\gamma_w + 3\gamma_w^2 - 2\left(1+\gamma_w\right)^2 \mathsf{Ln}\left(1+\gamma_w\right)\right)}{2\gamma_w^3}\right] \tag{4.106}$$

The term in square brackets of equations(4.106) defines the overall mass transfer resistance which is defined, in dimensional form, as

$$k_o = \frac{\frac{1}{2\pi}\int_0^{2\pi}(-D_f\ \frac{\partial c}{\partial r}\big|_{r=a^-})d\theta}{c_{mf} - \langle c\rangle_w}. \tag{4.107}$$

and in nondimensional form (overall Sherwood number) based on hydraulic diameter, as

$$\frac{1}{Sh_o} = \frac{D_f}{4k_o R_{\Omega_f}} = \frac{1}{Sh_e} + \frac{\mu}{4}\gamma_w \frac{1}{Sh_{\Omega i}} \tag{4.108}$$

where the external and internal Sherwood numbers are as defined previously.

For the special case of linear kinetics ($R\left(\langle c\rangle_w\right) = \langle c\rangle_w$), the inlet condition given by equations (4.104) simplifies to

$$c_{mf}(0) = \frac{\langle 1 + pDa\ \chi, uc_{in}\rangle_f}{\langle 1 + pDa\ \chi, u\rangle_f} = \alpha_1\ c_{m,in} + O(p^2) \tag{4.109}$$

The second equality in equations(4.109) defines the Fourier coefficient $\alpha_1$, which approaches unity for $p \rightarrow 0$ while $Da$ is of order unity. This coefficient also depends on the type of inlet release and approaches unity for the special case in which the inlet concentration is independent of the transverse coordinates. This result is consistent with analytical and numerical solutions presented in the literature (Bhattacharya et al., 2004a,b; Gupta and Balakotaiah, 2001) where it was observed that $\alpha_1$ depends only on the product $pDa$ and $\alpha_1 = 1 + O\left((pDa)^2\right)$. We note that for nonlinear kinetics or for the case of fast reactions (where $pDa$ is of order unity), the inlet condition, equations (4.104) has to be solved in combination with the local equation (4.106) to determine $c_{mf}(0)$ and $\langle c\rangle_w(0)$. As discussed elsewhere, these equations could have multiple solutions (Gupta and Balakotaiah, 2001).

As stated earlier, an analytical solution may be obtained for the exit cup-mixing concentration for the special case of linear kinetics. In this case, the solution of equations (4.105, 4.106) and (4.109) leads to

$$c_{mf}(x) = [1 + O(\phi_s^4]\ c_{m,in}\ \exp\left(-\frac{1}{p}\frac{\phi_s^2}{1+\frac{\phi_s^2}{Sh_o}}x\right), \tag{4.110}$$

where $\phi_s^2 = p\gamma_w Da$. Thus, for the special case of linear kinetics and uniform inlet condition, the exit conversion is given by

$$\varkappa_e = 1 - \exp\left(-\frac{1}{p}\frac{\phi_s^2}{\left[1+\frac{\phi_s^2}{Sh_o}\right]}\right) \tag{4.111}$$

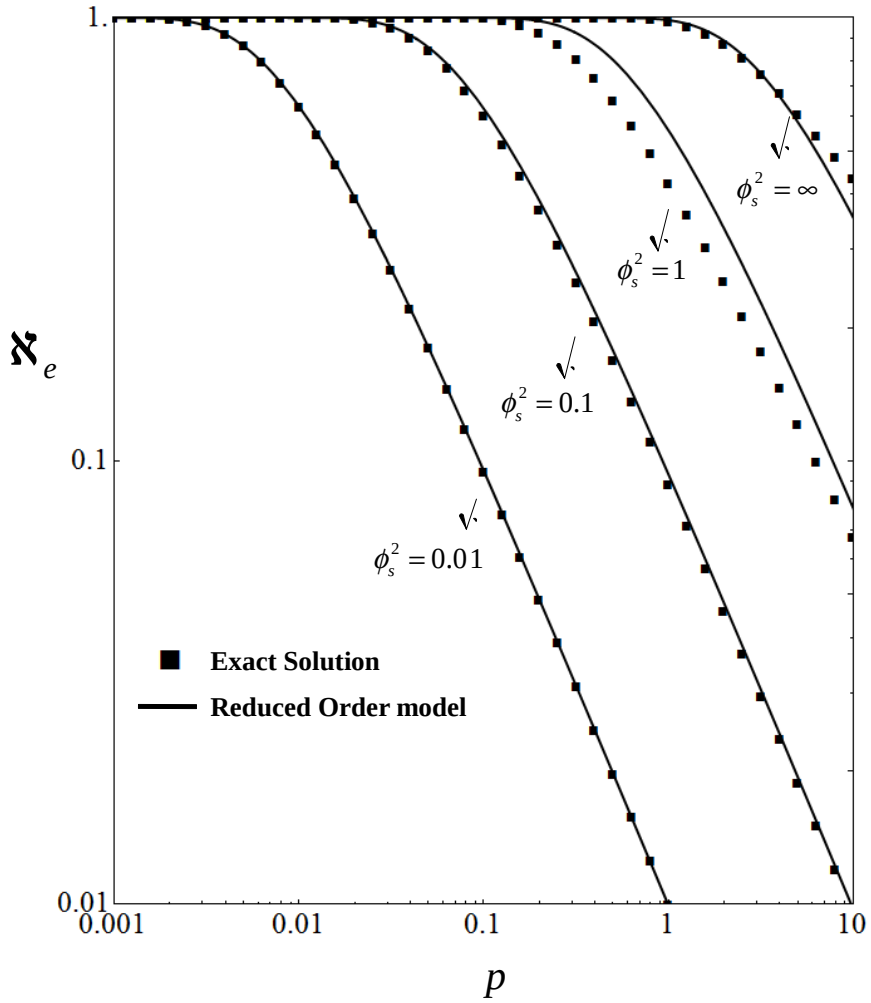


Figure 4.3: Steady state exit conversion $\varkappa_e$ corresponding to uniform feed conditions versus transverse peclet number p at various Thiele modulus for wall reaction case (comparison to exact solution).

This result shows the main advantage of the reduced order models, i.e., simple and explicit expressions for quantities of practical interest (such as the exit reactant conversion) in terms of the parameters characterizing the system. Figure 4.3 shows a plot of the exit conversion as a function of $p$ for different values of $\phi_s^2$ for the special case of wall reaction (where $\phi_s^2 = pDa_s$ and $Sh_o = \frac{48}{11}$). When the predicted conversion is compared to the exact numerical solution (Bhattacharya et al., 2004), the agreement is found to be excellent for small $p$ and $\phi_s^2$ values (as can be expected). While the model validity is restricted to small values of $\phi_s^2$, it is

found that even in the limit of very high local Damköhler number or Thiele modulus $\left(\phi_s^2 \to \infty\right)$, the exit conversion is predicted with reasonable accuracy in the mass transfer controlled regime:

$$\varkappa_{e,\infty} = 1 - \exp\left(-\frac{48}{11p}\right);\ p < 1. \tag{4.112}$$

Comparing equations(48a) with the exact solution (Balakotaiah and West, 2002)

$$\varkappa_{e\infty,exact} = 1 - 0.819\exp\left(-\frac{3.656}{p}\right);\ p < 1 \tag{4.113}$$

we observe that the first Fourier coefficient and the asymptotic Sherwood number decrease by about 20 and 30%, respectively as $\phi_s^2$ increases from zero to infinity. As discussed elsewhere (Tronconi and Forzatti, 1992 ; Joshi et al., 2009a), the accuracy of the low-dimensional model may be improved by making $\alpha_1$ and $Sh_o$ a function of position and $\phi_s^2$. Also, as stated in the introduction, the main advantages of the reduced order model are for nonlinear reactions, where the bifurcation features can be analyzed more easily, and the determination of kinetics or effective diffusivity from measured exit conversions. While these applications are the main motivation for the present work, we do not pursue them here.

### 4.5.3 Taylor dispersion with diffusion into the washcoat

The third limiting case we consider is that of transient dispersion of a non-reactive solute in laminar flow in a channel with diffusion into the porous washcoat. In this case, the reduced order model may be simplified by setting $Da = 0$, which gives

$$\frac{\partial \langle c \rangle}{\partial t} + \langle u \rangle \frac{\partial c_{mf}}{\partial x} = 0 \tag{4.114}$$

$$c_{mf} - \langle c \rangle = \frac{p}{\langle u \rangle} \langle \Gamma, u' \rangle \frac{\partial c_{mf}}{\partial x} + O(p^2) \quad , \tag{4.115}$$

with inlet/initial conditions as follows:

$$c_{mf} = \langle u\, c_{fin} \rangle_f + O\left(p^2\right) \quad @ \quad x = 0 \tag{4.116}$$

$$\langle c \rangle = \langle c_0 \rangle + p \left\langle \Gamma, \frac{\partial c_0}{\partial x} \right\rangle + O\left(p^2\right) \ @\, t = 0 \qquad , \tag{4.117}$$

where the first equation (4.114) represents the species balance in fluid plus wash-coat and second equation (4.115) is due to solute transfer between convective mode $c_{mf}$ and stationary mode $\langle c \rangle$. It should be pointed out that this case was considered by Balakotaiah and Chang (2003) but they did not derive the $O\left(p\right)$ corrections to the inlet and initial conditions. For this non-reactive case, the model can be written in terms of single convective mode $c_m$ in hyperbolic form as follows:

$$\frac{\partial c_{mf}}{\partial t} + \langle u \rangle \frac{\partial c_{mf}}{\partial x} + p\Lambda \frac{\partial^2 c_{mf}}{\partial x \partial t} = 0 \tag{4.118}$$

$$c_{mf} = c_{m,in} \quad @ \quad x = 0, \tag{4.119}$$

$$c_{mf} = \langle c_0 \rangle + p \left\langle \Gamma, \frac{\partial c_0}{\partial x} \right\rangle + \frac{p}{\langle u \rangle} \langle \Gamma, u' \rangle \frac{\partial \langle c_0 \rangle}{\partial x} \ @\, t = 0. \tag{4.120}$$

The last term in equations(4.118) represents the Taylor dispersion term that arises due to velocity gradients and transverse molecular diffusion. The dimensionless dispersion coefficient $\Lambda$ is given by

$$\begin{aligned} \Lambda &= -\frac{1}{\langle u \rangle} \langle \Gamma, u' \rangle \\ &= \frac{(1 + 6\gamma + 11\gamma^2)}{48\,(1+\gamma)^2} - \frac{\mu\gamma^2}{8\,(1+\gamma)^2\,\gamma_w^2} \left[ 2\gamma_w + 3\gamma_w^2 - 2\,(1+\gamma_w)^2\, \mathsf{Ln}\,(1+\gamma_w) \right]. \end{aligned} \tag{4.121}$$

It is interesting to note that the first term on R.H.S. of equations(4.121) is same as that derived by Balaokotaiah (2004) for capillary chromatography, where $\gamma$ represents the capacitance ratio of solid to fluid phases. Since the advantages of the

hyperbolic model were discussed by Balakotaiah and Chang (2003), Mikelic et al. (2006) as well as other authors, we do not repeat them here. In stead, we consider the evolution of inlet condition only (i.e., $c_0 = 0$) and present solutions of the above model for a pulse input as these results are of practical interest in determining the effective diffusivities of species in porous washcoat. We examine the residence time distribution (RTD) curve or the dispersion curve which is the exit concentration $c_{mf}\left(x = 1, t\right)$ corresponding to a unit impulse (Delta function) input in the fluid phase $c_{mf}(0) = \delta\left(t\right)$. It can be seen easily from equations(4.118-4.120) that the dispersion curves in Laplace domain $(t \rightarrow \alpha)$ and time domain are given by

$$\overline{E\left(\alpha\right)} = \exp\left(-\frac{\alpha}{\langle u\rangle + p\Lambda\alpha}\right) \tag{4.122}$$

$$E\left(t\right) = \exp\left(-\frac{1+\langle u\rangle\ t}{p\Lambda}\right)\left[\delta\left(t\right) + \frac{1}{p\Lambda}\sqrt{\frac{\langle u\rangle}{t}}I_1\left(\frac{2\sqrt{\langle u\rangle\ t}}{p\Lambda}\right)\right] \quad . \tag{4.123}$$

The cumulative RTD function $F(t)$ is the integral of the density function $E(t)$. These are plotted against time for typical values of values of parameters used in monolith applications: $p = 1$, $\varepsilon_f = 0.8$ and $\varepsilon_{wc} = 0.5$ (or, $p = 1$, $\gamma_w = 0.25$ and $\gamma = 0.125$), in Figures 4.4 and 4.5, respectively. [Note: The Dirac-delta function of magnitude $\exp\left(-\frac{1}{p\Lambda}\right)$ is not shown in Figure 4.4]. It is interesting to note that the dispersion curve has longer tails for higher value of the diffusivity ratio $\mu$. This is due to the fact that the solute is trapped in the washcoat and takes much longer time to exit the system when the diffusivity in the washcoat is small compared to that in the fluid. [In catalytic after-treatment applications, typical $\mu$ values are between 10 and 1000]. It should be noted that the model results are only qualitatively correct for very large values of $\mu$ since scale separation breaks down in the limit $\mu \rightarrow \infty$. (Note: In deriving the model, we have implicitly assumed that $\mu$ is of order unity, or equivalently the diffusion time of the reactant in the washcoat is small compared to the convection time. Thus, the reduced order model is accurate for large values of

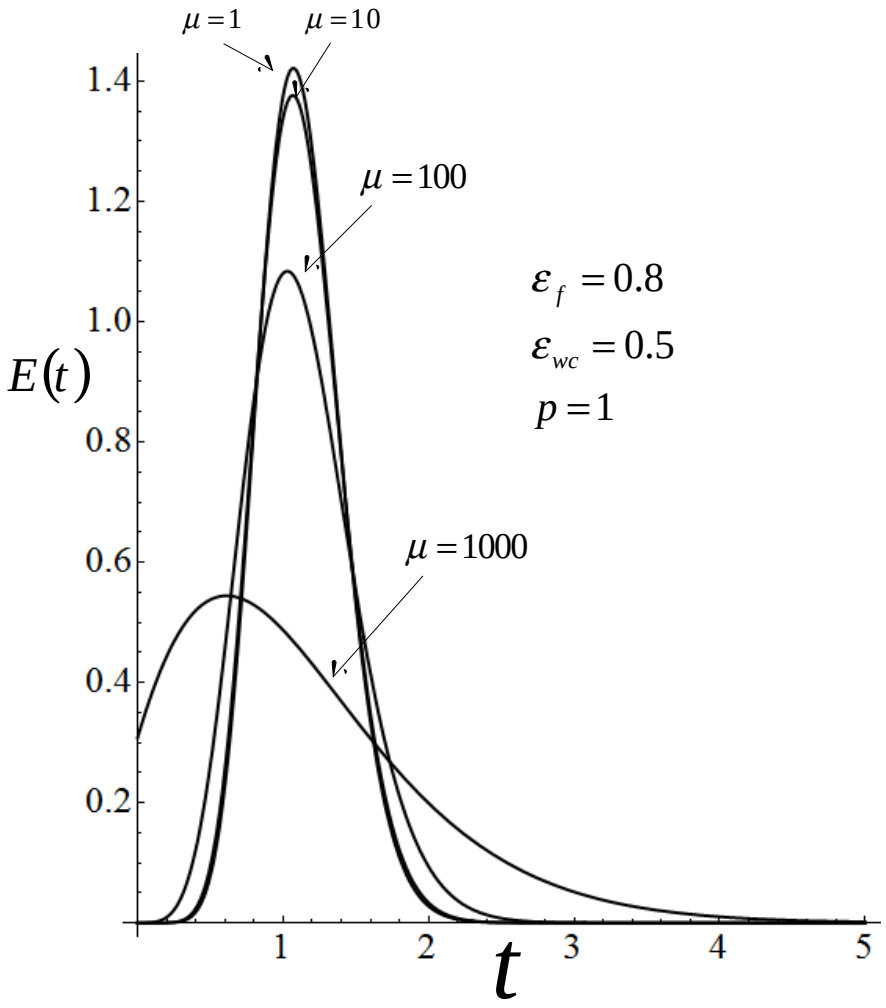


Figure 4.4: Predicted dispersion/RTD curves for non-reacting case corresponding to various diffusivity ratios $\mu$ at $\varepsilon_f = 0.8$, $\varepsilon_{wc} = 0.5$ (or, $\gamma_w = 0.25$, $\gamma = 0.125$) and $p = 1$.

$\mu$ only if $\mu p$ is small).

The dimensionless variance of the dispersion curve is given by

$$\sigma_D^2 = 2p\Lambda \tag{4.124}$$

which is shown in the Figure 4.6 against $\varepsilon_f$ for $\varepsilon_{wc} = 0.5$ at various diffusivity ratio $\mu$. We see that as expected, the variance increases as the washcoat thickness increases, i.e., the more solute get trapped in the washcoat if its thickness is large.

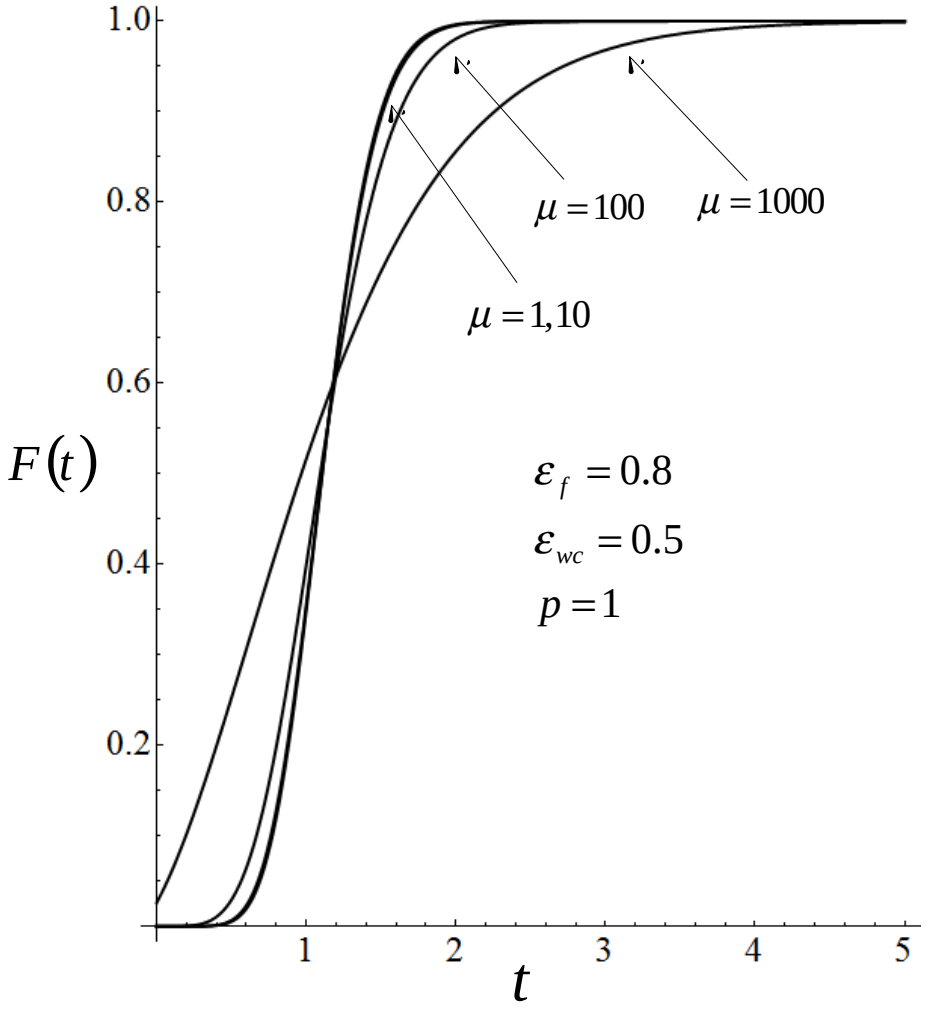


Figure 4.5: Predicted cumulative RTD function or F-curve for non-reacting case corresponding to various diffusivity ratio $\mu$ at $\varepsilon_f = 0.8$, $\varepsilon_{wc} = 0.5$ (or, $\gamma_w = 0.25$, $\gamma = 0.125$) and $p = 1$.

It can also be seen from equations(4.121) and (4.124) that the variance increases linearly w.r.t.. the diffusivity ratio $\mu$ for any value of $\varepsilon_f$. However, in the limit of very thin washcoat ($\varepsilon_f \to 1$), we get the Taylor limit given by $\sigma_D^2 = \frac{p}{24}$.

In the limit of small $p$ and large times, the dispersion curve is simplified as follows:

$$E_\infty(t) = \frac{1}{\sqrt{4\pi p\Lambda}} \left(\frac{\langle u \rangle}{t^3}\right)^{\frac{1}{4}} \exp\left(-\frac{1}{p\Lambda}\left(\sqrt{\langle u \rangle\ t} - 1\right)^2\right) \tag{4.125}$$

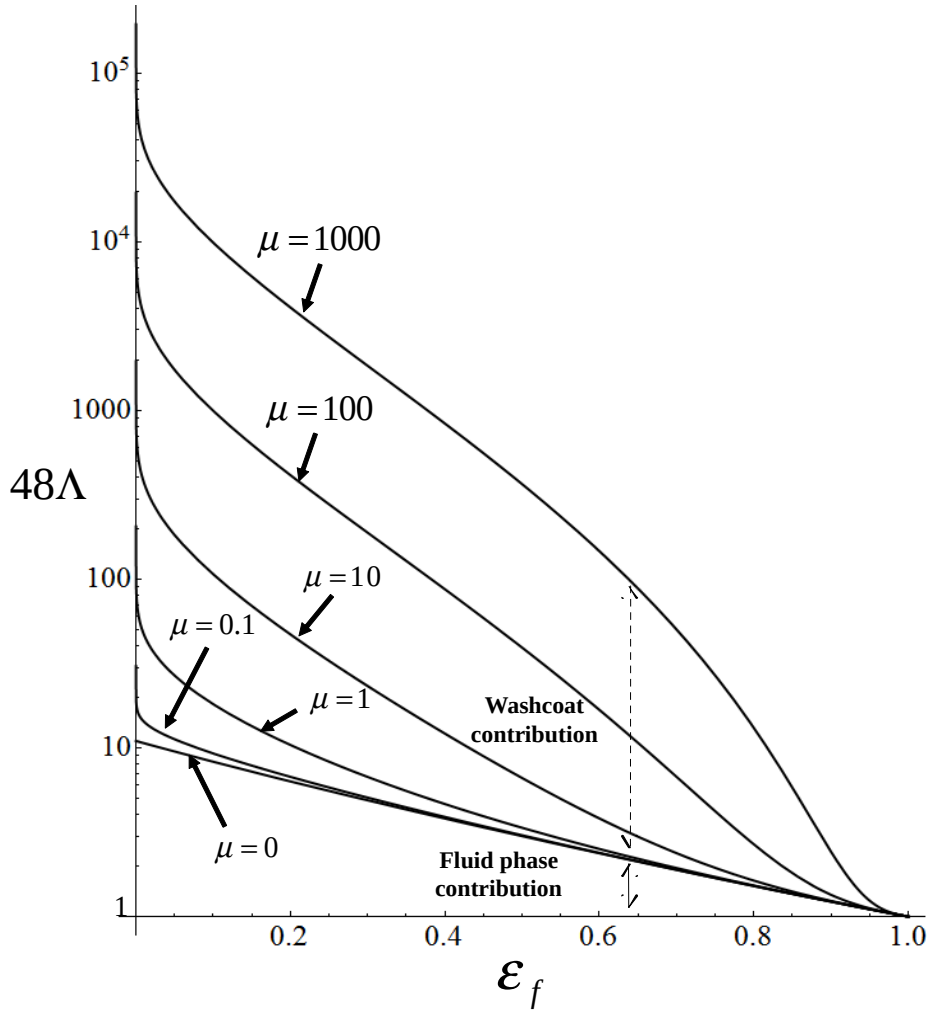


Figure 4.6: Dimensionless dispersion coefficient for various difusivity ratios for Taylor dispersion with diffusion into washcoat with parabolic velocity profile for $\varepsilon_{wc}\left(=\frac{\gamma}{\gamma_w}\right)=0.5$.

equations(4.125) indicates that instead of the extremely rapid Gaussian decay of the density function at large times from the mean value, the tail of the dispersion curve decays much more slowly as $t^{-\frac{3}{4}}\exp\left(-\frac{\langle u\rangle}{p\Lambda}\,t\right)$. This result and equations(4.121) may be used to determine the value of $\mu$ from measured RTD curves.

### 4.5.4 Flat Velocity Profile

The last limiting case we consider is that of a flat velocity profile in the channel. This limit may be attained in developing laminar flows with a low Schmidt number.

The transverse functions for this case are listed in the Table 4.2.

Table 4.2: Transverse functions and coefficients for flat velocity profile/developing flow

| | |
|---|---|
| $\Gamma$ = -$\frac{\gamma}{\gamma_w}\chi$ | Fluid $\Gamma_f = \frac{\gamma}{4(1+\gamma)}\xi^2 - \frac{\gamma(1+\gamma)}{8(1+\gamma)^2} + \frac{\mu\gamma^2}{8(1+\gamma)^2\gamma_w^2}\left[2\gamma_w + 3\gamma_w^2 - 2\left(1+\gamma_w\right)^2 \mathsf{Ln}\left(1+\gamma_w\right)\right]$<br>Washcoat $\Gamma_w = \frac{\mu\gamma}{4(1+\gamma)\gamma_w}\left[-\xi^2 + 2\left(1+\gamma_w\right)\mathsf{Ln}\left(\xi\right)\right] + \frac{\gamma}{8(1+\gamma)^2} + \frac{\mu\gamma}{8(1+\gamma)^2\gamma_w^2}\left[2\gamma_w + 4\gamma\gamma_w + 3\gamma\gamma_w^2 - 2\gamma\left(1+\gamma_w\right)^2 \mathsf{Ln}\ \left(1+\gamma_w\right)\right]$ |
| $\sigma$ | Fluid $\sigma_f = -\frac{\xi^2}{4} + \frac{(1+2\gamma)}{8(1+\gamma)} + \frac{\mu\gamma^2}{8(1+\gamma)\gamma_w^2}\left[2\gamma_w + 3\gamma_w^2 - 2\left(1+\gamma_w\right)^2 \mathsf{Ln}\left(1+\gamma_w\right)\right]$<br>Washcoat $\sigma_w = \frac{\mu\gamma}{4\gamma_w}\left[-\xi^2 + 2\left(1+\gamma_w\right)\mathsf{Ln}\left(\xi\right)\right] - \frac{1}{8(1+\gamma)} + \frac{\mu\gamma}{8(1+\gamma)\gamma_w^2}\left[2\gamma_w + 4\gamma\gamma_w + 3\gamma\gamma_w^2 - 2\gamma\left(1+\gamma_w\right)^2 \mathsf{Ln}\ \left(1+\gamma_w\right)\right]$ |
| $\langle\Gamma, u'\rangle$ = $\frac{\gamma^2}{\gamma_w^2}\langle\chi, \beta'\rangle$ = $-\frac{\gamma}{\gamma_w}\langle\chi, u'\rangle$ = $-\frac{\gamma}{\gamma_w}\langle\Gamma, \beta'\rangle$ | -$\frac{\gamma^2}{8(1+\gamma)^3} + \frac{\mu\gamma^2}{8(1+\gamma)^3\gamma_w^2}\left[2\gamma_w + 3\gamma_w^2 - 2\left(1+\gamma_w\right)^2 \mathsf{Ln}\left(1+\gamma_w\right)\right]$ |
| $\langle\sigma, u'\rangle = -\frac{\gamma}{\gamma_w}\langle\sigma, \beta'\rangle$ | $\frac{\gamma}{8(1+\gamma)^2} + \frac{\mu\gamma^2}{8(1+\gamma)^2\gamma_w^2}\left[2\gamma_w + 3\gamma_w^2 - 2\left(1+\gamma_w\right)^2 \mathsf{Ln}\left(1+\gamma_w\right)\right]$ |
| $2\left.\frac{\partial\Gamma}{\partial\xi}\right\|_{\xi=1^-}$ | $\frac{\gamma}{(1+\gamma)}$ |
| $2\left.\frac{\partial\chi}{\partial\xi}\right\|_{\xi=1^-}$ | -$\frac{\gamma_w}{(1+\gamma)}$ |

For this special case, the cup-mixing concentration $c_{mf}$ and fluid phase averaged concentration $\langle c\rangle_f$ are identical and the intraphase dispersion terms due to velocity gradients vanish. It can also be seen from Table 4.2 and equations (4.77

and 4.78) that the difference between external modes ($c_m$ and $\langle c_s \rangle$) is proportional to the interfacial flux and can be written using the external transfer coefficient concept. Thus, the reduced order model can be simplified in this case as follows:

$$\frac{\partial \langle c \rangle_f}{\partial t} + \frac{\partial c_{mf}}{\partial x} = -J = -\left[\gamma \frac{\partial \langle c \rangle_w}{\partial t} + \gamma_w Da\, R\left(\langle c \rangle_w\right)\right] \tag{4.126}$$

$$J = \frac{(8\gamma_w^2)}{\left[2\gamma_w + 3\gamma_w^2 - 2\left(1+\gamma_w\right)^2 \mathsf{Ln}\left(1+\gamma_w\right)\right]} \frac{\left(\langle c_s \rangle - \langle c \rangle_w\right)}{\mu\, p} = \frac{8}{p}\left(c_m - \langle c_s \rangle\right) \tag{4.127}$$

We note that the expression for the internal Sherwood number has not changed and is identical to that obtained for the parabolic case while the external Sherwood number has changed from $\frac{48}{11}$ to $8$. The inlet and initial conditions are in similar form as in equations(4.70, 4.71) except that the transverse functions and coefficients should be determined by Table 4.2. For the case of no reaction, the evolution of inlet condition is simplified to the form of telegrapher's like equation as follows:

$$\frac{\partial c_{mf}}{\partial t} + \langle u \rangle \frac{\partial c_{mf}}{\partial x} + \frac{p\left(1 - \langle u \rangle\right)}{Sh_o}\left(\frac{\partial^2 c_{mf}}{\partial t^2} + \frac{\partial^2 c_{mf}}{\partial x \partial t}\right) = 0 \tag{4.128}$$

$$c_{mf} = c_{m,in} \quad @x = 0;\; c_{mf} = \frac{\partial c_{mf}}{\partial t} = 0 \quad @t = 0 \tag{4.129}$$

where, $Sh_o$ is overall Sherwood number. The above equations (4.128, 4.129) can be simplified further by using the leading order approximation,

$$\frac{\partial c_{mf}}{\partial t} = -\langle u \rangle \frac{\partial c_{mf}}{\partial x} + O\left(p\right)$$

to write in terms of mixed derivative form of the hyperbolic model:

$$\frac{\partial c_{mf}}{\partial t} + \langle u \rangle \frac{\partial c_{mf}}{\partial x} + p\Lambda \frac{\partial^2 c_m}{\partial x \partial t} = 0,\; x, t > 0;\;\; c_m = c_{m,in} \;\; @ \;\; x = 0. \tag{4.130}$$

We note that the above model is of the same form as the reduced order model

for Taylor-dispersion with diffusion into the washcoat with parabolic velocity profile except that the dimensionless dispersion coefficient $\Lambda$ for this case is given by

$$\begin{aligned}\Lambda &= \frac{1}{Sh_o}\left(\frac{\gamma}{1+\gamma}\right)^2 = \left(\frac{\gamma}{1+\gamma}\right)^2\left(\frac{1}{Sh_{e,flat}}+\frac{\mu\gamma_w}{4}\frac{1}{Sh_{\Omega i}}\right) \\ &= \left(\frac{\gamma}{1+\gamma}\right)^2\left[\frac{1}{8}+\frac{\mu\left[2\gamma_w+3\gamma_w^2-2\left(1+\gamma_w\right)^2\mathsf{Ln}\left(1+\gamma_w\right)\right]}{\left(8\gamma_w^2\right)}\right] \end{aligned} \quad (4.131)$$

and is plotted in Figure 4.7 against $\varepsilon_f$ for $\varepsilon_{wc}=0.5$ at various diffusivity ratio $\mu$. We see that as expected, the variance increases as the washcoat thickness increases, i.e., more solute is trapped in the washcoat if its thickness is more. Thus, even with the flat velocity profile with no reaction case, the RTD curve is asymmetric and may have longer tail if the diffusivity ratio $\mu$ is high.

### 4.5.5 Comparison of Two-phase and Reduced Order Models

As discussed above, the reduced order model derived here leads to the same results as those obtained by the traditional two-phase model for steady-state conditions. However, in the transient reacting case where the cross-section average concentration $\langle c\rangle_f$ and cup-mixing concentration $c_m$ differ at order $p$ (given by equations 4.59), the two-phase model may lead to an error in the solution at order $p$. We demonstrate this here by examining the accuracy of the two-phase model by comparing the solution with that of the reduced order model for the case of wall reaction or very thin washcoat ($\varepsilon_w \to 0$). In this case, the traditional two-phase model (in dimensionless form) is given by

$$\frac{\partial c_{mf}}{\partial t}+\frac{\partial c_{mf}}{\partial x} = -J = -Da_s\, R\left(\langle c\rangle_w\right) \quad , \quad (4.132)$$

$$c_{mf}-\langle c\rangle_w = \frac{11}{48}pJ = \frac{11}{48}p\, Da_s\, R\left(\langle c\rangle_w\right) \quad , \quad (4.133)$$

$$c_{mf}|_{x=0} = c_{m,in}\left(t\right) \quad \text{and} \quad c_{mf}|_{t=0}=0. \quad (4.134)$$

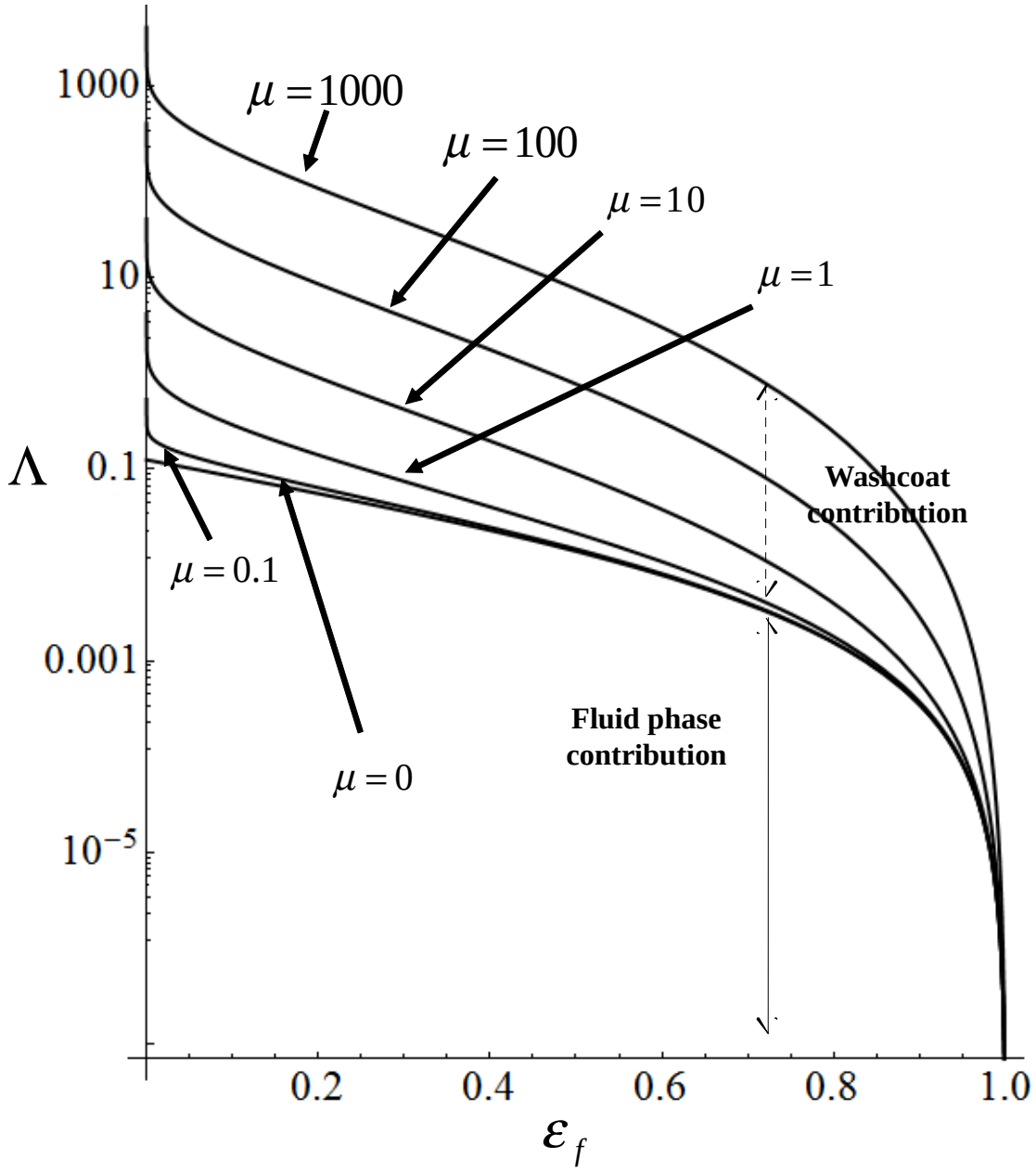


Figure 4.7: Dimensionless dispersion coefficient for various difusivity ratios for Taylor dispersion with diffusion into washcoat with flat velocity profile for $\varepsilon_{wc}\left(=\frac{\gamma}{\gamma_w}\right)=0.5$.

The above model may be solved to determine the exit concentration for the case of linear kinetics. In the Laplace domain $(t \rightarrow \alpha)$, the solution (transfer function) may be expressed as

$$\frac{\overline{c}_{two-phase}(\alpha)}{\overline{c}_{m,in}(\alpha)} = \exp\left[-\left(\alpha + \frac{Da_s}{1+\frac{11}{48}pDa_s}\right)\right] \tag{4.135}$$

Similarly, for the case of wall reaction, the reduced order model describing the evolution of inlet condition, in dimensionless form, may be expressed as follows:

$$\frac{\partial \langle c\rangle_f}{\partial t} + \frac{\partial c_{mf}}{\partial x} = -J = -Da_s\, R(\langle c\rangle_w), \tag{4.136}$$

$$c_{mf} - \langle c\rangle_f = p\left[\frac{-1}{48}\frac{\partial c_{mf}}{\partial x} + \frac{1}{24}\, Da_s\, R(\langle c\rangle_w)\right], \tag{4.137}$$

$$c_{mf} - \langle c\rangle_w = p\left[\frac{-1}{16}\frac{\partial c_{mf}}{\partial x} + \frac{1}{6}\, Da_s\, R(\langle c\rangle_w)\right], \tag{4.138}$$

$$c_{mf}|_{x=0} = c_{m,in}(t) \quad \text{and} \quad \langle c\rangle_f\Big|_{t=0} = 0. \tag{4.139}$$

It can be seen that the main difference between the reduced order model, equations(4.136-4.139), and the two-phase model, equations(4.132-4.134), is the (Taylor) dispersion in the fluid phase. The two-phase model does not distinguish between the cup-mixing concentration $c_m$ and the cross-section average concentration $\langle c\rangle_f$. As we have shown above, in general, the difference between $c_m$ and $\langle c\rangle_f$ is of order $p$ and hence can not be ignored. This difference may be higher for non-uniform feeding of solute. For example, for a feed at the central location of the channel, the cup-mixing concentration is twice the average concentration, i.e., $c_m = 2\langle c\rangle_f$.

When the reduced order model, equations(4.136-4.139), is solved for the exit cup-mixing concentration for the case of linear kinetics, the solution (transfer function) in Laplace domain $(\alpha)$ may be expressed as

$$\frac{\overline{c}(\alpha)}{\overline{c}_{m,in}(\alpha)} = \exp\left[-\left(\frac{\alpha + Da_s + \frac{p\alpha Da_s}{8}}{1+\frac{p\alpha}{8}+\frac{11}{48}pDa_s\left(1+\frac{p\alpha}{264}\right)}\right)\right]. \tag{4.140}$$

Thus, the ratio of exit concentrations predicted by the traditional two-phase model and the reduced order model can be simplified to order $p$ as

$$\frac{\overline{c}_{two-phase}(\alpha)}{\overline{c}(\alpha)} = 1 - \frac{p}{48}\alpha(\alpha + 6Da_s) + O\left(p^2\right) \tag{4.141}$$

Since the reduced order model is accurate to order $p,$ it can be seen from equations (4.141) that the two-phase model has an error of order $p$ (as can be expected intuitively). This error may be significant even at low-frequencies ( or slowly varying inlet conditions), depending on the values of transverse Peclet number $p$ and the Damköhler number, $Da_s$. Similarly, the error may be significant at moderate to high frequencies even for small values of $p$. For example, for typical values of $\alpha \approx 1$, $p \approx 0.2$, $Da_s = 10$, the error in two-phase model is about $25\%$. Thus, for the general transient reacting case, where the dispersion effect in the fluid phase is significant, the use of three-mode reduced order model is recommended.

## 4.6 Conclusions and Discussion

The main contribution of this work is the derivation of an averaged multi-mode model for a monolith reactor with a porous washcoat on the wall. The reduced order model given by equations(4.66-4.71), consists of the governing equations along with the initial and inlet conditions to first order accuracy in the transverse diffusion time. We have also examined various limiting cases of the model and given a physical interpretation of the various terms and the effective coefficients that appear in the reduced order description.

A second contribution of this work is the derivation and interpretation of an expression for the flux of the reacting species at the fluid-washcoat interface and how it may expressed in terms of various concentration modes. We have shown that for steady-state conditions, the interfacial flux may be expressed as the product of a transfer (exchange) coefficient times the driving force, and the driving force

appears as the difference between the two concentration modes. This traditional description also applies when the velocity gradient in the fluid phase is neglected or in the absence of reactions. However, in the general case of varying inlet conditions, velocity gradients and reaction in the washcoat, the interfacial flux depends on the interfacial mode as well as two external concentration modes, namely, the cup-mixing and fluid phase average concentrations. In our view, this is an important result that extends to many other multi-phase reacting systems (e.g. gas-liquid and gas-liquid-solid reactors).

The results of this work also support our earlier observation that a minimum number of modes are required in the reduced order description of reacting systems so that the reduced order model captures the main qualitative features of the detailed model. As shown in this work, a reduced order model expressed in terms of single concentration mode (that can not be related to directly measurable quantities) has a much smaller domain of validity in the parameter space compared to the regularized multi-mode form. For example, a single mode model may lead to unphysical results (such as negative effective diffusivity), especially for fast reactions or short times. Single mode models are also ineffective in distinguishing between kinetic and mass transfer controlled regimes. In contrast, regularized multi-mode models using the concept of transfer or exchange between various modes do not have these deficiencies.

As stated in the introduction, the main utility of the reduced order model developed here is in the real time simulations of catalytic after-treatment systems in which the inlet conditions vary with time (Joshi et al., 2009a). The models used in these simulations do not make a distinction between $\langle c \rangle_f$ and $c_{mf}$ and hence ignore the dispersion in the fluid phase. As shown in this work, the error due to this approximation for general transient reacting case is of order $p$. This can be significant even for low frequency inlet condition, depending on the value of the

Damkohler number. In addition, even for small $p$, the error may be large for inlet conditions having variation with moderate to high frequency.

# Chapter 5 Summary and Future Scope of the Work

## 5.1 Summary

We presented a systematic averaging procedure based on the Lyapunov-Schmidt (L-S) method for deriving coarse-grained low-dimensional models from the detailed diffusion-convection-reaction equations for various reactors such as catalytic monoliths, tubular reactor and two-compartment system. We demonstrated the several advantages of this method compared to other methods presented in the literature such as center manifold (CM) or method of moments. For example, (i) the L-S method can be applied to steady-state or equilibrium models where the governing equation is not an evolution equation either in space or time. In contrast, the CM method has limited applicability to such models. (ii) In the L-S method, the base state can be time dependent, and, time dependent inlet conditions/sources can be treated. In the CM method, base state (fixed point) is generally assumed to be time independent. Also, in the CM approach, the initial/inlet conditions are assumed to be close to the fixed point. In contrast, there is no restriction on initial/inlet conditions in the L-S technique. (iii) When applied to the averaging of transient models, the L-S method can capture exponentially small terms in time while these terms are ignored in the CM method. As illustrated earlier, the L-S method leads to reduced order model containing higher order derivatives in time when a perturbation expansion is used for small $p$. These higher order time derivatives extend the validity of the model to short times (or, capture the exponentially small transients). (iv) When a perturbation expansion is used to solve for the CM, the range of validity of the CM expansion can not be greater than that given by $\left|\frac{\omega\, p}{\gamma}\right| < 1$, where $\gamma$ is the real part of eigenvalue close to zero and $\omega$ is frequency or wave number. In contrast, when a perturbation expansion is used to solve the local equation in the L-S method, the region of convergence of the expansion appears

to be at least as large as that given by $\left|\frac{\omega\, p}{\gamma}\right| < 1$. In addition, time scale separation is convenient but not necessary in the L-S formalism. In contrast, the application of CM method requires time scale separation.

When there is scale separation in the detailed model, the L-S method is equivalent to the exact Maclaurin's series expansion of the detailed model in terms of the small parameter representing the scale separation. While we have illustrated it here only for few cases, it can be applied to a wide range of reacting as well as non-reacting cases described by diffusion-convection-reaction models. For the case of classical Taylor dispersion problem and two-compartment system, we have derived the reduced order model to all orders in the transverse diffusion time. By summing the resulting infinite series in closed functional form, we were able to show that the reduced order model derived by the L-S technique is exact. For example, in case of laminar dispersion, it can predict the moments of the solute distribution exactly for all times. In case of two-compartment model where exact solution can be determined, the reduced order model matches the exact solution when all order of terms are included. Here we also show that the higher order terms (appearing as higher order time derivatives) in reduced order model contribute less to the spreading process at longer times but are very important at shorter time.

We analyze the solute dispersion at short times using the coarse-grained model derived spatial moments for general sources including point sources. Specifically, we have shown that there is no centroid displacement or variance deficit in the solution. For a point release at $(r_0, \theta_0)$, the centroid moves with the local fluid velocity $u(r_0)$ at short times while it moves with the mean velocity at large times. Thus, it is not possible to predict the location of centroid (and hence the second central moment or the variance) correctly by any coarse-grained model that is not valid for $t \to 0$. Similarly, the short time approximation of variance shows that solute spreading process evolves with pure diffusion for $t \to 0$, and after some critical time

$\tau_{CD} = \frac{D_m}{\langle u \rangle^2}$, convection effects start to contribute and introduce asymmetry in the concentration distribution. For long times ($t \gg \tau_D = \frac{a^2}{D_m}$), the spreading process is governed by the Taylor (when $Pe_r \approx O(\frac{1}{\sqrt{p}})$) or Taylor-Aris mechanism (when $Pe_r \approx O(1)$). Thus, the solute spreading process may be divided into three time intervals; $0 < t < \tau_{CD}$ where axial molecular diffusion dominates, $t \in (\tau_{CD}, \tau_D)$ where the dispersion is due to the combined effects, and $t >> \tau_D$ where convection and transverse diffusion dominates. Our analysis in section 4.1 also shows that for the practical case of $Pe_r >> 1$, the skewness of the solute concentration profile increases as $\left(\frac{t}{\tau_D}\right)$ for short times while it decreases as $\sqrt{\frac{\tau_D}{t}}$ for long times. Thus, while the Gaussian profile is approached for $t \to \infty$, the skewness is never zero for any finite time and goes through a maxima for $t$ values of order $\tau_D$. In our view, this important observation has not been recognized in the literature.

We show the clear distinction between the dominant convective mode represented by the cup-mixing concentration ($c_m$) and the dominant diffusive mode represented by the cross-sectional averaged concentrations ($\langle c \rangle$). These modes arise naturally and quantify the local gradients more accurately in terms of transfer coefficient as compared to the traditional use of a single concentration mode with dispersion coefficient. In our opinion, there is a fundamental physical inconsistency in representing the Taylor dispersion phenomenon using a single diffusive mode (the cross-section averaged concentration) and its large scale gradient. This parabolic description of the dispersion flux, first used by Taylor and later by many others, makes the local phenomenon of exchange of solute between the (fast moving or large scale) convective mode ($c_m$) and nearly stationary and small scale diffusive mode($\langle c \rangle$) into a large scale phenomenon (effective diffusion on the larger scale). It is mainly for this reason, the traditional coarse-grained parabolic models fail to describe the solute dispersion process accurately for short times or for the case of a reactive solute, for fast reactions and for finite values of the transverse diffusion

time. In fact, the single mode description of the Taylor dispersion phenomenon for reacting flows in terms of $\langle c \rangle$ can lead to negative effective dispersion coefficients! Based on these and other comparisons, we conclude that Taylor dispersion phenomena are better described in terms of hyperbolic models using either a single convective mode (for the non-reactive case) or multiple concentration modes coupled through the concept of a transfer coefficient. It is one of the most important result for developing the low-dimensional model for various complex systems.

Here, we derive and interpret an expression for the flux of the reacting species at the fluid-washcoat interface and how it may expressed in terms of various concentration modes. We have shown that for steady-state conditions, the interfacial flux may be expressed as the product of a transfer (exchange) coefficient times the driving force, and the driving force appears as the difference between the two concentration modes. This traditional description also applies when the velocity gradient in the fluid phase is neglected or in the absence of reactions. However, in the general case of varying inlet conditions, velocity gradients and reaction in the washcoat, the interfacial flux depends on the interfacial mode as well as two external concentration modes, namely, the cup-mixing and fluid phase average concentrations. In our view, this is an important result that extends to many other multi-phase reacting systems (e.g. gas-liquid and gas-liquid-solid reactors).

The main utility of the reduced order model developed here is in the real time simulations of catalytic after-treatment systems in which the inlet conditions vary with time. Therefore, we show that a minimum number of modes are required in the reduced order description of reacting systems so that the reduced order model captures the main qualitative features of the detailed model. As shown in this work, a reduced order model expressed in terms of single concentration mode (that can not be related to directly measurable quantities) has a much smaller domain of validity in the parameter space compared to the regularized multi-mode

form and may lead to unphysical results (such as negative effective diffusivity), especially for fast reactions or short times. Single mode models are also ineffective in distinguishing between kinetic and mass transfer controlled regimes. In contrast, regularized multi-mode models using the concept of transfer or exchange between various modes do not have these deficiencies. For example, the models used for catalytic monoliths in the literature do not make a distinction between $\langle c \rangle_f$ and $c_{mf}$ and hence ignore the dispersion in the fluid phase. As shown in this work, the error due to this approximation for general transient reacting case is of order $p$. This can be significant even for low frequency inlet condition, depending on the value of the Damkohler number. In addition, even for small $p$, the error may be large for inlet conditions having variation with moderate to high frequency.

## 5.2 Future Scope

Now we discuss some possible extension of the work. Here, we applied L-S procedure for diffusion-convection-reaction in simple geometries with linear kinetics. One straightforward extension is for other flow geometries such as porous media or washcoat with arbitrary shapes and to include effect of axial diffusion in both the solid and fluid phases. A second possible extensions is to include the non-isothermal effect and multiple reacting species and average the coupled species and energy balances simultaneously. A third possible extension is to derive higher order averaged models and examine the convergence of the reduced order model. For the case of flow in a tube with a wall reaction, our earlier work has shown that whenever the local expansion does not converge, it is possible to obtain azimuthally asymmetric solutions. In our view, convergence and accuracy aspects are an important component of reduced order description of chemical reactors.

# Part II

# Reactive Transport of Gelling Acids and Wormhole Formation in Carbonates

# Chapter 6 Introduction

## 6.1 Preamble

One of the main activities of the production engineers is the reservoir stimulation where a solvent is injected into the formation. It has been observed that the hydrocarbon production rate decreases with time as a result of production operations. In particular, when hydrocarbons flow from far-field to the wellbore during production, particles eroded from the reservoir migrate and deposit near wellbore region that restrict the flow of hydrocarbons into the well. Similarly, formation damage near the wellbore during drilling operation reduces the flow conductivity in the reservoir that again leads to diminution of hydrocarbon production. Therefore, matrix stimulation is very necessary to enhance the permeability of the damaged zone near wellbore region to increase the production rate. Figure 6.1 shows a schematic diagram of a reservoir with damaged zone near wellbore. Typical radii of wellbore, damaged zone and reservoir are $0.33$ ft, $1-10$ ft $500-2000$ ft, respectively. The permeability of the damaged zone, $K_{dmg}$, is much lower (typically 10 times lower) than the permeability, $K_{res}$, of the undamaged reservoir (Economides, 1993). Therefore, a solvent is injected into the formation for matrix stimulation to dissolve some of the material present that greatly enhance or recover the permeability of near the wellbore region.

The most common matrix treatment is acidizing where an acidic solution such as mineral acids like HCl, organic acids like formic or acetic acids, chelating agents like EDTA is injected into the wellbore (William et al., 1979; Schechter, 1992; Economides et al., 1993; Economides and Nolte, 2000). It involves dissolution of the rock by a reactive fluid that enhance oil flow to the wellbore and increases the hydrocarbon production rate from a reservoir. When an acid is injected through the wellbore, it dissolves the formation rock and increases the flow conductivity.

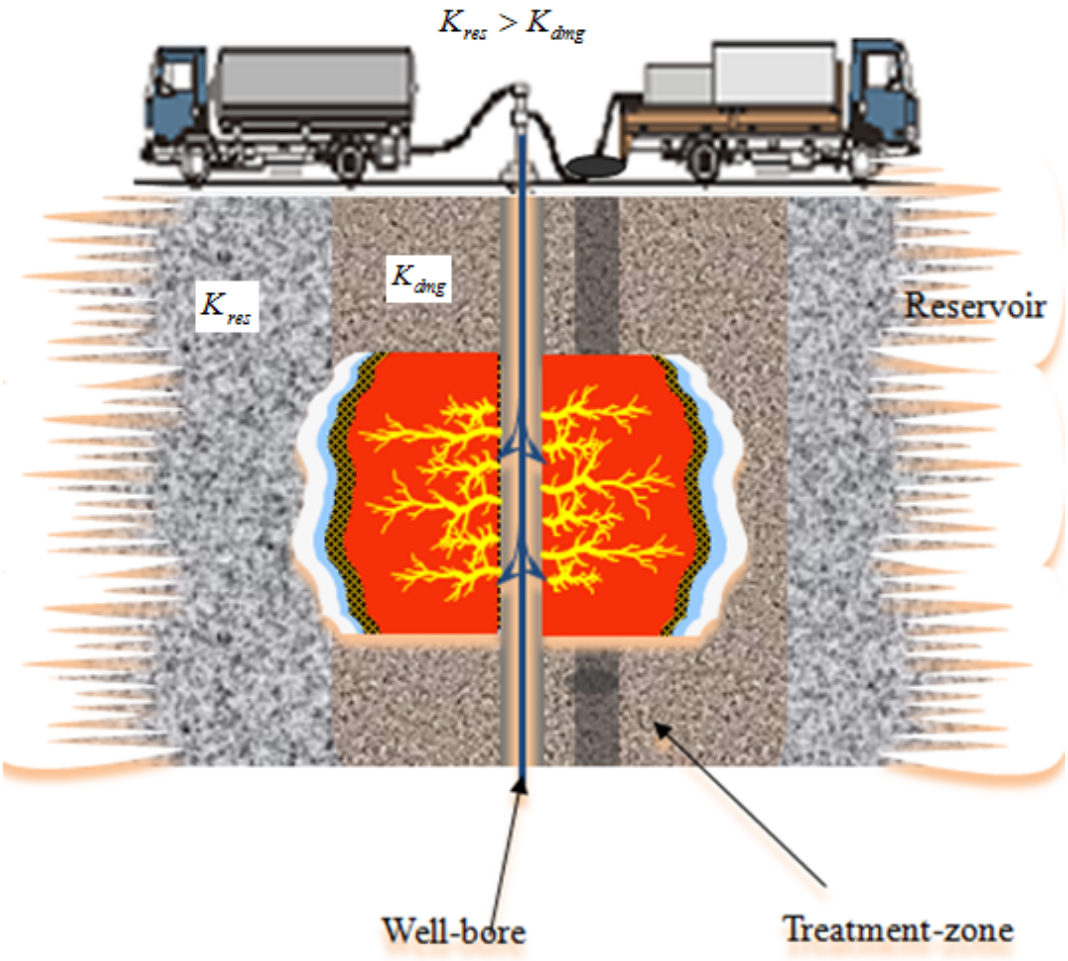


Figure 6.1: Schematic view of a wellbore, damaged zone and reservoir.

Dissolution results in the production of $CO_2$ from the acid-carbonate reactions as follows

$$\begin{aligned} Ca\ C\ O_3 + 2\ H^+ &\leftrightarrow Ca_2 + H_2O + CO_2 \\ Ca\ Mg\ (CO_3)_2 + 4\ H^+ &\leftrightarrow Ca^{2+} + Mg^{2+} + 2H_2O + CO_2 \end{aligned} \tag{6.1}$$

where, calcite ($Ca\ C\ O_3$) is the typical carbonate. $CO_2$ is assumed to be in the liquid phase under high pressure reservoir conditions. $HCl$ is the most commonly used acid because it is inexpensive and reacts with the carbonate with a high rate

of reaction. Slower reacting acids like organic acids or the chelating agents are used when the reservoir temperature is high or when retardation of reaction rate is desired. As the acid penetrates into the porous rocks, it dissolves the rock and increases the flow conductivity by creating conductive channels called wormholes (Daccord, 1987; Hung et al., 1989; Hoefner and Fogler, 1988; Fred and Fogler, 1998, 1999; Bazin, 2001). The wormholes bypass the damaged zone around the wellbore, leaving highly permeable channels for oil to flow back after the treatment. The formation of wormholes depends on various factors such as acid injection rate, volume of acid injected, types of acid, mineralogy, heterogeneity (i.e., non-uniformities in porosity or permeability) in the formation and temperature (Williams et al., 1979, Wang et al., 1993; Fred and Fogler, 1998, 1999; Buijse, 2000; Panga et al., 2005; Kalia and Balakotaiah, 2007, 2009, 2010). For example, the uniform dissolution patterns are formed at very high injection rate while face dissolution patterns are formed at very low injection rate (Fredd and Fogler, 1998) as can be seen from Figure 6.2. Similar effects on dissolution patterns at various injection rates are observed in other experimental studies (Economides et al., 1993; Economides and Nolte, 2000; Golfer et al., 2002). These experiments are performed with a core of few inches, where acidic solution is injected at constant rate and pressure at the exit is fixed. When acid is injected at a very high rate, it penetrates into the medium but gets out unreacted due to insufficient residence time. As a result, the porosity of the medium increases slowly and uniformly that leads to an uniform dissolution pattern shown in Figure 6.2. At low injection rates, most of the acid is spent just before it can penetrate further into the medium. As a result, the whole face of the medium get dissolved as flow of acids proceeds that leads to a compact or face dissolution pattern shown in Figure 6.2. At intermediate flow rates, resident time is comparable to the reaction time and hence narrow conductive channels called wormholes are created shown in Figure 6.2. Thus, though acid injection increases

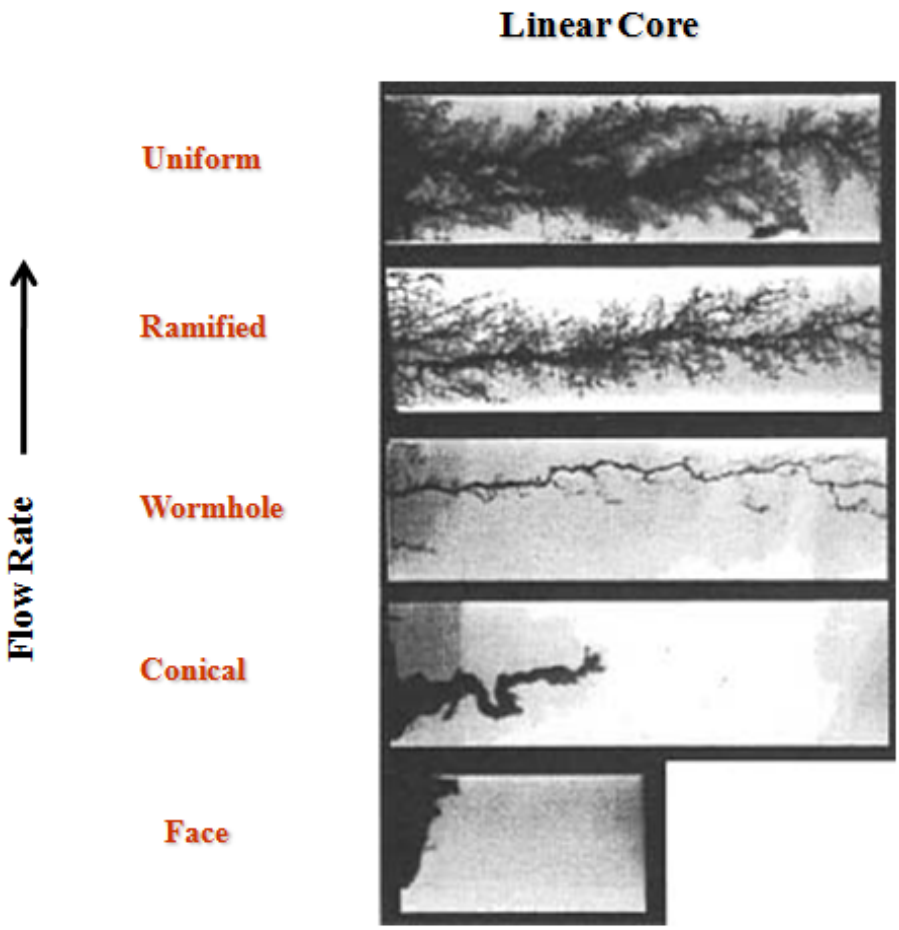


Figure 6.2: Dissolution patterns formed at different injection rates of acidic solution (Fredd and Fogler, 1998).

the flow conductivity of reservoir near the wellbore, due to difference in dissolution patterns at various injection rates, different rates of permeability enhancement is observed at different injection rates (Fredd and Fogler, 1998) as shown in Figure 6.3. However, It is interesting to note from this Figure that the rate of increase in permeability is non-monotonic with injection rate of acidic solutions, the maximum rate of increase in permeability corresponds to some intermediate injection rate (0.06 $\mathrm{cm}^3\,\mathrm{min}^{-1}$) while low injection rate (0.01 $\mathrm{cm}^3\,\mathrm{min}^{-1}$) or high injection rate (1.0$\mathrm{cm}^3\,\mathrm{min}^{-1}$) of acidic solution leads to comparably slower increase in permeability as can be seen from Figure 6.3. In fact, when the amount of acid required to

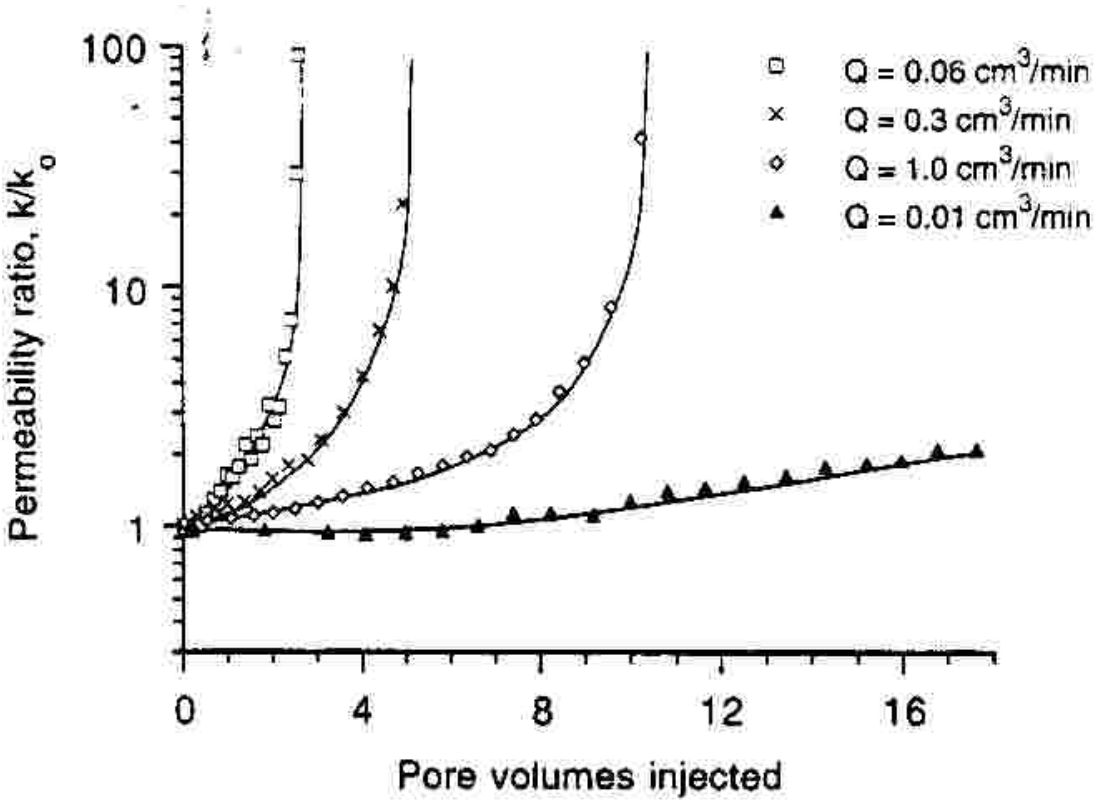


Figure 6.3: Increase in permeability due to dissolution with 0.25 M EDTA at various injection rates in a core (0.8-2 mD) of length 10.2 cm and diameter 3.8 cm (Fredd and Fogler, 1998).

increase the permeability by a given factor is noted for different types of patterns, it is found that the formation of wormholes requires the least amount of acid. This may be seen from breakthrough curve as shown in Figure 6.4, where the amount of acidic solution required in each experiment is plotted against the injection rate. Here, the number of pore volume of acidic solution is defined as the ratio of total volume of acidic solution injected and the initial pore volume of the rock at breakthrough and Q is the injection rate of the acid; and breakthrough is defined when permeability of the core increases by a certain factor (100 in this case) from its initial value.

Figure 6.4 shows that breakthrough curve has a minima where optimum amount of acid corresponds to some intermediate injection rate, $Q_{opt}$. The existence of the

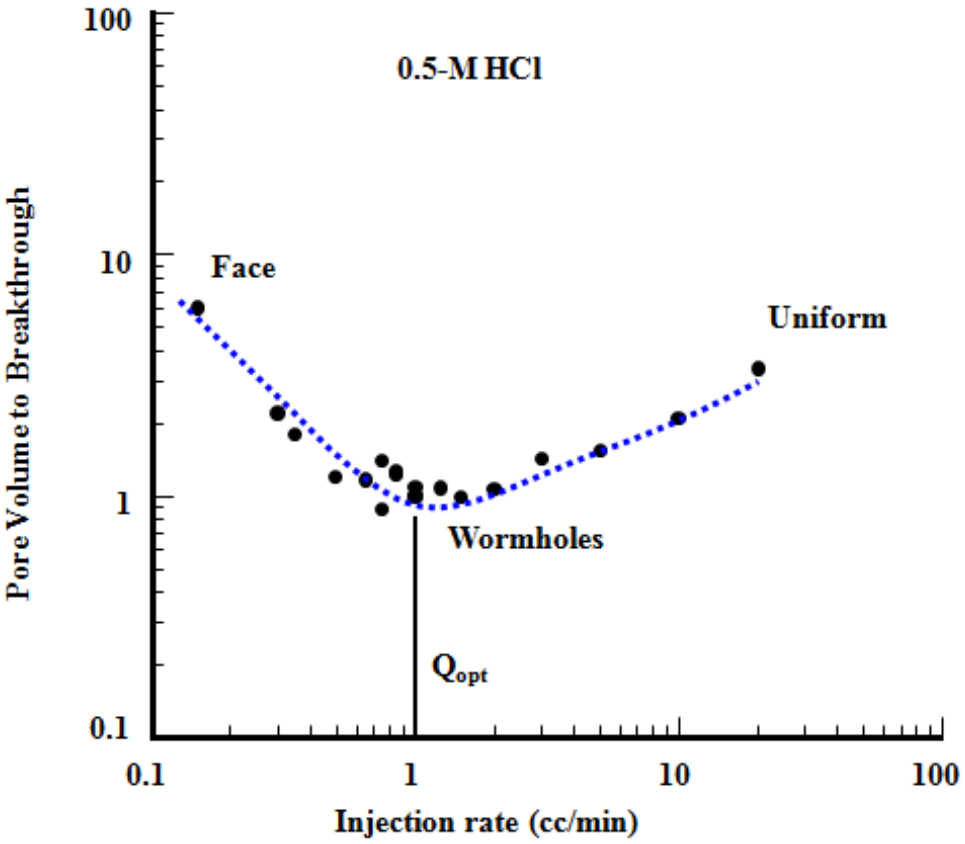


Figure 6.4: Breakthrough curve (here, pore volume to breakthrough is defined as the number of pore volume of acidic solution injected to increase the permeability of the core by a factor $100$).

optimum is due to the competition between transport and reaction phenomena. In other words, the optimum exists when residence time (time available for a particular proton to be in contact with the carbonate rock due to transport of acid) is comparable to the reaction time (the time it will take to consume a proton when it is in contact with the carbonate rock). Therefore, the injection rate higher or lower than $Q_{opt}$ leads to the higher pore volume of acid required for breakthrough as can be seen from Figure 6.4. This is because when acid is injected at higher rate, its resident time is smaller, i.e., it has very little time to react and hence, the core permeability increases very slowly (Figure 6.3) and the number of pore volume required for breakthrough, $\text{PV}_{BT}$ is larger. Similarly, when acid is injected slowly, it

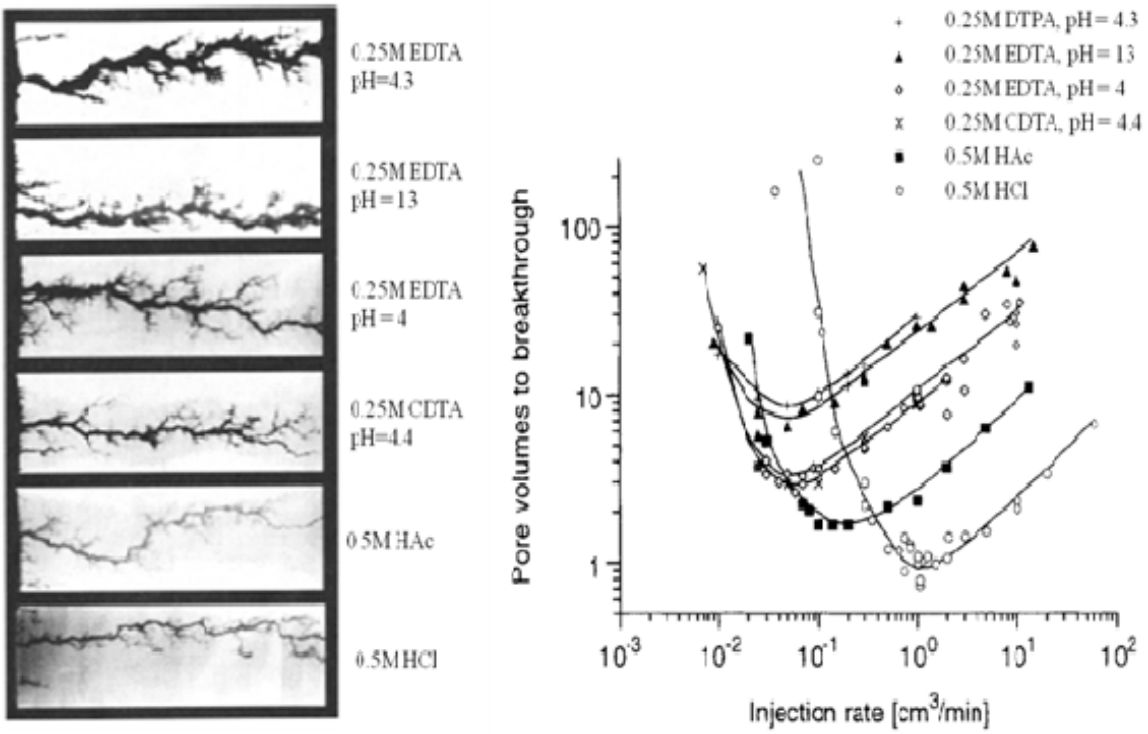


Figure 6.5: Breakthrough curve and wormhole patterns for various acids with different reactivity.

has more than enough time to react so lots of acids get consumed unnecessarily but acid front proceeds very slowly. As a result, in this case, the permeability increases slowly (Figure 6.3) and higher $PV_{BT}$ is required. Due to the same reason, lower optimum rate is observed for low-reacting acids as can be seen from Figure 6.5 where breakthrough curve and wormhole patterns are demonstrated for acids of different reactivity. Here, HCL is the strong acid and DTPA is the weakest one. From wormhole patterns in Figure 6.5 for various acids, it can be seen that the diameter of the conducting channel (wormhole) is bigger for slow reacting acids.

Since wormhole pattern is formed corresponding to some optimum injection rate where $PV_{BT}$ (the pore volume of acidic solution required for breakthrough) is minimum, the wormhole formation is of great importance for the economic purposes. While the experimental discussed above describes the influence of some of the factors on optimum injection rate ($Q_{opt}$), one of the main design parameters

of interest, and on wormhole formation, they do not provide sufficient insight into scale-up of laboratory results on to actual field-scale treatments. For example, in laboratory experiments where length of the core is larger than the diameter of the core, only one conducting channel (wormhole) is formed while at the field scale where the height of treatment zone is much larger than the radius of penetration, several conducting channels (wormholes) are formed. Similarly, the quantitative analysis from these experiments is not straightforward. In addition, most of these studies are performed for Newtonian type acids, which in case of heterogeneity in the reservoir (permeability variation within the reservoir), flow preferentially to the high-perm region and increase its permeability further. As a result, more acids are drawn to the high-perm region that over-stimulated the high-perm region while the low-perm region is under-stimulated. Therefore, diverting acids like gelled acids, surfactant based viscoelastic acids or emulsified acids are used in the field to get more uniform stimulation (MaGee et al., 1997; Buijse and Domelen, 2000; Chang et al., 2001; Lynn and Nasr-El-Din, 2001; Taylor and Nasr-El-Din, 2003; Nasr-El-Din et al., 2006, 2008; Gomaa and Nasr-El-Din, 2010; Gomaa et al., 2011).

In-situ gelled acids use pH to control the cross-linking of the polymer chains in the solution, which controls the fluid viscosity and flow diversion. For example, at very low pH, polymer chains are not cross-linked but as pH increases to a certain point, they start cross-linking until pH exceeds some limit (Rose, 2004; MaGee et al., 1997). Therefore, when a in-situ gelling acid at very low pH (and hence low viscosity) is injected, it preferentially flows to the high-perm zone and dissolves it. Consequently, the pH of the fluid increases as it gets spent at the rock face. Once the pH reaches to certain range, the polymer chains in the fluid start cross-linking and form a gel that creates a plug of high resistance (low mobility) in the high-perm zone and divert the fluid from high-perm to the low-perm region where the flow resistance is lower. Thus, the diversion of the acid leads to stimulation of hard-

to-access low-perm zones and increases the overall permeability of the reservoir uniformly. The following section gives a summary of experimental and theoretical studies performed on acidizing.

## 6.2 Literature Review

Several experimental and theoretical studies have been performed to predict conditions under which wormholes are formed and to understand the effect of injection rate, temperature, reaction kinetics, geometry of the system, heterogeneity, mineralogy etc. In the following sections, we briefly review the experimental observations and predictions by existing models in the literature on wormhole formation.

### 6.2.1 Experimental Studies with Newtonian Acids

One of the earliest works on carbonate acidization has been reported by Williams et al. (1979) where highest possible injection rates was recommended to avoid face dissolution near the well-bore. The earlier studies were based mostly on limestones (Lund et al. 1973, 1975) where hydrochloric acid (HCl) were injected from one end of the linear core. In these studies, one wormhole with multiple branches were observed. Experiments on radial and linear cores made of plaster were performed by Daccord et al. (1987, 1993a, 1993b) where water is used as injecting fluid. Since plaster is soluble in water, the patterns in these studies found to be similar to the patterns formed during reactive dissolution of a porous medium with an acidic solution due to chemical reaction. For example, at very slow injection rate, only the front part of the core was dissolved while at very high injection rate, entire core was dissolved uniformly. However, at intermediate injection rate, only selective part of the core was dissolved that formed wormholes as shown in Figure 6.6. Similar to Lund et al. (1973, 1975), Hoefner and Fogler (1989) conducted linear core experiments by injecting HCl in limestone and dolomite cores. Dissolution patterns and nature of breakthrough curves observed in these experiments were similar to ones shown in Figures 6.2 and 6.4, respectively, but due to the nature of

Figure 6.6: Wormholes created by injecting water through a radial core (of diameter 2 mm and length 50 mm) made of plaster (Daccord, 1987).

injection, one wormhole with multiple branches was observed at intermediate injection rates. Wang (1993) also performed experiments on limestone and dolomite to study the influence of rock mineralogy, acid concentration and temperature on optimum injection rate and $PV_{BT}$ and established the existence of a minima in breakthrough curves. Frick (1994) studied the effect of permeability, injection rate, acid concentration and temperature on wormhole formation by conducting radial core experiments on limestones. Bazin et al. (1995) conducted coreflow experiments on limestone and dolomite cores of diameter 50 mm and length 50 to 200

mm with 2M HCl at room temperature. They performed pre and post imaging of the cores using CT scanning (with $0.2\times0.2\times3$ mm pixel size) and found different types of dissolution patterns for different injection rates. They also studied the effect of heterogeneity by studying different types of carbonates and concluded that heterogeneity does not affect the type of dissolution pattern at a certain injection rate but change in the mineralogy of the rock changes the type of wormhole patterns. Similar effect of mineralogy was observed by Hoefner and Fogler (1989). Fredd and Fogler (1998) conducted linear core experiments on limestones (of diameter 3.8 cm and length 10.2 cm) by injecting various acids having significantly different reaction and transport rates compared to HCl, at constant injection rate. They studied the influence of reaction and transport mechanisms on wormhole formation and optimum injection rates; and observed more branched and thinner wormholes for fast reacting acids while less branched and thicker wormholes for slow reacting acids as in Figure 6.5. As reactivity of acid increased, $PV_{BT}$ was found to decrease and optimum injection rate was found to increase. Golfier et al. (2002) performed dissolution experiments by injecting under-saturated salt solution into a porous medium made of salt grains and observed the dissolution patterns very similar to the patterns formed during acidization. Ziauddin and Bize (2007) conducted core flow experiments and studied the effect of heterogeneity in the carbonate samples using several imaging techniques where they categorized different carbonate types according to spatial porosity distribution based on imaging and acidizing results.

### 6.2.2 Experimental Studies with Diverting Acids

Most of the experiments with diverting acids involve the study of pressure profile in single core and flow diversion in dual core set-ups. In a single core set-up, diverting acids are injected with a constant rate, pressure at the exit is fixed and inlet pressure is monitored with time. A dual core set-up consists of two cores (usually

of identical geometry but of different initial permeability) which are mounted parallel to each other so that pressure drop across both the cores be the same at all times. The pressure at exit of both the cores is same and kept constant, and, acid is injected with constant rate that splits into both the cores according to the ratio of their mobilities. Experiments have shown that unlike Newtonian acids, diverting acids leads to enormous increase in pressure drop across the core/cores (MaGee et al., 1997; Buijse and Domelen, 2000; Chang et al., 2001; Lynn and Nasr-El-Din, 2001; Taylor and Nasr-El-Din, 2003; Nasr-El-Din et al., 2006, 2008; Gomaa and Nasr-El-Din, 2010; Gomaa et al., 2011). It is because the viscosity of these acids increases in certain pH range ( MaGee et al., 1997; Rose, 2004). MaGee at al. (1997) showed that the in-situ cross-linked acids crosslink in the formation during treatment and are a thin gel during pumping and cleanup and hence, are ideally suited for acid diversion in carbonate formations. Buijse and Domelen, (2000) conducted experiments with emulsified based diverting acids and concluded that low diffusivity of these acids provides for efficient wormholing at low injection rates, forms thinner wormholes and penetrates deep into the formation. Chang et al. (2001) experimented with viscoelastic surfactant (VES) based in-situ gelled acids and suggested that these acids have superior diversion capability by its sustained viscosity as opposed to polymer based in situ gelled acid, which breaks down the viscosity when pH exceeds the higher limit of pH range of gel formation. Lynn and Nasr-El-Din (2001) showed that adding polymer to a regular acid changes its physical and chemical properties such that it behaves as a shear-thinning and slow reacting fluid. Nasr-El-Din et al. (2006) and Amro (2006) concluded that in-situ-gelled acid improved acid placement in carbonate reservoirs by offering the benefit of increasing viscosity inside the formation. Welton and van Domelen (2008) discussed the development of a unique in-situ-crosslinkable acid system that uses a blend of HCl/formic acid as the base acid and a synthetic polymer-gelling agent.

They noted that HCl/formic acid blends were more robust and maintained higher viscosities for longer periods and some synthetic polymer-acid-gelling agents provided high initial viscosity. Gomaa et al. (2011) examined flow of in-situ-gelled acid in dual-core experiments on carbonates with Computed-tomography (CT) scan as can be seen from Table 6.1 and Figure 6.7, and noted that at low or high flow rates

| | | | | | Permeability, md | | Wormhole | | Acid volume | | |
|---|---|---|---|---|---|---|---|---|---|---|---|
| No. | Injection Rate, $cm^3/min$ | Core | Length, in | $PV_{core}$ | Initial | Final | Length, in. | Diameter, mm | In-Situ -Gelled Acid, $PV_{core}$ | Regular Acid, $PV_{core}$ | Diversion Ability |
| 1 | 5 | 1 | 6 | 41.88 | 62 | acid breakthrough | 6 | 3.3 | 0 | 0.79 | No diverter used |
| | | 2 | 6 | 40.89 | 58 | 83 | 2.16 | 1.6 | 0 | 0.44 | |
| 2 | 5 | 3 | 6 | 48.70 | 102 | acid breakthrough | 6 | 4.5 | 0.60 | 0.43 | Achieved |
| | | 4 | 6 | 40.77 | 52 | 250 | 5.04 | 1.5 | 1.03 | 0.56 | |
| 3 | 1 | 5 | 6 | 46.04 | 88 | 40 | 1.68 | 1.5 | 0.6 | 0.2 | Not achieved |
| | | 6 | 6 | 37.2 | 3.5 | 0 | 0 | 0 | 0 | 0 | |
| 4 | 1.5 | 7 | 6 | 40.21 | 109 | 25 | 2.01 | 2.5 | 1.03 | 0.01 | Achieved |
| | | 8 | 6 | 36.8 | 5 | acid breakthrough | 6 | 1.6 | 0 | 1.4 | |
| 5 | 2.5 | 9 | 6 | 44.74 | 96 | 28 | 3.12 | 4.5 | 2.74 | 0.04 | Achieved |
| | | 10 | 6 | 36.51 | 4.5 | acid breakthrough | 6 | 1.5 | 0.18 | 1.06 | |
| 6 | 5 | 11 | 6 | 42.15 | 84 | 41 | 3.91 | 5.1 | 2.98 | 0.06 | Achieved |
| | | 12 | 6 | 35.90 | 4 | acid breakthrough | 6 | 1.7 | 0.20 | 1.1 | |
| 7 | 10 | 13 | 6 | 41.89 | 136 | 98 | 4.56 | 5.8 | 3.06 | 0.08 | Achieved |
| | | 14 | 6 | 34.12 | 7 | acid breakthrough | 6 | 1.8 | 0.25 | 1.2 | |
| 8 | 15 | 15 | 6 | 38.28 | 97 | acid breakthrough | 6 | 4.8 | 4.25 | 0.56 | Not achieved |
| | | 16 | 6 | 34.10 | 5 | 6 | 0 | 0 | 0 | 0 | |
| 9 | 5 | 17 | 20 | 156.96 | 106 | acid breakthrough | 20 | 3.4 | 4.36 | 0.82 | Not achieved |
| | | 18 | 20 | 110.10 | 5 | 5 | 0 | 0 | 0 | 0 | |
| 10 | 2.5 | 19 | 20 | 155.89 | 105 | acid breakthrough | 20 | 3.3 | 1.53 | 0.03 | Achieved |
| | | 20 | 20 | 124.20 | 5 | 10 | 7.3 | 3.5 | 0.83 | 0.25 | |

Table 6.1: Set of dual-core experiments with diverting acids at various injection rates (Gomaa et al., 2011).

of acids (experiments 3: 1 $cm^3\,min^{-1}$, $\frac{K_{high}}{K_{low}} \sim 25$; experiments 8: 15$cm^3\,min^{-1}$,

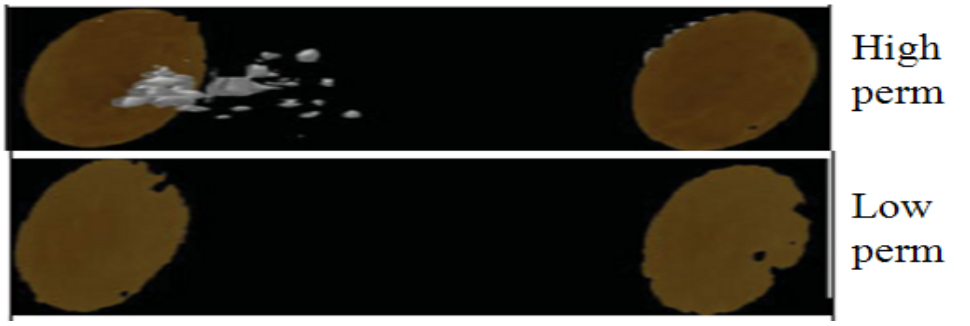


(a)

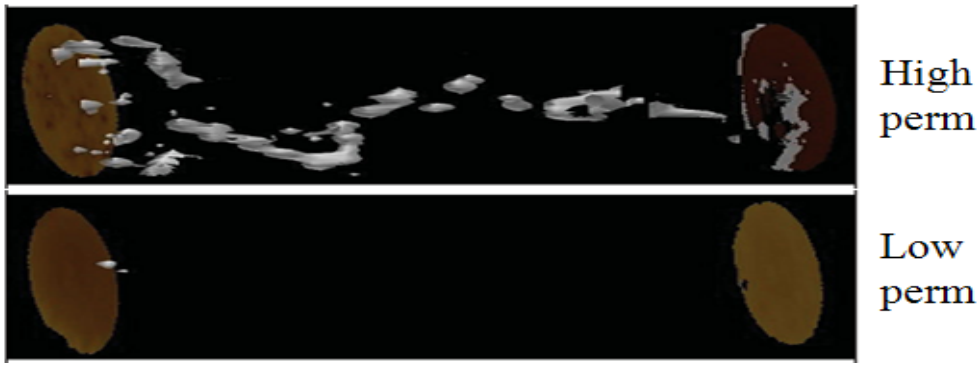


(b)

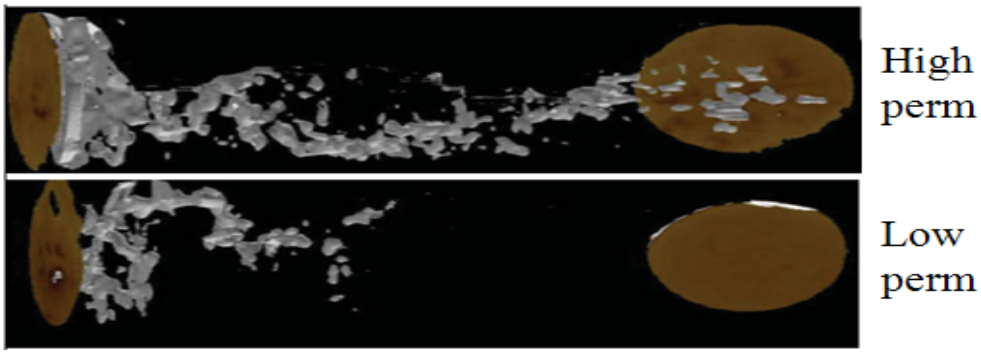


(c)

Figure 6.7: Dissolution patterns and flow diversion in dual-core experiments with diverting acids at various injection rates (a) experiments 3 (Gomaa et al., 2011) with injection rate, $Q = 1cm^3min^{-1}$ and permeability ratio, $\frac{K_{high}}{K_{low}} \sim 25$, (b) experiments 8 (Gomaa et al., 2011) with injection rate, $Q = 15cm^3min^{-1}$ and permeability ratio, $\frac{K_{high}}{K_{low}} \sim 20$, (c) experiments 10 (Gomaa et al., 2011) with injection rate, $Q = 2.5cm^3min^{-1}$ and permeability ratio, $\frac{K_{high}}{K_{low}} \sim 21$.

$\frac{K_{high}}{K_{low}} \sim 20$), diversion is negligible while at intermediate injection rates (experiments 4: 1.5 cm$^3\,\mathrm{min}^{-1}$, $\frac{K_{high}}{K_{low}} \sim 22$; experiments 10: 2.5cm$^3\,\mathrm{min}^{-1}$, $\frac{K_{high}}{K_{low}} \sim 21$), diversion is significant.

### 6.2.3 Mathematical Studies

Numerous mathematical models are developed in literature to describe the acidization process in reservoirs with Newtonian acids. These models can be classified mainly into four categories: (a) network models developed by Daccord et al. (1993a, 1993b), Fredd and Fogler (1998), etc., (b) the capillary tube models developed by Hung at al. (1989), Huang et al. (1997, 1999), Buijse et al. (2005), Gdanski (1999), and (c) continuum models reported by Liu et al. (1996), Golfier et al. (2002), Panga et al. (2005), Kalia and Balakotaiah (2007, 2009), Ratnakar et al. (2012).

#### Network Models

Network models developed by Daccord et al. (1993a, 1993b) and Fredd and Fogler (1998), describe the reactive dissolution by representing the porous medium as a network of tubes which are interconnected at the nodes. In these models, the flow of tube is described by Hagen-Poiseulle equation where reaction occurs at the wall of tube that increases tube radius. While these models predict the experimentally observed trends, the PV$_{BT}$ predicted by these models are much higher than the experimental results. To improve the predictions, Fredd and Fogler used physically representative network model that includes the channeling effects. However, predictions even after some improvements, were quantitatively very high as compared to experimental ones. In addition, since these models are applied at pore scale ($\sim \mu m$), the lab/core scale ($\sim cm$) or field scale predictions ($\sim km$) involve very high magnitude of length scale separation ($10^4 - 10^9$) and require huge number of mesh and hence, these models are computationally prohibitive and almost impractical. Also, the effect of heterogeneity and change in pore connectivity due

to dissolution are very difficult to incorporate in network models.

**Capillary Models**

Capillary tube models assume the existence of wormholes. In these models, a wormhole is represented as a capillary tube where transport and reaction are analyzed in detail (Hung at al., 1989; Huang et al., 1997, 1999; Buijse et al., 2005; Gdanski, 1999). This semi-analytical approach on the contrary with network models, is very simple and computationally very fast and can describe the wormhole propagation and its interaction with other wormholes. For example, Bujse(2000) and Huang et al. (1997) showed that the growth rates of multiple wormholes in a domain depends on separation distance between them, which is in accordance with experimental observations.

While these models are very simple, they need prior informations such as wormhole densities and expression for fluid leakage (which depends on wormhole structure and medium heterogeneity), which are very difficult to obtain. In fact there is no theoretical or experimental works available in literature on wormhole density. In addition, capillary models do not capture wormhole initiation, dissolution patterns and effect of heterogeneity or pore scale reaction and transport on wormhole formation.

**Continuum Models**

Continuum models (Liu et al., 1996; Golfier et al., 2002; Panga et al., 2005; Kalia and Balakotaiah, 2007, 2009; Ratnakar et al., 2012) describe the transport and reaction phenomena at intermediate or Darcy scale (that is bigger than the pore scale and smaller than the core/field scale). Darcy-scale ($\sim mm$) are the length scale where Darcy-law is applicable. These models requires information on the pore-scale processes, which are obtained from a pore scale model. Thus, these models are computationally less expensive as compared to the network models and can describe the effect of pore-scale reaction and transport mechanisms,

heterogeneities, wormhole density, geometries, etc. on carbonate dissolution and optimum conditions, unlike the capillary tube models. However, the model developed by Liu et al. (1996) does not consider the effect of mass transfer on the reaction rate and is valid only in the kinetic regime where dissolution is very slow as compared to transfer of solute from bulk to the soild-fluid interface. Similarly, though Golfier et al. (2002) reproduced the experimentally observed dissolution patterns numerically by using Darcy-Brinkman formulation and a local non-equilibrium model, the model is valid only in the mass transfer controlled regime where the transfer of solute from bulk to fluid-solid interface is slower than the rate of dissolution. These limitations were removed in two-scale continuum models (Panga et al. 2005; kalia and Balakotaiah, 2007, 2009; Ratnakar et al., 2012) which captured both the extremes of reaction (kinetic and mass transfer controlled) simultaneously by using two concentration variables and a mass transfer coefficient. A good match was obtained when the model predictions are compared with 2D salt pack experiments conducted by Golfier et al. (2002). Panga et al. (2005) introduced a qualitative optimum criterion to predict wormhole formation that depended on the fluid petro-physical properties but was independent of the domain size. The continuum model approach has also been adapted to model infiltration flow of a reactive fluid in porous medium.

Mathematical models discussed above, describe the reactive dissolution of porous media with Newtonian acids only which can not describe the carbonate acidizing with diverting acids due to strong dependency of pH on fluid viscosity. Unfortunately, viscosity of diverting acids depends strongly on pH and there are no rheological models available in literature that describe pH dependent viscosity and reactive transport of in-situ gelling acids in porous media.

## 6.3 Objectives

Since gel dynamics is the key for flow diversion from high-perm zones to low-perm zones in formation and hence for optimal stimulation, the main objective of this work is to understand gel dynamics and mechanism of flow diversion, and, use these understanding to develop guidelines for optimal stimulation of carbonates at field scale. It involves developing a rheological model for in-situ gelling acids that can account for dependency of pH, temperature and shear rates on fluid viscosity and developing a two-scale continuum model that can describe the reactive transport of in-situ gelling acids in porous media such as carbonates.

This work is focused on reactive dissolution of carbonates by in-situ gelling acids and comparison with that by Newtonian acids. We also compare the theoretical results with available experimental predictions. This part of thesis is organized in following manner. In chapter 7, we develop an experimental based novel empirical rheological model for rheology of in-situ gelling acids that accounts for effects of temperature, pH and shear rates on its viscosity. Here, we develop equivalent Darcy law for in-situ gelling acids to describe the fluid flow in porous media at Darcy scale that include the non-Newtonian (shear thinning) and diverting behavior of in-situ gelling acids. In the end of this chapter, we incorporate rheological model and equivalent Darcy law into two-scale continuum (TSC) model that can describe the transport and reaction of in-situ gelling acids at Darcy scale where pore-scale effects are included by effective properties used in the model and by structure-property relations. In chapter 8, we present gel dynamics and flow diversion in single and dual core set-ups, respectively, using one dimensional (1-D) version of the model. Since 1-D model can not explain the dissolution patterns, in chapter 9, we use two dimensional (2-D) version TSC model to analyze the various dissolution patterns. Chapter 10 presents the three dimensional (3-D) simulations of wormhole formation that is more accurate when compared to experimental ob-

servations. In the last chapter 11, we conclude our main results and discuss the possible extension of the current work.

# Chapter 7 Mathematical Model for In-situ Gelling Acids

## 7.1 Preamble

There are three types of mathematical models in literature to study the dissolution phenomena in porous media: (i) network models, (ii) capillary tube models, and (ii) continuum models discussed in the previous chapter. Due to the length scale associated with carbonates as shown in Figure 7.1, the network models (which use conservation laws at pore scales ($\sim 0.1 - 10\mu m$) to describe core scale ($\sim 10 - 50cm$) phenomena) are computationally prohibitive. On the other hand, though capillary models are computationally very fast, due to their inabil-

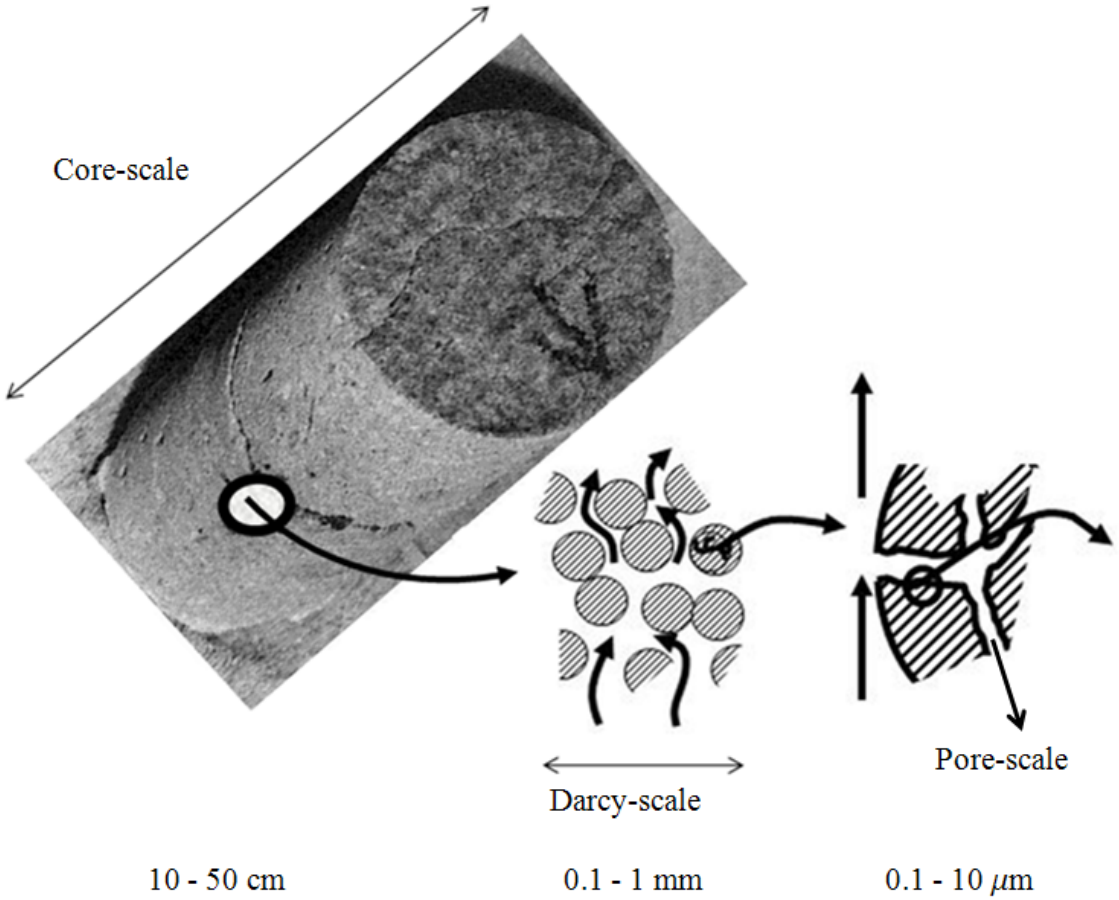


Figure 7.1: Schematic of different length scales associated in a lcarbonate core used in laboratory experiments.

ity to predict wormhole initiation and dissolution patterns, they can not be used to study the effect of pore-scale phenomena on wormhole formation. Thus, in this work, we use continuum models that describe the conservation laws at Darcy-scale (that makes it computationally less expensive than network models) and retains the pore-scale effects through pore-scale models for effective properties such as transfer/dispersion coefficients and structure-property-relations. However, these models in the literature are applicable only to Newtonian acids.

Diverting acids such as in-situ gelling acids are non-Newtonian (shear thinning) in nature and have viscosity that depends strongly on pH. In fact, the pH dependent viscosity is the main difference between diverting acids and other (Newtonian/non-Newtonian) acids. It is also the reason for gel formation, which is the key element for flow diversion from high-perm to low-perm zones in reservoirs. Therefore, the predictions of wormhole patterns (and other useful relationships such as the dependence of the optimum acid volume and wormhole density on injection rate or reaction parameters) in carbonate stimulation with diverting acids require a mathematical model that accounts for the flow, reaction and rheological effects of diverting fluids. Since, such model is not available in literature, in this chapter, we develop (i) an experimental based empirical rheological model for diverting acids that accounts for the effects of pH on viscosity; and, (ii) a mathematical model based on two-scale continuum model (Panga et al., 2005) that can describe the reactive transport of in-situ gelling acids in porous media at Darcy-scale and retain the essential features of pore-scale phenomena by pore-scale models.

## 7.2 Rheological Modeling for Diverting Acids

In general, the physio-chemical properties (viscosity, density etc.,) of a fluid depend on the three state variables, temperature, pressure/shear rate and concentration/pH. While several experimental studies are available on pH dependent viscosity of diverting acids, there are no theoretical or empirical pH dependent rhe-

ological models available in the literature. Therefore, we use experimental data by Rose (2004) to develop an empirical rheological model that accounts for the effect of pH on viscosity. Before we discuss it into detail, we briefly review the effect of temperature and shear rates on viscosity which is well established in literature.

### 7.2.1 Effect of Temperature on Viscosity

It is found that viscosity of most of the liquids decreases with increase in temperature while this may not be true for the gases. However, the effect of temperature on viscosity is very small and can be described mathematically as follows:

$$\mu = \mu_0 \, Exp\left[-\alpha \frac{T - T_0}{T_0}\right] \approx \mu_0 \, \left[1 - \alpha \frac{T - T_0}{T_0}\right]; \quad \alpha > 0 \text{ for liquids,} \tag{7.1}$$

where $T_0$ is the reference temperature, $\alpha$ is the temperature coefficient of viscosity and $\mu_0$ is the viscosity of fluid at reference temperature $T_0$. Experiments (Nasr-El-Din, 2008) show that viscosity of in-situ gelling acids also follow the same trends and decreases exponentially with temperature. It should be noted that the linear relationship is valid only in the small temperature range near $T_0$, i.e., $\frac{T-T_0}{T_0} << 1$ (For $\alpha = 1$ and $T_0 = 300K,$ equation (7.1) can be used over a $0 - 30 \ K$ change). However, the range of validity is larger for smaller $\alpha$. The temperature coefficient of viscosity, $\alpha$ varies from fluid to fluid and is positive for most of the liquids. The effect of $\alpha$ on viscosity as a function of temperature is shown in Figure 7.2. It can be seen from Figure 7.2 that for small values of $\alpha$, viscosity decreases linearly with temperature. In fact, experimental data for gelled acids (Nasr-El-Din et al., 2008) shows that the viscosity of in-situ gelling acids decreases almost linearly with temperature. Since, $\alpha$ is small for most liquids, the effect of temperature on viscosity may be negligible. However, viscosity may change significantly if temperature change is very large.

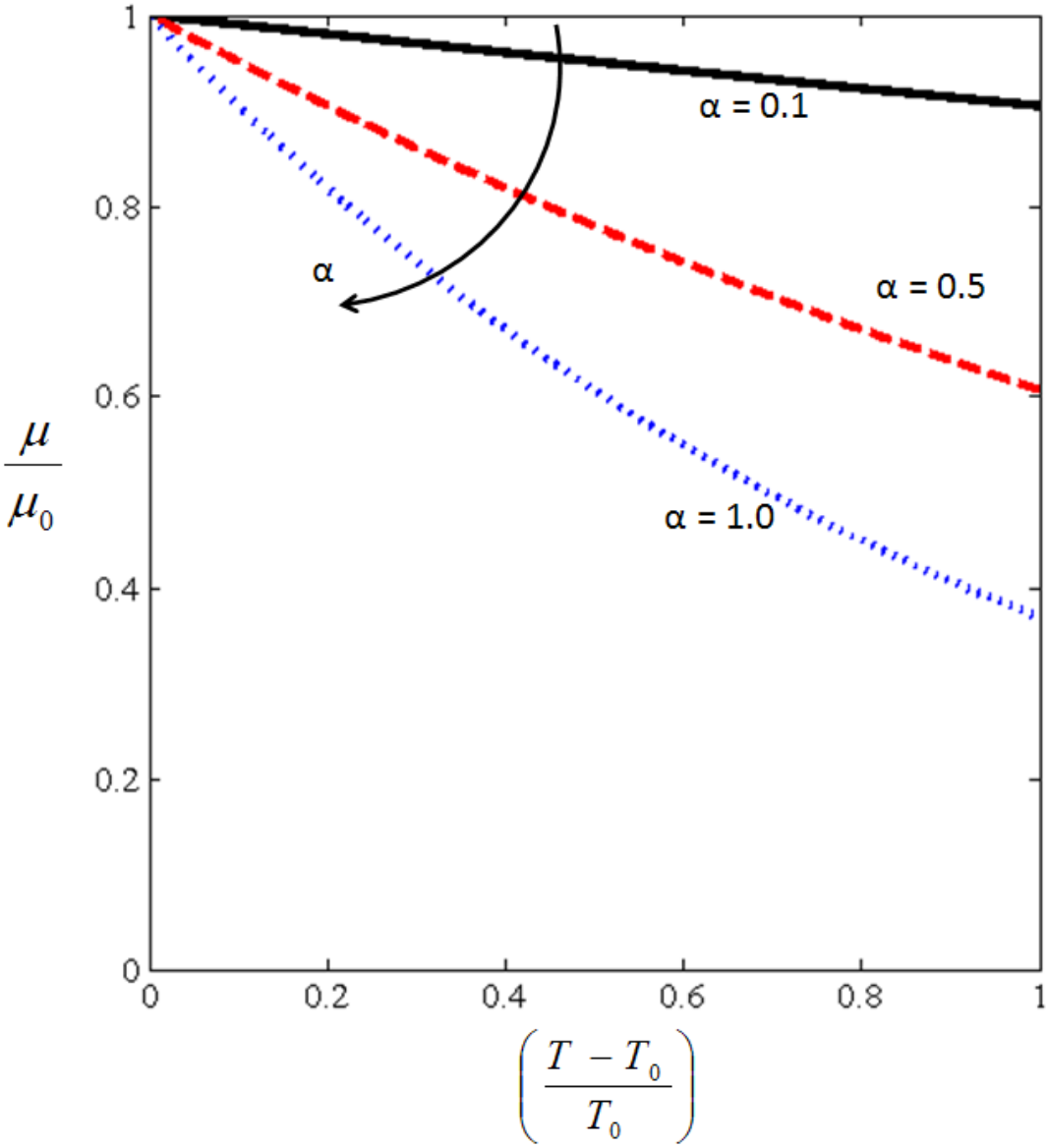


Figure 7.2: Effect of temerature coefficient of viscosity, $\alpha$, on viscosity vs temperature profile.

### 7.2.2 Effect of Pressure/Shear Rate on Viscosity

Several experimental studies have been performed to study the flow behavior of non-Newtonian fluids. The experimental data for steady-state laminar flow of polymeric fluids in tubular reactors (Bird et al., 1987) suggests that the non-Newtonian shear thinning fluids exhibit more blunt velocity profile than the Newtonian fluids. Also, the pressure drop increases much less rapidly with the mass flow rate for these fluids as compared to the Newtonian fluids (where it is linear). This implies that the viscosity of the polymeric fluids depends on the velocity gradient (or shear rate, $\dot{\gamma}$). Furthermore, the 'recoiling effect' is observed after cessation of steady-state flow for polymeric fluids (Fredrickson, 1964), i.e., when a dye is released in a steady flow of polymeric fluids, the dye line stretches to parabola. But, when flow is stopped, the die line comes back towards the inlet. This is a manifestation of elasticity or the notion of fading memory. Similarly, tube siphon effects (Tranner, 1970) indicate the existence of non-zero normal stresses for polymeric fluids.

Non-Newtonian fluids are generally classified into three groups depending on the relationship between shear rate and stress : (1) time-independent non-Newtonian fluids, (2) time dependent non-Newtonian fluids, and (3) viscoelastic non-Newtonian fluids. Time-independent fluids are those for which shear rate ($\dot{\gamma}$) is a unique but may be non-linear function of shear stress ($\tau$) at all times (Bird et al., 1960), i.e.,

$$\dot{\gamma} = f(\tau), \tag{7.2}$$

where $f$ may be a non-linear function. These fluids are also named as 'generalized Newtonian fluids' and can be characterized by flow curves of $\tau$ vs. $\dot{\gamma}$ as in Figure 7.3. These are: (i) Bingham plastic and yield-pseudoplastic for which a threshold shear stress is required to shear the fluid and cause flow, (ii) Pseudoplastic or shear thinning fluids whose apparent viscosity decreases with increase

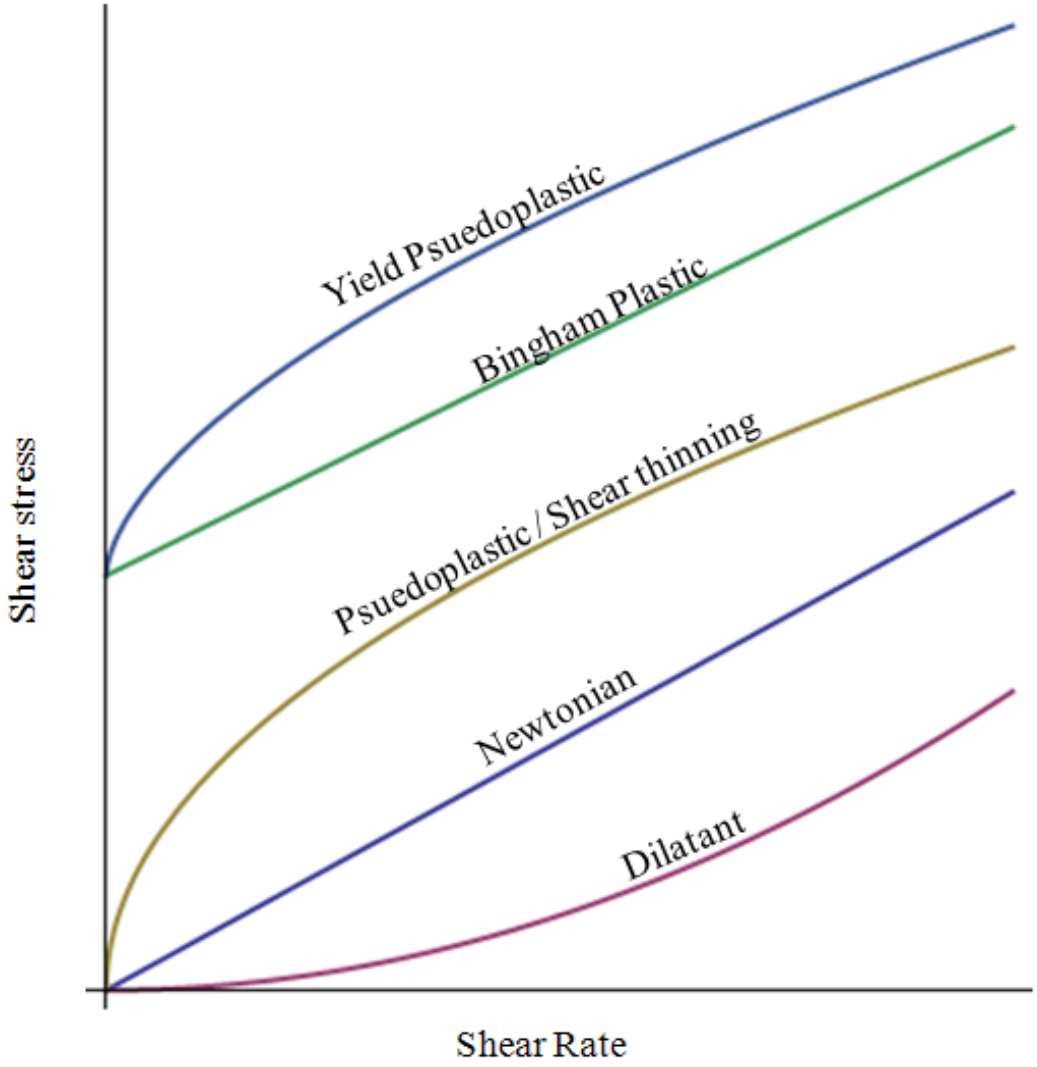


Figure 7.3: Schematic diagram illustrating the time independent non-Newtonian fluid behavior.

in shear rate or stress, and (iii) dilatant or shear thickening fluids whose apparent viscosity increases with increases in shear rate. Time-dependent fluids are those for which shear rate depends not only on shear stress but also on the shearing time or shear stress rate history. These are thixotropic or rheopectic fluids, depending upon whether the shear stress decreases or increases w.r.t. shearing time at a given shear rate. Thixotropic fluids are also called time-dependent shear thinning fluids, and rheopectic fluids are known as time-dependent shear thickening fluids. Viscoelastic fluids are those that exhibit both the elastic and the viscous properties, and shows partial recovery upon removal of the imposed shear stress. Various rheological models are published to explain the behavior of non-Newtonian fluids. Here, we review some of the well-known models.

**Generalized Newtonian Models**

The generalized Newtonian fluid models (Oldroyd, 1949, 1950) are obtained by simply replacing the constant viscosity by a non-Newtonian viscosity as follows:

$$\boldsymbol{\tau} = -\eta(\dot{\gamma})\,\dot{\boldsymbol{\gamma}}, \tag{7.3}$$

where $\eta$ is the non-Newtonian apparent viscosity and $\dot{\gamma} = \sqrt{\frac{1}{2}\left(\dot{\boldsymbol{\gamma}} : \dot{\boldsymbol{\gamma}}\right)}$ is the magnitude of the rate of shear tensor $\dot{\boldsymbol{\gamma}}$. This is the simplest non-Newtonian model which can describe only the non-Newtonian viscosity, but none of the normal stress, time-dependent and elastic effects. For Bingham fluids, $\boldsymbol{\tau}$ is replaced by $\boldsymbol{\tau} - \boldsymbol{\tau}_0$, because they exhibits a yield stress $\boldsymbol{\tau}_0$. Numerous empirical models for the non-Newtonian viscosity $\eta$ as a function $\dot{\gamma}$ or $\boldsymbol{\tau}$ are proposed (summarized in Corapcioglu, 1996). The most widely used rheological model to describe flow through porous media is the power-law model (Bird et al., 1960) that represents the non-Newtonian viscosity $\eta$ as

$$\eta(\dot{\gamma}) = H\dot{\gamma}^{n-1}, \tag{7.4}$$

where $H$ is called the consistency coefficient and $n$ is called the power index. This is a two-parameter model that gives a linear log-log plot of shear stress vs. shear rate. For the special case of $n = 1$, it represents the Newtonian fluid where the consistency coefficient $H$ is equal to the viscosity of the fluid. Because of its inherent simplicity, the power-law is of considerable interest in applications and is used to approximate the rheological behavior of both the shear thinning or psuedoplastic ($n < 1$) and the shear thickening or dilatant ($n > 1$) fluids over a large range of flow conditions. However, the major limitation of this model is that it predicts infinite viscosity at vanishingly small shear rate/stress. In other words, it can not describe the constant viscosities $\mu_0$ and $\mu_\infty$ at very low and very high shear rates where most of the fluids follow Newtonian behavior (Figure 7.4). These trends can be described only by the models containing at least four parameters. The simplest four-parameter model (Meter and Bird, 1964) is given by,

$$\eta = \mu_\infty + \frac{\mu_0 - \mu_\infty}{1 + \left(\frac{\tau}{\tau_m}\right)^{\alpha_1 - 1}} \tag{7.5}$$

where, $\mu_\infty$ and $\mu_0$ are minimum and maximum limiting viscosities at infinitely large and infinitely small shear rate (or stress), respectively. The parameter $\alpha_1$ is a dimensionless parameter and $\tau_m$ represents the shear stress at which the ratio $\frac{\eta - \mu_\infty}{\mu_0 - \mu_\infty}$ reduces to half. For the case of $\alpha_1 = 1$, $\eta$ reduces to Newtonian viscosity $\mu = \frac{\mu_0 + \mu_\infty}{2}$. We do not discuss time-dependent non-Newtonian fluids as they are rarely used.

**Viscoelastic Models**

The third category of non-Newtonian fluids is the viscoelastic non-Newtonian fluids (we do not review here the time dependent non-Newtonian fluids as they are not of interest in acidization). A good description of the viscoelastic behavior of these fluids can be illustrated by 'silly putty' which bounces when rolled and

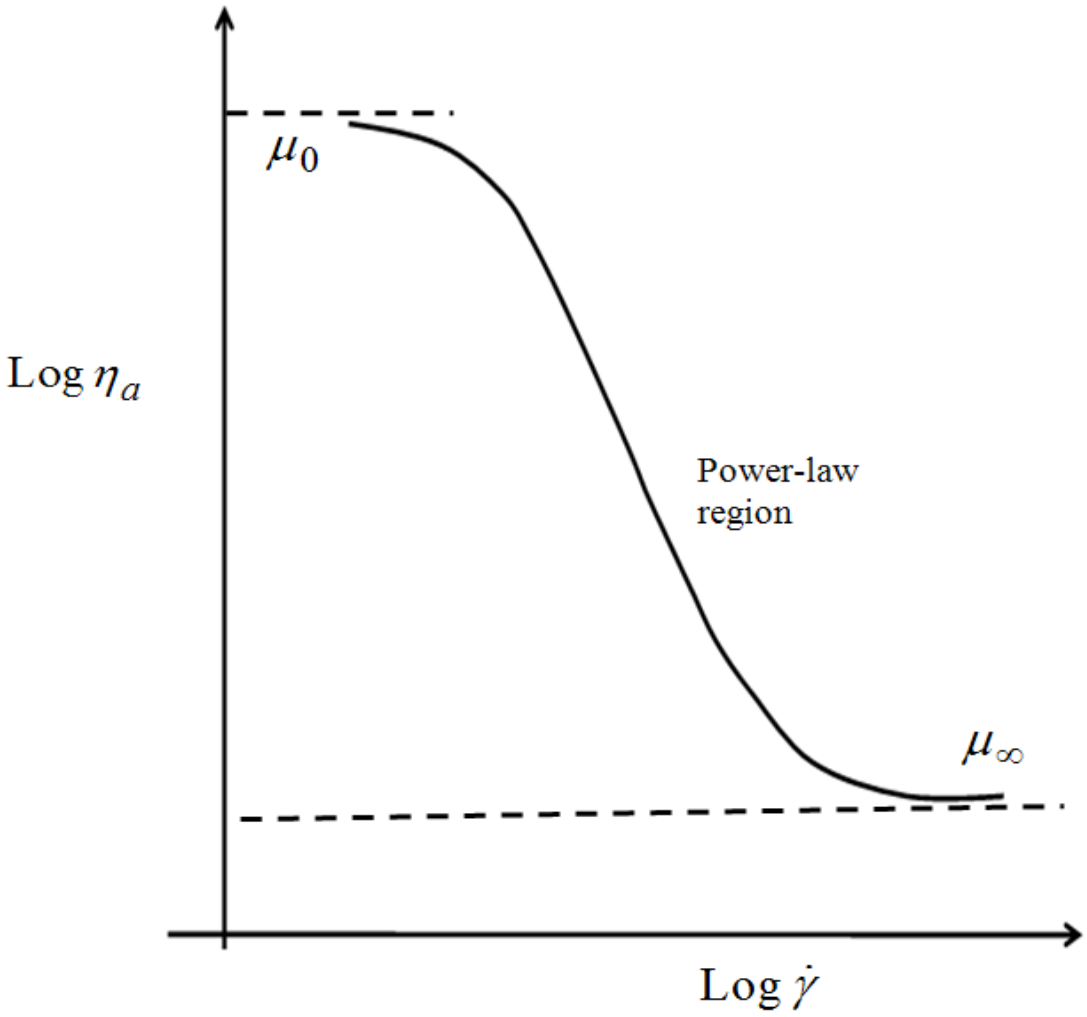


Figure 7.4: Schematic diagram illustrating the general viscosity behavior of a shear thinning fluid.

dropped onto a hard surface, while flows easily when squeezed slowly. The time-independent fluids can not explain the fading memory and elastic effects exhibited by the viscoelastic fluids as the time derivative or time integral is excluded in construction of these models. The viscous effects can be described by the Newton's law of viscosity while elastic effects can be described by the analogy of Hooke's expression which represents perfect memory i.e., the solid/fluid returns to its original position after removal of imposed shear stress.

One of the simplest mechanical models used to describe both the viscous and elastic effects is the Maxwell's model (Maxwell, 1867):

$$\boldsymbol{\tau}+\lambda_1\frac{\partial\boldsymbol{\tau}}{\partial t}=-\mu_0\dot{\boldsymbol{\gamma}}, \tag{7.6}$$

where $\lambda_1$ is a time constant called the relaxation time and $\mu_0$ is zero shear rate viscosity. When the relaxation time is negligible or the stress tensor changes very slowly with time, the derivative term is negligible and the model becomes Newtonian model with viscosity $\mu_0$. Similarly, if there are rapid changes in stress tensor with time or the relaxation time is very high, the derivative term dominates and the model becomes Hookean solid with elastic modulus $\frac{\mu_0}{\lambda_1}$. This is a linear viscoelastic model. If time derivative of the shear rate is included in Maxwell's model (Maxwell, 1867), it results in Jeffrey's model (Jeffrey, 1929) given as

$$\boldsymbol{\tau}+\lambda_1\frac{\partial\boldsymbol{\tau}}{\partial t}=-\mu_0\left(\dot{\boldsymbol{\gamma}}+\lambda_2\frac{\partial\dot{\boldsymbol{\gamma}}}{\partial t}\right), \tag{7.7}$$

where $\lambda_2$ is known as retardation time. If we have a mixture of Newtonian solvent $\left(\boldsymbol{\tau}_s=-\mu_s\dot{\boldsymbol{\gamma}}\right)$ and a Maxwellian polymeric fluid $\left(\boldsymbol{\tau}_p+\lambda_1\frac{\partial\boldsymbol{\tau}_p}{\partial t}=-\mu_p\dot{\boldsymbol{\gamma}}\right)$ where $\boldsymbol{\tau}_s+\boldsymbol{\tau}_p=\boldsymbol{\tau}$, it can be better described by Jeffrey's model (with $\mu_0=\mu_s+\mu_p$ and $\lambda_2=\frac{\mu_s}{\mu_s+\mu_p}\lambda_2$) that gives better flexibility in fitting experimental data.

Though there are various types of rheological models (described above) that

accounts for the effect of shear rates on viscosity, Lynn and Nasr-El-Din (2001) showed that diverting acids like in-situ gelling acids are shear thinning acids. For this reason, we adopt power-law model described in equation (7.4), with power index, $n$, less than unity. In addition, power-low models are the simplest and most widely used in the literature, and, can account for the effect of shear rate on viscosity for most of the practical cases.

### 7.2.3 Effect of pH on Viscosity

As discussed previously, in-situ gelled acids use pH to control the cross-linking of polymeric chains in solution to form a gel in a certain pH range and increase the viscosity enormously that leads to flow diversion and hence uniform stimulation of the carbonate formation. Though the experimental data for viscosity of in-situ gelling acids depending on pH are available in literature, there are no theoretical or empirical rheological models which exist to describe the effect of pH on viscosity of in-situ gelling acids. Since, fluid rheology (depending on pH) is one of the key factor for flow diversion, here, we develop an empirical model for pH dependent viscosity based on experimental data (Rose, 2004) shown in Figure 7.5. We note from Figure 7.5 that (i) the polymeric solution starts cross-linking to form the gel in the pH range 4 - 6, (ii) the pH corresponding to maximum viscosity remains constant, i.e., does not depend on the shear rate ($pH_m$= 5.47) and, (iii) viscosity vs. pH profile is asymmetric, i.e., viscosity increases slowly before maxima and decreases sharply thereafter. Based on the above observations, we need a model with at least four parameters to describe the base value, mean, variance and skewness of the viscosity curve that can be given by the expression

$$\mu\left(pH\right) = \mu_0 \left[1 + \left(\mu_m - 1\right) Exp\left\{\frac{-a\left(pH - pH_m\right)^2}{pH\left(7 - pH\right)}\right\}\right], \tag{7.8}$$

where, $\mu_0$, $\mu_m$, $pH_m$ and $a$ are the four parameters used in the model.

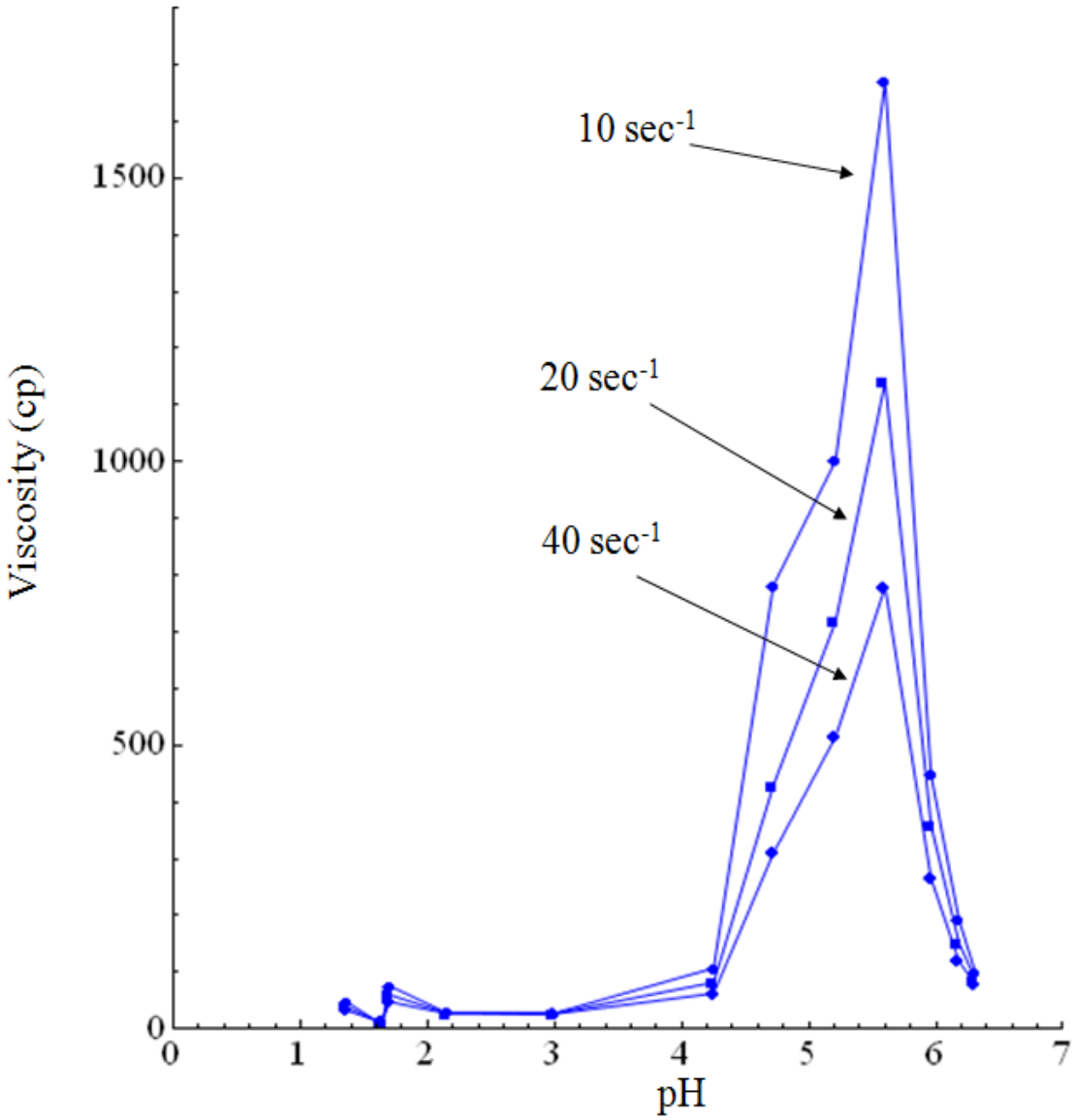


Figure 7.5: Experimental data for viscosity of ZCA (1.5 % SGA-III) vs pH.

It should be noted that four-parameter pH dependent rheological model in equation (7.8) can describe all types of diverting acids having profile same as in Figure 7.5. This is due to the most general form of the model where each parameter represents the particular feature of the viscosity behavior of in-situ gelling acids. For example, $\mu_0$ is the base viscosity at pH = 0 or 7. It represents the viscosity of the fluid before it starts cross-linking. The parameter $\mu_m$ is the maximum possible increment in the viscosity w.r.t. base value due to gel formation as can be seen from Figure 7.6. In this figure, increase in viscosity from the base value is plotted against pH for different values of $\mu_m$ (= $10,\ 20,\ 30$) while other parameters are kept constant ($a = 10.0$ and $pH_m = 5.0$). We note from this figure that (i) higher $\mu_m$ leads to higher increase in viscosity due to gel formation, (ii) $\mu_m$ equals to the same factor by which viscosity of diverting acid increases from the base value due to gel formation. Similarly, the parameter $pH_m$ is the pH value where increase in viscosity due to gel formation is maximum as can be seen from Figure 7.7 In this figure, viscosity profile is plotted against pH at $pH_m = 2.0,\ 3.5$ and $5.0$ while other parameters are kept constant ($\mu_m = 20$ and $a = 10$). It can be seen from this figure that the parameter $pH_m$ also introduce asymmetry in profile. For example, when $pH_m = 3.5$ (exactly in the middle), the profile is symmetric while $pH_m < 3.5$ and $> 3.5$ leads to asymmetric profile with positive and negative skewness, respectively. The parameter $a$ is the measure of the pH-range of gel formation which is, loosely, inverse of the variance (width) of the viscosity vs pH profile, i.e., if $a$ increases, pH range of gel formation decreases as can be seen from Figure 7.8. Thus, all the features of viscosity vs. pH profile for in-situ gelling acids can be represented by the four parameter empirical model given by equation (7.8) indicating that it is the most general model possible (to describe the effect of pH on viscosity). Now, based on the effects of temperature, pressure/shear rates and pH on fluid viscosity discussed above, a complete rheological model for diverting acids can be developed

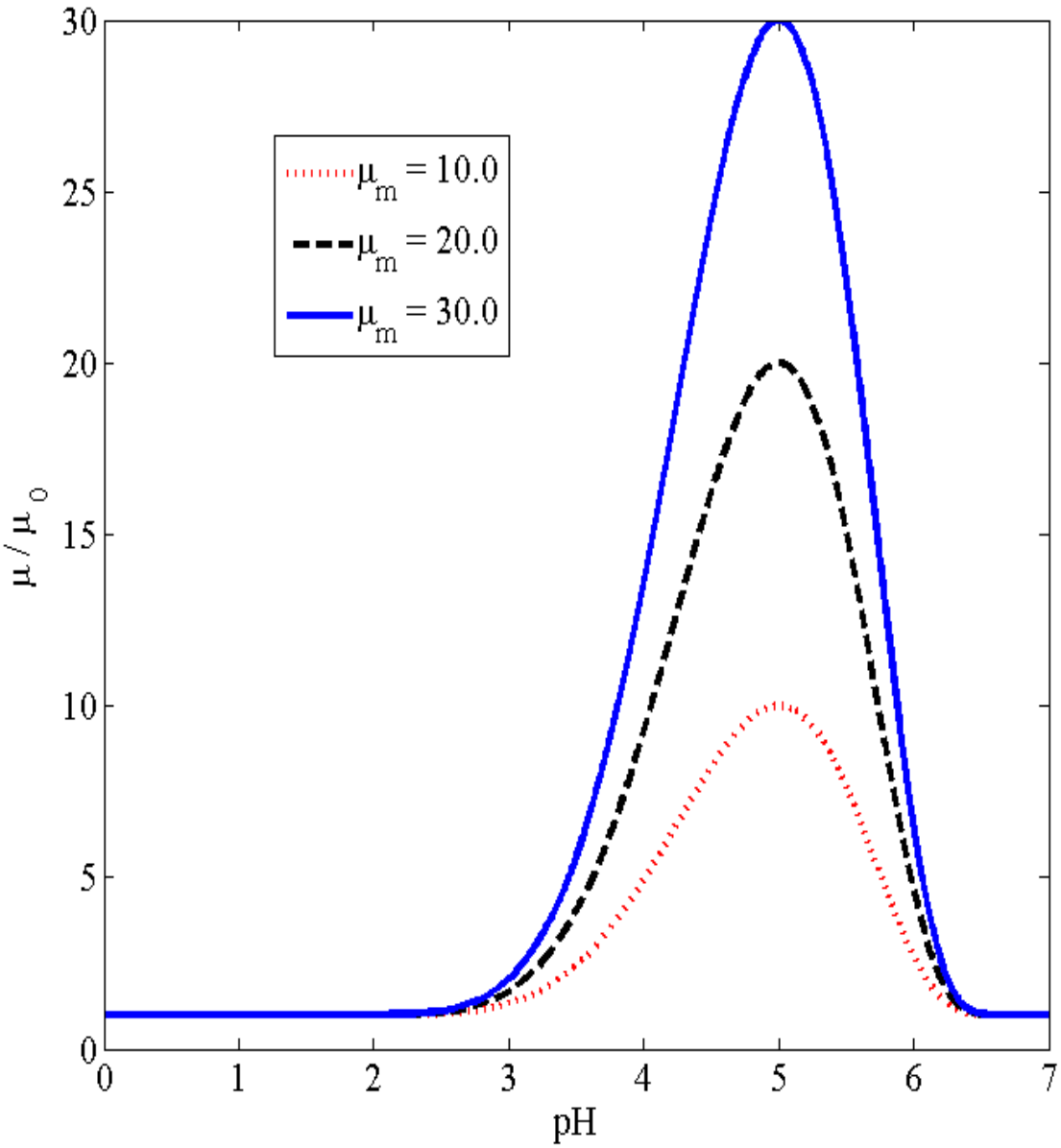


Figure 7.6: Effect of $\mu_m$ on viscosity vs pH profile for $a = 10$ and $pH_m = 5$.

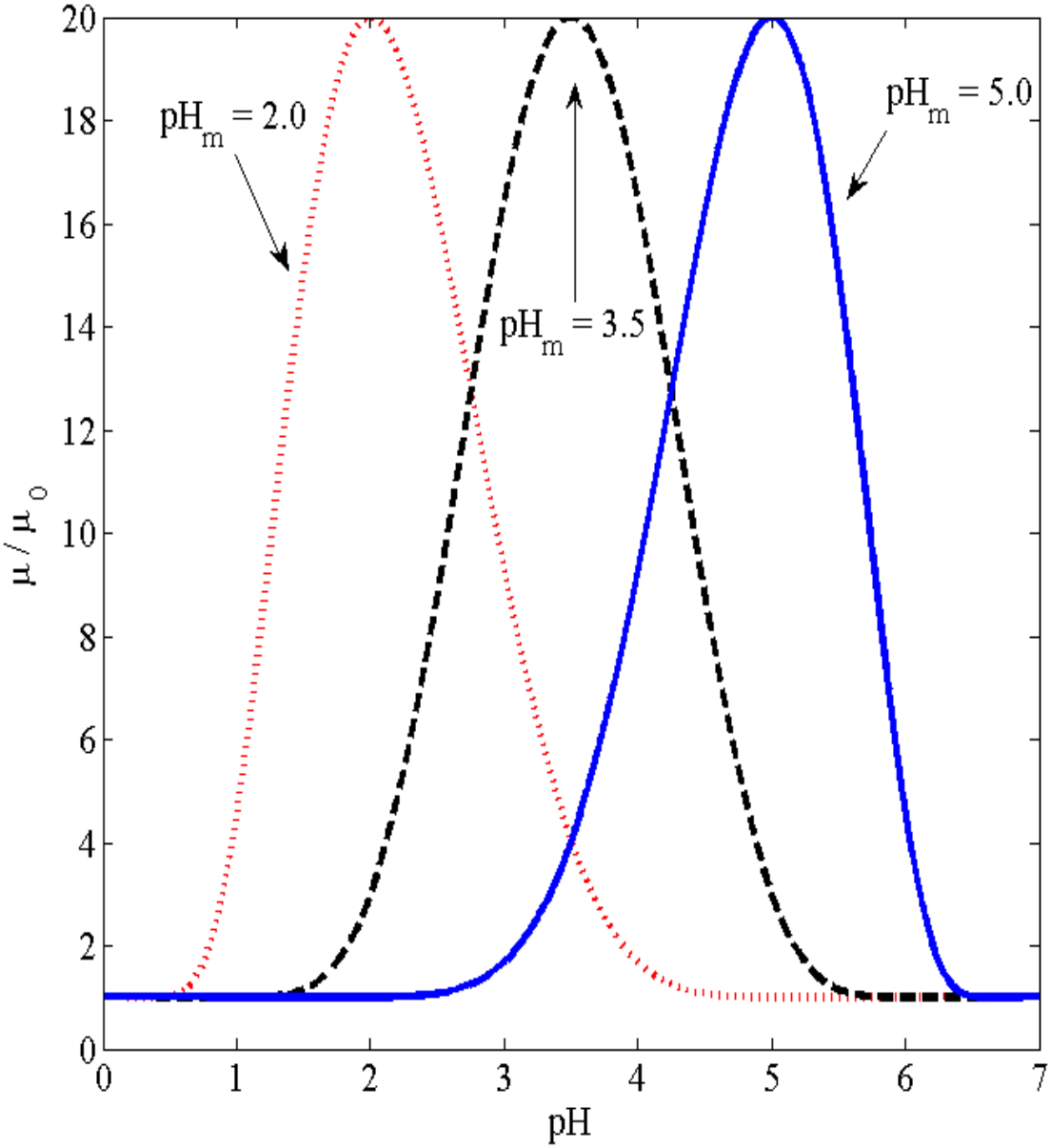


Figure 7.7: Effect of $pH_m$ on viscosity vs. pH profile for $\mu_m = 20$ and $a = 10$.

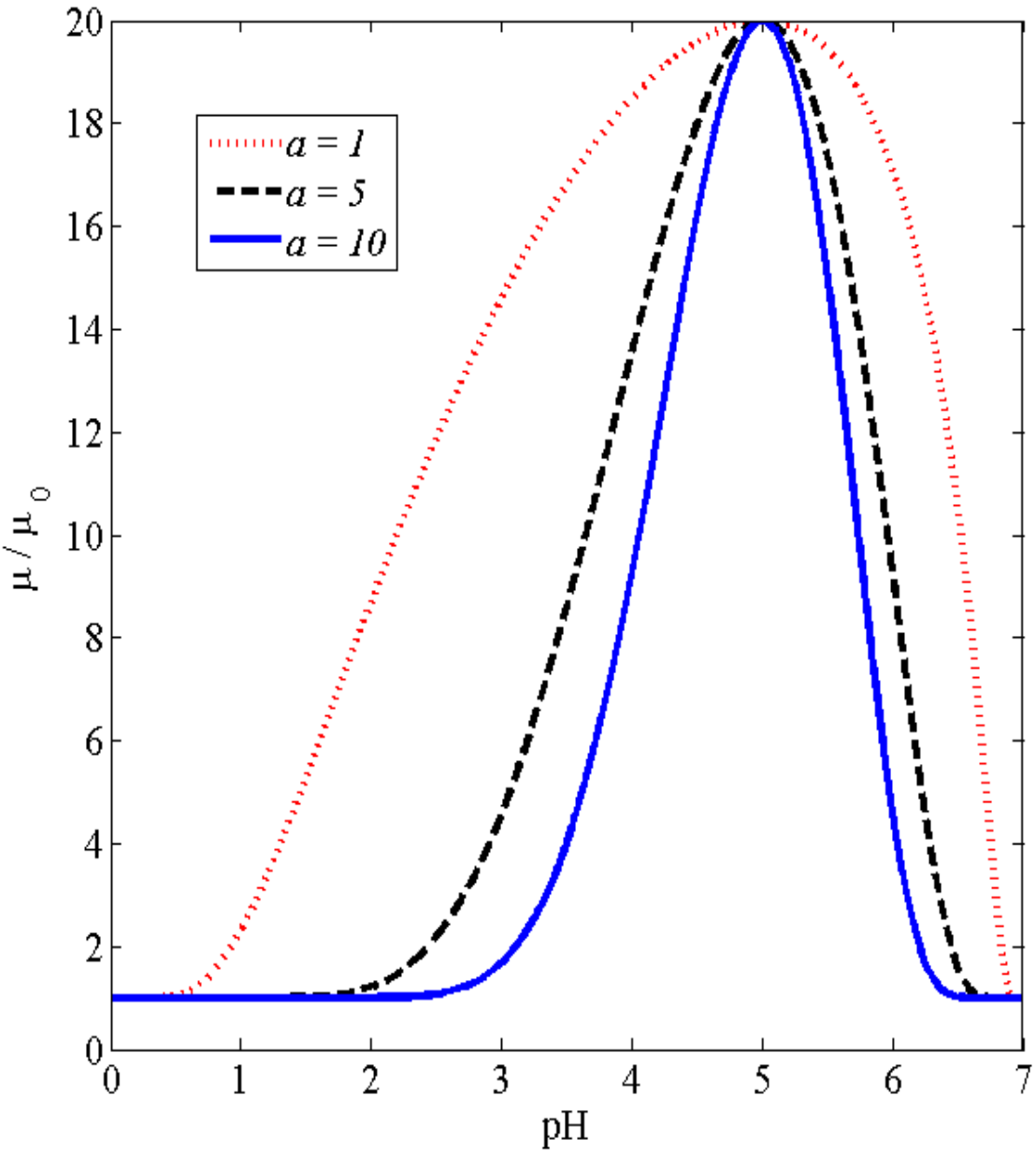


Figure 7.8: The effect of the parameter $a$ on viscosity vs. pH profile.

as explained in following section.

### 7.2.4 A Complete Rheological Model

A complete rheological model for in-situ gelling acids can be obtained by combining equations (7.1), (7.4) and (7.8) which describe the effect of temperature, shear rate and pH on viscosity, respectively. Thus, the complete rheological model can be given as follows:

$$\eta_a\left(T,\dot{\gamma},pH\right)=\mu_0\dot{\gamma}^{n-1}\left(1-\alpha\frac{T-T_0}{T_0}\right)\left[1+\left(\mu_m-1\right)Exp\left\{\frac{-a\left(pH-pH_m\right)^2}{pH\left(7-pH\right)}\right\}\right], \tag{7.9}$$

where $\eta_a$ is the apparent viscosity. The above model contains six parameters: (i) $\mu_0$, the base viscosity that is equivalent to consistency factor in the power-law model. (ii) $n$, the power index that accounts for the effect of shear rate. (iii) $\alpha$, the temperature coefficient of viscosity that includes the effect temperature in the model. (iv) $\mu_m$, the maximum increment in viscosity w.r.t. base viscosity due to in-situ gelling (this may depend on the polymer concentration) (v) $pH_m$, the pH value that corresponds to the maximum viscosity, and (vi) $a$, the parameter that measures the range of pH values in which polymer starts cross-linking leading to the gel formation. The last three parameters account the effect of pH/concentration. These parameters, in general, depends on types of polymers/cross-linkers/additives and their concentrations and the kinetics for cross-linking and breaking of the gel [Note: If the cross-linking and breaking is due to metal ions such as $Fe^{+++}$, the kinetics may be assumed to be fast and the effect of kinetics on the rheological model may be neglected].

Since the rheological model in equation (7.9) is empirical, these parameters must be determined experimentally. Using the isothermal experimental data (Rose, 2004) shown in Figure 7.5, the following set of values of the parameters (for the

isothermal case, $\alpha = 0$) is the best fit:

$$\mu_0 = 195.96; n = 0.5; \mu_m = 23.83; a = 23.4; pH_m = 5.47 \tag{7.10}$$

The non-linear least square fitting of the data is performed based on the Levenberg-Marquardt method which minimizes the square error function (sum of squares of the difference between the theoretical and experimental values at given pH points) and evaluates the best fit of the parameters iteratively. It can be seen from Figure 7.9 that the empirical rheological model given by equation (7.9) is a reasonable fit to the experimental data (Rose, 2004). However, in most of the lab experiments and works reported in literature (MaGee et al., 1997), the pH range of gel formation is designed typically between 2-4, so we adopt following rheological parameters

$$\mu_0 = 1; n = 1; \mu_m = 23.83; a = 23.4; pH_m = 2.47 \tag{7.11}$$

in our simulations to compare with existing experimental results in literature. However, these parameters depend on types of polymers and additives and their concentrations.

Now, we have the complete rheological model (7.9) for in-situ gelling acids to account for the effect of temperature, shear rate and pH (gelling phenomena) on viscosity. In the next section, we discuss the extension of two-scale continuum model to describe the reaction and transport of in-situ gelling acids in carbonates rocks (porous media).

## 7.3 Two-scale Continuum Model (TSC) for in-situ gelling Acids

The two-scale continuum model was developed by Panga et al. (2005) and used by Kalia and Balakotaiah (2007, 2009, 2010) to analyze the phenomenon of reactive dissolution of the carbonate rocks with Newtonian acids. In this case,

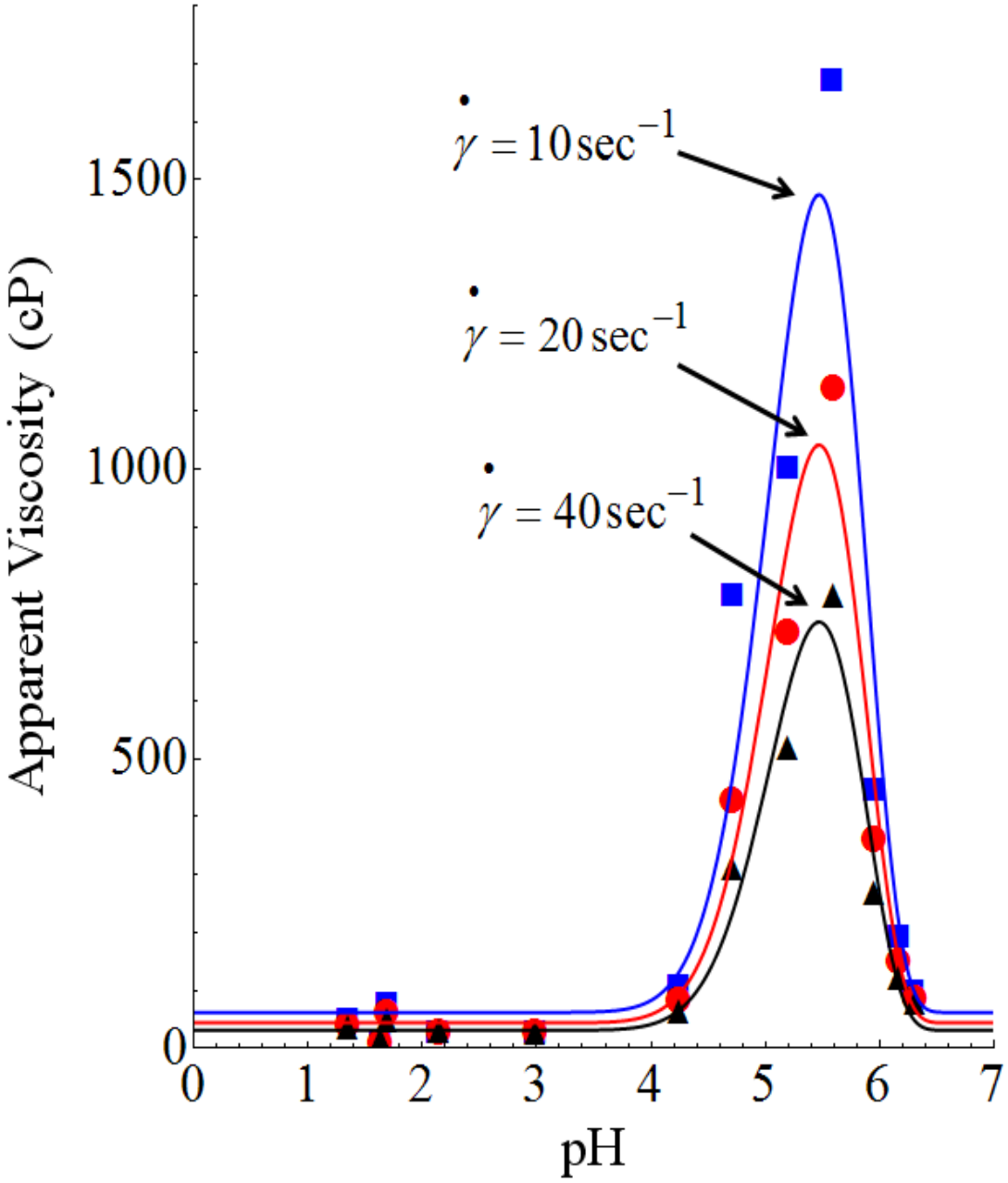


Figure 7.9: Comparison of experimental and theoretical plot for viscosity vs. pH for various shear rates.

the fluid viscosity remains constant and flow equation is represented by Darcy law. Since in the current work, the viscosity is non-linear function of concentration, shear rate even in isothermal case, we modify the model for in-situ gelling acids by incorporating general rheological model given in equation (7.9) and by developing an equivalent Darcy-law that is valid for all types of fluids including non-Newtonian ones.

### 7.3.1 Darcy Law for in-situ gelling Acids

The non-linear relationship between velocity and pressure drop adds to the challenges in understanding the flow dynamics of non-Newtonian fluid in porous media. Since length-scales associated with porous media vary from micro-scale to macro-scale, it is very important to find the momentum equation or Darcy law equivalent at mesoscale. Here, we explain in brief the development of Darcy law equivalent model using the procedure described by Christopher and Middleman (1965). We start with well-known Blake-Kozeny equation given by

$$\frac{\varepsilon^3 d_p}{\rho v_s^2(1-\varepsilon)}\frac{(-\Delta P)}{L} = \frac{150\mu(1-\varepsilon)}{\rho v_s d_p}, \tag{7.12}$$

for flow of Newtonian fluids through a packed bed, where $\varepsilon$ is the porosity, $d_p$ is the particle diameter, $\rho$ is the fluid density, $L$ is the bed length, $\mu$ is the fluid viscosity, $(-\Delta P)$ is the overall pressure drop across the bed and $v_s$ is the superficial velocity. The above relation reproduces experimental data for packed bed of uniform spheres rather well up to Reynolds number of about 10. From the Blake-Kozeny equation, we can derive Darcy equation as follow:

$$v_s = \frac{\varepsilon^3 d_p^2}{150(1-\varepsilon)^2}\frac{1}{\mu}\frac{(-\Delta P)}{L} = \frac{k_d}{\mu}\frac{(-\Delta P)}{L}, \tag{7.13}$$

where $k_d$ is the permeability of the porous media and is defined as

$$k_d = \frac{\varepsilon^3 d_p^2}{150(1-\varepsilon)^2}. \tag{7.14}$$

Now, we obtain Hagen–Poiseuille equation (Bird et al., 1960) for in-situ gelling acids (or power-law fluids) by solving one dimensional momentum balance (assuming steady, laminar and incompressible flow) through a capillary with no-slip boundary condition that leads to the average velocity, $\langle v \rangle$ , as

$$\langle v \rangle = \left( \frac{(-\Delta P)}{4HL} D \right)^{1/n} \frac{n\ D}{2(3n+1)}, \tag{7.15}$$

where $D$ is the capillary diameter. Similarly, we can find the average fluid velocity corresponding to other rheological models (Corapcioglu,1996).

Once we know the relationship between overall pressure drop and average velocity for a capillary, we can derive the Darcy-law equivalent for porous media by substituting (i) average velocity, $\langle v \rangle$ , in capillary with $\frac{v_s}{\varepsilon}$, where $v_s$ is the superficial/Darcy velocity; (ii) capillary diameter, $D$, with hydraulic diameter of porous media, $D_H$, given by,

$$D_H = \frac{4\ \times \text{ flow area}}{\text{wetted perimeter}} = \frac{4\varepsilon}{a_v(1-\varepsilon)} = \frac{2\varepsilon\ d_p}{3(1-\varepsilon)}, \tag{7.16}$$

where $a_v$ is the area per unit volume of the solid; (iii) particle diameter, $d_p$, with $\frac{(1-\varepsilon)}{\varepsilon}\sqrt{\frac{150k_d}{\varepsilon}}$, and scaling the length of capillary $L$ by tortuosity $\sigma$(=$\frac{25}{12}$), i.e., $L = \sigma L$. Thus, the Darcy law equivalent for a non-Newtonian fluid flowing through a porous medium can be given by

$$v_s = \left( \frac{k_d}{\mu_{eff}} \frac{(-\Delta P)}{L} \right)^{1/n}, \tag{7.17}$$

where $\mu_{eff}$ is the viscosity term given by

$$\mu_{eff} = \frac{H}{12}\left(9 + \frac{3}{n}\right)^{n} (150 k_d \varepsilon)^{\frac{(1-n)}{2}}, \tag{7.18}$$

where the constant '$150$' in the bracket depends on pore connectivity and should be measured experimentally.

It should be noted that $\mu_{eff}$ does not have the same units as viscosity and is given in terms of power-law parameters (consistency factor, $H$ and power-law index, $n$) and rock-properties such as permeability, $k_d$, and porosity, $\varepsilon$. Since permeability, $k_d$, depends only on the porous media, the rheological properties of fluids are accounted by effective viscosity terms. In addition, these models are valid for non-uniform particle sizes as none of the parameters are directly dependent on particle diameter. The above model in equation (7.17) was tested experimentally with dilute polymer solution flowing through packed porous material and the accuracy of the correlation was acceptable for most engineering design purposes (Christopher and Middleman, 1965).

### 7.3.2 Two-Scale Continuum Model

Here we describe briefly the main features of the two-scale continuum model (TSC) and refer to Panga et al. (2005) for details. The TSC model describes the phenomenon of reactive dissolution in carbonates as a coupling between transport and reaction processes occurring at two scales: Darcy scale and pore scale. The transport process such as convection and dispersion are important at core scale (much larger than the pore scale or darcy-scale), whereas, diffusion and reaction are the main mechanism at the pore scale. The transport processes are described by conservation laws such as continuity equation, momentum balance, species balances and dissolution equation at darcy-scale, whereas, reactive dissolution changes the pore-structure continuously, which changes effective properties (such

as transfer/dispersion coefficients) and rock properties such as (permeability, pore radius etc.) used in the model and hence, these properties must be expressed at pore-scale.

**Darcy-scale Models**

Darcy-scale models contains the momentum balance, continuity equation, species balance and dissolution equation. The momentum balance for in-situ gelling (power-law) acids is given by equivalent Darcy law as follows:

$$\|\mathbf{U}\|^{n-1}\,\mathbf{U} = -\frac{1}{\mu_{eff}}\mathbf{K}\cdot\boldsymbol{\nabla}P, \tag{7.19}$$

where

$$\mathbf{U} = \left(U_{x'}, U_{y'}, U_{z'}\right),$$

is the Darcy velocity vector, $\|\bullet\|$ represents the norm of a vector/matrix, $\mathbf{K}$ is permeability tensor, $\mu_{eff}$ is the pH-dependent effective viscosity term that is given by

$$\mu_{eff} = \eta_0\mu_0\left(\frac{K\varepsilon}{K_0\varepsilon_0}\right)^{\frac{(1-n)}{2}}\left[1+(\mu_m-1)\,Exp\left\{\frac{-a\left(pH-pH_m\right)^2}{pH\,(7-pH)}\right\}\right], \tag{7.20}$$

$P$ is pressure,

$$\boldsymbol{\nabla} = \left(\frac{\partial}{\partial x'}, \frac{\partial}{\partial y'}, \frac{\partial}{\partial z'}\right),$$

represents the gradient vector and $\mu_0$ is the base viscosity (equivalent to that of the brine solution). It should be noted that the effective viscosity term given in Equation (7.20) is defined only for pH in between 0 and 7. If pH is out of this range, the effective viscosity term is independent of pH and does not contain the terms in the square bracket. In addition, the parameters such as $\eta_0$, $\mu_m$, $a$ and $pH_m$ depend on polymer concentrations. Based on the literature on polymers, it is reasonable to assume that $\mu_m$ and $\eta_0$ vary exponential and linearly, respectively while $a$ and $pH_m$ remain constant, i.e.,

$$\frac{\mu_m - 1}{\mu_{\max} - 1} = \frac{1 - \exp\left(-\alpha_1 \frac{C_p}{C_{p,in}}\right)}{1 - \exp\left(-\alpha_1\right)} \tag{7.21}$$

$$\frac{\eta_0 - 1}{\mu_{p0} - 1} = \frac{C_p}{C_{p,in}} \tag{7.22}$$

where, the typical values of $\mu_{\max}$, $a$ and $pH_m$ are given by

$$\mu_{\max} = 23.83; a = 23.4; pH_m = 2.47 \tag{7.23}$$

The porosity increment due to dissolution on velocity profile is described by overall mass balance or continuity equation in fluid phase given by

$$\frac{\partial \varepsilon}{\partial t'} + \boldsymbol{\nabla} \cdot \mathbf{U} = 0, \tag{7.24}$$

where the first term ($\frac{\partial \varepsilon}{\partial t'}$) represents the change in pore volume due to reactive dissolution that leads to increase in local porosity ($\varepsilon$). Similarly, we keep track of concentrations of acid and polymers to analyze gel dynamics using species balance that is given by diffusion-convection-reaction model as follows:

$$\frac{\partial \left(\varepsilon C_f\right)}{\partial t'} + \boldsymbol{\nabla} \cdot \left(\mathbf{U}\, C_f\right) = \boldsymbol{\nabla} \cdot \left(\varepsilon \mathbf{D}'_e \cdot \boldsymbol{\nabla} C_f\right) - k_c a_v \left(C_f - C_s\right), \tag{7.25}$$

$$\frac{\partial \left(\varepsilon C_p\right)}{\partial t'} + \boldsymbol{\nabla} \cdot \left(\mathbf{U}\, C_p\right) = \boldsymbol{\nabla} \cdot \left(\varepsilon \mathbf{D}'_{ep} \cdot \boldsymbol{\nabla} C_p\right), \tag{7.26}$$

where $C_f$ and $C_p$ are the cup-mixing concentrations of the acid and polymer, respectively. $C_s$ is concentration of the acid at fluid-solid interface, $\mathbf{D}'_e$ and $\mathbf{D}'_{ep}$ are effective dispersion tensor of acid and polymer, respectively, $k_c$ is local mass transfer coefficient and $a_v$ is the interfacial area per unit volume of solid available for reaction.

It should be noted that the amount of acid diffusing from bulk fluid phase to

fluid-solid interface is the same as being consumed during dissolution. Thus, the flux balance at the fluid-solid interface can be written as

$$k_c \left( C_f - C_s \right) = R \left( C_s \right), \tag{7.27}$$

where $R(C_s)$ is the reaction rate. We can also write the evolution of porosity field by equating the amount of solid dissolved to the amount of acid consumed using the stoichiometry of the reaction as follows:

$$\frac{\partial \varepsilon}{\partial t'} = \frac{R \left( C_s \right) a_v \alpha_c}{\rho_s}, \tag{7.28}$$

where $\rho_s$ is the density of the solid phase and $\alpha_c$ is the dissolving power of the acid defined as grams of solid dissolved per mole of acid reacted. It should also be noted that the reaction, in general, may be highly non-linear and very complex. But for simplicity, we assume linear kinetics, i.e., $R(C_s) = k_s C_s$, where $k_s$ is the reaction rate constant. In this case, the interfacial concentration $C_s$ can be written in terms of the cup-mixing concentration of acid as

$$C_s = \frac{k_c C_f}{k_c + k_s}. \tag{7.29}$$

In addition, we also use the Stokes-Einstein relation:

$$\mu_{eff} \mathbf{D}'_e = \text{constant}; \quad \mu_{eff} \mathbf{D}'_{ep} = \text{constant}, \tag{7.30}$$

that relates the local diffusion coefficient as the fluid viscosity changes due to gel formation.

**Initial and Boundary Conditions**

The initial, inlet and boundary conditions depend on specific problems and are discussed in detail in literature (Kalia and Balakotaiah, 2009). For example, inlet conditions for Darcy-law (for velocity and pressure) depends on whether the system is being operated at constant injection rate or at constant pressure drop. Here, we consider injection rate is constant and exit pressure is fixed, i.e.,

$$\mathbf{U}= (U_{x'}, U_{y'}, U_{z'}) = (u_0, 0, 0) \quad @\ x' = 0, \tag{7.31}$$

$$P = P_{exit} \qquad @\ \ x' = L, \tag{7.32}$$

where $L$ is the length of the core. Similarly, for species balance equations (concentrations of acid and polymer), we use Danckwert's condition at inlet and zero flux condition at the exit as follows:

$$U_x\, C_f - \varepsilon D'_{eX}\, \frac{\partial C_f}{\partial x'} = u_0 C_{f,in} \quad @\ \ x' = 0, \tag{7.33}$$

$$U_x\, C_p - \varepsilon D'_{epX}\, \frac{\partial C_p}{\partial x'} = u_0 C_{p,in} \ \ @\ \ x' = 0, \tag{7.34}$$

$$\frac{\partial C_p}{\partial x'} = \frac{\partial C_f}{\partial x'} = 0 \qquad @\ \ x' = L. \tag{7.35}$$

At transverse boundaries, zero-flux boundary conditions are used for pressure and concentrations as given by

$$\mathbf{n} \cdot \boldsymbol{\nabla} P = \mathbf{n} \cdot \boldsymbol{\nabla} C_f = \mathbf{n} \cdot \boldsymbol{\nabla} C_p = 0 \qquad \text{on transverse boundaries} \tag{7.36}$$

Initially, we assume that the core is saturated with brine solution, i.e., no acid or polymers is present in the core. Also the core is heterogeneous where porosity is generated by random number generation distributed uniformly with mean $\langle \varepsilon_0 \rangle = 0.2$

and heterogeneity magnitude $\triangle\varepsilon = 0.15$, i.e.,

$$C_f = C_p = 0; \;\; \varepsilon = \langle \varepsilon_0 \rangle + \varepsilon' \;\; @ \;\; t = 0, \tag{7.37}$$

where $\varepsilon'$ varies from - $\triangle\varepsilon$ to $\triangle\varepsilon$, randomly.

**Pore-scale Models**

The physio-chemical parameters like permeability, transfer coefficients, etc. that appear in Darcy scale model depend on pore-scale structure and must be evaluated at the pore scale. Thus, the Darcy-scale model given above from equation (7.19) to equation (7.30) is complete as long as all these parameters are specified.

**Structure-Property-relations:** The structure of carbonate matrix changes continuously with dissolution, which changes the local porosity, permeability, mean pore radius and area per unit volume available for reaction, continuously. Thus, the choice of correlations that relates the change in local permeability to porosity due to dissolution plays very important role, i.e., if bad correlations are used, the simulation results may lead to quantitative errors, though qualitative trends predicted may be correct. Since, a definite way of relating the change in medium properties to the change in medium structure does not exits in literature, we use semi-empirical relations proposed by Civan (2001) that relates medium property such as permeability to the structure parameter such as porosity as follows:

$$\frac{K}{K_0} = \frac{\varepsilon}{\varepsilon_0}\left(\frac{\varepsilon\left(1-\varepsilon_0\right)}{\varepsilon_0\left(1-\varepsilon\right)}\right)^{2\beta}; \;\; \frac{r_p}{r_{p0}} = \sqrt{\frac{K\varepsilon_0}{K_0\varepsilon}}; \;\; \frac{a_v}{a_{v0}} = \frac{\varepsilon r_{p0}}{\varepsilon_0 r_p}; \tag{7.38}$$

where $\beta$ is a constant that depends on the structure of the medium. Here, $\varepsilon_0$, $K_0$, $rp_0$ and $a_{v0}$ are initial porosity, permeability, mean pore radius and the interfacial area available for reaction per unit volume of the core, respectively. Figures 7.10, 7.11 and 7.12 show the variation in permeability, pore radius and area per unit

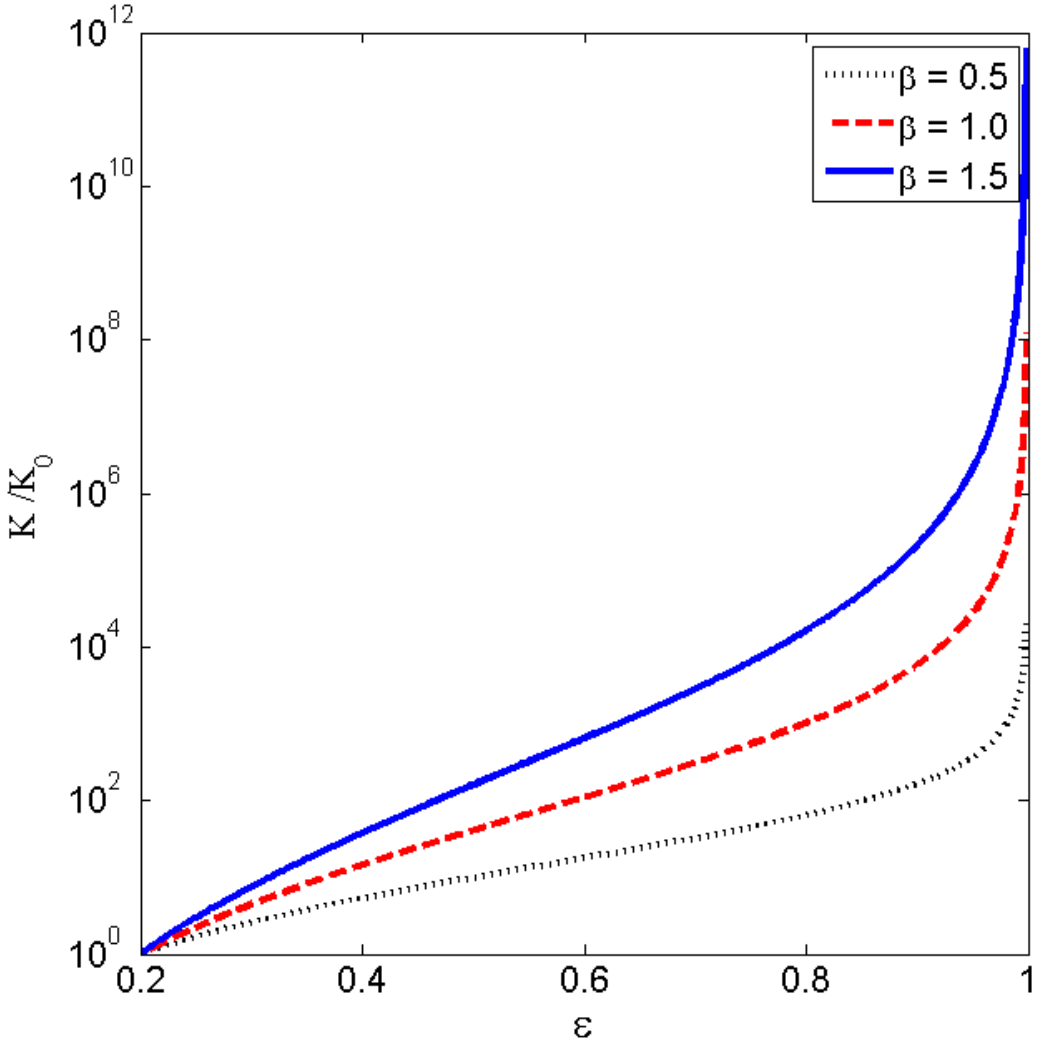


Figure 7.10: Variation in permeability with porosity due to dissolution for typical values of $\beta = 0.5$, $1.0$ and $1.5$.

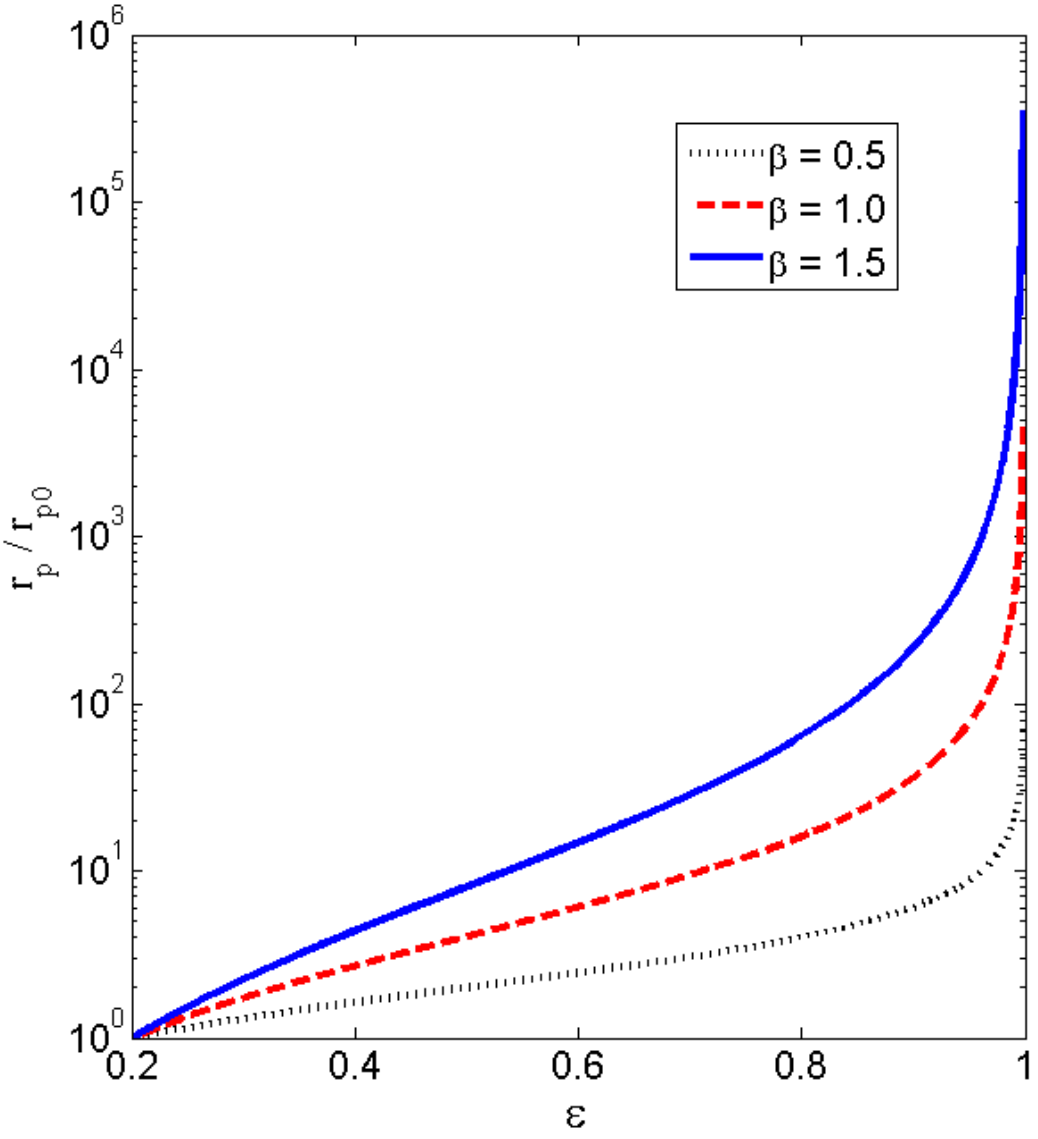


Figure 7.11: Change in pore radius with porosity due to dissolution for typical values of $\beta = 0.5$, $1.0$ and $1.5$.

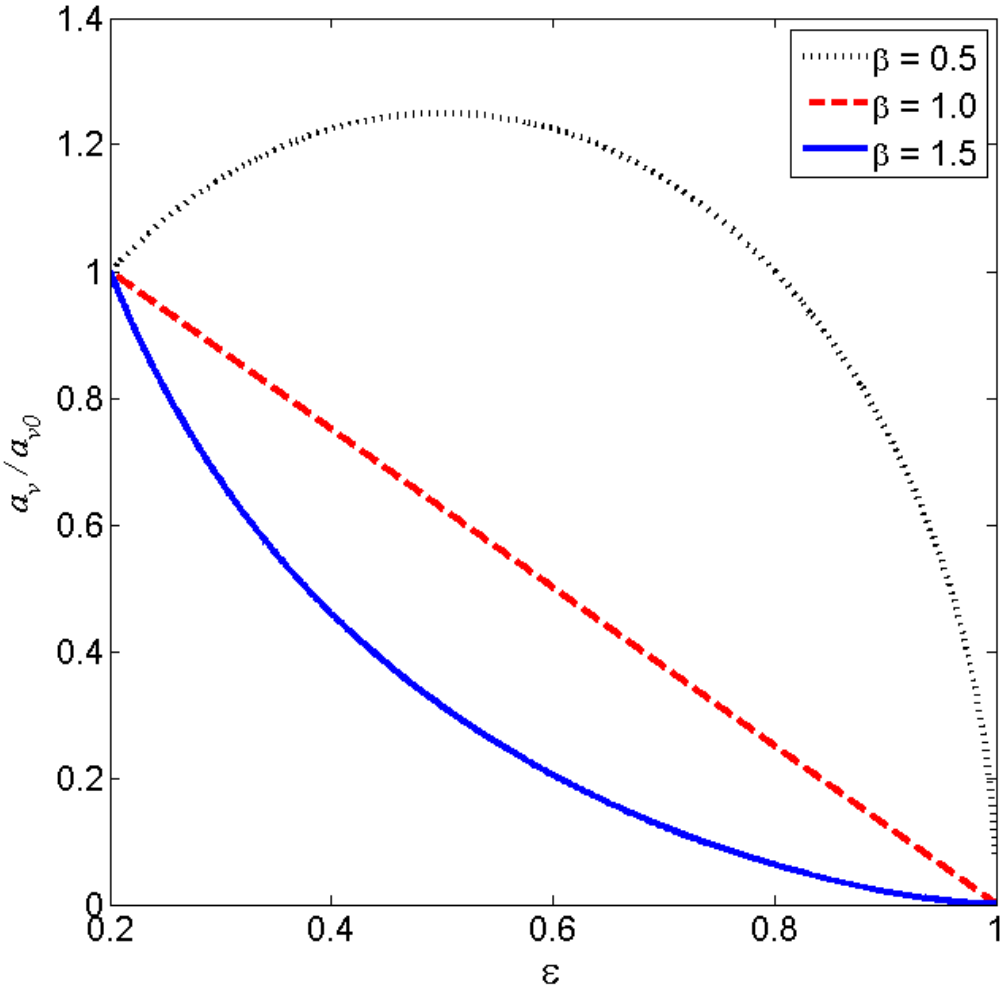


Figure 7.12: Change in area per unit volume available for reaction as porosity changes due to dissolution for typical values of $\beta = 0.5$, $1.0$ and $1.5$.

volume available for reaction as porosity of the medium changes. These figures are plotted for different values of $\beta$ that is one of the characteristics of carbonate rocks. Higher $\beta$ implies the higher rate of change in permeability for a fixed change in porosity due to dissolution. The same is true with the rate of increase in pore radius and rate of decrease in area per unit volume. However, the change in area per unit volume, $a_v$, is due to competition between increase in porosity and increase in pore radius, i.e., $a_v$ increases with porosity but decreases with pore radius; and

so for lower value of $\beta$ where initial rate of increase in pore radius is very small, the area per unit volume, $a_v$, may initially increase with porosity as can be seen in Figure 7.12.

It must be noted that the structural-property correlation gives the relation between the change in porosity and permeability due to dissolution, but the initial porosity $\varepsilon_0$ and the initial permeability $K_0$ are not correlated and depend on the types/characteristics of the rock. In other words, the high porosity rock may have very low initial permeability and vice-versa. However, the change in porosity and permeability due to dissolution follow the structural-property correlation (which is true when pores are connected).

**Transfer and Dispersion Coefficients:** The mass transfer and the dispersion of the acid at the pore scale are described by the following relations (Balakotaiah and West, 2002; Panga et al., 2005):

$$Sh = \frac{2k_c r_p}{D_m} = Sh_\infty + \frac{0.7}{m^{\frac{1}{2}}} \mathrm{Re}_p^{\frac{1}{2}} Sc^{\frac{1}{3}}; \tag{7.39}$$

$$D'_{eX} = \alpha_{0s} D_m + \frac{2\lambda_X \|\mathbf{U}\| r_p}{\varepsilon}; \quad D'_{eT} = \alpha_{0s} D_m + \frac{2\lambda_T \|\mathbf{U}\| r_p}{\varepsilon}; \tag{7.40}$$

where $Sh$ is the Sherwood number or dimensionless mass-transfer coefficient; $Sh_\infty$ is the asymptotic Sherwood number; m is the pore length to diameter ratio; $\mathrm{Re}_p$ is Reynolds number at pore scale that signifies the dominance of inertia over viscous forces and is expressed as $\mathrm{Re} = \frac{\|\mathbf{U}\| r_p}{\nu}$ where $\nu$ is kinematic viscosity; $Sc$ is the Schmidt number which is the ratio of kinematic viscosity, $\nu$, to the molecular diffusivity, $D_m$; $\alpha_{0s}$ and $Sh_\infty$ depend on tortuosity or pore geometries; $\lambda_T$ and $\lambda_X$ depend on pore connectivity and heterogeneity in the medium. The dispersion coefficient for the polymer can also be expressed in a similar way where diffusivity is smaller because of high molecular weight of polymers. The first terms in these

Figure 7.13: Schematic diagram of a single core set-up.

correlations represent the contributions due to molecular diffusion while second terms represent the convective contributions. Molecular contribution are dominant for smaller pores while for larger pores, convective contributions are comparable to the contributions by molecular diffusion.

The two-scale continuum model, described in previous section, is valid for kinetically controlled dissolution limit ($k_s << k_c$), where the acid is transferred from bulk to the rock surface very fast but the rate of consumption is slow, to mass-transfer controlled dissolution limit ($k_s >> k_c$), where consumption rate is fast but availability of acid at the rock is slow. It is very crucial, especially for in-situ gelling acids where dissolution process may start in kinetically controlled limit and end up in mass-transfer controlled limit due to enormous increase in viscosity that slows down the solute transfer rate.

### 7.3.3 Dimensionless Form of the Model

**Single Core Set-up**

The two-scale continuum (TSC) model described above is presented for a single core set-up shown in Figure 7.13, where $Q_0$ is the inlet flow rate of acidic solution to the core and is kept constant through out the dissolution process. $P_{exit}$ is the pressure at the exit of the core that is maintained at a constant value. $L$ is the length of the core. Now, we non-dimensionalize the TSC model by using dimensionless quantities listed in Table (7.1). Here, $u_0$ is the inlet velocity to the core; $C_{fin}$ and $C_{pin}$ are inlet concentrations of acid and polymer, respectively; $K_0$,

Table 7.1: List of dimensionless quantities used for single core analysis.

| Quantity | Dimensionless form | Quantity | Dimensionless form |
|---|---|---|---|
| $x$ | $\frac{x'}{L}$ | $k$ | $\frac{K}{K_0}$ |
| $t$ | $\frac{u_0 t'}{L}$ | $A_v$ | $\frac{a_v}{a_{v0}}$ |
| $\mathbf{u}$ | $\frac{\mathbf{U}}{u_0}$ | $r$ | $\frac{r_p}{r_{p0}}$ |
| $c_p$ | $\frac{C_P}{C_{p,in}}$ | $N_{ac}$ | $\frac{\alpha_c C_{f,in}}{\rho_s}$ |
| $c_f$ | $\frac{C_f}{C_{f,in}}$ | $Da$ | $\frac{k_s a_{v0} L}{u_0}$ |
| $c_s$ | $\frac{C_s}{C_{f,in}}$ | $\phi^2$ | $\frac{2k_s r_{p0}}{D_{m0}}$ |
| $p$ | $\frac{(P-P_{exit})K_0}{u_0 L \mu_0}$ | $\Phi^2$ | $\frac{k_s a_{v0} L^2}{D_{m0}}$ |
| $\mu$ | $\frac{\mu_{eff}}{\mu_0}$ | $Sh$ | $\frac{2k_c r_p}{D_m}$ |
| $D_e$ | $\frac{D'_e}{D_{m0}}$ | $Pe_L$ | $\frac{\Phi^2}{Da} = \frac{u_0 L}{D_{m0}}$ |
| $D_{ep}$ | $\frac{D'_{ep}}{D_{m0}}$ | $D_{pa}$ | $\frac{D_{m0}}{D_{mp0}}$ |

$a_{v0}$ and $r_{p0}$ are initial values of permeability, area per unit volume available for reaction and mean pore radius of the core, respectively; $\alpha_c$ is the acid capacity; $D_{m0}$ and $D_{mp0}$ are initial molecular diffusivities of the protons and polymer, respectively; and $\mu_0$ is the base viscosity. Thus, the TSC model in dimensionless form can be written as follows:

$$\begin{aligned}
\boldsymbol{\nabla}\cdot(\mathbf{M}\cdot\boldsymbol{\nabla}p) = -\boldsymbol{\nabla}\cdot\mathbf{u} &= Da\left(1+\frac{\phi^2 r\,\mu}{Sh}\right)^{-1} A_v\, c_f, \\
\frac{\partial\pi}{\partial t} + \boldsymbol{\nabla}\cdot(\mathbf{u}\, c_f) &= \frac{1}{Pe_L}\boldsymbol{\nabla}\cdot(\varepsilon\mathbf{D}_e\cdot\boldsymbol{\nabla}c_f), \\
\frac{\partial(\varepsilon c_p)}{\partial t} + \boldsymbol{\nabla}\cdot(\mathbf{u}\, c_p) &= \frac{1}{Pe_L}\boldsymbol{\nabla}\cdot(\varepsilon\mathbf{D}_{ep}\cdot\boldsymbol{\nabla}c_p), \\
\frac{\partial\varepsilon}{\partial t} &= N_{ac} Da\left(1+\frac{\phi^2 r\,\mu}{Sh}\right)^{-1} A_v\, c_f\,,
\end{aligned} \tag{7.41}$$

where the first equation for pressure is obtained by combining Darcy-law in equation (7.19), continuity equation (7.24) and dissolution equation (7.28) with mobility tensor, $\mathbf{M}$, and effective viscosity term, $\mu$, given by

$$
\begin{aligned}
M &= \frac{k}{\mu \left\|\mathbf{u}\right\|^{n-1}}, \\
\mu &= \eta_0 \left(k\frac{\varepsilon}{\varepsilon_0}\right)^{\frac{(1-n)}{2}} \left[1 + (\mu_m - 1)\, Exp\left\{\frac{-a\left(pH - pH_m\right)^2}{pH\,(7 - pH)}\right\}\right]; \\
\eta_0 &= 1 + \left(\mu_{p0} - 1\right) c_p; \\
\frac{\mu_m - 1}{\mu_{\max} - 1} &= \frac{1 - \exp\left(-\alpha_1 c_p\right)}{1 - \exp\left(-\alpha_1\right)}.
\end{aligned}
\tag{7.42}
$$

The second equation is obtained by combining species balance (7.25) and dissolution equation (7.28) where $\pi$ is given by

$$
\pi = \varepsilon \left(c_f + \frac{1}{N_{ac}}\right). \tag{7.43}
$$

The inlet/initial/boundary conditions are given by

$$
\begin{aligned}
\varepsilon = \varepsilon_0 + \widehat{f};\ c_f = 0 \quad @ \quad t = 0; \\
uc_f - \frac{\varepsilon D_{e,X}}{Pe_L}\frac{\partial c_f}{\partial x} = 1;\ u = 1;\ uc_p - \frac{\varepsilon D_{ep,X}}{Pe_L}\frac{\partial c_p}{\partial x} = 1 \quad @ \quad x = 0; \\
p = 0;\ \frac{\partial c_f}{\partial x} = 0;\ \frac{\partial c_p}{\partial x} = 0 \quad @ \quad x = 1; \\
\mathbf{n}\cdot\boldsymbol{\nabla} p = \mathbf{n}\cdot\boldsymbol{\nabla} c_f = \mathbf{n}\cdot\boldsymbol{\nabla} c_p = 0 \qquad \text{on transverse boundaries,}
\end{aligned}
\tag{7.44}
$$

where $u$ is the axial component of velocity, $x$ is axial coordinate and $\mathbf{n}$ is the transverse direction perpendicular to the flow. Here $\varepsilon_0$ is base porosity field and $\widehat{f}$ is a random fluctuation in the initial porosity field. Here, $Da$ is the core-scale Damkohler number that signifies the ratio of convection time to reaction time, $\phi^2$ is pore-scale Thiele modulus that signifies the ratio of diffusion time to reaction time at pore scale, $Sh$ is the Sherwood number that signifies the effect of mass-transfer due

to convection to molecular diffusion, $Pe_L$ is the axial Peclet number that signifies the ratio of axial diffusion time to the convection time, and $N_{ac}$ is the acid capacity number defined as the volume of solid dissolved per unit volume of the acid. When mean pore radius is very small as compared to mean pore length, i.e., $\frac{r_p}{L_p} << 1$, i.e., the convective contribution to mass transfer at the pore scale can be neglected and the Sherwood number ($Sh$) remains almost constant ($= Sh_\infty \sim 3.0$). The structural property-relationship in dimensionless form is given as follows:

$$k = \frac{\varepsilon}{\varepsilon_0}\left(\frac{\varepsilon\left(1-\varepsilon_0\right)}{\varepsilon_0\left(1-\varepsilon\right)}\right)^{2\beta};\ r = \sqrt{\frac{k\varepsilon_0}{\varepsilon}};\quad A_v = \frac{\varepsilon}{\varepsilon_0 r}; \tag{7.45}$$

Now, the above continuum model in equation (7.41) with the rheological model in equation (7.42) and structural-property correlation in equation (7.45) is closed and highly non-linear in nature. Next, we present the dimensionless form of the model for general multicore set-ups.

**Multi-core Set-ups**

The TSC model described above can also be written for the multi-core set-up shown in Figure 7.14, where an acidic solution is injected at a constant rate $Q_0$, pressure at the exit, $P_{exit}$ is maintained a constant value and $n\_core$ number of cores are mounted in a parallel flow arrangement. In this case, through the total inlet flow rate is constant, the inlet flow rate through individual core is not constant and depend on the effective mobilities of all the cores at any given time. Due to this reason, the TSC model and boundary and initial conditions for each core in this system is similar to that given for a single core set-up except the inlet conditions for pressure equation. Thus, instead of constant flow condition, the following conditions are appropriate in this case due to parallel arrangement:

$$P_i = P_j\ \forall\ i,j = 1 : n\_core\text{; and } \sum_{i=1}^{n\_core} U_{x,i} = u_0\ \ @x' = 0, \tag{7.46}$$

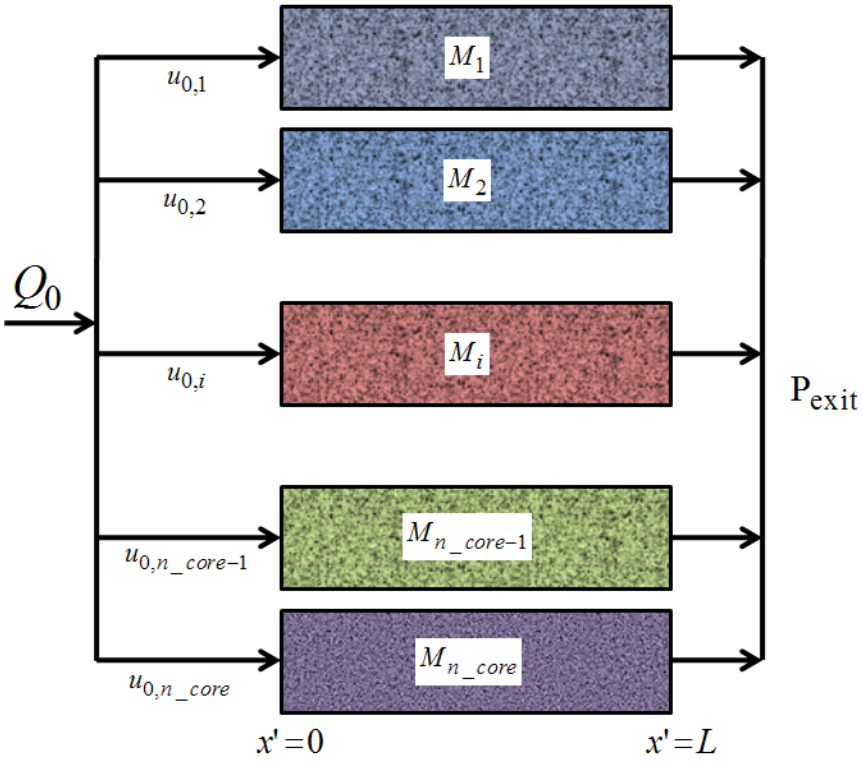


Figure 7.14: Schematic diagram of a multicore set-up.

where, $P_i$ and $U_{x,i}$ are pressure and x-velocity in $i^{th}$ core.

Now we non-dimensionalize the model using the dimensionless quantities listed in Table 7.2, where $M_{0i}$ is the initial mobility of the fluid in the $i^{th}$ core, $\gamma_{ri}$ is the ratio of initial pore radius of $i^{th}$ core to the reference value ($r_{p0}$), $\gamma_{vi}$ is the ratio of initial interfacial area per unit volume of the $i^{th}$ core available for reaction to the reference value ($a_{v0}$), and other quantities are same as discussed in previous section. We can choose reference value of rock properties ($K_0, r_{p0}$ and $a_{v0}$) corresponding to one of the cores (say low-perm core). Thus, the continuum model for multicore with linear kinetics can be written similar to equation (7.41) as follows:

$$\boldsymbol{\nabla}\cdot(\mathbf{M}_i\cdot\boldsymbol{\nabla}p_i) = -\boldsymbol{\nabla}\cdot\mathbf{u}_i = Da\left(1+\frac{\phi^2\gamma_{ri}\,r_i\mu_i}{Sh}\right)^{-1} A_{vi}\,c_{fi}\;;$$

Table 7.2: List of dimensionless quantities used for dual core analysis.

| **Quantity** | Dimensionless form |
|---|---|
| $x$ | $\frac{x'}{L}$ |
| $t$ | $\frac{u_0 t'}{L}$ |
| $u_i$ | $\frac{U_i}{u_0}$ |
| $c_{pi}$ | $\frac{C_{Pi}}{C_{f,in}}$ |
| $c_{fi}$ | $\frac{C_{fi}}{C_{f,in}}$ |
| $c_{si}$ | $\frac{C_{si}}{C_{f,in}}$ |
| $p_i$ | $\frac{(P_i - P_{exit})K_0}{u_0^n L \eta_0}$ |
| $\eta_0$ | $\frac{\mu_0}{12\mu_{p0}}\left(9+\frac{3}{n}\right)^n (150 K_0 \varepsilon_0)^{\frac{(1-n)}{2}}$ |
| $\mu_i$ | $\frac{\mu_{eff,i}}{\eta_0}$ |
| $k_i$ | $\frac{K_i}{K_{0,i}}$ |
| $M_{0i}$ | $\frac{K_{0,i}}{K_0}$ |
| $A_{vi}$ | $\frac{a_{v,i}}{a_{v0,i}}$ |
| $\gamma_{ai}$ | $\frac{a_{v0,i}}{a_{v0}}$ |
| $r_i$ | $\frac{r_{p,i}}{r_{p0,i}}$ |
| $\gamma_{ri}$ | $\frac{r_{p0,i}}{r_{p0}}$ |
| $N_{ac}$ | $\frac{\alpha_c C_{f,in}}{\rho_s}$ |
| $Da$ | $\frac{k_s a_{v0} L}{u_0}$ |
| $\phi^2$ | $\frac{2k_s r_{p0}}{D_{m0}}$ |
| $\Phi^2$ | $\frac{k_s a_{v0} L^2}{D_{m0}}$ |
| $Sh$ | $\frac{2k_c r_p}{D_m}$ |
| $Pe_L$ | $\frac{\Phi^2}{Da} = \frac{u_0 L}{D_{m0}}$ |
| $D_{pa}$ | $\frac{D_{m0}}{D_{p0}}$ |

$$\frac{\partial \pi_i}{\partial t} + \boldsymbol{\nabla}\cdot\left(\mathbf{u}_i\, c_{fi}\right) = \frac{1}{Pe_L}\boldsymbol{\nabla}\cdot\left(\varepsilon_i \mathbf{D}_{e_i}\cdot\boldsymbol{\nabla} c_{fi}\right)\ ;$$
$$\frac{\partial\left(\varepsilon_i c_{pi}\right)}{\partial t} + \boldsymbol{\nabla}\cdot\left(\mathbf{u}_i\, c_{pi}\right) = \frac{1}{Pe_L}\boldsymbol{\nabla}\cdot\left(\varepsilon_i \mathbf{D}_{epi}\cdot\boldsymbol{\nabla} c_{pi}\right); \tag{7.47}$$
$$\frac{\partial \varepsilon_i}{\partial t} = N_{ac} Da \left(1 + \frac{\phi^2 \gamma_{ri}\, r_i \mu_i}{Sh}\right)^{-1} A_{vi}\, c_{fi} \qquad i = 1 : n\_core$$

where $\pi_i = \varepsilon_i\left(c_{fi} + \frac{1}{N_{ac}}\right)$. The mobility, $M_{i,}$ and effective viscosity term, $\mu_i$, are given by

$$M_i = \frac{M_{0i} k_i}{\mu_i \left\|\mathbf{u}_i\right\|^{n-1}},$$
$$\mu_i = \eta_{0i}\left(M_{0i} k_i \frac{\varepsilon_i}{\varepsilon_{0i}}\right)^{\frac{(1-n)}{2}}\left[1 + \left(\mu_{mi} - 1\right) Exp\left\{\frac{-a\left(pH_i - pH_m\right)^2}{pH_i\left(7 - pH_i\right)}\right\}\right] \tag{7.48}$$
$$\eta_{0i} = 1 + \left(\mu_{p0} - 1\right) c_{pi};$$
$$\frac{\mu_{mi} - 1}{\mu_{\max} - 1} = \frac{1 - \exp\left(-\alpha_1 c_{pi}\right)}{1 - \exp\left(-\alpha_1\right)}.$$

The inlet/initial/boundary conditions are given by

$$\varepsilon_i = \varepsilon_{0,i} + \widehat{f};\ \ c_{f,i} = 0 \quad @ \quad t = 0;$$
$$u_i c_{f,i} - \frac{\varepsilon_i D_{ei,X}}{Pe_L}\frac{\partial c_{f,i}}{\partial x} = u_i c_{fin};\ \ u_i c_{p,i} - \frac{\varepsilon_i D_{epi,X}}{Pe_L}\frac{\partial c_{p,i}}{\partial x} = u_i c_{pin};\ @ \quad x = 0; \tag{7.49}$$
$$\sum_{i=1}^{n\_core}\left(u_i\right) = 1;\ \ p_i = p_j \forall i, j = 1 : n\_core \quad @ \quad x = 0;$$
$$p_i = 0;\ \frac{\partial c_{fi}}{\partial x} = 0;\ \frac{\partial c_{pi}}{\partial x} = 0 \qquad @ \quad x = 1;$$
$$\mathbf{n}\cdot\boldsymbol{\nabla} p_i = \mathbf{n}\cdot\boldsymbol{\nabla} c_{fi} = \mathbf{n}\cdot\boldsymbol{\nabla} c_{pi} = 0 \qquad \text{on transverse boundaries,}$$

and the structural property-relationship in dimensionless form is given as follows:

$$k_i = \frac{\varepsilon_i}{\varepsilon_{0,i}}\left(\frac{\varepsilon_i\left(1 - \varepsilon_{0,i}\right)}{\varepsilon_{0,i}\left(1 - \varepsilon_i\right)}\right)^{2\beta};\ r_i = \sqrt{\frac{k_i \varepsilon_{0,i}}{\varepsilon_i}};\quad A_{v,i} = \frac{\varepsilon_i}{\varepsilon_{0,i} r_i};\quad \forall\ i = 1 : n\_core. \tag{7.50}$$

It should be noted that unlike for Newtonian acids, the continuum model for in-situ

gelling acids have the strong coupling between momentum balance (Darcy-law) and species balances through the highly non-linear viscosity term. In case of multi-core set-up, since the inlet condition through each core is coupled with other cores, the solution in each core depends on the solution in other cores. In the following chapter, we present the solution technique for the general case of multi-core set-up.

**Disclaimer:**

*It must be noted that diverting acids like in-situ gelling acids have very complex rheological behavior that depends strongly on pH of the medium and concentration of additives such as polymer, cross-linkers and breakers. They are also non-Newtonian (shear thinning) in nature. Since, there are no theoretical models available in the literature that describe these behavior, as a first attempt performed on theoretical studies of reactive dissolution of carbonates with in-situ gelling acids, we use various simplifications in the two-scale continuum model presented in this work. Based on these simplifications/assumptions, we present the simulation results and analyze the dissolution process. Therefore, as long as these assumptions are valid, the model results are valid. We list these assumptions one by one as follows:*

1. *The rheological model developed here is based on the experimental data (Rose, 2004) as shown in Figure 7.9 that may not have the similar features of other in-situ gelling acids. Therefore, the parameters used in the rheological model may have to be modified accordingly.*

2. *The two-scale continuum model developed here does not account the polymer filtration. In some cases, cross-linked polymer molecules are very big in size as compared to micropores in carbonates, and so, they get filtered as dissolution proceeds. As a results, diffusivity and reaction rate of protons with carbonates changes that change the gel formation and its dynamics.*

*However, for simplicity, we neglected the filtration (adsorption/desorption) of polymers and cross-linkers in this work.*

3. *The kinetics of cross-linking and breaking of the gel is also neglected in this work. Here, we assume that kinetics of cross-linking and breaking is very fast and depends on pH and polymer concentration. Also, cross-linkers and breakers have different properties than the polymer, and may propagate at different speed as dissolution occurs. But, here we have considered all the additives (polymer, cross-linkers and breakers) as a single species and used only one species balance for these constituents (along with one species balance for protons).*

4. *The multi-step chemistry and ionic equilibrium due to formation of carbonic acids are neglected in these studies. Here, we have assumed the reaction is irreversible and occurs in a single step (which might not be the case for retarding acids such as EDTA, DTPA etc.). In addition,* $CO_2$, *produced due to dissolution of carbonates with acids, are dissolved in the solution and form carbonic acids. As a result, ionic equilibrium is achieved that restrict the pH in narrow range (around pH 4). This effect is very important for in-situ gelling acids as the pH-range of gel formation may overlap this equilibrium.*

5. *The relation between local permeability and porosity due to dissolution is described by modified Kozeny relation, which is well suitable to packed-bed but may not be applicable to porous media in general. In addition, the porosity and permeability may not be correlated in practice, whereas in this work, these are correlated as the same (Kozeny) relation. Similarly, the correlations for dispersion and transfer coefficients are taken from packed bed literature.*

6. *Initially, the porosity field is distributed using uniform random number generation. However, this may not be true in general. For example, initial porosity*

*field may be distributed randomly with normal or log normal distribution.*

# Chapter 8 Numerical Techniques for Wormhole Formation

## 8.1 Preamble

In this chapter, we present the solution techniques to determine the numerical solution of the two-scale continuum (TSC) model described in chapter 7. Here we consider the general case of multicore set-ups as shown in Figure 7.14, where $n\_core$ is the number of cores (identical in shape and size) mounted in parallel flow arrangement. $n\_core = 1$ corresponds to single core set-up while $n\_core = 2$ represents the dual core set-up. $Q_0$ (or $u_0$) is the total inlet flow rate (velocity) that is kept constant. The pressure at the exit, $P_{exit}$ is maintained at a fixed value. The inlet flow-rate through each cores, $u_{0,i}$ is split according to their mobility ratio.

The TSC model contains Darcy-law and material balance equations (continuity equation, species balance equations and dissolution equations) as given below:

$$\boldsymbol{\nabla}\cdot(\mathbf{M}_i\cdot\boldsymbol{\nabla}p_i) = -\boldsymbol{\nabla}\cdot\mathbf{u}_i = Da\left(1+\frac{\phi^2\gamma_{ri}\,r_i\mu_i}{Sh}\right)^{-1} A_{vi}\,c_{fi}\,; \tag{8.1}$$

$$\frac{\partial\pi_i}{\partial t} + \boldsymbol{\nabla}\cdot(\mathbf{u}_i\,c_{fi}) = \frac{1}{Pe_L}\boldsymbol{\nabla}\cdot(\varepsilon_i\mathbf{D}_{e_i}\cdot\boldsymbol{\nabla}c_{fi})\;; \tag{8.2}$$

$$\frac{\partial(\varepsilon_i c_{pi})}{\partial t} + \boldsymbol{\nabla}\cdot(\mathbf{u}_i\,c_{pi}) = \frac{1}{Pe_L}\boldsymbol{\nabla}\cdot(\varepsilon_i\mathbf{D}_{epi}\cdot\boldsymbol{\nabla}c_{pi})\,; \tag{8.3}$$

$$\frac{\partial\varepsilon_i}{\partial t} = N_{ac}Da\left(1+\frac{\phi^2\gamma_{ri}\,r_i\mu_i}{Sh}\right)^{-1} A_{vi}\,c_{fi} \qquad i=1,2, \tag{8.4}$$

where

$$\pi_i = \varepsilon_i\left(c_{fi}+\frac{1}{N_{ac}}\right); \tag{8.5}$$

the subscript $i$ stands for $i^{th}$ core; the mobility, $M_{i,}$ is given by

$$M_i = \frac{M_{0i}k_i}{\mu_i \left\|\mathbf{u}_i\right\|^{n-1}}; \tag{8.6}$$

and effective viscosity term, $\mu_i$, is given by

$$\mu_i = \eta_{0i}\left(M_{0i}k_i\frac{\varepsilon_i}{\varepsilon_{0i}}\right)^{\frac{(1-n)}{2}}\left[1+\left(\mu_{mi}-1\right)Exp\left\{\frac{-a\left(pH_i-pH_m\right)^2}{pH_i\left(7-pH_i\right)}\right\}\right] \quad ; \tag{8.7}$$

$$\eta_{0i} = 1+\left(\mu_{p0}-1\right)c_{pi};$$

$$\frac{\mu_{mi}-1}{\mu_{\max}-1} = \frac{1-\exp\left(-\alpha_1 c_{pi}\right)}{1-\exp\left(-\alpha_1\right)}.$$

The inlet/initial/boundary conditions are given by

$$\varepsilon_i = \varepsilon_{0,i}+\widehat{f};\ \ c_{f,i}=0; c_{p,i} \quad @ \quad t=0; \tag{8.8}$$

$$u_i c_{f,i} - \frac{\varepsilon_i D_{ei,X}}{Pe_L}\frac{\partial c_{f,i}}{\partial x} = u_i c_{fin,i};\ \ u_i c_{p,i} - \frac{\varepsilon_i D_{epi,X}}{Pe_L}\frac{\partial c_{p,i}}{\partial x} = u_i c_{pin,i};\ @ \quad x=0;$$

$$\frac{\partial c_{fi}}{\partial x}=0;\ \frac{\partial c_{pi}}{\partial x}=0 \quad @ \quad x=1; \tag{8.9}$$

$$\mathbf{n}\cdot\boldsymbol{\nabla}c_{fi} = \mathbf{n}\cdot\boldsymbol{\nabla}c_{pi} = 0 \quad \text{on transverse boundaries,}$$

$$p_i = p_j \forall \quad i,j = 1{:}n\_core; \quad \sum_{i=1}^{n\_core}\left(u_i\right)=1; \quad @ \quad x=0;$$

$$p_i = 0;\ @ \quad x=1; \tag{8.10}$$

$$\mathbf{n}\cdot\boldsymbol{\nabla}p_i = 0 \quad \text{on transverse boundaries,}$$

and the structural property-relationship in dimensionless form is given as follows:

$$k_i = \frac{\varepsilon_i}{\varepsilon_{0,i}}\left(\frac{\varepsilon_i\left(1-\varepsilon_{0,i}\right)}{\varepsilon_{0,i}\left(1-\varepsilon_i\right)}\right)^{2\beta};\ r_i = \sqrt{\frac{k_i\varepsilon_{0,i}}{\varepsilon_i}}; \quad A_{v,i} = \frac{\varepsilon_i}{\varepsilon_{0,i}r_i}; \quad \forall\ i=1,2. \tag{8.11}$$

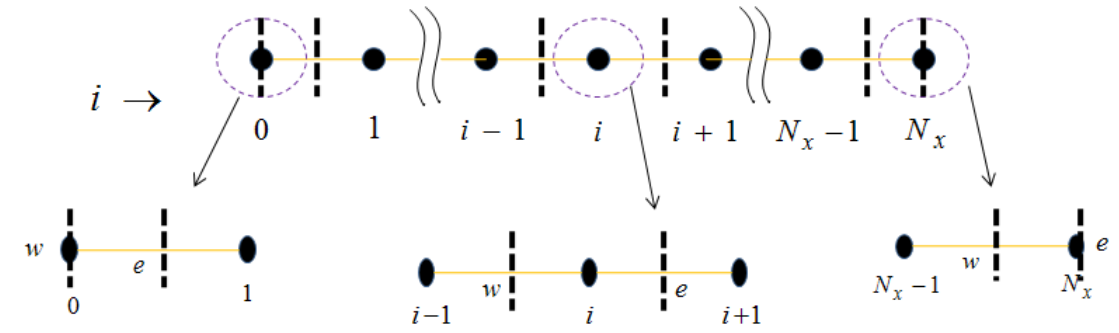


Figure 8.1: Finite volume descretization in 1D (solid circles denote the node points where concentrations, porosity and pressure are defined; w and e define the west and east face of the element where velocity vector are defined).

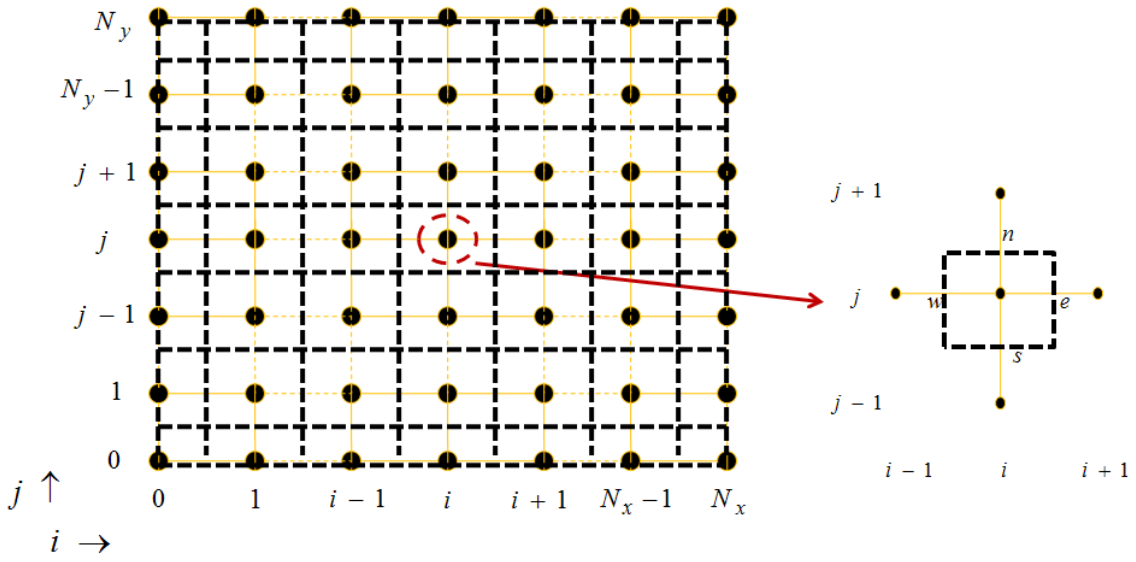


Figure 8.2: Finite volume descretization in 2D (solid circles denote the node points where concentrations, porosity and pressure are defined; w and e denote the west and east faces of the element where x-component of velocity vector are defined; s and n denote the south and east faces of the element where y-component of velocity vector are defined).

Here, we use finite volume discretization for spatial gradients as shown in Figures (8.1, 8.2 and 8.3) implicit first order Euler method coupled with extrapolation techniques for time derivatives. The discretization of these derivatives leads to large number of linear equations that we solve using multigrid linear solvers. Figure 8.4

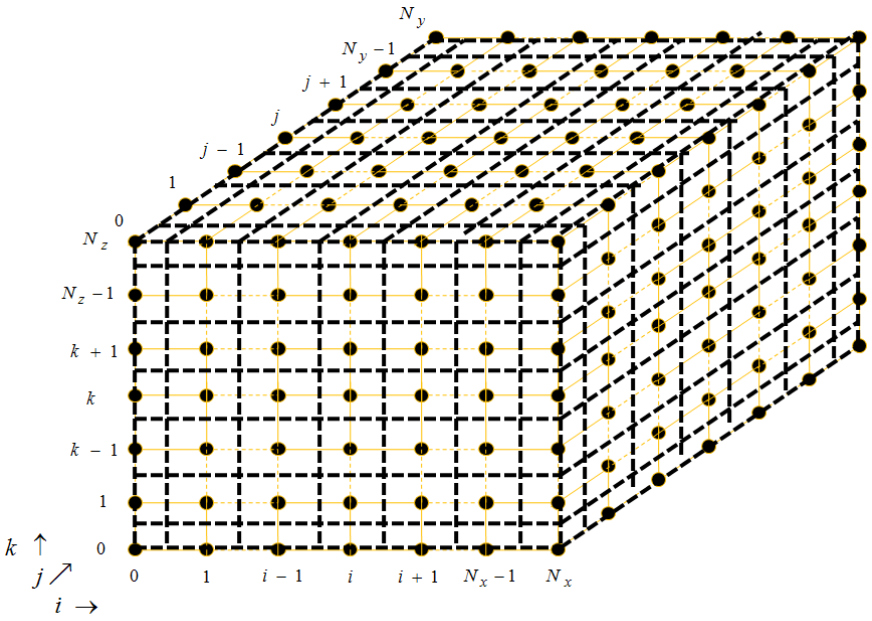


(a)

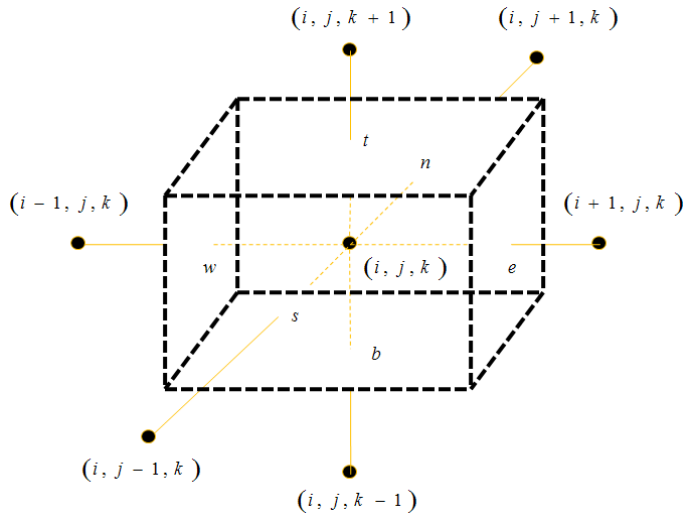


(b)

Figure 8.3: Finite volume descretization in 3D (solid circles denote the node points where concentrations, porosity and pressure are defined; w and e denote the west and east faces of the element where x-component of velocity vector are defined; s and n denote the south and east faces of the element where y-component of velocity vector are defined; b and t denote the bottom and top faces of the element where z-component of velocity vector are defined), (a) meshing (b) control volume.

shows the main steps involved in obtaining the numerical solution of the model. Initially, the concentration (of acid and polymer) and porosity field are given and boundary conditions are specified. Based on these input, we solve for pressure and velocity field in each core. Once, we have velocity profile, we use them to solve for concentration and porosity fields at next time step, then update the pressure and velocity profile at that time. We continue the procedure until breakthrough is achieved, i.e., the overall pressure across the core drops by the factor 100.

As described earlier, we start with the initial and boundary conditions given for concentration (of protons and polymer) and porosity field as well as the quantities (such as permeability, viscosity, mobility etc.) that appear in the model equations. Initially, porosity is field is generated using random number generation distributed uniformly between 0.05 to 0.35 with average porosity, $\langle \varepsilon_0 \rangle = 0.2$ and heterogeneity magnitude, $\triangle \varepsilon = 0.15$. Initial mobility, $M_{0,i}$ for $i^{th}$ core is known that gives the inlet velocity, $u_{in,i}$ through each core (identical in shape and size) as follows:

$$u_{in,i} = \frac{M_{0,i}}{\sum_{j=n\_core}^{j=1} M_{0,i}}. \tag{8.12}$$

Once, we have the inlet velocities, we replace the inlet conditions given in equation (8.10) for pressure equation by equation (8.12) and rewrite the boundary equations for pressure as follows:

$$\begin{aligned} -M\frac{\partial p}{\partial x} = u_i = u_{in,i} = \frac{M_{eff,i}}{\sum_{j=n\_core}^{j=1} M_{eff,i}}; \quad @ \quad x = 0; \\ p_i = 0; \ @ \quad x = 1; \\ \mathbf{n} \cdot \boldsymbol{\nabla} p_i = 0 \qquad \text{on transverse boundaries,} \end{aligned} \tag{8.13}$$

Initially, the cores are assumed to be saturated with brine solution, so we assume

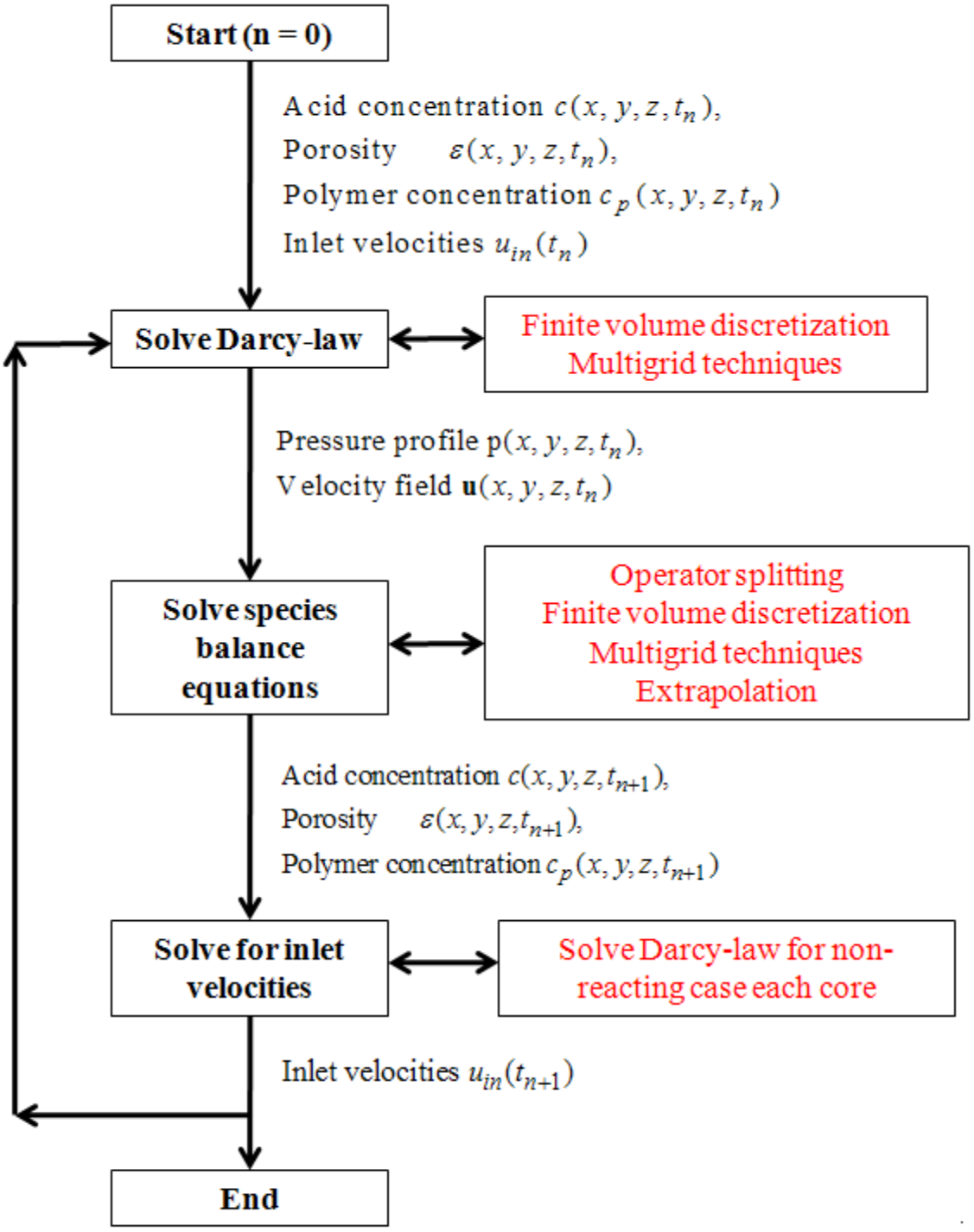


Figure 8.4: The main steps used in obtaining numerical solution of the two-scale continuum models in single or dual core set ups.

there are no acid or polymer present in the cores initially and $|u| = 1$. Now we explain the main steps used in solving the model one by one in detail.

## 8.2 Pressure Profile

To solve for the pressure profile, we first discretize the pressure equation (8.1) using control volume approach. Figure 8.3 (b) shows a schematic of the control volume used for discretization. The faces of the control volume are placed at the center of two adjacent nodes and are denoted by e, w, n and s corresponding to east, west, north and south boundaries of the control volume, i.e.,

$$\triangle x = \frac{\triangle x_e + \triangle x_w}{2}; \triangle y = \frac{\triangle y_n + \triangle y_s}{2}; \triangle z = \frac{\triangle z_t + \triangle z_b}{2}; \tag{8.14}$$

where, $\triangle x_e$, $\triangle x_w$, $\triangle y_n$, $\triangle y_s$, $\triangle z_t$ and $\triangle z_b$ are distance from node point to east, west, north, south, top and bottom boundaries, respectively and are given by

$$\begin{aligned} \triangle x_e &= x_{i+1} - x_i; \quad \triangle x_w = x_i - x_{i-1}; \\ \triangle y_n &= y_{j+1} - y_j; \quad \triangle y_s = y_j - y_{j-1}; \\ \triangle z_n &= z_{k+1} - z_k; \quad \triangle z_b = z_k - z_{k-1}; \end{aligned} \tag{8.15}$$

where $(x_{i,}y_j, z_k)$ denotes the coordinate of the node $(i, j, k)$ . Here, we assume the uniform

meshing, i.e.,

$$\triangle x_e = \triangle y_n = \triangle z_t = \frac{1}{N_x - 1}$$

and

$$x_i = i\triangle x_e, y_j = j\triangle y_n, z_k = k\triangle z_t.$$

for internal nodes.

At the boundaries of the core domain, the control volume is shown in Figure 8.1. Though this Figure corresponds to one-dimensional grids, it is same for 2D

and 3D discretization as shown in Figure 8.5, i.e., at $i = 1$, the node lies on west

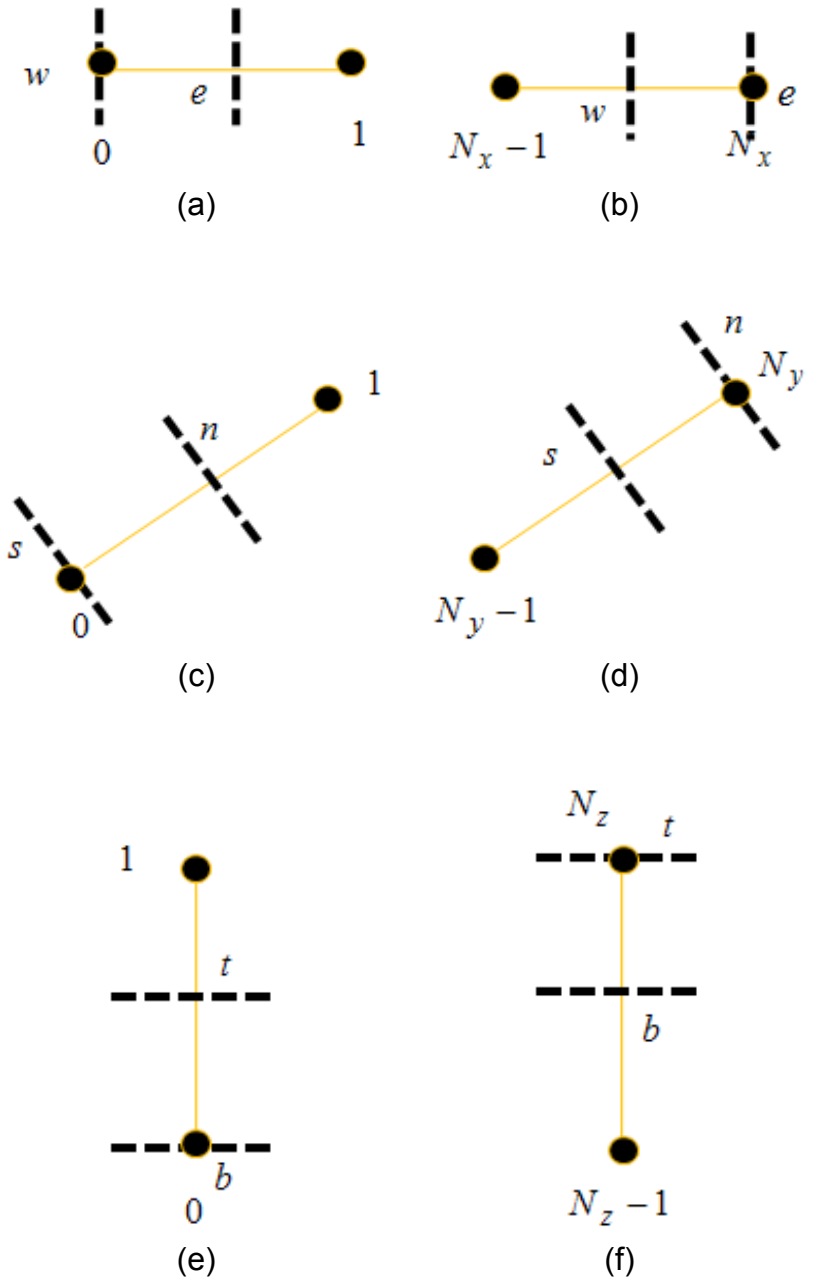


Figure 8.5: Surface of control volume at the boundaries, (a) west boundary, $i = 1$, (b) east boundary, $i = N_x$, (c) south boundary, $j = 1$, (d) north boundary, $j = N_y$, (e) bottom boundary, $k = 1$, (a) top boundary, $k = N_z$.

boundary ($\triangle x_w = 0$); at $i = N_x$, the node lies on east boundary ($\triangle x_e = 0$); at $j = 1$, the node lies on south boundary ($\triangle x_s = 0$); at $j = N_y$, the node lies on north

boundary ($\triangle x_n = 0$); at $k = 1$, the node lies on bottom boundary ($\triangle x_b = 0$); and, at $k = N_z$, the node lies on top boundary ($\triangle x_t = 0$).

Now we use integrate the pressure equation (8.10) over the control volume ($x$ from $w$ to $e$; $y$ from $s$ to $n$; $z$ from $b$ to $t$; depending on dimension of the problem) for each core as follows:

$$\frac{1}{\triangle x \triangle y \triangle z} \int_w^e \int_s^n \int_b^t \boldsymbol{\nabla} \cdot (\mathbf{M} \cdot \boldsymbol{\nabla} p)\, dxdydz$$
$$= \frac{1}{\triangle x \triangle y \triangle z} \int_w^e \int_s^n \int_b^t Da \left(1 + \frac{\phi^2 \gamma_r\, r\mu}{Sh}\right)^{-1} A_v\, c_f\, dxdydz, \tag{8.16}$$

which leads to discretized equation as follows:

$$\frac{1}{\triangle x} \left[ M \frac{\partial p}{\partial x} \right]_w^e + \frac{1}{\triangle y} \left[ M \frac{\partial p}{\partial y} \right]_s^n + \frac{1}{\triangle z} \left[ M \frac{\partial p}{\partial z} \right]_b^t$$
$$= \left[ Da \left(1 + \frac{\phi^2 \gamma_r\, r\mu}{Sh}\right)^{-1} A_v\, c_f \right]_{i,j,k} = f_{i,j,k}. \tag{8.17}$$

It should be noted that r.h.s. of above equation is calculated based on earlier values of concentrations, porosity and velocity profile. Now, we can write derivative terms in equation (8.17) using central difference and boundary conditions (8.13) as follows:

$$M \frac{\partial p}{\partial x}\bigg|_e = \begin{cases} M_e \frac{p_{i+1,j,k} - p_{i,j,k}}{\triangle x_e}, & i < N_x \\ 0, & i = N_x \end{cases} \tag{8.18}$$

$$M \frac{\partial p}{\partial x}\bigg|_w = \begin{cases} M_w \frac{p_{i,j,k} - p_{i-1,j,k}}{\triangle x_w}, & i > 1 \\ -u_{0,icore}, & i = 1 \end{cases} \tag{8.19}$$

$$M \frac{\partial p}{\partial y}\bigg|_n = \begin{cases} M_n \frac{p_{i,j+1,k} - p_{i,j,k}}{\triangle y_n}, & j < N_y \\ 0, & j = N_y \end{cases} \tag{8.20}$$

$$M\frac{\partial p}{\partial y}\bigg|_s = \begin{cases} M_s\frac{p_{i,j,k}-p_{i,j-1,k}}{\triangle y_s}, & j>1 \\ 0, & j=1 \end{cases} \tag{8.21}$$

$$M\frac{\partial p}{\partial z}\bigg|_t = \begin{cases} M_t\frac{p_{i,j,k+1}-p_{i,j,k}}{\triangle z_t}, & k<N_z \\ 0, & k=N_z \end{cases} \tag{8.22}$$

$$M\frac{\partial p}{\partial z}\bigg|_b = \begin{cases} M_b\frac{p_{i,j,k}-p_{i,j,k-1}}{\triangle z_b}, & k>1 \\ 0, & k=1 \end{cases} \tag{8.23}$$

Thus the equation (8.17) can further be written for internal nodes as

$$\begin{aligned} &\frac{1}{\triangle x}M_e\frac{p_{i+1,j,k}-p_{i,j,k}}{\triangle x_e} - \frac{1}{\triangle x}M_w\frac{p_{i,j,k}-p_{i-1,j,k}}{\triangle x_w} \\ &\frac{1}{\triangle y}M_n\frac{p_{i,j+1,k}-p_{i,j,k}}{\triangle y_n} \quad - \frac{1}{\triangle y}M_s\frac{p_{i,j,k}-p_{i,j-1,k}}{\triangle y_s} \\ &\frac{1}{\triangle z}M_t\frac{p_{i,j,k+1}-p_{i,j,k}}{\triangle z_t} - \frac{1}{\triangle z}M_b\frac{p_{i,j,k}-p_{i,j,k-1}}{\triangle z_b} = f_{i,j,k}, \end{aligned} \tag{8.24}$$

$\Rightarrow$

$$\begin{aligned} &\frac{M_e}{\triangle x\triangle x_e}p_{i+1,j,k} + \frac{M_w}{\triangle x\triangle x_w}p_{i-1,j,k} + \frac{M_n}{\triangle y\triangle y_n}p_{i,j+1,k} \\ &+\frac{M_s}{\triangle y\triangle y_s}p_{i,j-1,k} + \frac{M_t}{\triangle z\triangle z_t}p_{i,j,k+1} + \frac{M_b}{\triangle z\triangle z_b}p_{i,j,k-1} \\ &\quad -\left(\begin{array}{l} \frac{M_e}{\triangle x\triangle x_e} + \frac{M_w}{\triangle x\triangle x_w} + \frac{M_n}{\triangle y\triangle y_n} \\ +\frac{M_s}{\triangle y\triangle y_s} + \frac{M_t}{\triangle z\triangle z_t} + \frac{M_b}{\triangle z\triangle z_b} \end{array}\right) p_{i,j,k} = f_{i,j,k}, \end{aligned} \tag{8.25}$$

where, since the effective properties like mobilities are known at node points based on earlier values of concentration, porosity and velocity profile, the mobilities at the surfaces are calculated as follows:

$$\frac{\triangle x_e}{M_e} = \frac{x_{i+1}-x_e}{M_{i+1,j,k}} + \frac{x_e-x_i}{M_{i,j,k}}, \tag{8.26}$$

$$\frac{\triangle x_w}{M_w} = \frac{x_i-x_w}{M_{i,j,k}} + \frac{x_w-x_{i-1}}{M_{i-1,j,k}}, \tag{8.27}$$

$$\frac{\triangle y_n}{M_n} = \frac{y_{j+1} - y_n}{M_{i,j+1,k}} + \frac{y_n - y_j}{M_{i,j,k}}, \tag{8.28}$$

$$\frac{\triangle y_s}{M_s} = \frac{y_j - y_s}{M_{i,j,k}} + \frac{y_s - y_{j-1}}{M_{i,j-1,k}}, \tag{8.29}$$

$$\frac{\triangle z_t}{M_t} = \frac{z_{k+1} - z_t}{M_{i,j,k+1}} + \frac{z_t - z_k}{M_{i,j,k}}, \tag{8.30}$$

$$\frac{\triangle z_b}{M_b} = \frac{z_k - z_b}{M_{i,j,k}} + \frac{z_b - z_{k-1}}{M_{i,j,k-1}}. \tag{8.31}$$

The discretized equation (8.25) can further be written in standard form as

$$\begin{aligned} &east\ p_{i+1,j,k} + west\ p_{i-1,j,k} + north\ p_{i,j+1,k} + \\ &south\ p_{i,j-1,k} + top\ p_{i,j,k+1} + bottom\ p_{i,j,k-1} - \\ &(east + west + north + south + top\ + bottom)\, p_{i,j,k} = source, \end{aligned} \tag{8.32}$$

where,

$$east = \frac{M_e}{\triangle x \triangle x_e}, \tag{8.33}$$

$$west = \frac{M_w}{\triangle x \triangle x_w}, \tag{8.34}$$

$$north = \frac{M_n}{\triangle y \triangle y_n}, \tag{8.35}$$

$$south = \frac{M_s}{\triangle y \triangle y_s}, \tag{8.36}$$

$$top = \frac{M_t}{\triangle z \triangle z_t}, \tag{8.37}$$

$$bottom = \frac{M_b}{\triangle z \triangle z_b}, \tag{8.38}$$

$$source = f_{i,j,k}. \tag{8.39}$$

Similarly, equation (8.17) can be simplified for the boundaries using relation given in equations (8.18-8.23) that gives the similar form form of discretized equation as given in equation (8.24), except there will be no term containing $east$ for $i = N_x$ and

so on., i.e.,

$$east = 0 \text{ for } i = N_x \tag{8.40}$$

$$west = 0 \text{ for } i = 1 \tag{8.41}$$

$$north = 0 \text{ for } j = N_y \tag{8.42}$$

$$south = 0 \text{ for } j = 1 \tag{8.43}$$

$$top = 0 \text{ for } k = N_z \tag{8.44}$$

$$bottom = \text{for } k = 1, \tag{8.45}$$

$$source = \begin{cases} f_{i,j,k} + \frac{u_{in,icore}}{\triangle x} & \text{for } i = 1 \\ f_{i,j,k} & \text{else} \end{cases} \tag{8.46}$$

Thus, the discretized equation leads to system of linear equation that can be solved by using linear solvers (based on Gauss-Jacobi, Gauss-Seidel, SOR etc.). Since heterogeneity in the formation creates the transverse component of velocity, it very important to calculate the pressure profile as accurate as possible to capture the branching and dissolution patterns more accurately. For these reasons, we use advance multigrid techniques (Wesseling, 1992) that converges faster than any other technique available in the literature.

After we solve the pressure profile, we can determine the velocity profile at the faces of the control volumes using Darcy-law, $\mathbf{u} = -\mathbf{M} \cdot \boldsymbol{\nabla} p$. Thus, the velocity in x, y and z-directions for internal nodes can be given as,

$$u_{x,e} = -M_e \frac{p_{i+1,j,k} - p_{i,j,k}}{\triangle x_e};\ u_{x,w} = -M_w \frac{p_{i,j,k} - p_{i-1,j,k}}{\triangle x_w}; \tag{8.47}$$

$$u_{y,n} = -M_n \frac{p_{i,j+1,k} - p_{i,j,k}}{\triangle y_n};\ u_{y,s} = -M_s \frac{p_{i,j,k} - p_{i,j-1,k}}{\triangle y_s}; \tag{8.48}$$

$$u_{y,t} = -M_t \frac{p_{i,j,k+1} - p_{i,j,k}}{\triangle z_t};\ u_{y,b} = -M_b \frac{p_{i,j,k} - p_{i,j,k-1}}{\triangle z_b}; \tag{8.49}$$

It should be noted that

$$u_{x,e}|_{i,j,k} = u_{x,w}|_{i+1,j,k}\,; \quad u_{y,t}|_{i,j,k} = u_{y,b}|_{i,j+1,k}\,; u_{z,t}|_{i,j,k} = u_{z,b}|_{i,j,k+1}\,; \tag{8.50}$$

for internal nodes.

## 8.3 Concentration and Porosity Evolution

Once we calculate the velocity profile, we use them to solve the species balance and dissolution equations. We use the operator splitting method for species balance and dissolution equation, where upwind scheme is implemented for the convective term and second order discretization scheme for the dispersive term. For time derivative, we use the implicit first order (Euler) method and solve the system of linear equations using the multigrid techniques. We also use the extrapolation techniques to increase the order of accuracy of the solution.

### 8.3.1 Operator Splitting

The balance equations for concentrations and porosity given in equations (8.2 - 8.4), can be written as follows:

$$\frac{\partial \mathbf{F}_1}{\partial t} = \mathbf{L}_{DC}\mathbf{F} + \mathbf{L}_R\mathbf{F}, \tag{8.51}$$

where, $\mathbf{F}_1 = \begin{pmatrix} \pi \\ \varepsilon c_p \\ \varepsilon \end{pmatrix}$, the diffusion-convection operator, $\mathbf{L}_{DC}\mathbf{F}$, is given by

$$\mathbf{L}_{DC}\mathbf{F} = \begin{pmatrix} \frac{1}{Pe_L}\boldsymbol{\nabla}\cdot\left(\varepsilon\mathbf{D}_e\cdot\boldsymbol{\nabla}c_f\right) - \boldsymbol{\nabla}\cdot\left(\mathbf{u}\,c_f\right) \\ \frac{1}{Pe_L}\boldsymbol{\nabla}\cdot\left(\varepsilon\mathbf{D}_{ep}\cdot\boldsymbol{\nabla}c_p\right) - \boldsymbol{\nabla}\cdot\left(\mathbf{u}\,c_p\right) \\ 0 \end{pmatrix} \tag{8.52}$$

and reaction operator, $\mathbf{L}_R\mathbf{F}$, is given by

$$\mathbf{L}_R\mathbf{F} = \begin{pmatrix} 0 \\ 0 \\ N_{ac}Da\left(1+\frac{\phi^2\gamma_r\ r\mu}{Sh}\right)^{-1} A_v\ c_f \end{pmatrix}. \tag{8.53}$$

Now we use operator splitting where we solve the diffusion-convection operator first and then use the solution to solve the reaction operator as follows:

$$\frac{\mathbf{F}_1^* - \mathbf{F}_1^n}{\triangle t} = \overline{\mathbf{L}_{DC}}\mathbf{F}^*, \tag{8.54}$$

$$\frac{\mathbf{F}_1^{n+1} - \mathbf{F}_1^*}{\triangle t} = \overline{\mathbf{L}_R}\mathbf{F}^{n+1}, \tag{8.55}$$

where $\overline{\mathbf{L}_{DC}}$ and $\overline{\mathbf{L}_R}$ represents the discretized version of diffusion-convection and reaction operators, respectively. We repeat the same steps with half time steps and use extrapolation to find more accurate solution. It should be noted that we used implicit Euler (first order) method for discretization of time derivatives. Here, superscripts '*', '$n$' and '$n+1$' represent the intermediate (or virtual) time, older (previous) time and new (or next) time.

### 8.3.2 Finite Volume Discretization for Diffusion-Convection Operator

The diffusion-convection operator from first splitting (equation 8.54) can be written in operator form as follows:

$$\frac{\pi^* - \pi^n}{\triangle t} = \frac{\partial \pi}{\partial t} = \frac{1}{Pe_L}\boldsymbol{\nabla}\cdot\left(\varepsilon^*\mathbf{D}_e\cdot\boldsymbol{\nabla}c_f^*\right) - \boldsymbol{\nabla}\cdot\left(\mathbf{u}\ c_f^*\right), \tag{8.56}$$

$$\frac{(\varepsilon c_p)^* - (\varepsilon c_p)^n}{\triangle t} = \frac{\partial \varepsilon c_p}{\partial t} = \frac{1}{Pe_L}\boldsymbol{\nabla}\cdot\left(\varepsilon^*\mathbf{D}_{ep}\cdot\boldsymbol{\nabla}c_p^*\right) - \boldsymbol{\nabla}\cdot\left(\mathbf{u}\ c_p^*\right), \tag{8.57}$$

$$\frac{\varepsilon^* - \varepsilon^n}{\triangle t} = \frac{\partial \varepsilon}{\partial t} = 0. \tag{8.58}$$

The equation (8.58) leads to constant porosity through out this step, i.e., $\varepsilon^* = \varepsilon^n$. Now, we use this result and integrate equations (8.56 and 8.57) w.r.t. $x$ from $w$ to $e$, $y$ from $s$ to $n$, $z$ from $b$ to $t$ (as done in previous section) as follows:

$$\frac{\pi^* - \pi^n}{\triangle t} = \frac{1}{\triangle x \triangle y \triangle z} \int_w^e \int_s^n \int_b^t \boldsymbol{\nabla} \cdot (\mathbf{D} \cdot \boldsymbol{\nabla} c^* - \mathbf{u}\, c^*)\, dx dy dz \;, \tag{8.59}$$

with $c^* = c_f^*$; $\mathbf{D} = \frac{\varepsilon^* \mathbf{D}_e}{Pe_L}$ for acids and $c^* = c_p^*$; $\mathbf{D} = \frac{\varepsilon^* \mathbf{D}_{ep}}{Pe_L}$ for polymers. It simplifies the equation (8.56) as follows:

$$\varepsilon \frac{c^* - c^n}{\triangle t} = \frac{1}{\triangle x} \left[ D \frac{\partial c^*}{\partial x} - u_x c^* \right]_w^e + \frac{1}{\triangle y} \left[ D \frac{\partial c^*}{\partial y} - u_y c^* \right]_s^n + \frac{1}{\triangle z} \left[ D \frac{\partial c^*}{\partial z} - u_z c^* \right]_b^t . \tag{8.60}$$

Now, we can write derivative terms in equation (8.17) using central difference and convective term using upwinding scheme at internal nodes and boundaries (with boundary conditions (8.9) as follows:

$$D \frac{\partial c^*}{\partial x} - u_x c^* \Big|_e = \begin{cases} D_e \frac{c^*_{i+1,j,k} - c^*_{i,j,k}}{\triangle x_e} - (0, u_e)_{\max} c^*_{i,j,k} - (0, u_e)_{\min} c^*_{i+1,j,k}, & i < N_x \\ -u_e c^*_{i,j,k}, & i = N_x \end{cases} , \tag{8.61}$$

$$D \frac{\partial c^*}{\partial x} - u_x c^* \Big|_w = \begin{cases} D_w \frac{c^*_{i,j,k} - c^*_{i-1,j,k}}{\triangle x_w} - (0, u_w)_{\max} c^*_{i-1,j,k} - (0, u_w)_{\min} c^*_{i,j,k}, & i > 1 \\ -u_{in,icore} c_{in}, & i = 1 \end{cases} , \tag{8.62}$$

$$D \frac{\partial c^*}{\partial y} - u_y \Big|_n = \begin{cases} D_n \frac{c^*_{i,j+1,k} - c^*_{i,j,k}}{\triangle y_n} - (0, u_n)_{\max} c^*_{i,j,k} - (0, u_n)_{\min} c^*_{i,j+1,k}, & j < N_y \\ 0, & j = N_y \end{cases} , \tag{8.63}$$

$$D\frac{\partial c^*}{\partial y} - u_y\Big|_s = \begin{cases} D_s \frac{c^*_{i,j,k} - c^*_{i,j-1,k}}{\triangle y_s} - (0,u_s)_{\max} c^*_{i,j-1,k} - (0,u_s)_{\min} c^*_{i,j,k}, & j > 1 \\ 0, & j = 1 \end{cases}, \tag{8.64}$$

$$D\frac{\partial c^*}{\partial z} - u_z\Big|_t = \begin{cases} D_t \frac{c^*_{i,j,k+1} - c^*_{i,j,k}}{\triangle z_t} - (0,u_t)_{\max} c^*_{i,j,k} - (0,u_t)_{\min} c^*_{i,j,k+1}, & k < N_z \\ 0, & k = N_z \end{cases}, \tag{8.65}$$

$$D\frac{\partial c^*}{\partial z} - u_z\Big|_b = \begin{cases} D_b \frac{c^*_{i,j,k} - c^*_{i,j,k-1}}{\triangle z_b} - (0,u_b)_{\max} c^*_{i,j,k-1} - (0,u_b)_{\min} c^*_{i,j,k}, & k > 1 \\ 0, & k = 1 \end{cases}. \tag{8.66}$$

Thus the equation (8.60) simplifies further in following form:

$$\begin{aligned} &east\ c^*_{i+1,j,k} + west\ c^*_{i-1,j,k} + north\ c^*_{i,j+1,k} + \\ &south\ c^*_{i,j-1,k} + top\ c^*_{i,j,k+1} + bottom\ c^*_{i,j,k-1} - \\ &\left(nod_e + nod_w + nod_n + nod_s + nod_t\ + nod_b - \frac{\varepsilon}{\triangle t}\right) c^*_{i,j,k} = source - \frac{\varepsilon c^n}{\triangle t}, \end{aligned} \tag{8.67}$$

where,

$$east = \begin{cases} \frac{1}{\triangle x}\left(\frac{D_e}{\triangle x_e} - (0,u_e)_{\min}\right), & i < N_x \\ 0, & i = N_x \end{cases}, \tag{8.68}$$

$$west = \begin{cases} \frac{1}{\triangle x}\left(\frac{D_w}{\triangle x_w} + (0,u_w)_{\max}\right), & i > 1 \\ 0, & i = 1 \end{cases}, \tag{8.69}$$

$$nod_e = \begin{cases} \frac{1}{\triangle x}\left(\frac{D_e}{\triangle x_e} + (0,u_e)_{\max}\right), & i < N_x \\ \frac{u_e}{\triangle x}, & i = N_x \end{cases}, \tag{8.70}$$

$$nod_w = \begin{cases} \frac{1}{\triangle x}\left(\frac{D_w}{\triangle x_w} - (0,u_w)_{\min}\right), & i > 1 \\ 0, & i = 1 \end{cases}, \tag{8.71}$$

$$north = \begin{cases} \frac{1}{\triangle y}\left(\frac{D_n}{\triangle y_n} - (0,u_n)_{\min}\right), & j < N_y \\ 0, & j = N_y \end{cases}, \tag{8.72}$$

$$south = \begin{cases} \frac{1}{\triangle y}\left(\frac{D_s}{\triangle y_s} + (0,u_s)_{\max}\right), & j > 1 \\ 0, & j = 1 \end{cases}, \tag{8.73}$$

$$nod_n = \begin{cases} \frac{1}{\triangle y}\left(\frac{D_n}{\triangle y_n} + (0,u_n)_{\max}\right), & j < N_y \\ 0, & j = N_y \end{cases}, \tag{8.74}$$

$$nod_s = \begin{cases} \frac{1}{\triangle y}\left(\frac{D_s}{\triangle y_s} - (0,u_s)_{\min}\right), & j > 1 \\ 0, & j = 1 \end{cases}, \tag{8.75}$$

$$top = \begin{cases} \frac{1}{\triangle z}\left(\frac{D_t}{\triangle z_t} - (0,u_t)_{\min}\right), & k < N_z \\ 0, & k = N_z \end{cases}, \tag{8.76}$$

$$bottom = \begin{cases} \frac{1}{\triangle z}\left(\frac{D_b}{\triangle z_b} + (0,u_b)_{\max}\right), & k > 1 \\ 0, & k = 1 \end{cases}. \tag{8.77}$$

$$nod_t = \begin{cases} \frac{1}{\triangle z}\left(\frac{D_t}{\triangle z_t} + (0,u_t)_{\max}\right), & k < N_z \\ 0, & k = N_z \end{cases}, \tag{8.78}$$

$$nod_b = \begin{cases} \frac{1}{\triangle z}\left(\frac{D_b}{\triangle z_b} - (0,u_b)_{\min}\right), & k > 1 \\ 0, & k = 1 \end{cases}. \tag{8.79}$$

and

$$source = \begin{cases} -\frac{u_{in,icore}c_{in}}{\triangle x} & \text{for } i = 1 \\ 0 & \text{else} \end{cases}. \tag{8.80}$$

Here, the effective diffusivities are known based on earlier values of concentration, porosity and velocity. So, the effective diffusivities at the surfaces can be calculated as follows:

$$\frac{\triangle x_e}{D_e} = \frac{x_{i+1} - x_e}{D_{i+1,j,k}} + \frac{x_e - x_i}{D_{i,j,k}}, \tag{8.81}$$

$$\frac{\triangle x_w}{D_w} = \frac{x_i - x_w}{D_{i,j,k}} + \frac{x_w - x_{i-1}}{D_{i-1,j,k}}, \tag{8.82}$$

$$\frac{\triangle y_n}{D_n} = \frac{y_{j+1} - y_n}{D_{i,j+1,k}} + \frac{y_n - y_j}{D_{i,j,k}}, \tag{8.83}$$

$$\frac{\triangle y_s}{D_s} = \frac{y_j - y_s}{D_{i,j,k}} + \frac{y_s - y_{j-1}}{D_{i,j-1,k}}, \tag{8.84}$$

$$\frac{\triangle z_t}{D_t} = \frac{z_{k+1} - z_t}{D_{i,j,k+1}} + \frac{z_t - z_k}{D_{i,j,k}}, \tag{8.85}$$

$$\frac{\triangle z_b}{D_b} = \frac{z_k - z_b}{D_{i,j,k}} + \frac{z_b - z_{k-1}}{D_{i,j,k-1}}. \tag{8.86}$$

Thus, the discretization of transient diffusion-convection operator leads to system of linear equations (8.67) that can be solved by using linear solvers. We use advance multigrid techniques (Wesseling, 1992) to solve this equation. Similar disctretized system of equation for polymer concentration can be used by following the same procedure. Once, we solve for these concentrations and porosity field at intermediate step, we use these solution to solve the second splitting (reaction operator) given in equation (8.55) to find the solution at the next time step.

### 8.3.3 Solution of Reaction Operator

The second part of the operator splitting method is the solution of reaction operator given in equation (8.55) that can be rewritten as

$$\frac{\pi^{n+1} - \pi^*}{\triangle t} = \frac{\partial \pi}{\partial t} = 0, \tag{8.87}$$

$$\frac{(\varepsilon c_p)^{n+1} - (\varepsilon c_p)^*}{\triangle t} = \frac{\partial \varepsilon c_p}{\partial t} = 0, \tag{8.88}$$

$$\frac{\varepsilon^{n+1} - \varepsilon^*}{\triangle t} = \frac{\partial \varepsilon}{\partial t} = N_{ac} Da_{eff} c_f^{n+1}. \tag{8.89}$$

where effective Damkohler number, $Da_{eff}$, is given by

$$Da_{eff} = Da\left(1 + \frac{\phi^2 \gamma_r \, r\mu}{Sh}\right)^{-1} A_v. \tag{8.90}$$

The equation (8.87) leads to $\pi$ =constant, or, $\pi^{n+1} = \pi^* \Rightarrow$

$$c_f^{n+1} = \frac{\varepsilon^*}{\varepsilon^{n+1}}\left(c_f^* + \frac{1}{N_{ac}}\right) - \frac{1}{N_{ac}}. \tag{8.91}$$

Similarly, equation (8.88) gives,

$$c_p^{n+1} = \frac{\varepsilon^* c_p^*}{\varepsilon^{n+1}}. \tag{8.92}$$

Thus, if $\varepsilon^{n+1}$ is known, we can calculate concentration of acid and polymer from equation (8.91 and 8.92). To calculate $\varepsilon^{n+1}$, we rewrite equation (8.89) by using equation (8.91) as follows:

$$\frac{\varepsilon^{n+1} - \varepsilon^*}{\triangle t} = N_{ac} Da_{eff} c_f^{n+1} = Da_{eff}\left(\frac{\varepsilon^*}{\varepsilon^{n+1}}\left(N_{ac}c_f^* + 1\right) - 1\right), \tag{8.93}$$

that gives the quadratic equation in porosity $\varepsilon^{n+1}$ as

$$\left(\varepsilon^{n+1}\right)^2 - \left(\varepsilon^* - Da_{eff}\triangle t\right)\varepsilon^{n+1} - Da_{eff}\triangle t \; \varepsilon^*\left(N_{ac}c_f^* + 1\right), \tag{8.94}$$

that has two roots:

$$\varepsilon^{n+1} = \frac{1}{2}\left(\varepsilon^* - Da_{eff}\triangle t\right) \pm \sqrt{\left(\varepsilon^* - Da_{eff}\triangle t\right)^2 + 4Da_{eff}\triangle t \; \varepsilon^* N_{ac} c_f^*}. \tag{8.95}$$

One of these roots is negative and other is positive, we choose the positive roots (as porosity can not be negative). Thus the porosity at next time step is calculated

as

$$\varepsilon^{n+1} = \frac{1}{2}\left(\varepsilon^* - Da_{eff}\triangle t\right) + \sqrt{\left(\varepsilon^* - Da_{eff}\triangle t\right)^2 + 4Da_{eff}\triangle t\ \varepsilon^* N_{ac} c_f^*}. \tag{8.96}$$

Once we calculate the new porosity field, we update the concentrations of acid and polymer using equation (8.91 and 8.92).

### 8.3.4 Extrapolation

Earlier, we presented the numerical method to solve the concentrations of acid and polymer, and porosity field at next time step (at $t_{n+1}$) based on their values at the current time step (at $t_n$). The discretization for temporal derivatives are performed using implicit Euler method which has first order accuracy in time (O$(\triangle t)$). For 3-D problems which is computationally very expansive, very small time steps may be very difficult and time taking in obtaining solutions. For these reasons, higher order methods are used. But in literature, it is shown that first order method coupled with extrapolation technique is not only leads to higher order accuracy but also speed up the calculations.

It can be seen by simple example of solving a linear problem,

$$\frac{dc}{dt} = -\lambda c \tag{8.97}$$

$$c = c_0 \quad @t = 0, \tag{8.98}$$

which has exact solution as

$$c = c_0 \exp\left(-\lambda t\right) \tag{8.99}$$

that gives the exact solution at $n^{th}$ time step $(t_n = n\triangle t)$ as follows:

$$c_{n,exact} = c_0 \exp\left(-\lambda n\triangle t\right) \equiv c_0\left(1 - n\lambda\triangle t + \frac{n^2}{2}\lambda^2\triangle t^2 + O\left(\triangle t\right)^3\right) \tag{8.100}$$

Using the implicit first order Euler method, we get the solution at $n^{th}$ time step ($t_n = n\triangle t$) with step size $\triangle t$ as

$$c_{1n} = c_0 \left( \frac{1}{1 + \lambda \triangle t} \right)^n \equiv c_0 \left( 1 - n\lambda \triangle t + \frac{n\,(n+1)}{2} \lambda^2 \triangle t^2 + O\,(\triangle t)^3 \right) \tag{8.101}$$

while with step size $\frac{\triangle t}{2}$ as

$$c_{2n} = c_0 \left( \frac{1}{1 + \lambda \frac{\triangle t}{2}} \right)^{2n} \equiv c_0 \left( 1 - n\lambda \triangle t + \frac{n\left(n + \frac{1}{2}\right)}{2} \lambda^2 \triangle t^2 + O\,(\triangle t)^3 \right). \tag{8.102}$$

We can see that solutions from Implicit Euler method given in equations (8.101 and 8.102) have the first order accuracy. If we extrapolated these solution as follows:

$$c = 2c_{2n} - c_{1n} \equiv c_0 \left( 1 - n\lambda \triangle t + \frac{n^2}{2} \lambda^2 \triangle t^2 + O\,(\triangle t)^3 \right), \tag{8.103}$$

which has accuracy to second order.

Thus, here, based on the variables at current time step $t_n$, we determine the two solutions at next time steps $t_{n+1}$ with the step size, $\triangle t$ and $\frac{\triangle t}{2}$. Let $c_{f1},\, c_{p1},\, \varepsilon_1$ are solutions (acid concentration, polymer concentration and porosity, respectively) with step size $\triangle t$ and $c_{f2},\, c_{p2},\, \varepsilon_2$ are solutions when step size is $\frac{\triangle t}{2}$. Then the extrapolated solutions $(c_{f1}, c_{p1}, \varepsilon_1)$ can be written as

$$c_f = 2c_{f2} - c_{f1} \tag{8.104}$$

$$c_p = 2c_{p2} - c_{p1} \tag{8.105}$$

$$\varepsilon = 2\varepsilon_2 - \varepsilon_{1.} \tag{8.106}$$

As shown earlier, these extrapolated solution have second order accuracy O$(\triangle t^2)$ in time. In the following chapters, we use the solution technique describe here, to

determine the solution for pressure profile, concentrations of acid and polymer, and porosity evolution; analyze the acidization process with gelling acids; and, compare the results with that of Newtonian acids and those available in literature.

# Chapter 9 One Dimensional Analysis: Gel Dynamics and Flow Diversion

## 9.1 Preamble

As discussed earlier, stimulation with Newtonian acids leads to over-stimulation of high-perm zones and under-stimulation of low-perm zones. In particular, when Newtonian acids are injected into the wells, they preferentially flow through the high-permeability or low resistance region and increase the permeability of those regions. As a result, more acid is drawn to the high-perm region while low-perm region is under-stimulated. Therefore, in-situ gelling acids are used in stimulation that use pH to control viscosity. So, when in-situ gelling acids are injected into the wells, they also flow preferentially through the high-perm zones and increase their permeability. But, as dissolution occurs, pH of the medium increases and reaches to a threshold value where polymers added to acidic solution, start cross-linking. As a result, gel is formed in the high-perm regions that offers very high resistance due to enormous increase in viscosity. Consequently, acids are diverted to the low-perm regions and stimulate these regions. Thus, the use of in-situ gelling acids, unlike Newtonian acids, enable us to stimulate least-accessible low-perm zones that leads to uniform stimulation of carbonates. However, there are no theoretical studies performed with in-situ gelling acids and though, several experimental studies are presented in the literature, they are not sufficient enough to provide the information such as on the design a fluid (in terms of rheological parameters) and process conditions that lead to maximum diversion. Also, its very difficult to predict the optimum injection rates and amount of flow diversion for general acids.

Since gel formation is the key for optimal stimulation of carbonates with in-situ gelling acids, in this chapter, we study systematically the gel dynamics in a single core set-up as shown in Figure 9.1(a) and identify the mechanism of flow

diversion from high-perm core to low-perm core in a dual core set-up as shown in Figure 9.1(b). For this, we use simplest one-dimensional version of the TSC model

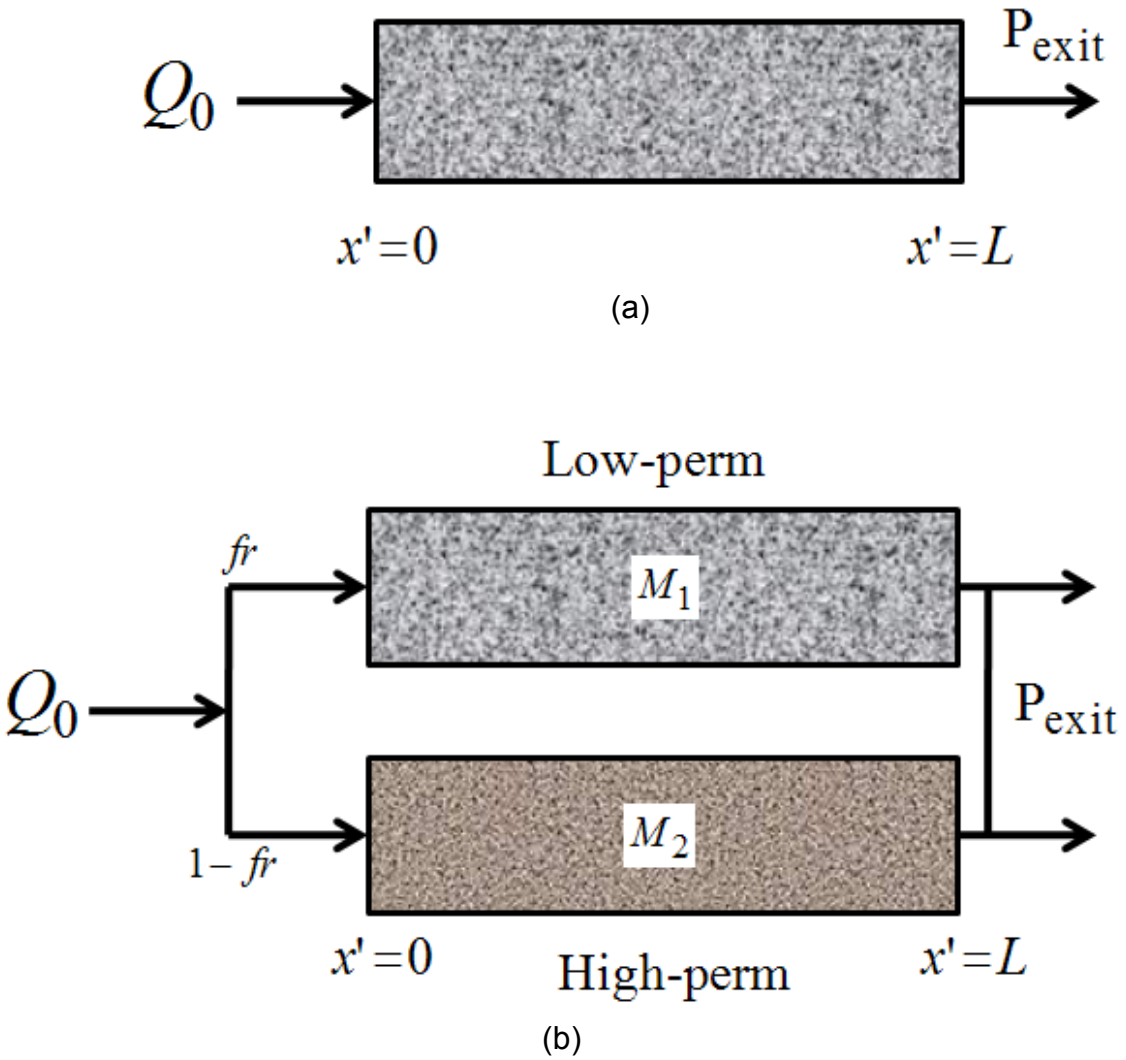


Figure 9.1: Schematic diagram of (a) single core set-ups (b) dual core set-ups in laboratory core experiments.

and simulate it using the techniques described in previous chapter. In the single core set-up shown in Figure 9.1(a), an acidic solution is injected at a constant rate through a carbonate core of length $L$ where pressure at the exit is kept constant. Similarly, in dual core set-ups as shown in Figure 9.1(b), two carbonate cores of different permeability are mounted parallel, where acid is injected at a constant

rate and pressure at the exit is fixed. In this set-up, the flow splits in both the cores depending on their effective mobility ratio. Here, we analyze the acidization with in-situ gelling acids in single and dual core set-ups one by one and estimate the gel properties such as front-speed and width and flow diversion using scaling analysis. We also analyze the effect of rheological parameters on optimum injection rates and dissolution phenomena and compare the predictions from simulation with available experimental results.

## 9.2 Single Core set-up

Figure 9.1(a) shows the schematic of a single core set-up where an acidic solution is injected through a carbonate core of length $L$ with a constant injection rate, $Q_0$ and exit pressure (back pressure), $P_{exit}$, is fixed. Since, the two-scale continuum model for acidization process contains several (flow, kinetics and rheological) parameters, the dimensionless form of the model which has minimum number of parameters, is better to analyze the effects of those parameters on dissolution process. For this reason, we use the dimensionless form of the model to analyze the acidization process.

### 9.2.1 Dimensionless TSC Model

The dimensionless form of the two-scale continuum model is described in previous chapter. Here, we use the one-dimensional version of the model for single core set-up that is given as follows:

$$\begin{aligned}
\frac{\partial}{\partial x}\left(M\frac{\partial p}{\partial x}\right) = -\frac{\partial u_x}{\partial x} &= Da\left(1+\frac{\phi^2 r\ \mu}{Sh}\right)^{-1} A_v\ c_f, \\
\frac{\partial \pi}{\partial t} + \frac{\partial u_x c_f}{\partial x} &= \frac{1}{Pe_L}\frac{\partial}{\partial x}\left(\varepsilon D_e \frac{\partial c_f}{\partial x}\right), \\
\frac{\partial\left(\varepsilon c_p\right)}{\partial t} + \frac{\partial u_x c_p}{\partial x} &= \frac{1}{Pe_L}\frac{\partial}{\partial x}\left(\varepsilon D_{ep} \frac{\partial c_f}{\partial x}\right), \\
\frac{\partial \varepsilon}{\partial t} &= N_{ac} Da\left(1+\frac{\phi^2 r\ \mu}{Sh}\right)^{-1} A_v\ c_f\ ,
\end{aligned} \tag{9.1}$$

where first equation for pressure is the combination of Darcy-law, continuity equation and dissolution equation. The second equation is the combination of species balance and dissolution equation, where $\pi$ is given by

$$\pi = \varepsilon \left( c_f + \frac{1}{N_{ac}} \right). \tag{9.2}$$

The third and forth equations represent the species balance for polymer and porosity evolution, respectively. The effective mobility, $M$, and effective viscosity term, $\mu$, are given by

$$\begin{gathered} M = \frac{k}{\mu \left\| u_x \right\|^{n-1}}, \\ . \qquad \mu = \eta_0 \left( k \frac{\varepsilon}{\varepsilon_0} \right)^{\frac{(1-n)}{2}} \left[ 1 + (\mu_m - 1)\, Exp \left\{ \frac{-a \left( pH - pH_m \right)^2}{pH \left( 7 - pH \right)} \right\} \right]; \\ \eta_0 = 1 + \left( \mu_{p0} - 1 \right) c_p; \\ \frac{\mu_m - 1}{\mu_{\max} - 1} = \frac{1 - \exp\left( -\alpha_1 c_p \right)}{1 - \exp\left( -\alpha_1 \right)}. \end{gathered} \tag{9.3}$$

The inlet/initial/boundary conditions are given by

$$\begin{gathered} \varepsilon = \varepsilon_0 + \widehat{f};\ c_f = 0 \quad @ \quad t = 0; \\ u c_f - \frac{\varepsilon D_{e,X}}{Pe_L} \frac{\partial c_f}{\partial x} = u_{in} c_{fin};\ u = u_{in};\ u c_p - \frac{\varepsilon D_{ep,X}}{Pe_L} \frac{\partial c_p}{\partial x} = u_{in} c_{pin} \quad @ \quad x = 0; \\ p = 0;\ \frac{\partial c_f}{\partial x} = 0;\ \frac{\partial c_p}{\partial x} = 0 \quad @ \quad x = 1; \end{gathered} \tag{9.4}$$

where $u$ is the axial component of velocity, $x$ is axial coordinate. Here $\varepsilon_0$ is base porosity field and $\widehat{f}$ is a random fluctuation in the initial porosity field. Here, $Da$ is the core-scale Damkohler number, $\phi^2$ is pore-scale Thiele modulus, $Sh$ is the Sherwood number, $Pe_L$ is the axial Peclet number and $N_{ac}$ is the acid capacity number defined as the volume of solid dissolved per unit volume of the acid. In this case, we assume that the $\frac{r_p}{L_p} << 1$, i.e., the convective contribution to mass transfer

at the pore scale is neglected and hence the Sherwood number ($Sh$) is almost constant ($= Sh_\infty = 3.0$). The structural property-relationship in dimensionless form is given as follows:

$$k = \frac{\varepsilon}{\varepsilon_0}\left(\frac{\varepsilon\left(1-\varepsilon_0\right)}{\varepsilon_0\left(1-\varepsilon\right)}\right)^{2\beta};\ r = \sqrt{\frac{k\varepsilon_0}{\varepsilon}};\quad A_v = \frac{\varepsilon}{\varepsilon_0 r}; \tag{9.5}$$

Now, we simulate the model using the technique described in previous chapter. We use the typical values of flow and reaction parameters, listed in Table 9.1, for simulation. In following sections, we present the simulation results based on these values of parameters.

Table 9.1: List of parameters and dimensionless numbers used in the simulation

| **Quantity** | **Value** |
|---|---|
| $C_{f,in}$ | 20%$(wt) = 0.68$ M |
| $C_{p,in}$ | 2%$(wt)$ |
| $\varepsilon_0$ | 0.2 |
| $k_s$ | $1.4 \times 10^{-4}$ cm/s |
| $D_{m0}$ | $6.0 \times 10^{-6}$cm$^2$/s |
| $\alpha_c$ | 200.04 g(solid)/mol(acid) |
| $\rho_s$ | 2.71 g/cm$^3$ |
| $N_{ac}$ | 0.05 |
| $\mu_{p0}$ | 10 cp |
| $\mu_0$ | 1 cp |
| $\mu_m$ | 23.83 |
| $a$ | 23.4 |
| $pH_m$ | 2.47 |
| $n$ | 1 |
| $K_0$ | 1 mD |
| $r_{p0}$ | 10 $\mu m$ |
| $a_{v0}$ | 50 cm$^{-1}$ |
| $L$ | 10 cm |
| $Sh_\infty$ | 3.0 |
| $\phi^2$ | 0.047 |
| $\Phi^2$ | $1.17 \times 10^5$ |
| $\beta$ | 1 |
| $\alpha_{0s}$ | 0.5 |

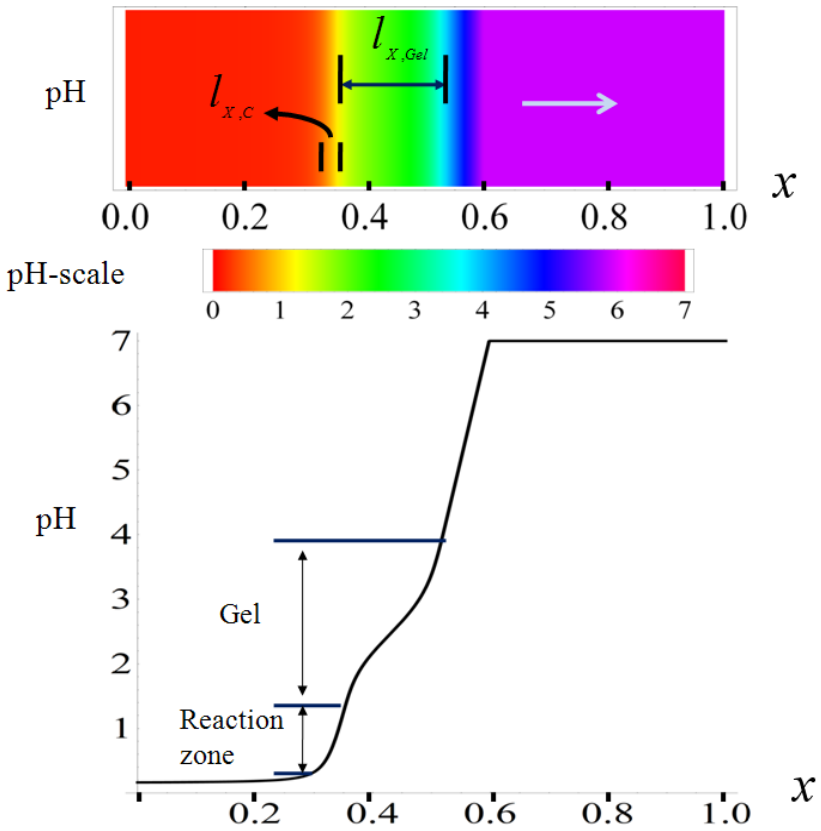


Figure 9.2: PH/concentration profile from 1-D simulation for $Da = 100$.

### 9.2.2 Gel Dynamics

Here, we solve the one-dimensional (1-D) version of the model and observe the variation of concentration/pH in axial direction as shown in Figure 9.2. It can be easily seen from this figure that there are two fronts (reaction and gel) present in the core, unlike for the case of Newtonian acids where only one (reaction) front is observed. In this figure, the red color represents the inlet concentration (at pH =0.68), the light orange color represents the reaction zone where most of the protons are used to dissolve the medium (in pH range, $0.68 \sim 1.7$), the pink color represents the brine solution (at pH = 7) and green color represents the pH range of gel formation ($pH = 1.6 \sim 3.8$) as can be seen from viscosity profile in Figure 9.3. Since, polymers is not consumed during dissolution, it propagates faster assuming there is no filtration (polymer molecules are too small compared to smallest pore

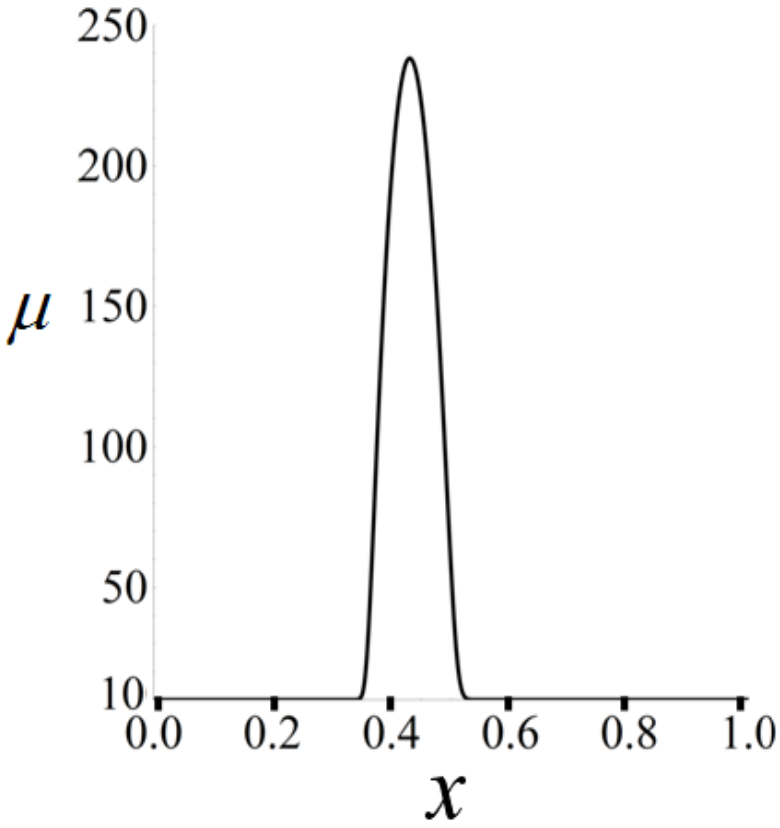


Figure 9.3: Viscosity profile (presence of gel) in the core the from 1-D simulation for $Da = 100$.

size in the core to get filtered or adsorbed on the rock). Thus, polymers are present everywhere in the core after very short time. Hence, when proton concentration falls sufficiently (pH increases to 1.6), the polymers start cross-linking and form gel.

Since, pH-range of reaction zone (where most of the reaction takes place or pH falls significantly from inlet value) corresponds to $pH = 0.68 \sim 1.7$ and pH-range of gel formation corresponds to $pH$ = $1.6 \sim 3.8$, the reaction front lies behind the gel front. However, the speed of propagation of both the fronts are same and can be expressed by scaling analysis (in appendix) as follows:

$$u_{front} = \frac{1 - \exp\left(-N_{ac}\right)}{1 - \varepsilon_0 \exp\left(-N_{ac}\right)} u_0, \tag{9.6}$$

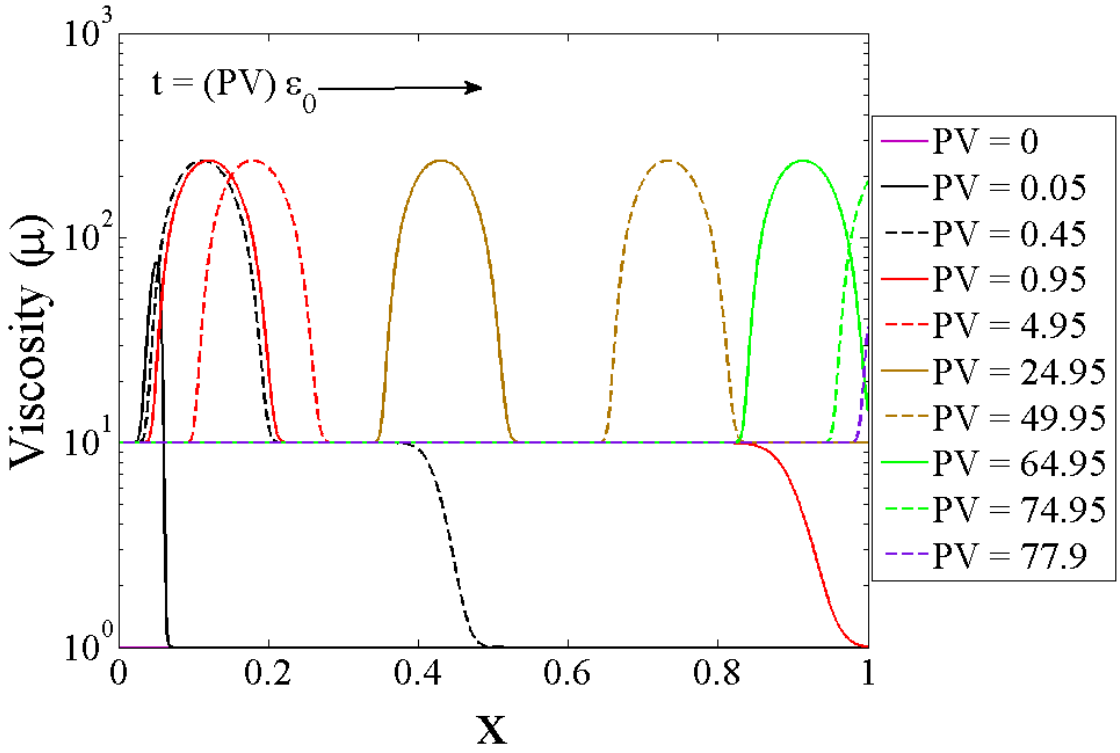


Figure 9.4: Gel propagation (viscosity profile) at $Da = 100$ in the core for various pore volume of acid injected.

where, $u_{front}$ is the front speed in steady propagation. It can be seen that the front speed $u_{front}$ depends on the injection speed, $u_0$, as well as the acid capacity number, $N_{ac}$. For $N_{ac} = 0.05$ and $\varepsilon_0 = 0.2$, the dimensionless front speed in equation (9.6) from scaling analysis corresponds to roughly $0.06$ that matches the simulation results in Figure 9.4, where gel front travels dimensionless distance $x = 0.25$ when pore volume of acid is injected from $4.95$ to $24.95$ in dimensionless time $t = 4$ (which leads to the same value of front velocity, $\frac{x}{t} = 0.06$). While the speed of both (reaction and gel) fronts are same, the diffusivity of protons in reaction zone is much higher compared to that in gel due to very high viscosity in the later regions. Therefore, the width of reaction front, $l_{X,C}$, is much smaller as compared to the width of gel front, $l_{X,Gel}$, (in mass-transfer controlled dissolution) as can be seen from Figure 9.2. The scaling analysis leads to the width of these fronts in

dimensionless form as follows:

$$
\begin{aligned}
l_{X,C} &= \frac{u_0}{a_v}\left[\frac{1}{k_s}+\frac{2r_p}{D_{m0}Sh}\left\langle\mu\right\rangle_c\right]\left\langle\triangle pH\right\rangle_C \exp\left(-N_{ac}\right)\mathsf{Ln}10 \\
l_{x,Gel} &= \frac{u_0}{a_v}\left[\frac{1}{k_s}+\frac{2r_p}{D_{m0}Sh}\left\langle\mu\right\rangle_{gel}\right]\left\langle\triangle pH\right\rangle_{gel} \exp\left(-N_{ac}\right)\mathsf{Ln}10
\end{aligned}
\tag{9.7}
$$

where $\left\langle\triangle pH\right\rangle_C$ is the pH-range of reaction zone and $\left\langle\triangle pH\right\rangle_{Gel}$ is the pH-range of gel formation. $r_p$ is average pore radius that depends on initial permeability as $r_p \sim \sqrt{K_0}$ and $\langle a_v\rangle$ is average area per unit volume available for reaction that depends on initial permeability as $a_v \sim \frac{1}{\sqrt{K_0}}$. $\left\langle\mu\right\rangle_c$ and $\left\langle\mu\right\rangle_{gel}$ are average viscosity of reaction zone and gelled acid, respectively and are given by

$$
\begin{aligned}
\left\langle\mu\right\rangle_c &= \frac{1}{\left\langle\triangle\mathsf{pH}\right\rangle_c}\int\limits_{\mathsf{pH}_c}\mu\, dpH \sim \mu_{p0}. \\
\left\langle\mu\right\rangle_{gel} &= \frac{1}{\left\langle\triangle\mathsf{pH}\right\rangle_{Gel}}\int\limits_{\mathsf{pH}_{Gel}}\mu\, dpH \sim 13.13\mu_{p0}.
\end{aligned}
\tag{9.8}
$$

Thus, the width of both the fronts increases as the injection rate ($Da^{-1}$) increases or initial permeability increases. The increase in the width of these fronts with initial permeability is also observed from simulation as shown in Figure 9.5 that verifies the scaling analysis at least qualitatively. It can be seen easily from equations (9.7) that if the dissolution process is kinetically controlled $\left(\frac{\phi^2}{Sh}\left\langle\mu\right\rangle_{gel} << 1\right)$, the width of both fronts is almost same ($l_{X,C} \sim l_{X,Gel} \propto u_0\sqrt{K_0}$) and increases linearly with injection rate but non-linearly with initial permeability; while for mass transfer controlled dissolution $\left(\frac{\phi^2}{Sh}\left\langle\mu\right\rangle_{gel} >> 1\right)$, the width of gel front is bigger than that of reaction front ($l_{X,C} \propto \left\langle\mu\right\rangle_c u_0K_0$ and $l_{X,Gel} \propto \left\langle\mu\right\rangle_{gel} u_0K_0$). In the latter limit, the width of both the fronts increases linearly with injection rate and initial permeability. In the current analysis, $\left\langle\triangle pH\right\rangle_{Gel}$ equals to 2.2 (gel is formed between pH-range 1.6 - 3.8) and $\left\langle\mu\right\rangle_{gel}$ is $131.3$. The typical value of $\left\langle\triangle pH\right\rangle_{react}$ is 1.2 that leads to

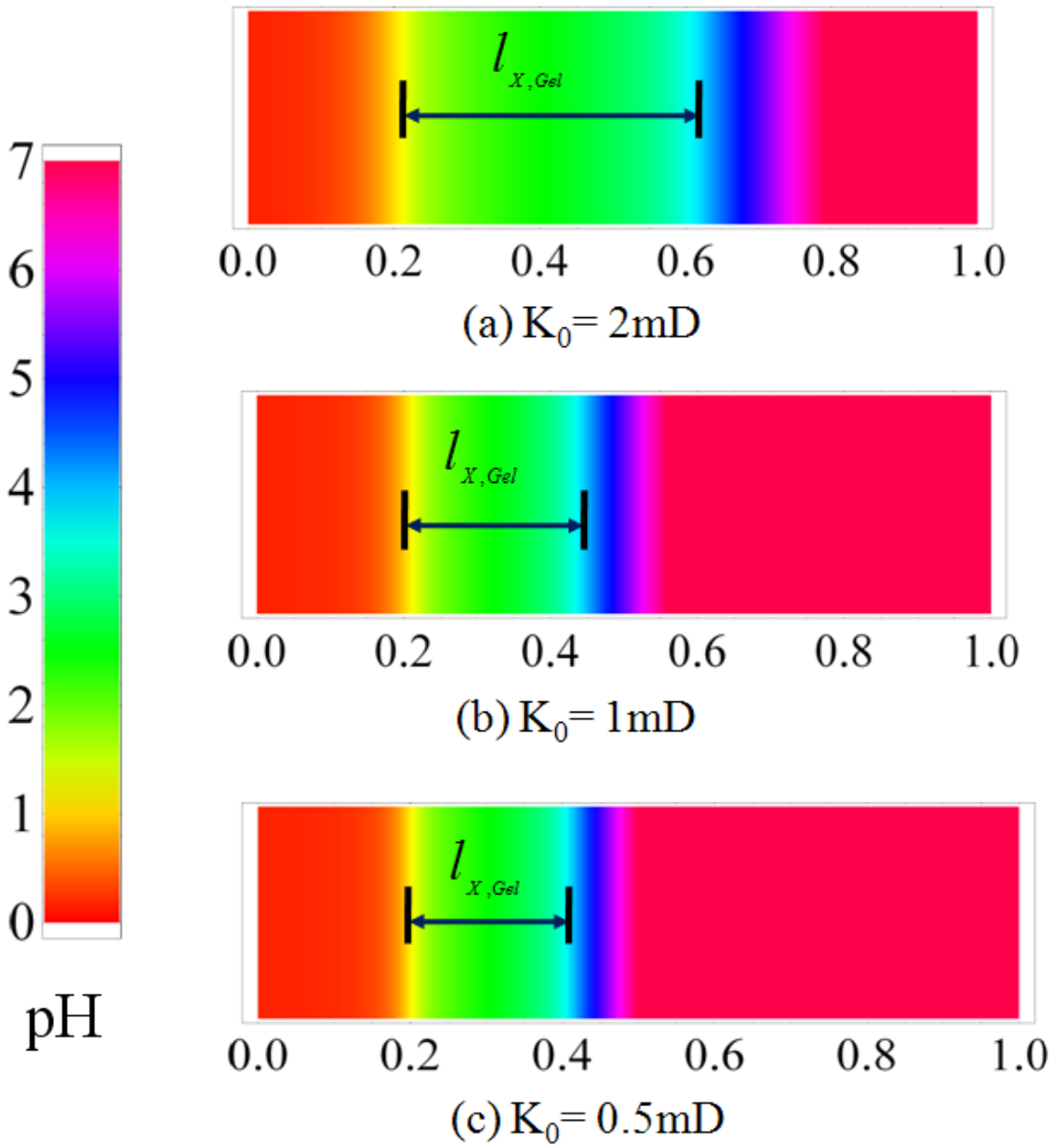


Figure 9.5: Width of gel and reaction fronts in cores of different initial permeabilities at constant injection rate, $u_0 = 9.8 \times 10^{-4}$cm $s^{-1}$.

$l_{X,C} = 0.025$ and $l_{X,Gel} = 0.15$ (which can be seen from Figure 9.2). Thus, for the case studied here, the dimensionless gel width is about $15\%$ of the domain size and about $13$ times larger than the width of reaction front, which can be seen from Figure 9.2.

**Overall Pressure-drop**

It must be noted that resistance offered by gel formation is the main difference between stimulation of carbonates with in-situ gelling acids and Newtonian acids. In the case of Newtonian acids, the viscosity remains constant while permeability is increased due to dissolution. As a result, effective mobility increases with dissolution and hence pressure drop across the core decreases with time. On the contrary, for the case of in-situ gelling acids, since effective viscosity of gel is very high, the effective mobility of in-situ gelling acids is reduced tremendously, which results in large increase in pressure drop as can be seen in Figure 9.6. Thereafter, as permeability of the core increases due to dissolution, the pressure drop decreases with time. Eventually, the gel exits the core, so the pressure drop falls sharply and we get the breakthrough. Thus, unlike for Newtonian acids where pressure drop decreases monotonically, the pressure profile for in-situ gelling acids is non-monotonic in time (Figure 9.6) and matches with the experimental trends (MaGee et al., 1997; Gomaa et al., 2011). This result plays very important role in designing lab experiments where pressure has to be stay within certain limit.

### 9.2.3 Breakthrough Curves and Optimum Injection Rate

The effect of injection rate on acidization curve is shown in Figure 9.7, where pore volume to breakthrough ($PV_{BT}$) is plotted against dimensionless injection rate ($Da^{-1}$). The pore volumes of breakthrough ($PV_{BT}$) is defined here as the number of pore volume of acid required to increase the effective mobility of the core by a factor 100. It can be seen from this figure that similar to the experimental observation (Fredd and Fogler, 1998), a minimum exists in breakthrough curves for both in-situ

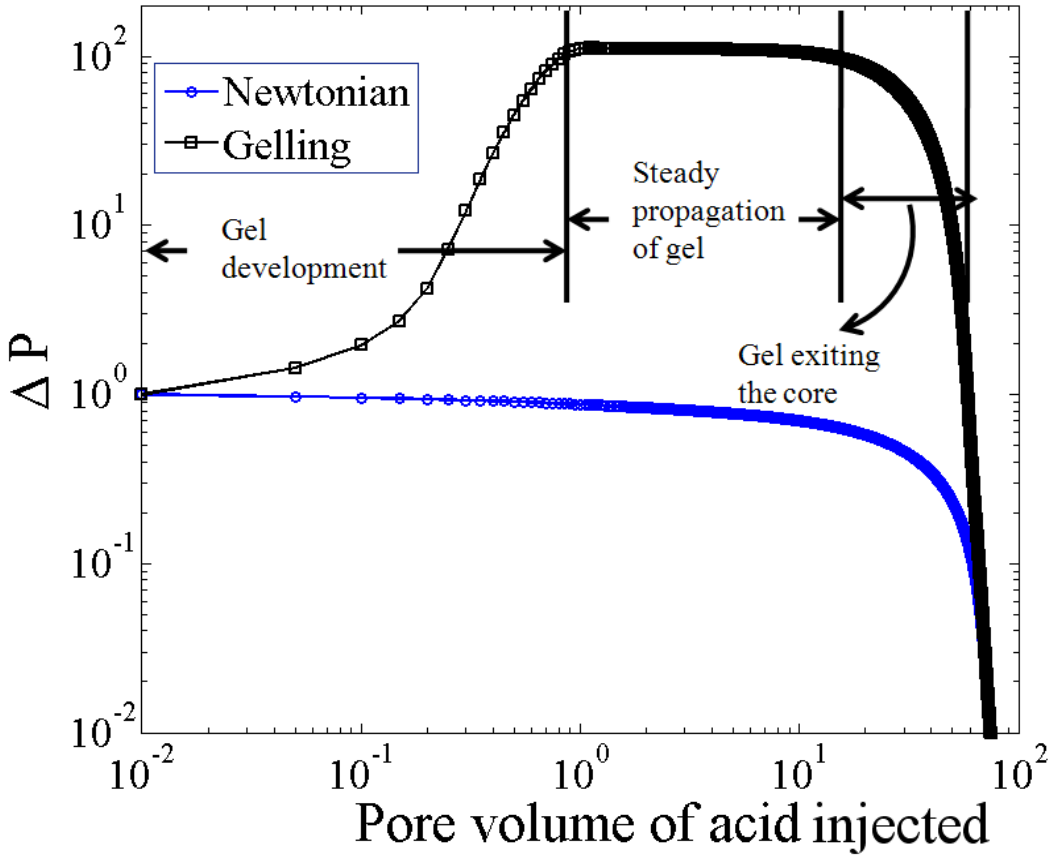


Figure 9.6: Overall pressure drop for gelling and Newtonian acids from 1-D simulation at $Da = 100$.

gelling acids and Newtonian acids. We note that the optimum injection rate ($Da^{-1}$) is smaller for in-situ gelling acids as compared to Newtonian acids. We estimate the optimum Damkohler number (injection rate at the minimum) for in-situ gelling acids using a procedure similar to that used by Panga at al. (2005) as follows:

$$\begin{aligned} u_{opt} &= \sqrt{\varepsilon D_e \frac{k_c k_c}{k_c + k_c} a_v}, \\ Da_{opt} &= \Phi \sqrt{\frac{\langle \mu \rangle_c}{\varepsilon_0 \langle A_v \rangle} \left(1 + \frac{\langle r \rangle \phi^2}{Sh} \langle \mu \rangle_c\right)}. \end{aligned} \tag{9.9}$$

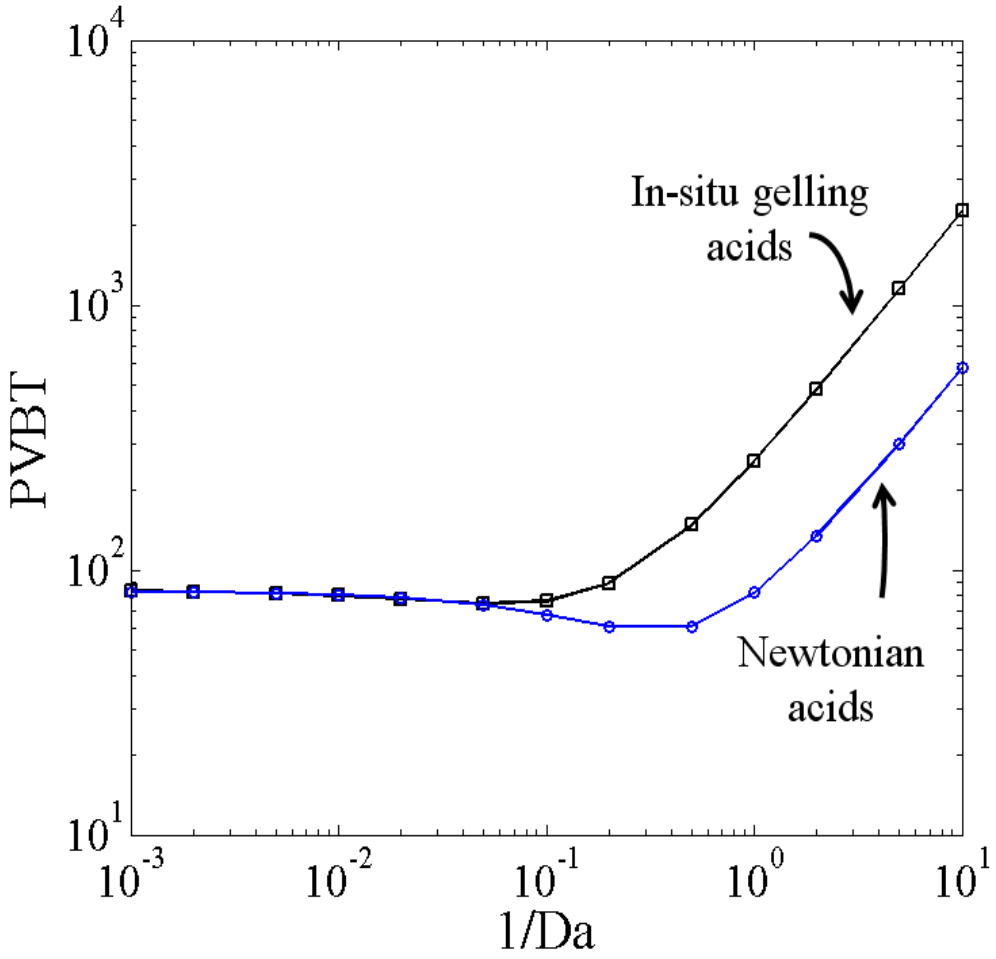


Figure 9.7: Comparison of breakthrough curves for gelling acids and Newtonian acids at $\phi^2 = 0.047$.

Thus, in the mass-transfer controlled dissolution ($k_c << k_s$), the optimum injection rate for in-situ gelling acids can be simplified as

$$u_{opt,Gel} = \frac{\langle u \rangle_{opt,New}}{\langle \mu \rangle_c}; \langle u \rangle_{opt,New} = \sqrt{\varepsilon_0 D_{m0} k_{c0} a_{v0}} \tag{9.10}$$

while in the kinetically controlled dissolution ($k_c << k_s$) as

$$u_{opt,Gel} = \frac{\langle u \rangle_{opt,New}}{\sqrt{\langle \mu \rangle_c}}; \langle u \rangle_{opt,New} = \sqrt{\varepsilon_0 D_{m0} k_s a_{v0}}. \tag{9.11}$$

Here, $\langle r \rangle$ is the overall increase in average pore radius from its base value while $\langle A_v \rangle$ is the overall decrease in area per unit volume from its base value, due to dissolution. Since we defined the breakthrough when mobility is increased by a factor 100, we assume $\langle r \rangle \sim 5$ and $\langle A_v \rangle \sim 0.2$. Thus it can be calculated from the equation (9.9), for the parameter values used in current analysis, the optimum injection rate ($Da^{-1}$) for in-situ gelling acid is less than that of the Newtonian acids by about a factor $4$, which can be verified by Figure 9.7. It is because, the gel formation slows down the mass-transfer of protons from bulk fluid phase to the solid surface. Therefore, lower injection rate corresponds to efficient stimulation or optimum for acidization. In addition, the pore volume of acid injected until breakthrough is higher for in-situ gelling acids as compared to that for Newtonian acids. This is due to the fact that it is 1-D simulation where there is no place for flow diversion, thus gel formation retard the dissolution process without leak-off or flow diversion. Therefore, higher $PV_{BT}$ is required at optima as observed in experiments (Fredd and Fogler, 1998) where slow reacting acids lead to higher $PV_{BT}$. However, for 2-D and 3-D simulations lead to the lower $PV_{BT}$ for in-situ gelling acids as compared to the Newtonian acids, described in later sections.

It should also be noted from equations (9.10) and (9.11) that optimum injection rate for both types of acids (in-situ gelling and Newtonian) changes with initial permeability in the same manner, i.e., in the kinetically controlled dissolution,

$$u_{opt} \sim \sqrt{a_{v0}} \sim K_0^{1/4}, \tag{9.12}$$

while in the mass-transfer controlled dissolution,

$$u_{opt} \sim \sqrt{k_{c0} a_{v0}} \sim \sqrt{\frac{a_{v0}}{r_{p0}}} \sim K_0^{1/2}. \tag{9.13}$$

In other words, the optimum injection rate for both acids decreases with initial per-

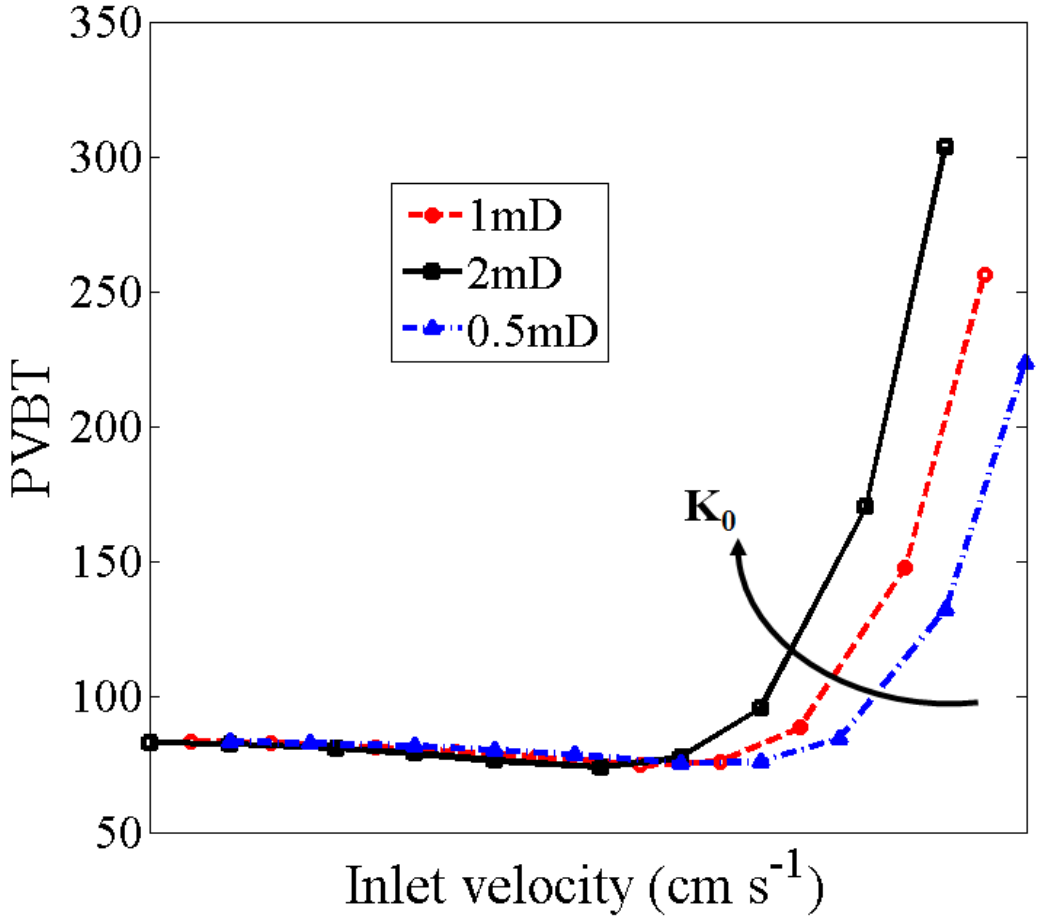


Figure 9.8: Effect of initial core permeability on breakthrough curves for gelling acids at $\phi^2 = 0.047$.

meability that can also be verified from Figure 9.8 where breakthrough curves for in-situ gelling acids are plotted for different initial permeability.

It should be noted from the breakthrough curves shown in figures 9.7 and 9.8 that in the face dissolution regime (for very low injection rate or $Da^{-1}$), $PV_{BT}$ is same and is independent of types of acid. In fact, in this asymptotic regime, $PV_{BT}$ can be estimated (Panga et al., 2005) as

$$PV_{BT,face} = \frac{1-\varepsilon_0}{\varepsilon_0 N_{ac}}, \tag{9.14}$$

which gives $PV_{BT,face} \sim 80$ for the parameters listed in Table 9.1 and used in current simulation, which matches with the simulation results. This validates the accuracy of the model as well as simulations.

## 9.3 Dual Core Analysis

In this section, we consider a dual core set-up as shown in the Figure 9.1(b) and identify the mechanism of flow diversion. Here, the total injection velocity, $u_0$, and exit pressure, $P_{exit}$, are kept constant, and, $fr$ signifies the flow diversion, the fraction of total injection rate flowing through low-perm core. As explained earlier, the dimensional form of two-scale continuum model has several parameters and so very difficult to analyze while the non-dimensional form of the model contains the minimum number of parameters and easy to analyze.

### 9.3.1 Dimensionless TSC Model

The dimensionless form of the continuum model for dual core with linear kinetics (as described in previous chapters) can be written in one dimension as follows:

$$\begin{aligned}
\frac{\partial}{\partial x}\left(M_i \frac{\partial p}{\partial x}\right) = -\frac{\partial u_{xi}}{\partial x} &= Da\left(1+\frac{\phi^2 \gamma_{ri}\, r_i \mu_i}{Sh}\right)^{-1} A_{vi}\, c_{fi}\ ; \\
\frac{\partial \pi_i}{\partial t} + \frac{\partial u_{xi} c_{fi}}{\partial x} &= \frac{1}{Pe_L}\frac{\partial}{\partial x}\left(\varepsilon_i D_{ei}\frac{\partial c_{fi}}{\partial x}\right)\ ; \\
\frac{\partial\left(\varepsilon_i c_{pi}\right)}{\partial t} + \frac{\partial u_{xi} c_{pi}}{\partial x} &= \frac{1}{Pe_L}\frac{\partial}{\partial x}\left(\varepsilon_i D_{epi}\frac{\partial c_{pi}}{\partial x}\right); \\
\frac{\partial \varepsilon_i}{\partial t} &= N_{ac} Da\left(1+\frac{\phi^2 \gamma_{ri}\, r_i \mu_i}{Sh}\right)^{-1} A_{vi}\, c_{fi} \qquad i=1,2,
\end{aligned} \tag{9.15}$$

where

$$\pi_i = \varepsilon_i\left(c_{fi}+\frac{1}{N_{ac}}\right).$$

The mobility, $M_i$, and effective viscosity term, $\mu_i$, are given by

$$M_i = \frac{M_{0i} k_i}{\mu_i \left\|u_{xi}\right\|^{n-1}},$$

$$\mu_i = \eta_{0i}\left(M_{0i}k_i\frac{\varepsilon_i}{\varepsilon_{0i}}\right)^{\frac{(1-n)}{2}}\left[1+(\mu_{mi}-1)\,Exp\left\{\frac{-a\,(pH_i-pH_m)^2}{pH_i\,(7-pH_i)}\right\}\right] \quad ;(9.16)$$

$$\eta_{0i} = 1+\left(\mu_{p0}-1\right)c_{pi};$$

$$\frac{\mu_{mi}-1}{\mu_{\max}-1} = \frac{1-\exp\left(-\alpha_1 c_{pi}\right)}{1-\exp\left(-\alpha_1\right)}.$$

The inlet/initial/boundary conditions are given by

$$\varepsilon_i = \varepsilon_{0,i}+\widehat{f};\;\; c_{f,i}=0 \quad @ \quad t=0;$$

$$u_i c_{f,i}-\frac{\varepsilon_i D_{ei,X}}{Pe_L}\frac{\partial c_{f,i}}{\partial x} = u_{in,i}c_{fin,i};\;\; u_i c_{p,i}-\frac{\varepsilon_i D_{epi,X}}{Pe_L}\frac{\partial c_{p,i}}{\partial x} = u_{in,i}c_{pin,i};\;@\quad x=0 \quad (9.17)$$

$$\sum_{i=1}^{2}(u_i)=1;\;\; p_1=p_2 \quad @ \quad x=0;$$

$$p_i=0;\frac{\partial c_{fi}}{\partial x}=0;\;\frac{\partial c_{pi}}{\partial x}=0 \quad @ \quad x=1;$$

and the structural property-relationship in dimensionless form is given as follows:

$$k_i = \frac{\varepsilon_i}{\varepsilon_{0,i}}\left(\frac{\varepsilon_i\,(1-\varepsilon_{0,i})}{\varepsilon_{0,i}\,(1-\varepsilon_i)}\right)^{2\beta};\; r_i=\sqrt{\frac{k_i\varepsilon_{0,i}}{\varepsilon_i}};\quad A_{v,i}=\frac{\varepsilon_i}{\varepsilon_{0,i}r_i};\quad \forall\;\; i=1,2 \qquad (9.18)$$

In this diversion study, we assume the initial permeability of the high-perm core is $4$ times higher than that of low-perm core, i.e., $M_{10}=1$, $M_{20}=4$; $\varepsilon_{0,1}=\varepsilon_{0,2}=\varepsilon_0$; $\gamma_{r1}=1$, $\gamma_{r2}=2$; and $\gamma_{a1}=1$, $\gamma_{a2}=0.5$. Now we use this1-D version of the two-scale continuum (TSC) model and simulate it with typical values of parameters listed in Table9.1 and identify the mechanism of flow diversion.

### 9.3.2 Flow Diversion in non-Reacting Case

Before we analyze the reactive dissolution, we first consider the non-reacting case where viscosity and overall permeability remain constant. In this case, the inlet velocity is given by Darcy-law and expression of mobility and viscosity in equation (9.16) as

$$u_i^n \sim \frac{M_{i0}}{M_{i0}^{\frac{1-n}{2}}} \text{ or, } u_i \sim M_{i0}^{\frac{1+n}{2n}}.$$

So, the flow splits through both the cores according to their effective mobility, and the fractional amount going through low-perm core is given by

$$fr = \frac{u_{10}}{u_{10} + u_{20}} = \left( \frac{M_1^{\frac{n+1}{2n}}}{M_1^{\frac{n+1}{2n}} + M_2^{\frac{n+1}{2n}}} \right) = \begin{cases} 0.20, & n = 1 \\ 0.11, & n = 0.5 \end{cases} . \tag{9.19}$$

Thus, we can see that if the power index $n$ is close to $1$ (Newtonian behavior), 20 % of the acid flows through low-perm core while if the power index $n$ is $0.5$ (highly non-Newtonian behavior), only 11 % of the acid goes through low-perm core. In other words, the higher power index is desired for practical purposes as it leads to more flow of acid through low-perm core.

### 9.3.3 Flow Diversion by in-situ gelling Acids

Now, we consider the case of reactive dissolution. As discussed in the previous section, the width of the gel front increases with the injection rate and the initial permeability of the core. Therefore, larger gel width is expected in high-perm core as compared in the low-perm core, which can be seen from simulation results shown in Figure 9.9. Since the effective viscosity of the gel is very high ($\langle \mu \rangle_{gel} \sim 131$), more resistance is offered in the high-perm core due to larger gel width and hence, the flow is diverted to the low-perm core as shown in Figure 9.10. Here, we can see that initially, the amount of acid that flows through each of the cores, is proportional to their initial permeability. Then, due to gel formation as dissolution proceeds, more flow is diverted from high-perm core to low-perm core due to larger gel width in the high-perm core. The amount of flow diversion keeps increasing until the gel is fully developed (to its maximum width) in high-perm core. Thereafter, gel propagates with a steady speed and gel width remains constant. As a result, flow diversion remains almost constant until the gel starts getting out of the high-perm core. For steady propagation, scaling analysis leads to the amount of flow

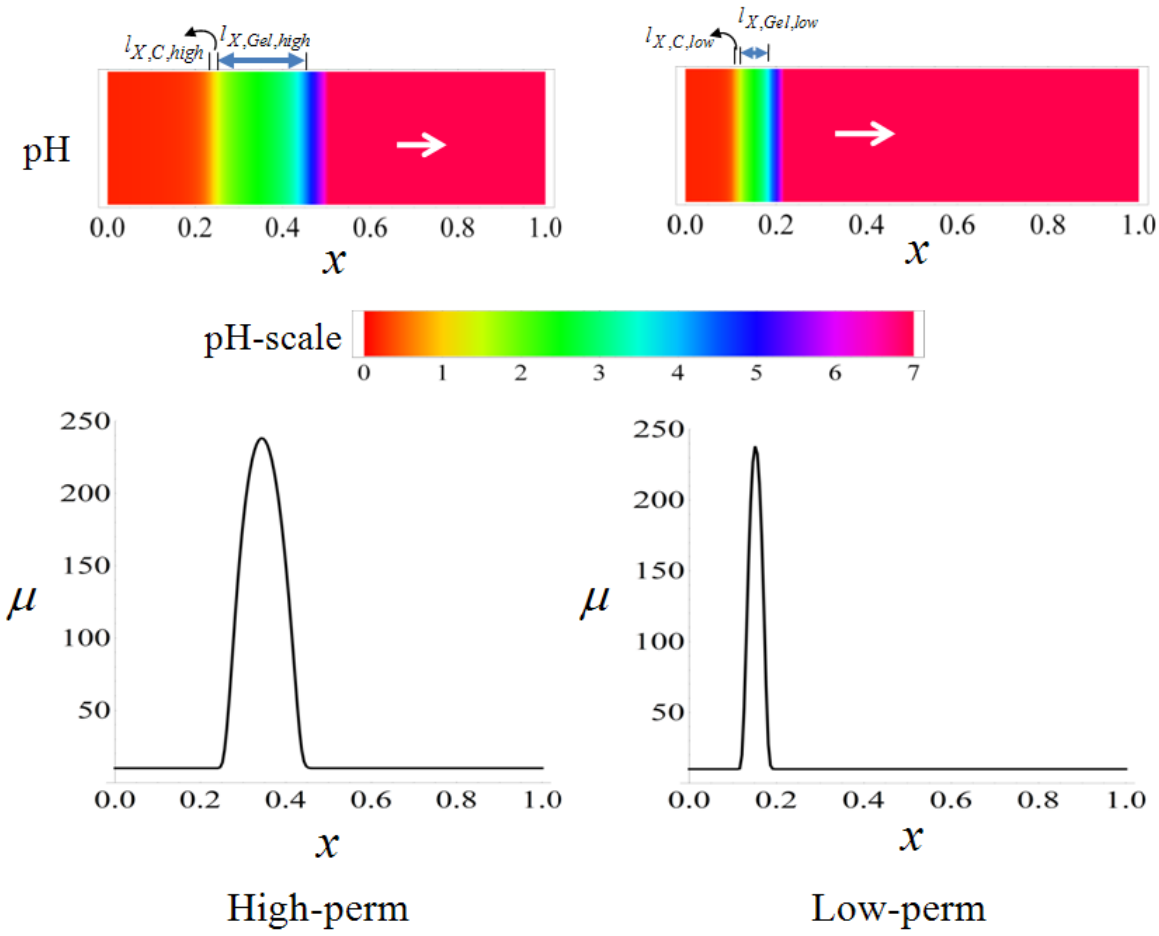


Figure 9.9: Gel dynamics in dual core set-up at $\phi^2 = 0.07$ and $Da = 100$ from 1-D simulation.

diversion, $fr$ that satisfies the following relation (details in appendix B):

$$\left.\frac{u_1}{u_2}\right|_{x=0} = \frac{fr}{1-fr} = \left(\frac{1+\delta_1\left(1-fr\right)\left(1+\delta_2\sqrt{M_2}\right)\sqrt{M_2}}{1+\delta_1\ fr\left(1+\delta_2\sqrt{M_1}\right)\sqrt{M_1}}\right)\left(\frac{M_1}{M_2}\right), \tag{9.20}$$

where $\delta_1$ and $\delta_2$ depend strongly on the rheological properties as given by the following expressions:

$$\delta_1 = \left(\frac{\langle\mu\rangle_{gel}}{\mu_{p0}} - 1\right)\langle\triangle\text{pH}\rangle_{Gel}\ \ \frac{\exp\left(-N_{ac}\right)}{Da}\text{Ln}10\quad ,$$
$$\delta_2 = \frac{\phi^2\langle\mu\rangle_{gel}}{Sh}. \tag{9.21}$$

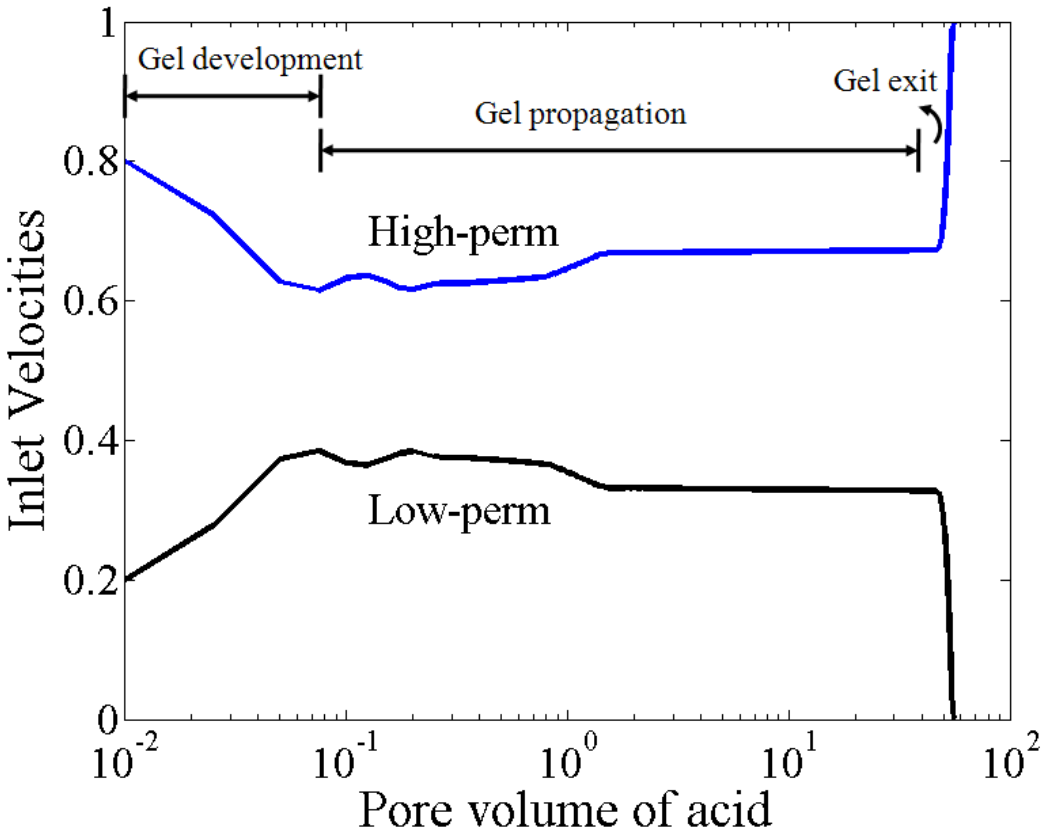


Figure 9.10: Flow splitting in dual core set-up at $\phi^2 = 0.047$ and $Da = 100$.

In the limit of mass-transfer controlled dissolution $\left(\delta_2 = \frac{\phi^2 \langle \mu \rangle_{gel}}{Sh} >> 1\right)$, equation (9.20) simplifies to

$$\left.\frac{u_1}{u_2}\right|_{x=0} = \frac{fr}{1-fr} = \frac{\delta_1\delta_2 + M_2^{-1}}{\delta_1\delta_2 + M_2^{-1}}. \tag{9.22}$$

For $Da = 100$, $\delta_1 = 0.58$ and $\delta_2 = 2.05$ corresponding to $\langle \mu \rangle_{gel} = 131.3$, $\mu_{p0} = 10$, $\langle \triangle pH \rangle_{Gel} = 2.2$, $N_{ac} = 0.05$, $\phi^2 = 0.047$ and $Sh = 3.0$ (Table 9.1). In this case, equation (9.20) leads to $fr = 0.4$, i.e., 40 % of acid flows through low-perm core that matches the simulation result shown in Figure 9.10. In this case, the ratio of amounts of acid flowing in low-perm and high-perm cores is 0.6 that can be seen from Figure 9.11. This ratio is measure of flow diversion. For example, if this ratio is unity, the diversion is maximum. Similarly, for Newtonian acids, this ratio is same as permeability ratio of cores. This ratio can be increased by increasing $\delta_1$ and

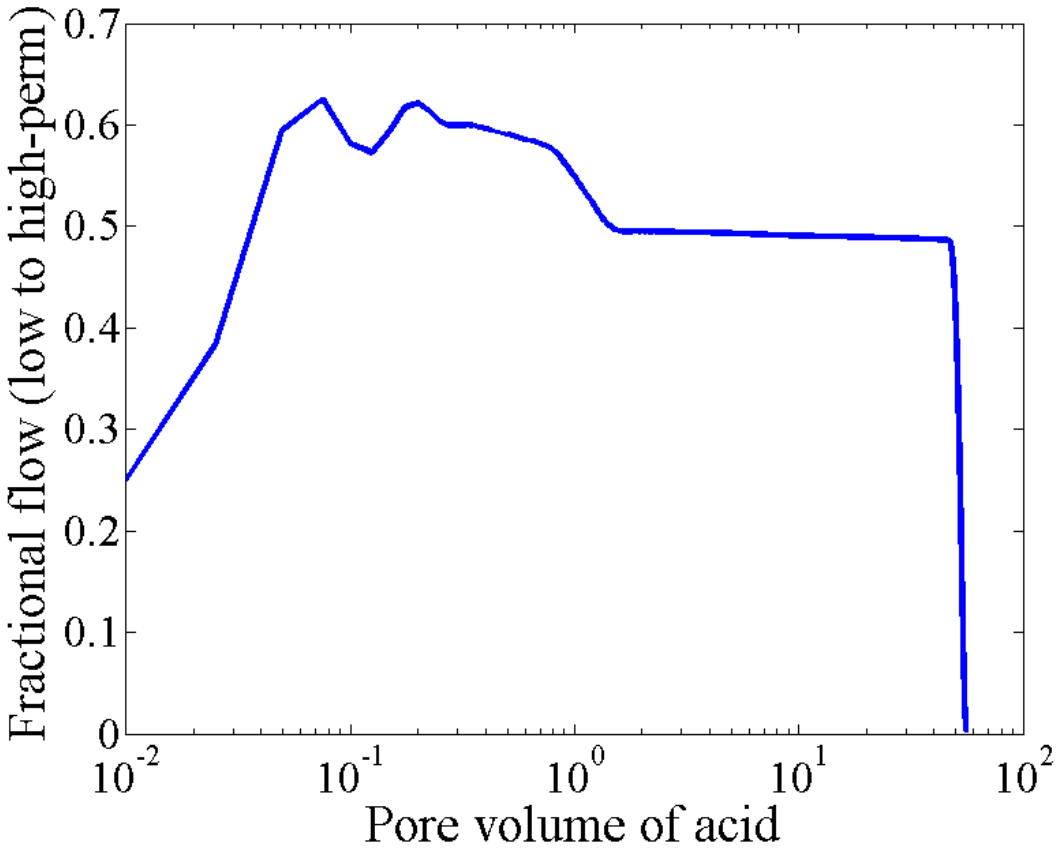


Figure 9.11: Ratio of inlet flow rates in low-perm to high-perm cores from 1-D simulation at $\phi^2 = 0.047$ and $Da$=100.

$\delta_2$, which depend strongly on rheological properties and injection rates (equation, 9.21). Since diversion occurs at short times until gel is fully developed as can be seen in Figure 9.11, this ratio can further be increased using intermittent flow condition where acidic solution is injected for short times followed by injection of non-reacting (brine) solution, repeatedly.

## 9.4 Conclusion and Discussion

We used the 1-D version of the two-scale continuum model to analyze the stimulation of single and dual core laboratory experiments with in-situ gelling acids for the case of constant injection rate. The scaling analysis, presented in the appendix B, for gel dynamics such as gel width and gel propagation in a single core, is

verified by the simulation results. For example, the scaling criteria show that the speed of reaction and gel fronts are independent of rheology and depend only on acid capacity number and injection rate, which is also observed in simulations. In particular, the speed of reaction front is found to be the same as that of gel fronts. Similarly, the scaling analysis shows that the width of these fronts are strongly dependent of rheological parameters which are also observed in the simulations. In fact, the width of gel front is found to be very large as compared to that of reaction front due to very high viscosity of the gelled acids.

Since the gelled acid has very high viscosity, the gel formation reduces the effective mobility. Hence, the pressure drop across the core increases tremendously unlike for the case of the Newtonian acid where pressure profile decreases monotonically. The similar trends is observed in laboratory experiments. Therefore, it is very important to estimate the increase in pressure drop for proper design of the laboratory experiments.

We showed from scaling analysis and from simulations that the high-perm core is offered more resistance due to larger gel width, which is the key mechanism for flow diversion. We express the amount of diversion in terms of rheological parameters, which can be used to design the injecting fluids to achieve maximum diversion by controlling the rheological parameters. We reasoned that the flow diversion, $fr$, can also be maximized by using intermittent flow conditions where acidic and non-reacting solutions are switched periodically until breakthrough.

We have developed the scaling criteria for optimum injection rate of in-situ gelling acid and showed that it is smaller by a factor $\langle\mu\rangle_c$ and $\sqrt{\langle\mu\rangle_c}$ in limits of mass-transfer and kinetically controlled dissolutions, respectively, when compared with Newtonian acids. Here $\langle\mu\rangle_c$ is the average viscosity of acidic solution in reaction zone. The same result is obtained from simulations. It is because the gel formation reduces the molecular diffusivity of protons. In addition to that, in mass-

transfer controlled dissolution, the gel formation hinders the transfer of protons from bulk to the rock surface. Both of these effects reduces the effective reaction rate or increases the reaction time. Since, wormhole formation is due to coupling between transport and reaction processes, the convection time also has to be increased to form a wormhole. Hence the lower injection rate is required corresponding to wormhole formation (or optimum).

# Chapter 10 Two-Dimensional and Three-Dimensional Simulations: Dissolution Patterns

## 10.1 Preamble

Though the one-dimensional analysis of acidization processes discussed in the previous chapter provides most of the qualitative features of the gel dynamics and flow diversion in single and dual core set-ups, they can not predict dissolution patterns due to absence of transverse direction. Because the formation of wormhole/dissolution patterns are due to competition between length-scales in flow and transverse directions (In the flow direction, convection and reaction are the dominant processes while in the transverse direction, dispersion and reaction are dominant processes), two-dimensional or three-dimensional simulations are needed to understand the different dissolution patterns. In addition, one-dimensional analysis gives the qualitative trends correctly but may be quantitatively less accurate, especially for high heterogeneity field. For these reasons, 2-D and 3-D simulations are very important to study the effect of rheological parameters or flow and reaction parameters on dissolution patterns.

In this chapter, we analyze the dissolution process by using the 2-D and 3-D version of the two-scale continuum model. First, we consider the 2-D dissolution in the single core set-up as shown in the Figure 9.1(a) where we use the model, expressed in dimensionless form in equations (9.1 - 9.5), and compare the results of in-situ gelling acids with that of Newtonian acids. Then, we study the flow diversion in dual core set-ups shown in Figure 9.1(b) where we use the dimensionless form of the model, expressed for dual core set-ups in equations (9.15 - 9.18), and compare the results with experimental data available. Finally, we consider the 3-D simulations in a single core set-up, where we show that the results from 2-D simulations contain all the essential feature of 3-D simulations.

## 10.2 2-D Simulations

### 10.2.1 Single Core Analysis

#### Model Equations

The 2-D version of the Two-scale continuum model for single core set-up can be written in dimensionless form as follows:

$$\begin{aligned}
\frac{\partial}{\partial x}\left(M_X\frac{\partial p}{\partial x}\right)+\frac{\partial}{\partial y}\left(M_T\frac{\partial p}{\partial y}\right) &= -\left(\frac{\partial u_x}{\partial x}+\frac{\partial u_y}{\partial y}\right)=Da\left(1+\frac{\phi^2 r\,\mu}{Sh}\right)^{-1}A_v\,c_f\,,\\
\frac{\partial \pi}{\partial t}+\frac{\partial u_x c_f}{\partial x}+\frac{\partial u_y c_f}{\partial y} &= \frac{1}{Pe_L}\left[\frac{\partial}{\partial x}\left(\varepsilon D_{eX}\frac{\partial c_f}{\partial x}\right)+\frac{\partial}{\partial y}\left(\varepsilon D_{eT}\frac{\partial c_f}{\partial y}\right)\right],\\
\frac{\partial\left(\varepsilon c_p\right)}{\partial t}+\frac{\partial u_x c_p}{\partial x}+\frac{\partial u_y c_p}{\partial y} &= \frac{1}{Pe_L}\left[\frac{\partial}{\partial x}\left(\varepsilon D_{epX}\frac{\partial c_p}{\partial x}\right)+\frac{\partial}{\partial y}\left(\varepsilon D_{epT}\frac{\partial c_p}{\partial y}\right)\right], \qquad (10.1)\\
\frac{\partial \varepsilon}{\partial t} &= N_{ac}Da\left(1+\frac{\phi^2 r\,\mu}{Sh}\right)^{-1}A_v\,c_f\,,
\end{aligned}$$

where subscript $'X'$ and $'T'$ denote the axial ($x-$) and transverse ($y-$) directions, respectively. The mobility, $M$, and effective viscosity term, $\mu$, are given by

$$\begin{aligned}
M &= \frac{k}{\mu\left\|\mathbf{u}\right\|^{n-1}},\\
\mu &= \eta_0\left(k\frac{\varepsilon}{\varepsilon_0}\right)^{\frac{(1-n)}{2}}\left[1+\left(\mu_m-1\right)Exp\left\{\frac{-a\left(pH-pH_m\right)^2}{pH\left(7-pH\right)}\right\}\right]; \qquad (10.2)\\
\eta_0 &= 1+\left(\mu_{p0}-1\right)c_p;\\
\frac{\mu_m-1}{\mu_{\max}-1} &= \frac{1-\exp\left(-\alpha_1 c_p\right)}{1-\exp\left(-\alpha_1\right)}.
\end{aligned}$$

and $\pi$ is given by

$$\pi=\varepsilon\left(c_f+\frac{1}{N_{ac}}\right). \qquad (10.3)$$

The inlet/initial/boundary conditions are given by

$$\varepsilon=\varepsilon_0+\widehat{f};\ c_f=0 \quad @ \quad t=0;$$

$$uc_f - \frac{\varepsilon D_{e,X}}{Pe_L}\frac{\partial c_f}{\partial x} = u_{in}c_{fin};\ u = u_{in}; \quad @ \quad x = 0 \tag{10.4}$$

$$uc_p - \frac{\varepsilon D_{ep,X}}{Pe_L}\frac{\partial c_p}{\partial x} = u_{in}c_{pin} \quad @ \quad x = 0;$$

$$p = 0;\ \frac{\partial c_f}{\partial x} = 0;\ \frac{\partial c_p}{\partial x} = 0 \quad @ \quad x = 1; \tag{10.5}$$

$$\frac{\partial p}{\partial y} = \frac{\partial c_f}{\partial y} = \frac{\partial c_p}{\partial y} = 0 \qquad \text{on transverse boundaries.}$$

The structural property-relationship in dimensionless form is given as follows:

$$k = \frac{\varepsilon}{\varepsilon_0}\left(\frac{\varepsilon\left(1-\varepsilon_0\right)}{\varepsilon_0\left(1-\varepsilon\right)}\right)^{2\beta};\ r = \sqrt{\frac{k\varepsilon_0}{\varepsilon}}; \quad A_v = \frac{\varepsilon}{\varepsilon_0 r}. \tag{10.6}$$

Now, we use the technique describe in previous chapter to simulate the 2-D version of the model with parameter values given in Table 9.1. and present the results below.

**Effective Mobility**

The wormholing phenomena is very complex process that is governed by competition between transport and reaction mechanisms. When acid is injected through a core of finite length, it dissolves the medium and increases the porosity. As a result, permeability increases. Therefore, for Newtonian acids where viscosity is constant, the effective mobility increases monotonically with pore volume of acid injected as can be seen from Figure 10.1. However, in case of gelling acids, as dissolution proceeds, the pH is increased and polymer starts cross-linking that increases the viscosity enormously. The rate of increase in viscosity is much higher than the rate of increase in permeability. Therefore, effective mobility decreases in case of gelling acid as can be seen from Figure 10.2, which matches the experimental trends (Fred and Fogler, 1998), qualitatively. However, as discussed in earlier section that after gel reaches to its maximum width, it stops increasing the viscosity and starts propagating forward. But permeability keeps increasing due to dissolution. As a result, the effective mobility starts increasing as in Figure 10.2

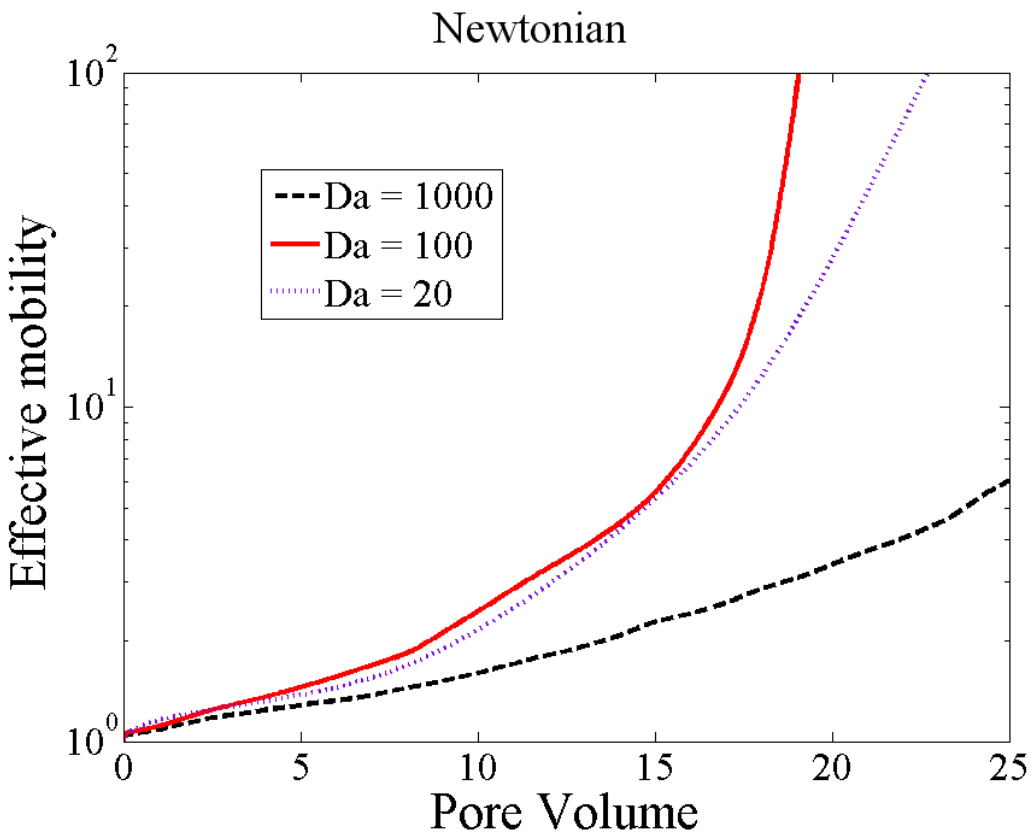


Figure 10.1: Evolution of effective mobility in time for Newtonian acids at various injection rates from 2-D simulation.

and we achieve the breakthrough.

**Pore volume to Breakthrough and Dissolution Patterns**

The rate of increase in flow conductivity depends on how fast the acid is being injected. It is observed experimentally (Fredd and Fogler, 1998) that the rate at which permeability increases due to reactive dissolution is non-monotonic with injection rate. Similar trend can also be seen from 2-D simulation with gelling acids and Newtonian acids as in Figures 10.1 and 10.2. For example, at very high injection rate, protons do not have sufficient time to react with the rock and most of the acid get out unreacted. Similarly, at very low injection rates, more acid is consumed, as most of the rock is dissolved. Therefore, to increase the flow conductivity to the same factor, large amount of acid is required in these extreme cases. In

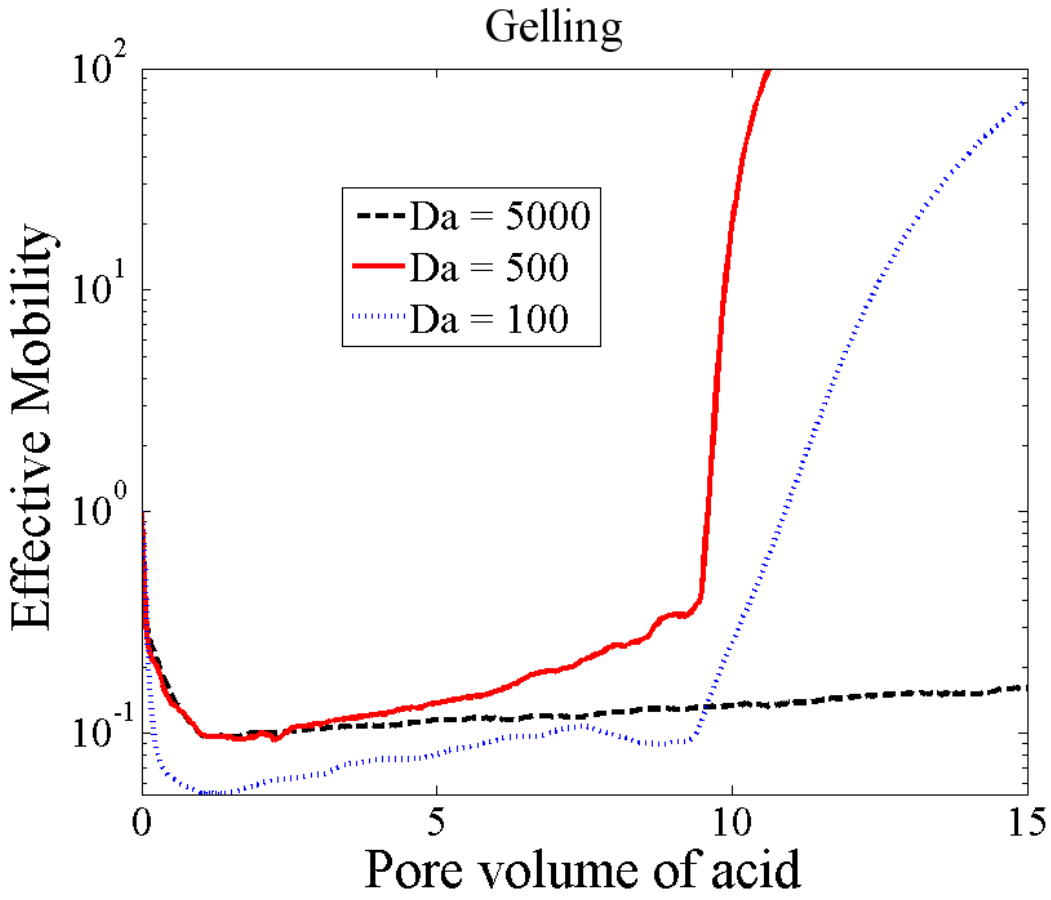


Figure 10.2: Evolution of effective mobility in time foi gelling acids at various injection rates from 2-D simulation.

fact, when pore volume of breakthrough (PVBT), defined here as pore volume of acid required to increase the effective mobility of the core by a factor 100, is plotted against injection rate ($Da^{-1}$), a minimum exists as shown in Figure 10.3. A similar trend is observed in experiments (Fredd and Fogler, 1998).

It should be noted that the optimum injection rate ($Da^{-1}$) is smaller for gelling acids as compared to Newtonian acids. As discussed in earlier sections that the scaling analysis leads to the optimum injection rate ($Da^{-1}$) for gelling acid less than that of the Newtonian acids by a factor $4$, the 2-D simulation matches that prediction which can be seen from Figure 10.3. It is because, the gel formation slows down the mass-transfer of protons from bulk fluid phase to the solid surface. Therefore,

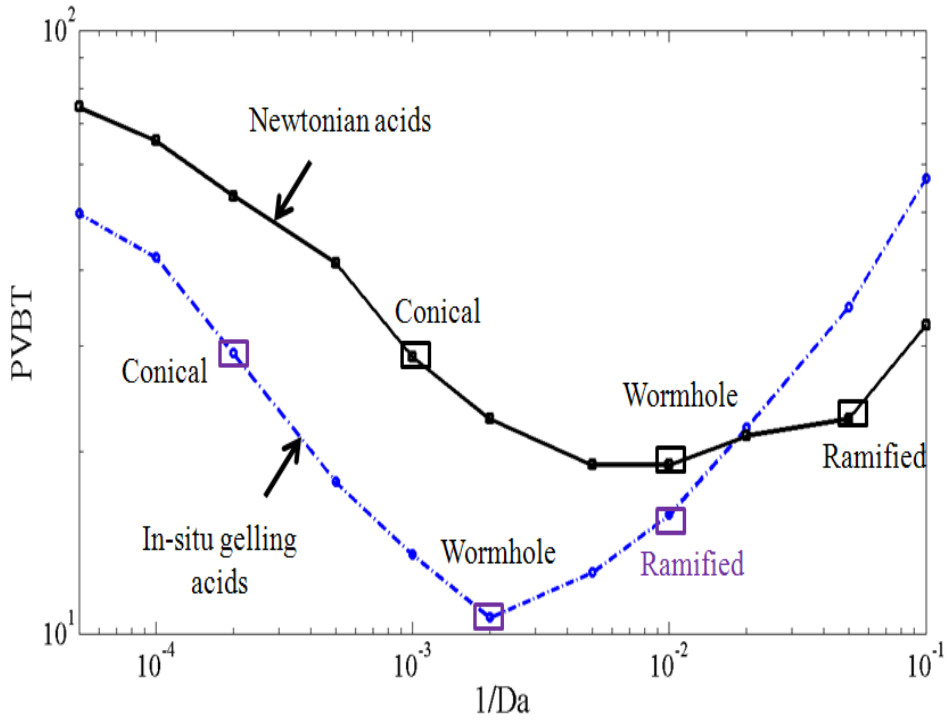


Figure 10.3: Breakthrough-curves for Newtonian and gelling acids at $\phi^2 = 0.047$.

lower injection rate corresponds to efficient stimulation or optimum for acidization. In addition, the pore volume of acid injected until breakthrough is smaller for gelling acids as compared to that for Newtonian acids at optimum. This is because of gel formation that bypasses the high-perm path and stimulates the least accessible zones as can be seen from Figure 10.4. When Newtonian acids are injected through the core, they flow preferentially through the least resistance or high-perm path, and form the conducting channels (wormholes). Since, these channels are bigger than the other pores, more acid is drawn to these channels which become wider due to dissolution. On the contrary, in case of gelling acids, due to gel formation, the acid is forced to go around the gel plugs. Figure 10.5 shows the profile of proton concentrations (pH) for Newtonian and gelling acids when one pore volume of acid is injected. It can be observed from this Figure that the pH-range of gel formation is right ahead to the reaction zone. Here the red color corresponds to in-

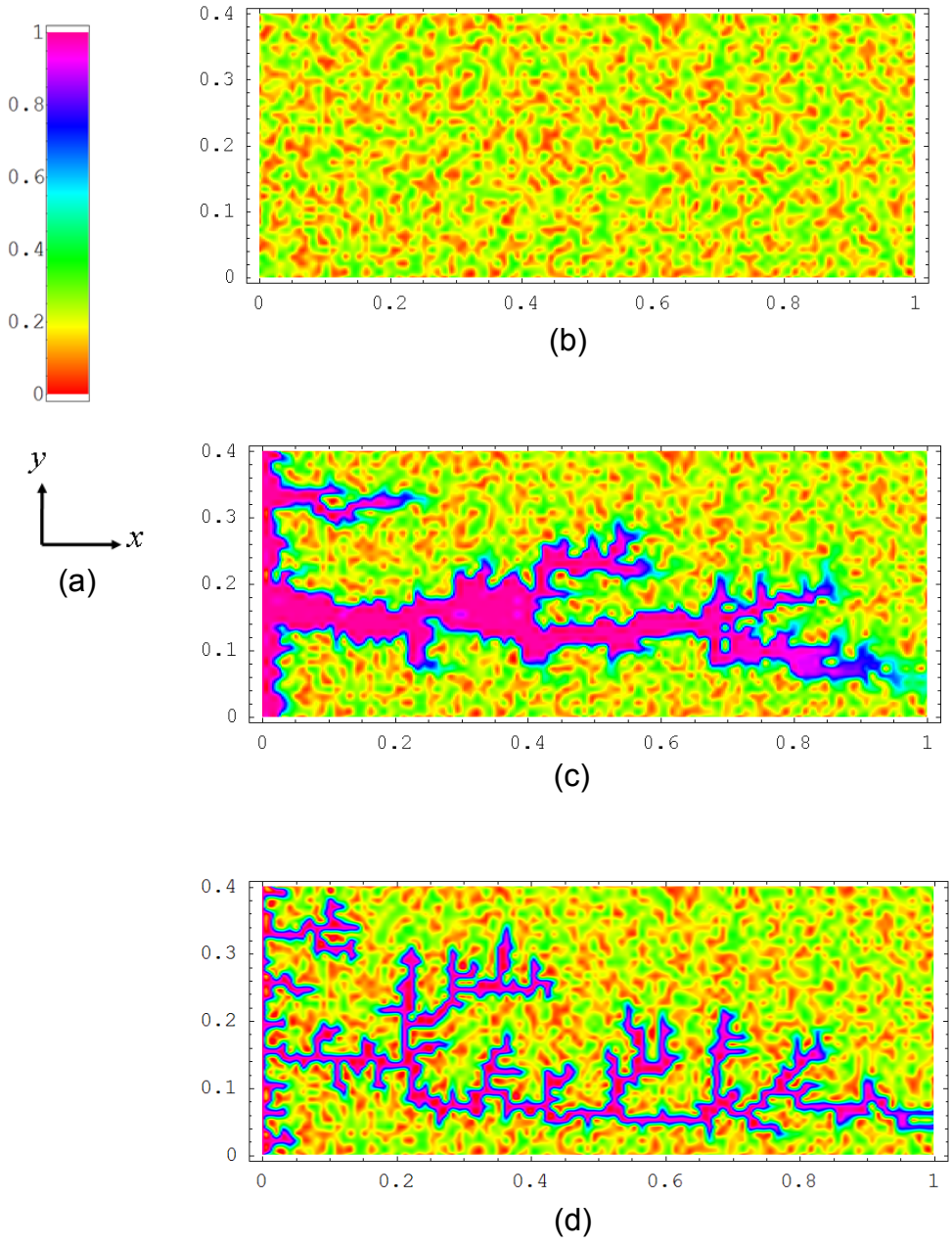


Figure 10.4: Dissolution patterns at optimum for gelling acids and Newtonian acids from 2-D simulation in a core of 5 cm length at (a) color-scale for porosity, (b) initial heterogeneious porosity field, (c) porosity field (wormhole structure) at breakthrough for Newtonian acids, and (d) porosity field (wormhole structure) at breakthrough for in-situ gelling acids.

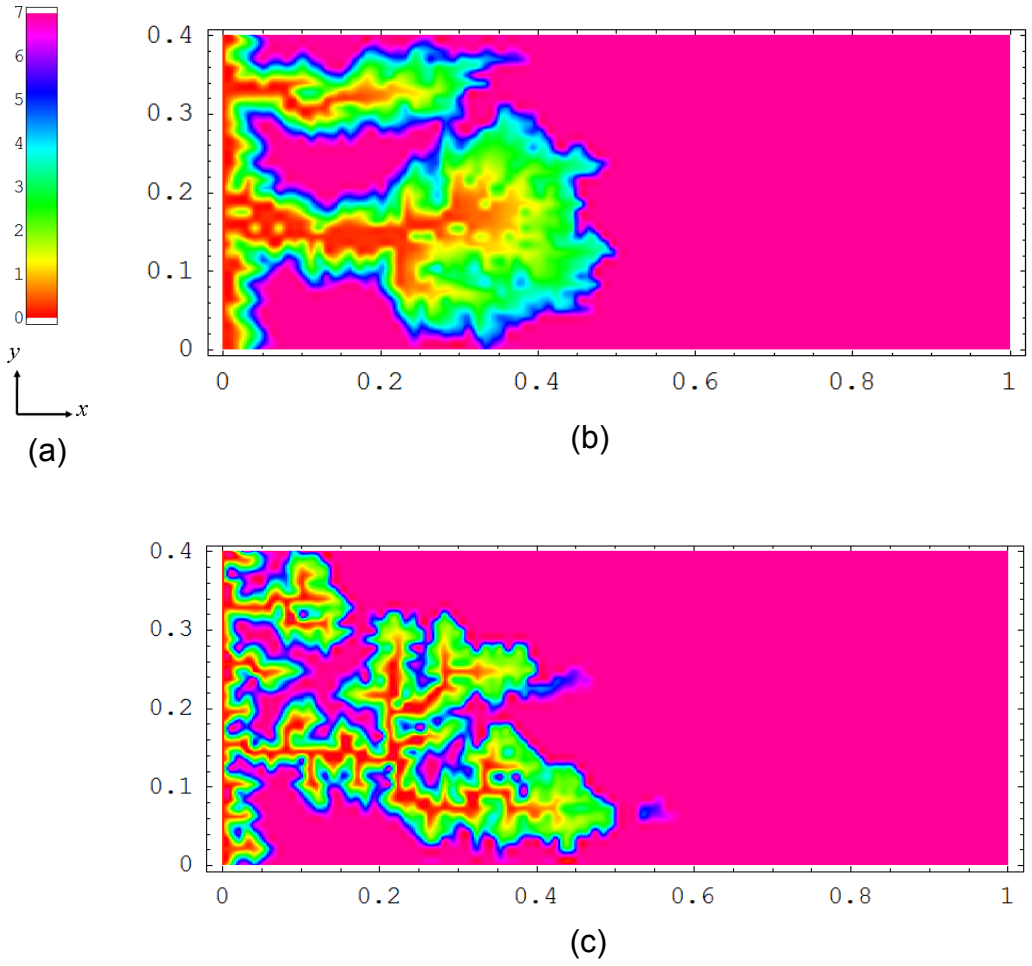


Figure 10.5: pH profile and demonstration of reaction and gelled zones (a) color-scale for pH, (b) Newtonian acids, and (c) in-situ gelling acids.

let concentration, pink color corresponds to brine solution, the yellow-orange color corresponds to reaction zones and green color corresponds to gelling zones. It is already shown that the width of gelling and reaction zone depends on flow and reaction parameters as well as rheological properties (Ratnakar et al., 2012). Since, unlike Newtonian acids, gelling acids lead to the gel formation around the wormhole, acid is forced to go around the gel plugs and thereby, creating a highly fractal wormhole pattern leading to more branching and more uniform stimulation. Thus, despite the additional branching in this case, the total amount of acid required for breakthrough with gelling acids is smaller as compared to Newtonian acids that

can be seen from PVBT-curve in Figure 10.3.

It may also be observed from Figure 10.4 that the average wormhole diameter in dissolution with Newtonian acids is larger than that obtained by using gelling acids. Scaling analysis, presented in appendix B, leads to the wormhole diameter, $d_w$, or characteristic transverse length scale, $\ell_T$, as follows:

$$d_w \approx \ell_T = \sqrt{\frac{\varepsilon D_e}{a_v}\left(\frac{1}{k_s}+\frac{1}{k_c}\right)}. \tag{10.7}$$

It is obtained by comparing the contribution of transverse dispersion to that of dissolution. In the mass-transfer controlled dissolution ($k_s >> k_c$), the wormhole diameter simplifies to $d_w \approx \sqrt{\frac{\varepsilon D_e}{a_v k_c}}$ that is independent of fluid rheology because both dispersion and mass-transfer coefficients decreases with the same factor due to increase in viscosity. However, in the current work, dissolution process is kinetically controlled ($k_s << k_c$), and wormhole diameter simplifies to $d_w \approx \sqrt{\frac{\varepsilon D_e}{a_v k_s}}$ that depends strongly on fluid rheology. Thus, in this case, the wormhole diameter is smaller for gelling acids as compared to Newtonian acids because the diffusion of protons is lowered due to gel formation. The same observation in Figure 10.4 validates the scaling criteria and simulations.

The dissolution patterns also depend on the injection rate of acidic solution as can be seen from Figure 10.6. For example, when acid is injected at fast rate, some acid exits unreacted and dissolves the medium slowly and uniformly that leads uniform dissolution. At very low injection rate, the acid dissolves whole face as it proceeds that leads to the face dissolution patterns. The intermediate injection rate leads to very localized porosity enhancement creating the narrow channels called wormholes. Similar trends are observed in experimental studies (Fredd and Fogler, 1998). It is interesting to note that the dissolution patterns formed by gelling acids and Newtonian acids are very different. Gelling acids leads to more

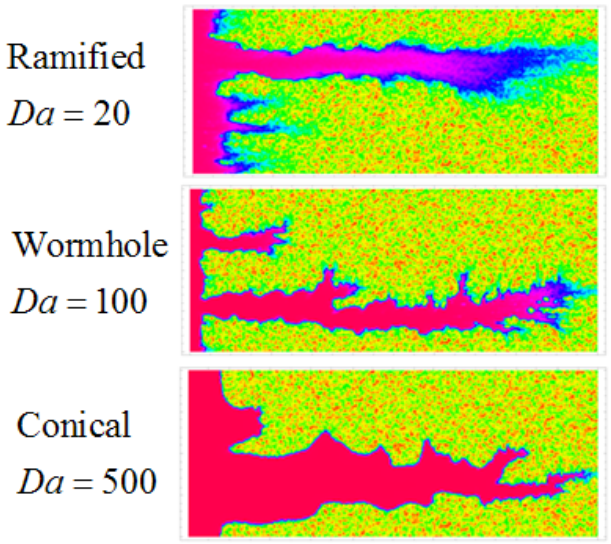


(a)

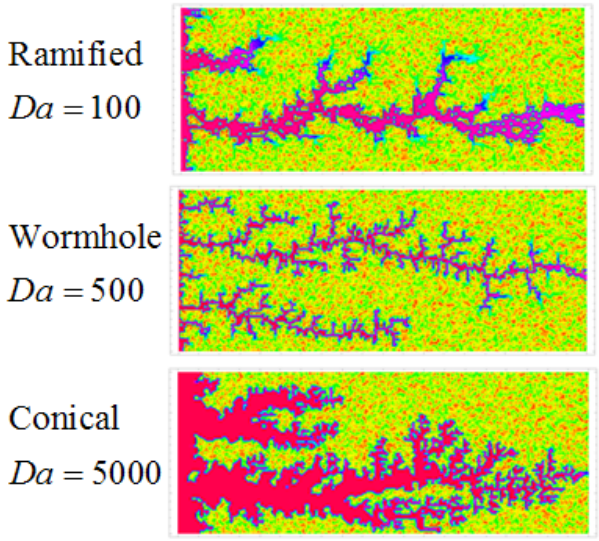


(b)

Figure 10.6: Dissolution patterns in a core of length 10 cm and height 4 cm at $\phi^2 = 0.047$ for (a) Newtonian acids and (b) in-situ gelling acids.

branching rather than widening the conducting channels that leads to more efficient stimulation. Since Newtonian acids preferentially flow through the least-resistance or high-perm zones, gelling acids are diverted from high-perm zones to the low-perm zones. There are two wormholes formed with both acids. But the wormhole in lower part of the core is dominant in case of stimulation with Newtonian acids which implies that the lower part of the core corresponds to high-perm zone and upper part corresponds to low-perm zones. But, when gelling acid is used for stimulation, the dominant wormhole is formed in upper part of the core. Thus, gelling acids enable us to achieve uniform stimulation by creating conducting channels in least-accessible low-perm zones. In the next section, we analyze the flow diversion from high-perm to low-perm zones in detail.

### 10.2.2 Dual Core Analysis

**Model Equations**

The 2-D version of the TSC model for dual core set-up in dimensionless form is given by

$$\frac{\partial}{\partial x}\left(M_{Xi}\frac{\partial p_i}{\partial x}\right)+\frac{\partial}{\partial y}\left(M_{Ti}\frac{\partial p_i}{\partial y}\right)=-\left(\frac{\partial u_{xi}}{\partial x}+\frac{\partial u_{yi}}{\partial y}\right)$$
$$=Da\left(1+\frac{\phi^2\gamma_{ri}\,r_i\mu_i}{Sh}\right)^{-1}A_{vi}\,c_{fi}; \tag{10.8}$$

$$\frac{\partial \pi_i}{\partial t}+\frac{\partial u_{xi}c_{fi}}{\partial x}+\frac{\partial u_{yi}c_{fi}}{\partial y}=\frac{1}{Pe_L}\left[\frac{\partial}{\partial x}\left(\varepsilon_i D_{eXi}\frac{\partial c_{fi}}{\partial x}\right)+\frac{\partial}{\partial y}\left(\varepsilon_i D_{eTi}\frac{\partial c_{fi}}{\partial y}\right)\right], \tag{10.9}$$

$$\frac{\partial\left(\varepsilon_i c_{pi}\right)}{\partial t}+\frac{\partial u_{xi}c_{pi}}{\partial x}+\frac{\partial u_{yi}c_{pi}}{\partial y}$$
$$=\frac{1}{Pe_L}\left[\frac{\partial}{\partial x}\left(\varepsilon_i D_{epXi}\frac{\partial c_{pi}}{\partial x}\right)+\frac{\partial}{\partial y}\left(\varepsilon_i D_{epTi}\frac{\partial c_{pi}}{\partial y}\right)\right], \tag{10.10}$$

$$\frac{\partial \varepsilon_i}{\partial t}=N_{ac}Da\left(1+\frac{\phi^2\gamma_{ri}\,r_i\mu_i}{Sh}\right)^{-1}A_{vi}\,c_{fi}\qquad i=1,2. \tag{10.11}$$

where

$$\pi_i = \varepsilon_i \left( c_{fi} + \frac{1}{N_{ac}} \right), \tag{10.12}$$

and effective mobility and viscosity term are given by

$$\begin{gathered} M_i = \frac{M_{0i} k_i}{\mu_i \left\| \mathbf{u}_i \right\|^{n-1}}, \\ \mu_i = \eta_{0i} \left( M_{0i} k_i \frac{\varepsilon_i}{\varepsilon_{0i}} \right)^{\frac{(1-n)}{2}} \left[ 1 + (\mu_{mi} - 1)\, Exp \left\{ \frac{-a \left( pH_i - pH_m \right)^2}{pH_i \left( 7 - pH_i \right)} \right\} \right] \\ \eta_{0i} = 1 + \left( \mu_{p0} - 1 \right) c_{pi}; \\ \frac{\mu_{mi} - 1}{\mu_{\max} - 1} = \frac{1 - \exp\left( -\alpha_1 c_{pi} \right)}{1 - \exp\left( -\alpha_1 \right)}. \end{gathered} \tag{10.13}$$

The inlet/initial/boundary conditions are given by

$$\begin{gathered} \varepsilon_i = \varepsilon_{0,i} + \widehat{f}; \;\; c_{f,i} = 0 \quad @ \quad t = 0; \\ u_i c_{f,i} - \frac{\varepsilon_i D_{ei,X}}{Pe_L} \frac{\partial c_{f,i}}{\partial x} = u_i; \;\; u_i c_{p,i} - \frac{\varepsilon_i D_{epi,X}}{Pe_L} \frac{\partial c_{p,i}}{\partial x} = u_i; \; @ \quad x = 0; \\ \sum_{i=1}^{2} (u_i) = 1; \;\; p_1 = p_2 \quad @ \quad x = 0; \\ p_i = 0; \frac{\partial c_{fi}}{\partial x} = 0; \; \frac{\partial c_{pi}}{\partial x} = 0 \quad @ \quad x = 1; \\ \frac{\partial p}{\partial y} = \frac{\partial c_f}{\partial y} = \frac{\partial c_p}{\partial y} = 0 \quad \text{on transverse boundaries,} \end{gathered} \tag{10.14}$$

and the structural property-relationship in dimensionless form is given as follows:

$$k_i = \frac{\varepsilon_i}{\varepsilon_{0,i}} \left( \frac{\varepsilon_i \left( 1 - \varepsilon_{0,i} \right)}{\varepsilon_{0,i} \left( 1 - \varepsilon_i \right)} \right)^{2\beta}; \; r_i = \sqrt{\frac{k_i \varepsilon_{0,i}}{\varepsilon_i}}; \quad A_{v,i} = \frac{\varepsilon_i}{\varepsilon_{0,i} r_i}; \quad \forall \;\; i = 1, 2. \tag{10.15}$$

Here also, we assume the initial permeability of high-perm core is $4$ times higher than that of low-perm core, i.e., $M_{10} = 1$, $M_{20} = 4$; $\varepsilon_{0,1} = \varepsilon_{0,2} = \varepsilon_0$; $\gamma_{r1} = 1$, $\gamma_{r2} = 2$; and $\gamma_{a1} = 1$, $\gamma_{a2} = 0.5$. Now we simulate the above 2-D version of model the

parameter values listed in Table9.1 and discuss the effect of injection rate on flow diversion.

**Flow Diversion**

Figure 10.5 shows that the pH range of gel formation lies right ahead to the reaction zone. Since viscosity of Newtonian acids remain constant, there is no diversion with these acids. But due to pH dependence viscosity of gelling acids, gel is formed ahead of the reaction zone and it forces the acid to go around the wormhole. Here, we consider a dual core set-up as shown in the Figure 9.1(b) and use 2-D version of the models (9.15 - 9.18) to study the mechanism of flow diversion.

The simulation results show that initially, flow is divided into the two cores based on initial permeability as can be seen from Figure 10.7 as observed from 1-D simulations. As the dissolution occurs, more acid is diverted to the low-perm core until gel reaches to its maximum width. Thereafter, the gel propagates with steady rate and offers almost constant resistance in both cores until the gel starts exiting one of the cores (Figure 10.7). The ratio of injection rates in low-perm to high-perm cores is shown in Figure (10.8). This ratio represents the amount of flow diversion. For example, if it is unity, it corresponds to maximum diversion and completely uniform stimulation. In the figure, it can be seen that this ratio reaches its maximum value in a very short time then starts decreasing slowly. In other words, the flow is diverted from high-perm to low-perm for very short time until gel is fully developed and exits the cores. Therefore, the intermittent injection or staged injection approach, where in-situ gelling fluid stage is followed by a neat acids (or brine solution) stage, may be more efficient than injecting a single stage of gelled acids and can lead to even more uniform diversion.

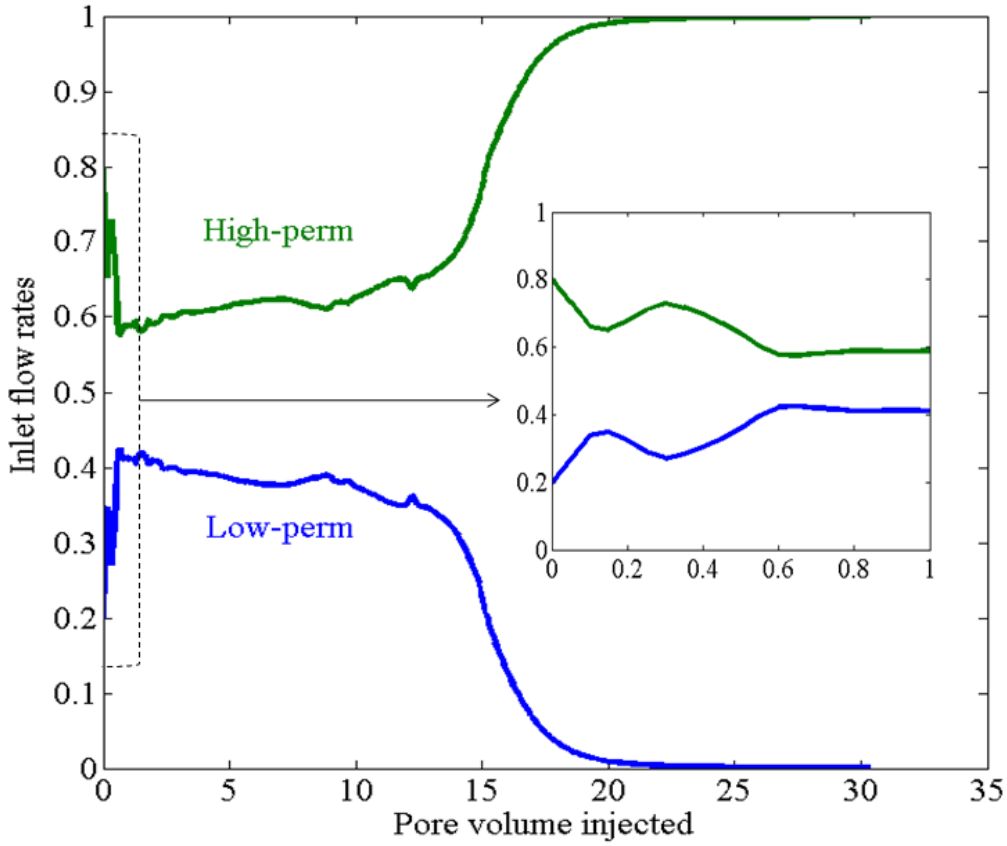


Figure 10.7: Flow diversion in a dual core set-up from 2-D simulation, inset show the plot at shorter times.

**Effect of Injection Rates**

Since, rate of increase in permeability (or mobility) is non-monotonic with inlet flow rates, it is possible that even when acidic solution is injected at constant rate, the rate of increase in mobility in both the low-perm or high-perm core may be different due to difference in flow regimes. For example, when inlet flow rate corresponds to the optimum in high-perm core, the low-perm core will lie in face or conical dissolution regime. In this case, the rate of increase in mobility may be higher in high perm core than the low-perm core. Similarly, when inlet flow rate corresponds to optimum in low-perm core, high-perm core will lie in uniform dissolution regime. And thus, in this case, rate of increase in mobility in low-perm core

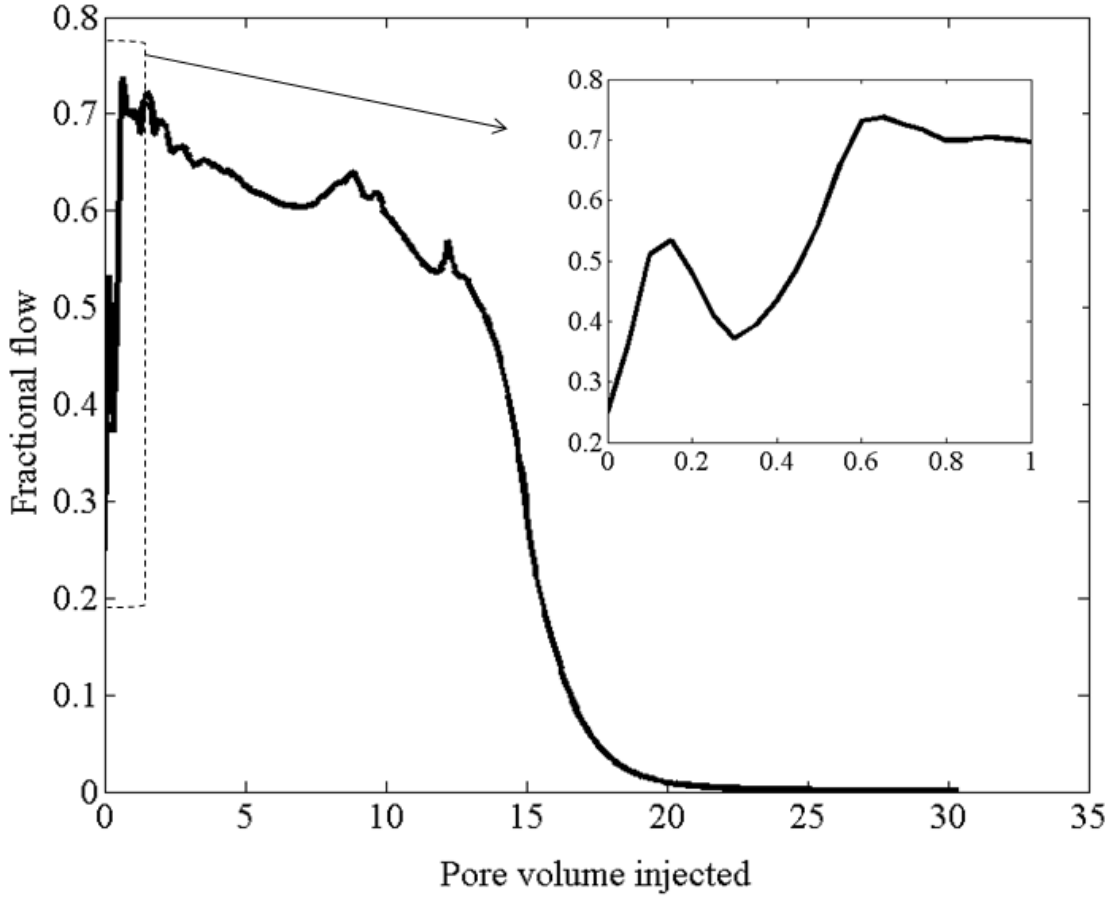

Figure 10.8: Fractional flow (ratio of flow rates in low-perm to high-perm cores), inset show the plot at shorter times.

may be quite high as compared to that in high-perm core. For these reasons, here we analyze the effect of injection rate on diversion for two cases: (i) when injection rate is corresponding to near the optimum in high-perm core, and (ii) when the injection rate is close to the optimum in the low-perm core. In the first case where injection rate corresponds to optimum in high-perm core, most of the acid flows in the high-perm core and less diversion occurs as can be seen from dissolution patterns in Figure 10.9(a). These patterns match the experimental results (Gomaa et al., 2011) shown in Figure 10.9(b) at least qualitatively. In this case, gel propagates faster in high-perm as compared to low-perm core and hence exits the high-perm core very fast while it stays in low-perm core for longer. As a result,

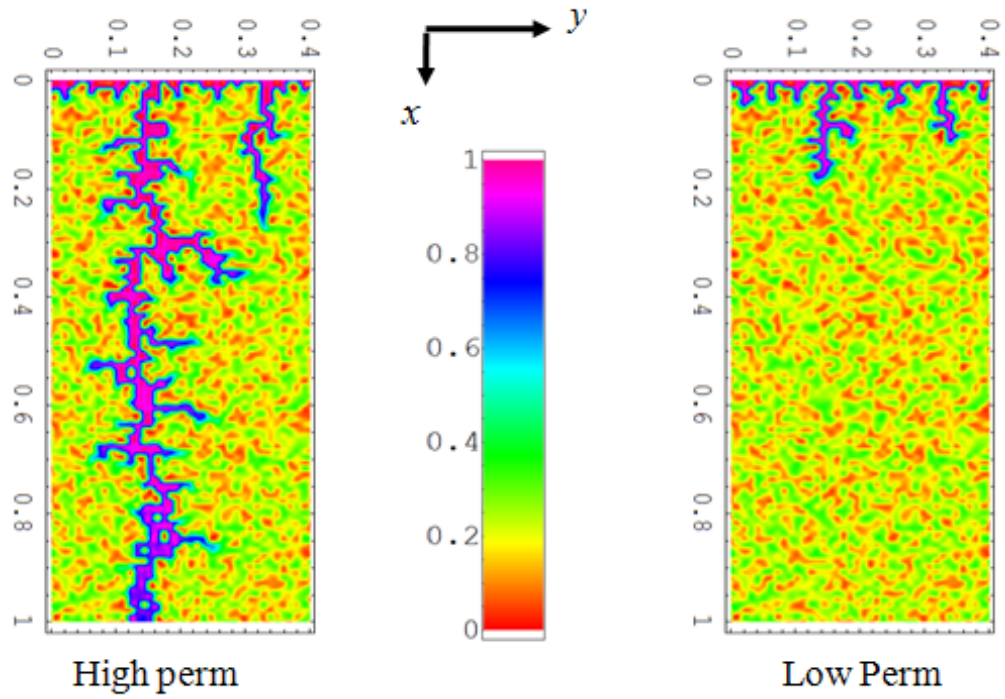


(a)

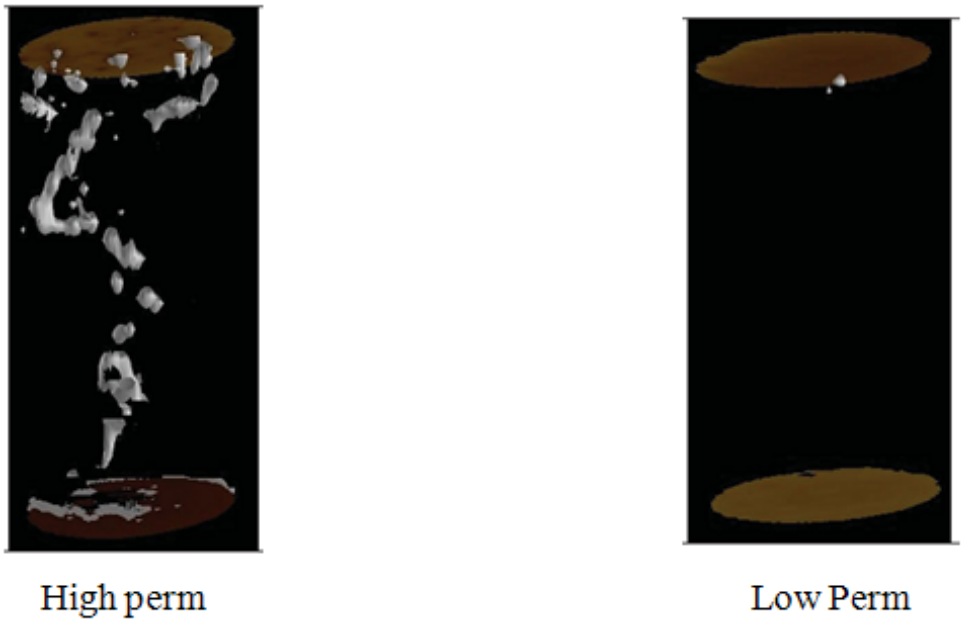


(b)

Figure 10.9: Disoolution pattern in dual core study when optimum exist in high-perm core (a) simulation results (b) experimental results (Gomaa, et al., 2011).

diversion occurs only for very short time and flow is diverted back from low-perm to high-perm core. In the second case where injection rate corresponds to optimum in low-perm core, acid penetrates the low-perm core to more depth and diversion occurs comparably for longer time as can be seen from Figure 10.10(a), which leads to more diversion from high-perm to low-perm core. The dissolution patterns in this case match the experimental observation (Gomaa et al., 2011) shown in Figure 10.10(b). Thus, by controlling the flow conditions, more uniform stimulation can be achieved using properly designed in-situ gelling acids.

Thus, 1-D and 2-D simulations provide sufficient insight on acidization process, at least qualitative. For example, dynamics of gel formation and mechanism of flow diversion remain same in both 1-D and 2-D simulations. In fact, results from low-dimensional simulations are easy to visualize and interpret. However, when simulation results need to be compared with experiments, 3-D simulations becomes very important as they are the correct representation of the experiments. In addition, 1-D and 2-D simulations predict the qualitative trends correctly but quantitatively may not be reliable. Therefore, in the next section, we use 3-D version of the model and compare the simulation results with available experimental data.

## 10.3 Three-dimensional Simulations of Wormholing with In-situ Gelling Acids

In this section, we consider the single core set-up as shown in Figure 9.1(a) with dimensions 5cm $\times$ 2cm $\times$ 2cm, and, simulate the 3-D version of the TSC model given in dimensionless form as follows:

$$\frac{\partial}{\partial x}\left(M_X\frac{\partial p}{\partial x}\right)+\frac{\partial}{\partial y}\left(M_T\frac{\partial p}{\partial y}\right)+\frac{\partial}{\partial z}\left(M_T\frac{\partial p}{\partial z}\right)$$
$$=-\left(\frac{\partial u_x}{\partial x}+\frac{\partial u_y}{\partial y}+\frac{\partial u_z}{\partial z}\right)=Da\left(1+\frac{\phi^2 r\,\mu}{Sh}\right)^{-1}A_v\,c_f, \qquad (10.16)$$

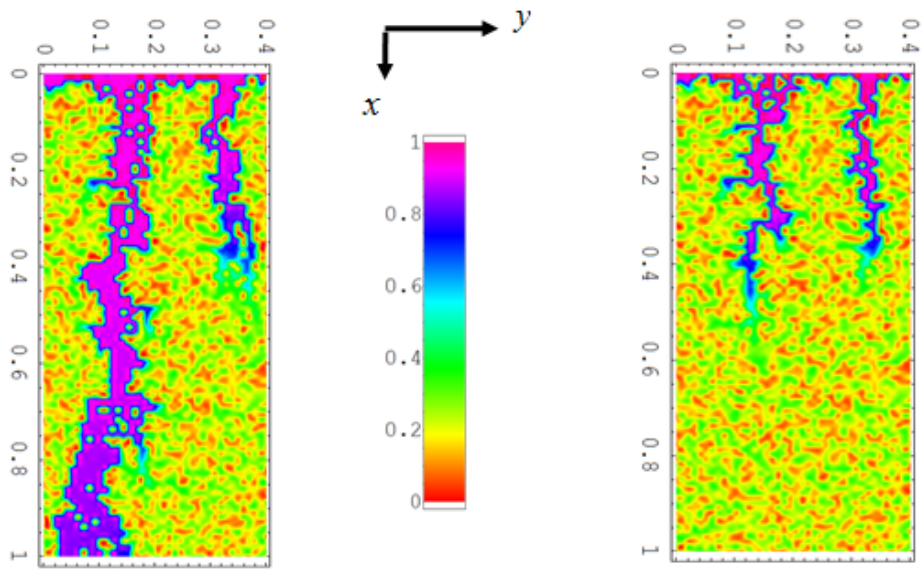


(a)

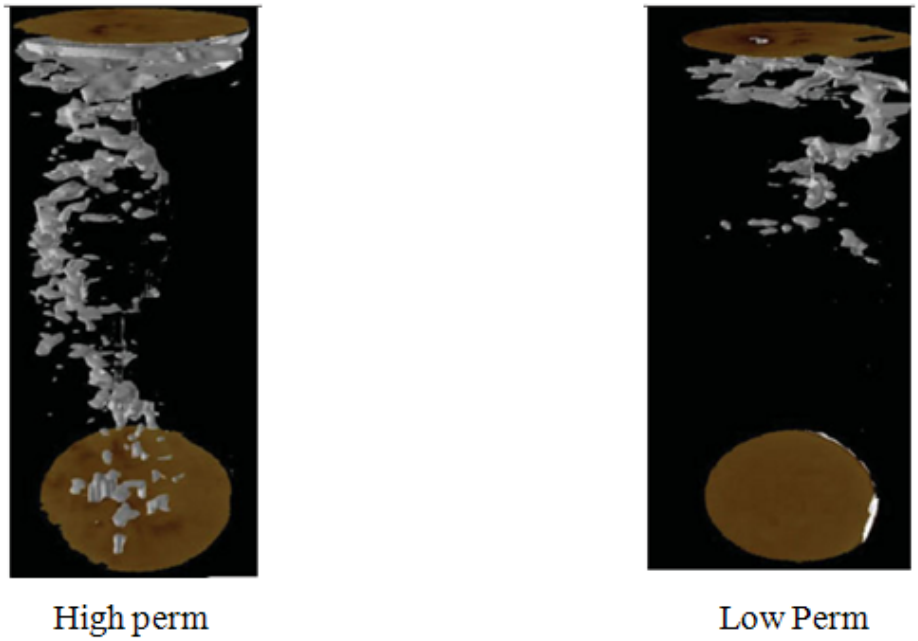


(b)

Figure 10.10: Disoolution pattern in dual core study when optimum exist in low-perm core (a) simulation results (b) experimental results (Gomaa, et al., 2011).

$$\frac{\partial \pi}{\partial t} + \frac{\partial u_x c_f}{\partial x} + \frac{\partial u_y c_f}{\partial y} + \frac{\partial u_z c_f}{\partial z} = \frac{1}{Pe_L}\left[\frac{\partial}{\partial x}\left(\varepsilon D_{eX}\frac{\partial c_f}{\partial x}\right) + \frac{\partial}{\partial y}\left(\varepsilon D_{eT}\frac{\partial c_f}{\partial y}\right) + \frac{\partial}{\partial z}\left(\varepsilon D_{eT}\frac{\partial c_f}{\partial z}\right)\right], \quad (10.17)$$

$$\frac{\partial (\varepsilon c_p)}{\partial t} + \frac{\partial u_x c_p}{\partial x} + \frac{\partial u_y c_p}{\partial y} + \frac{\partial u_z c_p}{\partial z} = \frac{1}{Pe_L}\left[\frac{\partial}{\partial x}\left(\varepsilon D_{epX}\frac{\partial c_p}{\partial x}\right) + \frac{\partial}{\partial y}\left(\varepsilon D_{epT}\frac{\partial c_p}{\partial y}\right) + \frac{\partial}{\partial z}\left(\varepsilon D_{epT}\frac{\partial c_p}{\partial z}\right)\right], \quad (10.18)$$

$$\frac{\partial \varepsilon}{\partial t} = N_{ac} Da \left(1 + \frac{\phi^2 r\, \mu}{Sh}\right)^{-1} A_v\, c_f\,, \quad (10.19)$$

where subscript $'X'$ and $'T'$ denote the axial ($x-$) and transverse ($y-$ and $z-$) directions, respectively. The mobility, $M$, and effective viscosity term, $\mu$, are given by

$$M = \frac{k}{\mu \left\|\mathbf{u}\right\|^{n-1}},$$
$$. \qquad \mu = \eta_0 \left(k\frac{\varepsilon}{\varepsilon_0}\right)^{\frac{(1-n)}{2}} \left[1 + (\mu_m - 1)\, Exp\left\{\frac{-a\,(pH - pH_m)^2}{pH\,(7 - pH)}\right\}\right]; \quad (10.20)$$
$$\eta_0 = 1 + \left(\mu_{p0} - 1\right) c_p;$$
$$\frac{\mu_m - 1}{\mu_{\max} - 1} = \frac{1 - \exp\left(-\alpha_1 c_p\right)}{1 - \exp\left(-\alpha_1\right)}.$$

and $\pi$ is given by

$$\pi = \varepsilon\left(c_f + \frac{1}{N_{ac}}\right). \quad (10.21)$$

The inlet/initial/boundary conditions are given by

$$\varepsilon = \varepsilon_0 + \widehat{f};\ c_f = 0 \quad @ \quad t = 0; \quad (10.22)$$

$$uc_f - \frac{\varepsilon D_{e,X}}{Pe_L}\frac{\partial c_f}{\partial x} = u_{in} c_{fin};\ u = u_{in};\ \ @ \quad x = 0; \quad (10.23)$$

$$uc_p - \frac{\varepsilon D_{ep,X}}{Pe_L}\frac{\partial c_p}{\partial x} = u_{in} c_{pin} \quad @ \quad x = 0; \quad (10.24)$$

$$p = 0;\ \frac{\partial c_f}{\partial x} = 0;\ \frac{\partial c_p}{\partial x} = 0 \quad @ \quad x = 1; \tag{10.25}$$

$$\frac{\partial p}{\partial y} = \frac{\partial c_f}{\partial y} = \frac{\partial c_p}{\partial y} = 0 \quad @ \ y = 0, L_y \tag{10.26}$$

$$\frac{\partial p}{\partial z} = \frac{\partial c_f}{\partial z} = \frac{\partial c_p}{\partial z} = 0 \quad @ \quad z = 0, \ \ L_z, \tag{10.27}$$

where $L_y\,(= 0.4)$ and $L_z\,(= 0.4)$ are dimensionless size of the domain in $y-$ and $z-$ directions, respectively. The structural property-relationship in dimensionless form is given as follows:

$$k = \frac{\varepsilon}{\varepsilon_0}\left(\frac{\varepsilon\,(1-\varepsilon_0)}{\varepsilon_0\,(1-\varepsilon)}\right)^{2\beta};\ r = \sqrt{\frac{k\varepsilon_0}{\varepsilon}};\quad A_v = \frac{\varepsilon}{\varepsilon_0 r}. \tag{10.28}$$

Now, we solve the above model with parameter values given in Table 9.1 by using the numerical technique described in earlier chapter and present the results below.

### 10.3.1 Overall pressure drop

The main difference between gelling acids and Newtonian acids is the fluid rheology. Because of the dependence of fluid viscosity on pH for gelling acids, it is found that the pressure response (pressure drop across the core with time) depends on the type of fluid being injected. This may be seen in Figure 10.11(a) and (b) where overall pressure drop across the core is plotted against the number of pore volumes of acid injected. It can be seen that the pressure drop across the core for Newtonian acids decreases monotonically as dissolution occurs but for gelled acids, the pressure first increases and then decreases which is also found in the experiments (Gomaa and Nasr-El-Din, 2010) as in Figure 10.11(c). As the dissolution proceeds, the porosity and hence permeability is increased, so for Newtonian acids where viscosity is constant, pressure drops monotonically. But in case of gelling acids, gel is formed that offers high resistance to the flow and hence pressure is increased tremendously. Once the gel is fully developed (i.e., the point of maximum resistance is achieved), it is pushed forward with steady speed by the incoming

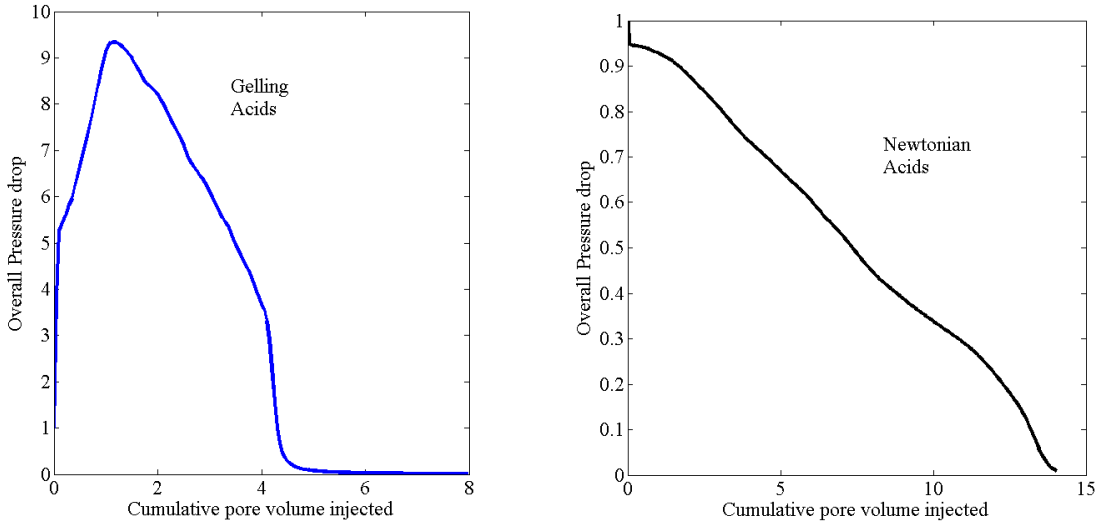


(a) (b)

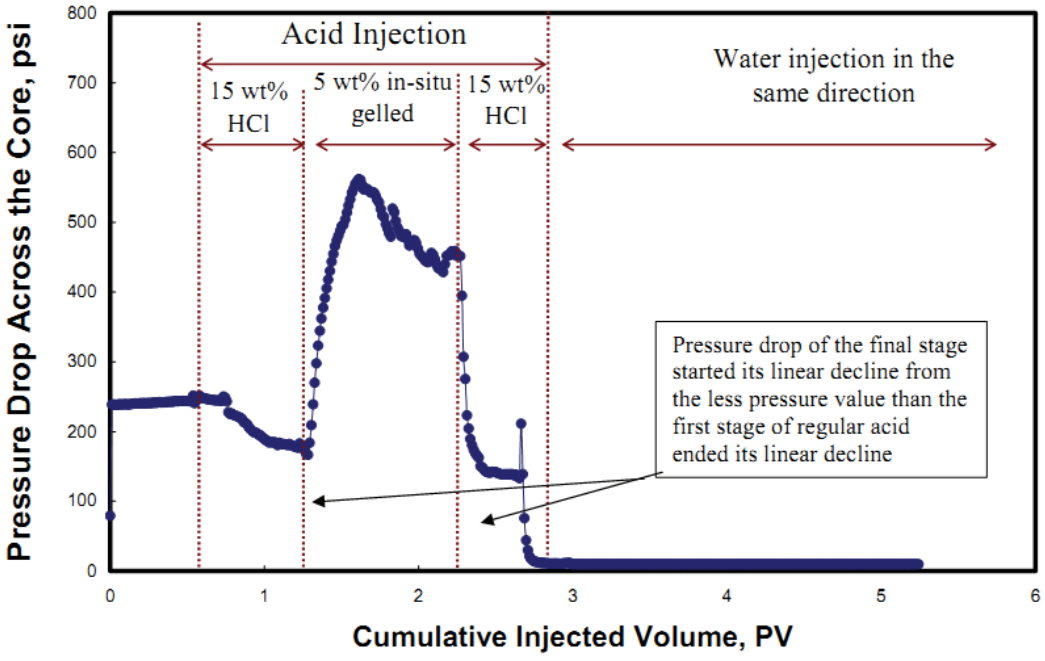


(c)

Figure 10.11: Comparison of pressure profile from 3-D simulations and experiments; (a) Pressure profile for gelling acids, (b) pressure profile for Newtonian acids, and (c) experimental profile (Gomaa, et al., 2011).

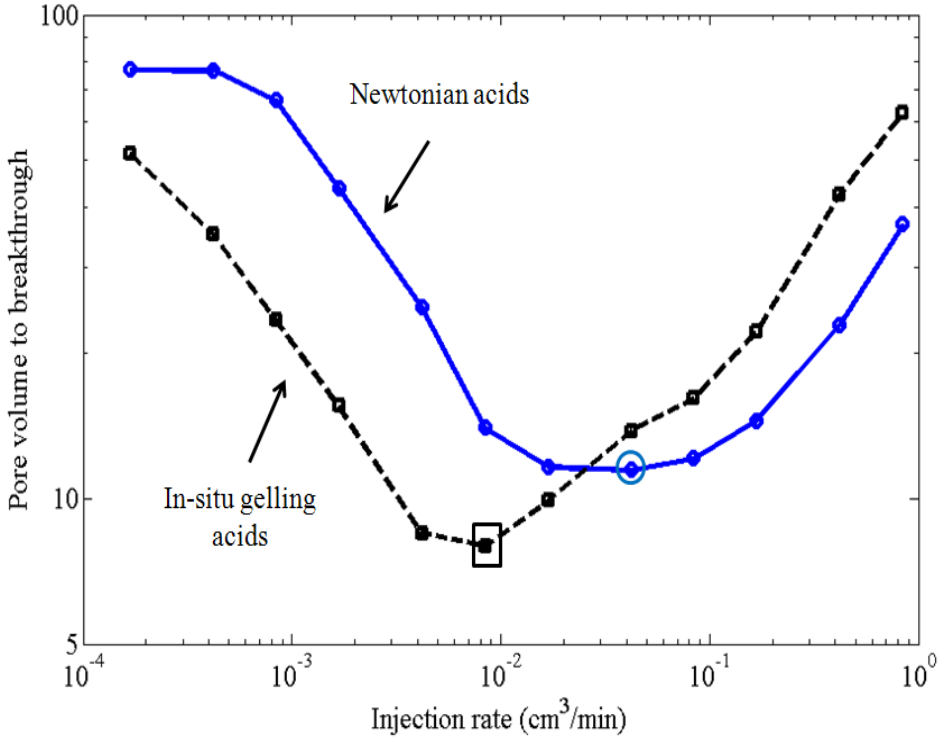


Figure 10.12: Breakthrough curves for gelling acids and newtonian acids from 3-D simulation at $\phi^2 = 0.047$.

injecting fluid. As a result, the overall permeability increases but viscosity remains almost constant. Thus, the pressure starts decreasing. This non-monotonic pressure profile for gelling acids plays very important role in designing and interpreting laboratory core experiments. Note that in these simulations, we use 3-dimensional version of the model for a single core set-up with dimensions 5cm $\times$ 2cm $\times$ 2cm, where acid is injected at constant rate and exit pressure is kept fixed. Once the gel starts exiting, the pressure decreases sharply and breakthrough is achieved eventually.

### 10.3.2 Breakthrough Curves and Dissolution Patterns

Here, we define breakthrough time as the time it takes to increase the overall mobility by a factor 100. When pore volume of acid to breakthrough (PVBT) is plotted against injection rate as in Figure 10.12, the model predicts the trend that

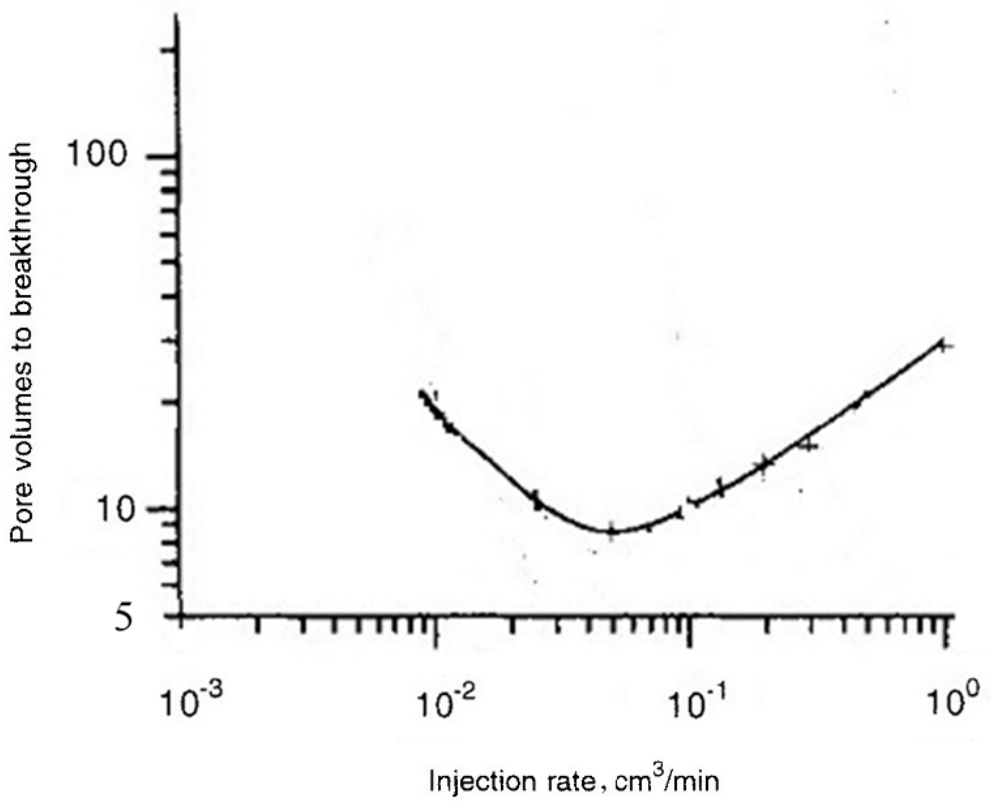


Figure 10.13: Experimental breakthrough curve for DTPA (Fredd and Fogler, 1998).

is similar to that found in lab experiments and for Newtonian acids, it matches very close to that of DTPA (Fredd and Fogler, 1998) shown in Figure 10.13. In fact, it can be seen from the figure 10.12 for Newtonian acids and Figure 10.13, the optimum injection rate is very close to each other ($\sim 0.05$ cm$^3\,\mathrm{min}^{-1}$) and the pore volume to breakthrough, $PV_{BT}$ at the optimum is also very close ($\sim 10\ PV$). It should be noted that the optimum injection rate for gelling acids is smaller as compared to the Newtonian acids and matches the scaling criteria discussed in earlier sections. In case of gelling acids where gel is formed during dissolution, the viscosity increases enormously that lowers the diffusivity and mass-transfer coefficient. Therefore, the optimum stimulation for gelling acids corresponds to smaller injection rate as compared to Newtonian acids. It is interesting to note from Figures 10.14(a) and (b) that the dissolution pattern formed at breakthrough by gelling acids and by Newtonian

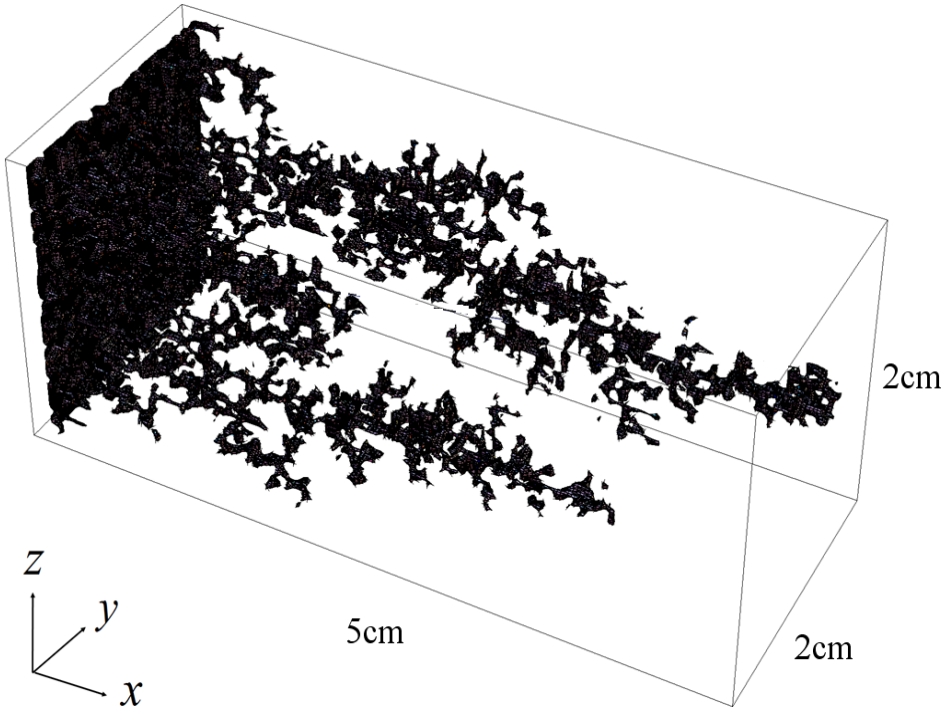


(a)

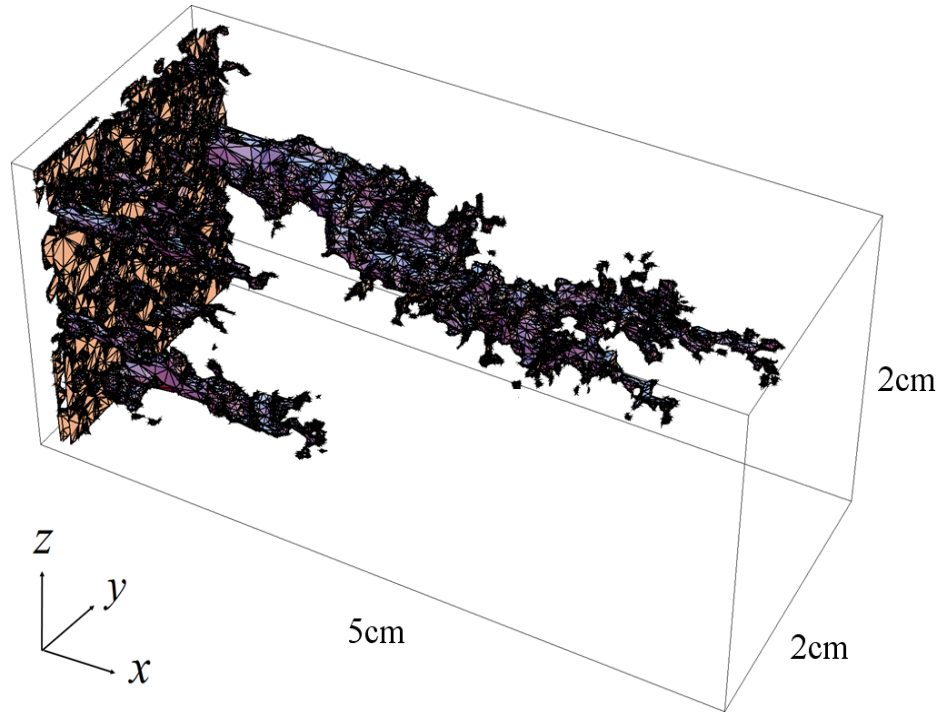


(b)

Figure 10.14: 3-D dissolution patterns at optimum for (a) Gelling acids ($0.01cm^3s^{-1}$) and (b) Newtonian acids ($0.04cm^3s^{-1}$).

acids are very different. Here, we start with 3-dimensional randomly distributed porosity field with average porosity, $\langle\varepsilon_0\rangle$=$0.2$, heterogeneity magnitude, $\Delta\varepsilon = 0.15$ and heterogeneity length scale, $\ell_{HT} = 0.5mm$, and obtain these dissolution patterns by contour plot of porosity = 0.9 at breakthrough. We can see from these patterns that use of gelling acids leads to more branching rather than widening the conducting channel (as observed from 2-D simulations) and hence leads to more uniform stimulation.

Similarly, the effect of inlet flow rate on dissolution patterns can be seen from Figure 10.15, where dissolution patterns are shown for three dissolution regimes, namely, conical, wormhole and ramified, for in-situ gelling acids, Newtonian acids and from experiments (Fredd and Fogler). The corresponding regime is shown on the breakthrough curve. It can be seen from this figure that the qualitative results from simulation match with that from experiments. For example, the breakthrough curve has a minima, i.e., the rate of increase in mobility of the core is non-monotonic with injection rate and is the highest at some intermediate injection rate. The number of pore volume to breakthrough at this intermediate injection rate is least. This intermediate injection rate leads to thinner channels (wormholes) in the core as compared to the case when acidic solution is injected with lower or higher flow rates than this intermediate value. When acid is injected with higher rate, the some acid gets out unreacted that gives the ramified dissolution patterns. Similarly, when acid is injected with lower rates, it proceeds slowly and dissolve more rocks that creates conical/face dissolution patterns.

## 10.4 Conclusion and Discussion

We used the 2-D and 3-D version of the two-scale continuum model to analyze the stimulation of core laboratory experiments with in-situ gelling acids for the case of constant injection rate. We showed that effective mobility of the core increases monotonically when Newtonian acids are used for stimulation, which is also found

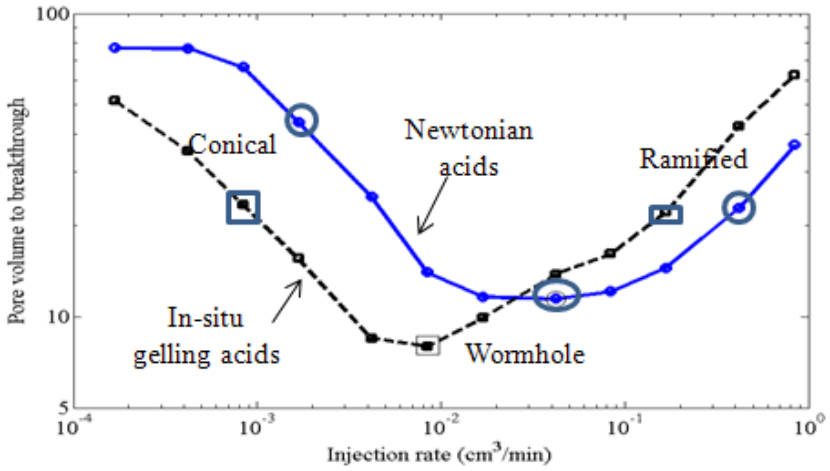


(a)

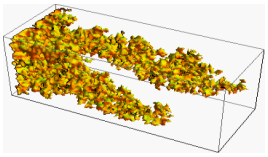

conical

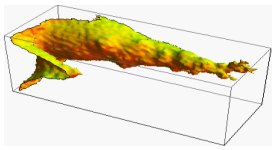

conical

conical

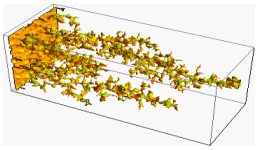

wormhole

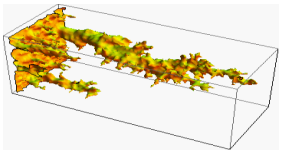

wormhole

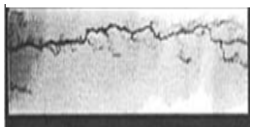

wormhole

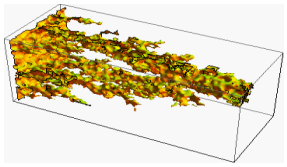

ramified

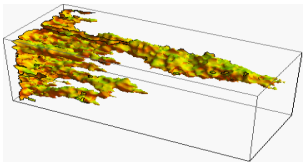

ramified

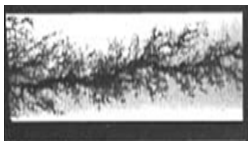

ramified

(b) (c) (d)

Figure 10.15: (a) Breakthrough curves for in-situ gelling acids and Newtonian acids; Dissolution patterns in wormhole, conical and ramified dissolution regimes (b) for in-situ gelling acids, (c) for Newtonian acids, and (d) from experiments (Fredd and Fogler, 1998).

in the laboratory experiments. However, the effective mobility of the core changes non-monotonically when in-situ gelled acids are used for stimulation. Due to dissolution, porosity of the rock increases and so, the permeability of the rock increases. However, in case of in-situ gelling acids, due to the gel formation, viscosity of the fluid increases enormously and so the effective mobility decreases as along as gel is present in the core. When gel gets out, the effective mobility starts increasing continuously.

The rate of increase in mobility is found to be the highest for some intermediate injection rate that leads to the existence of a minimum in the breakthrough curve (as observed in experimental studies). This optimum injection rate depends on types of acid. For example, we showed using scaling analysis that the optimum injection rate for in-situ gelling acid is smaller by a factor $\langle \mu \rangle_c$ and $\sqrt{\langle \mu \rangle_c}$ in limits of mass-transfer and kinetically controlled dissolutions, respectively, when compared with that for Newtonian acids. In case of in-situ gelling acids, gel is formed during dissolution process that not only decreases the molecular diffusivity of the protons but also hinders the transfer of protons from bulk to the rock surface. As a result, effective rate of reaction is retarded or the reaction time is increased. Therefore, to form a wormhole, acidic solution needs to be injected at smaller rates so that it has high enough convection time to compete with reaction time, which is verified by simulations.

We also show that the gel front is ahead of the reaction front in case of in-situ gelling acids. Hence, when in-situ gelling acids are injected, protons are forced to go around the wormhole and bypass the high-perm path. As a result, least-accessible low-perm zones are stimulated and more branched but thinner wormholes are created. In fact, the wormhole diameter, when estimated using scaling analysis, is found to be smaller for in-situ gelling acids as compared to that for Newtonian acids. Due to thinner and branched wormholes, the number of pore

volumes to breakthrough for in-situ gelling acids is less as compared to that of Newtonian acids. In addition, the dissolution patterns obtained from 2-D and 3-D simulations match the qualitative trends of experimental observations, i.e., the conical wormholes are formed at smaller injection rate, ramified wormholes are formed at higher injection rates, and, thinner and more branched wormholes are formed at the intermediate injection rates.

The effect of inlet flow rate on flow-diversion is also presented. We show that for optimal stimulation, inlet flow rate should correspond to wormholing in low-perm core and uniform or ramified in high-perm core. Finally, when compared the results from simulations and scaling laws to that with available experimental data, we showed that 2-D simulations results predict the experimental trends very well; and 3-D simulation results matches very accurately with experimental observation. For example, we were able to match the optimum injection rate and $PV_{BT}$ for DTPA with that of experimental results by Fredd and Fogler (1998).

# Chapter 11 Summary and Future Scope of the Work

## 11.1 Summary

One of the main results of this work is the formulation of an empirical four-parameter model to describe the effect of pH on viscosity of in-situ gelling acids that form gel in certain pH range. The model fits the experimental data (Rose, 2004) very well and describes all the key feature of the rheology of in-situ gelling acids. The four parameters $\mu_0$, $\mu_m$, $pH_m$ and $a$ involved in the model signify the base viscosity (at pH =7), maximum increase in viscosity from its base value, pH point where viscosity is maximum and pH-range of gel formation, respectively. This model is the simplest to implement. For example, three parameters, $\mu_0$, $\mu_m$ and $pH_m$, of this model can be evaluated directly from the profile of viscosity against pH. In other words, only one parameter is required to be determined by regression, which is much easier work as compared to regression in terms of more than one parameter.

A second result of this work is the extension of the two-scale continuum model to describe reaction and transport of in-situ gelling acids in carbonate rocks. We developed equivalent Darcy law for in-situ gelling acids, where permeability depends only on the porous media while the effect of non-Newtonian and gelling behaviors are accounted in the effective viscosity term that depends on temperature, pH and other medium properties. We also used the well known Stokes-Einstein relation to account for the effect of viscosity on the diffusivity of acid and additives.

We solve the two-scale continuum model, using operator splitting and implicit finite volume discretization where discretized equations are solved by advanced multigrid techniques, to analyze the stimulation of single and dual core laboratory experiments with in-situ gelling acids for the case of constant injection rate. As observed in experimental studies, our simulation results show that when Newtonian

acids are injected, the overall pressure drop across the core decreases monotonically with pore volume of acid injected. But when in-situ gelled acids are used, the pressure increases first and then decreases. The increases in pressure is due to gel formation. When in-situ gelled acids is injected, it dissolves the rock and increases the pH. As a result, polymer start cross-linking and form a gel that increases the viscosity of the fluid enormously. Therefore, even though dissolution increases permeability by increasing porosity, very high increase in viscosity leads to the large decrease in effective mobility and hence large increase in overall pressure drop across the core. Therefore, it is very important to estimate the increase in pressure drop for proper design of the laboratory experiments.

This process occurs in three stages. The first stage is the gel development where gel formation starts and gel width keeps increasing. At this stage, permeability not changed much but due to gel formation viscosity of the fluid increases enormously. So, the effective mobility drops very low and overall pressure drop across the core builds up very high. The next stage is gel propagation where gel has achieved its maximum width and propagates with a steady speed. At this stage, viscosity is almost constant while permeability keeps increasing slowly. As a result, effective mobility starts increasing slowly and overall pressure drop starts decreasing slowly until the third stage is reached which is gel exiting the core. This is the last stage where gel starts exiting the core. So the viscosity drops down very fast or the effective mobility increases very fast and hence, overall pressure drop start decreasing very fast.

The rate of increase in mobility is found to be the highest at some intermediate injection rate rather than at low of high flow rate. It leads to the existence of a minimum in the breakthrough curve, which is also observed in experimental studies. This optimum injection rate depends on types of acid. For example, we showed using scaling analysis that the optimum injection rate for in-situ gelling acid

is smaller by a factor $\langle\mu\rangle_c$ and $\sqrt{\langle\mu\rangle_c}$ in limits of mass-transfer and kinetically controlled dissolutions, respectively, when compared with that for Newtonian acids. In case of in-situ gelling acids, gel is formed during dissolution process that not only decreases the molecular diffusivity of the protons but also hinders the transfer of protons from bulk to the rock surface. As a result, effective rate of reaction is retarded or the reaction time is increased. Therefore, to form a wormhole, acidic solution needs to be injected at smaller rates so that it has high enough convection time to compete with reaction time, which is verified by simulations.

We also show that the gel front is ahead of the reaction front in case of in-situ gelling acids. Hence, when in-situ gelling acids are injected, protons are forced to go around the wormhole and bypass the high-perm path. As a result, least-accessible low-perm zones are stimulated and more branched but thinner wormholes are created. In fact, the wormhole diameter, when estimated using scaling analysis, is found to be smaller for in-situ gelling acids as compared to that for Newtonian acids. Due to thinner and branched wormholes, the number of pore volumes to breakthrough for in-situ gelling acids is less as compared to that of Newtonian acids. In addition, the dissolution patterns obtained from 2-D and 3-D simulations match the qualitative trends of experimental observations, i.e., the conical wormholes are formed at smaller injection rate, ramified wormholes are formed at higher injection rates, and, thinner and more branched wormholes are formed at the intermediate injection rates.

We presented the scaling analysis for gel dynamics such as gel width and gel propagation in a single core, and showed that the speed of both (reaction and gel) fronts depends on the injection velocity as well as on the acid capacity number. We also showed that while the front speed is independent of the rheological parameters, the gel width depends strongly on the rheological parameters. The width of both the reaction and the gel fronts larger in high-perm core and increases with

injection rate. The larger gel width in the high-perm core is the key mechanism for flow diversion. Due to larger gel width, the high-perm core is offered more resistance that diverts the acid to flow through low-perm core. We also obtained an expression for the amount of diversion in terms of rheological parameters, which can be used to design the injecting fluids to achieve maximum diversion by controlling the rheological parameters. The flow diversion, $fr,$ can also be maximized by using intermittent flow conditions where acidic and non-reacting solutions are switched periodically until breakthrough.

The effect of inlet flow rate on flow-diversion is also presented. We show that for optimal stimulation, inlet flow rate should correspond to wormholing in low-perm core and uniform or ramified in high-perm core. Finally, we compare the results from simulations and scaling laws to that from experiments available in literature and showed that 1-D and 2-D simulations results very well predict the experimental trends; and 3-D simulation results matches very accurately with experimental observation. For example, we were able to match the optimum injection rate and $PV_{BT}$ for DTPA with that of experimental results by Fredd and Fogler (1998). Similarly the scaling criteria developed in this work for gel properties such as front width and speed, optimum injection rate and amount of flow diversion, matches very well with the simulation results.

## 11.2 Future Work

The diverting acids like in-situ gelling acids have very complex rheological behavior that depends strongly on pH of the medium and concentration of additives such as polymer, cross-linkers and breakers. They are also non-Newtonian (shear thinning) in nature. The current (six parameter) rheological model is empirical. therefore, one of the important extension of the current work can be evaluation of parameters based on fluid composition and chemistry of gel formation (kinetics of cross-linking and gel break-up).

The two-scale continuum model developed here does not account the effect of polymer filtration or adsorption/desorption. In some cases, cross-linked polymer molecules are very big in size as compared to micropores in carbonates, and so, they get filtered as dissolution proceeds. As a results, diffusivity and reaction rate of protons with carbonates changes that change the gel formation and its dynamics. Therefore, the current model can be extended to include the effect of filtration or adsorption/desorption of polymers and cross-linkers. In addition, we have taken all additives (polymer, cross-linker and breakers) as a single species assuming they all have similar properties. However, in general, they may possess different physio-chemical properties such. In that case, the current model may be extended in terms of more concentration modes corresponding to these additives, which can also account for kinetics of cross-linking and breaking.

Here, we have assumed the reaction is irreversible and occurs in a single step, which might not be the case for retarding acids such as EDTA, DTPA etc.). In addition, $CO_2$, produced due to dissolution of carbonates with acids, are dissolved in the solution and form carbonic acids. As a result, ionic equilibrium is achieved that restrict the pH in narrow range (around pH 4). This effect is very important for in-situ gelling acids as the pH-range of gel formation may overlap this equilibrium. So, the another important extension of the work is to include the multistep chemistry and effect of ionic-equilibria in dissolution process.

We presented scaling analysis for gel dynamics, gel width, propagation speed, etc. and validated with numerical simulations. Another important extension of current work is to design the lab/core experiment to verify the model as well as the results predicted by scaling analysis.

Other possible extensions include the analysis 3-D models, radial flow and field scale operation to estimate wormhole properties such as density, length, fractal dimension etc. in extended domains; improvement of pore scale mass-transfer and

dispersion effects; analysis of constant pressure operation, analysis of acidification with time dependent inputs; sensitivity analysis with respect to reaction kinetics and structure-property-relations; and, extension to other diverting acids such as emulsified and viscoelastic acids.

# References


Ambrosetti, A. and Prodi, G., *A Primer of Nonlinear Analysis* (Cambridge University Press, NY, 1993).

Amro, M.M., "Extended Matrix Acidizing Using Polymer-Acid Solutions," SPE 106360 (2006).

Aris, R., "On the dispersion of a solute in a fluid flowing through a tube," Proc. Roy. Soc. Lond. A **235,** 67 (1956).

Balakotaiah, V. , "Hyperbolic homogenized models for describing dispersion effects in chromatographs and reactors," Korean Journal of Chem. Eng. **21,** 318 (2004).

Balakotaiah, V. , "Comment on "Taylor dispersion with absorbing boundaries: A stochastic approach," Physical Review Letters **100,** Issue 2 (2008).

Balakotaiah, V. and Chakraborty, S., "A Novel approach for describing micromixing effects in homogeneous reactors," Chemical Engineering Education., **36**, 250 (2002).

Balakotaiah, V. and Chang, H-C., "Dispersion of chemical solutes in chromatographs and reactors," Phil. Trans. R. Soc. Lond. A. **351,** 39 (1995).

Balakotaiah, V. and Chang, H-C., "Hyperbolic homogenized models for thermal and solutal dispersion," SIAM J. Appl. Math. **63**, 1231 (2003).

Balakotaiah, V. and Dommeti, S.M.S., “Effective models for packed bed catalytic reactors”, *Chem. Eng. Sci.*, **54**, 1621–1638 (1999).

Balakotaiah, V., Luss, D. and Keyfitz, B.L., "Steady state multiplicity analysis of lumped parameter systems described by a set of algebraic equations," Chem. Eng. Commun. **36,** 121 (1985).

Balakotaiah, V., and Ratnakar, R.R., "On the Use of Transfer and Dispersion Coefficient Concepts in Low-dimensional Diffusion-Convection-Reaction Models," Chem. Eng. Research and Design **88,** Issue 3, 342 (2010).

Balakotaiah, V. and West, DH., "Shape normalization and analysis of the mass transfer controlled regime in catalytic monoliths," Chem Eng Sci., **57**, 1269 (2002).

Baldyga, J., and Bourne, J. R., *Turbulent Mixing and Chemical Reactions* (Wiley, New York, 1999).

Barton, N.G., "On the method of moment for solute dispersion," J. Fluid Mech. **126,** 205 (1983).

Bazin, B., "From matrix acidizing to acid fracturing: A laboratory evaluation of acid/rock interactions," SPE Prod. & Facilities, 22 (2001).

Bazin, B., Roque, C. and Bouteca. M., "A Laboratory Evaluation of acid propagation in relation to acid fracturing: results and interpretation," European Formation Damage Conference, SPE 30085 (1995).

Bhattacharya, M., Harold, M.P., Balakotaiah, V., "Shape normalization for catalytic monoliths," Chem. Eng. Science, **59**, 3737 (2004).

Bird, R.B., Armstrong, R.C. and Hassager., O., *Dynamics of Polymeric Liquids, Vol. 1., Fluid Mechanics* (Wiley-Interscience, New York, $2^{nd}$ ed., 1987).

Bird, R.B., Stewart, W.E. and Lightfoot, E.N., *Transport Phenomena* (Wiley, New York, N.Y., 1960).

Biswas, R.R. and Sen, P.N., "Taylor dispersion with absorbing boundaries: A stochastic approach," Physical Review Letters **98,** Issue 16 (2007).

Bodenstein, M., and Wolgast, K., “Reaktionsgeschwindigkeit in strömenden Gasen,” Ztschr. Phys. Chem., **61**, 422 (1908).

Bourne, J.R., and Toor, H.L., “Simple criteria for mixing effects in complex reactions,” *AIChE J.*, **23**, 602 (1977).

Boussinesq, J., "Thorie de l’coulement tourbillant. Mem," Presents par Divers Savant Acad. Sci. Inst. Fr., **23**, 46-50 (1877).

Brenner, H. and Edwards, D.A., *Macrotransport Processes* (Butterworth-Heinemann, Boston, 1993).

Brodkey, R.S., and Lewalle, J., “Reactor selectivity based on first-order closures of the turbulent concentration equations,” *AIChE J.,* **31**, 111. (1985).

Buijse, M.A., "Understanding wormholing mechanisms can improve acid treatments in carbonate formations," SPE Prod. & Facilities,168 (2000).

Buijse, M.A. and Domelen, M.S., "Novel Application of Emulsified Acids to Matrix Stimulation of Heterogeneous Formations", SPE, 65355-PA (2000).

Camacho, J., "Purely global model for Taylor dispersion," PHYSICAL REVIEW E, **48**, 310 (1993).

Carr, J., *Application of Center Manifold Theory (*Springer, Berlin, 1981).

Chakraborty, S. and Balakotaiah, V., "Spatially averaged multi-scale models for chemical reactors," Advances in Chemical Engineering, **30**, 205 (2005).

Chang, F., Qu, Q. and Frenier, W., "A Novel Self-Diverting-Acid Developed for Matrix Stimulation of Carbonate Reservoirs," SPE, 65033 (2001).

Chatwin, P.C., "The approach to normality of the concentration distribution of a solute in a solvent flowing along a straight pipe," J. Fluid Mech. **43**, 321 (1970).

Choquet, C. and Mikelic, A., "Rigorous upscaling of the reactive flow with finite kinetics and under dominant Peclet number", Cont. Mech. and Therm. **21**, 125 (2009).

Christopher, R.H. and Middleman, S., "Power-law flow through a packed tube," I & EC Fundamentals, 4, 422 (1965).

Civan, F., "Scale Effect on Porosity and Permeability:Kinetics, Model, and Correlation," AIChE Journal, 47, 271 (2001).

Corapcioglu, M.Y., *Advances in Porous Media, Vol.3*, (Elsevier, Netherlands, 1996).

Cox, S.M. and Roberts, A.J., "Centre Manifolds of forced dynamical systems", J. Austral. Math. Soc. B **32**, 401 (1991).

Cox, S.M., and Roberts, A.J., "Initial conditions for models of dynamical systems", Physica D **85**, 126 (1995).

Cybulski, A. and Moulijn, J.A., *Structured catalysts and reactor* (CRC Press, 2006).

Daccord, G., "Chemical dissolution of a porous medium by a reactive fluid," Phys Rev Lett, 58, 479–482 (1987).

Daccord, G., Lenormand, R., and Lietard, O., "Chemical dissolution of a porous medium by a reactive fluid-1. model for the "wormholing" phenomenon," Chem. Eng. Sci., 48, 169 (1993a).

Daccord, G., Lenormand, R., and Lietard, O., "Chemical dissolution of a porous medium by a reactive fluid-2. convection vs reaction, behavior diagram," Chem. Eng. Sci., 48, 179 (1993b).

Damköhler, G., “Einflüsse der Strömung, Diffusion und Wärmeüberganges auf die Leistung von Reaktionsöfen. II. Die isotherme, raumbeständige, homogene Reaktion ester Ordnung,” *Z. Elektrochem.*, **43**, 1 (1937).

Danckwerts, P.V., “Continuous Flow Systems: Distribution of Residence Times,” Chem. Engng. Sci., **2**, 1 (1953).

Danckwerts, P.V., “The effect of incomplete mixing on homogeneous reactions”. *Chem. Engng. Sci.*, **8**, 93. (1958).

Dommeti, S.M.S., and Balakotaiah, V., “On the limits of validity of effective dispersion models for bulk reactions,” *Chem. Engng. Sci.*, **55**, 6169 (2000).

Dorfman, K.D. and Brenner, H., "Generalized Taylor-Aris dispersion in spatially periodic microfluidic networks. Chemical reactions," SIAM J. App. Math **63**, 962 (2003).

Dutta, A., and Tarbell, J.M., “Closure models for turbulent reacting flows,” *AIChE J.,* **35**, 2013 (1989).

Economides, M., Hill A, Ehlig-Economides C., *Petroleum Production Systems* (Prentice Hall Inc., 1993).

Economides, M. and Nolte, K., *Reservoir Stimulation* (Wiley, 2000).

Förster, V.T., and Geib, K.H., “Die theorietische Behandlung chemischer Reaktionen in strömenden Systemen,” *Annalen der Physik*, **5**, 250 (1934).

Fox, R.O., “Computation of turbulent reactive flows: first principle macro/micro mixing models using probability density function methods,” *Chem Engng Sci.,* **47,** 2853 (1992).

Fredd, C.N. and Fogler, H.S., "Influence of transport and reaction on wormhole formation in carbonate porous media." AIChE Journal, 44, 1933 (1998).

Fredd, C.N. and Fogler, H.S., "Optimum conditions for wormhole formation in carbonate porous media: Influence of transport and reaction," SPE J., 4, 196 (1999).

Fredrickson., A.G., *Principle and Application of Rheology* (Prentice Hall, Englewood Cliffs, N.J., 1964).

Frick, T., Mostofizadeh, B. and Economides, M., "Analysis of radial core experiments of hydrochloric acid interaction with limestones," Intl. Symposium on Formation Damage Control, SPE 27402 (1994).

Froment, G.F. and Bischoff, K.B., *Chemical Reactor Analysis and Design* (John Wiley and Sons, New York, 1990).

Gdanski, R., "A fundamentally new model of acid wormholing in carbonates," European Formation Damage Conf., SPE 54719 ( 1999).

Gill, W.N. and Subramanian, R.S., "On Laminar dispersion for flow through round tubes," J. App. Mech.-Trans. ASME **47,** 975 (1980).

Golfier, F., Zarcone, C., Bazin, B., Lenormand, R., Lasseux, D. and Quintard, M. "On the ability of a darcy-scale model to capture wormhole formation during the dissolution of a porous medium," J. Fluid Mech., 457, 213 (2002).

Golubitsky, M. and Schaeffer, D.G., *Singularities and Groups in Bifurcation Theory* (Springer, Berlin, 1984).

Gomaa, A.M., Mahmoud, M.A. and Nasr-El-Din, H.A., "A Study of Diversion Using Polymer-Based In-Situ Gelled Acids Systems," SPE 132535 (2011).

Gomaa, A.M. and Nasr-El-Din, H.A., "Propagation of Regular HCl Acids in Carbonate Rocks: The Impact of an In-Situ Gelled Acid StageA," SPE 130586 (2010).

Gupta, N. and Balakotaiah, V., "Heat and mass transfer coefficients in catalytic monoliths," Chem. Eng. Science, **56**, 4771 (2001).

Heck, R.M. and Farrauto, R.J., *Catalytic air pollution control: commercial technology* (John Wiley and Sons (WIE), 2009).

Himmelblau, D.M. and Bischoff, K.B., *Process analysis and simulation* (Wiley, NY, 1968).

Hoefner, M. L. and Fogler, H. S., "Fluid-velocity and reaction-rate effects during carbonate acidizing: application of network model," SPE Production Engineering, 56 (1989).

Hoefner, M.L. and Fogler, H.S., "Pore evolution and channel formation during flow and reaction in porous media," AIChE J, 34, 45–54 (1988).

Huang, T., Hill, A. and Schechter, R., "Reaction rate and fluid loss: The key to wormhole initiation and propagation in carbonate acidizing," Intl. Symposium on Oilfeld Chemistry, SPE 37312 (1997).

Huang, T., Zhu, D., and Hill, A., "Prediction of wormhole population density in carbonate matrix acidizing," European Formation Damage Conf., SPE 54723 (1999).

Hung, K.M., Hill, A.D., Sepehrnoori, K., "A mechanistic model of wormhole growth in carbonate matrix acidizing and acid fracturing.," Journal of Petroleum Technology, 40 (1989).

Jeffreys., H., *The Earth* (*Cambridge University Press*, $2^{nd}$ Ed., 1929).

Joshi, S.Y., Harold, M.P. and Balakotaiah, V., "Low-dimensional model for real time simulation of catalytic monoliths," AIChE J., **55**, 1771 (2009a).

Joshi, S.Y., Harold, M.P. and Balakotaiah, V., "On the use of internal mass transfer coefficient in modeling of diffusion and reaction in catalytic monoliths," Chemical Engineering Science., **64**, 4976 (2009b).

Kalia, N. and Balakotaiah, V., "Modeling and analysis of wormhole formation in reactive dissolution in carbonate rocks," Chemical Engineering Science, 62, 919 (2007).

Kalia, N. and Balakotaiah, V., "Effect of medium heterogeneities on reactive dissolution of carbonates," Chemical Engineering Science, 64, 376 (2009).

Kalia, N. and Balakotaiah, V., "Wormholing in perforated completions," SPE, 127347 (2010).

Kays, W.M., Crawford, M.E., and Weigand, B., *Convective heat And mass Transfer (*McGraw-Hill Professional, 2004).

Langmuir, I., “The velocity of reactions in gases moving through heated vessels and the effect of convection and diffusion,” J. Am. Ceram. Soc., **30**, 656 (1908).

Lee, J., Kulla, E., Chauhan, A. and Tripathi, A., "Taylor dispersion in polymerase chain reaction in a microchannel," Phy. Fluids, **20**, Art N 093601 (2008).

Levenspiel, O., *Chemical Reaction Engineering*, Wiley, New York (1999).

Lewis, W.K., "The principles of counter-current extraction," Industrial and Engineering Chemistry, **8,** 825 (1916).

Lewis, W.K., and Whitman, W.G., "Principles of gas absorption," Industrial and Engineering Chemistry, **16,** 1215 (1924).

Li, K.T., and Toor, H.L., “Turbulent reactive mixing with a series-parallel reaction–effect of mixing on yield,” *AIChE J.,* **32**, 1312 (1986).

Liu, X., Ormond, A., Bartko, K., Li, Y. and Ortoleva, P., "A geochemical reaction-transport simulator for matrix acidizing analysis and design," J. Pet. Sci. Eng., 181 (1996).

Lund, K., Fogler, H., and McCune, C., "Acidization. I: The dissolution of dolomite in hydrochloric acid," Chem. Eng. Sci., 28, 691 (1973).

Lund, K., Fogler, H., McCune, C., and Ault, J., "Acidization.2: The dissolution of calcite in hydrochloric acid," Chem. Eng. Sci., 30, 825 (1975).

Lynn, D.L. and Nasr-El-Din, H.A., "A core based comparison of the reaction characteristics of emulsified and in-situ gelled acids in low permeability, high temperature, gas bearing carbonates," SPE, 65386 (2001).

MaGee, J., Buijse, M.A. and Pongratz, R., "Method for effective fluid diversion when performing a matrix acid stimulation in carbonate formation," SPE 37736 (1997).

Mass, C., "A hyperbolic dispersion equation to model the bounds of a contaminated groundwater body," Journal of Hydrology, **226**, 234 (1999).

Mauri, R., "Dispersion, convection, and reaction in porous media," Phys. Fluids A, **3**, 743 (1991).

Maxwell., J.C., Phill. Trans. Roy. Soc., A, **157**, 49 (1867).

Mercer, G.N. and Roberts, A.J., "A Centre Manifold description of contaminant dispersion in channel with varying flow properties," SIAM J. Appl. Math. **50,** 1547 (1990).

Mercer, G.N. and Roberts, A.J., "A complete model of shear dispersion in pipes," Jap. J. Indust. Appl. Math. **11,** 499 (1994).

Meter, D.M. and Bird., R.B., AIChE J., **10,** 878 (1964).

Mikelic, A., Devigne, V. and Van Duijn, C.J., "Rigorous upscaling of the reactive flow through a pore, under dominant Peclet and Damkohler numbers," SIAM J. Math. Anal. **38,** 1262 (2006).

Nasr-El-Din, H.A., Al-Mohammad, A.M., Al-Aamri, A.M. and Al-Fuwaires, O., "Reaction of Gelled Acids With Calcite," SPE, 103979-PA (2008).

Nasr-El-Din, H.A., Chesson, J.B., Cawiezel, K.E. and Devine, C.S., "Field Success in Carbonate Acid Diversion, Utilizing Laboratory Data Generated by Parallel Flow Testing," SPE, 102828 (2006).

Oldroyd., J.G., Proc. Camb. Phil. Soc., **45**, 595 (1049).

Oldroyd., J.G., Proc. Camb. Phil. Soc., **47**, 410 (1950).

Panga, M.K.R., Ziauddin, M. and Balakotaiah, V., "Two-scale continuum model for simulation of wormholes in carbonate acidification," AIChE J., 51, 3231 (2005).

Prandtl, L., "Ueber Flussigkeitsbewegung Bei Sehr Kleiner Reibung. Third International Mathematical Congress, Heidelberg, Germany, 574–584 (1904) [English Translation: "On motion of fluids with little viscosity," NASA-TM-452 (1928)].

Ratnakar, R.R. and Balakotaiah V., "Exact averaging of laminar dispersion," Phy. Fluids., **23**, 023631 (2011a).

.

Ratnakar, R.R., Kalia, N. and Balakotaiah, V., "Carbonate matrix acidizing with gelled acids: An experiment-based modeling study," SPE 154936 (2012).

Ratnakar, R.R., Bhattacharya, M. and Balakotaiah V., "Reduced order models for describing dispersion and reaction in monoliths," Chem. Eng. Sc., **doi:10.1016/ j.ces.2011.09.056** (2011b).

Roberts, A.J., "Boundary conditions for approximate differential equations", J. Austral. Math. Soc. B **34**, 54 (1992).

Rose, B., *HTPPAC0689-116-01*, Halliburton Energy Services (2004).

Schechter, R.S., *Oil Well Stimulation* (New Jersey: Prentice Hall Inc., 1992).

Smith, R., "Entry and exit conditions for flow reactors", IMA J. App. Math. **41**, 1 (1988).

Takeshi, O., "Surface equation of falling film flows with moderate Reynolds number and large but finite Weber number," Phy. Fluids. **11,** 3247 (1999).

Taylor, G.I., "Dispersion of soluble matter in solvent flowing slowly through a tube," Proc. Roy. Soc. Lond. A **219,** 186 (1953).

Taylor, G.I., "The Dispersion of matter in turbulent flow through a pipe," Proc. Roy. Soc. Lond. A **223**, 446 (1954).

Taylor, K.C., and Nasr-El-Din, H.A., "Laboratory Evaluation of In-Situ Gelled Acids for Carbonate Reservoirs," SPE, 87331 (2003).

Tranner, R.I., Trans. Soc. Rheology., **14**, 483 (1970).

Tronconi, E. and Forzatti, P., "Adequacy of lumped parameter models for SCR reactors with monolith structure," AIChE J. **38**, 201 (1992).

Vandenbroeck, C., "Taylor dispersion revisited," Physica A **168,** 677 (1990).

Villermaux, J. “Mixing effects on complex chemical reactions in a stirred tank”, *Rev. Chem. Eng.*, **7** (1), 51 (1991).

Von Karman, T., "Uber laminare und turbulent reibung," J. F. A. M. M., **1,** 233 (1921) [English Translation: "On laminar and turbulent friction," NASA-TM-1092 (1946)].

Wang, Y., Hill, A.D., "Schechter RS. The optimum injection rate for matrix acidizing of carbonate formations," SPE, 26578 (1993).

Watson, G.N., *A Treatise on the Theory of Bessel Functions* (Cambridge University Press, New York, 1995).

Watt, S.D. and Roberts, A.J., "The accurate dynamic modelling of contaminant dispersion in channels," SIAM J. Appl. Math. **55,** 1016 (1995).

Wehner, J.F. and Wilhelm, R.H., "Boundary conditions for flow reactor," Chemical Engineering Science **6**, 89 (1956).

Welton, T.D. and van Domelen, M.S., "High-Viscosity-Yield Acid Systems for High-Temperature Stimulation," SPE-98237 (2008).

Wen, C.Y. and Fan, L.T., *Models for flow systems and chemical reactions* (Marcel Dekker, NY, 1975).

Wesseling, P., *An introduction to multigrid methods* (John Wiley & Sons, 1992).

William, B., Gidley, J., Schechter, RS., *Acidizing Fundamentals* (SPE, Monograph Series, 1979).

Young, W.R. and Jones, S., "Shear dispersion," Phys. Fluids. **3**, 1087 (1991).

Ziauddin M., and Bize, E., "The effect of pore-scale heterogeneities on carbonate stimulation treatments". SPE Middle East Oil & Gas Show and Conference, SPE 104627 (2007).

Zwietering, T.N., “The degree of mixing in continuous flow systems,” *Chem. Eng. Sc.*, **11**, 1 (1959).

# Appendices

# Appendix A: Solution of Local equation in Laminar Dispersion

In this appendix, we solve the local equation given in chapter 3 by equation (3.27) to determine the exact concentration profile of a non-reacting solute in a laminar flow in a tube. We also analyze the first few moments and present the asymptotic behavior at very small and large times.

## A.1 Eigenvalue problem in Cylindrical Coordinate

The eigenvalue problem (EVP) in 2D cylindrical coordinate $(\xi, \theta)$ with no flux boundary condition on the wall is given by

$$\begin{aligned} \mathbb{L}\psi \equiv \nabla_{\perp}^{2}\psi = \frac{1}{\xi}\frac{\partial}{\partial\xi}\left(\xi\frac{\partial\psi}{\partial\xi}\right) + \frac{1}{\xi^{2}}\frac{\partial^{2}\psi}{\partial\theta^{2}} = -\mu\,\psi \text{ in } \Omega \quad , \\ \bigtriangledown\psi\cdot\mathbf{n} = 0 \text{ on } \partial\Omega. \end{aligned} \tag{A.1}$$

The boundary condition can also be written as $\frac{\partial\psi}{\partial\xi} = 0$ @ $\xi$=0,1 and $\psi(\theta + 2\pi) = \psi(\theta)$. Using separation of variables, we write $\psi(\xi,\theta) = \psi_{\xi}(\xi)\ \psi_{\theta}(\theta)$ and multiply the EVP (A.1) by $\frac{\xi^{2}}{\psi(\xi,\theta)}$ that simplify the problem as follows:

$$\begin{aligned} \frac{\xi}{\psi_{\xi}}\frac{\partial}{\partial\xi}\left(\xi\frac{\partial\psi_{\xi}}{\partial\xi}\right) + \mu\,\xi^{2} = -\frac{1}{\psi_{\theta}}\frac{\partial^{2}\psi_{\theta}}{\partial\theta^{2}},\ 0<\xi<1,\ 0<\theta<2\pi \\ \frac{\partial\psi_{\xi}}{\partial\xi} = 0 \quad @ \quad \xi = 0,1 \\ \psi_{\theta}(\theta + 2\pi) = \psi_{\theta}(\theta)\,. \end{aligned} \tag{A.2}$$

We see in equation (A.2) that the L.H.S. is solely function of $\xi$ while R.H.S. is that of $\theta$. Hence Both the L.H.S. and the R.H.S. must be a constant (independent of $\xi$ and $\theta$). From the boundary condition in $\theta$, this constant must be positive and square of

any integer, i.e.,

$$\frac{\xi}{\psi_\xi}\frac{\partial}{\partial\xi}\left(\xi\frac{\partial\psi_\xi}{\partial\xi}\right)+\mu\,\xi^2=-\frac{1}{\psi_\theta}\frac{\partial^2\psi_\theta}{\partial\theta^2}=n^2,\quad n=0,1,2,... \tag{A.3}$$

which gives the normalized $\psi_\theta$ as

$$\psi_{\theta n}=\begin{cases}\psi^s_{\theta n}=\sqrt{2}\,\sin\left(n\theta\right), & n\neq 0\\ \psi^c_{\theta n}=\sqrt{2}\,\cos\left(n\theta\right), & n\neq 0\\ \psi_0=1, & n=0\end{cases}. \tag{A.4}$$

Now, the EVP in $\xi$ can be given by arranging the equation A.3 as follows:

$$\begin{aligned}\xi^2\frac{\partial^2\psi_\xi}{\partial\xi^2}+\xi\frac{\partial\psi_\xi}{\partial\xi}+\left(\mu\,\xi^2-n^2\right)\psi_\xi,\ 0<\xi<1,\\ \frac{\partial\psi_\xi}{\partial\xi}=0\quad @\quad \xi=0,1.\end{aligned} \tag{A.5}$$

The solution of above equation A.5 is given in terms of linear combination of Bessel functions of first and second kind. However, the boundary condition at $\xi=0$ suggests that the coefficient of Bessel function of second kind has to be zero, implying the solution in the form:

$$\psi_\xi(\xi)=A\;J_n\left(\sqrt{\mu}\xi\right), \tag{A.6}$$

where $A$ is a constant and $\mu$ is obtained by using boundary condition at $\xi=1$. From the recurrence formula for Bessel functions (See Watson 1995, §3.2), we know that

$$\begin{aligned}\frac{d}{d\xi}J_n\left(\sqrt{\mu}\xi\right) &= -\sqrt{\mu}J_{n+1}\left(\sqrt{\mu}\xi\right)+\frac{n}{\xi}J_n\left(\sqrt{\mu}\xi\right)\\ &= \sqrt{\mu}J_{n-1}\left(\sqrt{\mu}\xi\right)-\frac{n}{\xi}J_n\left(\sqrt{\mu}\xi\right)\end{aligned} \tag{A.7}$$

$$= \frac{\sqrt{\mu}}{2}\left[J_{n-1}\left(\sqrt{\mu}\xi\right) - \sqrt{\mu}J_{n+1}\left(\sqrt{\mu}\xi\right)\right].$$

Hence, the eigenvalues $\mu_{nm}$ are roots of the following equation

$$J_n'\left(\sqrt{\mu}\right) = -\sqrt{\mu}J_{n+1}\left(\sqrt{\mu}\right) + nJ_n\left(\sqrt{\mu}\xi\right) = \sqrt{\mu}J_{n-1}\left(\sqrt{\mu}\right) - nJ_n\left(\sqrt{\mu}\right) = 0. \quad \text{(A.8)}$$

The constant $A$ is determined by normalizing the eigenfunction $\psi_\xi(\xi)$, i.e.,

$$A^2 \int_0^1 2\xi J_n^2\left(\sqrt{\mu}\xi\right) d\xi^{-1} = 1.$$

From the property of Bessel function (see Watson 1995, §5.11), we can write

$$\int_0^1 2\xi J_n^2\left(\sqrt{\mu}\xi\right) d\xi = \left(1 - \frac{n^2}{\mu}\right) J_n^2\left(\sqrt{\mu}\right) + J_n'^2\left(\sqrt{\mu}\right). \quad \text{(A.9)}$$

But, $J_n'^2\left(\sqrt{\mu}\right) = 0$ (boundary condition at $\xi = 1$), so the normalization constant is given by

$$A^2 = \left[\left(1 - \frac{n^2}{\mu}\right) J_n^2\left(\sqrt{\mu}\right)\right]^{-1}, \text{ or, } A = \frac{1}{\left[\sqrt{\left(1 - \frac{n^2}{\mu}\right)} J_n\left(\sqrt{\mu}\right)\right]}. \quad \text{(A.10)}$$

Hence, the eigenfunction in $\xi$ is given by,

$$\psi_{nm\xi}(\xi) = \frac{J_n\left(\sqrt{\mu_{nm}}\xi\right)}{\sqrt{\left(1 - \frac{n^2}{\mu_{nm}}\right)} J_n\left(\sqrt{\mu_{nm}}\right)}. \quad \text{(A.11)}$$

Thus, the eigenfunctions of transverse operator $\mathbb{L}$ ($= \nabla_{\perp}^2$) is given as follows:

$$\psi_{nm}(\xi,\theta) = \begin{cases} \psi_{nm}^{s} = \sqrt{2}\ \sin(n\theta)\ \frac{J_n\left(\sqrt{\mu_{nm}}\xi\right)}{\sqrt{\left(1-\frac{n^2}{\mu_{nm}}\right)}J_n\left(\sqrt{\mu_{nm}}\right)}, & n \neq 0 \\ \psi_{nm}^{c} = \sqrt{2}\ \cos(n\theta)\ \frac{J_n\left(\sqrt{\mu_{nm}}\xi\right)}{\sqrt{\left(1-\frac{n^2}{\mu_{nm}}\right)}J_n\left(\sqrt{\mu_{nm}}\right)}, & n \neq 0\ , \\ \psi_{m} = \frac{J_0\left(\sqrt{\mu_{0m}}\xi\right)}{J_0\left(\sqrt{\mu_{0m}}\right)}, & n = 0 \end{cases} \tag{A.12}$$

where $\mu_{nm}$ are m$^{th}$ roots of the equation:

$$J_n'(\sqrt{\mu}) = -\sqrt{\mu}J_{n+1}(\sqrt{\mu}) + nJ_n(\sqrt{\mu}) = 0. \tag{B11b}$$

## A.2 Solution of Local Equation

The local equation in case of solute dispersion in a laminar flow is given in chapter 3 by equation (3.27) as follows:

$$\nabla_{\xi,\theta}^2 c' = p\ \left[\frac{\partial c'}{\partial \tau} + u(\xi)\frac{\partial c'}{\partial z} - \left\langle u(\xi), \frac{\partial c'}{\partial z}\right\rangle - \frac{p}{Pe_r^2}\frac{\partial^2 c'}{\partial z^2} + h'(\xi,\theta,z,\tau)\right] \text{ in } \Omega \tag{A.13}$$
$$\bigtriangledown\psi \cdot \mathbf{n} = 0 \text{ on } \partial\Omega,$$

where $\langle c', 1\rangle = 0$ and the source function $h'$ is given by

$$h'(\xi,\theta,z,\tau) = u'(\xi)\frac{\partial \langle c\rangle}{\partial z} - s'(\xi,\theta,z,\tau), \tag{A.14}$$

with $\langle s', 1\rangle = 0$. We take Laplace Transformation of equation (A.13) w.r.t. $t \rightarrow \omega$ and $z \rightarrow \alpha$ and write the equation in Laplace domain as

$$\nabla_{\xi,\theta}^2 \widehat{c'} = p\ \left[\omega\widehat{c'} + u(\xi)\alpha\widehat{c'} - \left\langle u(\xi), \alpha\widehat{c'}\right\rangle - \frac{p}{Pe_r^2}\alpha^2\widehat{c'} + H'(\xi,\theta,\alpha,\omega)\right] \tag{A.15}$$

where, $\widehat{c'}$ and $H'$ are Laplace transform of $c'$ and $h'$, respectively.

It may be seen from the equation (A.15) that $\widehat{c'} = 0$ around base state $p = 0$, Hence $\widehat{c'}$ can be expanded around the base sate using Liapunov-Schmidt expansion as,

$$\widehat{c'} = \sum_{m=1}^{\infty} p^m \, \widehat{c'}_m \tag{A.16}$$

where $\widehat{c'}_m$ are given as

$$\begin{aligned}
\nabla^2_{\xi,\theta} \, \widehat{c'}_1 &= H' \\
\nabla^2_{\xi,\theta} \, \widehat{c'}_2 &= \omega \widehat{c'}_1 + \alpha \left( u\widehat{c'}_1 - \left\langle u, \widehat{c'}_1 \right\rangle \right) \\
\nabla^2_{\xi,\theta} \, \widehat{c'}_{n+1} &= \omega \widehat{c'}_n + \alpha \left( u\widehat{c'}_n - \left\langle u, \widehat{c'}_n \right\rangle \right) - \frac{1}{Pe_r^2} \alpha^2 \widehat{c'}_{n-1} \qquad (n \geq 2)
\end{aligned} \tag{A.17}$$

If we let

$$\widehat{c'}_n = \sum_{j=1}^{n} \omega^{n-j} \; \alpha^{j-1} \; \widehat{c'}_{n,j}, \tag{A.18}$$

then we have,

$$\nabla^2_{\xi,\theta} \, \widehat{c'}_{1,1} = H'(\xi, \theta, \alpha, \omega) \tag{A.19}$$

and

$$\begin{aligned}
&\omega^{n+1-j} \alpha^{j-1} \nabla^2_{\xi,\theta} \, \widehat{c'}_{n+1} \\
&= \omega \sum_{j=1}^{n} \omega^{n-j} \alpha^{j-1} \widehat{c'}_{n,j} + \alpha \sum_{j=1}^{n} \omega^{n-j} \alpha^{j-1} \left( u\widehat{c'}_{n,j} - \left\langle u, \widehat{c'}_{n,j} \right\rangle \right) \\
&\qquad - \frac{\alpha^2}{Pe_r^2} \sum_{j=1}^{n-1} \omega^{n-j} \alpha^{j-1} \widehat{c'}_{n-1,j} \\
&= \sum_{i=1}^{n} \omega^{n+1-i} \alpha^{i-1} \widehat{c'}_{n,i} + \sum_{i=2}^{n+1} \omega^{n+1-i} \alpha^{i-1} \left( u\widehat{c'}_{n,i-1} - \left\langle u, \widehat{c'}_{n,i-1} \right\rangle \right) \\
&\qquad - \frac{1}{Pe_r^2} \sum_{i=3}^{n+1} \omega^{n+1-1} \alpha^{i-1} \widehat{c'}_{n-1,i-2}
\end{aligned} \tag{A.20}$$

$\Rightarrow$

$$\nabla^2_{\xi,\theta}\,\widehat{c'}_{1,1} = H'(\xi,\theta,\alpha,\omega) \tag{A.21}$$

$$\nabla^2_{\xi,\theta}\,\widehat{c'}_{n+1,j} = \widehat{c'}_{n,j} + \left(u\widehat{c'}_{n,j-1} - \left\langle u, \widehat{c'}_{n,j-1}\right\rangle\right) - \frac{1}{Pe_r^2}\widehat{c'}_{n-1,j-2,} \tag{A.22}$$

where $\widehat{c'}_{n,j} = 0\ \forall\ j > n\ \&\ \ j\ < 0$ and $\left\langle \widehat{c'}_{n,j}, 1\right\rangle = 0$. [Remark: It must be noted that all $\widehat{c'}_{i,j}$ are solely function of $\xi$, i.e., independent of $\theta$, because the fluctuation velocity $u'(\xi)$ is independent of $\theta$.]. Thus, the solution of local equation is given by combining and taking inverse Laplace Transform of equations(A.16, A.18 and A.22) that leads to the result as follows:

$$c' = \sum_{n=1}^{\infty} p^n \sum_{j=1}^{n} \frac{\partial^{n-1} c'_{n,j}}{\partial z^{j-1}\,\partial \tau^{n-j}},\ . \tag{A.23}$$

where, $c'_{n,j}$s are given by

$$\nabla^2_{\xi,\theta}\,c'_{1,1} = h'(\xi,\theta,z,\tau) \tag{A.24}$$

$$\nabla^2_{\xi,\theta}\,c'_{n+1,j} = c'_{n,j} + \left(uc'_{n,j-1} - \left\langle u, c'_{n,j-1}\right\rangle\right) - \frac{1}{Pe_r^2}c'_{n-1,j-2,}$$

Thus, the cup-mixing concentration,

$$c_m = \langle c\rangle + \langle u'c'\rangle\,,$$

can be written in Laplace domain as follows:

$$\widehat{c_m} - \widehat{\langle c\rangle} = \sum_{n=1}^{\infty} p^n \sum_{j=1}^{n} \left\langle u', \omega^{n-j}\alpha^{j-1}\,\widehat{c'}_{n,j}\right\rangle = \sum_{n=1}^{\infty} p^n \sum_{j=1}^{n} \left\langle \omega^{n-j}\alpha^{j-1}H', \Lambda_{n,j}\right\rangle, \tag{A.25}$$

where $\Lambda_{n,j}$ are given by

$$\nabla^2_{\xi,\theta}\ \Lambda_{1,1} = u' \tag{A.26}$$

$$\nabla^2_{\xi,\theta}\Lambda_{n+1,j} = \Lambda_{n,j} + (u\Lambda_{n,j-1} - \langle u, \Lambda_{n,j-1}\rangle) - \frac{1}{Pe_r^2}\Lambda_{n-1,j-2}$$

with $\Lambda_{n,j} = 0\ \forall\ j > n\ \&\ \ j\ < 0$ and $\langle \Lambda_{n,j}, 1\rangle = 0$. After taking inverse Laplace Transform, the cup-mixing concentration can be given as follows:

$$c_m - \langle c\rangle = \sum_{n=1}^{\infty} p^n \sum_{j=1}^{n} \left\langle \frac{\partial^{n-1} h'}{\partial z^{j-1}\ \partial \tau^{n-j}},\ \Lambda_{n,j} \right\rangle. \tag{A.27}$$

Thus, by using the equation (A.14), the cup-mixing concentration $c_m$ is given by

$$c_m - \langle c\rangle = \sum_{n=1}^{\infty} p^n \sum_{j=1}^{n} \langle u',\ \Lambda_{n,j}\rangle \frac{\partial^n \langle c\rangle}{\partial z^j\ \partial \tau^{n-j}} - \sum_{n=1}^{\infty} p^n \sum_{j=1}^{n} \left\langle \frac{\partial^{n-1} s'}{\partial z^{j-1}\ \partial \tau^{n-j}},\ \Lambda_{n,j} \right\rangle \tag{A.28}$$

## A.3 Moment Analysis

The coarse grained model for the classical Taylor dispersion problem in an infinitely long tube with initial release $\zeta(\xi, \theta, x^*)$ is obtained in chapter 3 from equation (3.69) as follows:

$$\frac{\partial \langle c\rangle}{\partial t^*} + Pe_r \frac{\partial \langle c\rangle}{\partial x^*} + Pe_r^2 \sum_{n=1}^{\infty}\sum_{j=1}^{n} \langle u',\ \Gamma_{n,j}\rangle \frac{\partial^{n+1} \langle c\rangle}{\partial x^{*j+1}\ \partial t^{*n-j}} - \frac{\partial^2 \langle c\rangle}{\partial x^{*2}} - \langle \zeta\rangle\, \delta(t^*)$$
$$- Pe_r \sum_{n=1}^{\infty}\sum_{j=1}^{n} \left\langle \frac{\partial^j \zeta'}{\partial x^{*j}},\ \Gamma_{n,j} \right\rangle \delta^{n-j}(t^*) = 0, \tag{A.29}$$

where $\Gamma_{n+1,\ j}$ are given by equations (3.67, 3.68). Now, using the following definition of 2-D spatial moments,

$$m_j(t^*) = \frac{1}{A_\Omega} \int_{-\infty}^{\infty}\int_{0}^{2\pi}\int_{0}^{1} x^{*j}\xi\ c(\xi, \theta, x^*, t^*)\ d\xi\ d\theta\ dx^* = \int_{-\infty}^{\infty} x^{*j}\ \langle c\rangle\,(x^*, t^*)\ dx^* \tag{A.30}$$

with the following relations,

$$\int_{-\infty}^{\infty} x^{*j} \frac{\partial^i \langle c \rangle}{\partial x^{*i}} dx^* = \begin{cases} (-1)^i \prod_{n=1}^{i} (j-n+1) m_{j-i} & if\ j \geq i \\ 0 & if\ j < i \end{cases}, \tag{A.31}$$

$$\zeta_j(\xi, \theta) = \int_{-\infty}^{\infty} x^{*j}\ \zeta(\xi, \theta, x^*)\ dx^*, \qquad \left\langle \zeta_j \right\rangle = \left\langle \zeta_j(\xi, \theta), \psi_0 \right\rangle \tag{A.32}$$

and the properties of distributional derivative of Dirac-delta function,

$$\int_{-\infty}^{\infty} f(x^*) \delta^r (x^* - x_0^*) dx^* = (-1)^r \frac{\partial^r f}{\partial x^{*r}}|_{x^*=x_0^*}, \tag{A.33}$$

the equation for $k^{th}$ moment can be written as follows:

$$\begin{aligned} &\frac{dm_k}{dt^*} - k\ Pe_r\ m_{k-1} - k(k-1)\ m_{k-2} - \langle \zeta_k \rangle\ \delta(t^*) \\ &\quad + Pe_r^2 \sum_{n=1}^{\infty} \sum_{j=1}^{n} \langle u',\ \Gamma_{n,j} \rangle \frac{\partial^{n-j} m_{k-j-1}}{\partial t^{*n-j}} (-1)^{j+1} \prod_{i=1}^{j+1} (k-i+1) \\ &\quad - Pe_r \sum_{n=1}^{\infty} \sum_{j=1}^{n} \left\langle \zeta'_{k-j},\ \Gamma_{n,j} \right\rangle\ \delta^{n-j}(t^*)\ (-1)^j \prod_{i=1}^{j} (k-i+1) = 0. \end{aligned} \tag{A.34}$$

This equation can be used to obtain the spatial moments sequentially. We can also write the moment equation in the Laplace domain ($m_k(t^*) \rightarrow M_k(\omega)$) as follows:

$$\begin{aligned} \omega M_k = &\ k\ Pe_r\ M_{k-1} + k(k-1)\ M_{k-2} + \langle \zeta_k \rangle \\ &- Pe_r^2 \sum_{n=1}^{\infty} \sum_{j=1}^{n} \langle u',\ \Gamma_{n,j} \rangle\, \omega^{n-j} M_{k-j-1} (-1)^{j+1} \prod_{i=1}^{j+1} (k-i+1) \\ &+ Pe_r \sum_{n=1}^{\infty} \sum_{j=1}^{n} \left\langle \zeta'_{k-j},\ \Gamma_{n,j} \right\rangle\ \omega^{n-j}\ (-1)^j \prod_{i=1}^{j} (k-i+1). \end{aligned} \tag{A.35}$$

If we assume

$$Y_{n,j} = \omega^{n-j}\ \Gamma_{n,j} \qquad \text{and} \quad Y_j = \sum_{n=1}^{\infty} Y_{n,j} = \sum_{n=1}^{\infty} \Gamma_{n,j}\omega^{n-j}, \tag{A.36}$$

then $Y_j = 0\ \forall\ j \leq 0$, and by definition of $\Gamma_{n,j}$, we can write

$$\begin{aligned}
\mathbb{L}\ Y_1 &= u'(\xi) + \omega Y_1, \\
\mathbb{L}\ Y_2 &= \omega Y_2 + Pe_r\left(u(\xi)\ Y_1 - \langle u(\xi),\ Y_1\rangle\right), \\
\mathbb{L}\ Y_j &= \omega Y_j + Pe_r\left(u(\xi)\ Y_{j-1} - \langle u(\xi),\ Y_{j-1}\rangle\right) - Y_{j-2}, \qquad j \geq 3
\end{aligned} \tag{A.37}$$

and express the solution as

$$\begin{aligned}
Y_1 &= -\sum_m \frac{\langle u', \psi_m\rangle}{\mu_m + \omega}\psi_m \\
Y_2 &= -Pe_r \sum_m \frac{\langle u\ Y_1, \psi_m\rangle}{\mu_m + \omega}\psi_m = Pe_r \sum_m \sum_n \frac{\langle u', \psi_n\rangle}{\mu_n + \omega}\frac{\langle u\ \psi_n, \psi_m\rangle}{\mu_m + \omega}\psi_m \\
Y_j &= -\sum_m \frac{\langle Pe_r\ u\ Y_{j-1} - Y_{j-2}, \psi_m\rangle}{\mu_m + \omega}\psi_m, \qquad \forall\ \ j \geq 3
\end{aligned} \tag{A.38}$$

where $\psi_m$ are eigenfunction of transverse Laplacian operator corresponding to non-zero eigenvalues $\mu_m$.

[Remarks: Since $\Gamma_{n,j}$ are solely function of $\xi$, i.e., independent of $\theta$, so $Y_{n,j}$ and $Y_j$. Hence eigenfunctions $\psi_m$ are given as

$$\psi_m = \psi_{0m} = \frac{J_0\left(\sqrt{\mu_{0m}}\xi\right)}{J_0\left(\sqrt{\mu_{0m}}\right)}, \tag{A.39}$$

where $J_0\left(\sqrt{\mu_{0m}}\xi\right)$ is the zeroth order bessel function and $\mu_m\ (= \mu_{0m})$ are the zeroes of the equation

$$J_0'\left(\sqrt{\mu_m}\right) = \sqrt{\mu_m} J_1\left(\sqrt{\mu_m}\right) = 0, \tag{A.40}$$

because other eigenfunctions contain sine and cosine functions which leads to zero after taking inner product with the function that are independent of $\theta$ such as $u'(\xi)$ or $u'(\xi)Y_j(\xi)$. Now, using relations (A.36), we can further simplify the moment equation (A.35) in the Laplace domain as follows:

$$\omega M_k = k\ Pe_r\ M_{k-1} + k(k-1)\ M_{k-2} + Pe_r^2 \sum_{j=1}^{k-1} (-1)^j\ \frac{k!}{(k-j-1)!}\ \langle u',\ Y_j \rangle\ M_{k-j-1}$$
$$+ \langle \zeta_k \rangle\ +\ Pe_r \sum_{j=1}^{k} (-1)^j \frac{k!}{(k-j)!}\ \left\langle \zeta'_{k-j},\ Y_j \right\rangle\ . \tag{A.41}$$

### A.3.1 Zeroth Moment

The zeroth moment ($k = 0$) given by,

$$\omega M_0 = \langle \zeta_0 \rangle \Longrightarrow M_0 = \frac{\langle \zeta_0 \rangle}{\omega} \Longrightarrow m_0(t^*) = \langle \zeta_0 \rangle \tag{A.42}$$

For the case of unit amount of solute released, $\langle \zeta_0 \rangle = 1,$

$$m_0(t^*) = 1. \tag{A.43}$$

### A.3.2 First Moment

From equation (A.41), the first moment may be expressed as

$$\omega M_1 = Pe_r\ M_0 + \langle \zeta_1 \rangle -\ Pe_r \langle\ \zeta'_0, Y_1 \rangle\, . \tag{A.44}$$

Using the relation (A.38) for $Y_1$ we get,

$$M_1 = Pe_r\ \frac{\langle \zeta_0 \rangle}{\omega^2} + \frac{\langle \zeta_1 \rangle}{\omega} +\ Pe_r \sum_m \frac{\langle u', \psi_m \rangle \langle\ \zeta'_0, \psi_m \rangle}{\omega(\mu_m + \omega)}, \tag{A.45}$$

which after inverting the Laplace transform, gives,

$$m_1(t^*) = \langle \zeta_1 \rangle + Pe_r \ \langle \zeta_0 \rangle \ t^* + \ Pe_r \sum_m \frac{\langle u', \psi_m \rangle \langle \ \zeta_0', \psi_m \rangle}{\mu_m} \left(1 - e^{-\mu_m t^*} \ \right). \quad \text{(A.46)}$$

For the case of $\langle \zeta_0 \rangle = 1$ and $\langle \zeta_1 \rangle = 0$ (unit amount of solute released with zero first moment or symmetrically placed around $x^* = 0$), the first moment can be written as,

$$m_1(t^*) = Pe_r \ t^* + \ Pe_r \sum_m \frac{\langle u', \psi_m \rangle \langle \ \zeta_0', \psi_m \rangle}{\mu_m} \left(1 - e^{-\mu_m t^*} \ \right). \quad \text{(A.47)}$$

For the case of cross-sectionally uniform release, $\zeta_j'(\xi, \theta) = 0 \ \forall \ j$, the expression for the first moment simplifies to,

$$m_{1,uniform}(t^*) = Pe_r \ t^*. \quad \text{(A.48)}$$

For $t^* \to \infty$ (the long time approximation), $e^{-\mu_m t^*} \ \to 0$, and the fist moment becomes

$$\begin{aligned} m_{1,long}(t^*) &= Pe_r \ t^* + \ Pe_r \sum_m \frac{\langle u', \psi_m \rangle \langle \ \zeta_0', \psi_m \rangle}{\mu_m} \\ &= Pe_r \ t^* - \ Pe_r \langle \ \zeta_0', \Gamma_{11} \rangle \, , \end{aligned} \quad \text{(A.49)}$$

where, $\Gamma_{11} = -\sum_m \frac{\langle u', \psi_m \rangle, \psi_m}{\mu_m} = -\frac{1}{24} \left(2 - 6\xi^2 + 3\xi^4\right)$.

For the case of short time ($t^* \to 0$), the first moment can be written by using the series expansion of $e^{-\mu_m t^*}$ as follows:

$$\begin{aligned} m_{1,short}(t^*) &= Pe_r \ t^* + \ Pe_r \sum_m \frac{\langle u', \psi_m \rangle \langle \ \zeta_0', \psi_m \rangle}{\mu_m} \left(\mu_m t^* + O(t^{*2}) \ \right) \\ &= Pe_r \ t^* + \ Pe_r t^* \sum_m \langle u', \psi_m \rangle \langle \ \zeta_0', \psi_m \rangle \, t^* + O(t^{*2}) \\ &= Pe_r \ t^* \left(1 + \langle u', \ \zeta_0' \rangle\right) + O(t^{*2}) \, , \end{aligned}$$

or,

$$m_{1,short}(t^*) = Pe_r \ \langle u,\ \zeta_0 \rangle \, t^* + O(t^{*2}) \ . \tag{A.50}$$

### A.3.3 Second Moment

The second moment is given from equation (A.41) as,

$$\omega M_2 = 2 \ Pe_r \ M_1 + 2 \ M_0 - 2Pe_r^2 \langle \ u', Y_1 \rangle \ \ M_0 + \langle \zeta_2 \rangle - 2Pe_r \langle \ \zeta_1',\ Y_1 \rangle + \ 2Pe_r \langle \ \zeta_0',\ Y_2 \rangle \, . \tag{A.51}$$

Using the relation (A.38) for $Y_1$ and $Y_2$, we get

$$\begin{aligned} M_2 \ = \ & 2 \ Pe_r \ \left( Pe_r \ \frac{\langle \zeta_0 \rangle}{\omega^3} + \frac{\langle \zeta_1 \rangle}{\omega^2} + \ Pe_r \sum_m \frac{\langle u', \psi_m \rangle \langle \ \zeta_0', \psi_m \rangle}{\omega^2 (\mu_m + \omega)} \right) \\ & + 2 \ \frac{\langle \zeta_0 \rangle}{\omega^2} + 2Pe_r^2 \ \langle \zeta_0 \rangle \sum_m \frac{\langle u', \psi_m \rangle^2}{\omega^2 (\mu_m + \omega)} \\ & + \frac{\langle \zeta_2 \rangle}{\omega} + 2Pe_r \sum_m \frac{\langle u', \psi_m \rangle \langle \ \zeta_1', \psi_m \rangle}{\omega (\mu_m + \omega)} + \\ & 2Pe_r^2 \ \sum_m \sum_n \frac{\langle u', \psi_n \rangle \langle u \ \psi_n, \psi_m \rangle \langle \ \zeta_0', \psi_m \rangle}{\omega \ (\mu_n + \omega) \ (\mu_m + \omega)}, \end{aligned} \tag{A.52}$$

which after inverting the Laplace Transform, gives

$$\begin{aligned} m_2(t^*) \ = \ & \langle \zeta_2 \rangle + 2 \left( \langle \zeta_0 \rangle + \ Pe_r \ \langle \zeta_1 \rangle \right) t^* + Pe_r^2 \ \ \langle \zeta_0 \rangle \ t^{*2} \\ & + 2Pe_r \sum_m \frac{\langle u', \psi_m \rangle \langle \ \zeta_1', \psi_m \rangle}{\mu_m} \left( 1 - e^{-\mu_m t^*} \ \right) \\ & + 2Pe_r^2 \sum_m \frac{\langle u', \psi_m \rangle \langle \ \zeta_0' + \langle \zeta_0 \rangle \, u', \psi_m \rangle}{\mu_m} \left( t^* - \frac{1 - e^{-\mu_m t^*}}{\mu_m} \right) \\ & + 2Pe_r^2 \ \sum_m \frac{\langle u', \psi_m \rangle \langle u \ \psi_m, \psi_m \rangle \langle \ \zeta_0', \psi_m \rangle}{\mu_m} \left( \frac{1 - e^{-\mu_m t^*}}{\mu_m} - t^* e^{-\mu_m t^*} \right) \\ & + 2Pe_r^2 \ \sum_m \sum_{n \neq m} \frac{\langle u', \psi_n \rangle \langle u \ \psi_n, \psi_m \rangle \langle \ \zeta_0', \psi_m \rangle}{(\mu_n - \mu_m)} \left( \frac{1 - e^{-\mu_m t^*}}{\mu_m} - \frac{1 - e^{-\mu_n t^*}}{\mu_n} \right) . \end{aligned} \tag{A.53}$$

The last term in equation (A.53) can also be written in form as

$$2Pe_r^2 \sum_m \left\{ \sum_{n \neq m} \frac{\langle\, u\, \psi_n, \psi_m \rangle}{(\mu_n - \mu_m)} \left( \langle u', \psi_n \rangle \langle \zeta_0', \psi_m \rangle + \langle u', \psi_m \rangle \langle\, \zeta_0', \psi_n \rangle \right) \right\} \left( \frac{1 - e^{-\mu_m t^*}}{\mu_m} \right).$$

Hence, the variance $\sigma^2 = m_2 - m_1^2$, can be calculated from equations(A.46) and (A.53) as

$$\begin{aligned}
\sigma^2(t^*) &= \langle \zeta_2 \rangle + 2 \left( \langle \zeta_0 \rangle + Pe_r \langle \zeta_1 \rangle \right) t^* + Pe_r^2 \ \langle \zeta_0 \rangle \ t^{*2} \\
&+ 2Pe_r \sum_m \frac{\langle u', \psi_m \rangle \langle\, \zeta_1', \psi_m \rangle}{\mu_m} \left( 1 - e^{-\mu_m t^*} \right) \\
&+ 2Pe_r^2 \sum_m \frac{\langle u', \psi_m \rangle \langle\, \zeta_0' + \langle \zeta_0 \rangle\, u', \psi_m \rangle}{\mu_m} \left( t^* - \frac{1 - e^{-\mu_m t^*}}{\mu_m} \right) \\
&+ 2Pe_r^2 \sum_m \frac{\langle u', \psi_m \rangle \langle u\, \psi_m, \psi_m \rangle \langle\, \zeta_0', \psi_m \rangle}{\mu_m} \left( \frac{1 - e^{-\mu_m t^*}}{\mu_m} - t^* e^{-\mu_m t^*} \right) \\
&+ 2Pe_r^2 \sum_m \sum_{n \neq m} \frac{\langle u', \psi_n \rangle \langle u\, \psi_n, \psi_m \rangle \langle\, \zeta_0', \psi_m \rangle}{(\mu_n - \mu_m)} \left( \frac{1 - e^{-\mu_m t^*}}{\mu_m} - \frac{1 - e^{-\mu_n t^*}}{\mu_n} \right) \\
&- \left( \langle \zeta_1 \rangle + Pe_r \ \langle \zeta_0 \rangle \ t^* + Pe_r \sum_m \frac{\langle u', \psi_m \rangle \langle\, \zeta_0', \psi_m \rangle}{\mu_m} \left( 1 - e^{-\mu_m t^*} \right) \right)^2 .
\end{aligned} \tag{A.54}$$

For the case of $\langle \zeta_0 \rangle = 1$ and $\langle \zeta_1 \rangle = 0$,variance can be written as,

$$\begin{aligned}
\sigma^2(t^*) &= \langle \zeta_2 \rangle + 2t^* + 2Pe_r \sum_m \frac{\langle u', \psi_m \rangle \langle\, \zeta_1', \psi_m \rangle}{\mu_m} \left( 1 - e^{-\mu_m t^*} \right) \\
&+ 2Pe_r^2 \sum_m \frac{\langle u', \psi_m \rangle \langle\, \zeta_0' + u', \psi_m \rangle}{\mu_m} \left( t^* - \frac{1 - e^{-\mu_m t^*}}{\mu_m} \right) \\
&+ 2Pe_r^2 \sum_m \frac{\langle u', \psi_m \rangle \langle u\, \psi_m, \psi_m \rangle \langle\, \zeta_0', \psi_m \rangle}{\mu_m} \left( \frac{1 - e^{-\mu_m t^*}}{\mu_m} - t^* e^{-\mu_m t^*} \right) \\
&+ 2Pe_r^2 \sum_m \sum_{n \neq m} \frac{\langle u', \psi_n \rangle \langle u\, \psi_n, \psi_m \rangle \langle\, \zeta_0', \psi_m \rangle}{(\mu_n - \mu_m)} \left( \frac{1 - e^{-\mu_m t^*}}{\mu_m} - \frac{1 - e^{-\mu_n t^*}}{\mu_n} \right) \\
&- 2Pe_r^2 \ t^* \sum_m \frac{\langle u', \psi_m \rangle \langle\, \zeta_0', \psi_m \rangle}{\mu_m} \left( 1 - e^{-\mu_m t^*} \right) \\
&- \left( Pe_r \sum_m \frac{\langle u', \psi_m \rangle \langle\, \zeta_0, \psi_m \rangle}{\mu_m} \left( 1 - e^{-\mu_m t^*} \right) \right)^2 .
\end{aligned} \tag{A.55}$$

For the case of uniform release, the second moment is given by

$$\begin{aligned} m_{2,uniform}(t^*) &= \langle\zeta_2\rangle + 2t^* + Pe_r^2\, t^{*2} + 2Pe_r^2 \sum_m \frac{\langle u', \psi_m\rangle^2}{\mu_m}\left(t^* - \frac{1-e^{-\mu_m t^*}}{\mu_m}\right) \\ &= \langle\zeta_2\rangle + 2\left(1 - Pe_r^2\,\langle u', \Gamma_{11}\rangle\ \right) t^* + Pe_r^2 t^{*2} \\ &\quad -2Pe_r^2\,\langle u', \Gamma_{21}\rangle + 2Pe_r^2 \sum_m \frac{\langle u', \psi_m\rangle^2}{\mu_m^2} e^{-\mu_m t^*} \\ &= \langle\zeta_2\rangle + 2\left(1 + \frac{1}{48} Pe_r^2\,\langle\zeta_0\rangle\right) t^* + Pe_r^2\, t^{*2} \\ &\quad -\frac{Pe_r^2}{360} + 2Pe_r^2 \sum_m \frac{\langle u', \psi_m\rangle^2}{\mu_m^2} e^{-\mu_m t^*}, \end{aligned} \tag{A.56}$$

where,

$$\Gamma_{21} = \sum_m \frac{\langle u', \psi_m\rangle^2}{\mu_m^2} = \sum_m \frac{\langle \Gamma_{11}, \psi_m\rangle}{\mu_m} = \frac{1}{1152}(7 - 24\xi^2 + 18\xi^4 - 4\xi^6).$$

For the case of uniform release, the variance is,

$$\begin{aligned} \sigma^2_{uniform}(t^*) &= \langle\zeta_2\rangle + 2\left(1 + \frac{1}{48} Pe_r^2\right) t^* + Pe_r^2\, t^{*2} - \frac{Pe_r^2}{360} \\ &\quad +2Pe_r^2 \sum_m \frac{\langle u', \psi_m\rangle^2}{\mu_m^2} e^{-\mu_m t^*} - Pe_r^2\, t^{*2} \\ &= \langle\zeta_2\rangle - \frac{Pe_r^2}{360} + 2\left(1 + \frac{1}{48} Pe_r^2\right) t^* \\ &\quad +2Pe_r^2 \sum_m \frac{\langle u', \psi_m\rangle^2}{\mu_m^2} e^{-\mu_m t^*}. \end{aligned} \tag{A.57}$$

For $t^* \to \infty$ (the long time approximation), $e^{-\mu_m t^*} \to 0$, and the variance becomes

$$\begin{aligned} \sigma^2_{long}(t^*) &= \langle\zeta_2\rangle + 2t^* + 2Pe_r \sum_m \frac{\langle u', \psi_m\rangle\,\langle\ \zeta_1', \psi_m\rangle}{\mu_m} \\ &\quad +2Pe_r^2 \sum_m \frac{\langle u', \psi_m\rangle\,\langle\ \zeta_0' + u', \psi_m\rangle}{\mu_m}\left(t^* - \frac{1}{\mu_m}\right) \\ &\quad +2Pe_r^2 \sum_m \frac{\langle u', \psi_m\rangle\,\langle u\ \psi_m, \psi_m\rangle\,\langle\ \zeta_0', \psi_m\rangle}{\mu_m}\left(\frac{1}{\mu_m}\right) \end{aligned}$$

$$+2Pe_r^2 \sum_m \sum_{n \neq m} \frac{\langle u', \psi_n \rangle \langle u\, \psi_n, \psi_m \rangle \langle\, \zeta_0', \psi_m \rangle}{(\mu_n - \mu_m)} \left( \frac{1}{\mu_m} - \frac{1}{\mu_n} \right)$$

$$-2Pe_r^2\, t^* \sum_m \frac{\langle u', \psi_m \rangle \langle\, \zeta_0', \psi_m \rangle}{\mu_m} - \left( Pe_r \sum_m \frac{\langle u', \psi_m \rangle \langle\, \zeta_0', \psi_m \rangle}{\mu_m} \right)^2,$$

or,

$$\begin{aligned}
\sigma^2_{long}(t^*) &= \langle \zeta_2 \rangle + 2t^* - 2Pe_r \langle \zeta_1, \Gamma_{11} \rangle - 2Pe_r^2 t^* \ \langle u' + \zeta_0', \Gamma_{11} \rangle - 2Pe_r^2 \langle u' + \zeta_0', \Gamma_{21} \rangle \\
&\quad +2Pe_r \ \langle\, \zeta_0', \Gamma_{22} \rangle + 2Pe_r^2 t^* \langle\, \zeta_0', \Gamma_{11} \rangle - Pe_r^2 \ \langle\, \zeta_0', \Gamma_{11} \rangle^2 \\
&= \langle \zeta_2 \rangle - 2Pe_r^2 \langle u'\, , \Gamma_{21} \rangle + 2 \left( 1 - Pe_r^2 \langle u'\, , \Gamma_{11} \rangle \right) t^* - 2Pe_r^2 \langle \zeta_0', \Gamma_{21} \rangle \\
&\quad -2Pe_r \langle\, \zeta_1', \Gamma_{11} \rangle + 2Pe_r \ \langle\, \zeta_0', \Gamma_{22} \rangle - Pe_r^2 \ \langle\, \zeta_0', \Gamma_{11} \rangle^2 \\
&= \langle \zeta_2 \rangle - \frac{Pe_r^2}{360} + 2 \left( 1 + \frac{1}{48} Pe_r^2 \right) t^* - 2Pe_r^2 \langle \zeta_0, \Gamma_{21} \rangle - 2Pe_r \langle\, \zeta_1, \Gamma_{11} \rangle \\
&\quad +2Pe_r \ \langle\, \zeta_0, \Gamma_{22} \rangle - Pe_r^2 \ \langle\, \zeta_0, \Gamma_{11} \rangle^2,
\end{aligned}$$

or,

$$\begin{aligned}
\sigma^2_{long}(t^*) &= \langle \zeta_2 \rangle + 2 \left( 1 + \frac{1}{48} Pe_r^2 \right) t^* - 2Pe_r \left( \ \langle \zeta_1', \Gamma_{11} \rangle - \langle \zeta_0', \Gamma_{22} \rangle \right) \\
&\quad -Pe_r^2 \left( \frac{1}{360} + 2 \langle\, \zeta_0', \Gamma_{21} \rangle \ \ + \langle\, \zeta_0', \Gamma_{11} \rangle^2 \right),
\end{aligned} \tag{A.58}$$

where,

$$\begin{aligned}
\Gamma_{22} &= Pe_r \sum_m \sum_n \frac{\langle u', \psi_m \rangle \langle u\, \psi_m, \psi_n \rangle, \psi_n}{\mu_m \mu_n} = Pe_r\, \Lambda_{22} \\
&= \frac{Pe_r}{11520} \left( 101 - 420\xi^2 + 480\xi^4 + 240\xi^6 + 45\xi^8 \right).
\end{aligned}$$

For the case of short time ($t^* \rightarrow 0$) the variance can be simplified by using the series expansion of $e^{-\mu_m t^*}$ as follows:

$$\sigma^2_{short}(t^*) = \langle \zeta_2 \rangle + 2t^* + 2Pe_r \sum_m \frac{\langle u', \psi_m \rangle \langle\, \zeta_1', \psi_m \rangle}{\mu_m} \left( \mu_m t^* - \frac{\mu_m^2 t^{*2}}{2} + O(t^{*3}) \right)$$

$$
\begin{aligned}
&+2Pe_r^2 \sum_m \frac{\langle u', \psi_m \rangle \langle\, \zeta_0' + u', \psi_m \rangle}{\mu_m} \left( t^* - t^* + \frac{\mu_m t^{*2}}{2} + O(t^{*3}) \right) \\
&+2Pe_r^2 \sum_m \left[ \begin{array}{c} \frac{\langle u', \psi_m \rangle \langle u\, \psi_m, \psi_m \rangle \langle\, \zeta_0', \psi_m \rangle}{\mu_m} \\ \left( t^* - \frac{\mu_m t^{*2}}{2} - t^* (\, 1 - \mu_m t^*) + O(t^{*3}) \right) \end{array} \right] \\
&+2Pe_r^2 \sum_m \sum_{n \neq m} \left[ \begin{array}{c} \frac{\langle u', \psi_n \rangle \langle u\, \psi_n, \psi_m \rangle \langle\, \zeta_0', \psi_m \rangle}{(\mu_n - \mu_m)} \\ \left( t^* - \frac{\mu_m t^{*2}}{2} - t^* + \frac{\mu_n t^{*2}}{2} + O(t^{*3}) \right) \end{array} \right] \\
&-2Pe_r^2\, t^* \sum_m \frac{\langle u', \psi_m \rangle \langle\, \zeta_0', \psi_m \rangle}{\mu_m} \left( \mu_m t^* - \frac{\mu_m^2 t^{*2}}{2} + O(t^{*3}) \right) \\
&- \left( Pe_r \sum_m \frac{\langle u', \psi_m \rangle \langle\, \zeta_0', \psi_m \rangle}{\mu_m} \left( \mu_m t^* - \frac{\mu_m^2 t^{*2}}{2} + O(t^{*3}) \right) \right)^2 ,
\end{aligned}
$$

or,

$$
\begin{aligned}
\sigma^2_{short}(t^*) \;=\; & \langle \zeta_2 \rangle + 2t^* + 2Pe_r \sum_m \frac{\langle u', \psi_m \rangle \langle\, \zeta_1', \psi_m \rangle}{\mu_m} \left( \mu_m t^* - \frac{\mu_m^2 t^{*2}}{2} + O(t^{*3}) \right) \\
&+2Pe_r^2 \sum_m \frac{\langle u', \psi_m \rangle \langle\, \zeta_0' + u', \psi_m \rangle}{\mu_m} \left( \frac{\mu_m t^{*2}}{2} + O(t^{*3}) \right) \\
&+2Pe_r^2 \sum_m \frac{\langle u', \psi_m \rangle \langle u\, \psi_m, \psi_m \rangle \langle\, \zeta_0', \psi_m \rangle}{\mu_m} \left( \frac{\mu_m t^{*2}}{2} + O(t^{*3}) \right) \\
&+2Pe_r^2 \sum_m \sum_{n \neq m} \frac{\langle u', \psi_n \rangle \langle u\, \psi_n, \psi_m \rangle \langle\, \zeta_0', \psi_m \rangle}{(\mu_n - \mu_m)} \left( -\frac{\mu_m t^{*2}}{2} + \frac{\mu_n t^{*2}}{2} + O(t^{*3}) \right) \\
&-2Pe_r^2\, t^* \sum_m \frac{\langle u', \psi_m \rangle \langle\, \zeta_0', \psi_m \rangle}{\mu_m} \left( \mu_m t^* - \frac{\mu_m^2 t^{*2}}{2} + O(t^{*3}) \right) \\
&-Pe_r^2 t^{*2} \left( \sum_m \langle u', \psi_m \rangle \langle\, \zeta_0', \psi_m \rangle \right)^2 + O(t^{*3})
\end{aligned}
$$

or,

$$
\begin{aligned}
\sigma^2_{short}(t^*) = \langle \zeta_2 \rangle + 2t^* & \left[ 1 + Pe_r \sum_m \langle u', \psi_m \rangle \langle\, \zeta_1', \psi_m \rangle \right] \\
& -Pe_r^2 t^{*2} \sum_m \langle u', \psi_m \rangle \langle \zeta_0' + u', \psi_m \rangle \\
& +Pe_r^2 t^{*2} \sum_m \sum_n \langle u', \psi_n \rangle \langle u\psi_n, \psi_m \rangle \langle \zeta_0', \psi_m \rangle
\end{aligned}
\tag{A.59}
$$

$$-Pe_r t^{*2} \sum_m \langle u', \psi_m \rangle \langle \zeta_1', \psi_m \rangle \mu_m$$
$$-Pe_r^2 t^{*2} \left( \sum_m \langle u', \psi_m \rangle \langle \zeta_0', \psi_m \rangle \right)^2 + O(t^{*3}) \quad ,$$

but

$$\sum_m \sum_n \langle u', \psi_n \rangle \langle u\, \psi_n, \psi_m \rangle \langle\, \zeta_0', \psi_m \rangle = \sum_m \sum_n \langle u', \psi_n \rangle \langle \psi_n, u\psi_m \rangle \langle\, \zeta_0', \psi_m \rangle$$
$$= \sum_m \langle u', u\psi_m \rangle \langle\, \zeta_0', \psi_m \rangle = \sum_m \langle u'u, \psi_m \rangle \langle\, \zeta_0', \psi_m \rangle = \langle\, \zeta_0', u'u \rangle$$

so if we assume $\zeta_1 = 0$, the variance evolves as follows:

$$\begin{aligned}
\sigma^2_{short}(t^*) &= \langle \zeta_2 \rangle + 2t^* + Pe_r^2 t^{*2} \left[ \begin{array}{c} -\langle \zeta_0', u' \rangle + \langle u', u' \rangle \\ +\langle \zeta_0', u'u \rangle - \langle \zeta_0', u' \rangle^2 \end{array} \right] + O(t^{*3}) \\
&= \langle \zeta_2 \rangle + 2t^* + Pe_r^2 t^{*2} \left[ \begin{array}{c} 1 - \langle \zeta_0, u \rangle + \langle \zeta_0, uu \rangle \\ -\langle \zeta_0, u \rangle - \{\langle \zeta_0, u \rangle - 1\}^2 \end{array} \right] + O(t^{*3}) \\
&= \langle \zeta_2 \rangle + 2t^* + Pe_r^2 t^{*2} \left[ \begin{array}{c} 1 - 2\langle \zeta_0, u \rangle + \langle \zeta_0, u^2 \rangle \\ -\langle \zeta_0, u \rangle^2 + 2\langle \zeta_0, u \rangle - 1 \end{array} \right] + O(t^{*3}),
\end{aligned}$$

or,

$$\sigma^2_{short}(t^*) = \langle \zeta_2 \rangle + 2t^* + Pe_r^2 t^{*2} \left[ \langle \zeta_0, u^2 \rangle - \langle\, \zeta_0, u \rangle^2 \right] + O(t^{*3}). \qquad \text{(A.60)}$$

### A.3.4 Third Moment for uniform release

The third moment is given in Laplace domain by equation (A.41) as follows:

$$\omega M_3 = 3\ Pe_r\ M_2 + 6\ M_1 - 6Pe_r^2 \langle\, u', Y_1 \rangle\ M_1 + 6Pe_r^2 \langle\, u',\ Y_2 \rangle M_0 + \langle \zeta_3 \rangle\,, \qquad \text{(A.61)}$$

using relations (A.38-A.40), (A.42,A.43), (A.45) and (A.52) for uniform release, we have,

$$\begin{aligned} M_3 &= 6\ Pe_r^2\ \left(Pe_r\ \frac{\langle\zeta_0\rangle}{\omega^4}+\frac{\langle\zeta_1\rangle}{\omega^3}\right)+6\ Pe_r\ \frac{\langle\zeta_0\rangle}{\omega^3} \\ &+6Pe_r^3\ \sum_m \frac{\langle\zeta_0\rangle\ \langle u',\psi_m\rangle^2}{\omega^3(\mu_m+\omega)}+3\ Pe_r\frac{\langle\zeta_2\rangle}{\omega^2}+6Pe_r\ \frac{\langle\zeta_0\rangle}{\omega^3}+6\frac{\langle\zeta_1\rangle}{\omega^2} \\ &+6Pe_r^2\sum_m \frac{\langle u',\psi_m\rangle^2}{\mu_m+\omega}\ \left(Pe_r\ \frac{\langle\zeta_0\rangle}{\omega^3}+\frac{\langle\zeta_1\rangle}{\omega^2}\right) \\ &+6Pe_r^3\ \sum_m\sum_n \frac{\langle u',\psi_n\rangle\ \langle u\ \psi_n,\psi_m\rangle\ \langle\ u',\psi_m\rangle}{(\mu_n+\omega)\ (\mu_m+\omega)}\frac{\langle\zeta_0\rangle}{\omega^2}+\frac{\langle\zeta_3\rangle}{\omega}. \end{aligned} \tag{A.62}$$

Taking its Laplace inverse, we get the third moment as,

$$\begin{aligned} m_3(t^*) &= \langle\zeta_3\rangle+\langle\zeta_2\rangle\ 3\ Pe_r\ t^*+\langle\zeta_1\rangle \begin{pmatrix} 6t^*+3\ Pe_r^2\ t^{*2}+ \\ 6Pe_r^2\sum_m \frac{\langle u',\psi_m\rangle^2}{\mu_m}\left(t^*-\frac{1-e^{-\mu_m t^*}}{\mu_m}\right) \end{pmatrix} \\ &+\langle\zeta_0\rangle\left[Pe_r^3\ t^{*3}+6\ Pe_r t^{*2}+6Pe_r^3\ \sum_m \frac{\langle u',\psi_m\rangle^2}{\mu_m}\left(t^{*2}-\frac{2t^*}{\mu_m}+\frac{2\left(1-e^{-\mu_m t^*}\right)}{\mu_m^2}\right)\right] \\ &+6Pe_r^3\ \langle\zeta_0\rangle\sum_m \frac{\langle u',\psi_m\rangle^2\ \langle u\ \psi_m,\psi_m\rangle}{\mu_m^2}\left(t^*\left(1+e^{-\mu_m t^*}\right)-\frac{2\left(1-e^{-\mu_m t^*}\right)}{\mu_m}\right) \\ &+6Pe_r^3\ \langle\zeta_0\rangle\sum_m\sum_{n\neq m} \frac{\langle u',\psi_n\rangle\ \langle u\ \psi_n,\psi_m\rangle\ \langle\ u',\psi_m\rangle}{(\mu_n-\mu_m)}\left(\frac{t^*-\frac{1-e^{-\mu_m t^*}}{\mu_m}}{\mu_m}-\frac{t^*-\frac{1-e^{-\mu_n t^*}}{\mu_n}}{\mu_n}\right), \end{aligned} \tag{A.63}$$

the third central moments can be found from the above results. For the case of $\langle\zeta_0\rangle=1$ and $\langle\zeta_1\rangle=0$, the third central moment,

$$\nu_3=m_3-3m_1m_2+2m_1^3,$$

is given as,

$$
\begin{aligned}
\nu_3(t^*) &= \langle\zeta_3\rangle + 6Pe_r^3\ t^* \sum_m \sum_n \frac{\langle u', \psi_n\rangle \langle u'\psi_n, \psi_m\rangle \langle\ u', \psi_m\rangle}{\mu_m\ \mu_n} \\
&\quad +6Pe_r^3\ \sum_m \frac{\langle u', \psi_m\rangle^2 \langle u'\ \psi_m, \psi_m\rangle}{\mu_m^2} \left(t^*\ e^{-\mu_m t^*}\right) \qquad \text{(A.64)} \\
&\quad -12Pe_r^3\ \sum_m \frac{\langle u', \psi_m\rangle}{\mu_m^2} \left\{ \begin{array}{c} \frac{\langle u', \psi_m\rangle \langle u'\psi_m, \psi_m\rangle}{\mu_m} \\ +\sum_{n\ \neq\ m} \frac{\langle u', \psi_n\rangle \langle u'\ \psi_n, \psi_m\rangle}{(\mu_n - \mu_m)} \end{array} \right\} \left(1 - e^{-\mu_m t^*}\ \right).
\end{aligned}
$$

The long time approximation in this case will be as,

$$
\begin{aligned}
\nu_3(t^*) &= \langle\zeta_3\rangle + 6Pe_r^3\ t^* \sum_m \sum_n \frac{\langle u', \psi_n\rangle \langle u'\psi_n, \psi_m\rangle \langle\ u', \psi_m\rangle}{\mu_m\ \mu_n} \\
&\quad -12Pe_r^3\ \sum_m \frac{\langle u', \psi_m\rangle}{\mu_m^2} \left\{ \begin{array}{c} \frac{\langle u', \psi_m\rangle \langle u'\psi_m, \psi_m\rangle}{\mu_m} \\ +\sum_{n\ \neq\ m} \frac{\langle u', \psi_n\rangle \langle u'\ \psi_n, \psi_m\rangle}{(\mu_n - \mu_m)} \end{array} \right\} \\
&= \langle\zeta_3\rangle - 6Pe_r^3\ t^* \sum_n \frac{\langle u', \psi_n\rangle \langle u'\psi_n, \Gamma_{11}\rangle}{\mu_n} \\
&\quad -12Pe_r^3\ \sum_m \frac{\langle u', \psi_m\rangle}{\mu_m^2} \frac{\langle u', \psi_m\rangle \langle u'\psi_m, \psi_m\rangle}{\mu_m} \\
&\quad -6Pe_r^3\ \sum_m \sum_{n\ \neq\ m} \frac{\langle u', \psi_m\rangle \langle u', \psi_n\rangle \langle u'\ \psi_n, \psi_m\rangle}{(\mu_n - \mu_m)} \left(\frac{1}{\mu_m^2} - \frac{1}{\mu_n^2}\right) \\
&= \langle\zeta_3\rangle - 6Pe_r^3\ t^* \sum_n \frac{\langle u', \psi_n\rangle \left(\ \langle u\psi_n, \Gamma_{11}\rangle - \langle\psi_n, \Gamma_{11}\rangle\right)}{\mu_n} \\
&\quad -12Pe_r^3\ \sum_m \frac{\langle u', \psi_m\rangle}{\mu_m^2} \frac{\langle u', \psi_m\rangle \langle u'\psi_m, \psi_m\rangle}{\mu_m} \\
&\quad -6Pe_r^3\ \sum_m \sum_{n\ \neq\ m} \frac{\langle u', \psi_m\rangle \langle u', \psi_n\rangle \langle u'\ \psi_n, \psi_m\rangle}{\mu_n \mu_m} \left(\frac{1}{\mu_m} + \frac{1}{\mu_n}\right) \\
&= \langle\zeta_3\rangle + 6Pe_r^2\ t^* \left(\langle u', \Gamma_{22}\rangle - Pe_r \langle u'\Gamma_{21}\rangle\ \right) \\
&\quad -6Pe_r^3\ \sum_m \sum_n \frac{\langle u', \psi_m\rangle \langle u', \psi_n\rangle \langle u'\ \psi_n, \psi_m\rangle}{\mu_n \mu_m} \left(\frac{1}{\mu_m} + \frac{1}{\mu_n}\right).
\end{aligned}
$$

But the last term can be simplified as,

$$\sum_m \sum_n \frac{\langle u', \psi_m \rangle \langle u', \psi_n \rangle \langle u' \, \psi_n, \psi_m \rangle}{\mu_n \mu_m} \left( \frac{1}{\mu_m} + \frac{1}{\mu_n} \right)$$

$$= 2 \sum_m \sum_n \frac{\langle u', \psi_m \rangle \langle u', \psi_n \rangle \langle u' \, \psi_n, \psi_m \rangle}{\mu_m \mu_n^2}$$

$$= -2 \sum_n \frac{\langle u', \psi_n \rangle \langle u' \, \psi_n, \Gamma_{11} \rangle}{\mu_n^2} = -2 \sum_p \sum_n \frac{\langle u', \psi_n \rangle \left\langle \psi_p, u' \, \Gamma_{11} \right\rangle \left\langle \psi_n, \psi_p \right\rangle}{\mu_p \mu_n}$$

$$= 2 \sum_p \sum_n \frac{\left\langle \psi_p, u' \, \Gamma_{11} \right\rangle \left\langle \Gamma_{11}, \psi_p \right\rangle}{\mu_p} = -2 \langle u' \Gamma_{11}, \Gamma_{21} \rangle = \frac{17}{53760}.$$

This gives long time behavior of third central moment as follows:

$$\nu_3(t^*) = \langle \zeta_3 \rangle + \frac{Pe_r^3}{480} \left( t^* - \frac{17}{112} \right). \tag{A.65}$$

# Appendix B: Scaling Laws

In this appendix, we use scaling analysis to analyze gel dynamics in a single and dual core set-ups. Here, we estimate the speed and width of gel fronts and reaction fronts in a single core set-up and formulate the amount of flow diversion of acidic solution from high-perm to low-perm cores in a dual core set-up. We also develop scaling criterion for optimum injection rate for stimulation of carbonates using in-situ gelling acids.

## B.1 Gel Dynamics

### B.1.1 Speed of Reaction and Gel Fronts

To analyze the gel dynamics, we consider one-dimensional version of the two-scale continuum model described in previous section, as follows:

$$\varepsilon \frac{\partial c}{\partial t'} + u_0 \frac{\partial c}{\partial x'} = -k_{eff}\, c \quad , \tag{B.1}$$

$$\frac{\partial \varepsilon}{\partial t'} = N_{ac} k_{eff}\, c, \tag{B.2}$$

where $c = \frac{C_f}{C_{f,in}}$ is dimensionless acid concentration; $k_{eff} = a_v \left(k_s^{-1} + k_c^{-1}\right)^{-1}$ is overall reaction rate constant that signifies the effect of mass-transfer and true kinetics on dissolution; and $N_{ac} == \frac{\alpha_c C_{f,in}}{\rho_s}$ is acid capacity number. Here, we neglect the axial dispersion term and assume that the velocity profile is constant. Now, defining the wave coordinates as

$$t^* = t' \text{ and } x^* = x' - u_f\, t', \tag{B.3}$$

we simplify the model using coordinate transform $\left(\frac{\partial}{\partial t'} = \frac{\partial}{\partial t^*} - u_f \frac{\partial}{\partial x^*};\ \text{and}\ \frac{\partial}{\partial x'} = \frac{\partial}{\partial x^*}\right)$, as follows:

$$\varepsilon \frac{\partial c}{\partial t^*} + (u_0 - \varepsilon u_f) \frac{\partial c}{\partial x^*} = -k_{eff}\ c, \tag{B.4}$$

$$\frac{\partial \varepsilon}{\partial t^*} - u_f \frac{\partial \varepsilon}{\partial x^*} = N_{ac} k_{eff}\ c, \tag{B.5}$$

where $u_f$ is the front velocity. Assuming the steady wave propagation, we can further simplify the model by setting $\frac{\partial}{\partial t^*} = 0$, which leads to the model in steady wave coordinates as

$$(u_0 - \varepsilon u_f) \frac{\partial c}{\partial x^*} = -k_{eff}\ c \quad , \tag{B.6}$$

$$u_f \frac{\partial \varepsilon}{\partial x^*} = -N_{ac} k_{eff}\ c. \tag{B.7}$$

Now, we use the steady wave model given by equations (B.6, B.7) to estimate the speed of propagation and width of reaction and gelling fronts in single core set-up. The Reaction front is the zone where reaction occurs or proton concentration falls significantly, while the gel front is the zone where proton concentration corresponds to the pH-range of gel formation.

We can simplify equations (B.6, B.7) to write a single ordinary differential equation (ODE) as

$$\frac{(u_0 - \varepsilon u_f)}{u_f} \frac{\partial c}{\partial \varepsilon} = \frac{1}{N_{ac}}. \tag{B.8}$$

It should be noted that behind the reaction front, the core is dissolved completely, while ahead to front, the core remains undissolved because all the protons are consumed earlier. Thus, we can write the following boundary conditions:

$$\varepsilon = \varepsilon_0,\ c = 0\ @\ x \to \infty\ ;\ \text{and}\ \varepsilon = 1,\ c = 1\ @\ x \to 0. \tag{B.9}$$

From Integration of the equation (B.8 ) from $x \rightarrow 0$ to $x \rightarrow \infty$ with the conditions given in equation (B.9), the front speed can be expressed in terms of acid capacity number, $N_{ac}$, as follows:

$$u_f = \frac{1 - \exp\left(-N_{ac}\right)}{1 - \varepsilon_0 \exp\left(-N_{ac}\right)} u_0 \tag{B.10}$$

that can further be simplified for very small acid capacity ($N_{ac} << 1$) as

$$u_f = \frac{N_{ac}}{1 - \varepsilon_0} u_0. \tag{B.11}$$

It is interesting to note from equation B.10 that the speed of propagation, $u_0$ is independent of concentration profile and rheological and kinetic parameters, and depends only on acid capacity number. Therefore, both reaction and gel fronts propagate with the same speed, $u_f$. Also, the speed of fronts depends linearly on inlet flow rate and is higher for an acid of higher capacity number.

### B.1.2 Width of Reaction and Gel Fronts

It is well known that the width of front depends on strongly on dissolution kinetics. Since mass-transfer coefficient depends on flow profile and molecular diffusion, $D_m \left(= \frac{D_{m0}}{\mu}\right)$ and viscosity depends strongly on $pH$, the dissolution kinetics, $k_{eff}$ is very complex function of proton concentration and is given in terms of Sherwood number, $Sh \left(= \frac{2k_c r_p}{D_m}\right)$, as follows:

$$\frac{1}{k_{eff}} = \frac{1}{a_v}\left(\frac{1}{k_s} + \frac{2r_p}{Sh\ D_{m0}}\mu\right), \tag{B.12}$$

In equation (B.12), all the parameters except viscosity ($\mu$) are almost constant due to dissolution. Since viscosity depends on $pH$, we express the equation (B.6) in terms of $pH$ by setting concentration $c = \frac{10^{-pH}}{C_{in}}$ that leads the equation (B.6) to the

following form:

$$\frac{1}{a_v}\left(\frac{1}{k_s}+\frac{2r_p}{Sh\ D_{m0}}\mu\right)\mathrm{Ln}10\ dpH=\ \frac{dx^*}{(u_0-\varepsilon u_f)}\sim\frac{dx^*}{\exp\left(-N_{ac}\right)u_0}. \tag{B.13}$$

Thus, we can determine the widths of reaction front and gel front by integrating equation (B.13) in appropriate $pH$-range. For example, the width of reaction front, $l_{x,c}$, as follows:

$$l_{x,c}=\frac{u_0\exp\left(-N_{ac}\right)}{a_v}\left(\frac{1}{k_s}+\frac{2r_p}{Sh\ D_{m0}}\left\langle\mu\right\rangle_c\right)\mathrm{Ln}10\ \left\langle\Delta pH_c\right\rangle, \tag{B.14}$$

where $\left\langle\mu\right\rangle_c$ is the average viscosity of reaction front defined over pH-range of reaction-zone, $pH_c$ as

$$\left\langle\mu\right\rangle_c=\frac{1}{\left\langle\Delta pH_c\right\rangle}\int_{pH_c}\mu\ \ dpH. \tag{B.15}$$

Similarly, the width of gel front, $l_{x,gel}$, can be expressed as follows:

$$l_{x,gel}=\frac{u_0\exp\left(-N_{ac}\right)}{a_v}\left(\frac{1}{k_s}+\frac{2r_p}{Sh\ D_{m0}}\left\langle\mu\right\rangle_{gel}\right)\mathrm{Ln}10\ \left\langle\Delta pH_{gel}\right\rangle, \tag{B.16}$$

where $\left\langle\mu\right\rangle_{gel}$ is the average viscosity of gel defined over pH-range of gel formation, $pH_{gel}$ as

$$\left\langle\mu\right\rangle_{gel}=\frac{1}{\left\langle\Delta pH_{gel}\right\rangle}\int_{pH_{gel}}\mu\ \ dpH. \tag{B.17}$$

Thus, in mass-transfer controlled dissolution $(k_c << k_s)$, the ratio of width of these fronts simplifies to

$$\frac{l_{x,gel}}{l_{x,c}}=\frac{\left\langle\mu\right\rangle_{gel}\left\langle\Delta pH_{gel}\right\rangle}{\left\langle\mu\right\rangle_c\left\langle\Delta pH_c\right\rangle} \tag{B.18}$$

that depends strongly on rheological properties. Whereas in kinetically controlled dissolution, the width of these fronts are independent of rheology.

## B.2 Flow Diversion in Dual-core Set-up

We consider dual-core set-up, where $fr$ is the fraction of fluid flowing through low-perm core. The core 1 has lower permeability than core 2. The flow splits in the ratio of overall resistance ($\frac{k}{\mu}$) of these cores. The permeability is almost constant until gel develops but viscosity keep increasing due to gel formation. The speed of front propagation in low-perm core 1 ($u_{f1}$) and high perm core 2 ($u_{f2}$) can be given by

$$u_{f1} = \frac{1-\exp\left(-N_{ac}\right)}{1-\varepsilon_0 \exp\left(-N_{ac}\right)} fr\ u_0; \quad u_{f2} = \frac{1-\exp\left(-N_{ac}\right)}{1-\varepsilon_0 \exp\left(-N_{ac}\right)} \left(1-fr\right)\ u_{0.} \tag{B.19}$$

Here, we write rock properties as

$$K_1 = M_1 K_0; K_2 = M_2 K_0; r_{p1} = \sqrt{M_1} r_{p0}; r_{p2} = \sqrt{M_2} r_{p0}; a_{v1} = \frac{a_{v0}}{\sqrt{M_1}}; a_{v2} = \frac{a_{v0}}{\sqrt{M_2}};$$

which leads to width of gel fronts as

$$\frac{l_{x,gel,1}}{L} = fr\ \alpha_1 \sqrt{M_1}\left(1+\alpha_2\sqrt{M1}\right);\ \frac{l_{x,gel,2}}{L} = \left(1-fr\right)\alpha_1\sqrt{M_2}\left(1+\alpha_2\sqrt{M_2}\right), \tag{B.20}$$

where $\alpha_1$ and $\alpha_2$are given by

$$\alpha_1 = \frac{u_0 \exp\left(-N_{ac}\right) \mathsf{Ln}10\ \left\langle \Delta pH_{gel}\right\rangle}{k_s\ a_{v0}\ L} = \frac{\exp\left(-N_{ac}\right)\mathsf{Ln}10\ \left\langle \Delta pH_{gel}\right\rangle}{Da};$$
$$\alpha_2 = \frac{2k_s\ r_{p0}}{Sh\ D_{m0}} \left\langle \mu \right\rangle_{gel} = \frac{\phi^2}{Sh} \left\langle \mu \right\rangle_{gel}. \tag{B.21}$$

Thus, the flow splitting can be expressed in terms of ratio of overall resistances in both the cores as

$$\frac{fr}{1-fr} \quad = \quad \frac{M_{eff,1}}{M_{eff,2}} = \frac{\left[\frac{\mu_{p0}}{K_1}\left(1-\frac{l_{x,gel,1}}{L}\right)+\frac{\langle\mu\rangle_{gel}}{K_1}\frac{l_{x,gel,1}}{L}\right]^{-1}}{\left[\frac{\mu_{p0}}{K_2}\left(1-\frac{l_{x,gel,2}}{L}\right)+\frac{\langle\mu\rangle_{gel}}{K_2}\frac{l_{x,gel,2}}{L}\right]^{-1}}$$

$$= \frac{M_1}{M_2}\frac{\left[1+\left(\frac{\langle\mu\rangle_{gel}}{\mu_{p0}}-1\right)(1-fr)\,\alpha_1\sqrt{M_2}\left(1+\alpha_2\sqrt{M_2}\right)\right]}{\left[1+\left(\frac{\langle\mu\rangle_{gel}}{\mu_{p0}}-1\right)fr\;\alpha_1\sqrt{M_1}\left(1+\alpha_2\sqrt{M_1}\right)\right]},$$

which can be rewritten as

$$\frac{fr}{1-fr} = \frac{M_1}{M_2}\left(\frac{1+(1-fr)\,\delta_1\sqrt{M_2}\left(1+\delta_2\sqrt{M_2}\right)}{1+fr\;\delta_1\sqrt{M_1}\left(1+\delta_2\sqrt{M_1}\right)}\right), \tag{B.22}$$

where $\delta_1$ and $\delta_2$ are given by

$$\delta_1 = \alpha_1\left(\frac{\langle\mu\rangle_{gel}}{\mu_{p0}}-1\right) = \frac{\exp\left(-N_{ac}\right)\mathsf{Ln}10\;\langle\Delta pH_{gel}\rangle}{Da}\left(\frac{\langle\mu\rangle_{gel}}{\mu_{p0}}-1\right);$$
$$\delta_2 = \alpha_2 = \frac{\phi^2}{Sh}\langle\mu\rangle_{gel}\,. \tag{B.23}$$

It should be noted that equation (B.22) results into a quadratic equation in $fr$. However, there is only one solution feasible (in the range of $0 < fr < 1$). In mass-transfer controlled dissolution ($k_c << k_s$ or $\delta_2 >> 1$), equation (B.22) can further be simplified as

$$\frac{fr}{1-fr} = \frac{M_1}{M_2}\left(\frac{1+(1-fr)\,\delta_1\delta_2 M_2}{1+fr\;\delta_1\delta_2 M_1}\right), \tag{B.24}$$

that leads to a linear equation in the form

$$\frac{fr}{1-fr} = \frac{\delta_1\delta_2 + M_2^{-1}}{\delta_1\delta_2 + M_1^{-1}}. \tag{B.25}$$

It can be seen from equations (B.25) and (B.23) that the flow diversion strongly dependent on rheological parameters. For Newtonian acids, $\langle\mu\rangle_{gel} = \mu_{p0}$, i.e., $\delta_1 = 0$ and hence flow splits into the ratio of permeability of cores, $\frac{M_1}{M_2}$. For the case of in-situ gelling acids, $\delta_1$ and $\delta_2$ can be very large and so the flow diversion, i.e., $fr \to 0.5$ @ $\delta_1\delta_2 \to \infty$. Thus, in-situ gelling acids diverts the flow of protons in least accessible low-perm core leading to more uniform stimulation.

## B.3 Optimum Injection rate

The strong coupling between transport and reaction processes leads to various types of dissolution patterns for a given acid depending on the injection rates. Experiments with Newtonian acids show that for high injection rate, porosity and permeability increase uniformly and slowly that leads to uniform dissolution patterns and require large amount of acids. Similarly at low injection rates, lots face dissolution patterns are formed large amount of acids is required. At the intermediate injection rate, very thin factal type channels are formed that are called wormholes and require least amount of acids. Panga et al. (2005) compared the characteristic length scales in flow and transverse directions to estimate the criterion for optimum injection rate. Here, we use the same procedure to develop a criterion for optimum injection rate for the case of in-situ gelling acids.

In the transverse direction, transverse dispersion and reaction are the dominant processes. So, the transverse length scale can be obtained by solving following diffusion-reaction equation:

$$\varepsilon D'_{eT} \frac{\partial^2 C_f}{\partial y'^2} = k_{eff} C_f. \tag{B.26}$$

that gives the characteristic transverse length scale, $\ell_T$, as

$$\ell_T = \sqrt{\frac{\varepsilon D'_{eT}}{k_{eff}}}. \tag{B.27}$$

Similarly, in the flow direction, convection and reaction are dominant processes. So the axial/longitudinal length scale can be obtained by solving convection-reaction model:

$$\overline{u} \frac{\partial C_f}{\partial x'} = k_{eff} C_f, \tag{B.28}$$

that gives the longitudinal length scale, $\ell_x$, as

$$\ell_x = \frac{\overline{u}}{k_{eff}}. \tag{B.29}$$

Here, $\overline{u}$ is the averaged velocity inside the wormhole which is much greater than the average injection velocity, i.e.,

$$\frac{\overline{u}}{\langle u \rangle} \sim \left(\frac{L_T}{d_w}\right)^2,$$

where $d_w$ is the wormhole diameter and $L_T$ is the length of separation between wormholes in transverse direction. Since, wormholes are formed due to competition between these diffusion-convection-reaction processes, the flow and reaction parameters should be such that the characteristic transverse and longitudinal length scales must be comparable to each other to form a wormhole. In other words, wormholes are formed when $\ell_T \sim \ell_x$, which leads to criteria for optimum injection rate (that corresponds to wormhole formation) as follows:

$$\overline{u} \sim \sqrt{\varepsilon D'_{eT} k_{eff}}. \tag{B.30}$$

In case, where the ratio of wormhole diameter and length of separation is of same order, the optimum injection rate can be given as

$$\langle u \rangle_{opt} \sim \overline{u} \sim \sqrt{\varepsilon D'_{eT} k_{eff}}. \tag{B.31}$$

Here, $k_{eff}$ is the effective rate constant that is disguised by mass-transfer and is given as

$$\frac{1}{k_{eff}} = \left(\frac{1}{k_s} + \frac{1}{k_c}\right)\frac{1}{a_v} = \left(\frac{1}{k_s} + \frac{2r_p \langle \mu \rangle_c}{D_{m0} Sh}\right)\frac{1}{a_v} \tag{B.32}$$

and $D'_{eT}\left(\sim \frac{D_{m0}}{\langle\mu\rangle_c}\right)$ is the effective diffusivity, where $\langle\mu\rangle_c$ is the average viscosity of the fluid in reaction zone. This simplifies the optimum injection rate further as

$$\langle u\rangle_{opt} \sim \sqrt{\frac{\varepsilon D_m k_s a_v}{\langle\mu\rangle_c \left(1+\frac{2k_s r_p \langle\mu\rangle_c}{D_{m0} Sh}\right)}} \sim \sqrt{\frac{\varepsilon D_m k_s a_v}{\langle\mu\rangle_c \left(1+\frac{\phi^2 \langle\mu\rangle_c}{Sh}\right)}}. \tag{B.33}$$

Thus, it can be seen from above equation (B.33) that the optimum injection rate for in-situ gelling acids is smaller as compared to that of Newtonian acids. In particular, in mass-transfer controlled dissolution ($k_c << k_s$), the optimum injection rate for in-situ gelling acids is $\langle\mu\rangle_c$ times smaller than that for Newtonian acids, i.e., $\frac{\langle u\rangle_{opt,Gel}}{\langle u\rangle_{opt,New}} \sim \frac{1}{\langle\mu\rangle_c}$, while in kinetically controlled dissolution ($k_c >> k_s$), the optimum injection rate for in-situ gelling acids is $\sqrt{\langle\mu\rangle_c}$ times smaller than that for Newtonian acids, i.e., $\frac{\langle u\rangle_{opt,Gel}}{\langle u\rangle_{opt,New}} \sim \frac{1}{\sqrt{\langle\mu\rangle_c}}$. In other words, stimulation with in-situ gelling acids should be performed at lower injection rates as compared to stimulation with Newtonian acids.